NUREG/CR-6233, Vol. 3
BMI-2177

Crack Stability in a Representative Piping System Under Combined Inertial and Seismic/Dynamic Displacement-Controlled Stresses

Subtask 1.3 Final Report

Manuscript Completed: April 1997
Date Published: June 1997

Prepared by
P. Scott, R. Olson, G. Wilkowski,
C. Marschall, R. Schmidt

Battelle
505 King Avenue
Columbus, OH 43201

M. Mayfield, NRC Project Manager

Prepared for
Division of Engineering Technology
Office of Nuclear Regulatory Research
U.S. Nuclear Regulatory Commission
Washington, DC 20555-0001
NRC Job Code B5702

ABSTRACT

This report presents the results from Subtask 1.3 of the International Piping Integrity Research Group (IPIRG) program. The objective of Subtask 1.3 is to develop data to assess analysis methodologies for characterizing the fracture behavior of circumferentially cracked pipe in a representative piping system under combined inertial and displacement-controlled stresses. A unique experimental facility was designed and constructed. The piping system evaluated is an expansion loop with over 30 meters of 16-inch diameter Schedule 100 pipe. The experimental facility is equipped with special hardware to ensure system boundary conditions could be appropriately modeled. The test matrix involved one uncracked and five cracked dynamic pipe-system experiments. The uncracked experiment was conducted to evaluate piping system damping and natural frequency characteristics. The cracked-pipe experiments evaluated the fracture behavior, pipe system response, and stability characteristics of five different materials. All cracked-pipe experiments were conducted at PWR conditions. Material characterization efforts provided tensile and fracture toughness properties of the different pipe materials at various strain rates and temperatures. Results from all pipe-system experiments and material characterization efforts are presented. Results of fracture mechanics analyses, dynamic finite element stress analyses, and stability analyses are presented and compared with experimental results.

CONTENTS

CONTENTS

CONTENTS

CONTENTS

LIST OF FIGURES

LIST OF FIGURES
(Continued)

Page

LIST OF FIGURES
(Continued)

Page

LIST OF FIGURES
(Continued)

Page

LIST OF FIGURES
(Continued)

Page

LIST OF FIGURES
(Continued)

Page

LIST OF FIGURES
(Continued)

Page

LIST OF FIGURES
(Continued)

Page

LIST OF FIGURES
(Continued)

Page

LIST OF FIGURES
(Continued)

Page

LIST OF FIGURES
(Continued)

Page

LIST OF FIGURES
(Continued)

Page

LIST OF FIGURES
(Continued)

Page

LIST OF FIGURES
(Continued)

Page

LIST OF FIGURES
(Continued)

LIST OF FIGURES
(Continued)

Page

LIST OF FIGURES
(Continued)

Page

LIST OF TABLES

LIST OF TABLES
(Continued)

LIST OF TABLES
(Continued)

EXECUTIVE SUMMARY

This report presents the results from Subtask 1.3 of the International Piping Integrity Research Group (IPIRG) program. The IPIRG program was an international group program coordinated by the U.S. NRC and conducted at Battelle. The principal objective of the IPIRG program was to evaluate the mechanical behavior of nuclear piping containing flaws and subjected to dynamic loadings. Dynamic loading in this report refers to loading rates comparable to those for high amplitude seismic events.

The design of piping systems in nuclear power plants recognizes the existence of both inertial and displacement-controlled stresses. Uncertainties in the ability to characterize inertial stresses has, in part, led to a prevailing industry design practice that results in inherently stiff piping systems. However, stiff systems are less tolerant of displacement-controlled loads caused by thermal expansion and differential anchor motion. Furthermore, the hardware used to restrict pipe motion in nuclear plants, i.e., pipe hangers, snubbers, pipe whip restraints, etc., makes it difficult to adequately inspect piping systems using non-destructive techniques. As a result, operators and designers are beginning to consider inherently more flexible piping systems. A potential concern with flexible piping systems is the stability of cracks, or crack like defects, which are subjected to high inertial stresses or a combination of inertial and displacement-controlled stresses. Unfortunately, the experimental data base needed to evaluate such an issue was lacking. The vast majority of data on the fracture behavior of piping has been obtained under quasi-static displacement-controlled conditions (Refs. 1-4). There is a limited amount of dynamic data on small diameter pipe. Some of the lessons learned from these small diameter, dynamic pipe experiments were applied during the design of the IPIRG program. However, the small pipe diameters evaluated in these previous experiments always gave failures that occurred under Net-Section-Collapse conditions. Larger diameter dynamic pipe data were needed for which elastic-plastic fracture conditions would predominate. The impetus of the IPIRG program was to fill these voids.

Inertial Stresses - Subtask 1.1

The initial experimental subtasks within the IPIRG program were formulated to investigate the separate effects of both inertial (Subtask 1.1) and displacement-controlled stresses (Subtask 1.2) on flawed piping. The specific objective of Subtask 1.1 was to develop the experimental data necessary to assess the analysis methodologies for characterizing the fracture behavior of circumferentially cracked pipe subjected to inertial stresses. One of the most important observations made from these experiments was that once maximum load was achieved, there were very few additional cycles until the pipe essentially severed into two pieces. The implication is that for seismic applications, the stability of flawed pipe under pure inertial loading should be considered as if the loading conditions are load-controlled (i.e., a primary stress) rather than displacement-controlled (i.e., a secondary stress).

Displacement-Controlled Stresses - Subtask 1.2

The specific objective of Subtask 1.2 was similar to that of Subtask 1.1 except the loading history of interest was displacement-controlled. The experiments conducted as part of Subtask 1.2 expanded the data base developed at such places as Battelle (Ref. 1), DTRC (Ref. 2), NUPEC (Ref. 3), and MPA (Ref. 4) by considering such aspects as loading rate and cyclic loadings under displacement-controlled conditions. The results from this subtask allow comparison of quasi-static with dynamic loading and monotonic loading with cyclic loading interactions during fracture. Specifically it was found that for the carbon steel

evaluated, its ultimate strength and fracture toughness decreased at the dynamic rates, while the dynamic rates produced very little change in the strength or toughness values for the stainless steel evaluated at 288 C (550 F). The loss of strength and toughness for the carbon steel is believed to be related to dynamic-strain-aging for the A106 Grade B material evaluated.

Concerning the effects of cyclic loading, there are two important parameters. The first is the load ratio, i.e., minimum load divided by maximum load, and the second is the increment of plastic displacement between cycles. There was little effect on the fracture behavior for either the carbon or stainless steel evaluated for a minimum cyclic load of zero, i.e., a load ratio (R) of zero. However, for the case of fully reversed (R=-1) loading, there was a significant reduction in the load-carrying capacity and apparent toughness for both the A106 Grade B carbon steel and Type 304 stainless steel pipes. The effects of combined dynamic and cyclic loading were evaluated for these materials, and the fracture resistance was found to be lower than either effect taken separately. The second important parameter for understanding cyclic loading is the spacing or incremental plastic displacement between cycles. The smaller the cyclic displacement, the greater the effect of cyclic loading on lowering the apparent toughness. Under inertial loading, there are few cycles sustained near maximum load, and the cyclic plastic displacement becomes very large. Hence, the detrimental aspects of reverse cyclic loading are inherently mitigated for pure inertial loading.

Combined Stresses - Subtask 1.3

The objective of Subtask 1.3, which is the subject of this report, was to build on what was learned from the two separate effects studies in Subtask 1.1 (Ref. 5) and Subtask 1.2 (Ref. 6) by developing the experimental data necessary to assess the analysis methodologies for characterizing the fracture behavior of circumferentially cracked pipe under combined inertial and displacement-controlled stresses. This effort also built on the work of the joint EPRI/NRC Piping and Fitting Dynamic Reliability Program (Ref. 7), in which the stresses in an uncracked piping system subjected to both inertial and displacement-controlled stresses were assessed. The failure mechanism for the uncracked pipe experiments in the EPRI/NRC program was by ratcheting and eventual fatigue, rather than by fracture as was the case for the Subtask 1.3 cracked pipe experiments.

The piping system evaluated as part of Subtask 1.3 experiments was fabricated with an expansion loop with over 30 meters (100 feet) of 406-mm (16-inch) nominal diameter Schedule 100 pipe and five long radius elbows. Five different materials were evaluated as part of the cracked pipe experiments. These materials were an A106 Grade B carbon steel, a Type 304 stainless steel, a low toughness submerged-arc weld (SAW) for both of these materials, and an artificially aged cast stainless steel. The cracks introduced into the test specimens for the cracked pipe experiments were all relatively large internal circumferential surface cracks. All cracked pipe experiments were conducted at PWR conditions; all specimens contained subcooled water at 288 C (550 F) and at a pressure of 15.5 MPa (2,250 psi).

A unique experimental facility was designed and constructed to conduct these dynamic pipe experiments. The experimental facility is equipped with specially designed hardware to ensure that the pipe system has well-defined boundary conditions that can be adequately modeled. A finite element model of the piping system was analyzed using a commercially available finite element package, ANSYS, to aid in: (1) the design of the facility, (2) the determination of input test parameters for control of each experiment, and (3) the analysis of results.

As a result of the pipe-system experiments and associated material characterization and analysis efforts, several key observations and results, highlighted below, were identified.

Piping System Response

As part of the uncracked experiment, the piping system damping characteristics were evaluated. The experimentally determined damping value for the pipe loop was 0.5 percent. This value is quite low compared with what is assumed for most piping analyses, i.e., 2-3 percent per ASME Section III, Division I, Appendix N and up to 5 percent per ASME Code Case N-411-1. The reason for the low measured damping values lies in the hardware used to enforce the boundary conditions on the pipe system and the use of high strength pipe. The use of spherical bearings, linear bearings, and most importantly, hydrostatic bearings for vertical supports provides very little opportunity for energy to be dissipated as friction. The use of high strength pipe for the loop also minimizes plasticity and related energy absorption.

During the uncracked pipe experiment, the first few natural frequencies and mode shapes were experimentally determined. The first natural frequency of 4.4 Hz was determined in a number of ways, system ring-down, instrumented hammer tests, and actuator driven excitation. This experimentally determined value agreed within 4 percent of the values predicted using the ANSYS finite element code. The agreement between the experimentally determined values and predicted values was not as close for the higher natural frequencies.

Effects of Seismic Loading Rates

The results of the material characterization tests revealed important differences in the behavior of carbon and stainless steels. The two carbon steels evaluated [A106B and a submerged-arc weld] were found to be susceptible to dynamic strain aging. The elevated temperature tensile strength of both materials decreased significantly as the strain rate was increased. The fracture resistance of the carbon steel base metal also decreased at the dynamic strain rates. In addition, at the quasi-static loading rates, the carbon steel base metal exhibited bursts of unstable crack extension between periods of stable tearing. In contrast to the results for the carbon steels, the stainless steels exhibited no pronounced deleterious effects of elevated strain rates.

Results from dynamic pipe-system experiments from this program were compared with results from quasi-static pipe experiments conducted in previous studies. The inherent fracture margin, defined as the ratio of the measured failure stress to the predicted failure stress, was evaluated for each experiment using various predictive methods. For the carbon steel base metal, the calculated margins were significantly lower for the dynamic IPIRG pipe-system experiment than for the companion quasi-static experiment conducted in the Degraded Piping Program. This observation is consistent with the material property data. The results from the material characterization efforts and pipe experiments tend to indicate that it may be prudent to use dynamic properties to evaluate flawed carbon steel piping, especially if the pipe material is suspected of being susceptible to dynamic strain aging.

This finding appears to be somewhat in conflict with the findings of the carbon steel SAW pipe experiment. The carbon steel SAW was the only material that showed higher failure stresses at dynamic rates than at quasi-static rates even though this weld was in the same pipe used in the A106B base metal experiment, which had lower strength at higher strain rates. The fact that this material showed higher failure stresses at dynamic rates is not totally unexpected since the measured toughness of this weld is higher at the seismic loading rates. This may indicate that, perhaps, it is sufficient to use the quasi-static tensile properties to analyze a crack in this type of weld subjected to dynamic loadings. This is substantiated by the finite element results of Brickstad (Ref. 8), who showed by viscoplastic finite element analysis that quasi-static properties were sufficient for analysis since the strain rates were sufficiently low

in the uncracked pipe and most of the ligament. Further efforts may be needed to resolve this issue. The findings for the stainless steel materials are considerably less complex. For the three stainless steels evaluated (TP304, SAW, and CF8M), the results from both the material characterization efforts and pipe experiments indicate that quasi-static strength and toughness data are adequate.

Effects of Load Ratio

The effective load ratio, based on total stress, for the Subtask 1.3 experiments ranged from +0.23 to -0.34. From the stainless steel through-wall cracked pipe results of Subtask 1.2, one would not expect much effect of cyclic loading on the apparent toughness of these materials at these load ratios, especially for the values of the incremental cyclic plastic displacement of interest in these experiments. A similar conclusion was reached from the Subtask 1.1 experiments. Consequently, these experiments should be able to be effectively analyzed using monotonic specimen J-R curve data.

Stability

For the Subtask 1.3 experiments, the number of cycles after maximum load until either a DEGB condition was reached or the applied loadings died out was 10 to 20. This is in sharp contrast to what was observed for the Subtask 1.1 experiments for which there were very few cycles (2 or 3) after maximum load until a double-ended guillotine break (DEGB) occurred. It was concluded that in considering the stability of flawed piping, inertial loading (i.e., Subtask 1.1 experiments) should be considered as load-controlled. Thus, one would expect a relatively quick, but not quite instantaneous, break. For the Subtask 1.3 experiments, with a mixture of inertial and displacement-controlled stresses, one would expect a larger number of cycles between maximum load and a break.

Initially, Net-Section-Collapse predictions for the aged cast stainless steel experiment suggested that if the pressure at the cracked section were maintained at the saturation pressure after the surface crack penetrated the pipe wall, a DEGB would occur once the through-wall crack grew to 63 percent of the pipe circumference. However, in this experiment the through-wall crack grew to a length of 95 percent of the pipe circumference before the DEGB occurred. This discrepancy appears to be due to a restraint of bending moments, possibly provided by pipe-system boundary conditions, by inertial effects, or by the thrust forces caused by the fluid escaping through the through-wall crack. The bending restraint, whatever its source, can be beneficial in that the critical crack lengths due to pressure induced loadings will be greater than predicted by the Net-Section-Collapse analysis when free end boundary conditions are assumed. (Net-Section-Collapse calculations with an assumption of fixed ends provide a much better match to observed behavior.) As a result, if one does not account for this induced bending restraint, the margins on critical through-wall crack length in a pipe system for a leak-before-break analysis may be considerably greater than previously expected. A potential detrimental effect may occur if the pipe rotations, due to the axial (pressure) stresses, are mechanically restrained. For normal operating loads, this restraint would potentially cause a smaller crack opening and associated smaller leakage than may be calculated by current analysis methods. Hence, the leakage rate may be underestimated for LBB analyses.

Both the fully plastic J/T and energy balance stability analyses properly predict the instability behavior of the surface cracks. Superficially, it would also appear that both analyses, using displacement-controlled stress assumptions, did a reasonable job of predicting the stability of the resultant through-wall cracks. This may give some measure of confidence that these quasi-static methods are adequate for piping system stability analyses. However, under closer scrutiny, it appears that the correct predictions may only be fortuitous. Several inconsistencies and limitations were identified with both approaches.

The Accuracy of Elastic Stress Analysis

The accuracy of elastic stress analysis procedures was calculated and expressed as the ratio of either moments or stresses from an elastic analysis to the experimental moments or stresses. The ratios on total stress for the Subtask 1.3 experiments varied from 0.95 to 1.32. These were close to the ratios reported for the Subtasks 1.1 experiments (Ref. 5). However, these ratios are significantly below the ratios of elastic stress calculations to experimental measurements of 15 to 30 reported in the joint EPRI/NRC Piping and Fitting Dynamic Reliability Program (Ref. 7) in which experiments were performed on uncracked pipe. The order of magnitude difference in these ratios is due to the IPIRG pipe system being intentionally designed to avoid plasticity anywhere except at the cracked section, and the cracks being large enough to keep the pipe loop stresses below yield. The IPIRG system which used low friction supports, was constructed with high strength pipe, except for the cracked test section, and had a thicker elbow at a critical location intentionally to avoid plasticity. Pre- and post-test measurements indicated that the piping system did indeed experience very little plastic deformation during the course of the cracked pipe experiments. On the other hand, the EPRI/NRC systems were constructed of one material and without cracks. As a result, they experienced extensive plastic deformation during the course of those experiments. Hence, the margins associated with the IPIRG pipe-system experiments should be considered as severe lower bounds for the type of crack and materials evaluated. In a prototypical piping system for which extensive plasticity will occur, the ratios of calculated to measured stresses, when using linear elastic stress analysis, will be much greater.

The Accuracy of Fracture Analyses

The various fracture analyses used in this study were also assessed for their accuracy by comparing their predictions with experimental measurements. In this case, however, the ratios taken were of failure loads measured experimentally to failure loads predicted by analysis.

- For the Net-Section-Collapse analysis, the ratio of the experimental bending stress plus calculated axial stress to the predicted bending stress plus calculated axial stress was calculated. In all but one case, the ratios were the lowest of all such ratios calculated. In the exceptional case, the failure was not a limit-load failure and required an elastic-plastic analysis.

- The Dimensionless Plastic-Zone Screening Criterion is one of the simplest means of modifying the Net-Section-Collapse analysis for elastic-plastic corrections. With the exception of the three dynamic IPIRG base metal experiments, the analysis produced reasonably accurate predictions of the load-carrying capacity of the cracked pipe segments. For the three exceptions, the predicted bending stresses were greater than the corresponding bending stresses inferred from the experimental measurements.

- The ASME Section XI flaw evaluation procedures for ferritic piping (IWB-3650) using the Code values of S_m had the highest ratios of experimental bending stress plus calculated axial stress to calculated bending stress plus calculated axial stress. The ratios associated with the austenitic criterion (IWB-3640) tended to be much lower. In fact, the IPIRG dynamic pipe-system experiments with cracks in the Type 304 stainless steel base metal and the artificially aged cast stainless steel base metal both had ratios less than one (calculated bending stresses less than the experimental stresses). It is also of note that for the quasi-static pipe experiments, the calculated bending stresses were greater than the experimental stresses.

Consequently, the existing quasi-static pipe fracture data base used to verify IWB-3640 may not be sufficient. It may be appropriate to reconsider this criterion in light of the new IPIRG dynamic data.

When the actual properties of the materials are used to determine S_m, instead of using Code published values, the ratios of experimental to calculated bending stresses decrease significantly. This implies that for an austenitic pipe with Code minimum properties, the ratios may be significantly below one.

Finally, for both the ferritic and stainless steel weld IPIRG experiments, the ratio of the measured bending plus axial to the calculated bending plus axial stresses were above one. This may be partially due to the fact that the height of the weld crown was ignored in determining the flaw-depth-to-wall-thickness ratio during the analysis of these experiments. The weld crown increases the remaining ligament and tends to add some conservatism if it is ignored. For surface crack evaluations, it is recommended that the weld crown not be considered in determining the flaw-depth-to-wall-thickness ratio for the fracture analysis. The fact that the experimental-to-analytical ratio is greater than one for both weld experiments also may be partially explained by the fact that the weld strength is higher than the base metal strength. Base metal strength properties are used in these ASME Section XI flaw evaluation procedures.

- The ratio of experimental bending stress plus calculated axial stress to calculated bending stress plus axial stress was also calculated using the R6 Option 1 analysis procedure. In all cases, the calculated bending stress was less than the experimentally determined bending stress. The values ranged from 1.14 to 1.88.

- The SC.TNP J-estimation scheme tended to have the best agreement with the experimental data with the exception of the dynamic IPIRG carbon steel base metal experiment. This may be an artifact of using quasi-static material property data to analyze this experiment which involved a material highly susceptible to dynamic strain aging effects.

Finite Element Dynamic Analysis

The dynamic analysis of the few Subtask 1.3 pipe-system and Subtask 1.1 inertial experiments considered showed that using the simple nonlinear spring analysis gives good predictions of the dynamic fracture behavior up to maximum load. This was true as long as the nonlinear spring was properly calibrated by use of the SC.TNP J-estimation scheme.

J-Values Directly Calculated from Pipe-System Experiments

The J values at crack initiation for the three stainless steel pipe-system experiments were calculated using an η-factor approach. It was found that the stainless steel base metal has an initiation toughness determined from the pipe experiment that is only 76 percent of the quasi-static C(T) specimen value and 46 percent of the dynamic C(T) specimen value. When this lower J_i value from the pipe test was used in the Dimensionless Plastic Zone Screening Criterion, the stainless steel pipe test agreed much better with the rest of the Degraded Piping Program and IPIRG data. The results from this experiment agreed very poorly with the rest of the data when C(T) specimen J_i values were used in the analysis. Calculations showed that the J_i value from the stainless steel weld pipe test was significantly higher than the J_i values from the C(T)

specimen tests. The J_i values from the aged cast stainless steel pipe-system experiment agreed well with the C(T) specimen data.

References

1. Wilkowski, G. M., and others, "Degraded Piping Program - Phase II," Summary of Technical Results and Their Significance to Leak-Before-Break and In-Service Flaw Acceptance Criteria, March 1984-January 1989, by Battelle Columbus Division, NUREG/CR-4082, Vol. 8, March 1989.

2. Vassilaros, M. G., and others, "J-Integral Testing Instability Analyses for 8-inch Diameter ASTM A106 Steel Pipe," David Taylor Research Center, NUREG/CR-3740, April 1984.

3. Asada, Y., "Verification Test Program on Integrity of Carbon Steel Piping in LWR Plants," Proceedings of the Seminar on LEAK-BEFORE-BREAK: Progress in Regulatory Policies and Supporting Research, NUREG/CR-0092, pp 83-112, March 1988.

4. Sturm, D., Stoppler, W., Hippelein, K. W., Julisch, P., Muz, J., and Schiedermaier, J., Research Programme "Phenomenological Vessel Burst Experiments," 150 279, Final Report Phase I, Staatliche Materialpruefungsanstalt, University of Stuttgart, July 1985.

5. Scott, P., and others, "Subtask 1.1 Final Report - Stability of Cracked Pipe under Inertial Stresses," NUREG/CR-6233, Vol. 1, August 1994.

6. Vieth, P., and others, "Subtask 1.2 Final Report - Stability of Cracked Pipe Under Seismic/Dynamic Displacement-Controlled Stresses," NUREG/CR-6233, Vol. 2, No. 1, April 1997.

7. Tang, H. T., Duffey, R. B., Sing, A., and Bausch, P., "Experimental Investigation of High Energy Pipe Leak and Rupture Phenomena," ASME Special Publication PVP Volume 98-8, *Fracture, Fatigue and Advanced Mechanics*, 1985.

8. Brickstad, B., Swiss-Swedish Analysis Program: "Numerical Analysis of IPIRG Cracked Pipe Experiments with use of Nonlinear Fracture Mechanics," AB Statens Anläggningsprovning Report No. SA/Fou-RAPPORT, May 1989.

ACKNOWLEDGMENTS

The IPIRG program is an international group program being coordinated by the U.S. Nuclear Regulatory Commission's Materials Engineering Branch of the Office of Nuclear Regulatory Research under Contract No. NRC-04-86-106 to Battelle. Mr. M. Mayfield is the NRC program manager. Dr. R. Schmidt is the Battelle program manager.

The members of the IPIRG program and their representatives to the IPIRG Technical Advisory Group (TAG) are:

Canada	
- AECB[a]	Dr. Ali Omar[b] and Dr. B. Jarman
- Ontario Hydro	Mr. M. Kozluk
France	
- CEA[a]	Mr. Ph. Jamet[b]
- EDF	Mr. C. Faidy
- Framatome	Dr. S. Bhandari
Italy	
- ENEA[a]	Dr. P. Milella[b]
Japan	
- CRIEPI[a,c]	Dr. K. Kashima[b]
Republic of China	
- AIT[a]	Mr. Y. H. Cheng[b], Taiwan Power Co.
- ROC-AEC	Mr. R. Y. Wu
- INER	Dr. K. Ting
Sweden	
- SKi[a]	Dr. B. Brickstad[b], AB Statens Anläggningsprovning
Switzerland	
- HSK[a]	Mr. H. Njo[b]
- Kernkraftwerk Leibstadt	Dr. D. Burns

(a) Contractual organization.
(b) TAG representative.
(c) Other Japanese members include, Mitsubishi, Toshiba, Hitachi, IHI, and 13 electric utilities.

United Kingdom
- Nuclear Electric[a] Dr. B. J. Darlaston[b]

United States
- U. S. NRC-RES[a] Mr. M. Mayfield[b]
- U. S. NRC-NRR Mr. K. Wichman[b]
- EPRI[a] Mr. J. Gilman[b]

We would like to express our appreciation for the support and interest of the IPIRG members in this program.

A special note of appreciation is extended to Dr. C. Maricchiolo (ENEA, Italy) who, as a visiting scientist to Battelle, worked diligently to reduce much of the raw data acquired on these experiments.

Researchers and technicians at Battelle who also contributed to this work are: N. Frey, R. Gertler, N. Ghadiali, D. Hayes, P. Held, J. Kramer, P. Krishnaswamy, M. Landow, J. Meyer, J. Morris, M. Oliver, D. Rider, M. Rosenfield, J. Ryan, D. Shoemaker, P. Vieth, M. Wilson, and J. Wood. Quality assurance review was provided by E. Fromm, B. White, and D. Lozier. The important contributions of B. Saffell, who managed the IPIRG program when this work began, are also recognized. We would also like to acknowledge the assistance of Mrs. B. Blanton and Mrs. Verna Kreachbaum in coordinating this report.

Additional thanks go to C. Baxley, J. Anthony, R. Chaffin, T. Goodrich, and the rest of the Battelle machine shop for their diligence and efforts in all that was asked of them.

(a) Contractual organization.
(b) TAG representative.

NOMENCLATURE

1. SYMBOLS

a_e	Plastic-zone size connection to half crack length in GE/EPRI method
A	Parameter in Z-factor expression in IWB-3650
A_{ff}	Maximum amplitude of sinusoidal displacement for Subtask 1.3 forcing function
A_p	Cross-sectional area of pipe
A_{ps}	Area under M-ϕ curve or energy of pipe system
A_{sc}	Area under M-ϕ_c curve for surface crack
b	Half of the pipe circumference (πR)
b_{ff}	Subtask 1.3 forcing function parameter
c	Half crack length
c_{ff}	Subtask 1.3 forcing function parameter
C	Statistically-based parameter from plastic-zone-size screening criteria
C_s	Test system compliance
d	Crack depth
d_{CB}	Depth of weld counterbore
D	Pipe diameter
D_i	Inside pipe diameter
D_o	Outside pipe diameter
E	Elastic modulus
f_g	Correction factor for pipe size and flaw size for moment rotation curve
f_t	Correction factor for temperature for moment rotation curves
F	Applied load
F_b	Bending stress elastic function

F_i	Percent inertial loading
F_j	Parameter in J/T stability analysis which is a function of crack size
F_m	Membrane stress elastic function
F_s	Percent static loading
F_{slide}	Limiting force in spring-slider element
F_{T1}, F_{T2}, F_{T3}	Forces used in modeling multilinear crack behavior
G	Modulus of rigidity
h_{crown}	Weld crown height
h_1	Function in EPRI/GE J-estimation scheme to calculate plastic contribution of J
I	Area moment of inertia
J	J-integral fracture parameter
$J_{applied}$	Applied crack-driving force in terms of J
J_D	J based on deformation theory
J_e	Elastic component of J
J_i	J at crack initiation
J_{Ic}	Plane strain J at crack initiation by ASTM E813
J_m	Modified form of J
J_p	Plastic component of J
J_{total}	Total J applied, i.e., J_e plus J_p
k	Stiffness
k_{sc}	Stiffness of surface-cracked pipe
k_{tw}	Stiffness of through-wall-cracked pipe
K	LEFM stress intensity factor fracture parameter
K_I	Applied linear elastic stress intensity factor
K_{Ib}	Bending component of K_I

K_{Im}	Membrane component of K_I
K_r	Ratio of K_I to $K_r(a)$ from R6 analysis
$K_r(a)$	Toughness of the material as a function of crack growth in terms of K
l	Inner span length of pipe in four-point bend test
L	Outer span length of pipe in four-point-bend test
L_r	Load ratio in R6 analysis
M	Moment
M_a	Moment arm length in four-point bend test
M( )	Net-section-collapse moment for a given set of parameters
M'	Moment from moment-rotation curve corrected for differences in temperature, flaw size, and pipe size
M_b	Net-section-collapse analysis calculated moment at failure for pure bending
M_{b+p}	Net-section-collapse analysis calculated moment at failure for combined pressure and bending
M_{eq}	Equivalent bending moment
M_{exp}	Experimental moment
M_i	Moment at crack initiation
$M_{inertial}$	Inertial moment
M_{NSC}	Net-Section-Collapse moment
M_{pred}	Predicted moment
M_s	Static moment
$M_{(SAM\ el.)}$	Elastically calculated seismic anchor motion moment
$M_{(SP\ el.)}$	Moment from static push analysis
$M_{(SP\ exp.)}$	Moment from static push experiment
$M_{(Tot\ el)}$	Calculated elastic moment at crack section at time of maximum moment from the experiment

$M_{(Tot\ exp)}$	Experimental maximum moment
M_{tw}	Moment for through-wall-cracked pipe
n	Ramberg-Osgood parameter
N_m	Moment normalization parameter
NPS	Nominal pipe size
N_ϕ	Rotation normalization parameter
p	Pressure
P	Total failure stress
P_a	Axial force
P_m	Membrane stress
P_{NSC}	Net-section-collapse predicted tension and bending stress
P_o	Reference stress in J-estimation schemes
P_{sat}	Saturation pressure
R	Stress ratio
R	Pipe radius
R_i	Inside pipe radius
R_m	Mean pipe radius
R_o	Outside pipe radius
S	Total pipe length
S_{ff}	Pipe system forcing function ramp parameter
S_m	ASME Code design stress intensity
S_m(Actual)	S_m based on measured tensile properties
S_m(Code)	S_m based on Code properties
S_r	Stress ratio in R6 analysis
S_u	ASME Section III ultimate strength

S_y	ASME Section III yield strength
t	Time
t	Pipe wall thickness
t_{wall}	Pipe wall thickness
T	Tearing modulus
T*	An integral parameter based on incremental theory of plasticity
$T_{applied}$	Applied tearing modulus
$T_{material}$	Tearing modulus of the material
T_R	Thrust force
U_x, U_y, U_z	Displacements in X, Y, and Z directions
x	Height of CMO measurement device from pipe wall
W	Weight of half the pipe
Z	Stress multipliers in Section XI to account for low toughness flux welds
α	Ramberg-Osgood parameter
β	Angle from bottom of pipe to neutral bending axis
δ_d	Damping logarithmic decrement
Δa	Change in crack length or depth, i.e., crack growth
Δa_{cyclic}	Crack growth due to cyclic loading
Δa_{mono}	Crack growth due to monotonic loading
ΔJ	Change in J
ΔM	Moment reduction factor for adjusting moment-rotation curve
Δ_{xi}	Uncertainty of parameter x
$\dot{\epsilon}$	Strain rate
ε_h	Hoop strain
ε_l	Longitudinal strain

ε_o	Ramberg-Osgood parameter
ε_{45}	Strain from 45-degree gage in rossette
ν	Poisson's ratio
η	Geometric constant used in general analytical procedure where J_p is calculated using experimental load, displacement, and crack growth data
ϕ	Pipe rotation
ϕ_c	Critical kink angle
ϕ_{CI}	Rotation at crack initiation
ϕ_K	Critical crack length angle
ϕ_{CMO}	Pipe rotation due to crack-mouth-opening
ϕ_e^c	Elastic component of the rotation due to the crack
ϕ_p^c	Plastic component of the rotation due to the crack
ϕ_{PL}	Plastic increment of rotation in a cyclic experiment
σ	Stress
σ_b	Bending stress
σ_{bNSC}	Net-section-collapse predicted bending stress
$\sigma_{(expt\ bend\ \sigma)}$	Experimental bending stress at maximum moment
σ_f	Flow stress
σ_h	Hoop stress
σ_l	Longitudinal stress
σ_{NSC}	Net-Section-Collapse stress
σ_o	Ramberg-Osgood parameter
$\sigma_{(SAM\ el.)}$	Seismic anchor motion stresses
σ_t	Axial tensile stress
$\sigma_{t=0}$	Initial stress in piping system due to temperature and pressure only

$\sigma_{(ten)}$	Pressure induced axial tensile stress
$\sigma_{(Tot.\ el.)}$	Total calculated elastic stress; calculated elastic bending stress plus pressure induced axial tension stress
$\sigma_{(Tot.\ el.\ bend\ \sigma)}$	Calculated elastic bending stress from ANSYS calculated moments
$\sigma_{(Tot.\ expt.)}$	Total experimental stress; experimental bending stress plus pressure induced axial tension stress
σ_u	Ultimate strength
σ_{vm}	Von Mises stress
σ_y	Yield strength
σ_1	Maximum principal stress
σ_2	Minimum principal stress
τ	Shear stress
θ	Half crack angle
θ_i	Initial half crack angle
θ_{tot}	Total crack angle
ω	Forcing function frequency in radians/second
ς	Damping ratio (fraction of critical damping)

2. ACRONYMS AND INITIALISMS

AC	Alternating current
ACS	Aged cast stainless
A/D	Analog-to-Digital
AISI	American Iron and Steel Institute
AIT	American Institute of Taiwan
ANL	Argonne National Laboratories
ASME	American Society of Mechanical Engineers

ASTM	American Society for Testing and Materials
AWG	American Wire Gage
BWR	Boiling Water Reactor
CEA	Commissariat A L'Energie Atomique, France
CEGB	Central Electric Generating Board, United Kingdom (currently Nuclear Electric)
CMO	Crack-mouth-opening
CMOD	Crack-mouth-opening displacement
COD	Crack-opening displacement
CRIEPI	Central Research Institute of Electric Power Industry, Japan
CS	Carbon steel
CSW	Carbon steel weld
C(T)	Compact (Tension)
CTOA	Crack-tip-opening angle
D/A	Digital-to-analog
d-c	Direct current
d-c EP	Direct-current electric potential
DEGB	Double-ended guillotine break
DPZP	Dimensionless plastic zone parameter
DTRC	David Taylor Research Center, USA
EDF	Electricité de France
ENEA	dell'Energia Nucleare e delle Energie Alternative, Italy
EP	Electric potential
EPRI	Electric Power Research Institute, USA
ESR	Elastic stress analysis ratio
FFT	Fast Fourier transform

FM	Frequency modulated
GE	General Electric
HSK	Hauptabteilung für die Sicherheit der Kernanlagen, Switzerland
INER	Institute of Nuclear Energy Research, Republic of China
IPIRG	International Piping Integrity Research Group
JAERI	Japanese Atomic Energy Research Institute
J-R	J-resistance (curve)
LBB	Leak-Before-Break
L-C	Orientation that indicates crack plane is normal to longitudinal axis (L) and crack growth direction is circumferential (C)
LVDT	Linear variable differential transformer
MSS	Manufacturers Standardization Society
MTS	Materials Testing Systems (Supplier of servo-hydraulic equipment)
NPS	Nominal pipe size
NRC	Nuclear Regulatory Commission
NRC-NRR	Nuclear Regulatory Commission - Office of Nuclear Reactor Research
NSC	Net-Section-Collapse
PWR	Pressurized Water Reactor
QAP	Quality Assurance Plan
RMS	Root mean square
ROC-AEC	Republic of China - Atomic Energy Commission
RT	Room temperature
RVDT	Rotary-variable-differential transformer
SAM	Seismic anchor motion
SAW	Submerged-arc weld

SC	Surface crack
SKi	Statens Kärnkraftinspektion (Swedish Nuclear Power Inspectorate)
SMAW	Shielded-metal-arc weld
SMTS	Specified minimum tensile strength
SMYS	Specified minimum yield strength
SS	Stainless steel
SSW	Stainless steel weld
STA	Science and Technology Agency, Japan
TAG	Technical Advisory Group
TWC	Through-wall crack
U.S.	United States
U.S. NRC	United States Nuclear Regulatory Commission
VHS	Video home system

GLOSSARY OF TERMS

ASME Section XI Safety Factors - Explicit safety factors incorporated in Section XI of the ASME Code to account for inaccuracies and uncertainties in the analysis procedures. For Normal Conditions a safety factor of 2.77 is incorporated in the Section XI circumferential-cracked-pipe flaw evaluation procedures. For Emergency and Faulted Conditions a safety factor of 1.39 is incorporated in the procedures.

Collapse Load - The maximum load a structure can carry on the basis of a limit analysis assuming that the structure is made of an ideally plastic material. At this load, the deformations of the structure increase without bound.

Crack Closure Marks - Distinctive marks which are evident on the fracture surface which occur when the cracked pipe section unloads. These marks were used to estimate the extent of the through-wall crack at defined times throughout the event.

Crack Initiation - The onset of stable crack extension. For the IPIRG Subtask 1.3 experiments crack initiation was defined as the point where the plot of the electric potential versus crack-mouth-opening displacement deviated from the initial slope.

Crack Stability - A condition where crack growth occurs at a slow rate that corresponds to the loading or displacement rate. In addition, when the crack section is unloaded the crack arrests.

Critical Crack Length - The length of a crack (either axial or circumferential) for which the crack will propagate unstably for a given set of loading conditions.

Cyclic Loads - A condition for which the applied loads and moments increase and then decrease in a periodic manner throughout the event.

Dead-Weight Stresses - The stresses imposed on the piping system due to the weight of the piping, insulation, and other loads permanently imposed on the piping.

Design Stress Intensity Value (Sm) - A strength based material property used for design purposes in the ASME Code. For ferritic steels the value of S_m at any temperature is the lowest of (1) one-third of the specified minimum tensile strength at room temperature, (2) one-third of the tensile strength at temperature, (3) two-thirds of the specified minimum yield strength at room temperature, or (4) two-thirds of the yield strength at temperature. For austenitic steels the value of S_m at any temperature is the lowest of (1) one-third of the specified minimum tensile strength at room temperature, (2) one-third of the tensile strength at temperature, (3) two-thirds of the specified minimum yield strength at room temperature, or (4) 90 percent of the yield strength at temperature. Values of S_m for a given material are defined as a function of temperature in Tables I-1.1 and I-1.2 of Section III, Division 1 Appendices of the 1989 ASME Code.

Displacement-Controlled Instability - A loading condition where an increase in displacements on the structure will start rapid crack growth.

Displacement-Controlled Stresses - Stresses that result from the application of displacements, such as those due to thermal expansion or seismic anchor motion.

Double-Ended Guillotine Break (DEGB) - A condition for which a circumferential through-wall crack propagates around the entire circumference of the pipe such that the cracked pipe section severs into two pieces and the two ends are displaced relative to their pipe axes to allow for full flow from each end.

Dynamic Loading - A condition for which the applied loads are changing rapidly with time. In this program the loading rates are comparable to those in high amplitude seismic events.

Dynamic Analysis - An analysis for which the applied loads are changing rapidly with time.

Dynamic Material Property Data - Material property data (tensile or fracture toughness) from laboratory specimens which were obtained under the conditions of high rate (dynamic) loading.

Dynamic Strain Aging - A phenomenon in which aging occurs simultaneously with straining at certain strain rates and temperatures. It results from the rapid diffusion of minute quantities of nitrogen and/or carbon dissolved in the steel. Dynamic strain aging can produce several effects such as changes in tensile strength and toughness with temperature and/or strain rate changes, and a susceptibility to intermittent crack jumps or instabilities preceded and succeeded by periods of stable crack growth.

Effective R-Ratio - The stress ratio (minimum stress divided by maximum stress) in which the stress includes the axial tensile stress due to internal pressure.

Elastic Analysis - An analysis based on the assumption of a linear relationship between stress and strain.

Emergency and Faulted Conditions - Refers to very low probability postulated incidents whose consequences are such that subsequent plant operation is not required and safe system shutdown is the only consideration.

Expansion Loop - A piping system configuration designed to accommodate the thermal expansion stresses which arise as a result of increasing the temperature of the piping system.

Expansion Stresses - Those stresses resulting from restrained boundary conditions of the piping system.

Experimental Stresses - In this program, the stresses inferred from the experimentally determined strain values.

Failure - A condition for which a component or system is no longer capable of performing its design function. Depending on the context, failure can be defined as either the condition for which the piping system is no longer capable of maintaining internal pressure, or when the pipe experiences a DEGB.

Flow Stress - A material parameter used to describe the tensile properties of a strain-hardening material in terms of an equivalent elastic-plastic material having a yield strength between the yield and ultimate strengths of the material.

Incremental Cyclic Plastic Displacement - The nonrecoverable plastic component of displacement (or rotation) between loading cycles during a cyclic event.

Inertial Stresses - Dynamic stresses that result from the mass of the piping. Inertial stress is the component of total dynamic stress not due to the static displacement of anchor points.

In-Service Flaw Evaluation - The process for determining the significance of flaws found in service, including the comparison the discovered flaws with acceptance criteria, i.e., ASME Section XI Articles IWB-3640 and 3650.

Instability - An event where a crack starts to propagate rapidly.

Instantaneous Break - A condition for which the cracked pipe section severs into two pieces instantaneously, or near instantaneously.

J-Estimation Scheme - A closed-form elastic-plastic analysis, based on the J-Integral fracture parameter, for predicting the moment and rotation response of a cracked pipe.

Leak-Before-Break - For nuclear piping this is generally referred to as a methodology whereby one shows that a crack can be detected by leakage under normal operating conditions and that crack would be stable at normal plus safe shut-down earthquake (SSE) loads. Sometimes also referred to as a condition whereby a surface crack breaks through the pipe thickness and remains stable even if the break-through occurs at emergency or faulted loads.

Level C Service Loads - A classification of loads for evaluating the effect of plant operating loads on the structural integrity of a component for situations which are not anticipated to occur for a sufficient number of times to affect fatigue life and for which large deformations in areas of structural discontinuities are not objectionable. (Used to be referred to by ASME as emergency loading condition.)

Level D Service Loads - A classification of loads for evaluating the effect of plant operating loads on the structural integrity of a component for situations in which gross general deformations, loss of dimensional stability, and damage requiring repair, excluding loss of pressure retaining function, are not objectionable. (Used to be referred to by ASME as faulted loading condition.)

Ligament - The uncracked region of the pipe in the plane of a crack.

Limit-Load Analysis - A special case of plastic analysis in which the material is assumed to be ideally plastic (non-strain hardening). In limit-load analysis, the equilibrium and flow characteristics at the limit state are used to calculate the maximum load.

Limit Load - See collapse load.

Load-Controlled Instability. A loading condition where an increase in load on the structure will start rapid crack growth.

Load-Controlled Stresses - Stresses that result from application of loads, such as internal pressure or the effects of gravity, whose magnitude is not reduced as a result of displacement. Inertial stresses are also frequently considered as load-controlled or primary stresses.

Load Ratio - The minimum load, moment, or stress divided by the maximum load, moment, or stress.

Margin - The difference between an analytical prediction and experimental data.

Margin on Elastic Stress Analysis - The ratio of the analytically predicted moments or stresses from an elastic analysis to the experimentally measured moments or stresses.

Margin on Fracture Analysis - An inherent margin in the fracture analysis defined as the ratio between the experimentally measured moments or stresses at a distinct instant in time (crack initiation or maximum moment) and the analytically predicted moments or stresses from a given fracture criterion (e.g., Net-Section-Collapse and R6).

Membrane Stress - The component of the normal stress which is uniformly distributed and equal to the average value of stress across the thickness of the section under consideration.

Monotonic Loading - A loading condition where the applied loads or displacements continue to increase up to maximum load or moment.

Normal Stress - The component of stress normal to the plane of reference. In the case of Subtask 1.3, the plane of reference is the plane of the circumferential crack.

Normal (Including Upset and Test) Conditions - Includes all design transients expected to occur during the course of system testing and operation, as well as upset conditions anticipated to occur frequently enough so that the system should be designed to accommodate them.

Operating Basis Earthquake (OBE) - An earthquake which could reasonably be expected to affect the plant site during the operating life of the plant considering the regional and local geology and seismology and specific characteristics of the local subsurface material.

Percent Inertial Loading - The ratio of the total moment (inertial plus static) minus the static moment to the total moment expressed as a percentage. The total moment at the crack section at any point in time can be calculated from a dynamic, time-dependent finite element analysis. The static moment at the crack section can be calculated from a static finite element analysis using thermal and pressure loading combined with an actuator displacement equal to the displacement of the actuator at the time of interest in the dynamic simulation.

Percent Static Loading - The ratio of the static moment to the total moment (inertial plus static) expressed as a percentage.

Pipe System Experiment - An experiment in the IPIRG Subtask 1.3 experimental facility.

Plastic Analysis - That method which computes the structural behavior under given loads, considering the plasticity characteristics of the materials, including strain hardening and the stress redistribution occurring in the structure.

Pressure Induced Stresses - The axial stress in the piping system due to the internal pipe pressure.

Primary Stresses - Any normal or shear stress developed by an imposed loading which is necessary to satisfy the laws of equilibrium of external and internal forces and moments. The basic characteristic of a primary stress is that it is not self-limiting.

Quasi-Static Loading - A condition for which the applied loadings are changing very slowly with time.

Quasi-Static Material Property Data - Material property data (tensile and fracture toughness) which were obtained under the conditions of slow rate (quasi-static) loading.

Quasi-Static Pipe Experiment - A pipe experiment for which the applied loads are changing very slowly with time.

R-Ratio - See Load Ratio.

Ratcheting - A progressive incremental inelastic deformation or strain which can occur in a component that is subjected to variations of mechanical stress, thermal stress, or both.

Seismic Anchor Motion (SAM) Stresses - Stresses imposed on the piping system due to the differential motion of piping system supports or anchors.

Safe Shutdown Earthquake (SSE) - An earthquake which is based upon an evaluation of the maximum earthquake potential considering the regional and local geology and seismology and specific characteristics of the local subsurface material. It is that earthquake which produces the maximum vibratory ground motion for which structures, systems, and components important for safety are designed to remain functional.

Secondary Stresses - A normal or shear stress developed by the constraint of adjacent material or by self-constraint of the structure. The basic characteristic of a secondary stress is that it is self-limiting.

Shear Stress - The component of stress tangent to the plane of reference. In the case of Subtask 1.3, the plane of reference is the plane of the crack.

Surface Crack - A crack or crack-like defect which penetrates only one of the pipe surfaces, either internal or external, but not both.

Surface Crack Instability - A condition where a surface crack grows through the remaining ligament in a rapid manner.

Surface Crack Penetration - The instant in time when the internal surface cracks for the Subtask 1.3 experiments penetrated the pipe wall creating a through-wall crack.

Thermal Stress - A self-balancing stress produced by a change in temperature. Thermal stress is developed in a solid body whenever a volume of material is prevented from assuming the size and shape that it normally should under a change in temperature.

Through-Wall Crack - A crack which penetrates both pipe surfaces.

Through-Wall Crack Instability - A condition where a through-wall crack grows around the pipe circumference in a rapid manner.

Thrust Forces - A force acting on the piping system at a through-wall crack as the result of high pressure, high velocity fluid escaping through the cracked pipe.

PREVIOUS REPORTS IN SERIES

Reports from this Program

"Evaluation and Refinement of Leak-Rate Estimation Models," NUREG/CR-5128, BMI-2164, Revision 1, June 1994.

"Loading Rate Effects on Strength and Fracture Toughness of Pipe Steels Used in Task 1 of the IPIRG Program," Topical Report, NUREG/CR-6098, BMI-2175, October 1993.

"Stability of Cracked Pipe Under Inertial Stresses," NUREG/CR-6233, BMI-2177, Volume 1, August 1994.

Reports from IPIRG-2 Program (IPIRG-2 reports were prepared after the conclusion of IPIRG-1, but prior to the IPIRG-2 reports being published)

"Summary of Results from the IPIRG-2 Round-Robin Analyses," NUREG/CR-6337, BMI-2186, January 1996.

"IPIRG-2 Task 1 - Pipe System Experiments With Circumferential Cracks in Straight-Pipe Locations," NUREG/CR-6389, BMI-2187, February 1997.

"The Effect of Cyclic and Dynamic Loads on Carbon Steel Pipe," NUREG/CR-6438, BMI-2188, February 1996.

"Design of the IPIRG-2 Simulated Seismic Forcing Function," NUREG/CR-6439, BMI-2189, February 1996.

"The Effect of Cyclic and Dynamic Loading on the Fracture Resistance of Nuclear Piping Steels," NUREG/CR-6440, BMI-2190, December 1996.

"Deterministic and Probabilistic Evaluations for Uncertainty in Pipe Fracture Parameters in Leak-Before-Break and In-Service Flaw Evaluations," NUREG/CR-6443, BMI-2191, June 1996.

"Fracture Behavior of Circumferentially Surface-Cracked Elbows," NUREG/CR-6444, BMI-2192, December 1996.

"Development of a J-Estimation Scheme for Internal Circumferential and Axial Surface Cracks in Elbows," NUREG/CR-6445, BMI-2193, June 1996.

"Fracture Toughness Evaluations of TP304 Stainless Steel Pipes," NUREG/CR-6446, BMI-2194, February 1997.

"The Second International Piping Integrity Research Group (IPIRG-2) Program - Final Report," NUREG/CR-6452, BMI-2195, May 1997.

Previous Related Documents from NRC's Short Cracks in Piping and Piping Welds Program

"Short Cracks in Piping and Piping Welds," First Semiannual Report, NUREG/CR-4599, BMI-2173, Vol. 1, No. 1, March 1991.

"Short Cracks in Piping and Piping Welds," Second Semiannual Report, NUREG/CR-4599, BMI-2173, Vol. 1, No. 2, April 1992.

"Short Cracks in Piping and Piping Welds," Third Semiannual Report, NUREG/CR-4599, BMI-2173, Vol. 2, No. 1, September 1992.

"Short Cracks in Piping and Piping Welds," Fourth Semiannual Report, NUREG/CR-4599, BMI-2173, Vol. 2, No. 2, February 1993.

"Short Cracks in Piping and Piping Welds," Fifth Semiannual Report, NUREG/CR-4599, BMI-2173, Vol. 3, No. 1, October 1993.

"Short Cracks in Piping and Piping Welds," Sixth Semiannual Report, NUREG/CR-4599, BMI-2173, Vol. 3, No. 2, March 1994.

"Short Cracks in Piping and Piping Welds," Progress Report, NUREG/CR-4599, BMI-2173, Vol. 4, No. 1, April 1995.

"Assessment of Short Through-Wall Circumferential Cracks in Pipes," NUREG/CR-6235, BMI-2178, April 1995.

"Fracture Behavior of Short Circumferential Short-Surface-Cracked Pipe," NUREG/CR-6298, BMI-2183, November 1995.

"Fracture Evaluations of Fusion Line Cracks in Nuclear Pipe Bimetallic Welds," NUREG/CR-6297, BMI-2182, April 1995.

"Effect of Dynamic Strain Aging on the Strength and Toughness of Nuclear Ferritic Piping at LWR Temperatures," NUREG/CR-6226, BMI-2176, October 1994.

"Effects of Toughness Anisotropy and Combined Loading on Fracture Behavior of Ferritic Nuclear Pipe," NUREG/CR-6299, BMI-2184, April 1995.

"Refinement and Evaluation of Crack-Opening Analyses for Circumferential Through-Wall Cracks in Pipes," NUREG/CR-6300, April 1995.

"Probabilistic Pipe Fracture Evaluations for Leak-Rate Detection Applications," NUREG/CR-6004, BMI-2174, April 1995.

"Stainless Steel Submerged Arc Weld Fusion Line Toughness," NUREG/CR-6251, BMI-2180, April 1995.

"Validity Limits in J-Resistance Curve Determination: Volume 1: An Assessment of the J_M Parameter," NUREG/CR-6264, BMI-2181, Vol. 1, February 1995.

"Validity Limits in J-Resistance Curve Determinations: Volume 2: A Computational Approach to Ductile Crack Growth Under Large-Scale Yielding Condition," NUREG/CR-6264, BMI-2181, Vol. 2, February 1995.

Previous Related Documents from NRC's Degraded Piping Program - Phase I Reports

"The Development of a Plan for the Assessment of Degraded Nuclear Piping by Experimentation and Tearing Instability Fracture Mechanics Analysis," NUREG/CR-3142, Vols. 1 and 2, June 1983.

Previous Related Documents from NRC's Degraded Piping Program - Phase II Reports

"Degraded Piping Program - Phase II," Semiannual Report, NUREG/CR-4082, BMI-2120, Vol. 1, Oct. 1984.

"Degraded Piping Program - Phase II," Semiannual Report, NUREG/CR-4082, BMI-2120, Vol. 2, June 1985.

"Degraded Piping Program - Phase II," Semiannual Report, NUREG/CR-4082, BMI-2120, Vol. 3, March 1986.

"Degraded Piping Program - Phase II," Semiannual Report, NUREG/CR-4082, BMI-2120, Vol. 4, July 1986.

"Degraded Piping Program - Phase II," Semiannual Report, NUREG/CR-4082, BMI-2120, Vol. 5, Dec. 1986.

"Degraded Piping Program - Phase II," Semiannual Report, NUREG/CR-4082, BMI-2120, Vol. 6, April 1988.

"Degraded Piping Program - Phase II," Semiannual Report, NUREG/CR-4082, BMI-2120, Vol. 7, March 1989.

"Degraded Piping Program - Phase II," Semiannual Report, NUREG/CR-4082, BMI-2120, Vol. 8, March 1989.

"NRC Leak-Before-Break (LBB.NRC) Analysis Method for Circumferentially Through-Wall Cracked Pipes Under Axial Plus Bending Loads," Topical Report, NUREG/CR-4572, BMI-2134, March 1986.

"Elastic-Plastic Finite Element Analysis of Crack Growth in Large Compact Tension and Circumferentially Through-Wall-Cracked Pipe Specimen--Results of the First Battelle/NRC Analysis Round Robin," Topical Report, NUREG/CR-4573, BMI-2135, September 1986.

"An Experimental and Analytical Assessment of Circumferential Through-Wall Cracked Pipes Under Pure Bending," Topical Report, NUREG/CR-4574, BMI-2136, June 1986.

"Predictions of J-R Curves With Large Crack Growth From Small Specimen Data," Topical Report, NUREG/CR-4575, BMI-2137, September 1986.

"An Assessment of Circumferentially Complex-Cracked Pipe Subjected to Bending," Topical Report, NUREG/CR-4687, BMI-2142, September 1986.

"Analysis of Cracks in Stainless Steel TIG Welds," Topical Report, NUREG/CR-4806, BMI-2144, November 1986.

"Approximate Methods for Fracture Analyses of Through-Wall Cracked Pipes," Topical Report, NUREG/CR-4853, BMI-2145, January 1987.

"Assessment of Design Basis for Load-Carrying Capacity of Weld-Overlay Repair," Topical Report, NUREG/CR-4877, BMI-2150, February 1987.

"Analysis of Experiments on Stainless Steel Flux Welds," Topical Report, NUREG/CR-4878, BMI-2151, February 1987.

"Experimental and Analytical Assessment of Circumferentially Surface-Cracked Pipes Under Bending," Topical Report, NUREG/CR-4872, BMI-2149, April 1987.

Other Related Program Reports

"Validation of Analysis Methods for Assessing Flawed Piping Subjected to Dynamic Loading," NUREG/CR-6234, ANL-94/22, BMI-2178, August 1994.

1.0 INTRODUCTION

This report provides results from Subtask 1.3 of the International Piping Integrity Research Group (IPIRG) program. The IPIRG program was an international group program managed by the U.S. Nuclear Regulatory Commission (U.S. NRC) and funded by a consortium of organizations from nine nations: Canada, France, Italy, Japan, Sweden, Switzerland, Taiwan, the United Kingdom, and the United States.

The objective of the program was to develop data that are needed to verify engineering methods for assessing the integrity of nuclear power plant piping that contains defects. The program encompassed numerous tasks including material characterization studies, updates of a pipe fracture data base, seminars, workshops and a leak-rate investigation that involved experiments, analysis, and computer code development. However, the primary focus of the program was an experimental task designed to investigate the fracture behavior of pipes and piping systems that contain circumferentially oriented cracks and that are subjected to high-rate loading typical of seismic events.

This report provides the results of the experiments and analyses performed to evaluate the behavior of a moderately large diameter piping system, representative of nuclear power plant piping which contains a circumferential flaw and which is subjected to high-rate cyclic loading where the loading rate is typical of seismic events. This work is applicable to evaluations of cracked pipe subjected to seismic or other dynamic loadings, and is considered essential in validating the fracture mechanics analyses used in leak-before-break (LBB) evaluations and in-service flaw assessments.

1.1 Background

There are basically two types of evaluations that make use of pipe fracture analyses -- LBB analyses and analyses of flaws detected during in-service inspections. In LBB analyses, a flaw is assumed to exist at critical locations in the piping system, which generally are the high stress locations. In some countries, the assumed flaw is a surface flaw and its growth due to service loads and environments is predicted. Fracture mechanics analyses are performed to predict the crack sizes and shapes that could lead to a large break in the piping or that could lead to a leak in the piping, given that some specified accident loading occurs. The accident loading most commonly assumed to be the limiting load is a seismic event, although in some cases there are other dynamic loads that are limiting.

Other countries follow the general procedure adopted by the U.S. NRC in its LBB analyses. In that procedure, a through-wall flaw is assumed, where the circumferential length of the flaw is based on predicted normal operating load levels and on the leak detection capability of the particular plant. Pipe fracture analyses are used to estimate the critical crack size under seismic loads. This crack size is then compared with the crack size determined for the normal operating loads to determine the margin against failure. There is a similar analysis performed to determine a margin against failure based on the loading levels for a fixed crack size.

For in-service flaw assessment criteria, the stresses of concern can be either quasi-static (normal and test conditions) or dynamic (emergency or faulted conditions). The flaw evaluation procedures generally involve the assessment of surface cracks, which can have axial, circumferential, or helical orientations. In the U.S., Section XI of the ASME Boiler and Pressure Vessel Code includes procedures to assess flaws in

austenitic (Ref. 1.1) or ferritic piping (Ref. 1.2). Several other countries use different assessment methods including the R6 method (Ref. 1.3).

Regardless of which LBB analysis method or in-service flaw evaluation procedure is used, whether by choice or regulation, verification of its validity and tendency to under- or overpredict critical crack sizes requires data from appropriate experiments. Many flawed-piping research programs have been conducted in the U.S. (Refs. 1.4 to 1.8) and internationally (Refs. 1.9 to 1.13). However, most of these programs involved quasi-static loading of cracked pipe, rather than the dynamic seismic loading that is more realistic for LBB and in-service flaw assessments. The IPIRG program was created to provide data for fracture evaluations of flawed piping and piping systems subjected to high-rate cyclic loading typical of seismic events.

Prior to the start of the IPIRG program, only two research programs had been completed on cracked nuclear pipe at dynamic loading rates. Both programs were funded by the EPRI BWR Owner's group and involved 4-inch diameter Schedule 80 stainless steel pipe tested at room temperature and without internal pressure.

The EPRI program conducted at GE San Jose (Ref. 1.14) involved constant amplitude fully reversed cyclic inertial loading. These were experiments similar to the IPIRG Subtask 1.1 experiments (Ref. 1.15), see Figure 1.1. A conclusion in that report is that "a Net-Section-Collapse criterion can be used as a conservative estimate of the load capacity of flawed pipe sections provided the change in the flaw shape due to (cyclic) crack growth (during the dynamic event) is properly accounted for".

The EPRI program at Battelle (Ref. 1.5), involved dynamic material property tests and dynamic blow-down cracked pipe experiments on TP304 stainless steel at room temperature. The material property tests showed that the wrought TP304 stainless steel had a higher strength and toughness at elevated strain rates. The dynamic blow-down loaded pipe experiments, see Figure 1.2, showed that the compliance from the through-wall cracked pipe and the plasticity at the crack lowered the dynamic blow-down loads so that the loads required to cause the crack to grow by ductile tearing were less than half of the loads predicted from an uncracked pipe dynamic analysis. This is illustrated in Figure 1.3, which shows a series of experiments in which the crack length had to be extended by more than a factor of 5 from the initial crack size, which was selected based on uncracked pipe stress analysis, in order for ductile tearing to start.

The lessons learned from these programs, that were applied in the IPIRG program, were:

A large number of constant amplitude cycles could cause fatigue crack growth which would complicate the analysis of the experiments. To minimize the fatigue crack growth complications in understanding dynamic IPIRG experiments, an increasing amplitude sinusoidal loading history was selected.

Compliance changes due to the presence of a crack, and plasticity at the crack section can change the dynamic loads relative to the loads calculated for an uncracked pipe. To design the IPIRG experiments, it was necessary to account for the effects of the crack on the dynamic response of the pipe. A nonlinear cracked-pipe element was conceived in the Degraded Piping program (Ref. 1.16) and implemented in the IPIRG design analysis.

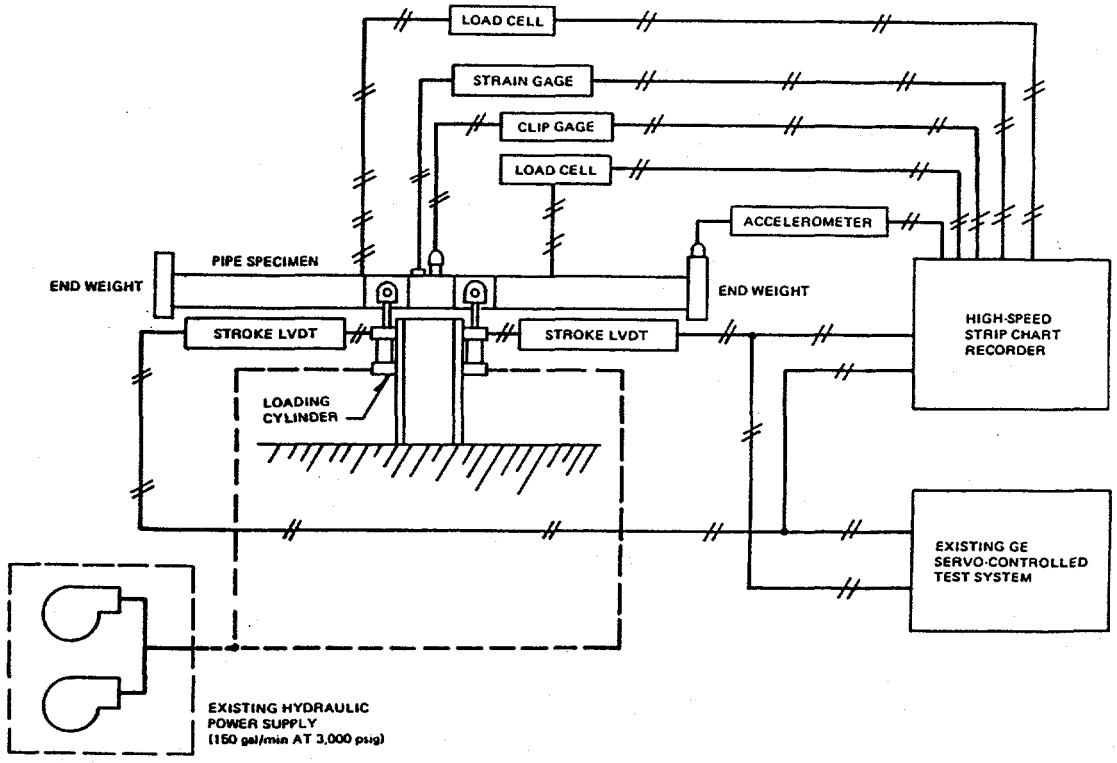

Figure 1.1 GE/EPRI dynamic pipe test system schematic
I1.3-10/90-F1.1

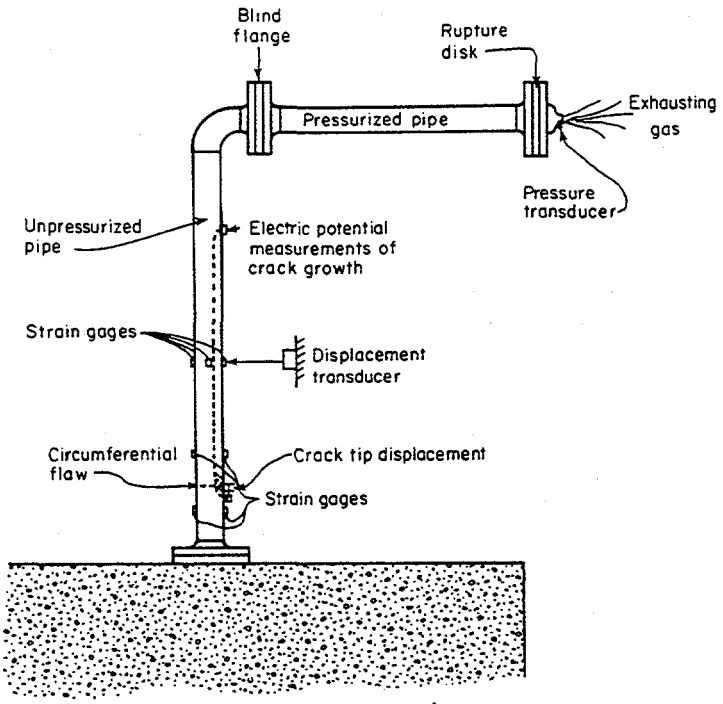

Figure 1.2 An experimental setup for inducing transient bending stresses in the dynamic pipe fracture experiments in Reference 1.5

I1.3-10/90-F1.2

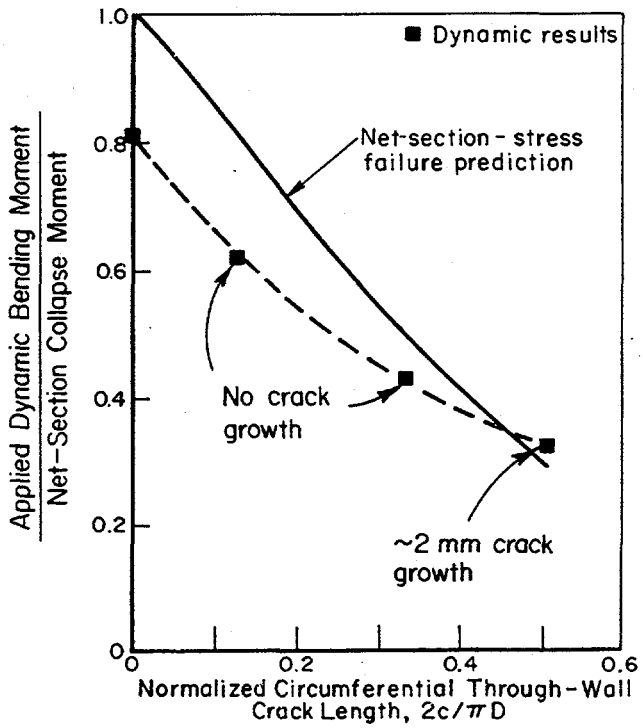

Figure 1.3 Change in dynamic moments at crack location due to increasing through-wall circumferential crack size (Same applied blow-down loads in each experiment from Reference 1.5)

I1.3-10/90-F1.3

During the course of the IPIRG program, two other dynamic cracked pipe programs were completed and reported in the open literature. Both of these were conducted in Japan, one by JAERI (Ref. 1.17) and the other at the Japanese National Research Center for Disaster Prevention with funding by the Science and Technology Agency (STA) (Ref. 1.18).

The JAERI program (Ref. 1.17) involved inertial pipe tests that were similar in design to the double-cantilever inertial tests in Reference 1.14 and the IPIRG program Subtask 1.1 experiments (Ref. 1.15), see Figure 1.4. These were pressurized tests conducted at room temperature, with a testing frequency of 12 Hz. Blocks of constant amplitude sinusoidal displacements were applied to the pipe. This load history was sufficiently low that low-cycle fatigue crack growth was significant. Hence, as in the case of the Reference 1.14 experiments, the Net-Section-Collapse analysis could be used only if the fatigue crack growth during the dynamic loading was accounted for, see Figure 1.5.

The program at the National Research Center for Disaster Prevention in Japan (Ref. 1.18) involved a cracked pipe system, unlike the EPRI and JAERI experiments. The pipe system evaluated was more complex than the IPIRG Subtask 1.3 pipe loop. Figure 1.6 is a sketch of the 4- and 6-inch diameter piping system used. Pressurized, room-temperature tests were conducted with and without initial flaws. The loading consisted of constant amplitude sinusoidal blocks at 8 Hz for 10 seconds or a seismic load history of similar duration. In the case of long circumferential surface flaw tests, a complete break occurred from four to seven cycles after the surface crack penetrated the pipe thickness. (Videotapes of these experiments clearly show the behavior.) Hence, these experiments with a more complicated (but smaller) pipe system than the IPIRG pipe-system experiments also showed inertial stresses can cause complete pipe failure.

As with the EPRI/GE and JAERI program experience, the failure loads were underpredicted by the Net-Section-Collapse analysis unless the cyclic crack growth in the "seismic" load history was used to increase the initial flaw to the flaw size at failure, see Figure 1.7. (Note, the Hasegawa (Ref. 1.19) and Kurihara (Ref. 1.20) analyses in Figures 1.7a and 1.7b are slight modifications of the Net-Section-Collapse analysis equations. The Net-Section-Collapse analysis equations are the basis of the ASME pipe flaw evaluation criteria.) Key aspects to understanding piping integrity from this work are:

> The results further substantiated that large numbers of cycles in the dynamic event can grow the crack so that the calculated failure loads, using the flaw size prior to the application of the dynamic loads, would over predict the actual failure loads.
>
> Inertial loading can cause a DEGB, but the break is not instantaneous and there may be several cycles of opening and closing of the growing through-wall crack prior to a pipe section severing into two pieces.

1.2 Overview of IPIRG Program

The IPIRG program was developed by the U.S. NRC with the objective of developing data needed to verify engineering methods for assessing the integrity of nuclear power plant piping that contains defects. The work within the IPIRG program is broken down into five tasks:

- Task 1 LBB Verification Under Simulated Seismic/Dynamic Loading,

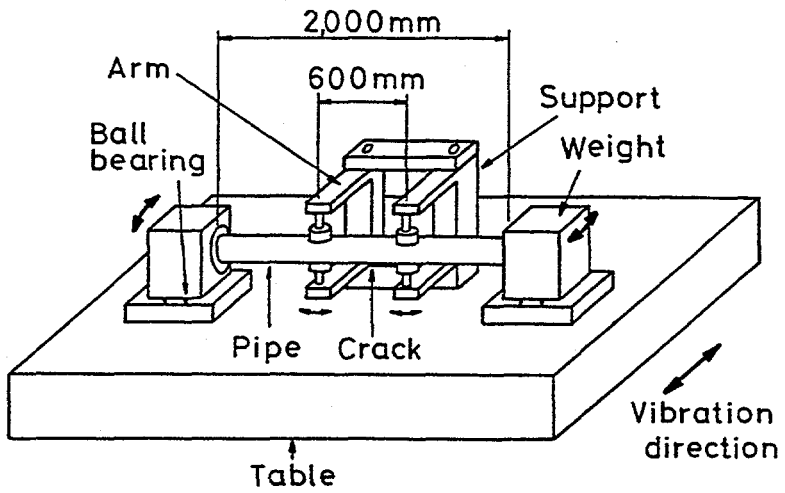

Figure 1.4 Schematic setup of JAERI vibration test from Reference 1.17
I1.3-10/90-F1.4

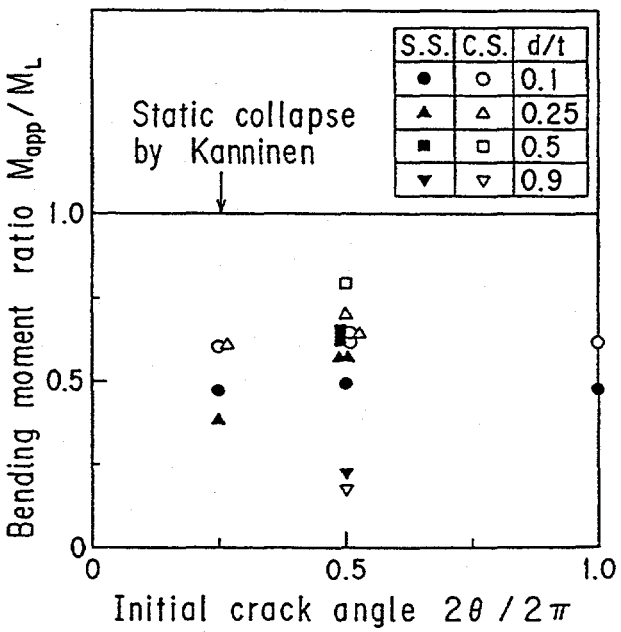

Figure 1.5 Comparison between applied maximum bending moment and Net-Section-Collapse moment for JAERI experiments using crack size prior to applied inertial loads
I1.3-10/90-F1.5

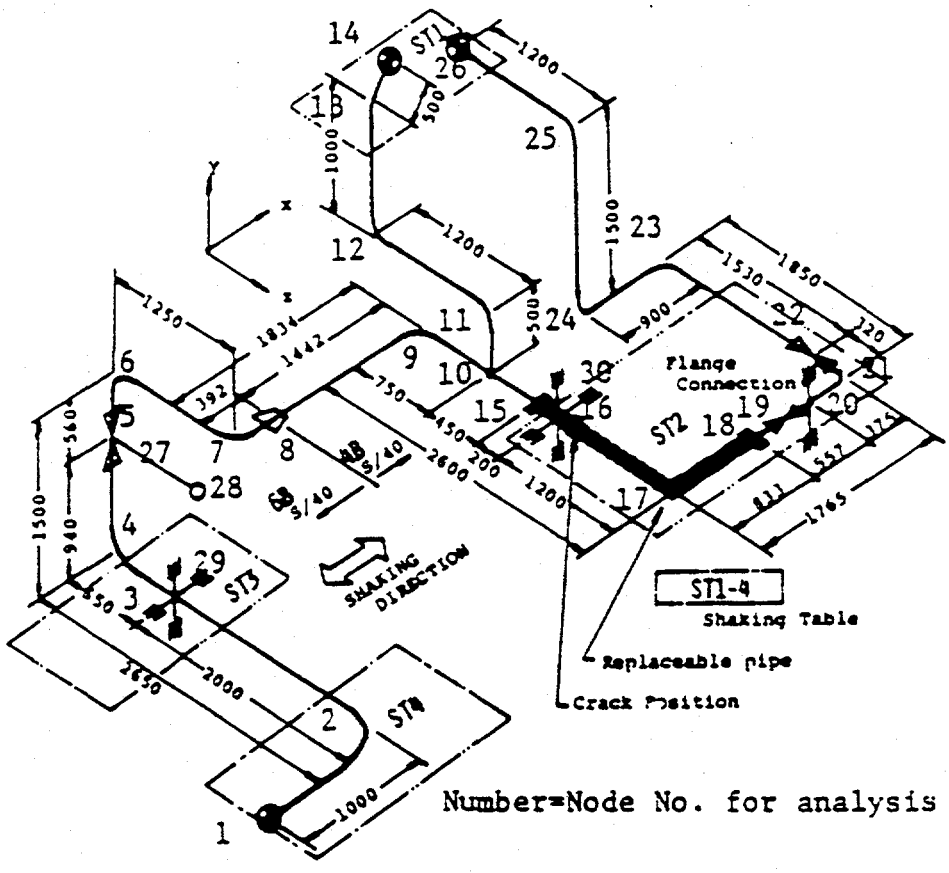

Figure 1.6 STA pipe system for dynamic flawed pipe tests
I1.3-10/90-F1.6

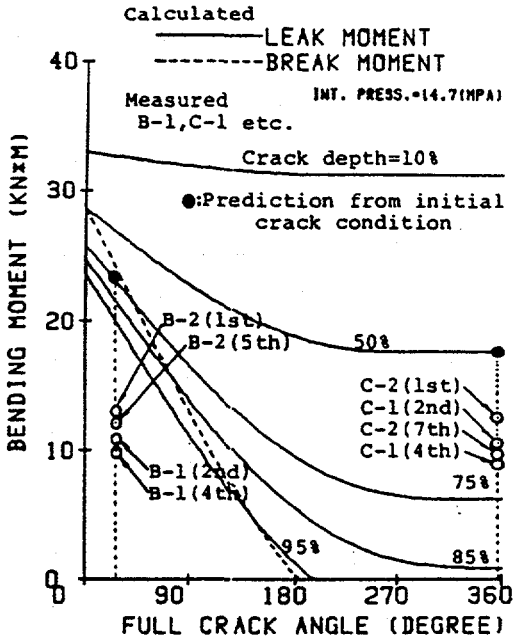

(a) Comparison between experiment and limit-load analysis by the formulation of Hasegawa and others (Ref. 1.19)

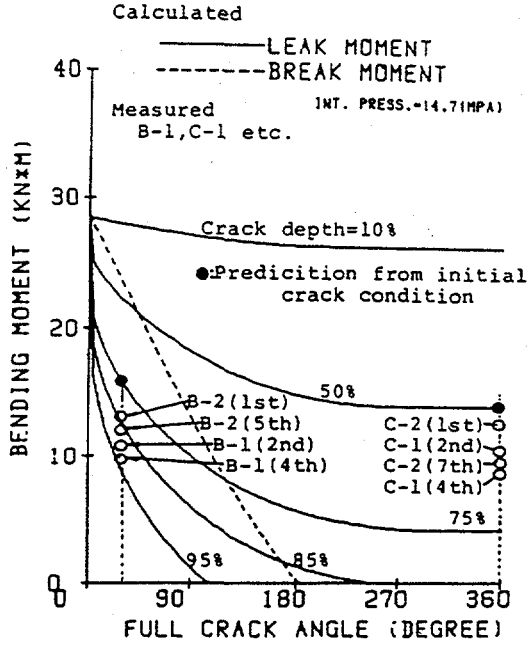

(b) Comparison between experiment and limit-load analysis by the formulation of Kurihara and Ueda (Ref. 1.20)

Figure 1.7 Comparison of STA pipe-system test failure loads with modified Net-Section-Collapse analyses using flaw size prior to dynamic load

I1.3-10/90-F1.7

- Task 2 Experimental Pipe Fracture and Material Property Data Base Development,

- Task 3 Fracture of Piping Containing High Energy Fluids,

- Task 4 Resolution of Unresolved Issues from the U.S. NRC Degraded Piping Program and IPIRG Research Tasks, and

- Task 5 Information Exchange Seminars and Program Administration.

The behavior of flawed piping and piping systems subjected to high-rate loading was investigated in Task 1 by conducting both "separate effects" experiments on simple pipe specimens and full-scale experiments on a representative piping system tested at PWR conditions. The separate effects experiments were designed to investigate the effects of inertial loads (Subtask 1.1, Ref. 1.15) and displacement-controlled loads (Subtask 1.2, Ref. 1.21) on pipe fracture behavior and stability. Combined effects of inertial and displacement-controlled loads were investigated in Subtask 1.3 on a full-scale representative piping system. The three subtasks in Task 1 are as follows:

- Subtask 1.1 Stability of Cracked Pipe Under Inertial Loading,

- Subtask 1.2 Stability of Cracked Pipe Under Seismic/Dynamic Displacement-Controlled Stresses, and

- Subtask 1.3 Crack Stability in Representative Piping System Under Combined Inertial and Seismic/Dynamic Displacement-Controlled Stresses.

This report describes the results from Subtask 1.3.

1.3 Objective and Rationale of Subtask 1.3

The objective of Subtask 1.3 was to provide data to assess the accuracy of analytical predictions of the stability of a circumferential crack in a representative piping configuration under combined inertial and displacement-controlled stresses resulting from a simulated seismic event. Results from the separate effects experiments conducted in Subtask 1.1 (Ref. 1.15), which involved primarily inertial loading with pressure and dead-weight loads, and in Subtask 1.2 (Ref. 1.21), which involved purely displacement-controlled bending, were used to evaluate the results of this subtask, which involved combined loading conditions. By developing data on a full-scale piping system designed to be representative of nuclear reactor piping systems, the complex interaction of loading conditions and system dynamics provided important test cases for assessing current analysis procedures, i.e., finite element stress analyses, in-service flaw assessment, and leak-before-break analyses. This assessment of current analysis procedures was facilitated by the construction of a test facility that incorporated well-defined boundary conditions, which greatly simplified the analytical modeling of the piping system. This was a distinct advantage over other similar piping test facilities, such as the German HDR facility.

By conducting these important experiments as part of an international forum, it was hoped that an international consensus on the implications of these results could be reached. Furthermore, by conducting these experiments in a group program, the costs of these very expensive experiments could be shared by

the various participants. Without such cooperation this program may not have been conducted at all. It is unlikely that any of the organizations could have committed sufficient resources to fund the entire program alone.

This subtask consists of analytical, experimental, and material characterization efforts. The pipe-system experiments involved one uncracked pipe experiment designed to investigate system dynamics and boundary conditions and five cracked pipe experiments, each on a different material. The material characterization studies were conducted on pipe-system and pipe-specimen materials under loading conditions similar to those in the pipe-system experiments. Analysis efforts consisted of extensive pre-test design of the piping system, design of the individual experiments, and post-test analysis of results.

1.4 References

1.1 "Evaluation of Flaws in Austenitic Piping," ASME Boiler and Pressure Vessel Code, Section XI, Appendix C, 1995 Edition, July 1995.

1.2 "Evaluation of Flaws in Ferritic Piping," ASME Boiler and Pressure Vessel Code, Section XI, Appendix H, 1995 Edition July 1995.

1.3 Milne, I., Ainsworth, R. A., Dowling, A. R., and Stewart, A. T., "Assessment of the Integrity of Structures Containing Defects," R/H/R6-Rev. 3, Published by Central Electric Generating Board, England, May 1986.

1.4 Wilkowski, G. M., and others, "Degraded Piping Program - Phase II," Summary of Technical Results and Their Significance to Leak-Before-Break and In-Service Flaw Acceptance Criteria, March 1984-January 1989, by Battelle Columbus Division, NUREG/CR-4082, Vol. 8, March 1989.

1.5 Kanninen, M. F., and others, "Instability Predictions for Circumferentially Cracked Type 304 Stainless Steel Pipes Under Dynamic Loadings," Final Report on EPRI Project T118-2, by Battelle Columbus Laboratories, EPRI Report Number NP-2347, April 1982.

1.6 Eiber, R. J., Maxey, W. A., and Duffey, A. R., "Investigation of the Initiation and Extent of Ductile Pipe Rupture," Battelle Memorial Institute Report, BMI-1908, 1971.

1.7 Vassilaros, M. G., Hays, R. A., Gudas, J. P., and Joyce, J. A., "J-Integral Testing Instability Analysis for 8-Inch Diameter ASTM A106 Steel Pipe," U.S. David W. Taylor Naval Ship Research and Development Laboratory, NUREG/CR-2347, April 1984.

1.8 Tang, H. T., Duffey, R. B., Sing, A., and Bausch, P., "Experimental Investigation of High Energy Pipe Leak and Rupture Phenomena," in ASME Special Publication PVP Volume 98-8, *Fracture, Fatigue and Advanced Mechanics*, June 1985.

1.9 Takumi, K., "Results of the Japanese Carbon Steel Pipe Fracture Program," presented at IPIRG Leak-Before-Break Seminar, Taipei Taiwan, May 11-12, 1989, NUREG/CP-0109, February 1990.

1.10 Darlaston, B. J. L. and Harrison, R. P., "Ductile Failure of Thin-Walled Pipes with Defects Under Combinations of Internal Pressure and Bending", *3rd International Conference on Pressure Vessel Technology, Part II, Materials and Fabrication*, pp 669-676, April 1977.

1.11 Maricchiolo C. and Milella, P. P., "Fracture Behavior of Carbon Steel Pipes Containing Circumferential Cracks at Room Temperature and 300 C," *Nuclear Engineering and Design*, 111, pp 35-46, 1989.

1.12 Faidy, C., Jamet, P., and Bhandari, S. "Developments in Leak Before Break Approach in France," in NUREG/CP-0092, pp 69-82, March 1988.

1.13 Sturm, D., Stoppler, W., Jurlisch, P., Hipplelein, K., and Muz, J., "Fracture Initiation and Fracture Opening under Light Water Reactor Conditions," *Nuclear Engineering and Design*, Vol. 49, pp 117-134, 1978.

1.14 Hale, D. A., and others, "The Growth and Stability of Stress Corrosion Cracks in Large-Diameter BWR Piping," EPRI report NP-2472 Volume 2, see Appendices B and C, July 1982.

1.15 Scott, P., and others, "Stability of Cracked Pipe Under Inertial Stresses - Subtask 1.1 Final Report," NUREG/CR-6233, Vol. 1, August 1994.

1.16 Wilkowski, G. M., and others, "Degraded Piping Program - Phase II," Semiannual Report, April 1985-September 1985, by Battelle Columbus Division, NUREG/CR-4082, Vol. 3, March 1986.

1.17 Murakami, E., and others, "Crack Growth of Nuclear Piping Under Dynamic Loading," ASME PVP special publication PVP 167, pp 115-120, July 1989.

1.18 Ogawa, N., "Experimental Study of Piping Stability under Strong Earthquake," ASME PVP special publication PVP 150, pp 69-80, July 1988.

1.19 Hasegawa, K., and others, "Predictions of Fracture Tolerances for Stainless Steel Pipes with Circumferential Cracks," PVP Vol. 95, June 1983.

1.20 Kurihara, R., and others, "Estimation of Ductile Unstable Fracture of Pipe with a Circumferential Surface Crack Subjected to Bending," *Nuclear Engineering and Design*, Vol. 106, pp 265-273, 1988.

1.21 Scott, P., and others, "The Effect of Dynamic and Cyclic Loading During Ductile Testing on Circumferentially Cracked Pipe: Experimental Results," PVP Vol. 280, pp 207-220, June 1994.

2.0 MATERIAL CHARACTERIZATION

In this section, the results of the material characterization efforts for the Subtask 1.3 materials are discussed. The discussion begins with a description of the materials selected for use as test specimens and materials used in the construction of the pipe loop. Next the results of the tensile (both quasi-static and dynamic), fracture toughness (both quasi-static and dynamic), and dynamic modulus tests are presented. The section concludes with a discussion of the results. Further details of these material characterization efforts are presented in Reference 2.1.

2.1 Material Selection

In this section, the materials selected for test specimens and for the fabrication of the piping loop are described.

2.1.1 Test Specimen Materials

Six different materials were evaluated for the six pipe-system experiments (one uncracked pipe and five cracked pipe experiments) conducted as part of Subtask 1.3, see Table 2.1. The test material for the uncracked pipe experiment was a section of ASTM A710, Grade A, Class 3 steel. This is the same material used in constructing the pipe loop. Details of this material are provided in the next section, Piping Loop Materials. The five materials chosen for the cracked-pipe experiments were an A106 Grade B carbon steel, an SA-358 Type 304 stainless steel, submerged-arc welds in these two materials, and a section of aged cast stainless steel donated to the program by the French company, Framatome. These five materials were chosen to provide a range of fracture toughness values typical of nuclear power plant piping.

The stainless steel and carbon steel base metals were nuclear grade materials obtained from canceled nuclear plants. The weld procedures used in fabricating the stainless steel and carbon steel welds were submerged-arc welding (SAW) procedures obtained from nuclear plant vendors in the United States. Each of these materials (base metals and welds) had been characterized at quasi-static loading rates as part of an earlier research program funded by the U.S. NRC (Ref. 2.2). The stainless steel is a very high toughness material which was expected to reach limit load conditions during the pipe fracture experiments. The carbon steel material has a toughness near the lower bound from the ASME Code, and its failure was expected to fall in the elastic-plastic fracture mechanics (EPFM) regime.

The carbon steel weld also had a very low fracture toughness. In fact, the J-resistance (J-R) curve for this particular weld formed the basis for the lower bound J-R curve incorporated into Section XI IWB-3650. The stainless steel weld had a toughness value close to the lower bound toughness value used in Section XI IWB-3640 for submerged-arc welds.

The aged cast stainless material was incorporated into the test plan because it was of special interest to a number of the IPIRG program members. Cast stainless steels are often used in the construction of the primary loop piping systems in U.S. nuclear plants, as well as being used in the fabrication of elbows and other fittings. Owing to the metallurgical structure of cast stainless steel, the mechanical properties of the materials can change with continued exposure to reactor operating temperatures. This behavior, commonly

Table 2.1 Materials evaluated as part of Subtask 1.3 pipe-system experiments

Experiment Number	Material	Material I.D. Number
1.3-1	ASTM A710, Grade A, Class 3 Carbon Steel	IP-F3
1.3-2	ASTM A106 Grade B Carbon Steel Base Metal	DP2-F29
1.3-3	ASTM A358 Type 304 Stainless Steel Base Metal	DP2-A8
1.3-4	Submerged-Arc Weld (SAW) in A106 Grade B Carbon Steel	DP2-F29W
1.3-5	Submerged-Arc Weld (SAW) in A358 Type 304 Stainless Steel	DP2-A8W
1.3-7	Aged ASTM A351 Grade CF8M Cast Stainless Steel Base Metal	DP2-A40

termed thermal aging, has been studied by several researchers around the world, including work performed by Argonne National Laboratories for the U.S. NRC (Ref. 2.3). Of specific interest in this application is the fact that the toughness of cast stainless steels has a tendency to thermally degrade with continued exposure to reactor operating temperatures. The section of cast stainless steel donated by Framatome was Type CF8M centrifugally cast stainless steel which had been artificially aged for 700 hours at 400 C (750 F) to simulate nine years of in-plant service for a cold-leg and two years of service for a hot-leg.

Each of these materials was selected in part, because a companion quasi-static pipe fracture experiment had been previously conducted as part of the Degraded Piping Program (Ref. 2.2) or a previous EPRI program conducted at Battelle (Ref. 2.4).

2.1.2 Piping Loop Materials

Two different materials were used in the fabrication of the pipe loop, one for the straight sections and another for the elbows. The straight pipe sections, manufactured by Cameron Iron Works of Houston, Texas, are seamless extrusions of ASTM A710, Grade A, Class 3 material. The elbows, which were fabricated by Flo-Bend Incorporated of Tulsa, Oklahoma, have a material designation WPHY-65, which is a designation of the Manufacturers Standardization Society of the Valve and Fitting Industry, Inc., in specification MSS SP-75. Both materials were used in 406-mm (16-inch) diameter Schedule 100 (26 mm [1.03 inch] thick) and Schedule 160 (41 mm [1.59 inch] thick) nominal sizes.

These particular materials were chosen for their strength and weldability. To use the pipe loop for multiple experiments, a material was needed with a sufficiently high yield strength to preclude yielding remote from the cracked section. If yielding did occur remote from the crack, energy supplied by the hydraulic actuator used to shake the pipe would have been absorbed at those locations so that there would be less energy available to drive the crack. If this was to happen, larger (i.e., more costly) servo-hydraulic equipment would have been required to conduct these experiments.

2.2 Tensile Test Results

Summary graphs and tables of longitudinal tensile test results are presented in this section. Unless otherwise stated, all specimens were machined from 406-mm (16-inch) diameter, Schedule 100 pipe. The procedures used in collecting the necessary stress-strain data at dynamic rates for these tensile tests are provided in detail in Reference 2.1.

2.2.1 A106B Carbon Steel

Specimens were machined from a section of the ASTM A106 Grade B carbon steel pipe material (DP2-F29) and subjected to quasi-static tests at room temperature, 149 C (300 F), and 288 C (550 F), and to dynamic tests at 288 C (550 F). All specimens were machined longitudinal to the pipe axis. The results of those tests are summarized in Table 2.2 and Figure 2.1. Notice in Figure 2.1 that the actual yield strength

Table 2.2 Tensile properties of ASTM A106 Grade B carbon steel pipe (DP2-F29)

Spec. Ident. No.	Temperature, C	Temperature, F	Strain, Rate, s^{-1}	0.2-Percent Offset Yield Strength, MPa	0.2-Percent Offset Yield Strength, ksi	Ultimate Tensile Strength, MPa	Ultimate Tensile Strength, ksi	Elongation, Percent in 25.4 mm (1.0 inch)
F29-1[a]	22	72	$2x10^{-4}$	277	40.2	524	76.0	29.6
F29-2[a]	22	72	$2x10^{-4}$	276	40.0	513	74.4	29.6
F29-3[a]	149	300	$2x10^{-4}$	252	36.6	610	88.5	18.1
F29-4[a]	149	300	$2x10^{-4}$	251	36.4	596	86.4	19.1
F29-5[a]	288	550	$2x10^{-4}$	241	34.9	618	89.7	24.0
F29-6[a]	288	550	$2x10^{-4}$	234	33.9	601	87.2	24.0
F29-101	288	550	1	235[b]	34.1	503	72.9	19.6
F29-103	288	550	1	230[b]	33.3	511	74.1	23.0
F-29-102	288	550	10	234[b]	34.0	443	64.2	24.1
F-29-104	288	550	10	228[b]	33.0	435	63.1	19.6
SA-106 Gr. B	22	72	QS	241[c]	35.0[c]	414[f]	60.0[d]	--
SA-106 Gr. B	288	550	QS	187[e]	27.1[e]	414[f]	60.0[f]	--

(a) Round-bar, threaded-ends specimens; all others were flat pin-loaded specimens.
(b) Approximate value only, due to uncertainties in stress-strain curves at small strains.
(c) S_y at 22 C (72 F) from ASME Section III.
(d) S_u at 22 C (72 F) from ASME Section III.
(e) S_y at 288 C (550 F) from ASME Section III.
(f) S_u at 288 C (550 F) from ASME Section III.

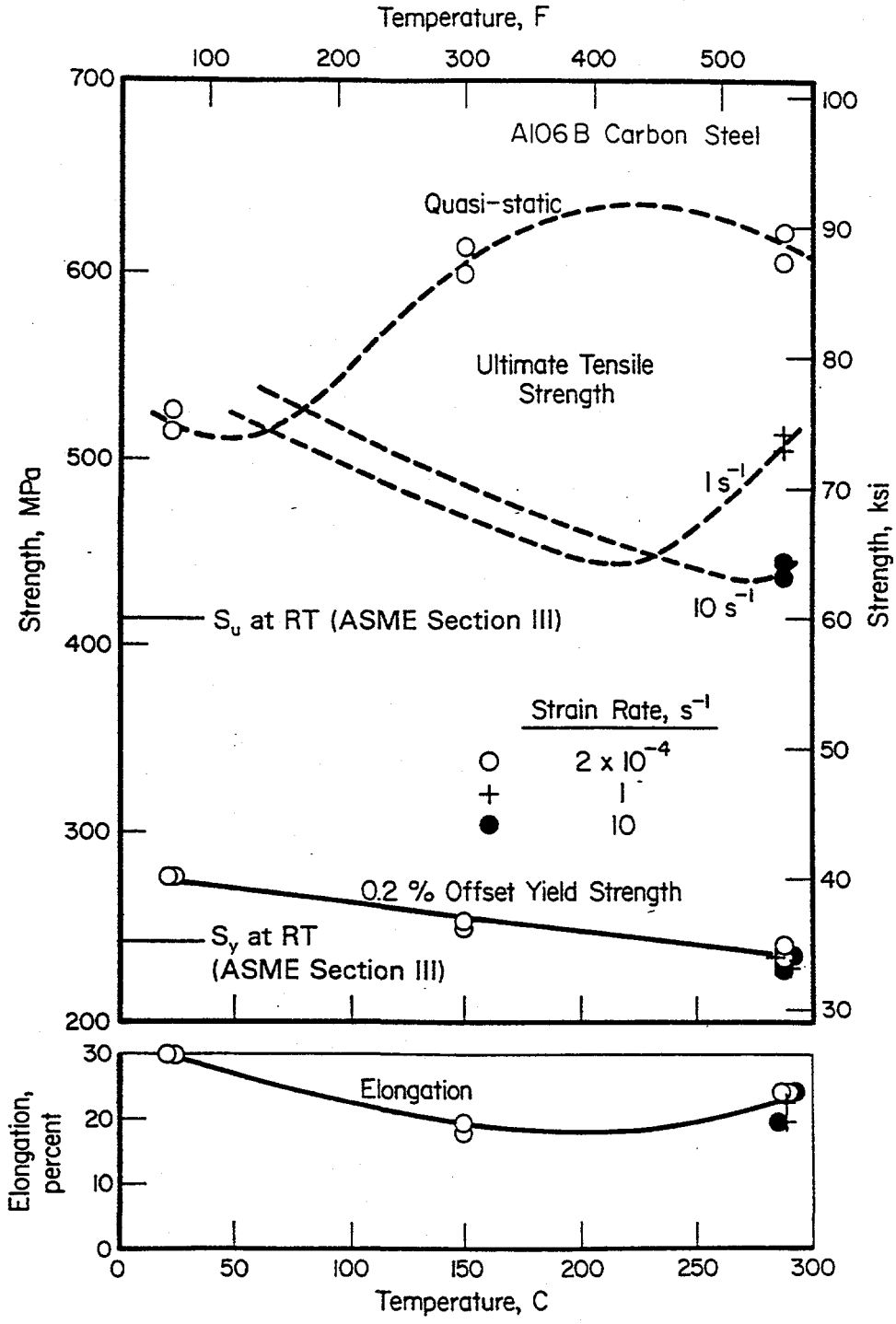

Figure 2.1 Tensile properties versus temperature for A106 Grade B carbon steel (DP2-F29)

I1.3-10/90-F2.2.1

at room temperature was approximately 115 percent of the ASME Section III specified minimum yield strength, and the actual tensile strength was approximately 125 percent of the ASME Section III specified minimum tensile strength. The elevation of the tensile strength at the higher temperatures in the quasi-static tests and the lowering of the strength at 288 C (550 F) with increasing strain rate are indications of dynamic strain aging (DSA) sensitivity (Refs. 2.5 to 2.7).

Figure 2.2 shows engineering stress-strain curves from tensile tests for this carbon steel at 288 C (550 F) for three different strain rates. This steel exhibited pronounced serrations on the stress-strain curves at the intermediate strain rate which is another indication of DSA.

Figure 2.3 shows the variation of strength and ductility with strain rate for this carbon steel tested at 288 C (550 F). As was noted earlier, the ultimate strength dropped significantly with increasing strain rate. However, the yield strength and ductility were relatively unaffected by increased strain rate.

The ASME Section III yield strength (S_y) and ultimate strength (S_u) values at 288 C (550 F) are also indicated in Figure 2.3. The actual yield strength was approximately 120 percent of the ASME code value for this pipe at 288 C (550 F). The ultimate strength at quasi-static test rates was approximately 145 percent of the ASME code value at 288 C (550 F), but decreased to approximately 105 percent of the ASME code value at a strain rate of 10/second at 288 C (550 F).

2.2.2 Type 304 Stainless Steel

Tensile properties are summarized in Table 2.3 for all tensile tests, both quasi-static and dynamic, conducted on the ASTM A358 Type 304 stainless steel pipe material (DP2-A8).* All specimens were machined longitudinal to the pipe axis. Figure 2.4 shows the effect of test temperature on tensile properties. Note that the tensile strength, yield strength, and fracture elongation were decreased by increasing the test temperature. As was noted earlier, strength decreases are the expected result of increasing the test temperature; however, the reason for the decrease in fracture elongation as temperature was raised is not known. The reduction in fracture elongation is too great to be attributed to experimental scatter.

Notice in Figure 2.4 that the actual yield strength of this material at room temperature was approximately 140 percent of the ASME Section III specified minimum yield strength (SMYS). The actual tensile strength at room temperature for this material was also approximately 140 percent of the ASME Section III specified minimum tensile strength (SMTS).

Figure 2.5 shows engineering stress-strain curves for tensile specimens for this stainless steel material tested at 288 C (550 F) at several different strain rates. Table 2.3 and Figure 2.6 summarize the effect of strain rate on tensile properties. Ultimate tensile strength values showed a slight decrease and yield strength values showed a slight increase with increasing strain rate. Strain-rate effects on fracture elongation were modest.

---

* Some of the quasi-static tensile test results were available from the Degraded Piping Program (Ref. 2.2).

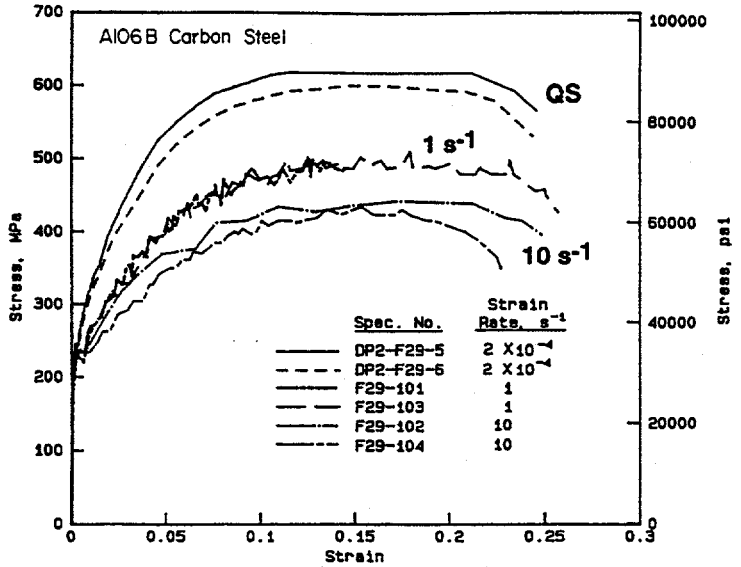

Figure 2.2 Engineering stress-strain curves at 288 C (550 F) for A106 Grade B carbon steel pipe (DP2-F29) tested at several different strain rates

I1.3-10/90-F2.2.2

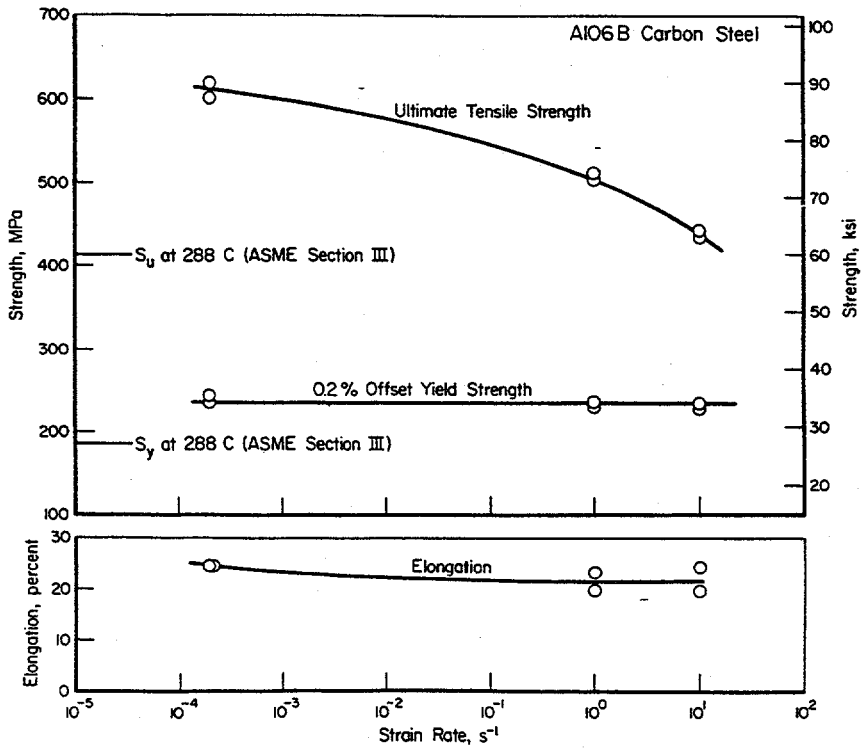

Figure 2.3 Tensile properties at 288 C (550 F) versus strain rate for A106 Grade B carbon steel pipe (DP2-F29)

I1.3-10/90-F2.2.3

Table 2.3 Tensile properties of ASTM A358 Type 304 stainless steel pipe (DP2-A8)

Specimen Identification Number	Temperature, C	Temperature, F	Strain Rate, s^{-1}	0.2-Percent Offset Yield Strength, MPa	0.2-Percent Offset Yield Strength, ksi	Ultimate Tensile Strength, MPa	Ultimate Tensile Strength, ksi	Elongation, Percent in 25.4 mm (1.0 inch)
A8-48[a]	22	72	$4x10^{-4}$	287	41.6	698	101.2	79.4
A8-35[a]	22	72	$4x10^{-4}$	295	42.8	743	107.8	75.9
A8-36[a]	22	72	$4x10^{-4}$	303	43.9	736	106.7	74.3
A8-37[a]	149	300	$4x10^{-4}$	225	32.6	481	69.8	43.5
A8-38[a]	149	300	$3x10^{-4}$	202	29.3	476	69.1	54.8
A8-105	288	550	$5x10^{-4}$	200[b]	29.0	443	64.3	45.7
A8-39[a]	288	550	$3x10^{-4}$	180	26.1	461	66.8	45.0
A8-40[a]	288	550	$4x10^{-4}$	171	24.8	456	66.2	47.0
A8-100	288	550	1	N.D.	N.D.	430	62.4	47.0
A8-101	288	550	1	200[b]	29.0	420	60.9	47.1
A8-102	300	572	1	190[b]	27.5	423	61.3	46.5
A8-103	288	550	10	200[b]	29.0	429	62.2	49.8
A8-104	288	550	10	194[b]	28.1	423	61.4	50.8
SA-358 TP304	22	72	QS	207[c]	30.0[c]	517[d]	75.0[d]	--
SA-358 TP304	288	550	QS	130[e]	18.8[e]	438[f]	63.5[f]	--

(a) Round-bar, threaded-ends specimen; all others were flat, pin-loaded specimens.
(b) Approximate value only, due to uncertainties in stress-strain curves at small strains.
(c) S_y at 22 C (72 F) from ASME Section III.
(d) S_u at 22 C (72 F) from ASME Section III.
(e) S_y at 288 C (550 F) from ASME Section III.
(f) S_u at 288 C (550 F) from ASME Section III.

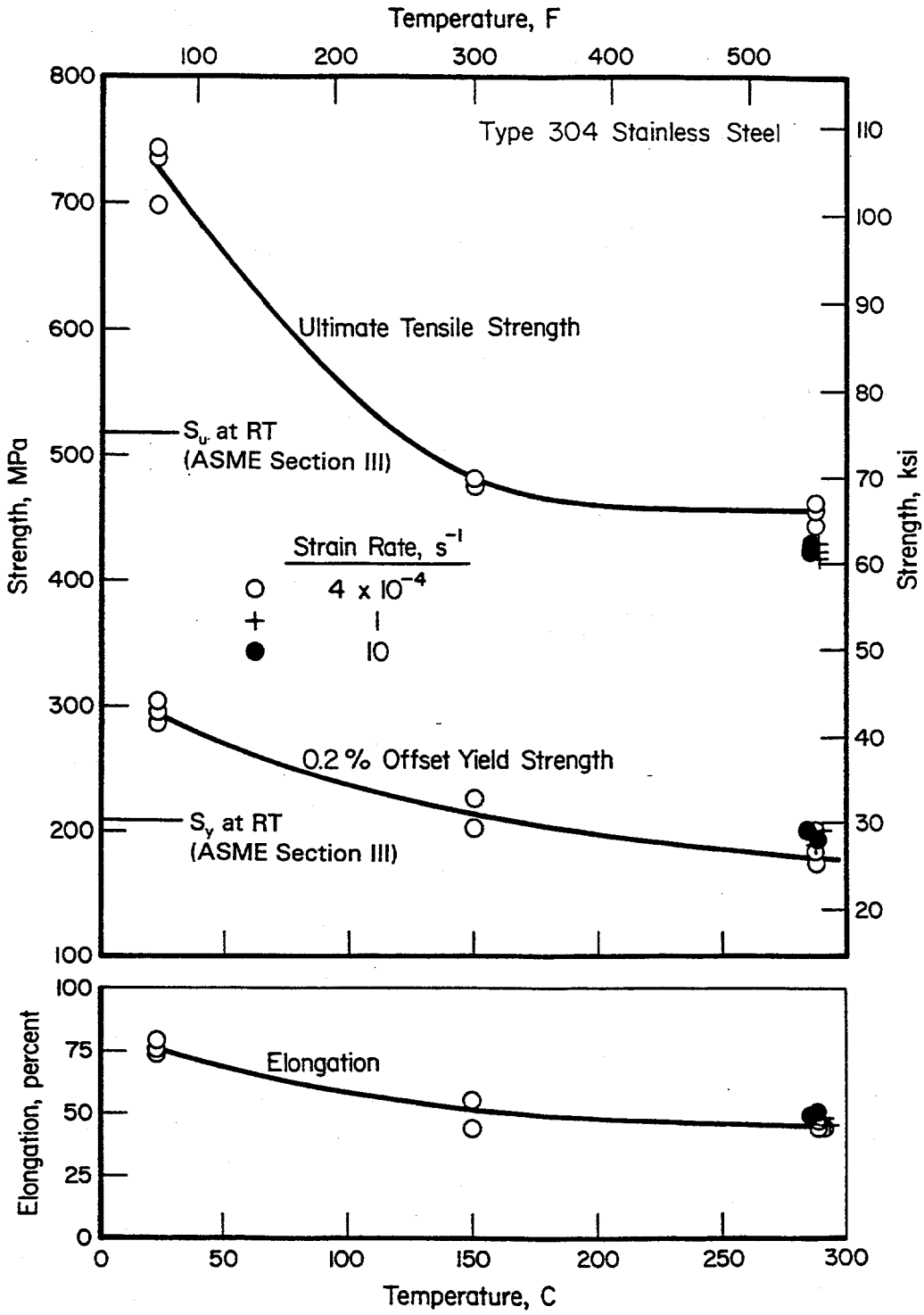

Figure 2.4 Tensile properties versus temperature for A358 Type 304 stainless steel pipe (DP2-A8)
I1.3-10/90-F2.2.4

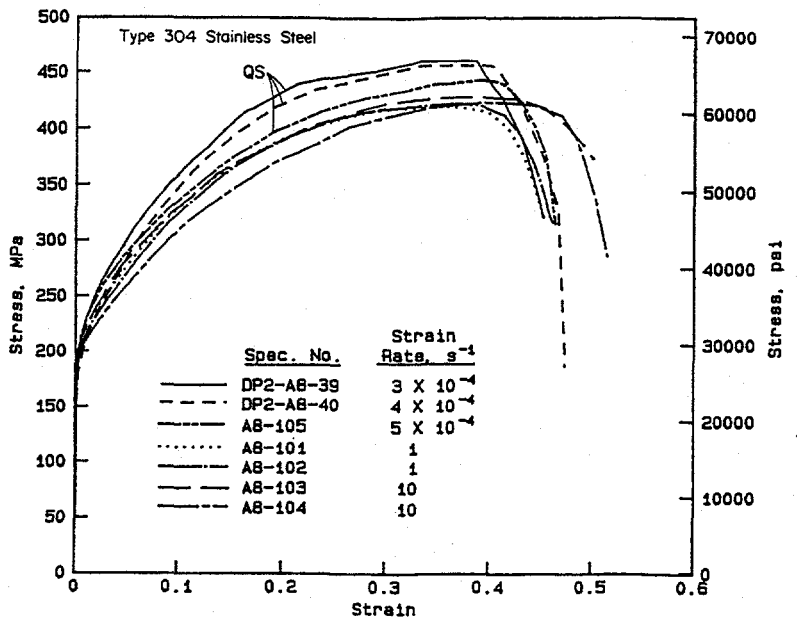

Figure 2.5 Engineering stress-strain curves at 288 C (550 F) for A358 Type 304 stainless steel pipe (DP2-A8) tested at several different strain rates

I1.3-10/90-F2.2.5

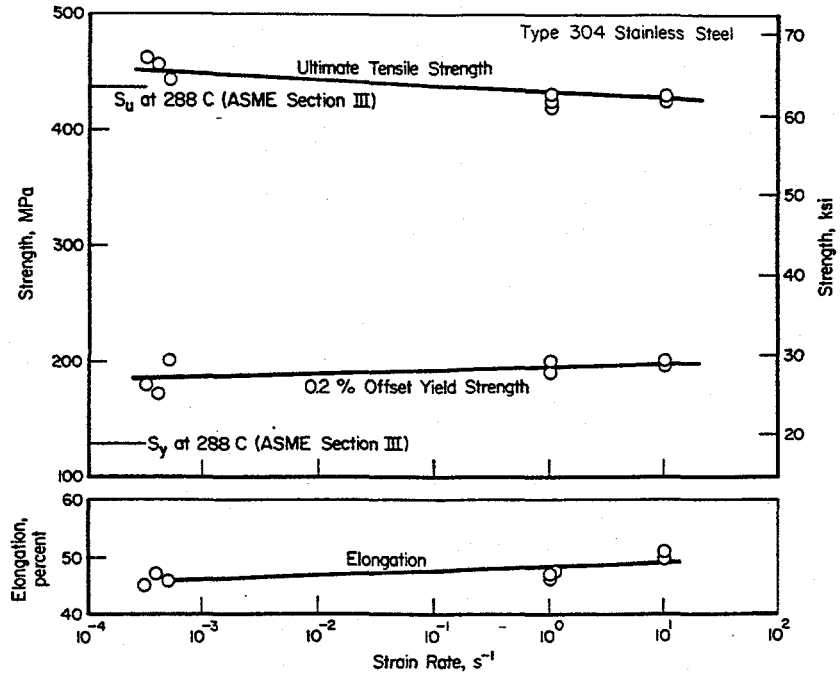

Figure 2.6 Tensile properties at 288 C (550 F) versus strain rate for A358 Type 304 stainless steel pipe (DP2-A8)

I1.3-10/90-F2.2.6

The ASME Section III yield strength (S_y) and ultimate strength (S_u) values at 288 C (550 F) are also indicated in Figure 2.6. The actual yield strength was above the ASME S_y value for all strain rates investigated. The actual ultimate strengths were above the ASME S_u value at low strain rates, and at the higher strain rates the actual ultimates were very close to the ASME S_u value.

2.2.3 Carbon Steel SAW

A submerged-arc girth weld (DP2-F29W) in the ASTM A106 Grade B carbon steel material was subjected to tensile tests only at 288 C (550 F) at three different strain rates. No tensile test results are available at other temperatures for this material. All specimens were machined longitudinal to the pipe axis with the test weld centered in the gage length of the specimen. Tensile properties are summarized in Table 2.4 and engineering stress-strain curves are presented in Figure 2.7. As was the case for the carbon steel base metal, this material exhibited very pronounced serrations at the intermediate strain rate, indicative of DSA.

Figure 2.8 shows the tensile properties of this submerged-arc weld as a function of strain rate in tests conducted at 288 C (550 F). Notice the similarity of the behavior exhibited by the carbon steel weld metal to that exhibited by the carbon steel base metal in Figure 2.3. In particular, the decreasing tensile strength with increasing strain rate is obvious. Thus, even though tensile tests on the pipe weld metal were conducted only at 288 C (550 F), it appears that the carbon steel weld metal was displaying susceptibility to DSA in a manner very similar to the carbon steel base metal.

In comparing the carbon steel base metal tensile test results to the carbon steel weld metal results, it was found that the weld metal ultimate strength at 288 C (550 F) was below that of the base metal at quasi-static rates and approached the base metal ultimate strength at a strain rate of 10/second. The weld metal yield strength was well above the base metal yield strength at all strain rates evaluated.

Table 2.4 Tensile properties of submerged-arc weld (DP2-F29W) in ASTM A106 Grade B carbon steel pipe at 288 C (550 F)

Spec. Ident. No.	Strain Rate, s^{-1}	0.2-Percent Offset Yield Strength,[a] MPa	ksi	Ultimate Tensile Strength, MPa	ksi	Elongation, Percent in 25.4 mm (1.0 inch)
F29W-107	$2x10^{-4}$	356	51.7	556	80.7	20.4
F29W-101	1	368	53.4	487	70.6	14.8
F29W-104	1	396	57.4	495	71.8	14.5
F29W-103	10	347	50.3	446	64.7	21.8
F29W-106	10	345	50.0	454	65.8	21.9

(a) Approximate values only, due to uncertainties in stress-strain curves at small strains.

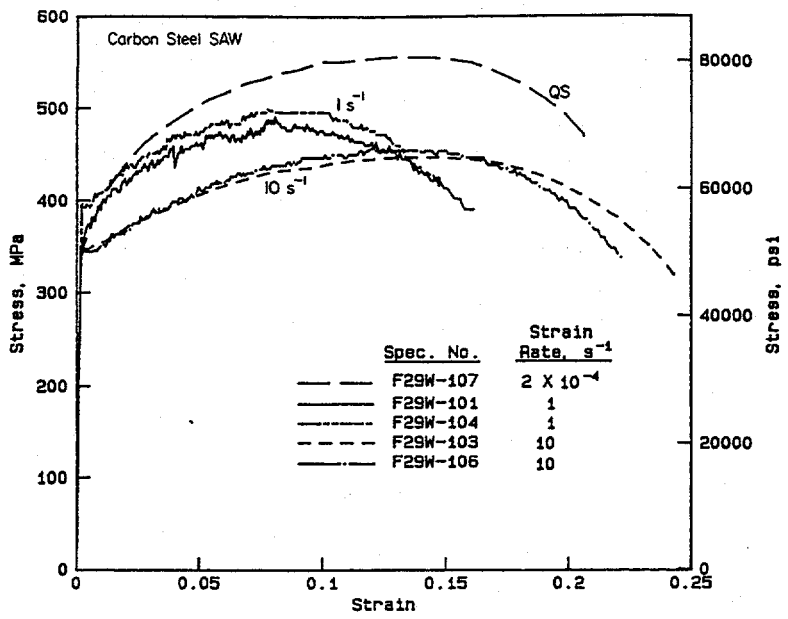

Figure 2.7 Engineering stress-strain curves at 288 C (550 F) for a submerged-arc weld (DP-F29W) in an A106 Grade B carbon steel pipe, tested at several different strain rates

I1.3-10/90-F2.2.7

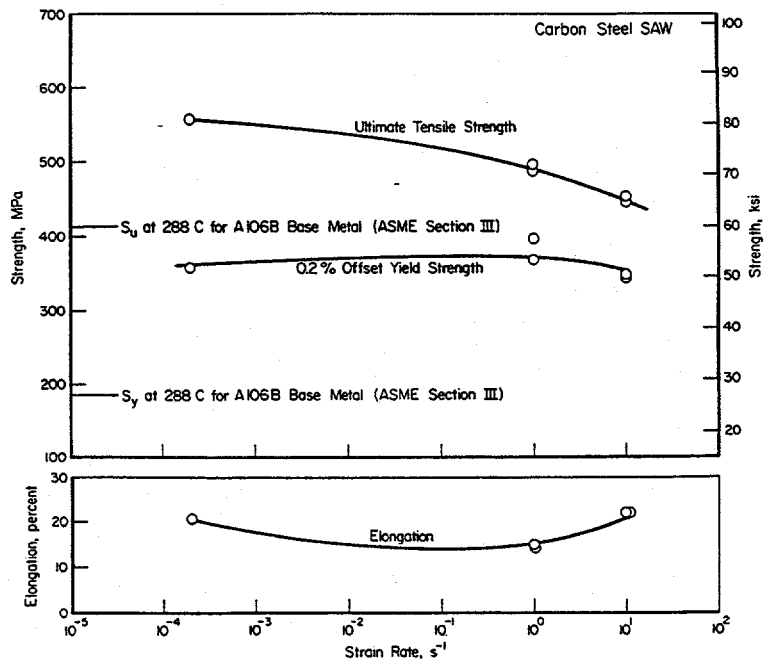

Figure 2.8 Tensile properties at 288 C (550 F) versus strain rate for a submerged-arc weld (DP2-F29W) in an A106 Grade B carbon steel pipe

I1.3-10/90-F2.2.8

2.2.4 Stainless Steel SAW

Figure 2.9 shows engineering stress-strain curves for the submerged-arc weld (SAW) metal (DP2-A8W) in ASTM A358 Type 304 stainless steel tested at 288 C (550 F) at several different strain rates. No tensile test results are available at other temperatures for this material. All specimens were machined longitudinal to the pipe axis with the test weld centered in the gage length of the specimen. Table 2.5 and Figure 2.10 summarize the effect of strain rate on the tensile properties at 288 C (550 F).

The results for the SAW are similar to those for the base metal in this pipe, see Figure 2.6. Both materials showed slightly lower ultimate tensile strength, slightly higher yield strength, and little change in fracture elongation with increasing strain rate.

In comparing the stainless steel base metal tensile test results to the stainless steel SAW results, it was found that the SAW yield strength values and ultimate strength values at 288 C (550 F) exceeded those of the base metal at all strain rates investigated.

2.2.5 Artificially Aged Cast Stainless Steel

Figure 2.11 shows engineering stress-strain curves for the artificially aged ASTM A351 Grade CF8M centrifugally cast stainless steel (DP2-A40) tensile specimens tested at 300 C (572 F). All test specimens were machined longitudinal to the pipe axis. No Battelle tensile test results are available at other temperatures for this material. However, additional room temperature tensile data have been developed at Framatome, who donated this pipe to the U.S. NRC's Degraded Piping Program (see data for Heat Y4331 in Reference 2.8). In addition, data are available from work done at David Taylor Research Center (DTRC) and Argonne National Laboratory (ANL). Table 2.6 and Figure 2.12 summarize the effect of strain rate on tensile properties at 300 C (572 F).

Table 2.5 Tensile properties of submerged-arc weld (DP2-A8W) in ASTM A358 Type 304 stainless steel pipe at 288 C (550 F)

Spec. Ident. No.	Strain Rate, s^{-1}	0.2-Percent Offset Yield Strength, MPa	ksi	Ultimate Tensile Strength, MPa	ksi	Elongation, Percent in 20.3 mm (0.8 inch)
A8W-106	2.0×10^{-4}	258	37.4	469	68.0	26.4
A8W-105	0.9	283	41.0	430	62.3	19.4
A8W-101	1.0	288	44.8	443	64.2	23.3
A8W-102[a]	1.1	270	39.1	436	63.2	30.1
A8W-103	8.0	308	44.6	442	64.1	22.8
A8W-104	13.7	266	38.6	444	64.4	24.5

(a) Tested at 300 C (572 F).

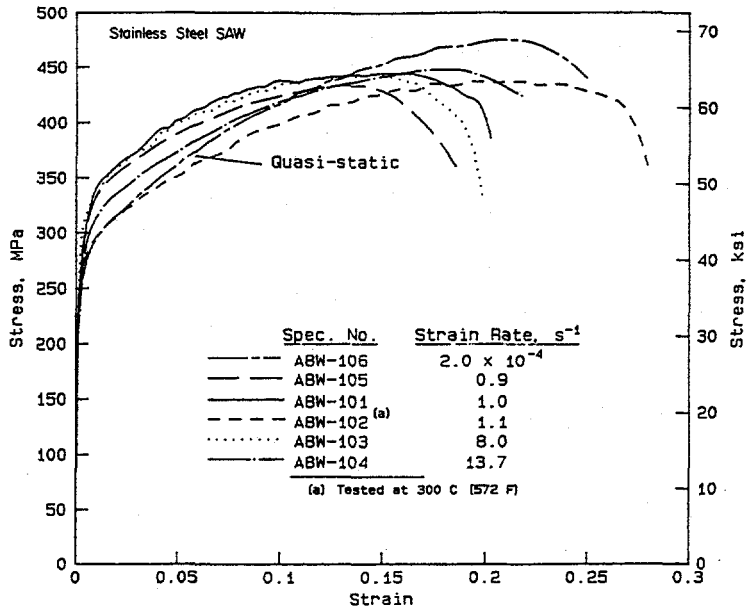

Figure 2.9 Engineering stress-strain curves at 288 C (550 F) for a submerged-arc weld (DP2-A8W) in A358 Type 304 stainless steel, tested at several different strain rates I1.3-10/90-F2.2.9

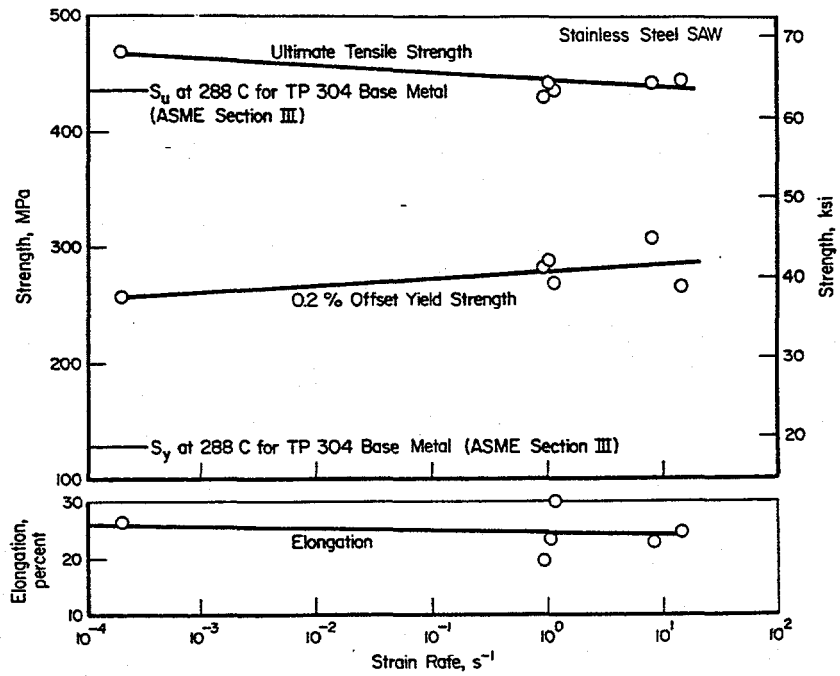

Figure 2.10 Tensile properties at 288 C (550 F) versus strain rate for submerged-arc weld (DP2-A8W) in A358 Type 304 stainless steel pipe I-T1.0-11/89-F3.25

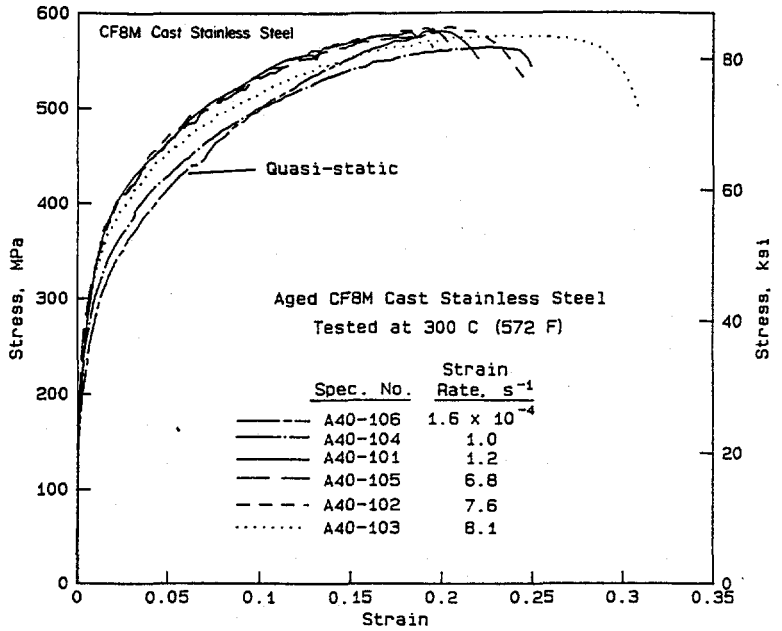

Figure 2.11 Engineering stress-strain curves at 300 C (572 F) for artificially aged A351 Grade CF8M cast stainless steel pipe (DP2-A40), tested at several different strain rates I1.3-10/90-F2.2.11

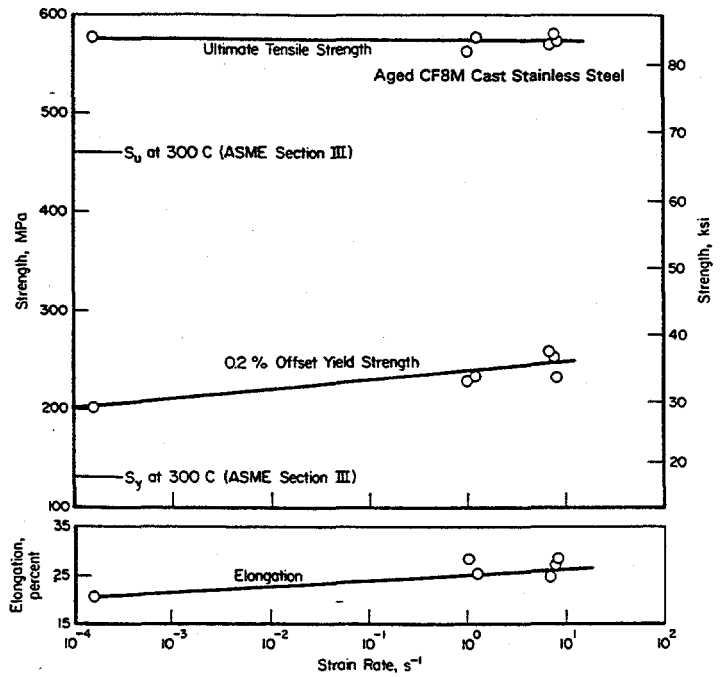

Figure 2.12 Tensile properties at 300 C (572 F) versus strain rate for artificially aged A351 Grade CF8M cast stainless steel pipe (DP2-A40) I1.3-10/90-F2.2.12

The results shown in Figure 2.12 indicate that the artificially aged cast stainless steel displayed increases in yield strength and fracture elongation but little change in ultimate tensile strength as the strain rate was increased.

2.2.6 ASTM A710 Carbon Steel Pipe Loop Material

The pipe loop was fabricated from ASTM A710, Grade A, Class 3, low carbon, age-hardening alloy steel in both Schedule 100 and 160 thicknesses (IP-F3 and IP-F4, respectively). Quasi-static longitudinal tensile tests were conducted by both the manufacturer of the pipe and Battelle. Table 2.7 summarizes the results. Figure 2.13 shows the Battelle stress-strain curves at room temperature and 288 C (550 F) for the Schedule 100 pipe. No data were developed at Battelle for the Schedule 160 pipe.

2.2.7 WPHY-65 Carbon Steel Elbow Material

Pipe loop elbows were manufactured from WPHY-65 carbon steel in both Schedule 100 and 160 thicknesses. Longitudinal tensile tests were conducted at room temperature by the manufacturer. Table 2.8 shows those results. Also shown in Table 2.8 are 0.2 percent offset yield strength values obtained in two different types of tests conducted at Battelle -- monotonic and cyclic. The cyclic tests were conducted to assess the susceptibility of this material to cyclic strain softening, as described in the next paragraph. The monotonic tests were conducted to provide baseline data and were discontinued at 1 percent strain, just as were the cyclic tests. Consequently, the Battelle tests provide no insight as to the ultimate strengths of these elbow materials. The room temperature yield strength values, determined from Battelle's monotonic tests (see Table 2.8), are in close agreement with the manufacturer's results for Elbow IP-FE7. However, for Elbow IP-FE6, the manufacturer's yield strength value is approximately 25 percent greater than the value determined at Battelle.

Incremental step shake-down tests were conducted by Battelle on the pipe loop elbow materials to assess the susceptibility of the elbows to cyclic strain softening. In this test, a tensile specimen is cycled in the following manner: (a) cycles are fully reversed, (b) starting at zero, the amplitude of each successive cycle is increased in a step-wise fashion to a maximum of 1.0 percent strain, and (c) at the maximum strain, the amplitude of each successive cycle is reduced back to zero strain. The cyclic loading history is repeated until the resulting stress-strain curve shows no further changes with cycling. Figures 2.14 and 2.15 show envelope data for the incremental step tests on the elbow materials and Table 2.8 gives values of the 0.2 percent offset yield strength determined from the curves. From the figures and the table, it is apparent that the elbow material cyclically softens at room temperature and that it cyclically hardens at elevated temperature.

Table 2.6 Tensile properties of aged ASTM A351 Grade CF8M cast stainless steel pipe (DP2-A40)

Spec. Ident. No.	Strain Rate, s^{-1}	0.2-Percent Offset Yield Strength, MPa	ksi	Ultimate Tensile Strength, MPa	ksi	Elongation, Percent in 25.4 mm (1 inch)
A40-106[a]	$1.6x10^{-4}$	201	29.2	578	83.9	20.2
A40-104[a]	1.0	228	33.1	563	81.6	28.3
A40-101[a]	1.2	234	34.0	578	83.8	25.4
A40-105[a]	6.8	259	37.6	571	82.8	24.7
A40-102[a]	7.6	252	36.6	581	84.3	26.9
A40-103[a]	8.1	232	33.7	574	83.3	33.1
SA-351 Gr. CF8M	QS	207[b]	30.0[b]	483[c]	70.0[c]	--
SA-351 Gr. CF8M	QS	134[d]	19.4[d]	462[e]	67.0[e]	--
B1-2[f]	QS	323	46.8	716	104	16.1

(a) Tested at 288 C (550 F).
(b) S_y at 22 C (72 F) from ASME Section III.
(c) S_u at 22 C (72 F) from ASME Section III.
(d) S_y at 300 C (572 F) from ASME Section III.
(e) S_u at 300 C (572 F) from ASME Section III.
(f) Average values for Specimens B1 and B2 tested at room temperature by Framatome (Ref. 2.8).

Table 2.7 Quasi-static tensile property data for ASTM A710, Grade A, Class 3, age-hardening, low-carbon alloy steel pipe (IP-F3 and IP-F4)

Pipe Ident.	Schedule	Heat	Temperature, C	F	0.2-Percent Offset Yield Strength, MPa	ksi	Ultimate Tensile Strength, MPa	ksi	Elongation, Percent	Red. of Area, Percent
IP-F3[a]	100	47453	20	68	555	80.5	678	98.3	27.1	78.0
IP-F3[b]	100	47453	22	72	530	76.9	653	94.7	27.5	76.6
IP-F3[b]	100	47454	22	72	560	81.2	665	96.4	27.3	76.7
IP-F3[a]	100	47453	288	550	463	67.1	621	90.1	21.8	72.9
IP-F4[b]	160	47549	22	72	538	78.0	656	95.1	27.3	75.9

(a) Battelle data.
(b) Manufacturer's data.

Table 2.8 Tensile properties for WPHY-65 carbon steel elbows

Spec. Ident. No.	Test Temperature, C	F	Test Type	0.2-Percent Offset Yield Strength, MPa	ksi	Ultimate Tensile Strength, MPa	ksi	Elongation, Percent	Reduction of Area, Percent
			Elbow IP-FE6, Schedule 100, Heat No. Y025 FN						
N.A.[a]	RT	RT	Conventional	545	79.0	662	96.0	32	75
IP-FE6-3	21	70	Monotonic	431	62.5	(b)	(b)	(b)	(b)
IP-FE6-4	21	70	Cyclic[c]	408	59.2	(b)	(b)	(b)	(b)
IP-FE6-1	288	550	Monotonic	346	50.2	(b)	(b)	(b)	(b)
IP-FE6-2	288	550	Cyclic[c]	556	80.7	(b)	(b)	(b)	(b)
			Elbow IP-FE7, Schedule 160, Heat No. 780419						
N.A.[a]	RT	RT	Conventional	448	65.0	593	86.0	36	66
IP-FE7-3	21	70	Monotonic	450	65.2	(b)	(b)	(b)	(b)
IP-FE7-4	21	70	Cyclic[c]	390	56.6	(b)	(b)	(b)	(b)
IP-FE7-1	288	550	Monotonic	418	60.6	(b)	(b)	(b)	(b)
IP-FE7-2	288	550	Cyclic[c]	574	83.2	(b)	(b)	(b)	(b)

(a) Tensile properties shown are from manufacturer's mill certifications.
(b) Ultimate strength, elongation, and reduction of area were not determined because tests were discontinued after 1 percent strain.
(c) Incremental step shake-down tests were conducted to assess susceptibility to cyclic strain softening.

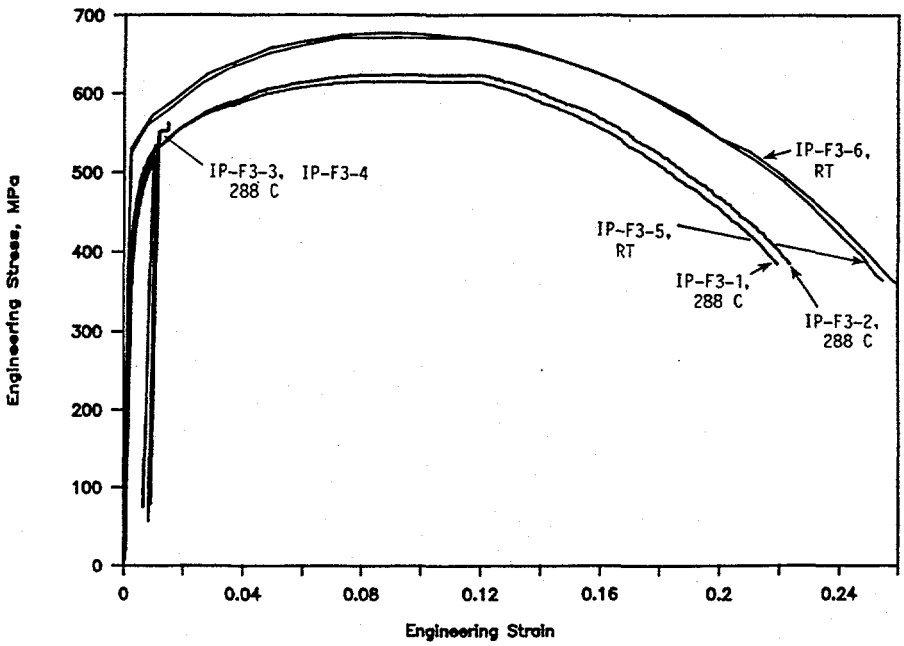

Figure 2.13 Engineering stress-strain curves for ASTM A710, Grade A, Class 3 pipe loop material (IP-F3) DRB/1.3-1/FA-1

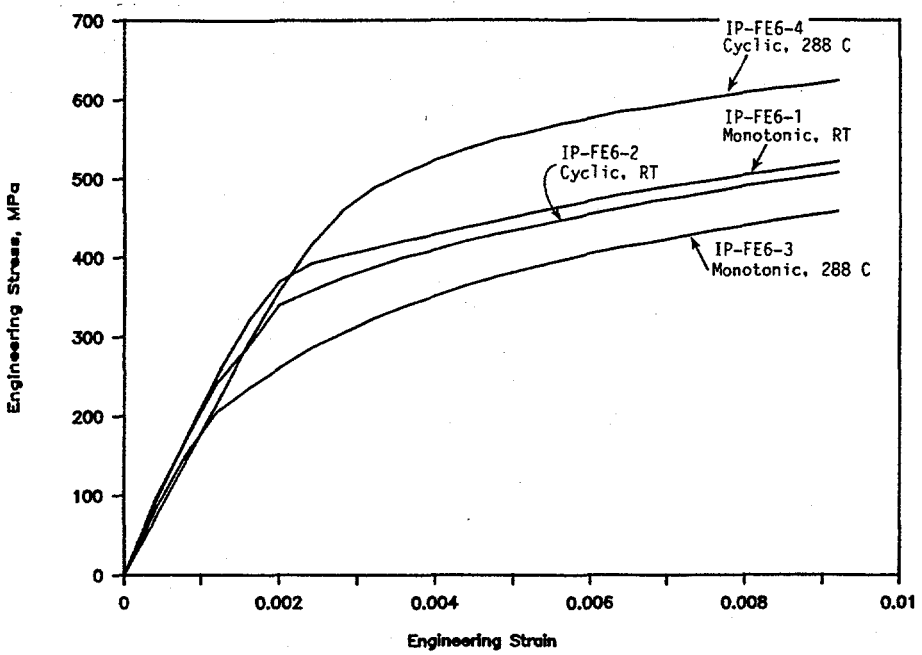

Figure 2.14 Envelopes of engineering stress-strain curves for WPHY-65, Schedule 100 elbow material (IP-FE6) from incremental step tests DRB/1.3-1/FA-5

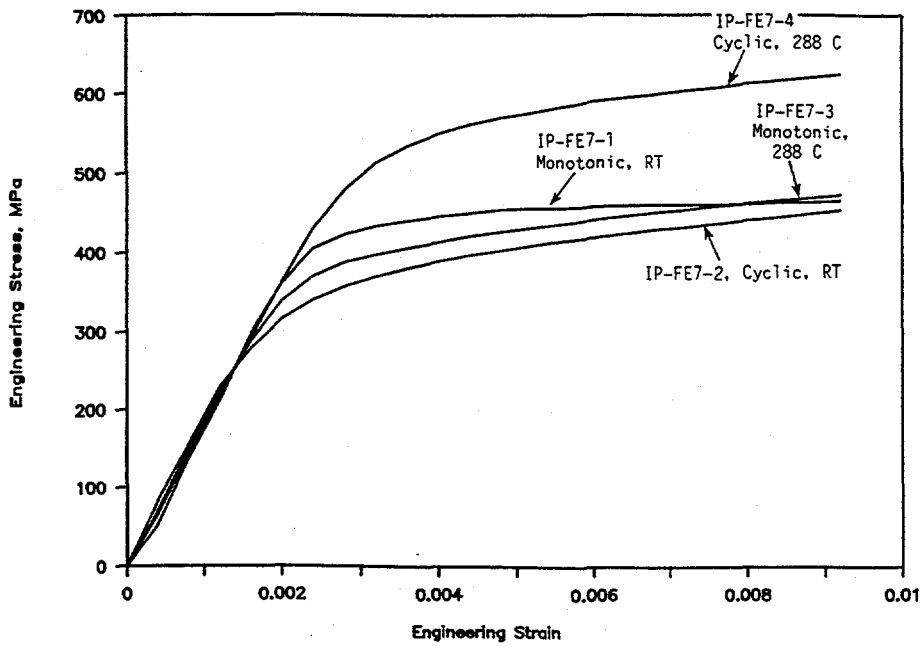

Figure 2.15 Envelopes of engineering stress-strain curves for WPHY-65, Schedule 160 elbow material (IP-FE7) from incremental step tests DRB/1.3-1/FA-3

2.3 J-R Curve Test Results

Summary graphs and tables of both quasi-static and dynamic J-R curve tests are presented in this section. All specimens were machined from 406-mm (16-inch) diameter, Schedule 100 pipe. All specimens were in the L-C orientation which simulates growth of a circumferential through-wall crack. The procedures used to convert the load, load-line displacement, and electric potential data into the J-resistance curves (J versus Δa) presented herein are provided in detail in Reference 2.1.

Actual rates of loading in compact (tension), C(T), tests, expressed as dJ/dt up to the point of crack initiation, are summarized in Table 2.9. The loading rates in the rapid loading tests were about 2,500 to 4,400 times faster, and averaged approximately 3,800 times faster, than those in quasi-static tests.

Table 2.9 Actual loading rates in tests of C(T) specimens

Pipe Identification Number	Material Type	Approximate dJ/dt, kJ/m²/s (in-lb/in²/s) Quasi-static	Rapid Loading	dJ/dt_{RL} / dJ/dt_{QS}
DP2-F29	ASTM A106, Grade B carbon steel	0.17 (0.97)	420 (2,400)	2,470
DP2-F29W	Submerged-arc girth weld in ASTM A106 Grade B	0.13 (0.74)	520 (2,970)	4,000
DP2-A8	ASTM A358, Type 304 stainless steel	1.8 (10.3)	7,250 (41,400)	4,025
DP2-A8W	Submerged-arc girth weld in ASTM A358, Type 304	0.13 (0.74)	570 (3,250)	4,385
DP2-A40	Aged ASTM A351, Grade CF8M centrifugally cast stainless steel	0.16 (0.91)	690 (3,940)	4,310
			Avg.	3,840

2.3.1 A106B Carbon Steel

Load-displacement curves for C(T) specimens machined from the ASTM A106 Grade B carbon steel pipe material (DP2-F29) and tested at 288 C (550 F) are shown in Figure 2.16. They reveal large effects of dynamic loading for this pipe, namely, substantial lowering of the load-displacement curve and virtual elimination of significant crack jumps that were observed in the quasi-static tests. The curve that lies above all the others in Figure 2.16 was for a specimen that was not side-grooved (Spec. No. F29-17).

J-resistance curves for this A106B steel are shown in Figure 2.17 and values of J_i and dJ/da are summarized in Table 2.10. For the quasi-static tests, the J-R curves were terminated at the point of the first significant crack jump because there is no agreed-upon method for calculating J during and after a crack instability. It is evident from the results in Figure 2.17 and Table 2.10 that both J_i and dJ/da were lowered as a result of increasing the displacement rate by a factor of approximately 2,500; J_i values decreased by approximately 35 percent and dJ/da values decreased by approximately 45 percent as the displacement rate was increased.

Included for comparison in Figure 2.17 are the ASME Section XI IWB-3650 reference J-R curves for A106 Grade B and A516 Grade 70 steel. Notice that the quasi-static test results for the carbon steel

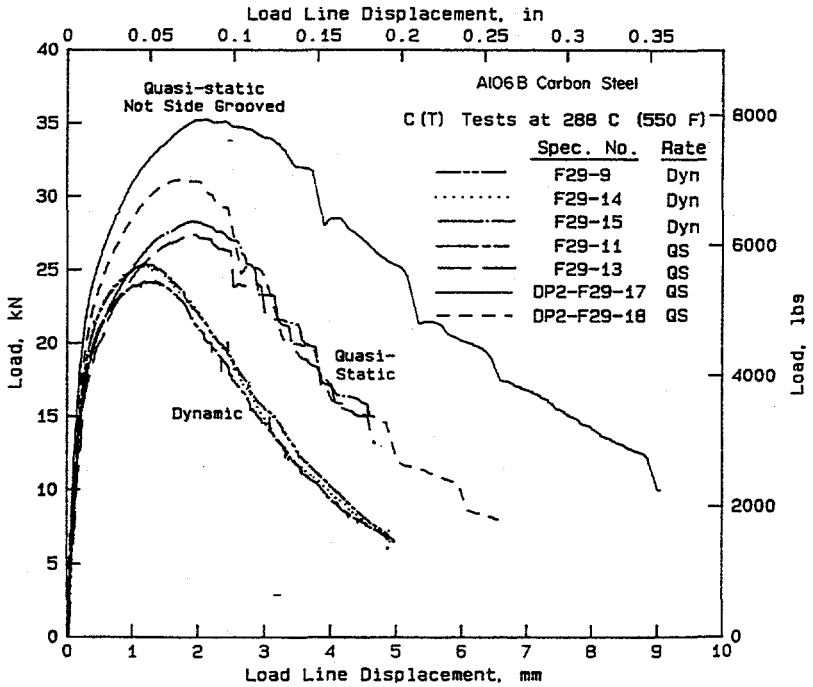

Figure 2.16 Load-displacement curves at 288 C (550 F) for C(T) specimens from A106 Grade B carbon steel pipe (DP2-F29)

I1.3-10/90-F2.3.1

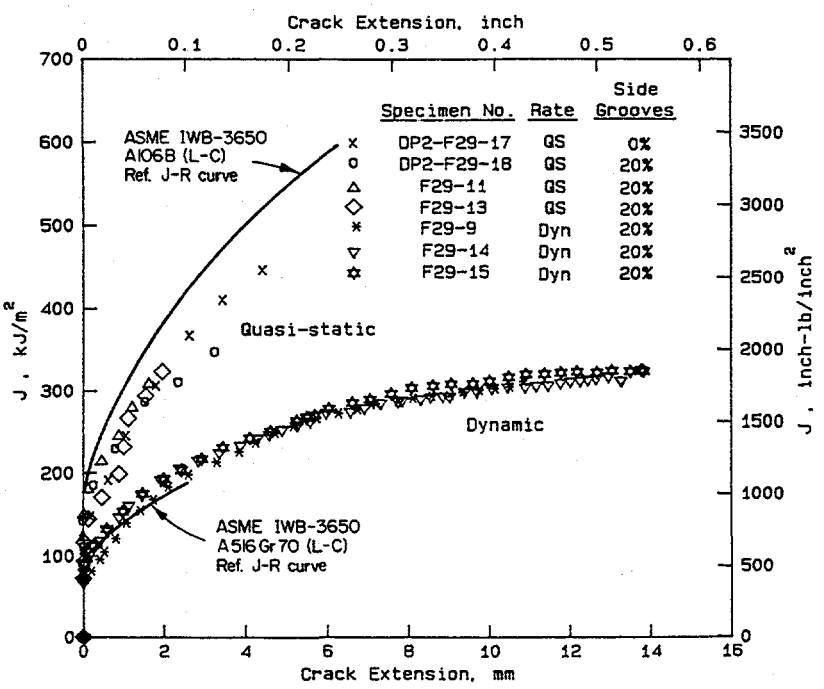

Figure 2.17 J-resistance curves for compact specimens from A106 Grade B carbon steel pipe (DP2-F29) tested at 288 C (550 F)

I-T1.0-11/89-F4.14

Table 2.10 Summary of J_i and dJ/da values for ASTM A106 Grade B carbon steel pipe (DP2-F29)

Specimen Identification Number	Percent Side-Grooves	Rate[a]	J at Initiation, kJ/m^2	J at Initiation, $in\text{-}lb/in^2$	dJ/da, MJ/m^3	dJ/da, $in\text{-}lb/in^3$
F29-17	0	QS	111	635	113	16,410
F29-18	20	QS	149	850	89	12,910
F29-11	20	QS	147	840	100	14,550
F29-13	20	QS	92	525	125	18,200
F29-9	20	Dyn	68	390	62	8,930
F29-14	20	Dyn	88	505	55	8,020
F29-15	20	Dyn	89	510	56	8,140

(a) QS = quasi-static, Dyn = dynamic.

specimens lie slightly below the ASME curve for A106 Grade B steel, and the dynamic test results lie significantly below the curve for A106 Grade B steel and approximately on the ASME curve for A516 Grade 70 steel.

2.3.2 Type 304 Stainless Steel

J-resistance curves for L-C orientation C(T) specimens machined from the ASTM A358, Type 304 stainless pipe material (DP2-A8) are presented in Figure 2.18 and values of J_i and dJ/da are summarized in Table 2.11. The results show that increasing the displacement rate by a factor of approximately 4,000 raised J_i significantly but had little effect on dJ/da.

Also shown for comparison in Figure 2.18 are results for a smaller diameter (152 mm [6 inch]) Type 304 stainless steel pipe (DP2-A23) tested in IPIRG Subtasks 1.1 and 1.2. Notice that the larger pipe (DP2-A8) exhibited somewhat greater toughness than did the smaller pipe (DP2-A23).

2.3.3 Carbon Steel SAW

Load-displacement curves are shown in Figure 2.19 for C(T) specimens machined from submerged-arc weld material (DP2-F29W) in ASTM A106 Grade B carbon steel pipe. Unlike the results obtained for the carbon steel base metal (see Figure 2.16) in which dynamic testing lowered the load-displacement curve, dynamic testing of the weld metal raised the load-displacement curve significantly. In addition, whereas quasi-static tests on base metal specimens produced significant crack jumps (see Figure 2.16), the single quasi-static test conducted on a weld metal specimen produced only very small jumps that are barely perceptible on the load-displacement curve in Figure 2.19.

J-resistance curves are shown in Figure 2.20 and values of J_i and dJ/da are summarized in Table 2.12. These results show that both J_i and dJ/da were increased approximately 50 percent as a result of increasing the displacement rate by a factor of approximately 4,000.

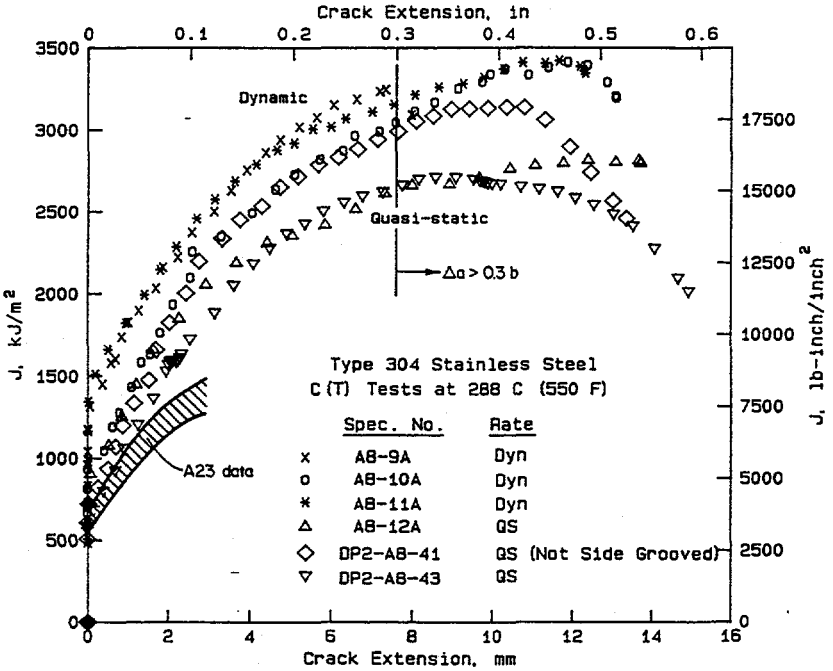

Figure 2.18 J-resistance curves for compact specimens from A358 Type 304 stainless steel pipe (DP2-A8) tested at 288 C (550 F) I1.3-10/90-F2.3.3

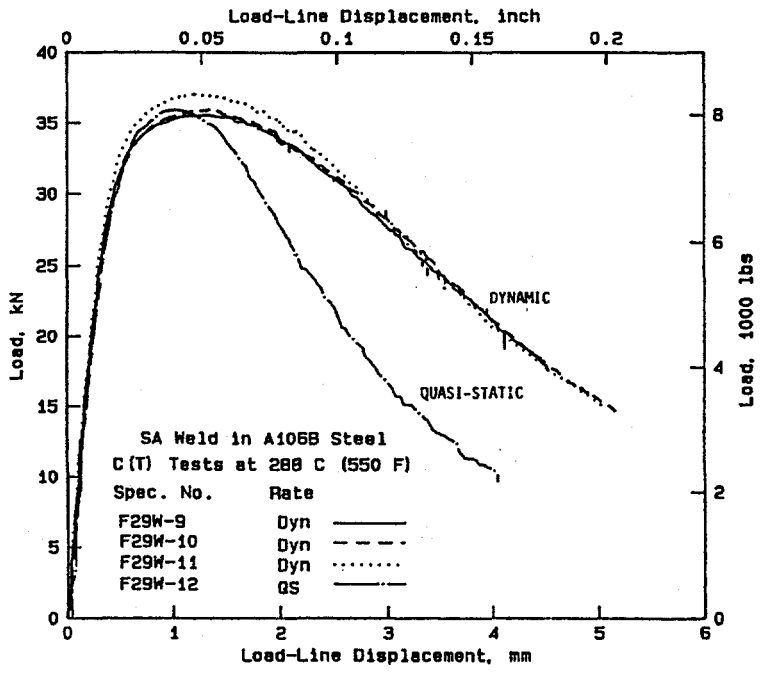

Figure 2.19 Load-displacement curves at 288 C (550 F) for C(T) specimens from a submerged-arc weld (DP2-F29W) in an A106 Grade B carbon steel pipe I1.3-10/90-F2.3.4

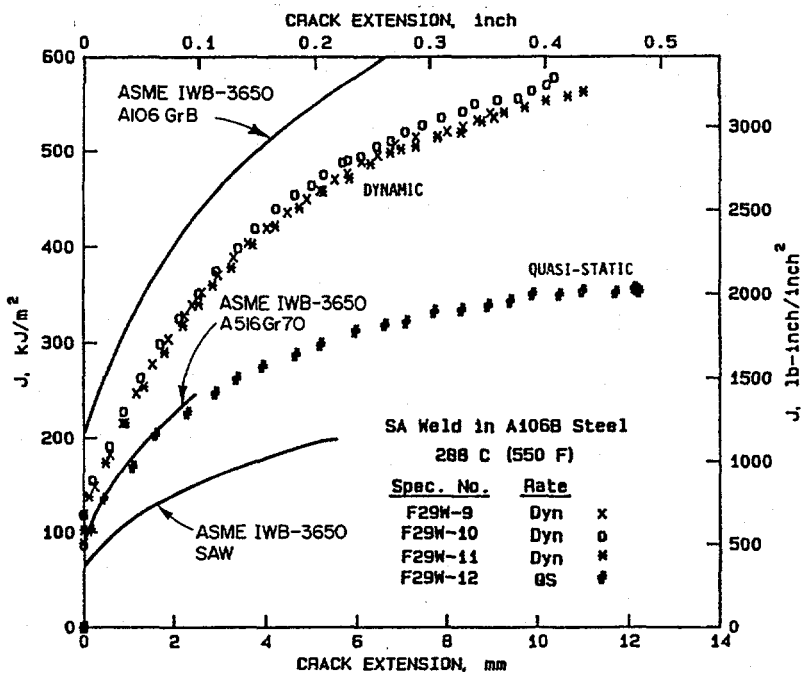

Figure 2.20 J-resistance curves for compact specimens for a submerged-arc weld (DP2-F29W) in A106 Grade B carbon steel pipe tested at 288 C (550 F) I1.3-10/90-F2.3.5

Table 2.11 Summary of J_i and dJ/da values for ASTM A358, Type 304 stainless steel pipe (DP2-A8)

Specimen Identification Number	Percent Side-Grooves	Rate[a]	J at Initiation, kJ/m²	J at Initiation, in-lb/in²	dJ/da, MJ/m³	dJ/da, in-lb/in³
A8-41	0	QS	710	4,050	610	88,500
A8-43	20	QS	623	3,555	524	76,000
A8-12A	20	QS	854	4,875	481	69,720
A8-9A	20	Dyn	1,302	7,430	500	72,470
A8-10A	20	Dyn	943	5,385	566	82,060
A8-11A	20	Dyn	1,399	7,985	388	56,320

(a) QS = quasi-static, Dyn = dynamic.

Table 2.12 Summary of J_i and dJ/da values for submerged-arc weld (DP2-F29W) in ASTM A106, Grade B carbon steel pipe

Specimen Identification Number	Percent Side-Grooves	Rate[a]	J at Initiation, kJ/m^2	J at Initiation, in-lb/in^2	dJ/da, MJ/m^3	dJ/da, in-lb/in^3
F29W-12	20	QS	82	470	68	9,860
F29W-9	20	Dyn	118	675	109	15,760
F29W-10	20	Dyn	131	745	102	14,820
F29W-11	20	Dyn	127	725	94	13,620

(a) QS = quasi-static, Dyn = dynamic.

Also shown in Figure 2.20 are the ASME IWB-3650 reference J-R curves for ferritic steel base metals and a ferritic steel submerged-arc weld. The ASME curve for the submerged-arc weld in Figure 2.20 is based on results obtained in the Degraded Piping Program in which a weld was prepared in a 25.4 mm (1 inch) plate of A516 Grade 70 steel, using the same procedures as for the weld studied here. J-R curves for 1T C(T) specimens machined from that earlier weld can be found in Figures 3.3.17 and 3.3.18 of Reference 2.9. Note in Figure 2.20 that the data from both quasi-static and dynamic tests on specimens machined from the carbon steel weld from this program lie above the ASME curve for a submerged-arc weld and, even in the worst case (quasi-static tests), are approximately equal to the ASME curve for A516 Grade 70 base metal.

It is also of note in comparing Figure 2.17 with Figure 2.20 that the quasi-static J-R curve for the base metal is higher than that for the weld, but the dynamic J-R curve for the base metal is lower than the dynamic J-R curve for the weld.

2.3.4 Stainless Steel SAW

J-resistance curves for L-C oriented C(T) specimens machined from submerged-arc weld metal (DP2-A8W) in ASTM A358 Type 304 stainless steel pipe are presented in Figure 2.21 and values of J_i and dJ/da are summarized in Table 2.13. The results indicate that the submerged-arc weld was affected somewhat more than was the base metal when the displacement rate was increased by a factor of approximately 4,400. J_i was more than doubled and dJ/da was increased by about 40 percent as a result of dynamic loading. Notice also in Figure 2.21 that the toughness of this submerged-arc weld metal was much lower than that of the base metal. That finding is in agreement with results obtained for Type 304 plate material, both base metal and submerged-arc weld metal, in the Degraded Piping Program (Ref. 2.9). The submerged-arc weld in Reference 2.9 was made by the same procedures as were used in this program and exhibited quasi-static J-R curves in 1T C(T) specimens that were very similar to that for the stainless steel weld studied here, whose quasi-static J-R curve is shown in Figure 2.21 (see Figures 3.3.14 and 3.3.15 in Reference 2.9).

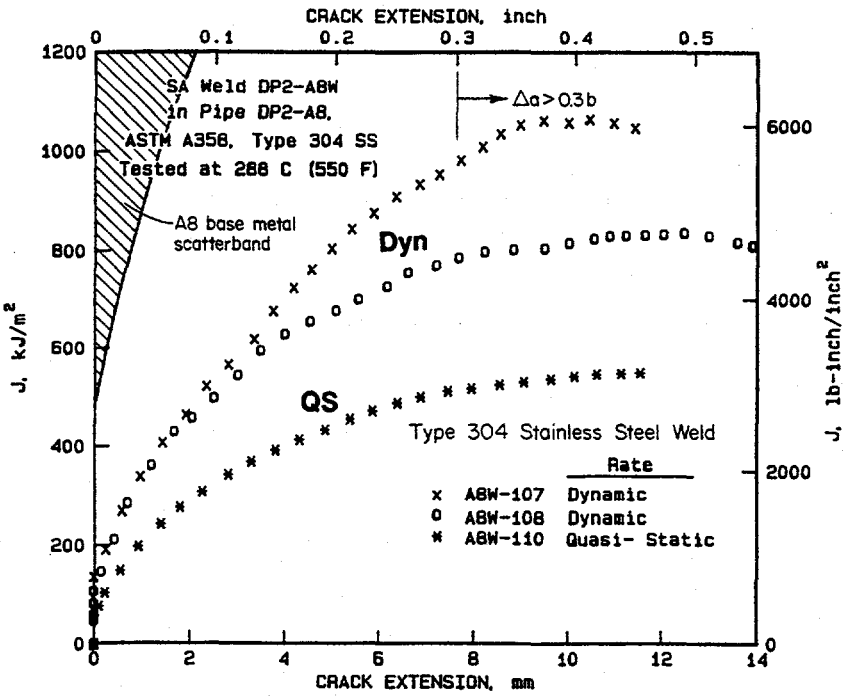

Figure 2.21 J-resistance curves at 288 C (550 F) for compact specimens from a submerged-arc weld (DP2-A8W) in an A358 Type 304 stainless steel pipe

I1.3-10/90-F2.3.6

Table 2.13 Summary of J_i and dJ/da values for submerged-arc weld (DP2-A8W) in ASTM A358, Type 304 stainless steel pipe (tested at 288 C [550 F]); L-C orientation

Specimen Identification Number	Percent Side-Grooves	Rate[a]	J at Initiation, kJ/m²	J at Initiation, in-lb/in²	dJ/da, MJ/m³	dJ/da, in-lb/in³
A8W-110	20	QS	55	315	135	19,550
A8W-107	20	Dyn	140	800	180	26,140
A8W-108	20	Dyn	116	660	205	29,700
A8W-111	20	Dyn	(b)	(b)	(b)	(b)

(a) QS = quasi-static, Dyn = dynamic.

(b) No electric potential data were obtained for Specimen No. A8W-111; hence the J-R curve could not be calculated.

2.3.5 Artificially Aged Cast Stainless Steel

Only a few small pieces of material were available for fabrication of C(T) specimens from the artificially aged CF8M cast stainless steel pipe (DP2-A40). The size of the pieces was such that three full-size 0.8T specimens and one 1T planform-size specimen, 22.9-mm (0.9-inch) thick could be obtained.

J-resistance curves are presented in Figure 2.22 and values of J_i and dJ/da are summarized in Table 2.14. The results indicate that increasing the displacement rate by a factor of about 4,300 increased J_i by approximately 30 percent and dJ/da by nearly 60 percent.

For comparison, the wrought stainless steel (DP2-A8) and the stainless steel submerged-arc weld (DP2-A8W) J-R curve scatter bands are also given in Figure 2.22. This comparison shows that this artificially aged cast stainless exhibited a toughness level that was comparable to that of submerged-arc weld metal in Type 304 stainless steel (A8W), but significantly lower than that of Type 304 stainless steel base metal (A8). Note that ASME Section XI does not have a reference J-R curve for cast stainless steel, but only requires the ferrite number to be less than 20. Under those requirements, a limit-load analysis is used for cast stainless steel in Article IWB-3640. Framatome reported the ferrite content for this material to be approximately 20 percent by volume.

2.4 Dynamic Modulus Test

2.4.1 A710 Carbon Steel Pipe Loop Material

From the results of some of the early quasi-static tensile tests on specimens machined from the 406-mm (16-inch) diameter, Schedule 100, ASTM A710, Grade A, Class 3, low-carbon, age-hardening alloy steel pipe (IP-F3), the Young's modulus of the pipe loop material appeared to be unrealistically low - 130 to 180 GPa (19 to 26 x 10^6 psi). Additional tests were conducted using a finer resolution extensometer; these gave a modulus of 160 to 165 GPa (23 to 24 x 10^6 psi). Again, these values seemed low. Because modulus is such an important factor in predicting the behavior of the pipe and in converting measured strains to bending moments, a direct determination of modulus as a function of temperature was made using a dynamic modulus device.

In a dynamic modulus measurement, the resonant frequency of a vibrating specimen is measured. Knowing the mass of the specimen and its geometry, and making corrections for thermal expansion, the modulus of the specimen can be inferred from the frequency equation for the specimen. The results are shown in Figure 2.23. At room temperature, the modulus was 210 GPa (30.5 x 10^6 psi), while at 289 C (552 F) the modulus was 195 GPa (28.3 x 10^6 psi). These data are consistent with published data for other steels, and thus seem more believable than the modulus values derived from the tensile stress-strain curves.

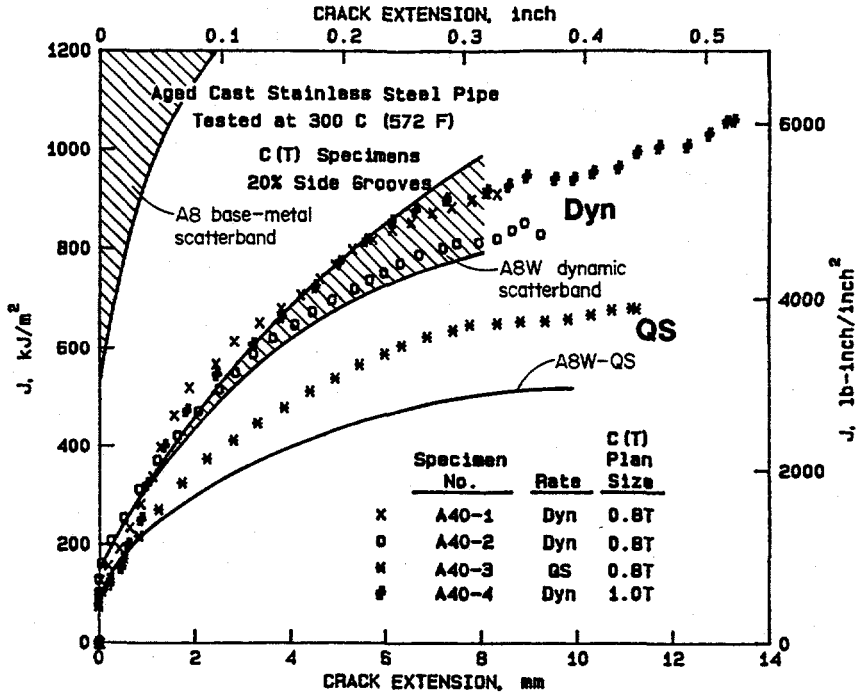

Figure 2.22 J-resistance curves at 300 C (572 F) for compact specimens from an aged A351 Grade CF8M cast stainless steel pipe (DP2-A40) I1.3-10/90-F2.3.7

Table 2.14 Summary of J_i and dJ/da values for aged ASTM A351 Grade CF8M cast stainless steel pipe (DP2-A40) tested at 300 C (572 F)

Specimen Identification Number	Size	Percent Side-Grooves	Rate[a]	J at Initiation, kJ/m²	J at Initiation, in-lb/in²	dJ/da, MJ/m³	dJ/da, in-lb/in³
A40-3	0.8T	20	QS	88	501	147	21,330
A40-1	0.8T	20	Dyn	109	621	253	36,700
A40-2	0.8T	20	Dyn	146	833	181	26,320
A40-4	1T	20	Dyn	93	553	263	38,150

(a) QS = quasi-static, Dyn = dynamic.

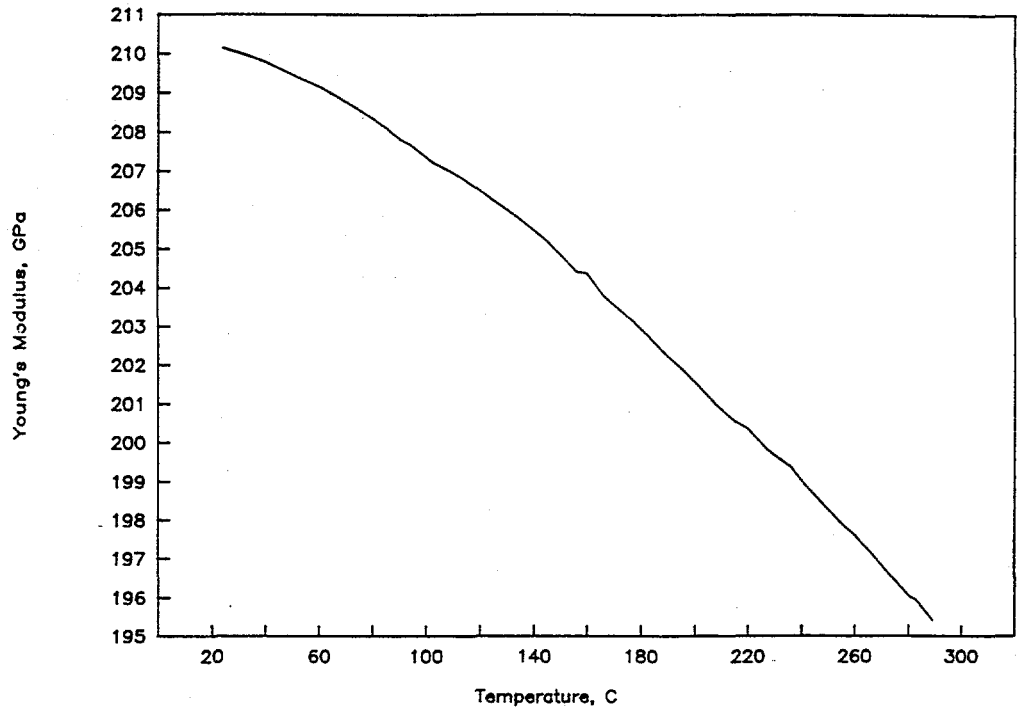

Figure 2.23 Dynamic modulus data for ASTM A710, Grade A, Class 3 pipe loop material (Pipe IP-F3) DRB/1.3-1/FA-7

2.5 Discussion of Results

2.5.1 Discussion of Dynamic-Rate Effects on Properties

The effect of increasing the rate of displacement in tensile and C(T) tests conducted at 288 C (550 F) for materials used in Subtask 1.3 is summarized in Table 2.15. Included in Table 2.15 are results from two 152-mm (6-inch) diameter pipes investigated in Subtask 1.1, A106B carbon steel (DP2-F30) and A376 Type 304 stainless steel (DP2-A23). Table 2.15 shows the approximate percentage change in tensile properties as the strain rate was increased by a factor of approximately 10^4 to 10^5, and the approximate percentage change in several toughness parameters (J_i, J at 2 mm of crack extension, and dJ/da) as the value of dJ/dt was increased by a factor of 2,500 to 4,400 times that in the quasi-static tests.

The results shown in Table 2.15 reveal that the carbon steel materials responded to increasing strain rate at 288 C (550 F) in a significantly different manner than did the stainless steel materials. The carbon steels, because of the fact that each was susceptible to dynamic strain aging, showed marked effects of strain rate on tensile strength. Of special importance to nuclear piping applications, the tensile strength of all three carbon steels and the fracture elongation of the two base metals were lowered substantially by the increased strain rate. The stainless steels, on the other hand, showed little change in either strength or elongation, except for the cast stainless steel, which showed increased elongation with increasing strain rate. Each of the stainless steels did exhibit a higher yield strength with increasing strain rate, whereas the yield strength of the carbon steels was virtually unchanged.

Table 2.15 Summary of dynamic effects on tensile properties and fracture resistance

Pipe Ident. Number	Type of Steel	Approximate Change in Indicated Property as Strain Rate was Increased[b]					
		Yield Strength	Ultimate Tensile Strength	Elongation	J_i	J at $\Delta a = 2mm$	dJ/da[b]
DP2-F30	A106B carbon steel	0	-20	-35	-15	-20[c]	+15
DP2-F29	A106B carbon steel	0	-30	-15	-35	-40	-45
DP2-F29W	Submerged weld in A106B carbon steel	0	-20	+5	+55	+70	+50
DP2-A23	A376 Type 304 stainless steel	+35	+5	+5	+5	+15	+20
DP2-A8	A358 Type 304 stainless steel	+10	-5	+10	+65	+20	-5
DP2-A8W	Submerged-arc weld in A358 Type 304 stainless steel	+10	-5	-10	+135	+60	+45
DP2-A40	Aged A351 Grade CF8M cast stainless steel	+25	0	+30	+30	+40	+60

(a) For tensile tests, strain rate was increased from approximately 10^{-4} s^{-1} to 10 s^{-1}; for C(T) tests, dJ/dt in dynamic tests was 2,500 to 4,400 times that in quasi-static tests.
(b) dJ/da was determined over the crack-extension range from 0.15 to 1.5 mm (0.006 to 0.060 in.).
(c) The change in J was determined at $\Delta a = 0.5$ mm because of limited stable crack growth in this material.

The observed differences between the two types of materials in tensile tests were carried over into the J-R curve tests as well. Each of the stainless steels increased in toughness as dJ/dt was increased, as evidenced by J values after 2 mm of crack extension and by dJ/da values.* In some cases, the gain was modest and in other cases the gain was substantial. In contrast to the relatively consistent behavior among the stainless steels, the behavior among the carbon steels was inconsistent in the C(T) tests. One of the carbon steels (152-mm [6-inch] diameter A106B, DP2-F30), exhibited a relatively modest reduction in crack-initiation toughness and a modest increase in dJ/da at the higher displacement rate, and experienced crack jumps at both rates. The carbon steel material used in this subtask (DP2-F29) showed a sizable reduction in toughness at the higher rate; however, the crack jumps observed in low displacement rate tests were not observed in the high rate tests. Finally, the submerged-arc weld material showed an impressive increase in toughness at the higher displacement rate, and was not susceptible to crack jumps at either rate.

The reasons for the different strain rate response of the three carbon steel materials are not known with certainty. It can be hypothesized that the differences in response are the result of differences in the way in which interstitial atoms (nitrogen and carbon) interact with dislocations at 288 C (550 F) to produce the many unusual effects associated with dynamic strain aging. These differences could give rise to different temperature- and strain-rate dependence of dynamic strain aging among the three steels. Thus, their strength-versus-temperature curves might show peak strengths occurring at different temperatures, or they might display serrations on the stress-strain curve over different temperature ranges, and so on.

* One exception was the 406-mm (16-inch) diameter stainless steel pipe (DP2-A8) which showed a slight decrease in dJ/da.

Even though the causes of the different behaviors among the three carbon steels cannot be adequately explained at this time, it is important to note that the results were clear in one regard; one of the carbon steels tested (406 mm [16 inch] diameter A106B) exhibited significant losses of both strength and toughness at the higher displacement rate. That result means that we must assume a similar response in any other carbon steel pipe unless contrary evidence is available.

In addition to measuring displacement-rate effects, this investigation confirmed a result obtained in the Degraded Piping Program, namely, the fracture resistance of submerged-arc welds in stainless steels is much poorer than that of base metal. The stainless steel SAW studied in this program for example, displayed a J_i value that was only about 10 percent of the value for its base metal counterpart, and of about the same magnitude as that for the carbon steel SAW.

2.5.2 Discussion of Cyclic Loading Effects

A literature review was conducted to assess the influence of cyclic loading on ductile fracture toughness from both experimental and analytical perspectives. Conclusions and recommendations from that review are summarized here.

2.5.2.1 Conclusions From Review of Experimental Work

The effect of cyclic loading on the J-resistance curve appears to be reasonably well understood and predictable for an R-ratio that is greater than zero. For those cases, total crack extension is given by $\Delta a_{mono} + \Delta a_{cyclic}$ where the value for Δa_{cyclic} is estimated from fatigue crack growth analyses. If Δa_{cyclic} is a small fraction of Δa_{mono}, which is the case when the number of unloading cycles is small, the net result on the cyclic J-R curve will be insignificant. However, the cyclic J-R curve can be significantly lower than the monotonic J-R curve if many cycles are applied.

The effect of cyclic loads on the J-R curve is less clear when unloading cycles are carried into the compression regime (i.e., $R < 0$). For these cases, the total crack extension exceeds $\Delta a_{mono} + \Delta a_{cyclic}$, where Δa_{cyclic} is estimated from da/dN versus ΔJ curves. That result suggests that degradation of the material properties at the crack tip occurs during compressive loading, which leads to reduced fracture toughness on the next loading cycle. At the present time, no rationale has been developed to bring the measured crack extension and the estimated crack extension into agreement.

The value of J_{Ic} obtained in cyclic J-R curve tests will be lower than that obtained monotonically only if load cycling begins before the point of monotonic crack initiation and if the value of Δa_{cyclic} prior to that point is significant. Such was the case in one investigation where the cyclic load J_{Ic} value was only about one-third of the monotonic value.

Cyclic load effects on J-R curves have not been extensively studied, so there is a paucity of data on strain rate effects, temperature effects, and negative R-ratio effects.

2.5.2.2 Conclusions From Analytical Considerations

A review of fracture mechanics parameters has shown that J based on deformation theory cannot account for irreversible processes during cyclic loading. Hence, a J-R curve calculated from the load-displacement envelope of a cyclic test may not give a unique material property. To use the current methodology, it would be necessary to conduct the J-R curve test using the anticipated service load history. Alternatively, it may be possible to develop a correlation between standard monotonic J-R curves and cyclic J-R curves.

Such correlations may depend on: (1) material toughness, (2) R-ratio, (3) frequency of unloading, (4) temperature, and (5) strain rate. It would be desirable to develop a model that will account for cyclic compressive loading. Another alternative is to pursue a more advanced fracture mechanics parameter capable of accounting for irreversible processes during cyclic loading. Unfortunately, most approaches require numerical solutions by finite element analysis. The versions of integral parameter based on the incremental theory of plasticity (for instance, T* and $\hat{J}$) are possible approaches that may evolve to simpler estimation schemes. Until a more advanced parameter for incremental plasticity fracture mechanics is developed, empirical correlations will have to be developed for current J-R curve methods to handle cyclic loading.

2.6 References

2.1 Marschall, C. W., Landow, M. P., and Wilkowski, G. M., "Loading Rate Effects on Strength and Fracture Toughness of Pipe Steels Used in Task 1 of the IPIRG Program," NUREG/CR-6098, October 1993.

2.2 Wilkowski, G. M., and others, "Degraded Piping Program - Phase II, Summary of Technical Results and Their Significance to Leak-Before-Break and In-Service Flaw Acceptance Criteria," March 1984 - January 1989, NUREG/CR-4082, Vol. 8, March 1989.

2.3 Chopra, O. K, "Estimation of Fracture Toughness of Cast Stainless Steels During Thermal Aging in LWR Systems," NUREG/CR-4153, Rev. 1, August 1994.

2.4 Kanninen, M. F., and others, "Instability Predictions for Circumferentially Cracked Type 304 Stainless Steel Pipes Under Dynamic Loadings," Final Report on EPRI Project T118-2, by Battelle Columbus Laboratories, EPRI Report Number NP-2347, April 1982.

2.5 Baird, J. D., "Strain Aging of Steel -- A Critical Review," *Iron and Steel*, pp 450-457, Sept. 1963.

2.6 Keh, A. S., Nakada, Y., and Leslie, W. C., "Dynamic Strain Aging in Iron and Steel," in *Dislocation Dynamics*, A. R. Rosenfield, and others, Eds., McGraw-Hill, New York, pp 381-408, 1968.

2.7 Manjoine, M. J., "Influence of Rate of Strain and Temperature on Yield Stresses of Mild Steel," *J. of Applied Mechanics*, December, pp A211-A218, 1944.

2.8 Meyzaud, V., Ould, P., Balladon, P., Bethmont, M., and Soulat, P., "Tearing Resistance of Aged Cast Austenitic Stainless Steels," *NUCSAFE 88*, Avignon, France, October, 1988.

2.9 Wilkowski, G. M. and others, "Degraded Piping Program--Phase II," Sixth Program Report, October 1986 - September 1987, by Battelle Columbus Laboratories, NUREG/CR-4082, Vol. 6, April, 1988.

3.0 PIPE-SYSTEM EXPERIMENTS

In this section, the six pipe experiments conducted as part of Subtask 1.3 of the IPIRG program will be discussed.

3.1 Test Matrix

The pipe diameter (406 mm [16 inch]) for the pipe-system experiments was chosen because previous programs (Ref. 3.1) tended to evaluate smaller diameter pipes (152 mm [6 inch]) for which fully plastic (limit-load) conditions would be expected regardless of the toughness of the material. Past research (Ref. 3.2) has clearly demonstrated that both material toughness and pipe size influence whether or not a cracked pipe section will reach fully plastic conditions. By evaluating larger diameter pipes, it was anticipated that the fracture process for the higher toughness steels would be governed by fully plastic (limit-load) conditions and that it would be governed by elastic-plastic fracture mechanics (EPFM) for the lower toughness steels. The wall thickness (25 mm [1 inch]) or schedule (Schedule 100) was chosen because it met Section III schedule requirements for pressure stress and the resultant pipe radius-to-wall thickness ratio (R/t) is close to that found in either Boiling Water Reactor (BWR) or Pressurized Water Reactor (PWR) piping systems. The piping in BWRs tends to be Schedule 80 while the piping in PWRs tends to be Schedule 160.

The test matrix for Subtask 1.3 of the IPIRG program is shown in Table 3.1. The test matrix consisted of six experiments, one series of uncracked pipe experiments and five cracked pipe experiments. The uncracked experiments had both a room temperature and an elevated temperature phase.

Table 3.1 Test matrix for Subtask 1.3

Experiment Number	Test Material	Crack Geometry
1.3-1	ASTM A710, Grade A, Class 3 Carbon Steel	Uncracked
1.3-2	A106 Grade B Carbon Steel Base Metal	Internal Surface Crack
1.3-3	SA-358 Type 304 Stainless Steel Base Metal	Internal Surface Crack
1.3-4	SA-106 Grade B Carbon Steel Submerged-Arc Weld	Internal Surface Crack
1.3-5	SA-358 Type 304 Stainless Steel Submerged-Arc Weld	Internal Surface Crack
1.3-7	SA-351 Grade CF8M Centrifugally Cast Aged Cast Stainless Steel	Internal Surface Crack

The uncracked pipe room temperature testing involved: (1) an assessment of the piping system response due to a pressurization to 15.5 MPa (2,250 psi) i.e., PWR pressure, (2) an eigenvalue assessment to determine the natural frequencies and mode shapes of the piping system, (3) a series of piping system damping evaluations, and (4) an assessment of the piping system response due to a dynamic excitation. The elevated temperature uncracked pipe testing involved: (1) an eigenvalue assessment, (2) an assessment of the piping system response due to a static push, and (3) an assessment of the piping system response due to a dynamic excitation.

The five cracked pipe experiments involved both an assessment of the piping system response, as well as an assessment of the fracture behavior of flawed pipe sections of different materials. The materials evaluated were a carbon steel base metal, a stainless steel base metal, a carbon steel weld, a stainless steel weld, and an aged cast stainless steel. For each of these materials, a comparison quasi-static pipe fracture experiment, using the same pipe and nominal crack size, had been previously conducted as part of the Degraded Piping Program - Phase II (Ref. 3.2) or in another Battelle program sponsored by the Electric Power Research Institute (EPRI) (Ref. 3.3). Relevant data from these studies are discussed in Section 4.1 of this report.

3.2 System Design Analyses

The pipe experiments conducted in IPIRG Subtask 1.3 were significantly more complex and technically sophisticated than those performed in earlier programs. The complexity of these experiments dictated that a detailed system design and analysis be performed to define the pipe configuration and to provide information for selecting components for the piping system.

There was an initial design effort which focussed solely on finding a piping system design that could reasonably be expected to be able to fail the test pipes, could be adequately modeled mathematically, and could be built within the cost constraints of the program. As the program progressed, and as the design evolved, it was analytically demonstrated that the above objectives could be met. However, an additional constraint was imposed on the design that there be a nearly equal mix of inertial- and displacement-controlled loads at the crack. This additional constraint forced a second design effort. In addition to the actual design work, there was an extensive effort to assess and ensure the accuracy of the analysis methods themselves.

3.2.1 Analysis Methods

A basic structural analysis capability was required to complete the design study. In addition, several supporting analytical developments or models were required to provide the data inputs to the structural analysis or to post-process the raw results from the analyses into system specifications.

3.2.1.1 Basic Structural Analysis Capability

In order to design the IPIRG Subtask 1.3 pipe loop, a basic structural analysis capability was needed. The requirements for the basic capability were:

- Linear and nonlinear capability
- Static, time-history, and natural frequency analyses
- Prescribed displacements, thermal load, internal pressure, and dead-weight loading.

The only reasonable alternative that embodied all of these features in a single package was finite elements.

After an in-depth examination of various finite element computer programs in terms of capabilities, maturity of the code, and estimated costs to conduct the analyses, it was decided that the commercial computer program ANSYS®, by Swanson Analysis Systems, would be used to design the IPIRG Subtask 1.3 pipe system. An Apollo Domain workstation served as the host computer.

The system models developed with the ANSYS® program used typical features found in many basic finite element programs; beam-type pipe elements (curved and straight, as necessary), lumped masses, Rayleigh structural damping, elbow flexibility factors, and time-history dynamic equation of motion solvers. In addition, some nonlinear capabilities of ANSYS® were also used, namely a nonlinear model of the crack, and to some extent, plasticity.

3.2.1.2 Nonlinear Modeling of Cracked Pipe Sections

In order to analyze the behavior of a piping system containing cracks, a simple nonlinear representation of the crack was developed. The model, a one-dimensional (i.e., moment versus rotation) nonlinear stiffness, accounted for the local plastic deformation due to the crack and stable crack growth which occurred during loading.

The starting point for the crack section modeling was static load-displacement test data for circumferentially cracked pipe under four-point bending. In calculating the stiffness of a cracked section, the material and crack section geometry (i.e., pipe diameter, thickness, crack length, and crack depth) for the proposed dynamic analysis had to be reasonably similar to conditions for a static bend test for which data were available. In addition to having static load-displacement data for a given crack geometry, several assumptions were made to generate the crack stiffness:

- For low-cycle high-amplitude loading, the cyclic load effect on the circumferential crack growth was assumed small; growth was assumed to be dominated by ductile tearing under increasing load amplitude.

- High strain rate effects on crack growth and on the constitutive relationship were ignored, even though they may tend to influence crack growth and the plastic flow to some extent for some materials. (In later pretest predictions, dynamic stress-strain and J-R curves were used to calculate moment-rotation response of the crack.)

- Only a separation mode (Mode I) of crack propagation under bending was assumed. This implies that the crack section is considered to be rigid in all degrees of freedom except the rotation corresponding to the crack opening.

- The rotational deformation due to the crack and relevant plastic deformations are confined to the crack section.

With these assumptions, and the static test data, a procedure for generating a bending moment, M, versus rotation, ϕ, due to a crack was developed.

Using the nomenclature shown in Figure 3.1 for a four-point bend test, the moment at the cracked section is

$$M = M_a + \frac{W(S - 2\ell)}{4} \tag{3-1}$$

and the total rotation due to the crack is

$$2\phi = 2 \tan^{-1} [(1/M_a) (\delta - F(L-\ell)^2(L+2\ell)/(24EI) - C_s(F+W))] \tag{3-2}$$

where

F	=	applied load
2W	=	pipe weight
S	=	total pipe length
L	=	length of outer span
ℓ	=	length of inner span
M_a	=	(L-ℓ)/2
δ	=	applied displacement
E	=	modulus of elasticity
I	=	second moment of area
C_s	=	test system compliance.

With suitable test data, a moment-rotation curve for a cracked pipe can be developed that can be used as the input for a finite element analysis. Also for later pretest predictions, the SC.TNP surface-cracked pipe J-estimation scheme developed as part of the Degraded Piping Program (Ref. 3.2), was used to develop the moment-rotation response for input into the finite element analysis.

3.2.1.3 Modifications to Cracked Pipe Section Model

The moment-rotation curve as described above provided the basic stiffness for a cracked section. At times, however, it was necessary to make modifications to the basic curve to establish an unknown machine compliance, to account for a difference in temperatures from the static test data and the proposed pipe-system test temperature, or to estimate the effect of internal pressure on a crack. In these cases, simple adjustments were made.

The method used to establish an unknown machine compliance was to use crack-mouth-opening (CMO) data as an independent measure of rotation and to adjust the compliance in Equation 3-2 so that the rotations from Equation 3-2 would be consistent with the CMO-based rotation. In equation form, and with respect to Figure 3.2, the rotation from CMO was assumed to be

$$2\phi_{cmo} = 2 \sin^{-1} [CMO/[2(D-t-x)]] \tag{3-3}$$

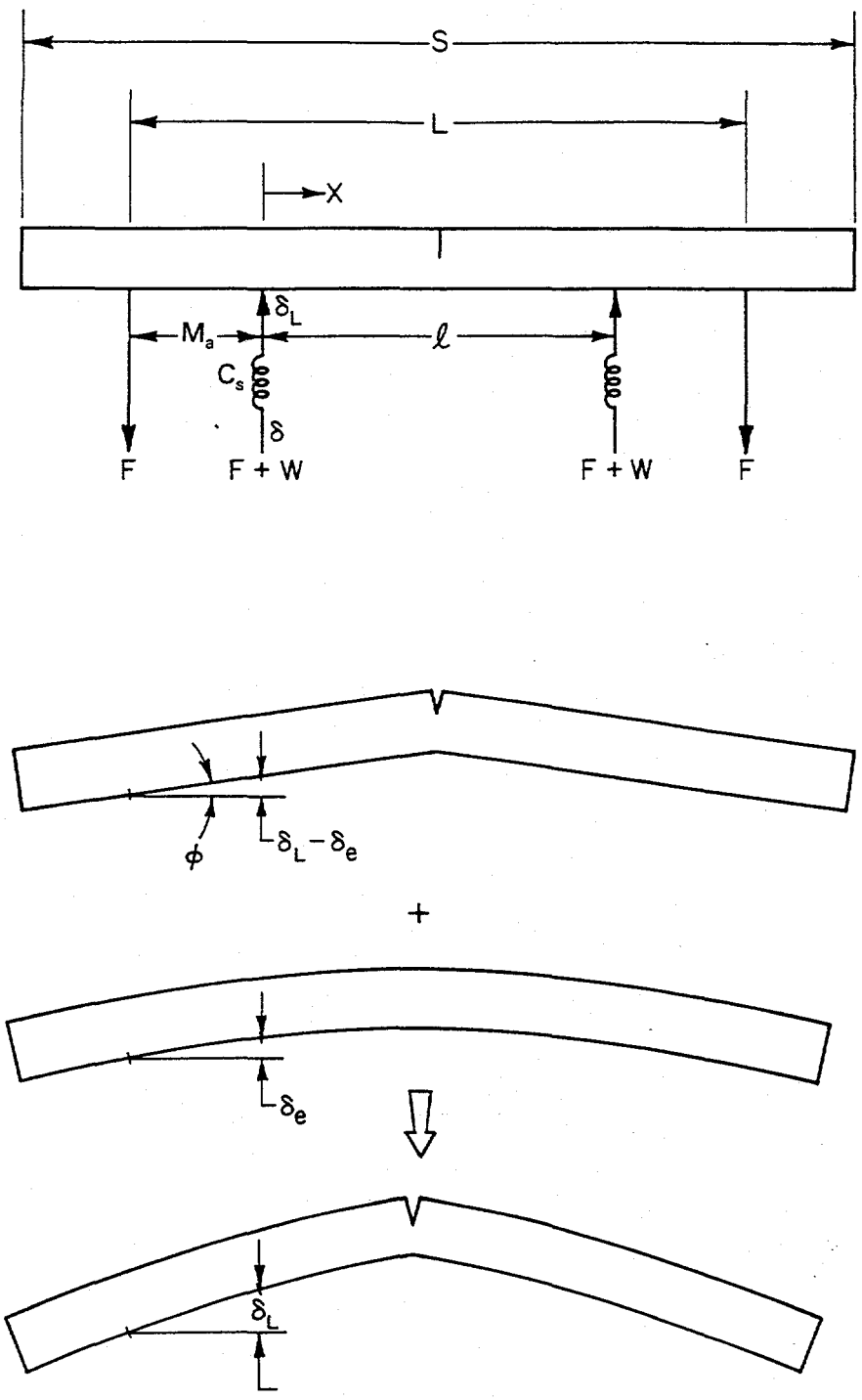

Figure 3.1 Static four-point bend test nomenclature

I1.3-10/90-F3.1

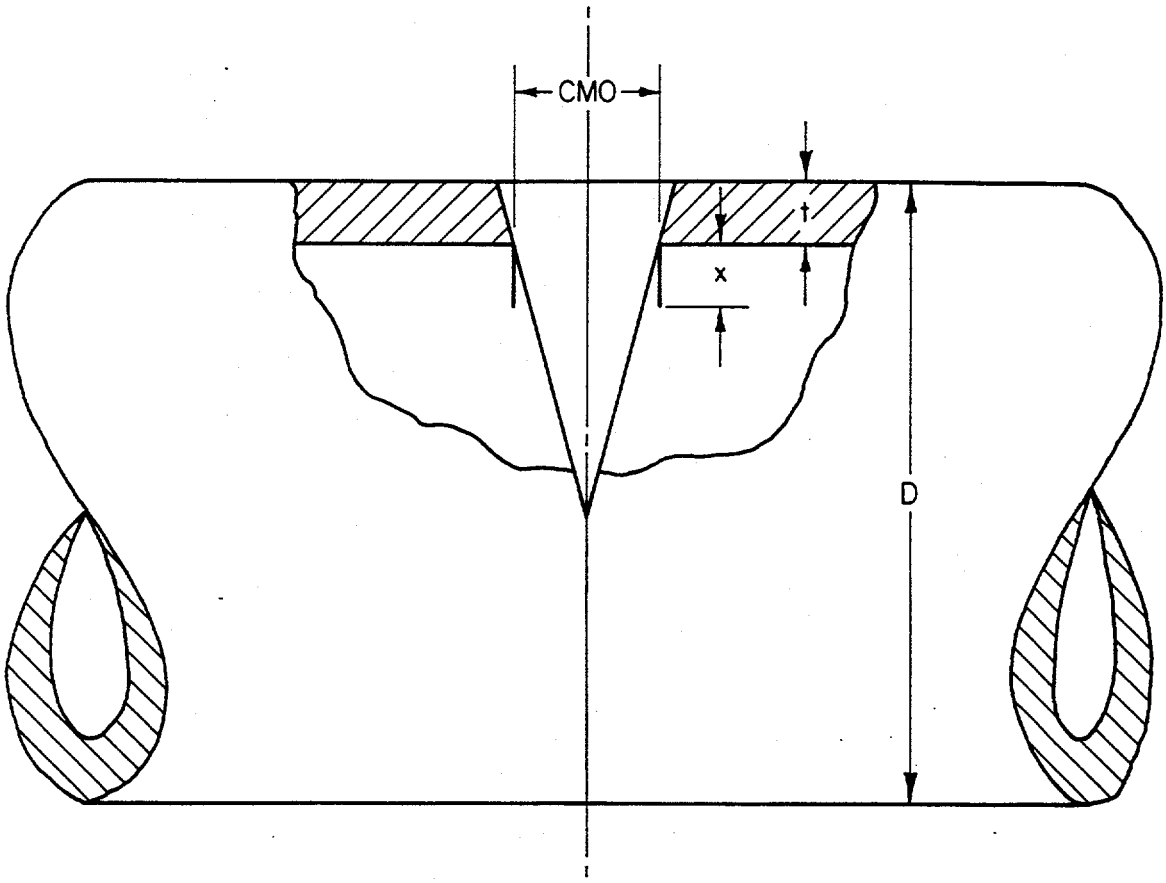

Figure 3.2 Nomenclature for crack rotation in terms of crack-mouth opening (CMO)
I1.3-10/90-F3.2

where

CMO	= crack mouth opening
D	= pipe diameter
t	= pipe wall thickness
x	= height of CMO measurement device from pipe wall.

Adjusting the compliance in Equation 3-2, the slope of the moment-rotation curve in the linear regime was forced to be consistent with Equation 3-3.

To accommodate differences in temperatures between quasi-static test data and the planned IPIRG Subtask 1.3 test conditions, the moment in the moment-rotation curve was multiplied by the ratio of the flow stresses at the respective temperatures.

Many of the Degraded Piping Program tests did not include pressure. As a consequence, a correction to the moment-rotation curve was needed to include pressure effects. Because the moment-rotation curve for a crack is basically a constitutive relationship, including the effect of pressure in the moment-rotation curve is not consistent, because pressure is a load. However, because the model of a crack used for the pretest design was only one dimensional, i.e., it does not respond to the axial load caused by pressure, the effect of pressure on crack separation could only be modeled by a reduction in the moment-carrying capacity of the crack by lowering the moment-rotation curve. To include the effect of pressure on the crack for the pretest design, the moments in the moment-rotation curve were all multiplied by the ratio of the Net-Section-Collapse analysis predicted moments with and without pressure.

3.2.1.4 Finite Element Implementation of Pipe Cracks

The basic approach used to model the flaw in the pipe is shown in Figure 3.3. Using load-displacement data for a static test of a flaw of the same size and the same material as would be used in the IPIRG tests, a moment-rotation curve for the crack was established as described above. This moment-rotation curve considered the crack in complete isolation, with all compliance due to the test machine and main body of the pipe removed. The resulting moment-rotation of the flaw then became the defined response between two adjacent pipe elements at the crack location.

Implementation of the crack moment-rotation response in a finite element analysis basically required definition of a nonlinear spring. Within ANSYS®, the most convenient means of achieving this was with spring-slider elements, one of which is shown in Figure 3.4. The spring-slider element is a two node, two degree-of-freedom element with a linear spring and a friction slider in series. At low loads, the slider is locked and the two nodes behave as if they have a linear spring between them. When the spring load reaches $\pm F_{slide}$, the force between nodes I and J remains constant. If the spring-slider reaches the limiting force and then is unloaded, a permanent displacement will remain when the load is brought back to zero. Putting two or more spring-slider elements in parallel, with different stiffness and F_{slide} values, allows one to model a multilinear load deflection curve. Figure 3.5 illustrates the modeling of a 3-segment curve.

Under monotonically increasing load, a multilinear spring-slider representation of a crack follows the curve as shown in Figure 3.5. With load reversals, as in the Subtask 1.3 experiments, compressive yield and hysteresis effects become important. Referring to Figure 3.6, at the point of first unloading, the spring-slider model unloads along a line parallel to the slope of the initial segment of the defined moment rotation curve. Unloading continues along this line until the load reaches a value of $2F_{T1}$ below the load at which unloading took place. At this point the system unloads along a line parallel to the slope of the second segment. If the system continues unloading to a load level that is $2(F_{T2} - F_{T1})$ below the slope change (yield), the system unloads along a line parallel to the third segment. Subsequent yielding and load reversals continue with the same pattern.

The behavior of the spring-slider elements described above is a model of the Baushinger effect, i.e, kinematic hardening in a plasticity analysis. For the pretest design, the implication of using a model like this is that energy is absorbed at the crack under cyclic loading.

(1) Take static cracked pipe data from a quasi-static bend test

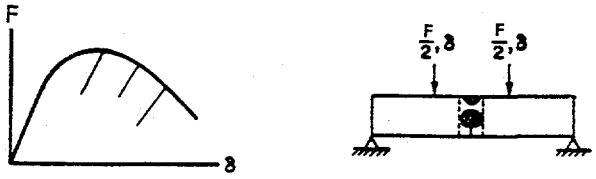

(2) Reduce F-δ into moment-rotation diagram only for the cracked pipe section

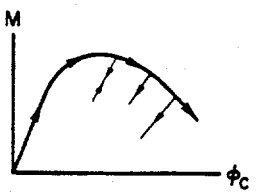

Crack (Growth) + Plasticity, Effects Included

(3) Incorporate incremental stiffness into the FEM code $[K]\{\Delta q\} + [C_s]\{\Delta \dot{q}\} + [m]\{\Delta \ddot{q}\} = \{\Delta F\}$

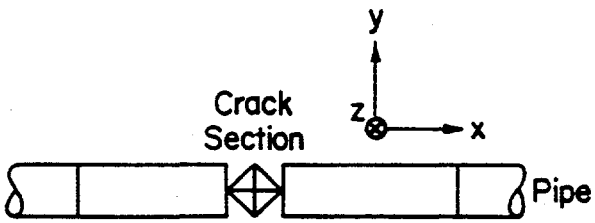

$$[K] = \begin{array}{c} \\ F_x \\ F_y \\ F_z \\ M_x \\ M_y \\ M_z \end{array} \begin{array}{c} \begin{array}{cccccc} u_x & u_y & u_z & \phi_x & \phi_y & \phi_z \end{array} \\ \begin{bmatrix} \infty & & & & & \\ & \infty & & -0- & & \\ & & \infty & & & \\ & & & \infty & & \\ & -0- & & & \infty & \\ & & & & & \frac{\partial M}{\partial \phi} \end{bmatrix} \end{array}$$

: positive definite

Figure 3.3 Nonlinear cracked pipe modeling

I1.3-10/90-F3.3

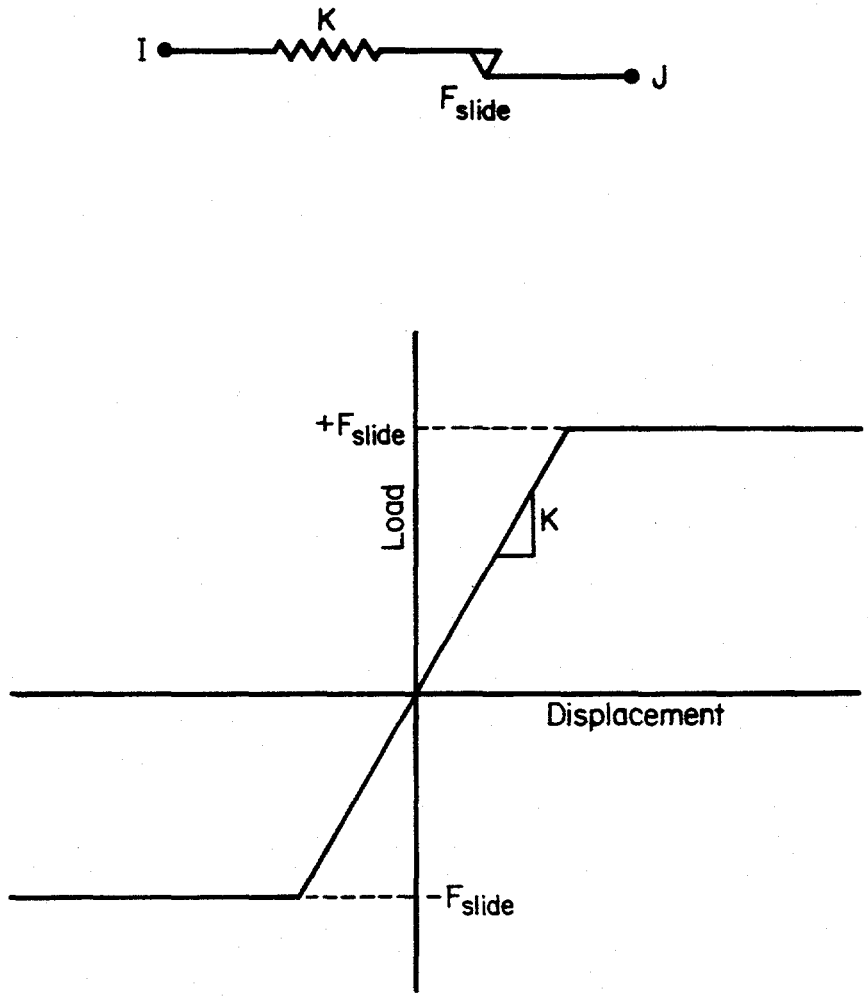

Figure 3.4 Basic spring-slider element

I1.0-9/87-F5

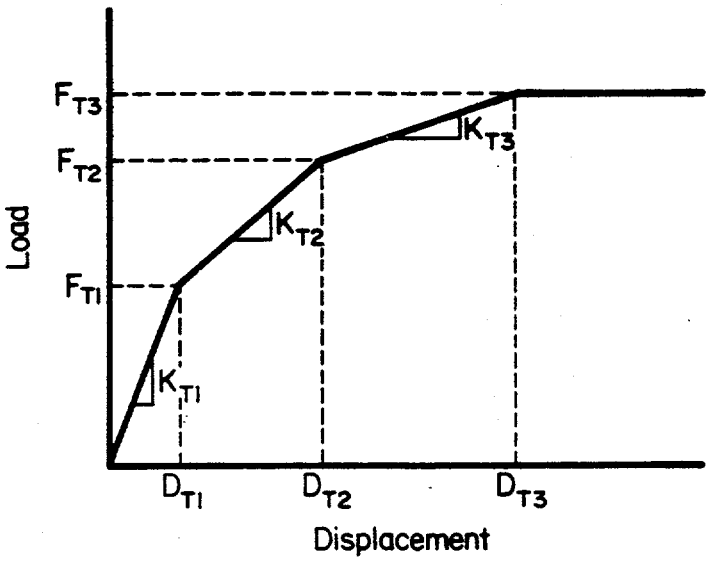

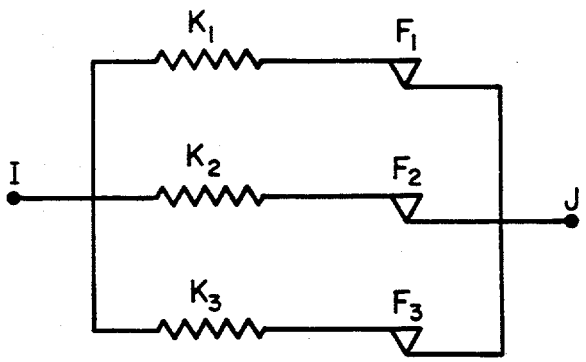

$$K_1 + K_2 + K_3 = K_{T1} \qquad F_1 + (K_2 + K_3)D_{T1} = F_{T1}$$

$$K_2 + K_3 = K_{T2} \qquad F_1 + F_2 + K_3 D_{T2} = F_{T2}$$

$$K_3 = K_{T3} \qquad F_1 + F_2 + F_3 = F_{T3}$$

Figure 3.5 Modeling of a multilinear load-displacement curve

I1.0-9/87-F6

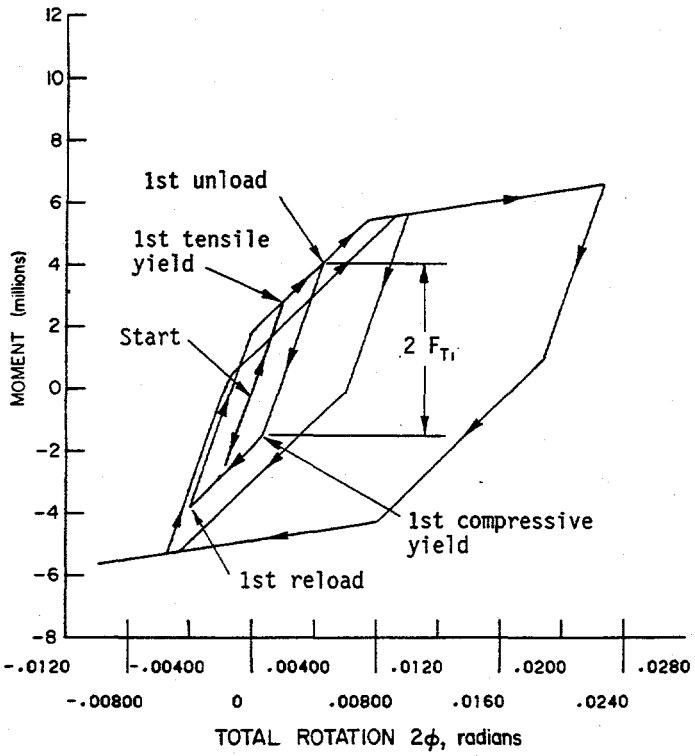

Figure 3.6 Spring-slider model of a crack under reversed loading
I1.3-10/90-F3.6

Given a moment-rotation curve for a particular crack, a multi-linear spring-slider model of the crack response was generated as described above (in this case, moment is the force and rotation in radians is the displacement). This multi-linear spring-slider model was then attached to a pair of coincident nodes at the crack location in the pipe model, coupling the two nodes together in the relative rotation bending degree of freedom of the attached pipe elements. The remaining five degrees of freedom; the two shears, the torsion, the axial displacement, and the other bending degree of freedom, were rigidly coupled with constraint equations. To accommodate crack closure in the nonlinear spring model, a very stiff spring was inserted that was "activated" when rotations tried to go negative.

The crack model as described above was used in all of the design analyses that included the crack. The model is quite simple, and as long as the loading does not take excessively large steps, closed hysteresis loops are traced on unloading and reloading as shown in Figure 3.7. Maximum moment in the crack occurs when all three spring-sliders are at the limiting slide force and the crack rotation becomes large. Details of the theory and development of the crack element are given in Reference 3.4.

3.2.1.5 Other Analytical Tools

In addition to the nonlinear crack model, several other analysis tools were developed. Among these were: (1) Fortran programs to calculate Rayleigh damping coefficients given system natural frequencies and damping ratios at those frequencies, (2) a servo-hydraulic system model that predicts the required rated servo-valve size and oil accumulator storage volume given load-displacement-time relationships for a

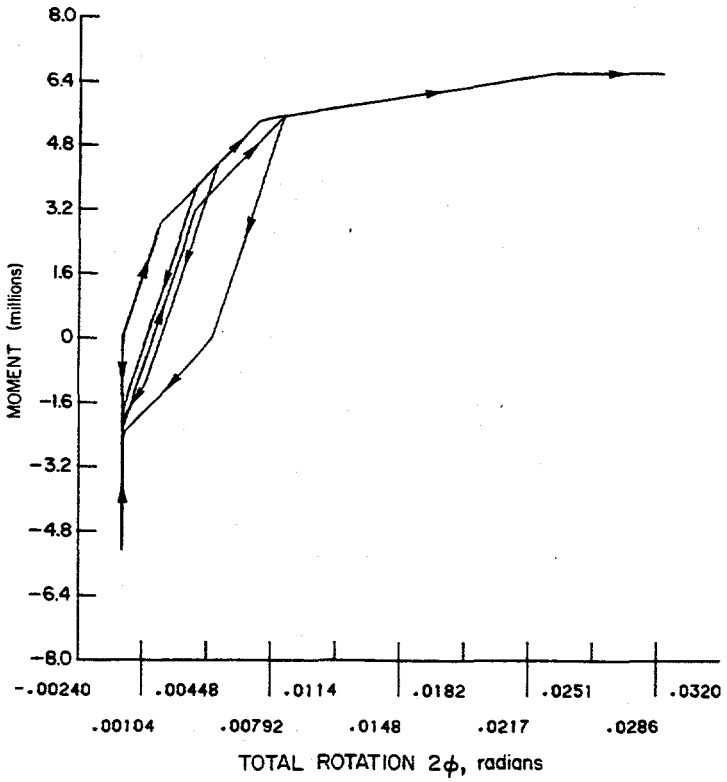

Figure 3.7 Typical moment-rotation behavior of multilinear spring-slider crack model including crack closure

I1.3-10/90-F3.7

hydraulic actuator, and (3) a program to calculate the spring stiffness and slide forces for the nonlinear crack model given a moment-rotation prescription.

3.2.2 Initial Design

The initial design of the Subtask 1.3 test system was an evolutionary process. Models were developed, analyses were conducted, results were reviewed, and changes were made to improve the design. Many configurations were considered, and some good ideas were abandoned for cost or fabrication difficulty reasons. The objective was to find a design that could: (1) reasonably be expected to be able to fail the test pipes, (2) be adequately modeled mathematically, and (3) be built within the cost constraints of the program.

3.2.2.1 Design Philosophy

The approach to performing the initial pretest design was based on the following four premises:

(1) The objective was to size components, not necessarily to predict detailed behavior of the pipe system during an actual test.

(2) In light of Item 1, analyses were only conducted to the point of achievement of maximum load (i.e., surface-crack penetration) in the test section, although the actual tests did not stop at this point.

(3) Only bounding cases of strength and toughness at the cracked section were considered, i.e., the pipe flaw geometries that would produce the greatest loads or largest rotation requirements were evaluated.

(4) The study was an engineering effort using reasonable assumptions.

This design philosophy provided a framework for selecting possible configurations, implementing analytical models of the configurations, selecting load cases, and a rationale for assessing the merits of competing design alternatives.

Implementing the design philosophy for the initial design used incremental analysis and review, with each succeeding stage of analysis incorporating more complex features of the problem. Linear-elastic analyses were used as a screening tool for preliminary evaluation of a number of potential configurations, followed by nonlinear analyses to confirm that the selection process was sound.

The basic steps of this approach were as follows:

(1) Perform linear-elastic analyses to determine:
   a. Static displacements and loads at candidate load points
   b. Natural frequency and mode shapes

(2) Select candidate flaw locations:
   a. In a straight section of pipe
   b. At least two pipe diameters from an elbow, hanger, or tee
   c. In a region having a high bending moment and low torque

(3) Screen the results to find the best configurations which have:
   a. Maximum resultant moment
   b. Minimum servo-hydraulic flow requirements based on estimated required actuator stroke and load to grow the crack at a test frequency near the system's first natural frequency
   c. Ease of fabrication
   d. Low torque to bending moment ratio

(4) Conduct linear transient analyses to:
   a. Determine best forcing function frequency
   b. Establish magnitude of dynamic amplification
   c. Select best geometry

(5) Conduct nonlinear transient analyses using the best configuration including a model of the flaw

(6) Refine the configuration to:
   a. Reduce undesirable high stresses
   b. Reduce load and hydraulic flow requirements
   c. Minimize logistics problems such as fabrication, siting, and damage control in the event of a double-ended break

(7) Analyze results to determine servo-hydraulic flow requirements.

3.2.2.2 Design Constraints

In implementing the design philosophy, several constraints were imposed during the initial design effort. First, only 406-mm (16-inch) diameter pipe was considered. Low toughness carbon steel pipes in this diameter range develop contained plasticity conditions that may occur in higher toughness pipes in larger pipe diameters typical of primary piping systems. Hence, experiments on 406-mm (16-inch) diameter pipe can reasonably represent large diameter pipe behavior without being excessively expensive. Also, material property data and quasi-static pipe bend test data were already available for carbon and stainless steels with flaws in 406-mm (16-inch) diameter pipe base metals and welds. There had been some early debate among the IPIRG Technical Advisory Group (TAG) Members suggesting that smaller diameter pipe may be adequate, but it was decided that the 406-mm (16-inch) diameter pipe size was the best alternative.

The second constraint on the designs was that the test system had to be reusable. For Subtask 1.3, six experiments were planned initially. To minimize the test costs, the test system had to be designed so that damage from each test was limited to the test section itself.

The test system had to be designed to fit into the existing facilities at Battelle. Considerations of access for replacement of test sections, possible effects as a result of a failure of the test sections, load frame design, ease of fabrication, and safety were all constraints on the designs.

The test system design had to be such that it could be adequately modeled mathematically. The boundary conditions had to be well defined.

The last constraint was cost and availability of materials. The subtask had a well defined scope of work, a schedule, and a budget. The test system coming out of the design study had to be compatible with all of these.

3.2.2.3 Results of Analysis Efforts

A number of potential configurations were investigated during the initial stages of the design analysis. The geometries included various numbers of elbows and hangers, different pipe lengths, expansion loops, relatively straight geometries, and a variety of forcing function locations and directions. In all, 23 different major designs were considered, with several minor variations on each major design. The configuration that was presented to the TAG after the design study, Option 23D16, is shown in Figure 3.8. All of the pipe in this design was 406-mm (16-inch) diameter Schedule 100 carbon steel pipe, except for the two vertical legs and the elbows in the expansion loop, which were Schedule 160.

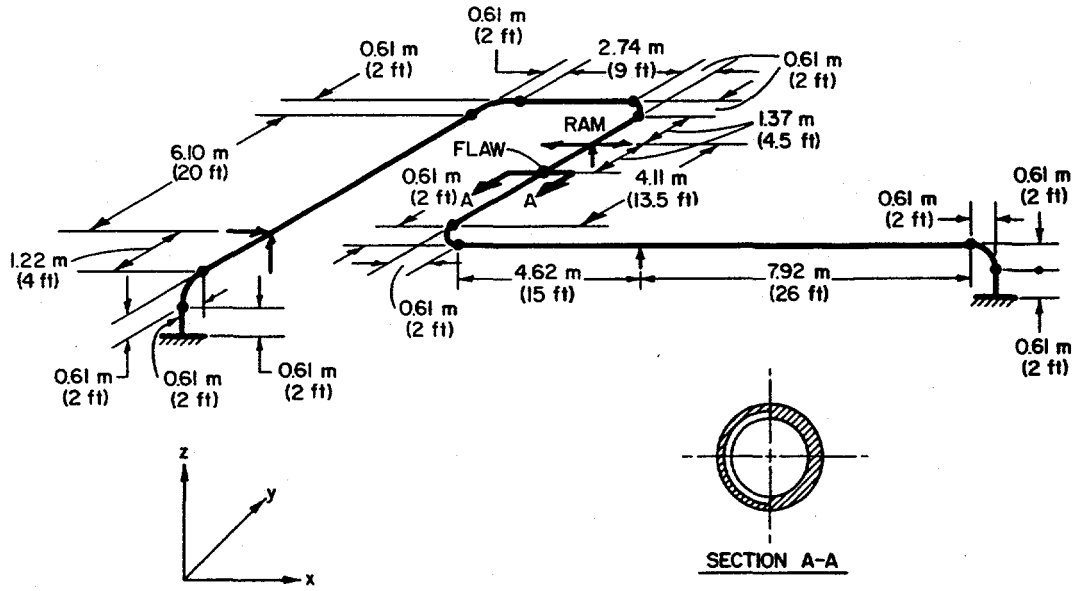

Figure 3.8 IPIRG Subtask 1.3 piping system Option 23D16 geometry

I1.0-9/87-F23

Using the crack model, quasi-static pipe bend test data and an ANSYS® finite element model of the Option 23D16 geometry, analyses were conducted of the carbon steel base metal and the stainless steel base metal experiments. The analyses assumed 5 percent critical damping in the first and fourth natural frequencies, PWR conditions in the pipe, and a forcing function shown in Figure 3.9 of the form:

$$U_x = S_{ff}*t + A_{ff}*[1-\exp(-b_{ff}*t)]*\sin(\omega*t) \qquad (3\text{-}4)$$

where

U_x = actuator displacement
t = time, seconds
S_{ff} = -38.1 mm/sec (-1.5 in/sec)
A_{ff} = 76.2 mm (3.0 in)
b_{ff} = 1.382
ω = 22.62 rad/sec (3.6 Hz).

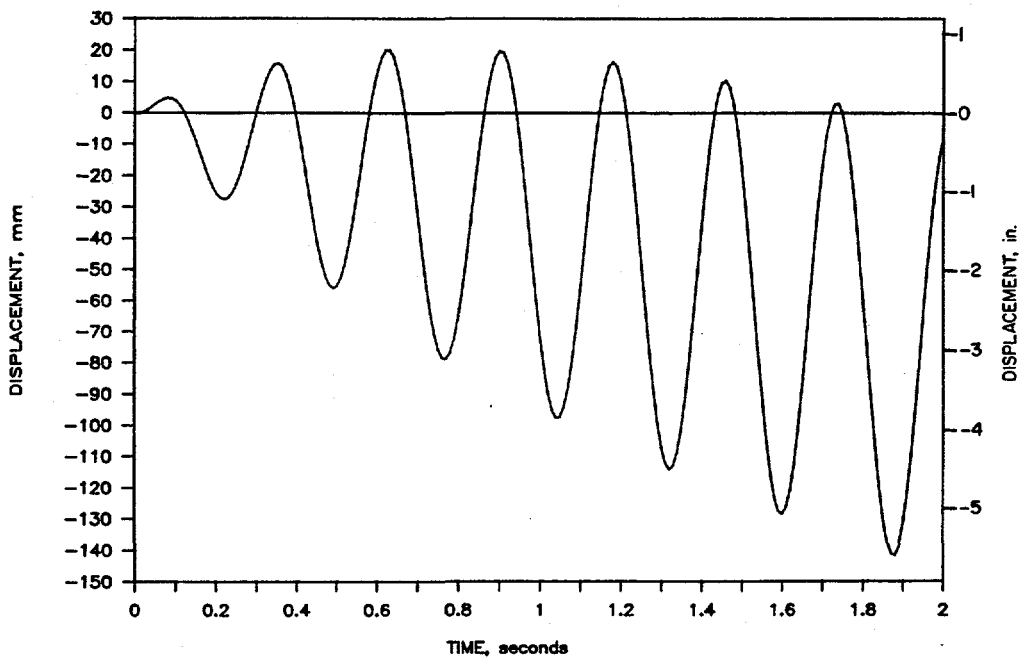

Figure 3.9 IPIRG Subtask 1.3 Option 23D16 displacement forcing function

I1.0-9/87-F26

The results of the analyses indicated that the cracked pipe could be failed using a servo-hydraulic system with the following minimum requirements:

Actuator area:	37,150 mm^2 (56.7 in^2)
Actuator stroke:	+19.8 mm (0.78 in) -97.9 mm (3.85 in)
Servo-valve rating:	3,340 liters/min (880 gpm)
Required oil volume:	25.5 liters (6.7 gallons).

Based on these results, a servo-valve, actuator, and accumulators were ordered that had the following capacities:

Actuator area:	74,200 mm^2 (115.0 in^2)
Actuator stroke:	±229 mm (±9.0 in)
Rated servo-valve flow:	7,600 liters/min (2,000 gpm)
Accumulator oil volume:	380 liters (100 gallons) .

With this capability, the servo-hydraulic system would have significant margins on force, stroke, and flow, even allowing for unknown potential flow losses in the hydraulic plumbing.

An issue that became apparent during the early stages of the initial design process was that it would be difficult to make the pipe loop reusable without using high strength pipe for all of the loop except the test section. Using A106 Grade B material, the analyses indicated that there would be progressive yielding in the pipe loop. Because this plasticity would act as a sink for energy being put into the system to fail the cracked pipe section, there was a chance that it might not be possible to fail the crack, in addition to making it necessary to replace significant portions of the loop for each test. As a consequence, high strength pipe was recommended for the loop.

3.2.3 System Redesign

During the presentation about the initial design, there was a discussion about the mixture of inertial and displacement-controlled loading at the proposed flaw location. Because design Option 23D16 intentionally took advantage of dynamic amplification, the fraction of the loading at surface-crack penetration due to inertia was substantial, on the order of 90 percent, according to the analyses. A second discussion focussed on stability of the crack after it penetrated the pipe wall. No analyses had been performed to assess whether a DEGB could be produced using Option 23D16. Although Option 23D16 met the original design criteria, the Technical Advisory Group decided that a more equal mix of inertial and displacement-controlled moments at failure would be better, and that crack stability should be investigated. As a consequence, a second round of design analyses was performed.

3.2.3.1 Approach

In conducting the system redesign, the original design criteria applied, as well as the new displacement-inertial mix criterion, and the need to be able to produce at least one DEGB. In addition, however, there were new constraints; the actuator and servo-valve sizes were fixed because they had already been ordered, and an order was pending for high strength pipe.

As in the initial design effort, a number of different possible configurations were investigated. Working from the basic Option 23D16 geometry, different crack locations, different actuator locations, adding lumped masses, different forcing functions, and changing the lengths of some the pipe runs were investigated.

3.2.3.2 Results

A configuration that met all of the design criteria, Option 33A40, and the new design forcing function are shown in Figures 3.10 and 3.11. The principal differences between Options 33A40 and 23D16 are the actuator location and the addition of a lumped mass to simulate a swing check valve. With the new forcing function, Option 33A40 had the following features:

- 10 cycles to failure for the stainless steel base metal
- Adequate design margins on the servo-hydraulic system
- 33 percent inertial loading

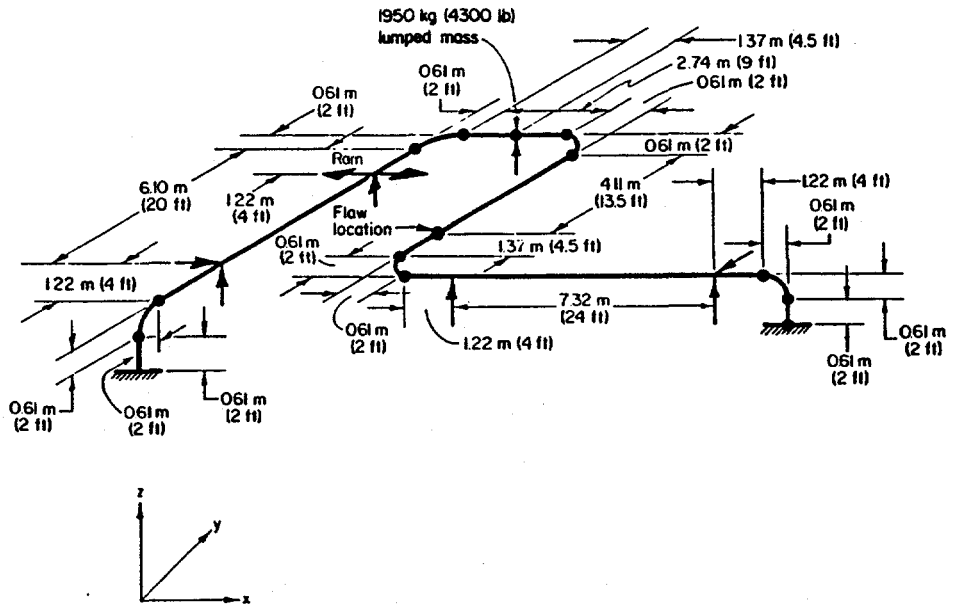

Figure 3.10 IPIRG Subtask 1.3 piping system Option 33A40 geometry

I1.3-10/90-F3.10

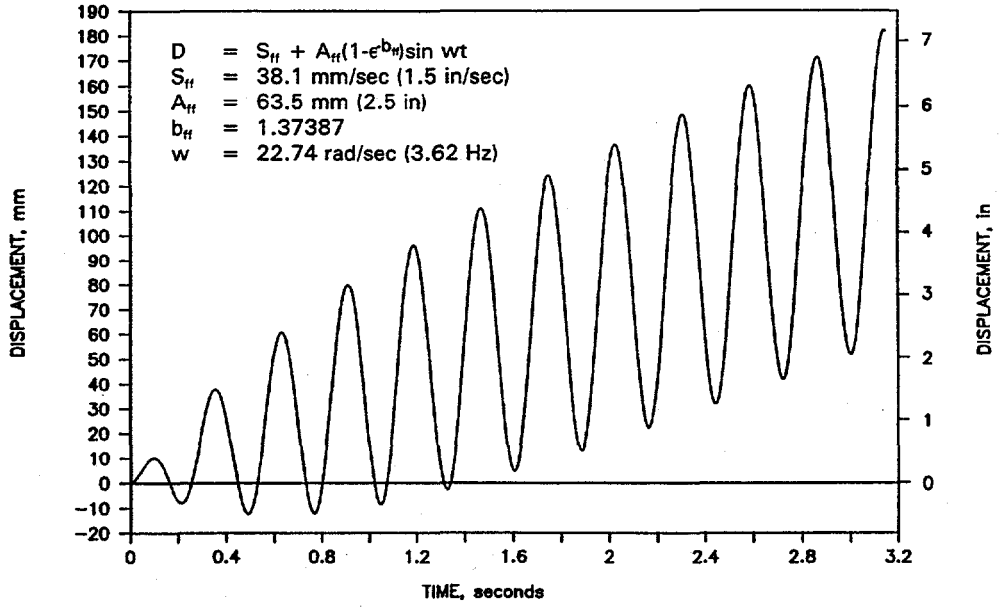

Figure 3.11 IPIRG Subtask 1.3 Option 33A40 displacement forcing function

I1.3-10/90-F3.11

- Peak stresses remote from the crack within the limits of the pipe material on order.

Regarding the issue of crack stability, two approaches for analyzing stability were considered, the J-T approach and an energy balance approach. The results of the calculations were mixed in that J-T suggested that only the carbon steel weld through-wall crack would be unstable, while the energy balance approach indicated that all but the stainless steel base metal through-wall crack would be unstable.

The results of the redesign were presented to the IPIRG Technical Advisory Group at the May 1988 meeting in Paris, France. It was agreed that the design and proposed forcing function, with some modest adjustments, could meet all of the objectives of the tests, and that detailed design and fabrication of the test facility should begin, using the Option 33A40 design.

3.2.3.3 Quality Assurance

All design calculations were checked and verified to assure accuracy and traceability. All design drawings for the test facility, including the loading frame, foundation, pipe supports, spherical bearings, hydrostatic bearings, plumbing, instrumentation fixtures, actuator load carriage, restraints, and shielding were checked by another engineer, and then filed.

3.2.4 Assessment of Analysis Procedures/Approach

Success of the Subtask 1.3 test facility design was contingent upon the quality of the finite element analyses that were used in the design process. In this case, quality implies correctly translating model concepts into data inputs for the finite element program, suitability of analysis assumptions such as amount of damping, time step, and analysis methods, efficacy of the nonlinear crack model, and overall accuracy of the finite element program.

3.2.4.1 Background

During the conduct of the pretest design, several Technical Advisory Group members reviewed Battelle's results and conducted analyses of their own. At several points in the design process, Technical Advisory Group members generated analytical solutions of the same system, using different software packages, that were not consistent with the Battelle solutions. In addition, discrepancies were discovered in Battelle solutions between two different versions of the ANSYS® software. As a consequence, a significant effort went into trying to discover the causes of the discrepancies and means to resolve the inconsistencies.

The solution assessments took three forms: comparison of dynamic cracked pipe experimental data with predictions using the cracked pipe model, a series of closed-form solutions to check basic finite element calculations, and a series of workshop problems for checking consistency between the various analysis programs.

3.2.4.2 Cracked Pipe Model Verification

One of the foundations of the Subtask 1.3 pretest design was the nonlinear cracked pipe element. Although the formulation of the element and its use appeared to be intuitively correct at the beginning of the Subtask 1.3 pretest design analyses, predictions of dynamic experiments using the element had not

been compared against test data. Unfortunately, there were no data available from previous pipe test programs, because all of that work had been done at quasi-static loading rates. However, the IPIRG Subtask 1.1 experiments were dynamic, and did generate data that could be used for verification of the nonlinear cracked pipe model, prior to completion of the Subtask 1.3 pretest design.

The objective of IPIRG Subtask 1.1 was to develop experimental data on the fracture behavior of circumferentially cracked pipe under predominately inertial loading. Both through-wall and surface-cracked pipe at PWR test conditions were tested in the loading fixture shown in Figure 3.12 using a prescribed displacement forcing function at the actuators. The final report for Subtask 1.1 (Ref. 3.5) provides details of the experiments.

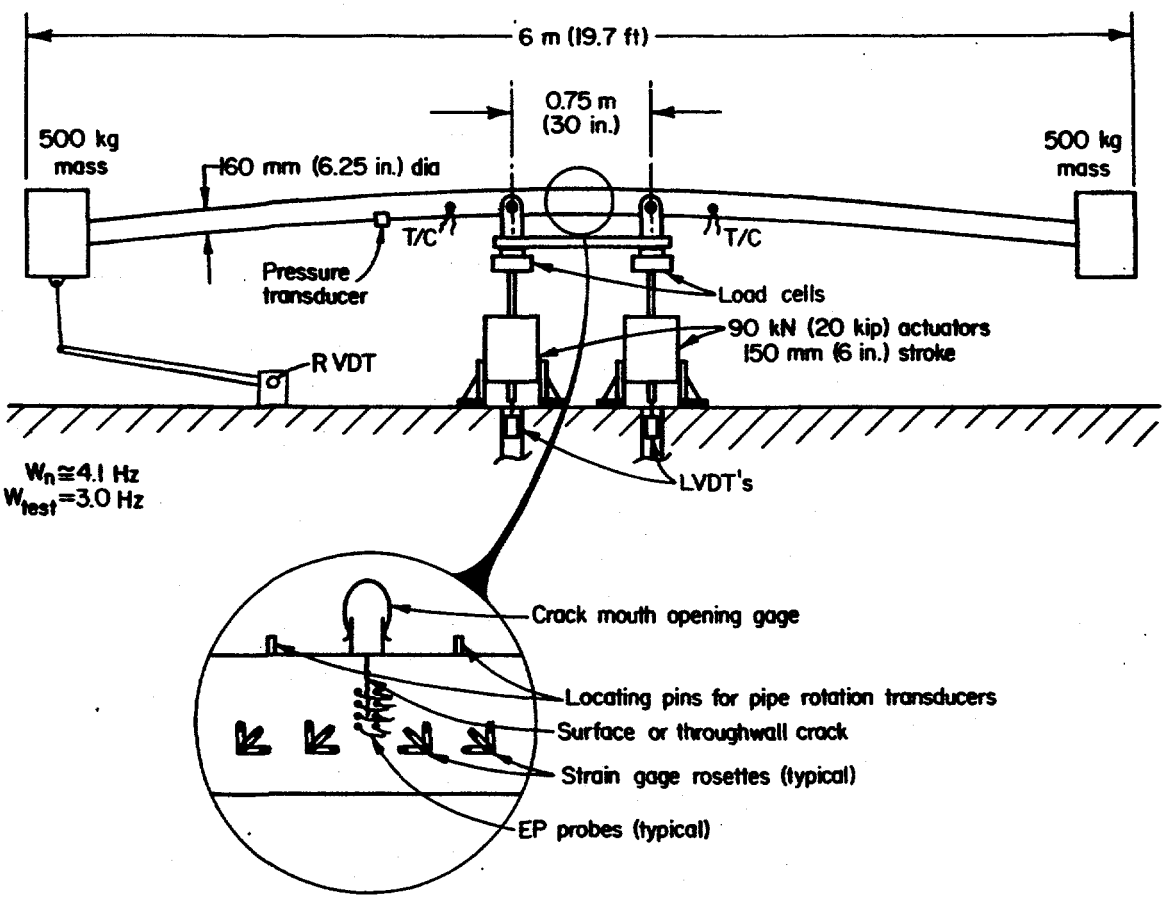

Figure 3.12 IPIRG Subtask 1.1 test system

I-11/87-E3-MW

Using the procedures previously described, a model of the crack for Experiment 1.1-3 (stainless steel through-wall crack) was developed, a finite element model of the Subtask 1.1 system prepared, and a nonlinear dynamic analysis performed. Comparisons of pretest predictions and the experiment are shown in Figures 3.13 to 3.15. Although there is a slight discrepancy between the test and the prediction (the prediction used a forcing function frequency of 3.0 Hz and the test was actually conducted using 3.5 Hz) the comparisons are exceptionally good, remembering that the finite element analysis can only be performed out to the point of maximum moment.

A second comparison between the nonlinear cracked pipe finite element model and an experiment was done for Experiment 1.1-2 (carbon steel through-wall crack). In this case, however, the moment-rotation behavior for the nonlinear crack was obtained from a J-estimation scheme using J-R curve and stress-strain data for the test material, rather than data from a previous quasi-static pipe test. The forcing function in both the analysis and experiment used a frequency of 3.5 Hz. Comparisons are shown in Figures 3.16 to 3.18. Again, the comparisons are exceptional

With the favorable comparisons between the nonlinear cracked-pipe finite element results and test data, the viability of the nonlinear cracked pipe model was confirmed. Although the comparisons were only made for through-wall-cracked pipe cases, the extension of the approach to surface-cracked pipe was deemed trivial.

3.2.4.3 Closed-Form Solutions

As indicated previously, the ANSYS® computer program was used in the design analyses for the Subtask 1.3 pipe loop. When the design effort started in March 1987, Version 4.2B of ANSYS® was used. The results using Version 4.2B, although not rigorously checked, appeared to be intuitively correct, consistent, and reasonable. In the early part of 1988, however, when the ANSYS® program was updated to Version 4.3, the reaction forces at the actuator changed very dramatically: they became very "noisy" and increased by an order of magnitude. In addition, it was discovered that linear transient solutions did not compare to nonlinear transient solutions that were performed without nonlinearities using the new version of ANSYS®. Because all of the design work on the pipe loop had been performed with the ANSYS® program, and because hardware orders had been placed based on the ANSYS® results, it was essential to understand the source of the discrepancies and to determine if any remedial action was necessary.

The approach used to determine the source of the discrepancies with ANSYS® involved a methodical step-by-step verification of the various parts of the finite element calculation using comparisons with closed-form solutions. The philosophy that guided the investigation was:

- The piping loop was too complicated to serve as a vehicle for diagnosing the discrepancies
- Simple problems with closed-form solutions were used to isolate the errors
- Static analyses were used to verify the stiffness matrix
- Eigenvalue analyses were used to verify the mass matrix

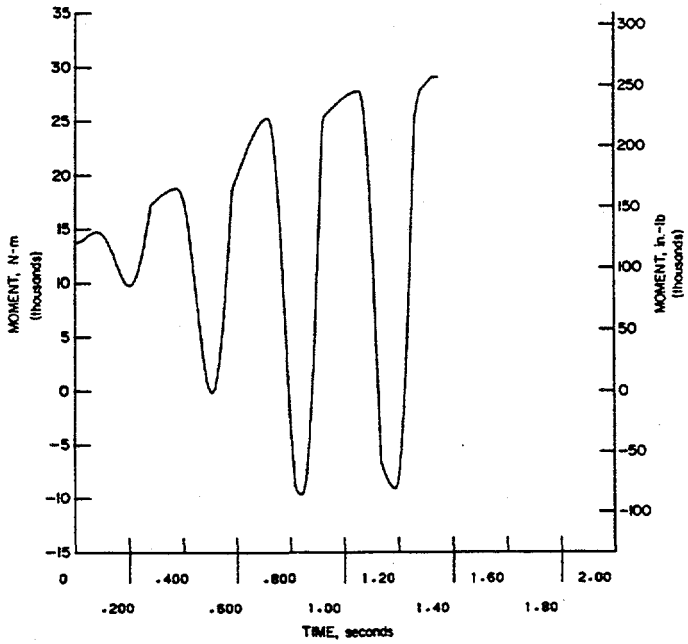

(a) Moment-time from analysis

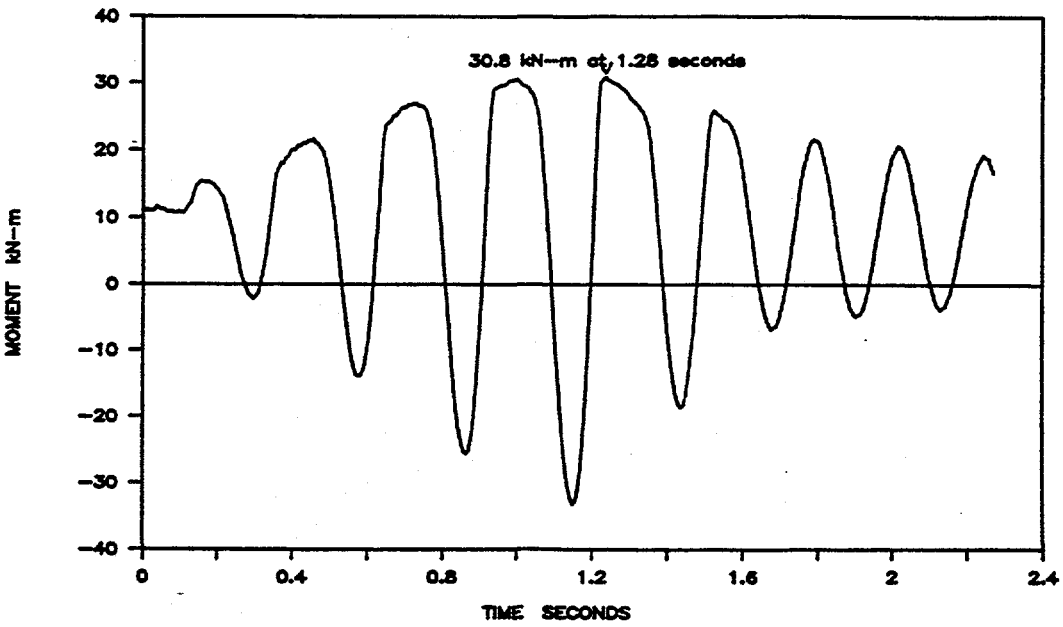

(b) Moment-time from experiment

Figure 3.13 Comparison of experiment and analysis for moment versus time plots for Experiment 1.1-3 (SS-TWC) (The analysis was valid only up to maximum moment) I1.1-10/89-F4.11

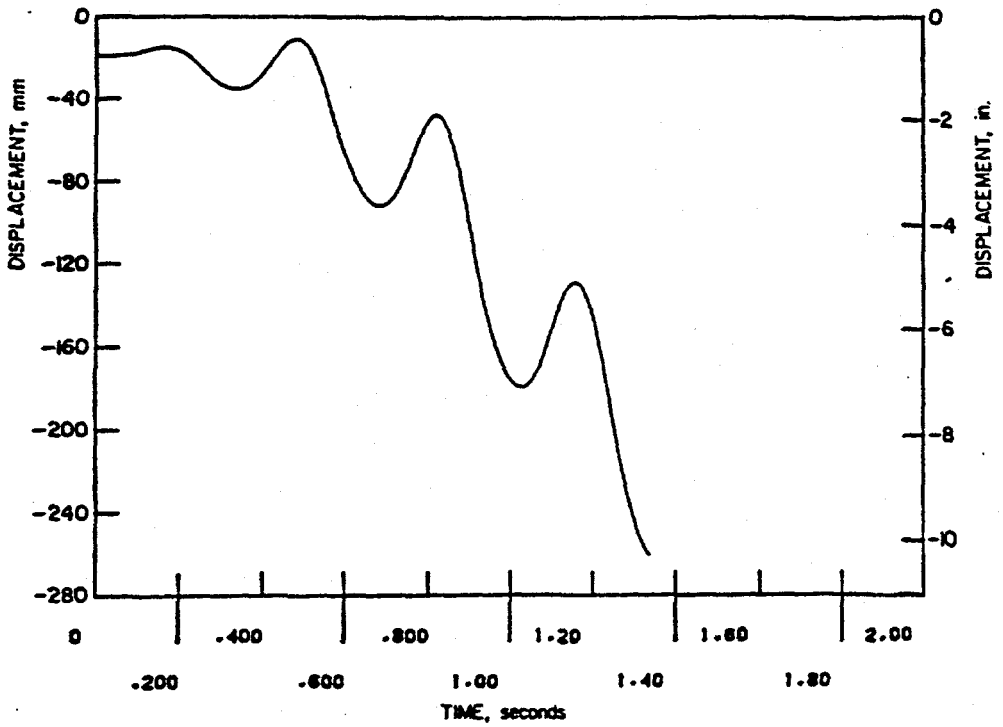

(a) Inertial mass displacement from analysis

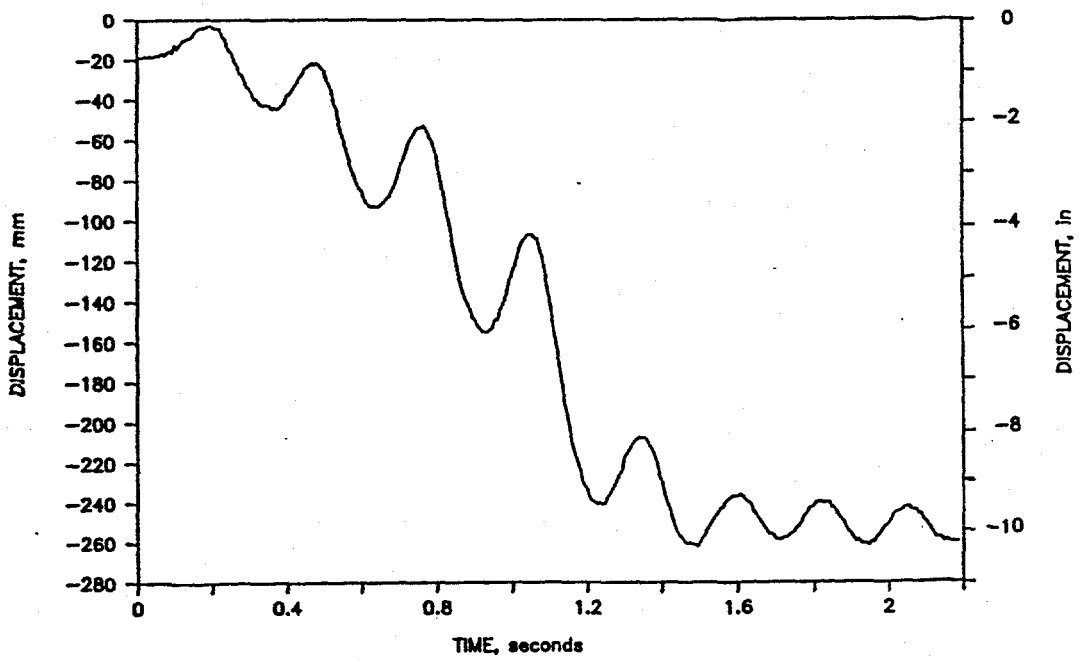

(b) Inertial mass displacements from experiment

Figure 3.14 Comparisons of experiment and pretest design analysis for displacements of the inertial mass for Experiment 1.1-3 (SS TWC)

I1.1-10/89-F4.12

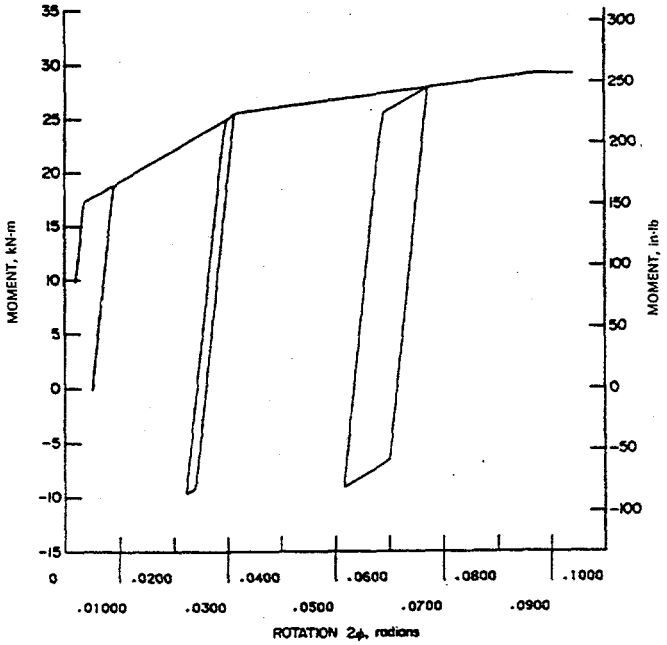

(a) Moment-rotation from analysis

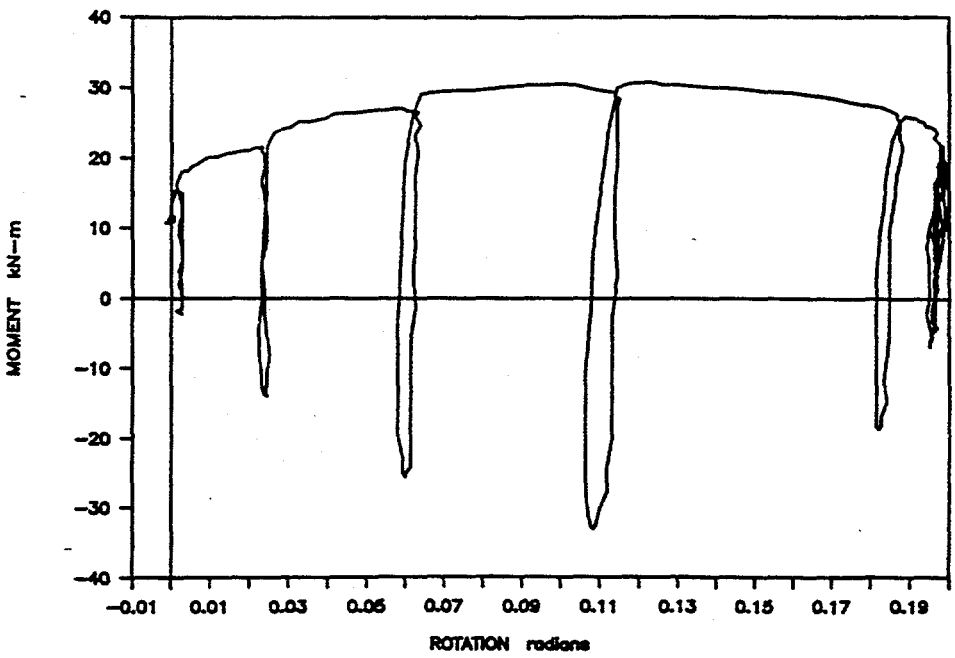

(b) Moment-rotation from experiment

Figure 3.15 Comparison of experiment and pretest design analysis for moment versus rotation for Experiment 1.1-3 (SS TWC)

I1.1-10/89-F4.13

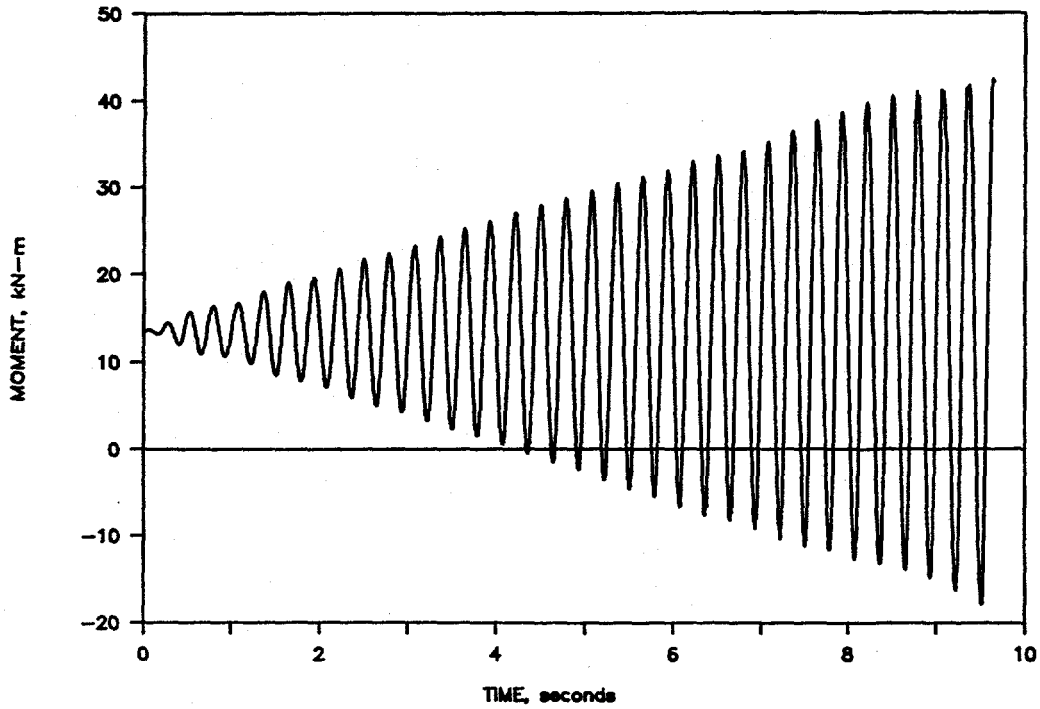

(a) Moment-time from analysis

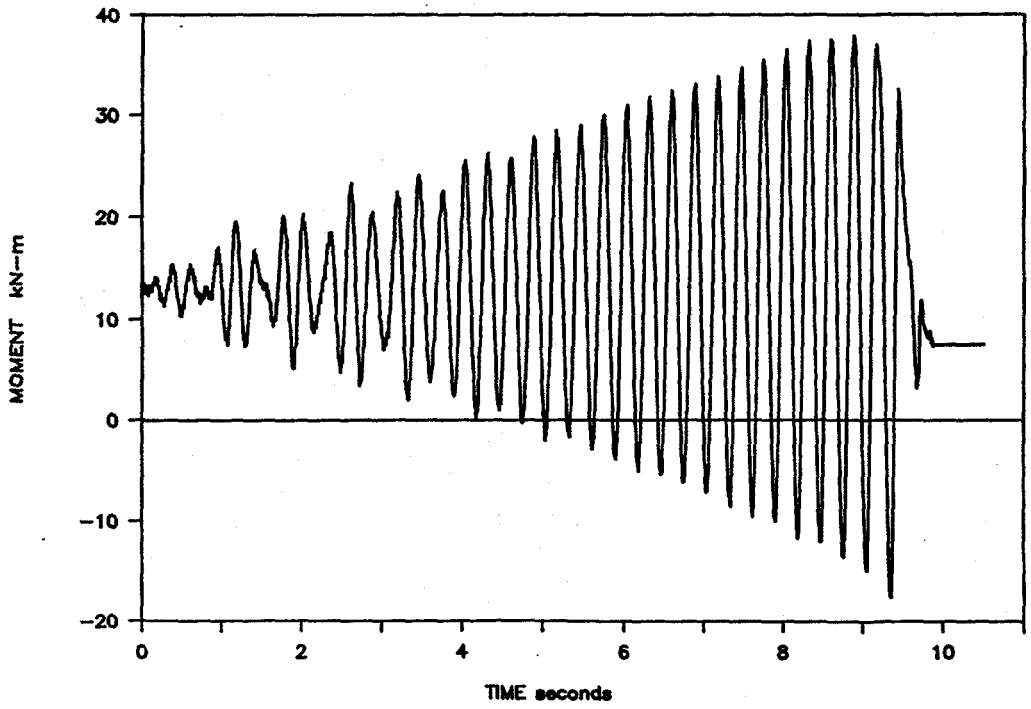

(b) Moment-time from experiment

Figure 3.16 Comparison of experiment and analysis for moment versus time plots for Experiment 1.1-2 (CS-TWC) IWS-11/880I6&I11-RO

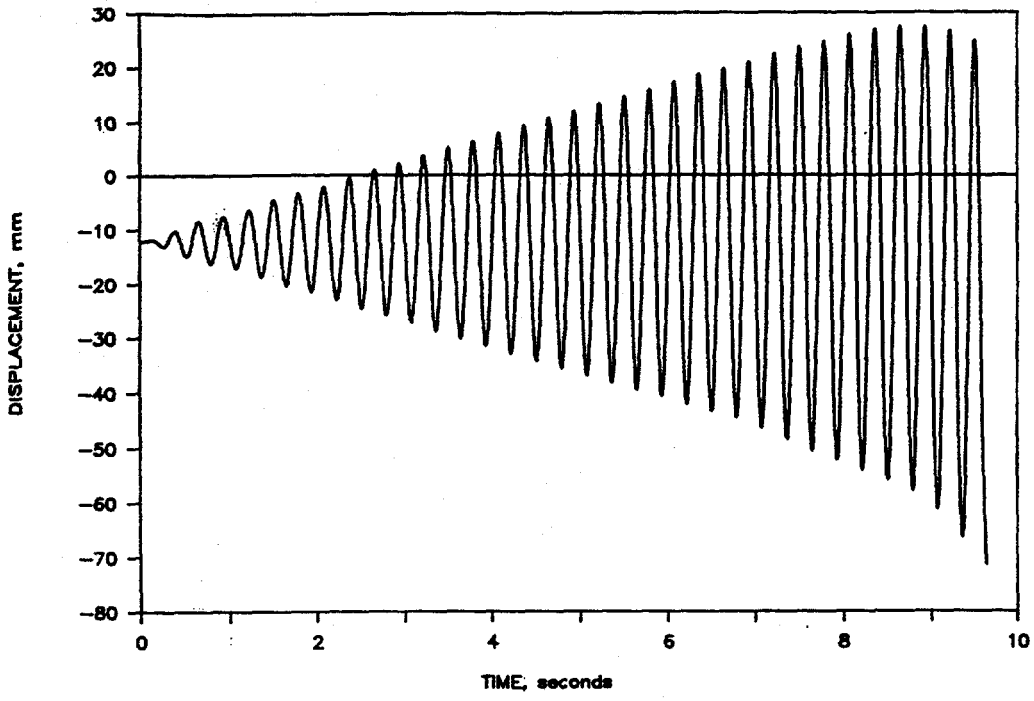

(a) Inertial mass displacements from analysis

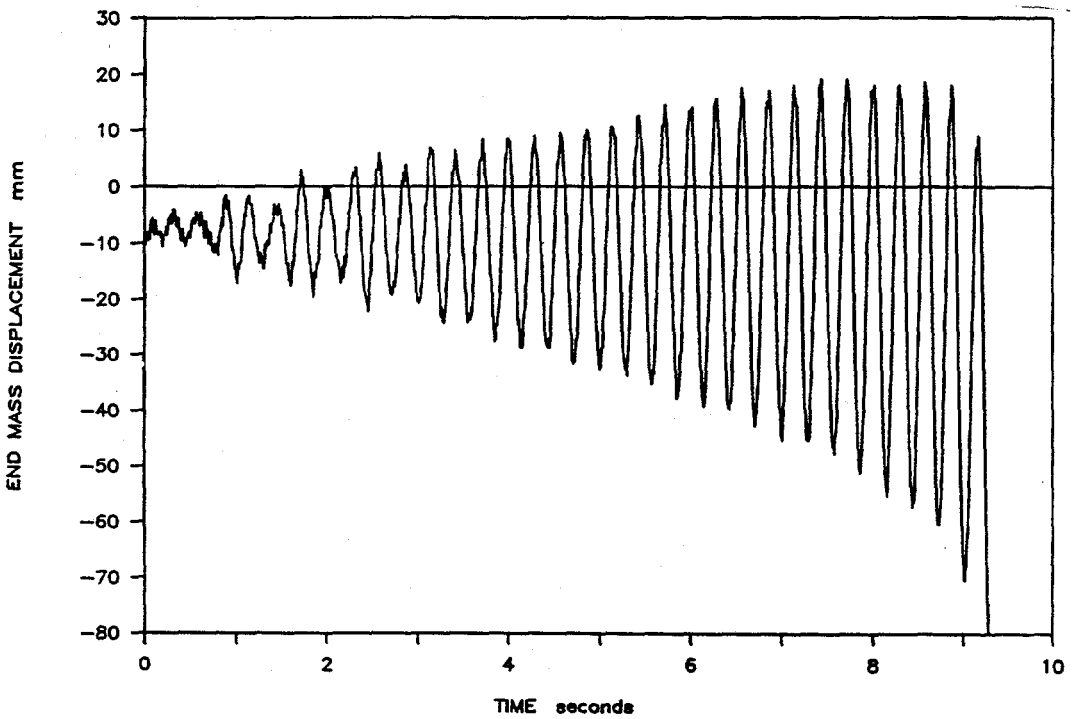

(b) Inertial mass displacements from experiment

Figure 3.17 Comparison of experiment and analysis for displacements of the inertial mass for Experiment 1.1-2 (CS-TWC) I1.1-10/89-F4.15

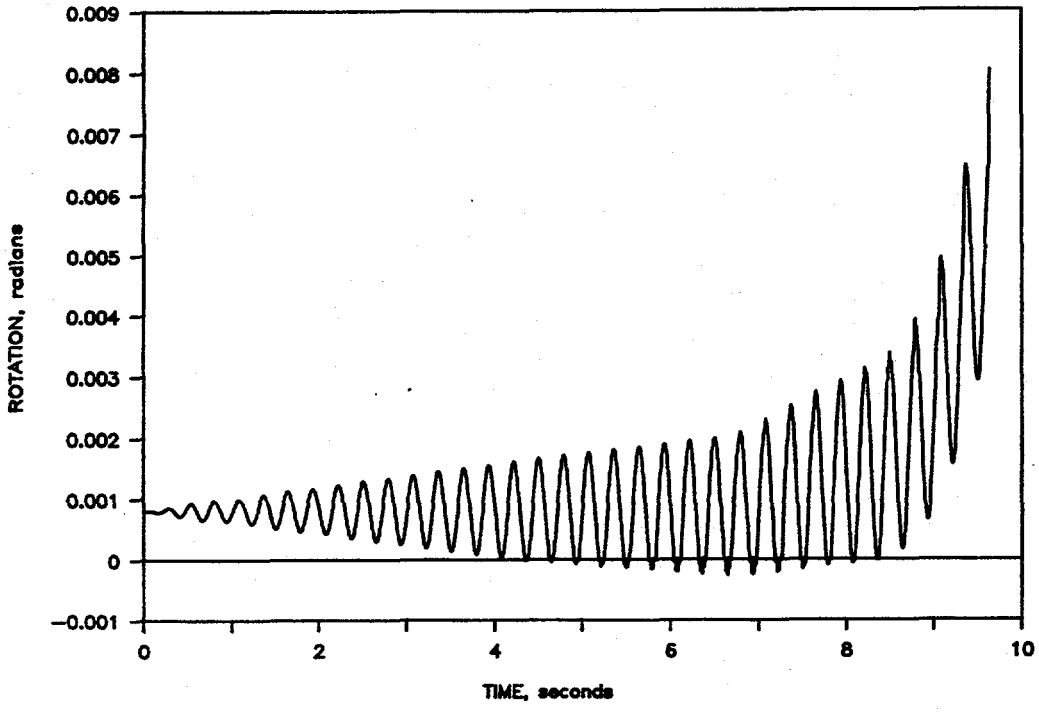

(a) Rotation-time from analysis

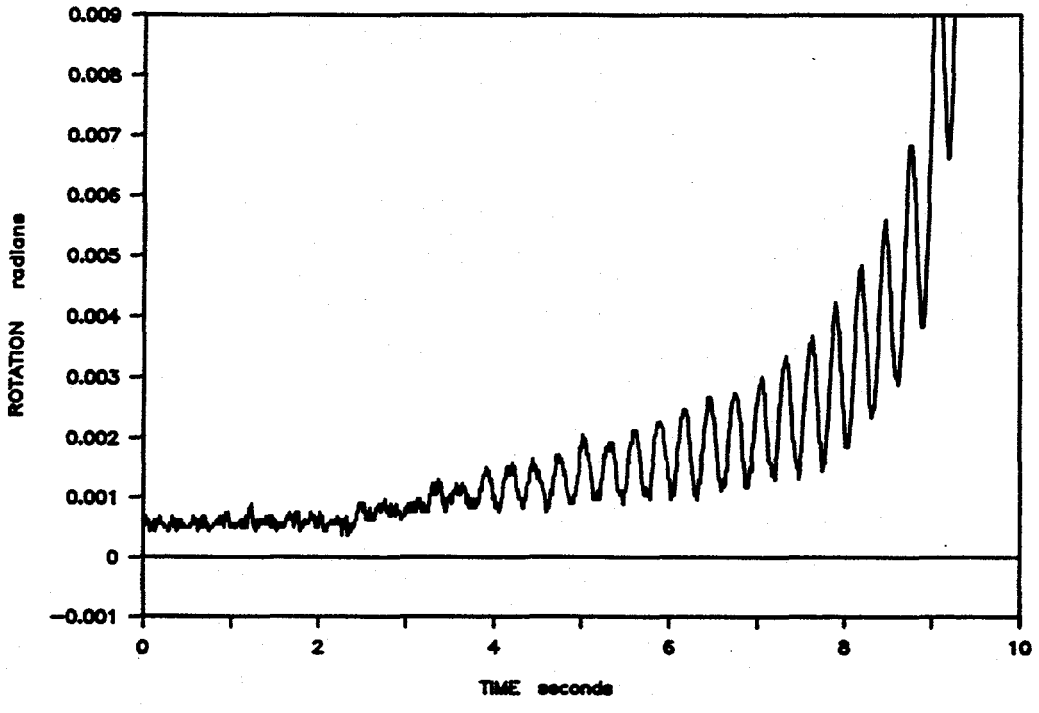

(b) Rotation-time from experiment

Figure 3.18 Comparison of experiment and analysis for rotations at the crack plane for Experiment 1.1-2 (CS-TWC) I1.1-10/89-F4.16

- Dynamic analyses were used to verify correctness of displacements and problems with reaction force recovery
- Dynamic analyses were used to isolate problems with the time integrator.

To apply this philosophy, closed-form solutions to the three problems shown in Figure 3.19 were compared with the finite element results.

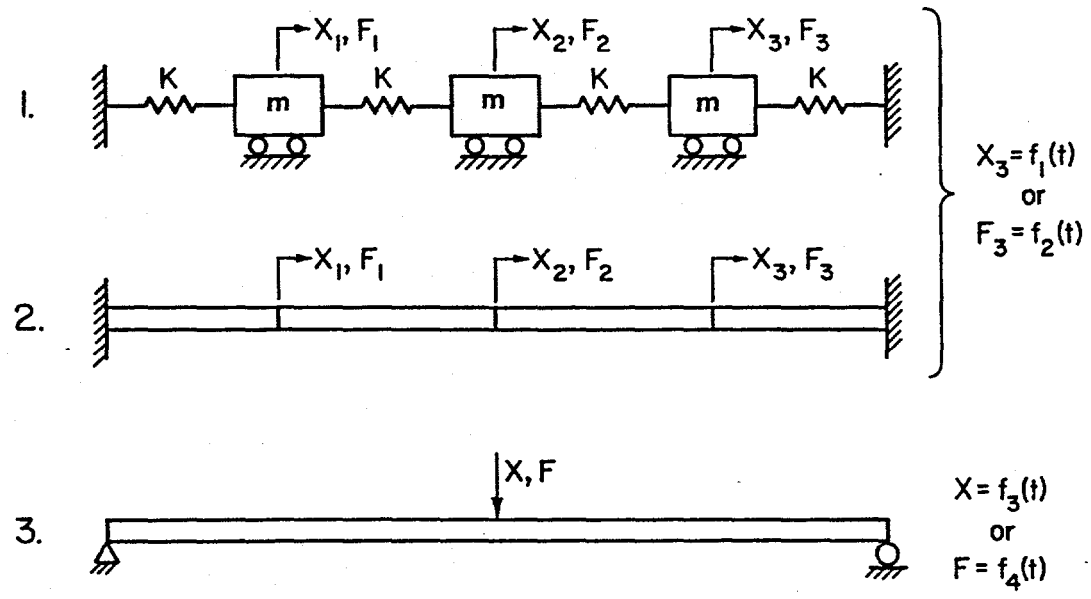

Figure 3.19 Closed-form problems used for comparison with finite element solutions I-5/88-ANSYS7-RO

Three problems were identified with Version 4.3 of ANSYS®:

(1) Reaction forces at locations where displacements are prescribed as a function of time in linear transient analyses are incorrectly recovered. Acceleration and velocity terms are ignored.

(2) The default time integrator in Version 4.3, the Newmark method, which uses a constant average acceleration assumption, introduced errors in the recovery of reaction forces at points where displacements are prescribed as a function of time. The Houbolt method of Version 4.2B makes a linear acceleration assumption and does not introduce significant errors.

(3) The iteration scheme for improving solution efficiency and quality of the equilibrium solution in ANSYS® is inappropriate for use in prescribed displacement dynamic problems. Displacements are linearly ramped between steps causing accelerations to go to zero.

Having identified these problems, three actions were implemented for all subsequent analyses:

(1) The ANSYS® nonlinear transient analysis was used for all dynamic calculations, even if the problem was clearly linear.

(2) The Houbolt integrator was invoked, instead of the default Newmark method, using an undocumented switch in the data input.

(3) No equilibrium iterations were performed. Instead, very small time steps were used.

Using these techniques, the solutions for the two versions of ANSYS® gave the same results, both agreeing with the closed-form solutions and both agreeing with the results from the previous pretest design work using Version 4.2B.

3.2.4.4 Round-Robin Problems

During the conduct of the pretest design, several of the Technical Advisory Group members were conducting independent analyses of the Subtask 1.3 experiments using their own analysis procedures and analysis programs. At times, discrepancies between the analyses were significant and controversial. To understand the source of the discrepancies, a series of round-robin workshop problems was devised in which all analysts supplied solutions to pertinent, well prescribed problems. The intent was to sort out whether there were inherent problems in the finite element programs, or whether the source of the errors was rooted in each analyst unintentionally solving a slightly different problem. The culmination of the efforts to understand the discrepancies was a meeting of analysts at Battelle to discuss and compare solutions to a step-by-step series of increasingly complex problems.

The discrepancies between the various analytical solutions generated by the Technical Advisory Group participants were focussed in three areas:

(1) Flexibility factors for elbows

(2) Discrepancies in eigenvalue solutions

(3) Poor agreement among the various dynamic piping analysis results, i.e., there was a factor of three between the largest and smallest predicted maximum moment at the future crack location for an uncracked dynamic pipe analysis, and the time zero displacement solutions were radically different.

A fourth apparent discrepancy, plasticity at one elbow in the pipe loop, was easily resolved when refined pretest analyses that allowed plasticity were performed. The consensus was that plasticity would occur, so the suspect elbow thickness was subsequently increased to Schedule 160.

Solutions were requested for three problems to resolve the outstanding inconsistencies. Five solutions were submitted, one from CEA, one from Framatome, two from CEGB, and one from Battelle. The three problems were: (1) a cantilever beam geometry in which static, eigenvalue, and dynamic analyses were performed with different pressure, temperature, and damping conditions, (2) a 90-degree elbow with pressure and end force loading, and (3) eigenvalue and dynamic uncracked pipe analyses of the Subtask 1.3 pipe loop. For the first two problems, closed-form solutions were available. The intent was to use the first two cases to sort out basic problems, before considering the complexities of the pipe loop.

At the Analysts meeting held at Battelle on September 25-26, 1989, the participants discussed their methods of solution and results. Discrepancies were discovered and rather easily resolved. In the end, each analyst at the meeting had discovered either something in the way that their computer program handled a certain aspect of an analysis or the way that the data were input that caused them to get different solutions. Armed with the information from the meeting, each participant submitted a revised solution to a subset of the three problems.

Figure 3.20 shows early results of an uncracked pipe analysis. Figures 3.21 through 3.24 show the results of the uncracked pipe analysis conducted after the Analysts meeting. Figures 3.21 through 3.24 also include the experimental test data for comparison purposes. Clearly, there was a vast improvement in the agreement between the analytical solutions and very good overall agreement with the experiment.

On a rather basic level, the lessons learned from the Analyst meeting were:

- Experienced analysts get different solutions to the same problem for four reasons:

  (1) Incomplete problem statements

  (2) Incorrect program inputs

  (3) Poorly documented program features

  (4) Program errors

- When everyone solves the same problem, all analysts, using different programs, get nearly the same solution.

On a much deeper level, there is a far more significant issue with implications far beyond the immediate scope of the IPIRG contract. With the design of nuclear power plants based on finite element analyses, it is difficult to envision how plant design could be immune from the same issues that caused problems in the

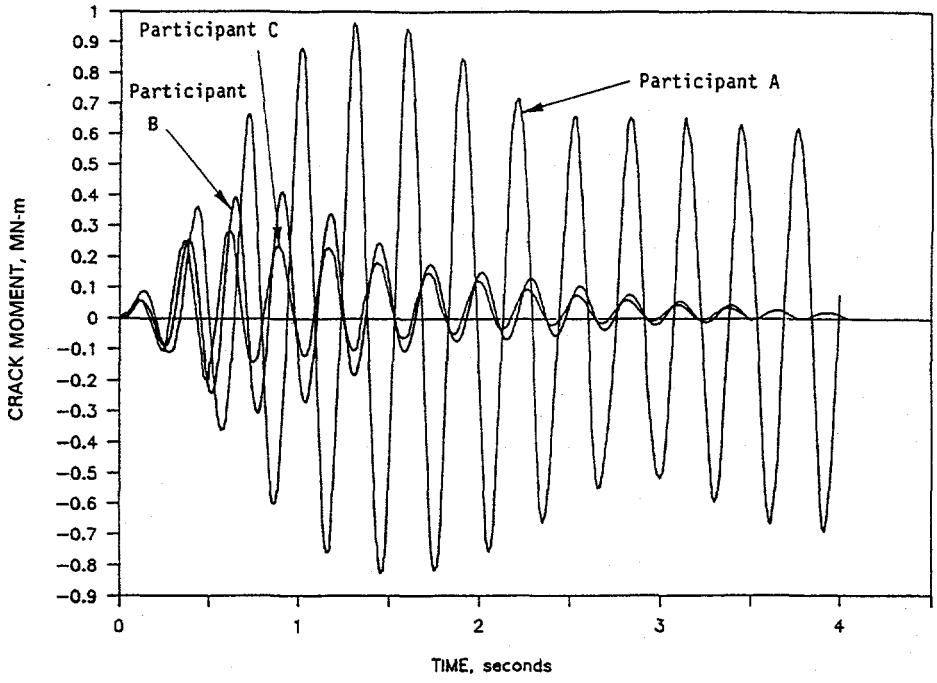

Figure 3.20 Early finite element predictions by different participants of crack location moment for the IPIRG pipe system I-10/89-F20-RO

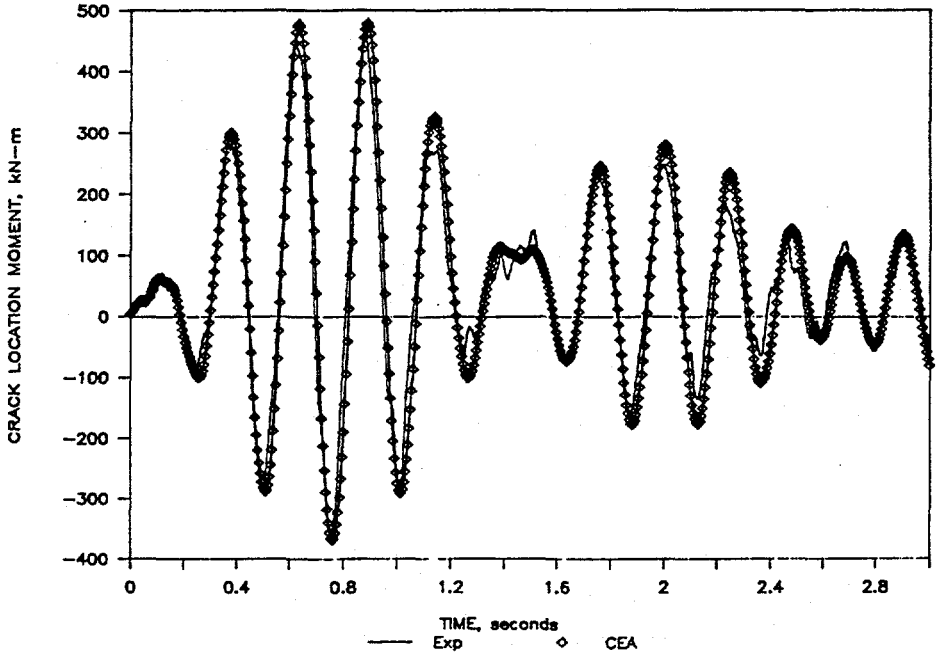

Figure 3.21 CEA prediction (using CASTEM 2000) of crack location moment in the IPIRG pipe system after Analyst Meeting I-10/89-F19-RO

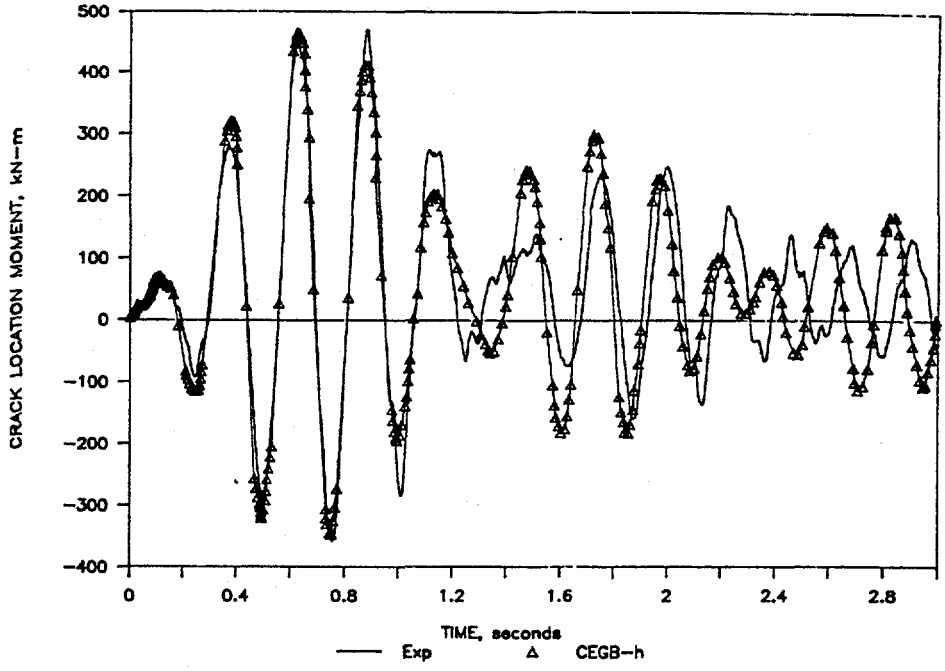

Figure 3.22 CEGB prediction (using ABAQUS) of crack location moment after Analyst Meeting I-10/89-F20-RO

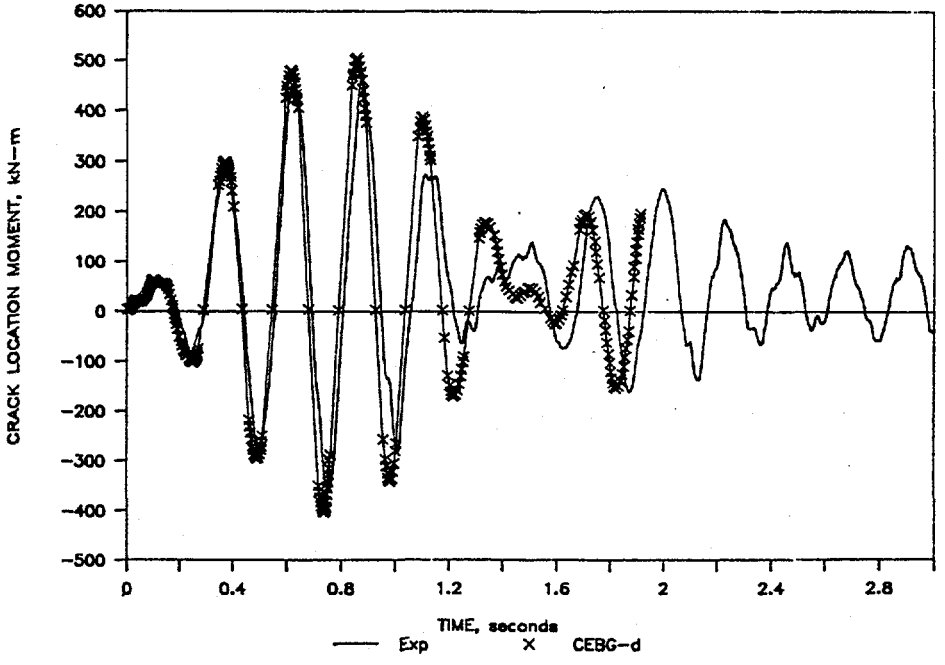

Figure 3.23 CEGB prediction (using ADLPIPE) of crack location moment after Analyst Meeting I-10/89-F21-RO

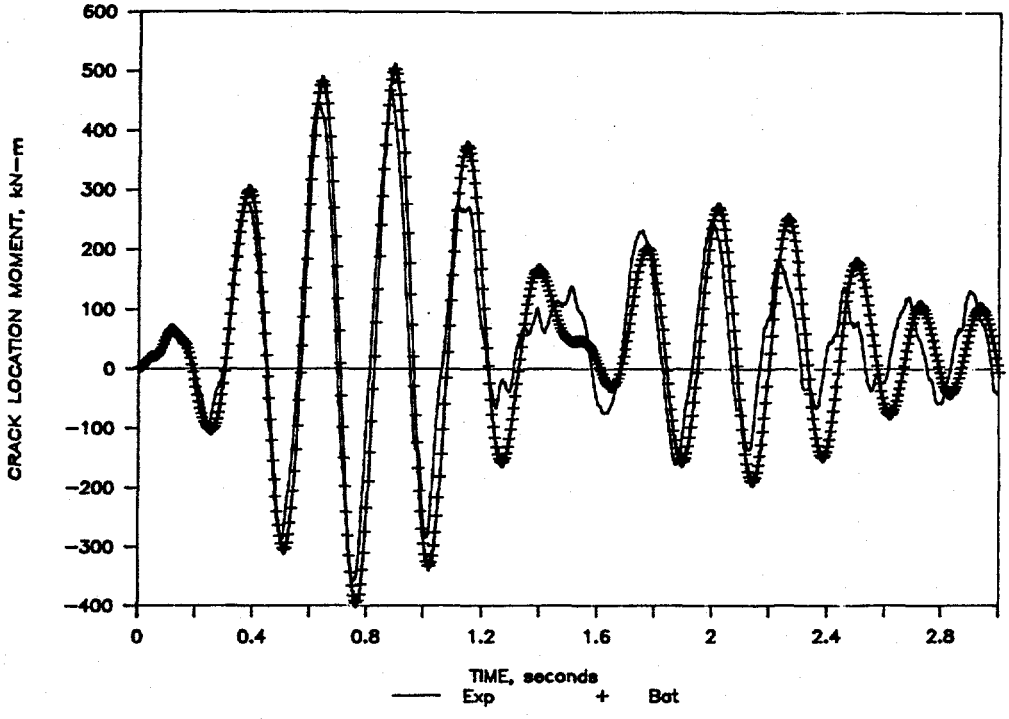

Figure 3.24 Battelle prediction of crack location moment after Analyst Meeting I-10/89-F18-RO

analysis of the IPIRG Subtask 1.3 system. All four of the reasons for different solutions of the Subtask 1.3 system could, and most likely do, affect plant design analyses.

Lest one be completely overcome by pessimism about the use of finite element analyses for plant design, the Analyst meeting also points the way to overcoming the problems:

- Program errors and poorly documented features can be discovered by computer code benchmarking and accreditation.

- Incomplete problem specification and program input errors can be uncovered by thoroughly reviewed independent redundant calculations performed by teams of highly qualified analysts using separate analysis programs.

Carefully selected, simple test cases with easily obtained closed-form solutions for the types of analyses to be performed were used in the IPIRG study to identify program deficiencies. From the broad perspective, submission of benchmark solutions could be a licensing prerequisite for acceptance of design analyses. The only weakness in applying the benchmarking on a broad basis is that some person or group has to be clever enough to think of all of the potential pitfalls and possible errors that may be hidden in computer codes. Conflicting independent redundant calculations, which alerted us to the possibility of the problems, is probably expensive to implement on a large-scale basis, but will probably uncover user or problem statement deficiencies and will also uncover computer code problems.

The larger issue of the quality of finite element calculations used in plant design is a subject that will need some attention from both the industry and the regulators. For the more local issue of IPIRG Subtask 1.3, resolving all of the analytical discrepancies was a major milestone. The agreement between the uncracked pipe test data and all of the analytical predictions provided confidence in the overall pretest design.

3.3 Description of Experimental Procedures

In this section of the report, a description of experimental procedures, i.e., instrumentation, data acquisition, test procedures, etc., will be presented.

3.3.1 Test Facility

A brief description of the IPIRG Subtask 1.3 experimental facility is provided in the following sections. Figure 3.25 is a photograph of the entire facility.

3.3.1.1 Piping Loop Description

Figure 3.26 is an artist's conception of the Subtask 1.3 experimental facility. Figure 3.27 shows the dimensions of the pipe loop. The pipe loop is fabricated from predominantly 406-mm (16-inch) nominal diameter Schedule 100 pipe. The straight pipe material is ASTM A710, Grade A, Class 3 steel. The elbows are 406-mm (16-inch) nominal diameter long radius elbows fabricated from WPHY-65 material. Elbows 1, 2, 3, and 5 are Schedule 100 and Elbow 4 is Schedule 160. End caps welded into the pipe loop at the two fixed ends provide the pressure boundary for the internal pressure. In addition, for all except the last experiment, i.e., the aged cast stainless experiment, the test section had internal end caps 914 mm (36 inches) on either side of the crack location, see Figure 3.28. The end caps had small holes in them to provide a flow path for the water which is circulated through the specimen and piping system. The end caps minimized the blowdown volume and mitigated the effects of the jet force when the crack broke through the pipe wall during the cracked pipe experiments. In the event the crack section completely severed, a system of wire ropes spanning the crack section was incorporated in the overall design to restrain the motion of the two halves of the pipe loop, see Figure 3.29. Finally, a large 1,950-kg (4,300-pound) mass which simulates a swing check valve is located in one leg of the pipe loop, see Figure 3.30.

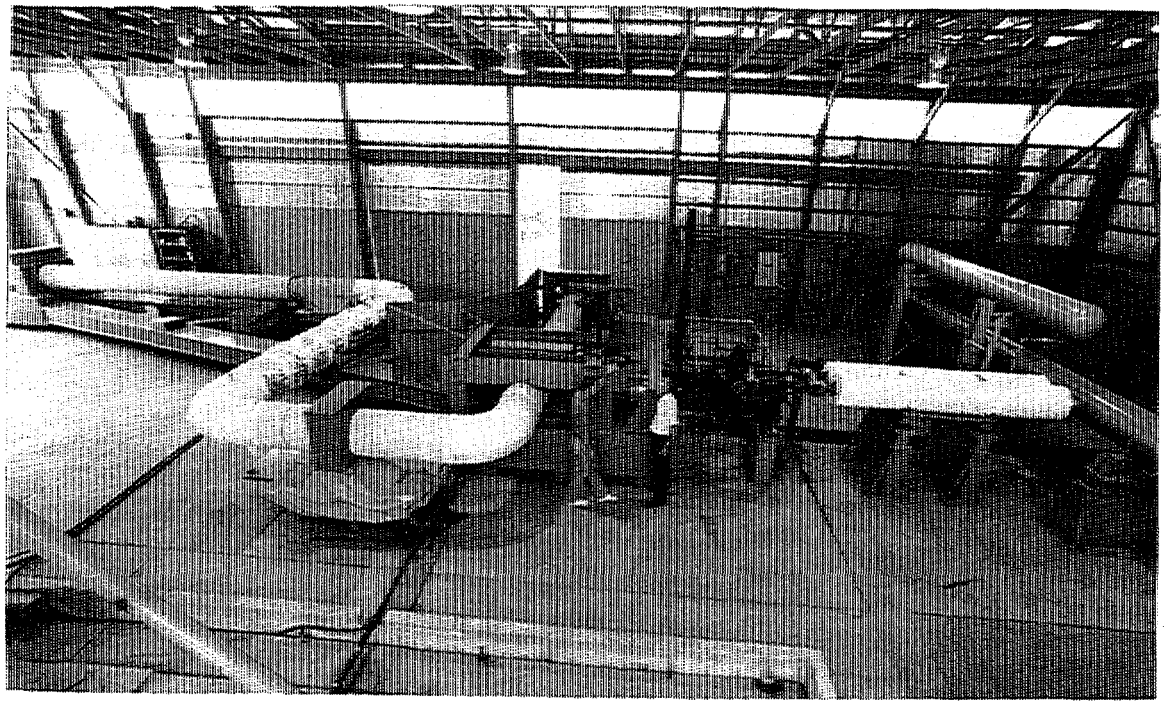

Figure 3.25 Overall photograph of IPIRG Subtask 1.3 experimental facility

F1.3-3/91-F3.25

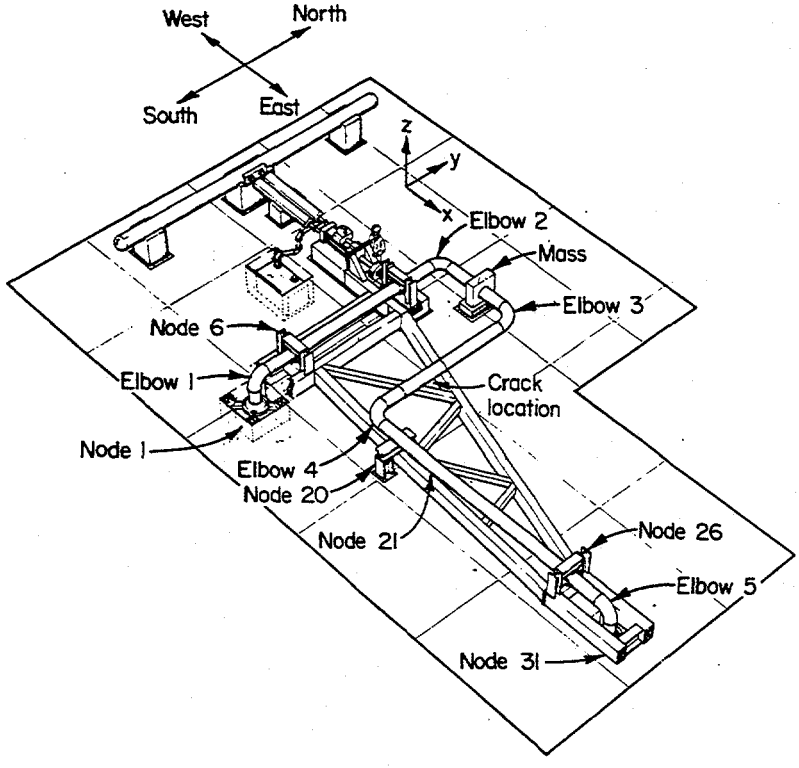

Figure 3.26 Artist's conception of the IPIRG Subtask 1.3 pipe loop

QL/1.3-4/F1

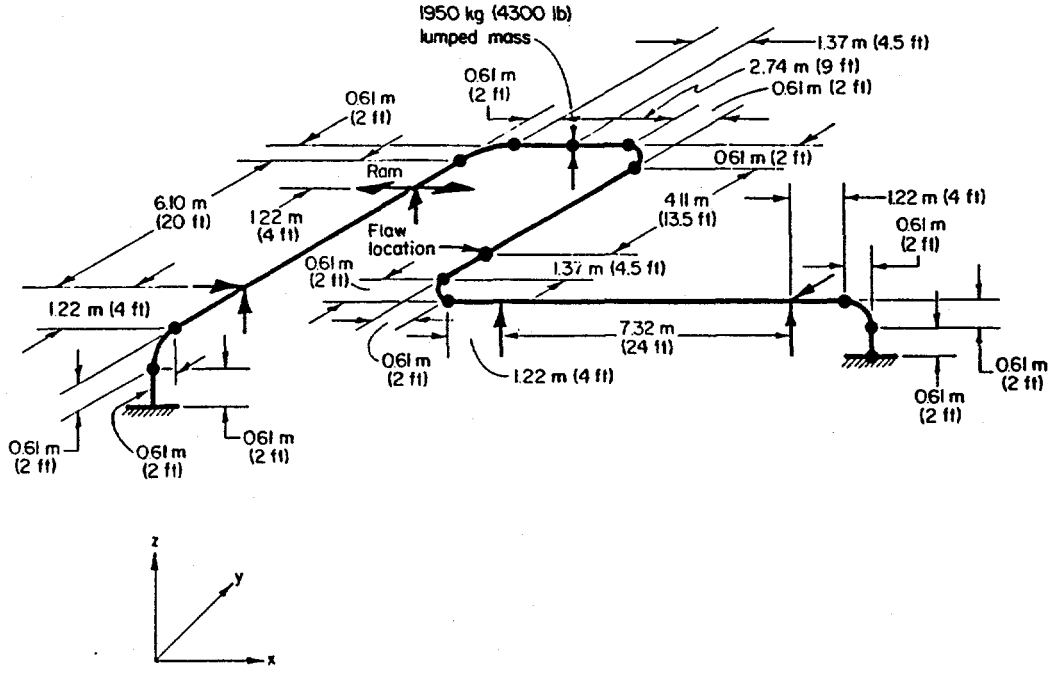

Figure 3.27 IPIRG Subtask 1.3 pipe loop geometry

DRB/1.3-1/F2

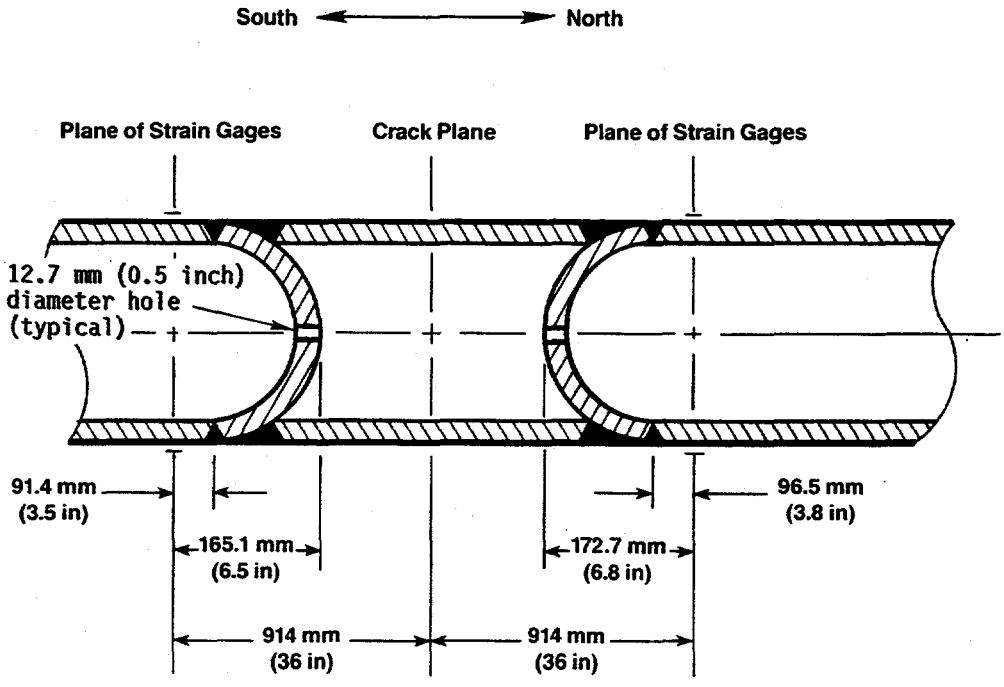

Figure 3.28 Details of end caps at test specimen used to minimize energy release in the event cracked pipe section severs I1.3-10/90-F3.28

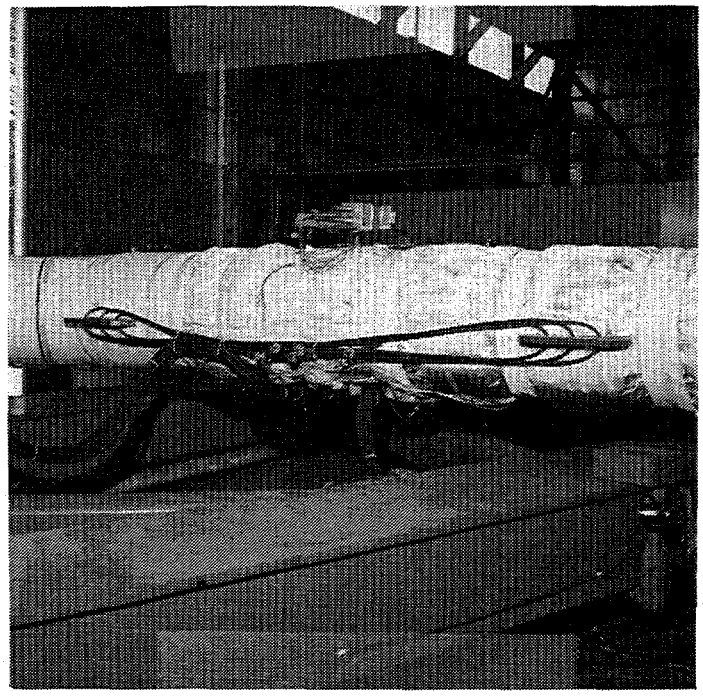

Figure 3.29 Photograph of wire rope system spanning the crack section incorporated in the overall design to restrain the motion of the two halves of the pipe loop in the event the crack section severs

F1.3-3/91-F3.29

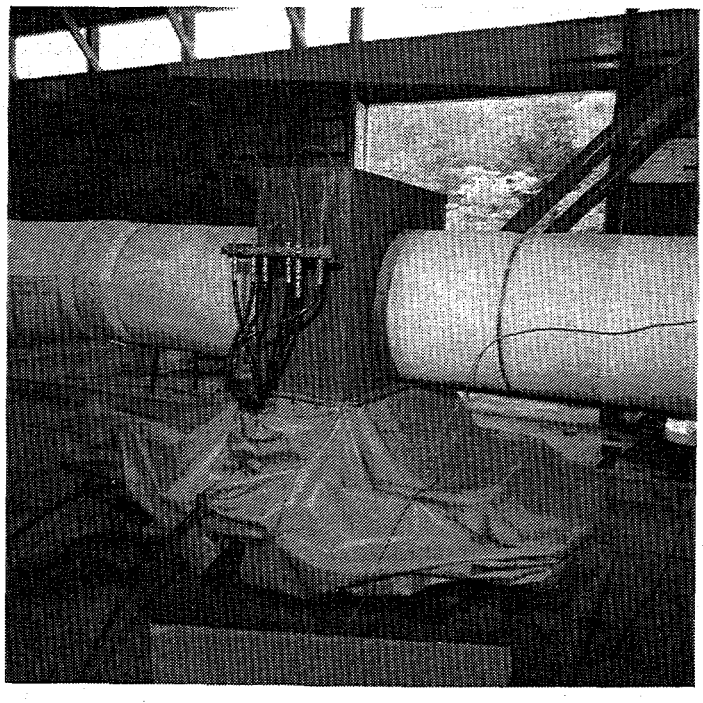

Figure 3.30 Photograph of large mass which simulates a swing check valve

F1.3-3/91-F3.30

3.3.1.2 Boundary Conditions

The boundary conditions for the piping loop are realized by using various specialized pieces of hardware. At the two fixed ends (Nodes 1 and 31), the pipe loop is welded to a 1,500-pound-class weld neck flange which is bolted to a large steel frame that is buried in a large, heavily reinforced concrete mass. At the actuator location, the pipe is restrained in the vertical direction with linear bearings (see Figure 3.31) and is free to rotate and translate in the other four degrees of freedom by use of a spherical bearing with a bronze bushing. At the two hanger locations (Nodes 6 and 26), the pipe is restrained in the vertical direction and the horizontal direction perpendicular to the pipe axis by spherical bearings, see Figure 3.32. The spherical bearings allow the pipe to rotate about all three axes and translate in the direction of the pipe axis. At the two vertical supports (at the mass and Node 20), the pipe is supported in the vertical direction by low friction hydrostatic bearings. Loads developed between the reaction points for the piping loop are reacted by a welded steel frame anchored in massive concrete blocks. The simplicity of the pipe loop boundary conditions makes finite element modeling of the pipe loop relatively simple.

3.3.1.3 Hardware

System loads are applied by a 1,560-kN (350,000-pound) Moog Model 85-454 double-ended piston actuator (equal piston areas for both push and pull) with a 457-mm (18-inch) stroke, see Figure 3.33. The actuator is driven by a 7,600 liter per minute (2,000 gpm) Moog Model 79-507 three-stage servo-valve which is supplied with oil at 21 MPa (3,000 psi) by piston-type accumulators with an oil capacity of 380 liters (100 gallons), see Figure 3.34. Nitrogen gas to drive the accumulators is stored in a separate pressure vessel.

The pipe loop is connected to an auxiliary expansion tank of 760 liters (200 gallons) capacity which is pressurized with air or dry nitrogen prior to the heat up. This tank accommodates the expansion of the water as it is heated from ambient temperature to 288 C (550 F). It also provides an accumulator effect for maintaining the pressure at the test conditions. Heat for bringing the pipe loop to test temperature is supplied by heater tapes wrapped continuously around the exterior of the pipe. Water in the pipe loop is circulated by a pump connected to the two fixed ends to provide an even temperature distribution. The pipe is completely covered with fiberglass insulation.

3.3.2 Test Specimen Preparation

The test specimens for the Subtask 1.3 experiments were short lengths (typically 300 mm [12 inches] or 760 mm [30 inches] in length) of 406-mm (16-inch) nominal diameter Schedule 100 pipe with an internal circumferential surface crack at the mid-length position of the test specimen. Table 3.2 lists the geometry details for the IPIRG 1.3 specimens. The five materials evaluated during the cracked pipe experiments were SA-106 Grade B carbon steel and SA-358 Type 304 stainless steel, their associated weldments, and a section of aged SA-351 Grade CF8M cast stainless steel donated to the program by the French company Framatome.

The internal circumferential surface cracks were machined into the test specimens using a horizontal milling machine with 150-mm (6-inch) diameter cutters. The initial portion of the machined notch was introduced using a 6.3-mm (0.25-inch) thick flat bottom cutter. The final 3.8 mm (0.150 inch) in depth

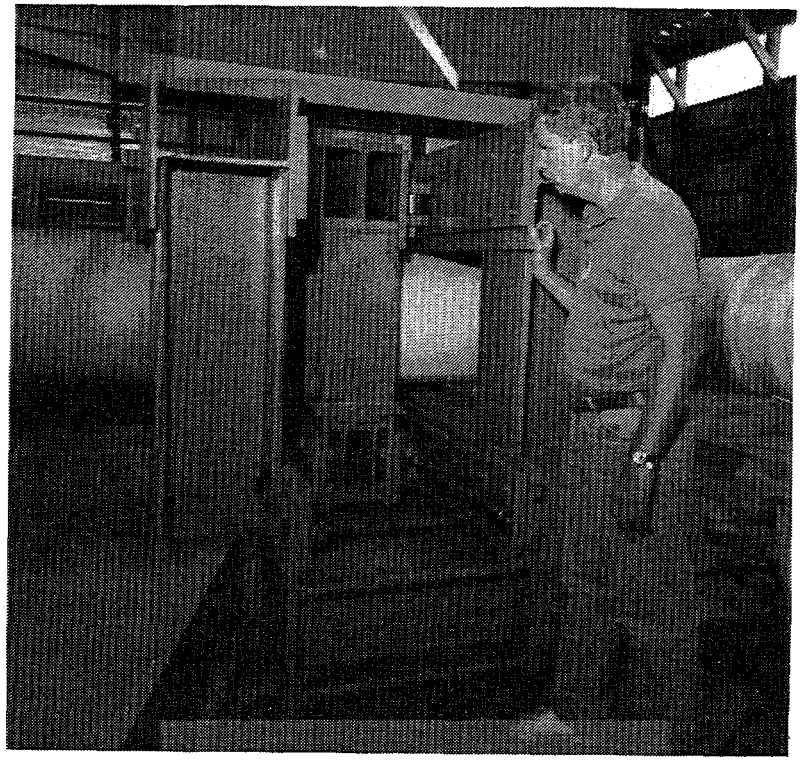

Figure 3.31 Photograph of carriage assembly at the actuator

F1.3-3/91-F3.31

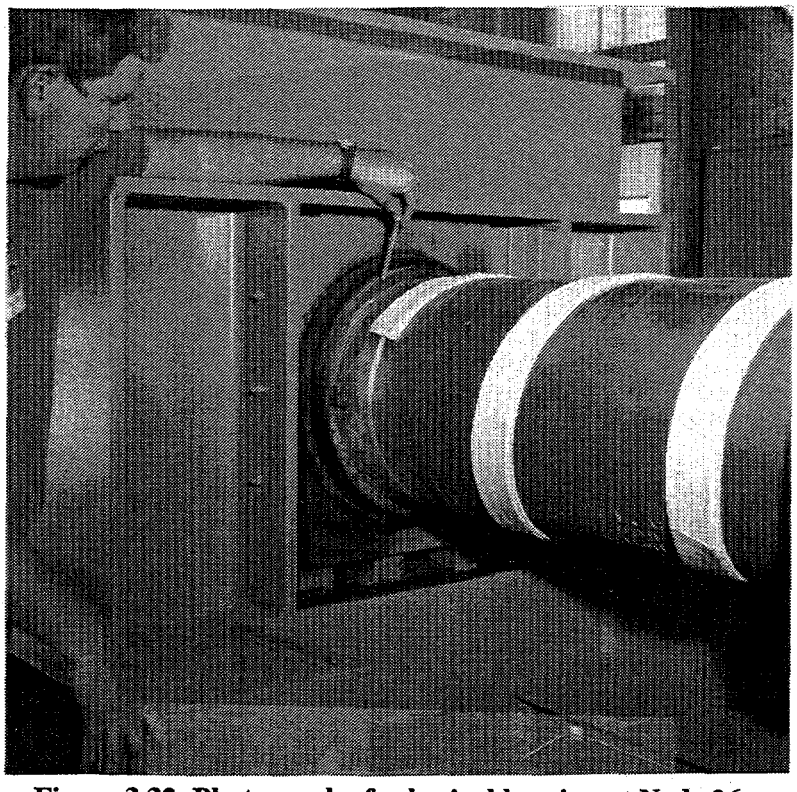

Figure 3.32 Photograph of spherical bearing at Node 26

F1.3-3/91-F3.32

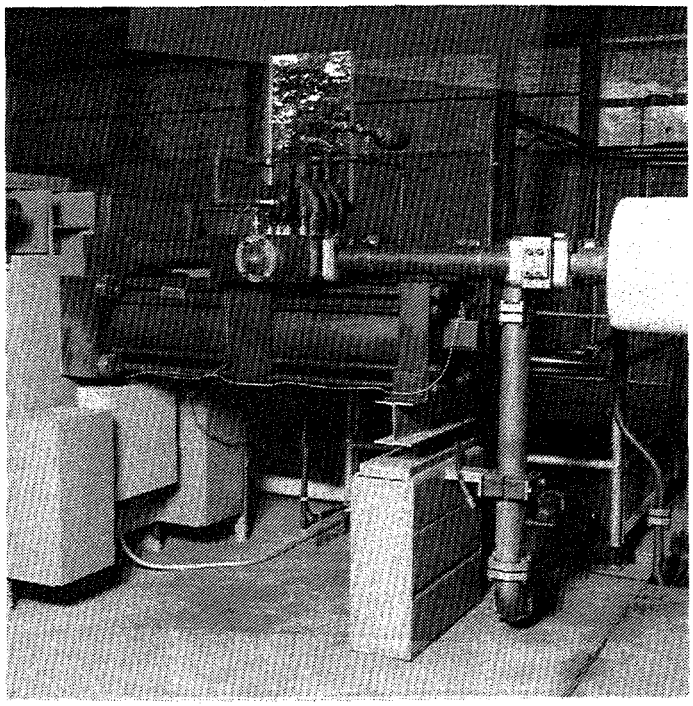

Figure 3.33 Photograph of hydraulic actuator with integral 7,600 lpm (2,000 gpm) servo-valve attached

F1.3-3/91-F3.33

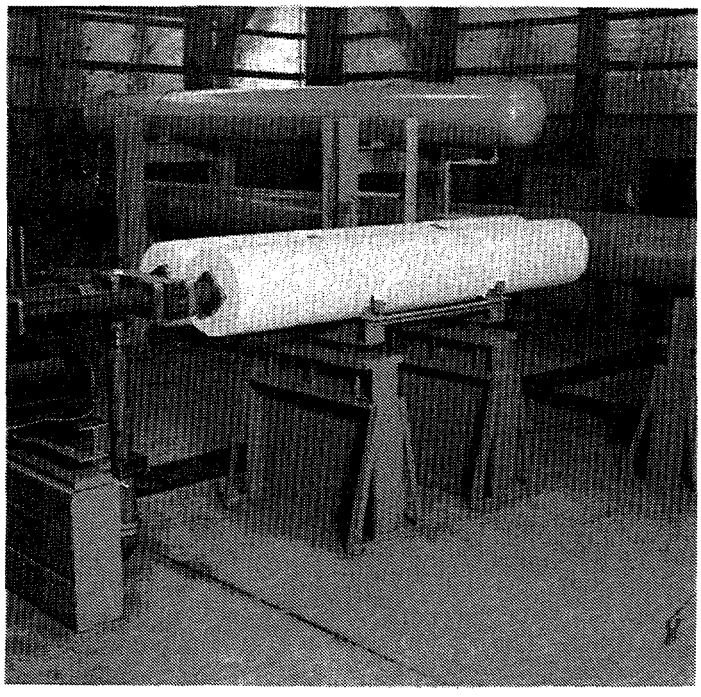

Figure 3.34 Photograph of piston-type hydraulic accumulators with nitrogen storage vessel and water circulation vessel in background

F1.3-3/91-F3.34

Table 3.2 Test specimens and flaw sizes evaluated as part of IPIRG Subtask 1.3

Experiment Number	Test Material	Pipe[c] Outside Diameter, mm (inch)	Length of Actual Test Specimen, mm (inch)	Maximum Crack Depth, mm (inch)	Pipe Wall Thickness, mm (inch)	Crack Length on Inside Surface, mm (inch)	Equivalent Crack Length, mm (inch)
1.3-1	ASTM A710 Carbon Steel Base Metal	406.4 (16.00)	N/A	N/A	27.4 (1.08)	N/A	N/A
1.3-2	SA-106B Carbon Steel Base Metal	403.9 (15.90)	762 (30)	18.81 (0.7405)	25.7 (1.012)	582 (22.9)	486 (19.12)
1.3-3	SA-358 Type 304 Stainless Steel Base Metal	415.8 (16.37)	762 (30)	16.95 (0.667)	26.2 (1.031)	630 (24.8)	534 (21.04)
1.3-4	SA-106B Carbon Steel Weld[a]	402.6 (15.85)	762 (30)	17.6 (0.693)	28.1 (1.106)[b] 25.5 (1.003)[c]	590 (23.3)	531 (20.9)
1.3-5	SA-358 Type 304 Stainless Steel Weld[a]	416.0 (16.38)	762 (30)	16.3 (0.642)[d]	26.2 (1.031)[b] 25.7 (1.011)[c]	610 (24.0)	506 (19.93)
1.3-7	SA-351 Grade CF8M Aged Cast Stainless Steel Base Metal	400.3 (15.76)	305 (12)	14.1 (0.555)	26.6 (1.047)	591 (23.25)	545 (21.46)

(a) Submerged-Arc Weld (SAW). Weld crowns left on.
(b) Includes the height of the weld crown (t_{wall} + h_{crown}, see Figure 3.36).
(c) Does not include the height of the weld crown (t_{wall}, see Figure 3.36).
(d) Includes the depth of the counterbore (d_c + d_{cb}, see Figure 3.36).

was introduced using a 3.2-mm (0.125- inch) thick cutter with the teeth ground to a 30 degree included angle, see Figure 3.35. This cutter geometry provided for a relative sharp machine notch. For the stainless steel base metal and the aged cast stainless steel experiments, the sharp machine notch was not fatigue precracked because previous experience in the Degraded Piping Program - Phase II (Ref. 3.6) had demonstrated that the fracture behavior for the stainless steel base metal and the aged cast stainless specimens was not influenced by the notch acuity. For the other materials evaluated (i.e., the carbon steel base metal, and the carbon and stainless steel weld metal specimens), the machine notch was fatigue precracked by pressure cycling with a minimum and maximum pressure of 1.72 MPa (250 psi) and 17.2 MPa (2,500 psi), respectively. Note, this notch/precrack geometry would not satisfy the constraints imposed in applicable ASTM standards such as E338 or E399 to avoid notch effects in fracture toughness specimens (i.e., side-edge notch or compact (tension) specimens). However, this was not considered to be a severe limitation based on our experience from the Degraded Piping Program (Ref. 3.6). Furthermore, Problem 3-1a of the Sixth IPIRG Workshop in Taipei, Taiwan involved finite element analyses of a 102-mm (4-inch) diameter Schedule 160 through-wall crack experiment (French Experiment Number 5). The through-wall crack geometry for this experiment also failed to satisfy the notch/precrack geometry constraints imposed in the applicable ASTM Standards. However, the finite element predictions of moment versus load-line displacements provided by Battelle, SKi, CEA, and EDF showed excellent agreement with the experimental results. Thus, it appears that the effect of this notch geometry was minimal. The depths of the internal surface cracks (including the fatigue precrack, where applicable) and the pipe wall thicknesses were measured post-test at nine locations along the lengths of the surface cracks. The maximum crack depths of the internal surface cracks and the average wall thicknesses for each of the experiments are included in Table 3.2.

For analysis purposes, it is frequently necessary to use the crack depth to thickness ratio. There are two complications in determining this ratio. The first is that the crack depth is not perfectly uniform. In this case, the maximum depth is most frequently used. The second complication occurs for the case of a crack in the weld. Either the pipe thickness or the pipe thickness plus weld crown height could be used in the depth-to-thickness ratio. In ASME Code applications, the pipe thickness is used, but in analyzing experimental data, the thickness plus weld crown height may be more appropriate. Both values are included in Table 3.2.

A further complication associated with the stainless steel weld specimen was that the inside pipe surface in the vicinity of the weld was counterbored prior to welding, see Figure 3.36. This counterbore was machined on the inside surface per the General Electric (GE) weld procedure that was followed. The weld procedure specified a counterbore to match up the weld lands to accommodate mismatches between different pipe inside diameters.

The total crack length (2c) for each specimen was measured post-test. The crack lengths (tip-to-tip) measured on the inside pipe surface are included in Table 3.2. In addition, Table 3.2 includes an equivalent crack length measurement. This equivalent crack length, which is frequently used in fracture analyses, was determined by dividing the actual crack area by the maximum crack depth.

3.3.3 Instrumentation

A wide range of instrumentation was used during the course of the six Subtask 1.3 experiments. The total instrumentation plan was an evolutionary process. As technical issues arose, and were subsequently

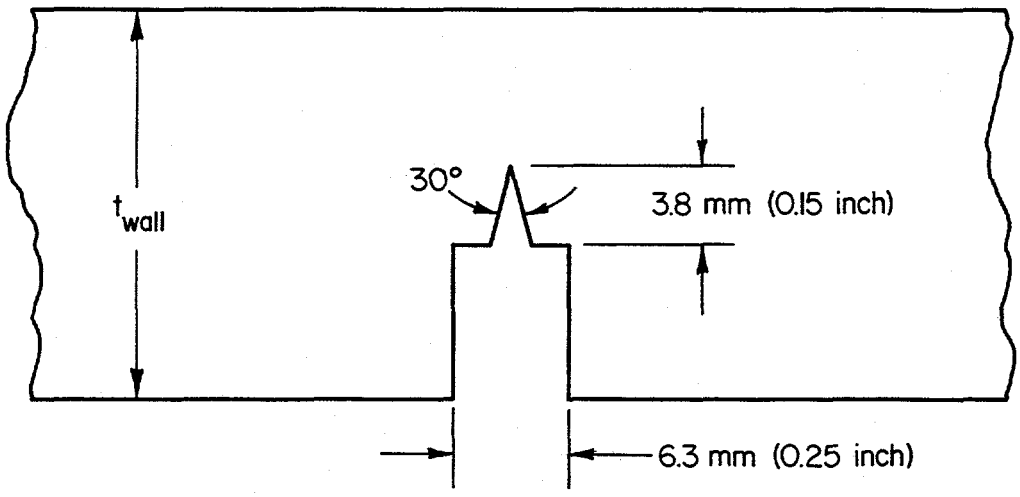

Figure 3.35 Geometry of machined notch used for Subtask 1.3 test specimens

I1.3-10/90-F3.35

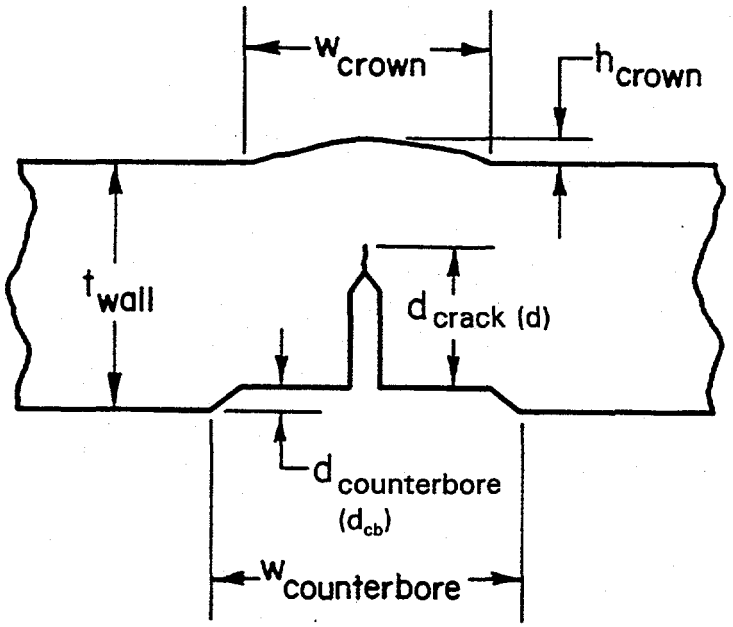

Figure 3.36 Weld joint geometry for stainless steel weld experiment

QL/1.3-5/F2

resolved, various pieces of the overall instrumentation plan were added or removed. For example, in the early experiments a pressing question was whether or not the two fixed ends were indeed fixed. In order to address this question, three orthogonally mounted accelerometers were attached to the steel pipe support framework. Ideally, by double integrating the accelerometer data, it would be possible to assess the magnitude of the displacements at these two locations. Once it was established that the displacements at the two fixed ends were indeed extremely small, these accelerometers were eliminated from future experiments. Table 3.3 lists all the instrumentation used throughout the course of this program Figure 3.37 shows the location of the various pieces of instrumentation listed in Table 3.3.

3.3.3.1 Actuator Displacements

At the actuator location, the applied displacement was measured using an MTS Temposonics Model 011018070109 (Moog A81840-018S-010) 457-mm (18.0-inch) range magnetostrictive position transducer integral with the actuator rod. Signal conditioning for the Temposonics was provided by an externally mounted MTS Temposonics Model 011018072603100 (Moog 96300B-018B-003) signal conditioner. In addition to being a measured output signal, the applied displacement was also the feedback signal for the servo-controller. Data from this transducer were collected for all experiments.

3.3.3.2 Actuator Loads

The applied forces were measured directly using a strain gage based load cell of 1,335 kN (300,000 pound) capacity manufactured by the Toroid Corporation. The load cell output was conditioned by a DC Signal Conditioner Module in the actuator servo-controller. In addition, as a backup, the pressure on both sides of the actuator piston was measured using Schaevitz P2593-0001, 24 MPa (3,500 psi) pressure transducers with internal signal conditioning. Knowing the cross-sectional area of the piston and the pressure of the oil being delivered to each side of the actuator, the applied force can be calculated. In dynamic tests, there is a pressure drop between the pressure transducers and the actuator piston that must be considered. Because there was never a failure of the load cell, the backup pressure transducer data were never needed to calculate load. The pressure transducer data were analyzed for one experiment and found to be in very close agreement with the load cell data.

3.3.3.3 Node 6 Reaction Force

Reaction force data in the horizontal plane was collected at Node 6 (the hanger nearest the actuator location) as shown in Figure 3.37. At this location, the lateral reaction force was derived from the pressure developed in a set of hydraulic jacks plumbed together in a closed system, see Figure 3.38. With reference to Figure 3.39, as the pipe loop loads against one column of the hanger, the pressure in the hydraulic jacks on that side increases because the check valves close off any oil flow out of the jacks. On the opposite side, the pressure drops until it reaches the pressure of the accumulator, 6.9 MPa (1,000 psi). At this pressure, the check valve on that side unseats and the jacks extend to take up any clearance that may have developed. Knowing the cross-sectional area of the jacks and the pressure in the jacks on both sides,

Table 3.3 Total list of instrumentation used during the IPIRG Subtask 1.3 experiments

Channel Name			
Actuator Displacement			
Actuator Load			
Node 6 Reaction Force			
Vessel Pressure			
Crack			
Elbow 3			
Elbow 4			
Crack-Mouth-Opening Displacements			
LVDT			
Clip Gage			
Rotation			
Fine			
Coarse			
Nodes 1 and 31 Displacements			
Accelerometers (Nodes 1 and 31)			
String Potentiometers (Node 1 only)			
d-c Electric Potential			
Internal #1	External #4		
Internal #2	External #5		
Internal #3	External #6		
Base Metal			
Battery Current			
Strain Gages			
South End Cap #1		Future Crack #7[1]	North End Cap #13
South End Cap #2		Future Crack #8	North End Cap #14
South End Cap #3		Future Crack #9	North End Cap #15
South End Cap #4		Future Crack #10	North End Cap #16
South End Cap #5		Future Crack #11	North End Cap #17
South End Cap #6		Future Crack #12	North End Cap #18
Elbow 4 Extrados #19			
3.2 m North of Elbow 4			
#20			
#21			
#22			
Elbow 3 Top #23			
Elbow 2 Top #24			
Elbow Strain Gages (room temperature)			
Elbow 3 (A-1 through D-3)			
Elbow 4 (E-1 through H-3)			
String Potentiometers			
Elbow 3 Displacement (Center, West, South)			
Crack Location Displacement (Center, East, South)			
Hydrostatic Bearing Displacement (Center, East, South)			

(a) Data taken during uncracked pipe experiment (1.3-1), crack location for subsequent cracked pipe experiments.

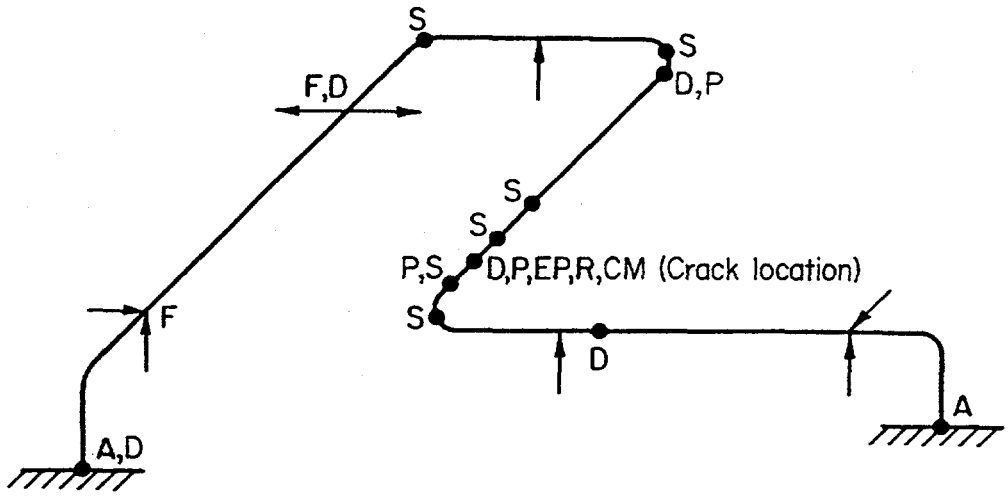

LEGEND

A	-	**Accelerations**
F	-	**Force**
D	-	**Displacement**
S	-	**Strain**
P	-	**Pressure**
EP	-	**Electric Potential**
R	-	**Rotation**
CM	-	**Crack-Mouth-Opening Displacement**

Figure 3.37 Overall instrumentation layout for Subtask 1.3

I1.3-10/90-F3.37

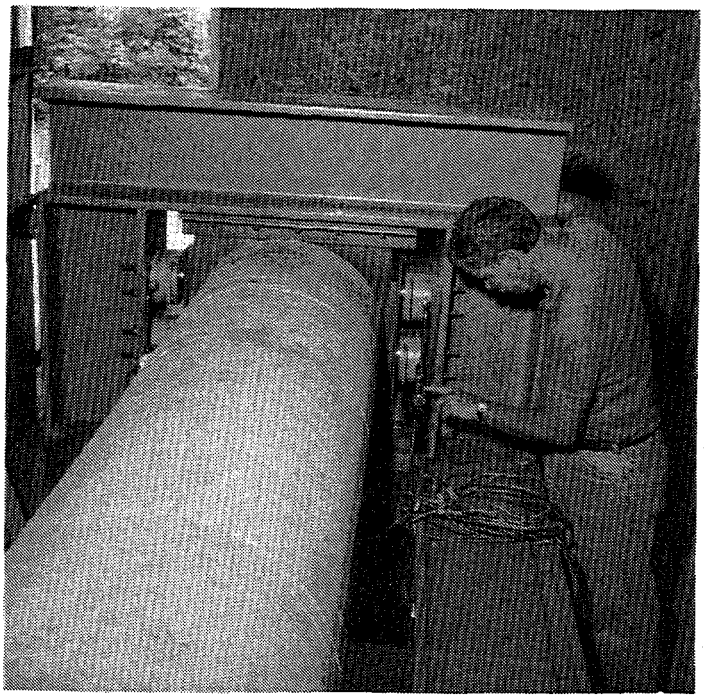

Figure 3.38 Photograph of hydraulic jacks at Node 6 used to infer reaction force F1.3-3/91-F3.38

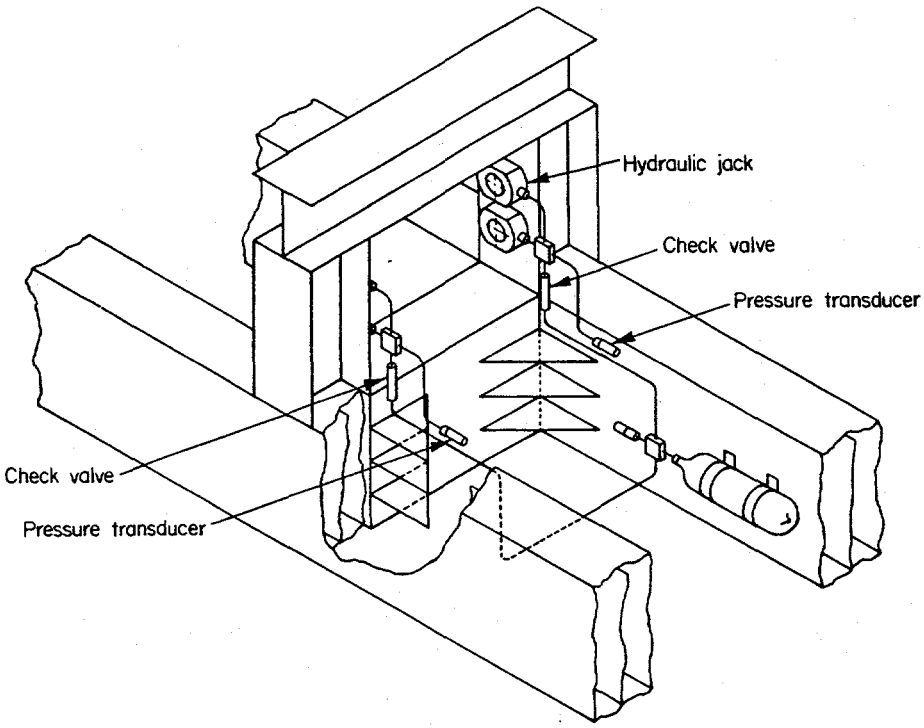

Figure 3.39 Node 6 hanger load cell details F1.3-3/91-F3.39

one can calculate the applied force. This load measuring system provides a simple, zero-lash method for determining the reaction load at the hanger. Four Enerpac RSM-1000 jacks were used in the system along with Sensotec TJE/744, 69 MPa (10,000 psi) pressure transducers with internal signal conditioning.

3.3.3.4 Pipe Displacements

At three locations on the pipe (Elbow 3, the crack location, and Node 21, see Figure 3.37), pipe loop displacements were measured using Genisco PT-50A 1.27 m (50 inch) range string potentiometers, see Figure 3.40. These devices utilize a precision potentiometer, a constant tension rotational spring, and a cable and to provide a resistance directly proportional to the extension of the cable from the base for the device. Using a precision, fixed-voltage power supply, the output of the string potentiometer is a voltage proportional to displacement. As shown in Figures 3.41 through 3.43, three displacement measurements were made at each location. Knowing the initial spacing between the three potentiometers and the pipe, and measured changes in the vector lengths between the base of the string potentiometers and the point of attachment on the pipe, the global X-Y-Z displacements of the pipe in space can be calculated using the procedure set forth in Appendix A.

Prior to conducting the first experiment, the dynamic response of these string potentiometers was assessed in Battelle's Fatigue Laboratory. Three string potentiometers were mounted in a high-rate MTS servo-hydraulic test frame, see Figure 3.44. The ends of the three cables were tied together and attached to the stationary load cell. The three housings were mounted 90 degrees to each other and attached to a common base plate which was attached to the hydraulic ram. The hydraulic ram was excited in displacement control.

The first test involved exciting the ram at a displacement rate of 50 mm/second (2 inches/second), see Figure 3.45. During the second test the ram was excited at a higher rate of 250 mm/second (10 inches/second), see Figure 3.46. It was thought that this higher displacement rate would be typical of what might be expected during the actual IPIRG Subtask 1.3 experiments. (Note, post-test it was found that the actual displacement rates for some of the potentiometers approached 1250 mm/second (50 inches/second.) In examining Figures 3.45 and 3.46, one sees that the predicted Z-displacements from the string potentiometers showed excellent agreement with the measured stroke of the actuator from the test machine's LVDT. In addition, the predicted X- and Y-displacements are small, as one would expect. (The base plate holding the string potentiometer housings was not moving in the X-Y plane.) Furthermore, comparing the agreement between the predicted (from string potentiometer data) and actual (LVDT) Z-displacements for the two different displacement rates reveals the fact that the response of the string potentiometers was better at the higher displacement rate typical of what we expected in the actual Subtask 1.3 experiments.

3.3.3.5 Fixed End (Node 1) Displacements

At the Node 1 fixed end, displacements were measured for the stainless steel base metal experiment to assess the suitability of the fixed node assumption made in the analytical modeling of the experiments. Two types of instrumentation were employed for these measurements as shown in Figure 3.47; three orthogonally mounted accelerometers attached to the steel framework support for the large weld neck flange at the end of the loop and two string potentiometers attached to the same flange in the

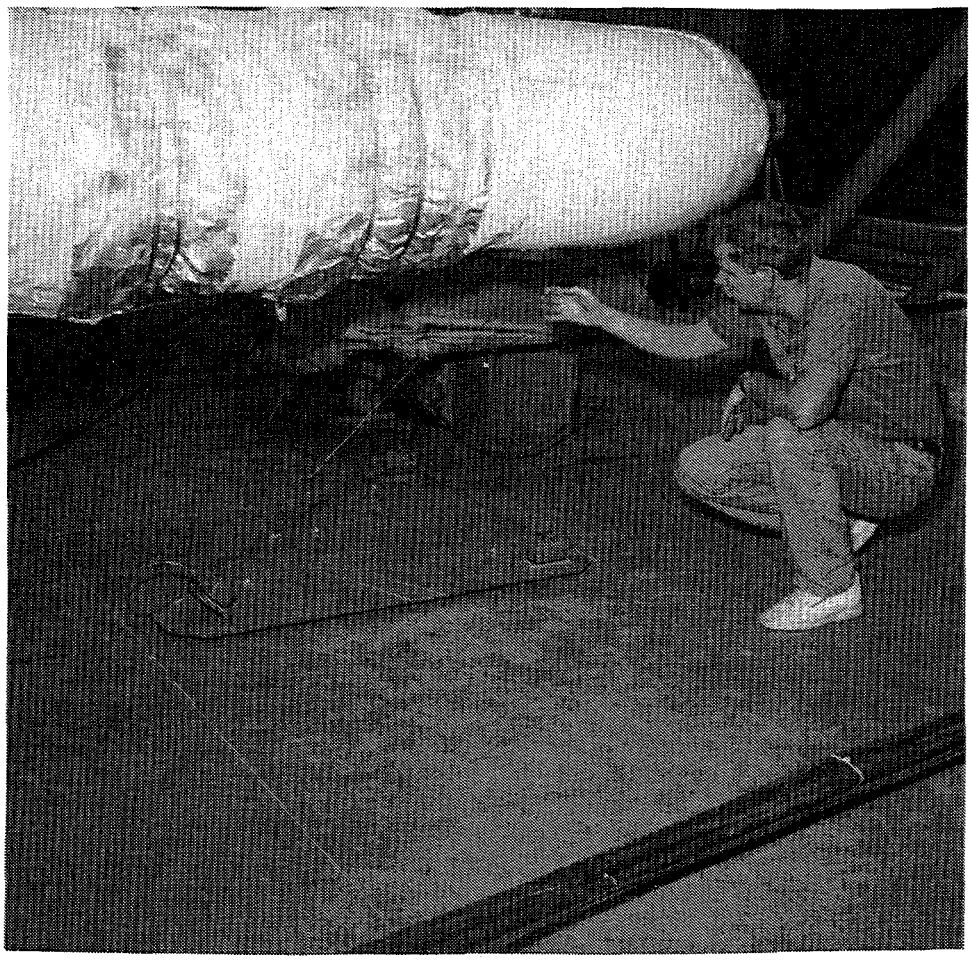

Figure 3.40 Photograph of three orthogonally mounted string potentiometers at Elbow 3 used to infer pipe displacement data F1.3-3/91-F3.40

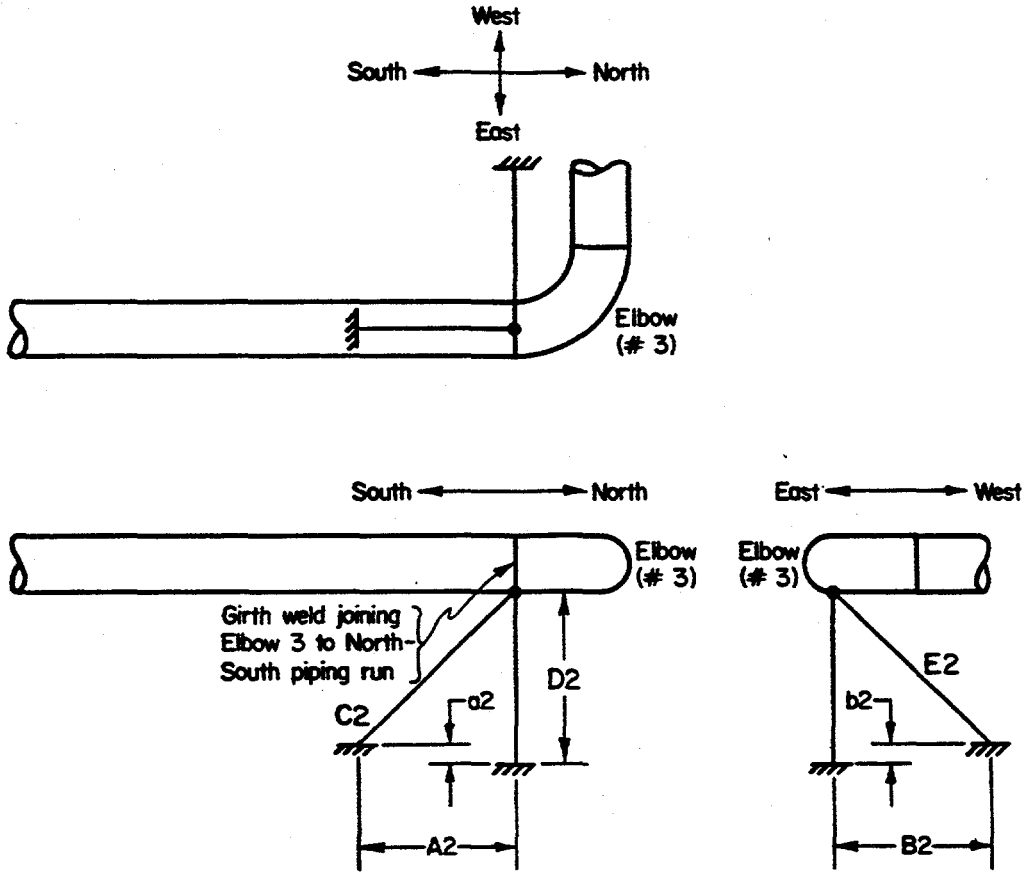

NOTE: Due to offsets of the entire pipe loop from previous tests, do not assume that the D2 measurement is perpendicular to the ground. The vector lengths C2, D2, and E2 define the initial position prior to pressurization and heat-up

Figure 3.41 Elbow Number 3 displacement measuring device initial geometry for Subtask 1.3 experiments

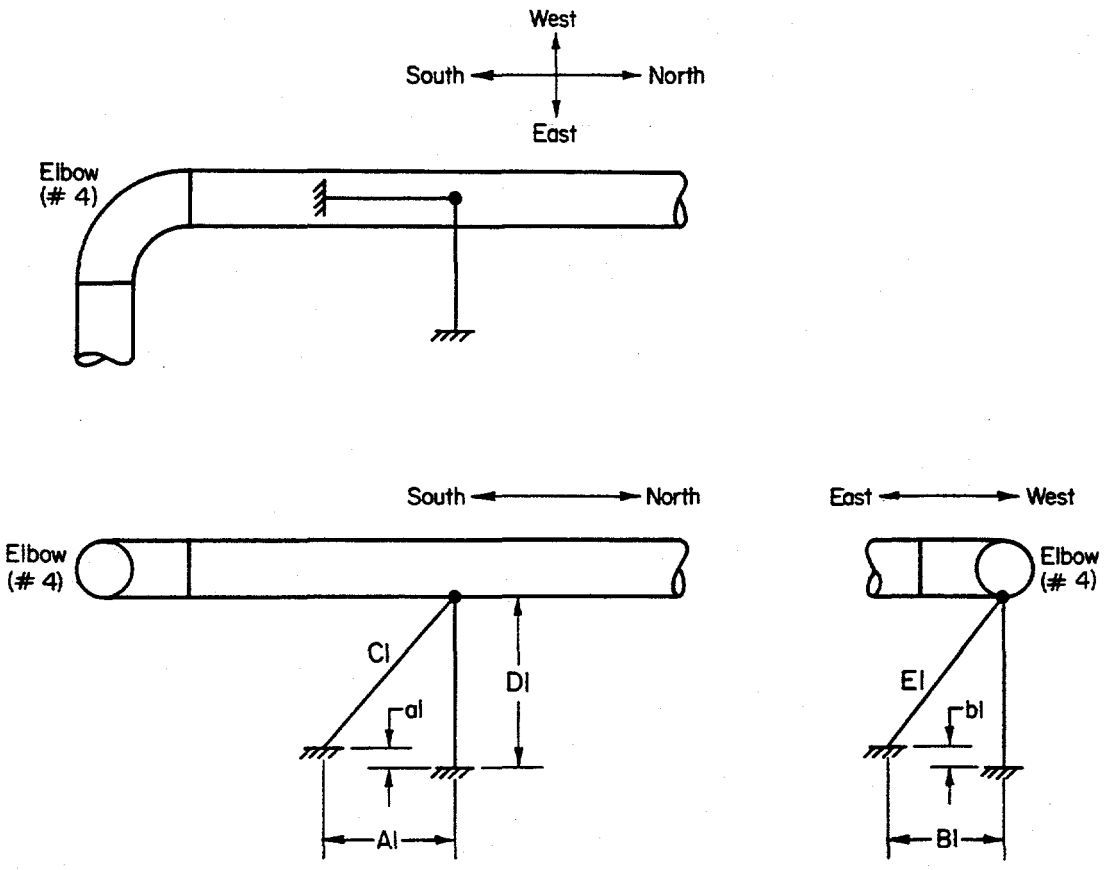

NOTE: Due to offsets of the entire pipe loop from previous tests, do not assume that the D2 measurement is perpendicular to the ground. The vector lengths C1, D1, and E1 define the initial position prior to pressurization and heat-up

Figure 3.42 Crack location displacement measuring device initial geometry for Subtask 1.3 experiments

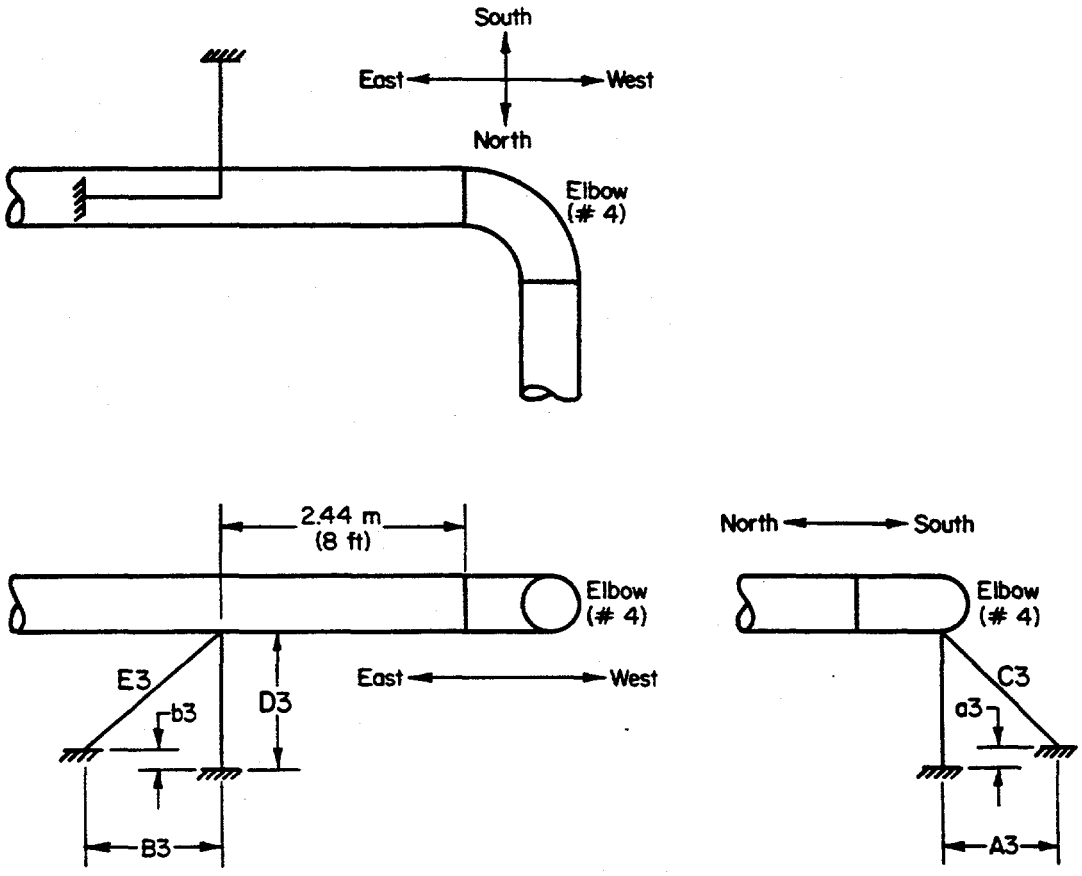

NOTE: Due to offsets of the entire pipe loop from previous tests, do not assume that the D2 measurement is perpendicular to the ground. The vector lengths C3, D3, and E3 define the initial position prior to pressurization and heat-up

Figure 3.43 Node 21 displacement measuring device initial geometry for Subtask 1.3 experiments

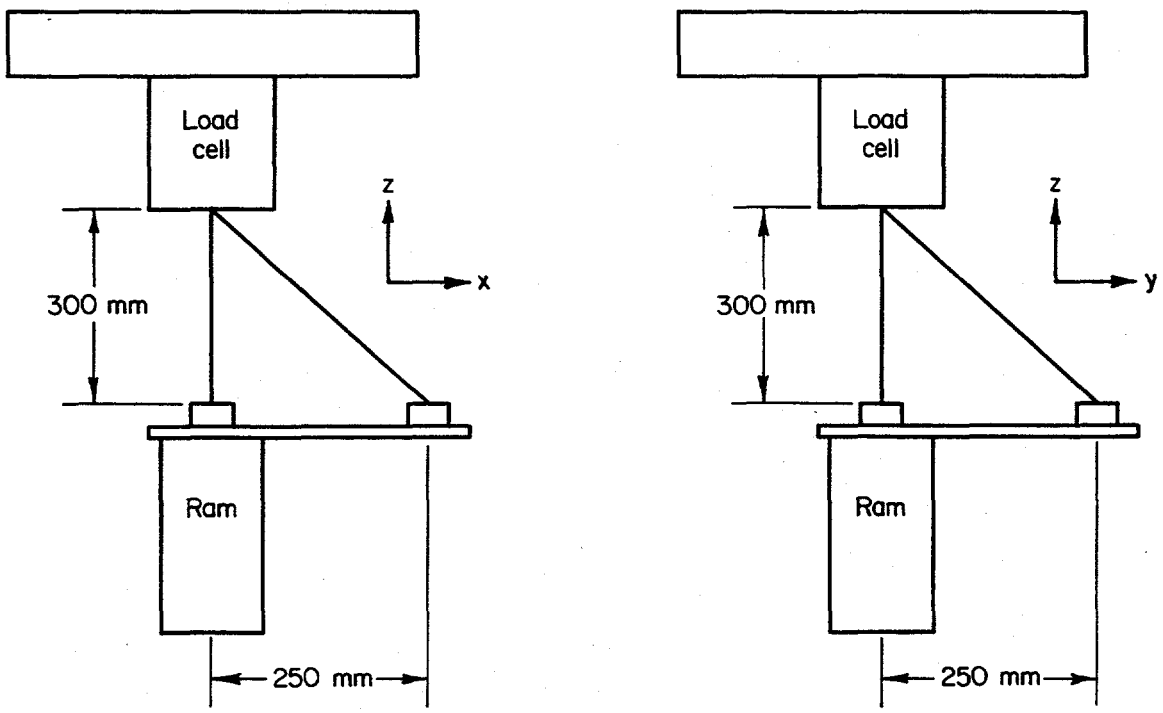

Figure 3.44 Setup of three string potentiometers in high rate fatigue machine used to assess dynamic response of string potentiometers F1.3-3/91-F3.44

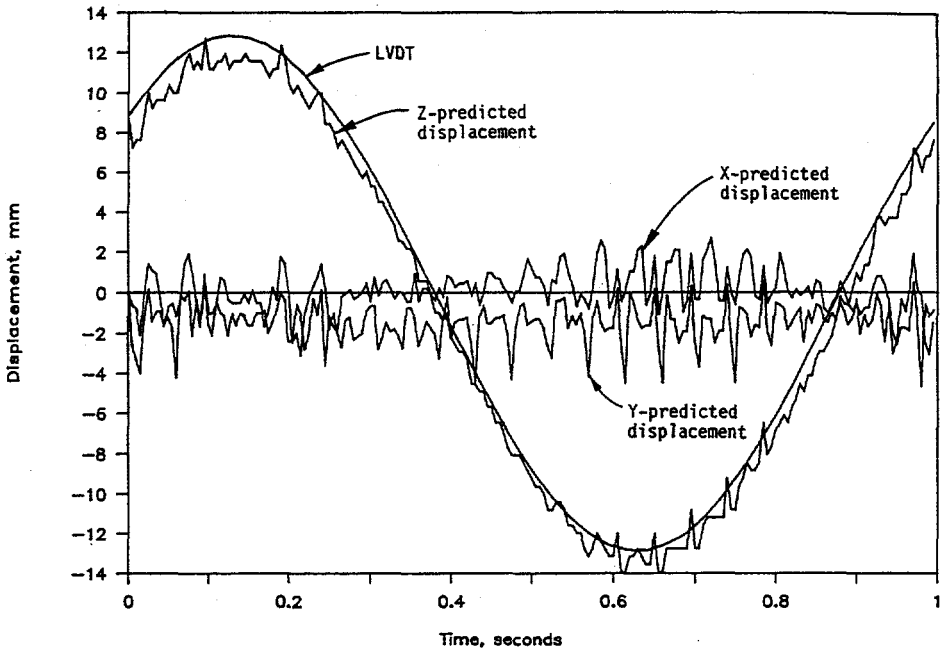

Figure 3.45 Predicted X, Y, and Z-direction response from string potentiometer data and actual Z-direction response from LVDT measurements for applied Z-directed displacement rate of 50 mm/sec (2 inches/sec) F1.3-3/91-F3.45

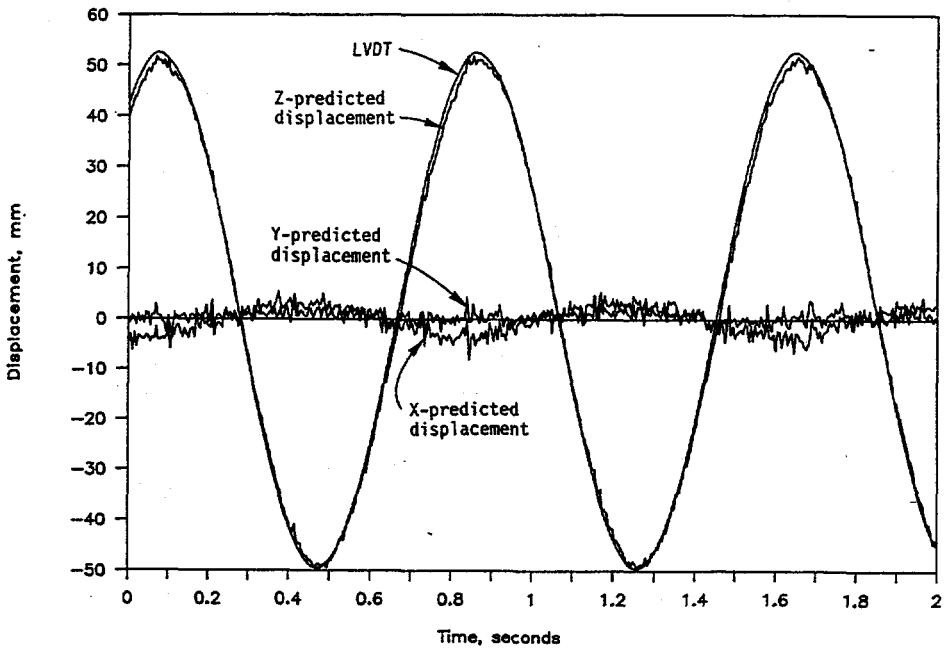

Figure 3.46 Predicted X, Y, and Z-direction response from string potentiometer data and actual Z-direction response from LVDT measurements for applied Z-directed displacement rate of 250 mm/sec (10 inches/sec) F1.3-3/91-F3.46

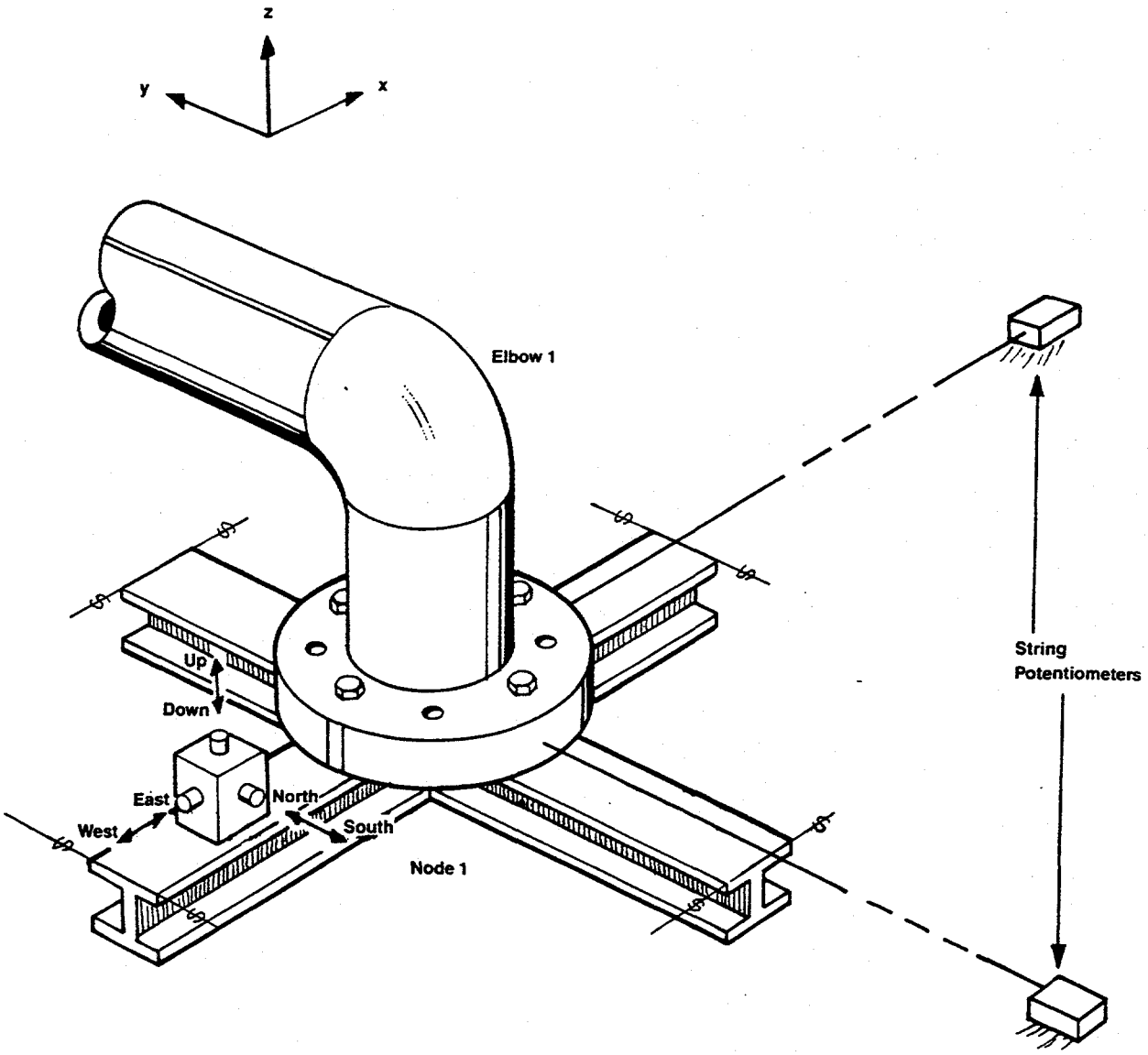

Figure 3.47 Accelerometers and string potentiometers used to check boundary conditions at Node 1 fixed end for stainless steel base metal experiment

horizontal plane. As shown in Figure 3.47, the bases for the string potentiometers were mounted on fixtures which were attached to the ground and isolated from the piping loop and loading frame. The string potentiometer cables were attached directly to the weld neck flange and consequently, the outputs of the string potentiometers were the relative displacements of the Node 1 fixed end with respect to ground.

The accelerometers were PCB Piezotronics Model 321A02 quartz accelerometers with built-in amplifiers and a 50 g range. Power and signal amplifying of the accelerometers were provided by a PCB Piezotronics accelerometer amplifying power unit, Model 482A07. The string potentiometers were Genisco PT-50A 1.27 m (50 inch) range string potentiometers. To increase the apparent sensitivity of the potentiometers, their outputs were amplified by Ectron 751 El-M563 amplifiers. To keep the amplified outputs within the range of the data acquisition system, the outputs of the string potentiometers were offset using the Ectron amplifiers in a differential mode with a precision constant voltage power supply as the second amplifier input.

3.3.3.6 Pipe Pressures

For all but the aged cast stainless experiment, the internal pressure at the test section was measured using a Schaevitz 2503-0001, 17.2 MPa (2,500 psi) pressure transducer. The aged cast stainless experiment used a Dynisco PT-1191, 17.2 MPa (2,500 psi) pressure transducer. For all experiments, the pressure transducer was conditioned using a Daytronic 3270 strain gage bridge signal conditioner. The signal was filtered at 200 Hz.

The output of the test section pressure transducer served two purposes; it was a measured signal, and it provided a control signal which triggered the shutdown of actuator motion for the cracked pipe experiments. Further details of this control logic are provided in the Data Acquisition and Control System section of this report.

In addition to measuring the pressure at the test specimen, for the aged cast stainless experiment, the pressure in the straight pipe run containing the crack was measured at its two ends, i.e., adjacent to Elbows 3 and 4 (see Figure 3.48). The pressures at these locations were measured using Schaevitz 2503-0001 17.2 MPa (2,500 psi) pressure transducers. These transducers were conditioned using Daytronic 3270 strain gage bridge signal conditioners. The pressure signals were filtered at 200 Hz.

3.3.3.7 Crack-Mouth-Opening Displacement (CMOD)

For each of the cracked pipe experiments, CMOD was measured across the crack centerline using a Schaevitz 250XS-ZT, ±6.5-mm (±0.250-inch) range extreme environment LVDT (Linear-Variable-Differential Transformer) displacement transducer. The LVDT was conditioned with a Schaevitz PCB-441 AC amplifier/demodulator. In addition, for the latter experiments (i.e., the stainless steel base metal and weld metal experiments, and the aged cast stainless steel experiment), the CMOD data from the LVDT was backed up by CMOD data collected at a position 38 mm (1.5 inch) offset from the crack centerline using a Battelle-built high-pressure/high-temperature clip gage. The geometry/layout of the CMOD devices is shown in Figure 3.49.

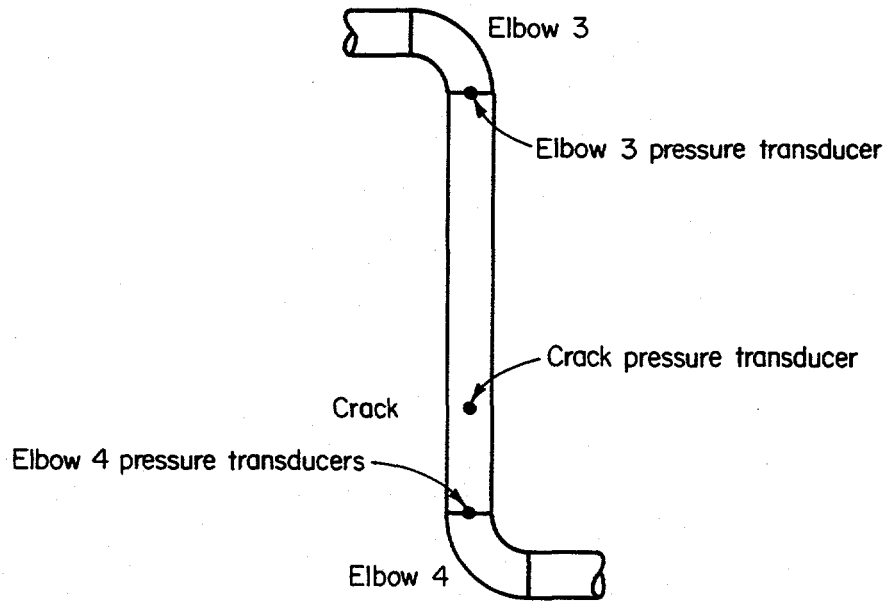

Figure 3.48 Location of pressure transducers for aged cast stainless steel experiment

I1.3-10/90-F3.48

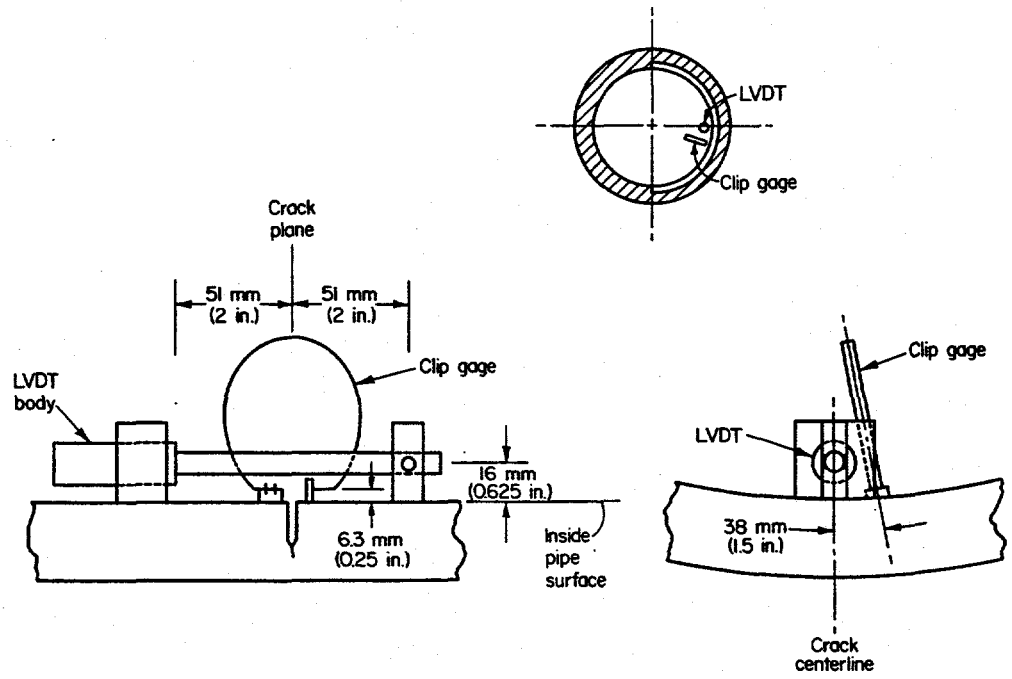

Figure 3.49 Layout/geometry of LVDT and clip gage used to determine crack-mouth-opening displacements

DRB/1.3-3/F8

3.3.3.8 Pipe Rotations

Pipe rotation data at the cracked section were collected for all experiments. For the first two cracked pipe experiments, rotation at the test section was measured using the device shown in Figure 3.50. With reference to Figure 3.51, the operation of this device is as follows:

- The axle of Wheel A is rigidly attached to the pipe. Wheel A does not rotate on the axle.
- The axle of Wheel B is also attached to the pipe but the wheel rotates in bearings around the shaft.
- Rotation of Wheel B relative to Point d (Angle c'-b'-d') is equal to the total rotation, 2ϕ, of the crack provided that Wheels A and B are of the same size and are located equal distances from the crack plane.

The rotation of Wheel B was measured with a Schaevitz R30D DC-RVDT. This device, internally conditioned rotary-variable-differential transformers, provides a d-c output voltage proportional to the rotation of the shaft relative to the housing. A redundant set of rotation measuring devices was deployed. The output of the RVDT was filtered at 100 Hz using Ectron 751 El-M563 amplifiers to eliminate noise from the internal RVDT modulator/demodulator.

Although the RVDT-based rotation device was used with success on the IPIRG Subtask 1.1 pipe tests, in the Subtask 1.3 experiments, the signal-to-noise ratio for the device precluded detection of the small rotations that occur prior to surface-crack penetration. After surface-crack penetration, signal values increased, but noise and drift caused by impingement of the escaping steam on the device rendered the data unusable. In any event, the data from the device were generally of little value.

In order to overcome the signal-to-noise ratio problem and to make a physically more robust rotation measuring system, the RVDT-based rotation device was replaced with an LVDT-based rotation device for the last three experiments, i.e., the stainless steel base metal, stainless steel weld metal, and the aged cast stainless experiments. For these three experiments, the pipe-rotation data at the crack section were obtained using the device shown in Figures 3.52 and 3.53. This rotation device utilized two LVDTs; a short stroke LVDT to measure small rotations up to surface-crack penetration and a long stroke LVDT to obtain the larger rotations which occur after the surface-crack penetrates the pipe wall and becomes a through-wall crack. In operation, the LVDT-based rotation device operates in the same fashion as a beam-type torque wrench; the relative displacement of the stiff rigid beam and the LVDTs is geometrically related to the total angle of rotation between the device's two points of attachment to the pipe.

The short stroke LVDT used in the LVDT-based rotation device was a Schaevitz GCA-121-250 hermetically sealed ±6.35-mm (±0.250-inch) spring-loaded LVDT, while the long stroke LVDT was a Schaevitz 1000 RBB-A Ultra-Tough ±25-mm (±1.00-inch) stroke precision gage head. Both of the LVDTs were conditioned by Schaevitz PCB-441 AC amplifier/demodulators.

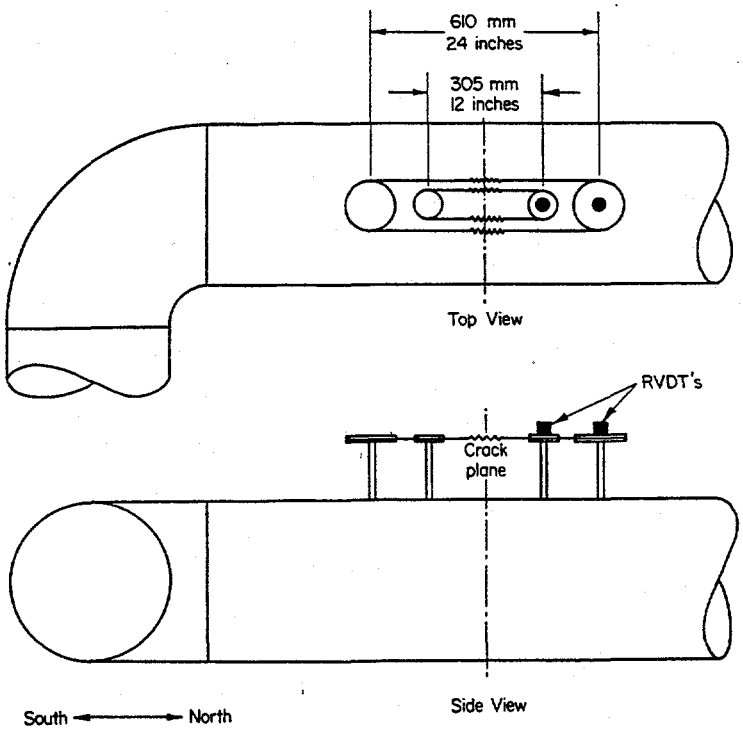

Figure 3.50 Crack rotation measuring device geometry used for carbon steel base metal and weld metal experiments

DRB/1.3-1/F9

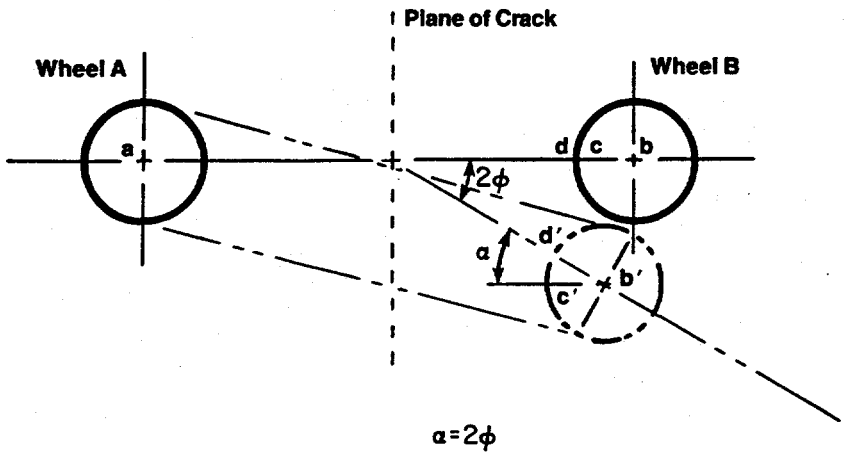

Figure 3.51 RVDT-based crack-rotation device operation

I1.3-10/90-F3.51

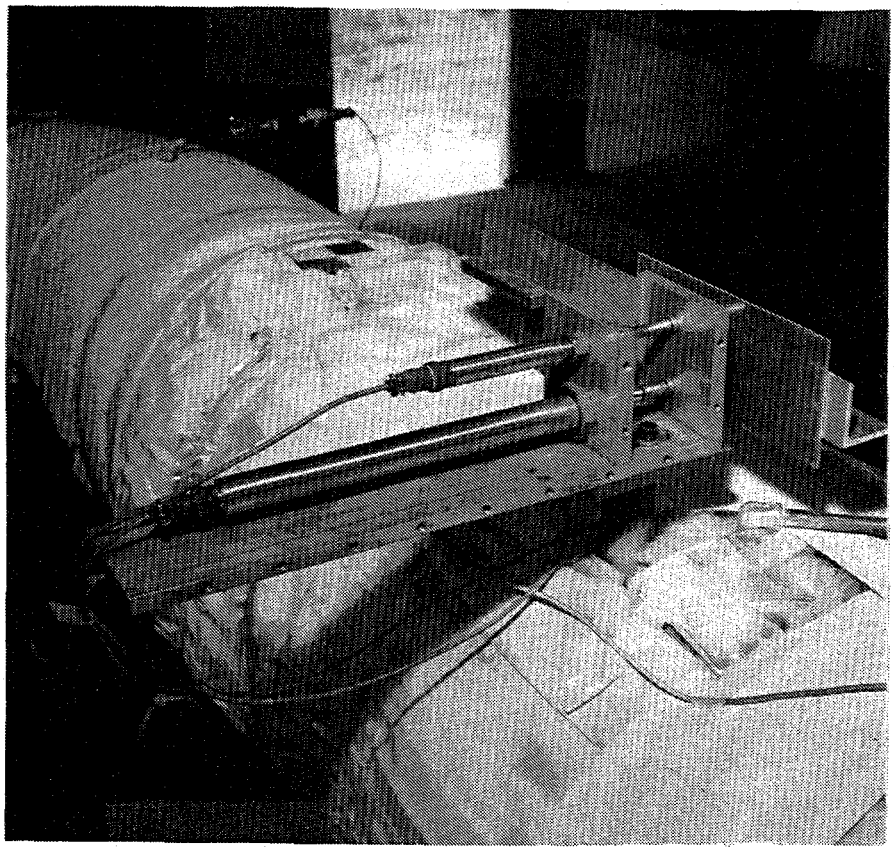

Figure 3.52 Photograph of LVDT-based rotation device used on three stainless steel experiments

F1.3-3/91-F3.52

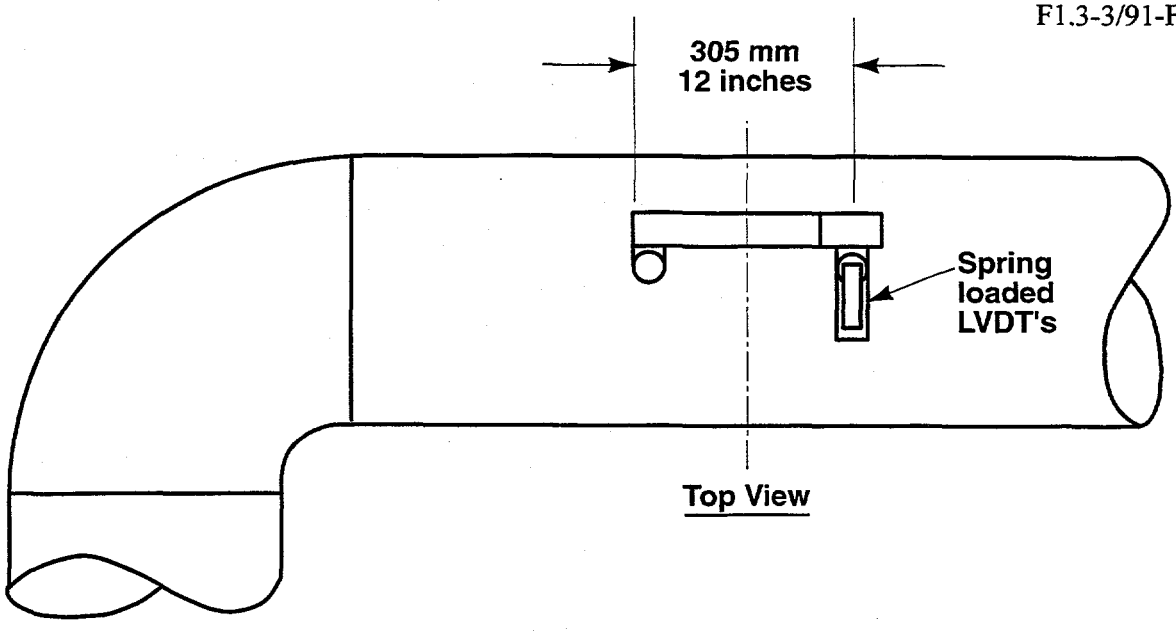

Figure 3.53 Layout/geometry of rotation device used for the three stainless steel experiments

DRB/1.3-3/F9

3.3.3.9 Electric Potential Data

Electric potential data were measured at several locations across the crack during the testing to provide an indication of crack initiation and a measure of crack growth. Typically, three probes were mounted across the crack on the inside diameter, three probes on the outside diameter, and one remote from the crack for a reference. The probes for the electric potential measurements were the iron wire of an iron-constantan (Type J) thermocouple. Figure 3.54 shows the location of each of the six probes at the crack plane. Voltages developed at the EP probes were amplified by Ectron 751 El-M563 amplifiers. The current source for the tests was an Exide Dynacell SD70 battery which was short circuited to supply current to the pipe. The short circuited battery provided currents on the order of thousands of amperes. Large currents were used in an attempt to overwhelm any dynamically self-induced potentials that may be developed (Ref. 3.8).

For every test except the aged cast stainless experiment, eight 5.7 m (225 inch) long, AWG 000 size current wires spaced 45 degrees apart around the pipe circumference carried the current to and from the battery. These wires were attached to the pipe approximately 762 mm (30 inches) on either side of the crack plane. This configuration gives a constant current density across the crack plane, which permits use of EP crack growth calibration curves for estimating crack growth. To provide a reference for the EP signals, reference EP probes were located on the base metal of the pipe about 150 mm (6 inches) from the crack plane with a 100 mm (4 inch) spacing along the axis of the pipe.

The major exception to this current wire arrangement was the arrangement used for the last experiment, i.e., the aged cast stainless experiment. Review of the data from the carbon steel experiments conducted prior to the aged cast stainless test indicated that in spite of the large currents being supplied, on the order of 4,000 amperes, the EP signal levels were still on the order of the dynamically self-induced potentials for these ferritic materials. In an attempt to concentrate the current at the crack centerline, and thus overcome the effect of this problem, the current wire arrangement shown in Figure 3.55 was used for the aged cast stainless experiment. In this arrangement, all eight current wires from one terminal of the battery were attached to a copper block which was silver soldered to the pipe 76 mm (3 inches) from the crack plane on the axis at the circumferential center of the crack. A similar copper block on the other side of the crack held the wires from the other battery terminal. The result of this modification was to increase the measured current supplied to the test specimen four-fold from approximately 4,000 to 16,000 amperes. Using this arrangement, the reference EP probes were separated by 25 mm (1 inch) and were located 25 mm (1 inch) from the crack plane between the current input blocks.

3.3.3.10 Strains

A number of permanently mounted strain gages were attached to the pipe loop to provide data for determining the moment at the test section, the moment at a location remote from the test section, and to provide some measure of the damage done to the elbows in the pipe loop. The permanent gages were located as follows on the pipe: Figures 3.56 and 3.57, six gages each on the north and south internal ends caps; Figure 3.58, one gage each at Elbows 2, 3, and 4; and Figure 3.58, three gages at a location 3.2 m (10.5 feet) north of Elbow 4.

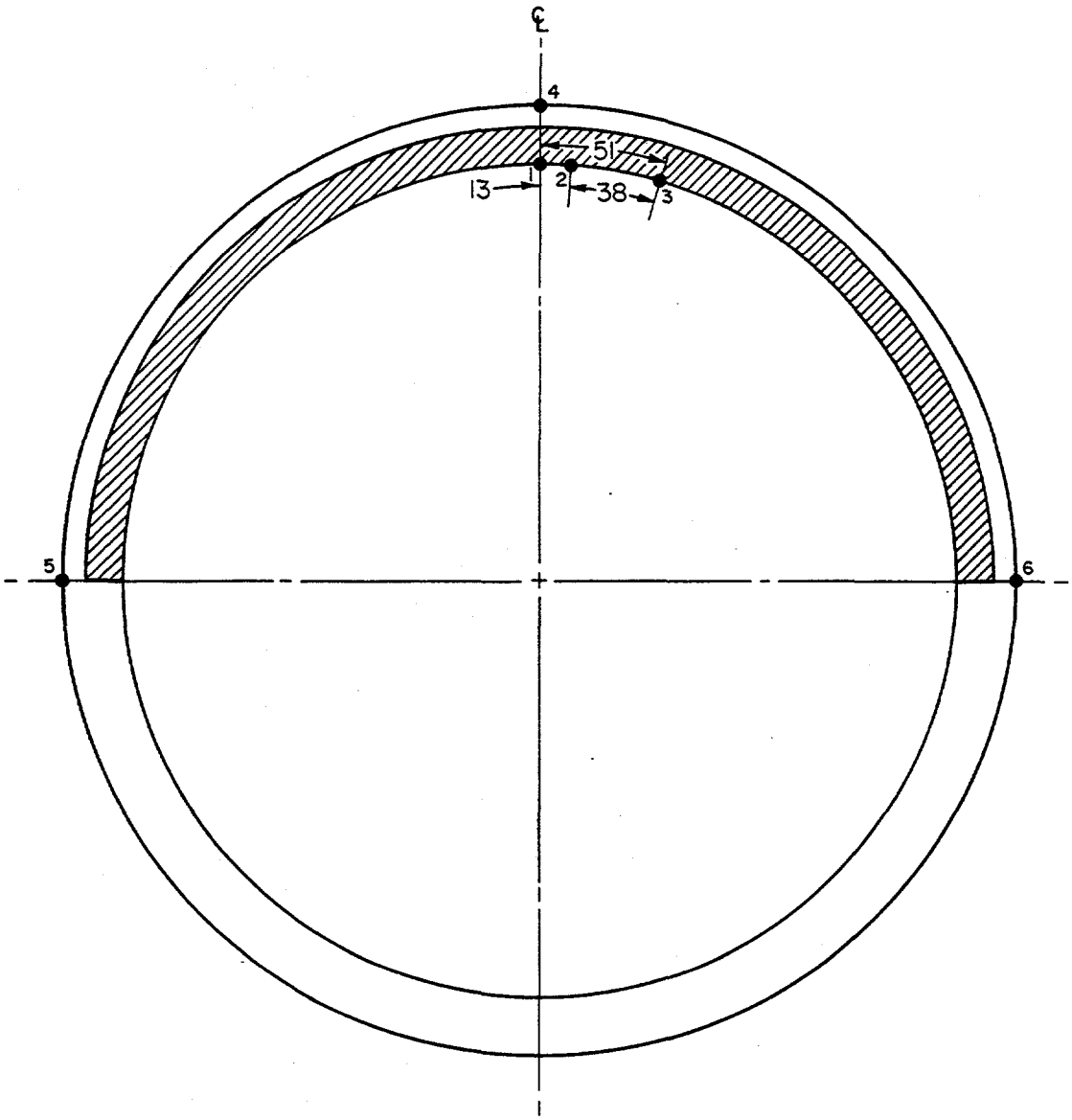

Figure 3.54 Location of d-c electric potential probes at the crack plane for Subtask 1.3 experiments QL/1.3-4/F3

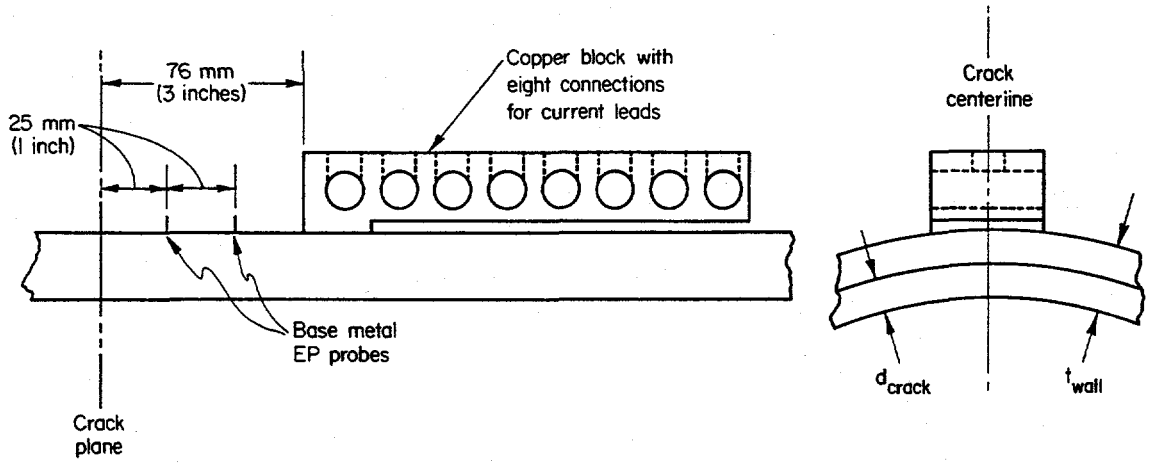

Figure 3.55 Details of current wire arrangement for aged cast stainless steel experiment I1.3-10/90-F3.55

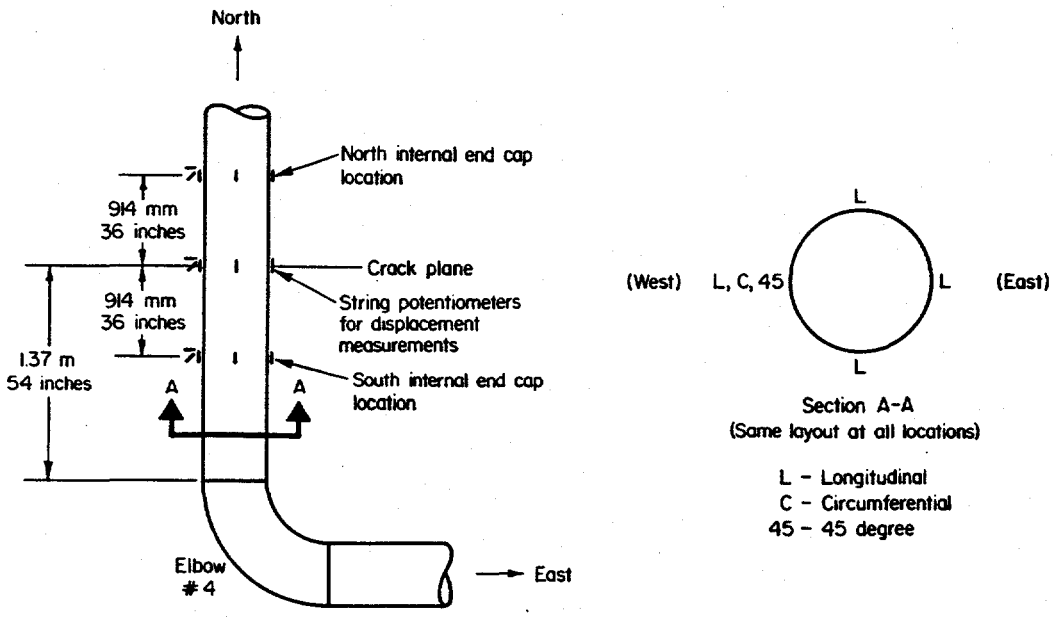

Figure 3.56 Strain gage layout at test section for uncracked pipe-system experiments QL/1.3-1/F3

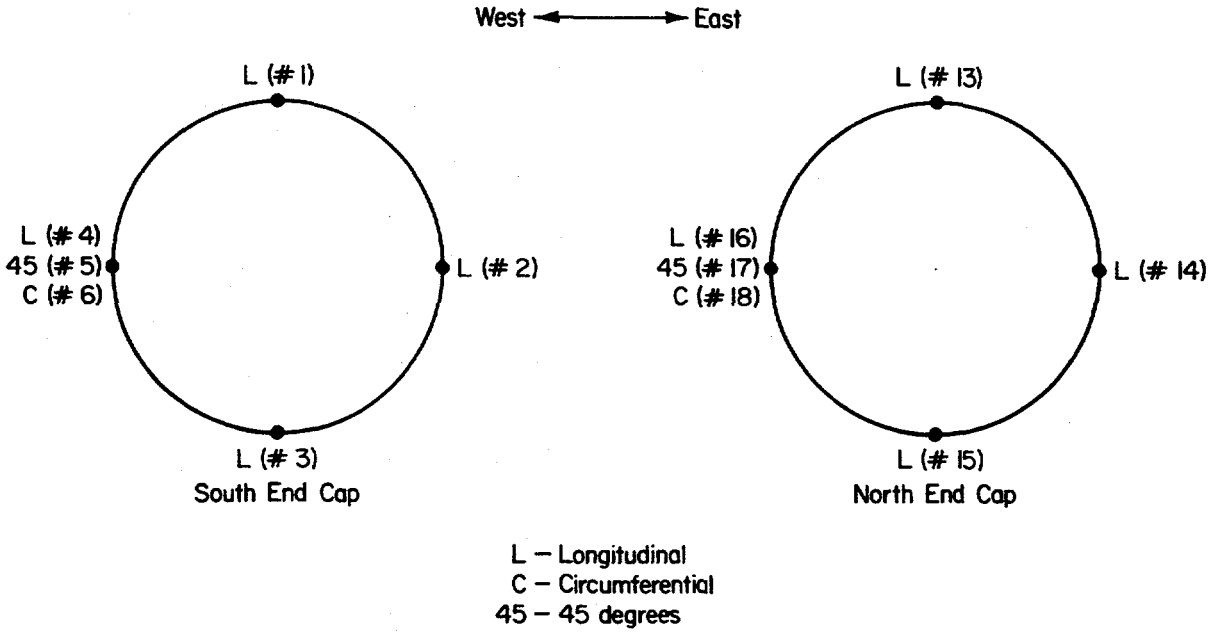

Figure 3.57 Strain gage numbering system for gages in vicinity of crack section for cracked-pipe experiments

QL/1.3-2/F4

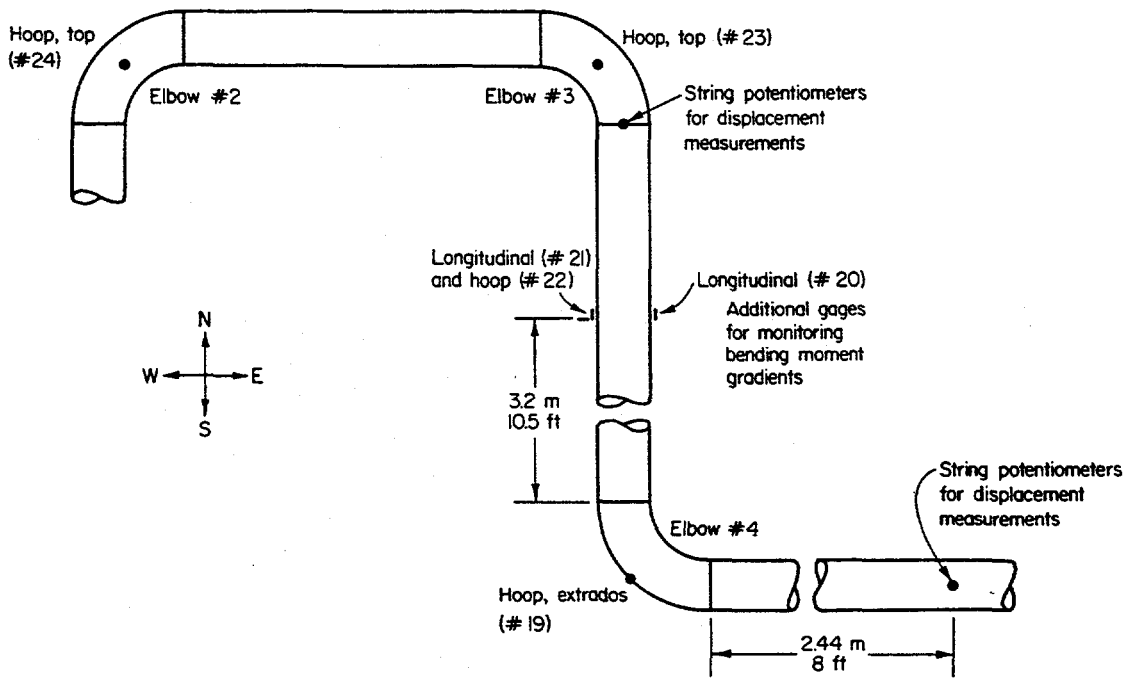

Figure 3.58 Pipe instrumentation remote from the crack

QL/1.3-1/F6

For all but the aged cast stainless experiment, the permanent gages were Eaton SG123-01-10-6S resistance strain gages. Characteristics of these gages are as follows: weldable installation; 27.8-mm (1.093-inch) gage length; nickel-chromium alloy; quarter bridge; 120 ohm; thermally compensated from 24 C to 316 C (75 F to 600 F); 3 m (120 inches) of three-conductor, fiberglass insulated, fiberglass jacketed cable; and thermal compensation for AISI 1018 plain carbon steel. For the aged cast stainless experiment, all of the gages except the gages at Elbows 2, 3, and 4 were replaced with Eaton SG125-01F-6-6S. These new gages were nominally identical to the other Eaton gages except that the cable was 1.8 m (72 inches) of MgO insulated wires in a stainless steel sheath with a 152-mm (6-inch) flexible lead end termination. It was felt that the more robust cabling would permit strain data to be collected past surface-crack breakthrough.

All of the weldable strain gages were conditioned using Measurements Group Model 2120 strain gage conditioner/amplifiers. Completion of the Wheatstone bridge circuits for the quarter-bridge strain gages was done near the active gages using three 120-ohm precision resistors.

In addition to the 18 permanent gages previously mentioned, as part of the uncracked pipe experiment, six additional temporary weldable strain gages (Eaton SG123-01-10-6S gages) were attached to the pipe at the eventual crack location (see Figures 3.56 and 3.59). These gages were incorporated into the instrumentation plan for the uncracked pipe experiment for two reasons. First, they provided a direct measurement of the strains, stresses, and moments at the crack location for the uncracked experiments. Second, they provided a "calibration" for the strain gages at the two end cap locations for inferring the crack section moments for the subsequent cracked pipe experiments. Appendix B provides a detailed discussion of how the strain gage data from the cracked pipe experiments were converted to moments and stresses and the procedures for inferring crack section moment data from the strain gage data at the two end cap locations.

A number of temporary gages were installed on the pipe at Elbows 3 and 4 for the room temperature uncracked pipe test to provide some indication of the stresses that are developed in the elbows under dynamic loading. Figure 3.60 shows the layout of the temporary strain gages at Elbows 3 and 4. Strain gage rosettes were attached to the outside surface of both elbows at the top, bottom, intrados, and extrados. The gages were Micro-Measurements EA-06-250RA-120 gages: open-faced general-purpose gage on a polyamide backing, self-temperature-compensated constantan alloy, 3.3 ppm/C (6 ppm/F) temperature compensation, 6.35-mm (0.250-inch) active gage length, 45-degree rectangular rosette (three gages at 45 degree spacings on a common substrate), quarter bridge each gage, 120 ohm resistance. These gages were glue-on gages and were suitable only for the room temperature portion of the uncracked experiment. The temporary gages were conditioned by two Ectron Model 4001, 14-channel signal conditioning systems. Completion of the bridges for each gage of the rosettes was done using three precision 120-ohm resistors near the active gages.

3.3.3.11 Temperatures

Temperatures of the pipe for controlling the heaters and for pipe temperature monitoring were measured with nickel chromium-nickel aluminum (Type K) thermocouples. Immersion thermocouples were installed at each fixed end to monitor the temperature of the water. Outputs of the thermocouples were read with two Doric Trendicator 402A thermocouple indicators and one Omega 871 digital thermometer.

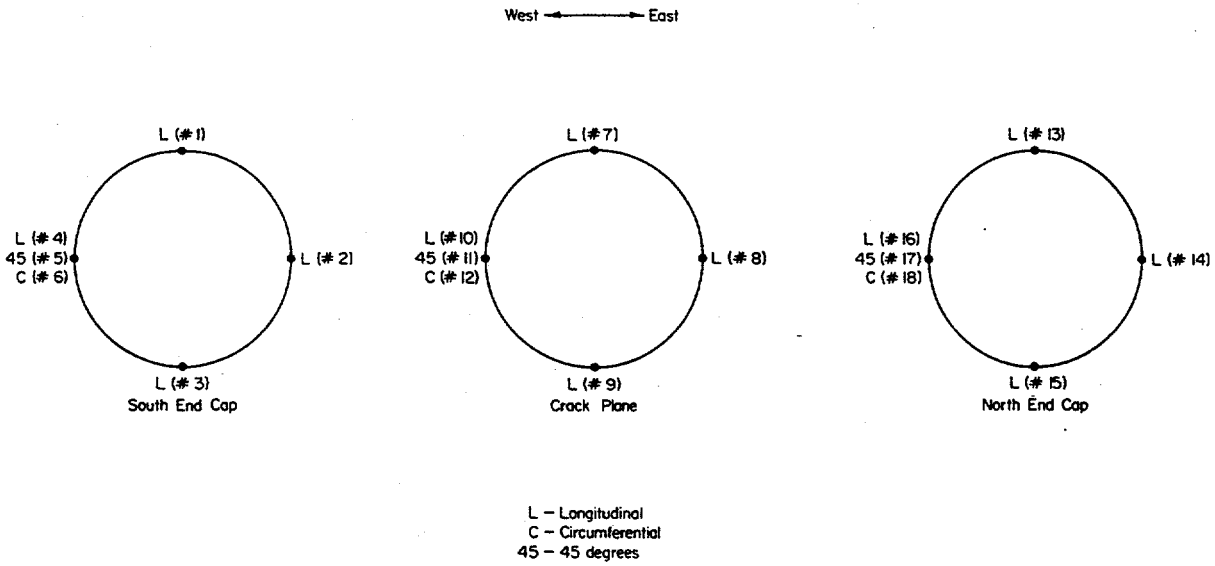

Figure 3.59 Strain gage numbering for gages in the vicinity of the crack plane for uncracked-pipe experiments

QL/1.3-1/F4

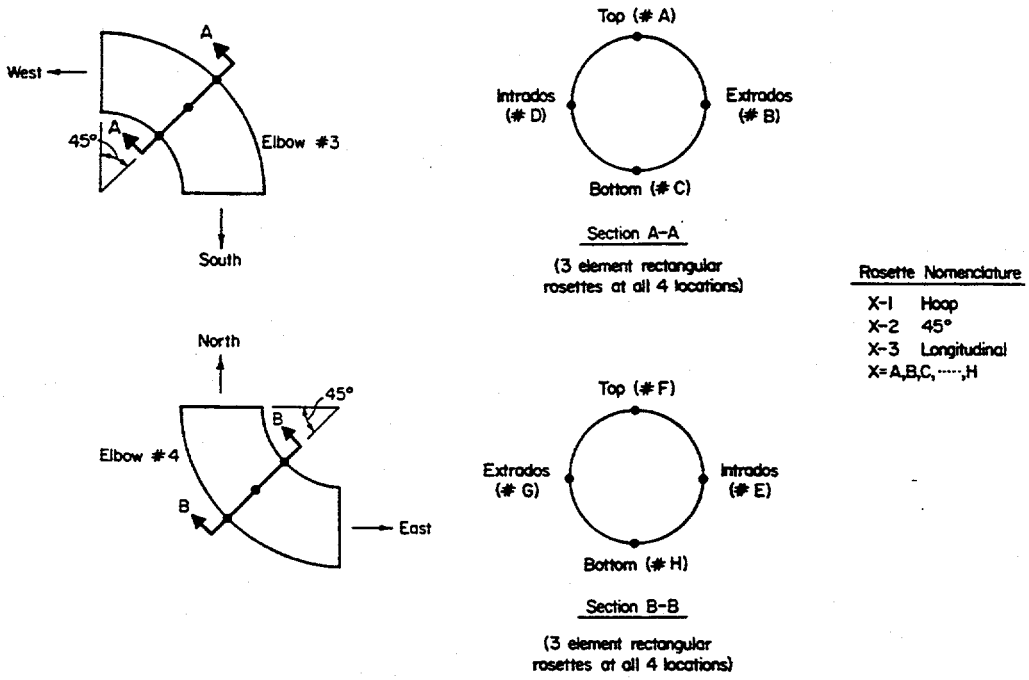

Figure 3.60 Elbow strain gage locations and numbering system for room temperature uncracked-pipe experiment

QL/1.3-1/F5

3.3.3.12 Video Recording

Each experiment conducted as part of Subtask 1.3 was recorded on videotape. Four standard VHS video cameras were placed at various strategic locations to capture the motion of the pipe. A fifth broadcast quality camera was also used. Figure 3.61 shows typical locations for the cameras.

3.3.3.13 Quality Assurance

The instrumentation used on the IPIRG Subtask 1.3 experiments was calibrated per IPIRG Quality Assurance Program Plan QAP No. 23 Subtask 1.3. Calibration records for the instruments are maintained and are on file in Battelle's Quality Assurance Section.

3.3.4 Data Acquisition and Control System

Figure 3.62 is a schematic of the data acquisition and control system for the pipe tests. The two systems are interconnected because several of the transducer inputs to the data acquisition system are feedback signals for the control system.

3.3.4.1 Data Acquisition system

The primary data acquisition system for the IPIRG Subtask 1.3 experiments consisted of four IBM-XT compatible computers using Metrabyte DAS-8, 8-channel, high speed, A/D converters with Metrabyte EXP-16 expansion multiplexer/conditioners. Each computer collected data for 16 channels using Labtech Notebook® data acquisition and control software running under MS-DOS 3.3.

The data acquisition system was set up for ±10 volt input signals, giving a basic resolution of 5 mv (12-bit A/D conversion). The data were collected at 200 Hz for a total of 30 seconds, with data acquisition beginning several seconds prior to the start of shaking the pipe. The four data acquisition computers were set up so that they had a common trigger which was manually initiated. All of the machines recorded the actuator displacement. For all but the uncracked and carbon steel base metal experiments, a voltage pulse that signaled the beginning of the forcing function command signal to the servo-controller was also recorded on all computers to unambiguously identify the actual start of the test.

In addition to the digital data acquired with the IBM PCS, backup analog data were recorded on tape using two Sangamo Sabre VI, 14-channel, reel-to-reel FM tape recorders and one 24-channel, Racal V-Store 24 tape recorder. The latter stores its data on video cassettes in FM format. Except for the case when motion of the fixed ends were being measured, no primary data were recorded on FM tape.

Although the primary data acquisition system used in these experiments (IBM PCS) was not sophisticated, it was more than adequate for the purpose. It was never necessary to resort to one of the back-up systems. The system collected data at 200 Hz and at that rate, it collected approximately 50 data points per cycle at the forcing frequency typically used in these experiments, approximately 4 Hz. Fifty data points adequately describes the response.

System Performance - Instrumentation

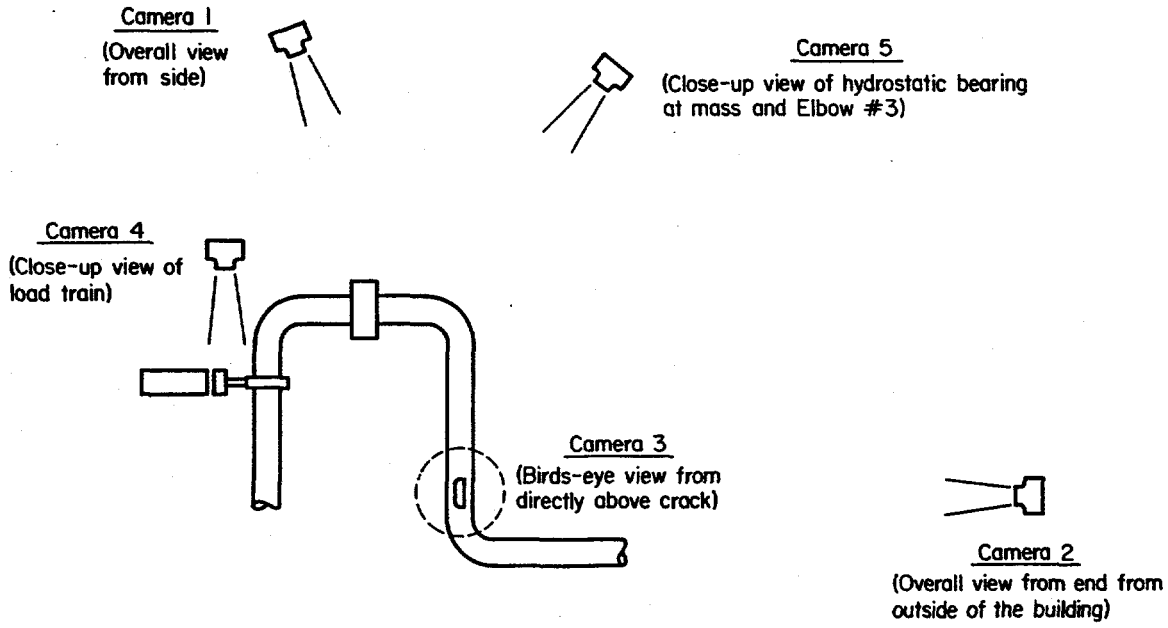

Figure 3.61 Typical locations for video cameras

I-10/89-B9-PS

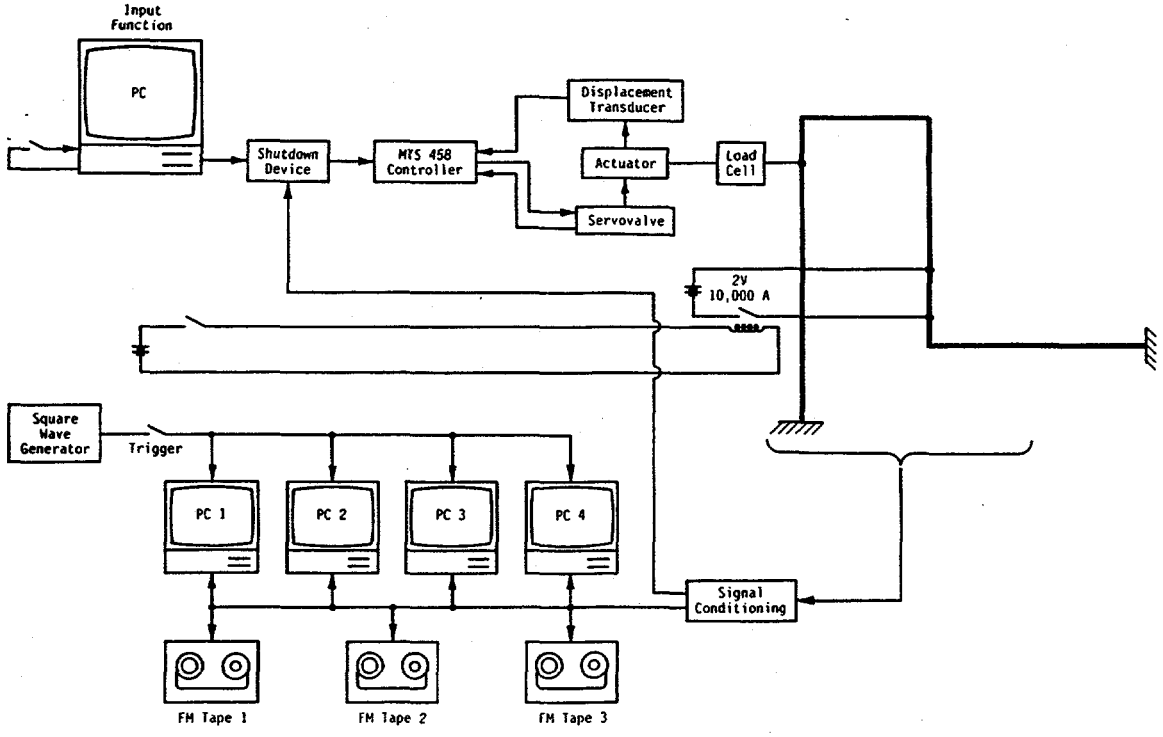

Figure 3.62 Data acquisition and control system for Subtask 1.3 experiments

I-10/89-B10-PS

3.3.4.2 Control System

The hardware used to control the motion of the actuator consisted of a computer to generate the forcing function signal, a shut-down device and a servo-controller. The command signal for the actuator was generated by an IBM compatible computer using a Metrabyte DAC-02, 12-bit, two-channel, analog-output board. In the first two cracked pipe experiments, the computer was an XT-class machine. For all of the remaining tests, the forcing function computer was a 386-class machine.

One channel of the D/A converter was used as the input to the servo-controller. For all but the uncracked and carbon steel base metal tests, the second channel of the D/A converter was used to generate a signal to set off a strobe light to synchronize the video recordings. The "flash" signal was also recorded by the data acquisition system to provide an unambiguous indication of when the forcing function was started.

The command computer produced an analog voltage derived from a digital data file of the forcing function. Using Labtech Notebook® data acquisition and control software under MS-DOS 3.3, analog values were output to the servo-controller at 200 Hz for the duration of the test. The output of the command signal was initiated manually, after it was established that the data acquisition system was taking data and functioning properly.

The output of the command function computer was fed to a Battelle-built programmable attenuator, which was used to shut down the cracked pipe experiments. The attenuator, referred to as the shut-down device, reduced the command function voltage linearly to zero in four seconds when an external trigger voltage dropped below a programmable threshold value. In this case, the trigger voltage was the output of the pipe test section pressure transducer.

The output of the shut-down device went to an MTS 458.20 servo-controller. The servo-controller had one MTS 458.11 DC Signal Conditioning Module and one MTS 458.13 AC Signal Conditioning Module. The DC module provided excitation and conditioning for the load cell. The AC module merely provided an interface for the actuator displacement transducer, because its signal was already conditioned and at a high level when it entered the servo-controller. The actuator was operated in displacement control using an MTS 458.15 three-stage valve driver for the Moog servo-valve. The feedback signal for the servo-controller was the output of the actuator displacement transducer.

During the course of the first two cracked pipe experiments, i.e., the carbon steel base metal and carbon steel weld metal experiments, it was evident that the amplitudes of the actuator displacements were somewhat less than expected, i.e., the dynamic displacements did not accurately follow the design basis equation that had been programmed as the command function. Through detailed review of the control system, it became apparent that the attenuation was caused by interplay in the proportional, integral, and derivative gain settings of the servo-controller, i.e., the servo-controller was not tuned perfectly. Because tuning of a high performance servo-hydraulic system can be difficult, and the risk exists of applying unstable loads to the pipe system, it was decided to adjust the forcing function to get better agreement between the equation and the actual displacements rather than adjusting the gains on the servo-controller, thus avoiding the possibility of inducing a control instability and potentially damaging the facility. The adjustment was made by increasing only the dynamic portion of the servo-valve command signal by 25 percent, because the static push portion of the command signal appeared to be correct. With the adjustment, actuator displacements from the last three experiments, the stainless steel base metal, stainless steel weld metal, and aged cast stainless tests, agreed with the forcing function equation very well, except for the first cycle.

3.3.4.3 Quality Assurance

The data acquisition and control hardware were all calibrated per IPIRG Quality Assurance Program Plan QAP No. 23, Subtask 1.3, Revision 0. Calibration records for these systems are maintained and are on file in Battelle's Quality Assurance Section.

3.3.5 Instrumentation and Data Acquisition Accuracy

The instrumentation and data acquisition system used on the IPIRG Subtask 1.3 experiments was selected on the basis of technical requirements, previous usage experience, availability, cost, and expected accuracy. There were, inevitably, tradeoffs that had to be made in the decision to use a particular piece of equipment that have influenced the accuracy of the measurements that were made during the conduct of the experiments. In order to quantify the effects of the use of the various components, an uncertainty analysis of the complete instrumentation and data acquisition system was performed.

All of the individual instrumentation components used in IPIRG Subtask 1.3 were calibrated to published manufacturers' specifications. Typically, these individual specifications indicate accuracy or nonlinearity on the order of less than one percent full scale. When these individual components are connected together into a system, however, the individual accuracy tolerances accumulate. In a typical situation the accuracy of the following components has to be considered:

(1) The individual transducer

(2) The excitation power supply for the transducer

(3) The voltmeter used to set and read the excitation

(4) Shunt calibration resistors and the voltmeter used to read the shunted outputs

(5) Multiple stages of amplifier gain

(6) The analog-to-digital conversion system.

Considering all of these items, the final data that are collected have an aggregate accuracy or uncertainty much larger than the accuracy of any one of the individual components.

The accuracy analysis performed on the Subtask 1.3 instrumentation and data acquisition system was founded on manufacturers' equipment specifications, Battelle calibrations, and knowledge of the pre-test setup procedures. In a number of cases, the total accuracy was merely the sum of the accuracy of the transducer and the analog-to-digital conversion system. An internally conditioned pressure transducer where the aggregate accuracy for Items 1 to 5 is quoted by the manufacturer for the whole device is an example of this. In other cases, analytical models of components and systems were built to be able to quantify the influence of some parameter being at the extreme of its tolerance. The strain measuring system is a good example of the latter. The calculations and models assume that all of the uncertainties are embedded in the equipment and that actions and intervention required during setup by the technicians and engineers were flawless, i.e., setting the shunt resistance value on a decade resistor box or adjusting the gain on an amplifier was done correctly and precisely.

Table 3.4 summarizes the results of the instrumentation and data-acquisition-system measurement-accuracy analysis. The total uncertainty quoted is for the worst case scenario, considering all of the various components to be at the extremes of their individual accuracies. Most uncertainties are quoted for the transducer full-scale output. In other cases, where the uncertainty is a function of the output level, due to nonlinearities, full scale in the table has been chosen as a value typical of what might be seen during an experiment. For the most part, even when considering the unlikely worst on worst situation, the aggregate uncertainties are on the order of less than 1 percent. For some measurements, such as the battery current, the uncertainty is quite large, but because the data are never really used, a large uncertainty is of no consequence. In the case of the weldable strain gages, two figures are quoted, the worst case and a likely value. Because the strains from the weldable strain gages are used to calculate one of the most important test parameters, bending moment, a few comments are warranted.

The accuracy of the strain measuring system is by far the most complex to calculate of any of the instrumentation systems used on the Subtask 1.3 experiments. It involves the most equipment and operations. Hence, due to the greater number of possible sources of inaccuracy, there is a larger uncertainty in the measurements. Items that contribute to the accuracy of the weldable strain gage system include:

- The basic resistance of the gage - the tolerance on resistance is typically ± 1.5 Ω. This results in Wheatstone bridge nonlinearities when a quarter bridge is completed with precision fixed resistors.
- The gage factor of weldable gages has a very large tolerance of ± 3 percent, when compared with typical glue-on gages, ± 0.5 percent.
- Resistance of the high temperature lead wires on the gage is quite high, on the order of 1 Ω for a 3 meter length. This causes bridge nonlinearities and apparent gage factor changes when the resistivity of the wire changes with temperature. Thus, the length of wire at an elevated temperature becomes important.
- The bridge completion resistors have some tolerance and temperature coefficient associated with them that has an effect on accuracy.
- The bridge shunt resistor, as set on a decade resistance box, and the precision of the digital multimeter used to read the shunted bridge output affects accuracy.
- Zeroing and shunting of the strain gage bridges at room temperature and then conducting the test at PWR temperatures has some effect.
- Drift in bridge excitation affects accuracy.
- The tolerance with which the amplifier gain remains fixed shows up as part of the overall accuracy.
- The analog-to-digital conversion system introduces additional uncertainties into the measurements.

Table 3.4 Instrumentation and data acquisition system measurement uncertainties

Measurement	Transducer	Full Scale	Total Uncertainty - ±
Actuator Force	Load cell	1560 kN	13 kN
	Pressure transducer	24 MPa	0.4 MPa
Actuator Displacement	Linear displacement transducer	±228 mm	0.43 mm
Pipe Displacement	String potentiometer	1270 mm	2.4 mm
Pipe Pressure	Pressure transducer	35 MPa	0.3 MPa
Node 6 Force	Pressure transducer	69 MPa	0.2 MPa
Electric Potential	Fe lead of type J TC	0.01 V	0.00001 V
		0.02 V	0.00002 V
		0.05 V	0.00005 V
		0.2 V	0.00020 V
		1 V	0.00099 V
		5 V	0.00494 V
Battery Current	Ammeter	1000 A	110 A
CMOD	LVDT	±6.35 mm	0.05 mm
	Clip gage	12.70 mm	0.61 mm
Crack Rotation	LVDT	±25.40 mm	0.10 mm
		±6.35 mm	0.03 mm
	RVDT	±30 deg	0.15 deg
Strain	Weldable gages	±1000 με	180 με/1000 με (worst case)
	Glue-on gages	±1000 με	66 με/1000 με (likely) 26 με/1000 με
Base Motion	Accelerometer	±50 g	0.12 g/5 g
	String potentiometer	±25.40 mm	0.048 mm
Temperature	Type K TC	288 C	0.6 C

All of these, when taken at their tolerance limits suggest that strains can only be assured to be within ± 180 microstrain at a ± 1000 microstrain level. Because of system nonlinearities, due to use of a voltage output type bridge for dynamic measurements as opposed to a null balance bridge, the tolerance band is larger at higher strain levels and lower at lesser strains. Adopting a less pessimistic point of view and in accordance with the excellent agreement between analytical predictions of moments versus measured moments, it can be argued that the accuracy of the strain measurements is primarily a function of the gage-factor variation, lead-wire resistivity changes, and A/D conversion uncertainty. This reduces the total worst uncertainty from ± 180 microstrain to ± 66 microstrain at a 1000 microstrain level. In the best possible scenario, the

smallest uncertainty that could be achieved would be ± 30 microstrain. This is on the same order as the worst case uncertainty for room temperature glue-on strain gages. From a probabilistic viewpoint, the measured values may be much closer to the actual values than the summation of the worst case errors would indicate.

In general, the instrumentation and data acquisition system accuracies are a reasonable compromise between cost and engineering requirements. The most significant uncertainties occur in the weldable strain gages. Accepting the "likely" scenario, the ± 66 microstrain at 1000 microstrain seems reasonable in an engineering sense. As in all measurement efforts, it becomes apparent, in hindsight, that there may be ways that the accuracy could be improved.

3.3.6 Experiment Design

Prior to the conduct of each of the cracked pipe experiments, dynamic finite element analyses were performed to select the forcing function. Considerations in the selection of the forcing function included the structural properties of the flawed test section and the test system capabilities.

3.3.6.1 Design Criteria

There were five basic criteria for selecting a forcing function:

(1) To avoid significant fatigue crack growth, the surface crack should ideally penetrate the wall of the pipe in approximately 10 cycles and not require more than 30 cycles.

(2) The selected forcing function should provide a reasonable margin on predicted force, stroke, flow rate, and oil usage for the servo-hydraulic system.

(3) The forcing function should be of the form

$$U_x = S_{ff}*t + A_{ff}*[1-\exp(-b_{ff}*t)]*\sin(\omega*t) \qquad (3\text{-}5)$$

where,

U_x	= actuator displacement
t	= time, seconds
S_{ff}, A_{ff}, b_{ff}	= equation constants
ω	= forcing function frequency.

(4) There should be a nearly equal mix of inertial and displacement-controlled loading on the crack.

In addition, other minor criterion were applied such as: (1) the forcing function frequency should be kept below the first natural frequency of the system, (2) it was deemed desirable to use the same forcing function for a number of experiments, if possible, and (3) loading that tended to have equal tension and compression bending moments (stress-ratio) was favored. The meaning and rationale for most of these criterion is fairly clear. However, the mix of inertial- and displacement-controlled loading and the stress-ratio criterion deserve further clarification.

At the outset of the design process for the IPIRG Subtask 1.3 pipe loop and test facility, the focus was on finding a configuration that could reasonably be expected to fail the test pipes and that could be built within the cost constraints of the program. As the program progressed, and as the design evolved, it was analytically demonstrated that the above objectives could be met. However, an additional constraint was imposed on the design that there be a nearly equal mix of inertial- and displacement-controlled loads at the crack. There was, however, no existing method for defining the mixture of inertial- and displacement-controlled loading, so one was created.

The definition used to design the first two experiments was based on a calculation of time-averaged effective crack-opening moments. The procedure was as follows:

(1) Conduct dynamic analysis of the piping system including the crack to determine the total moment at the crack as a function of time, using "m" total time steps

(2) Conduct static analysis of the piping system including the crack using the same "m" displacements as in Step 1 to find the statically induced moment at the crack

(3) Considering only the subset of the calculated moments that tend to open the crack, calculate the effective (RMS) crack-opening moment for both the static and dynamic analyses

$$M_{rms} = \sqrt{(1/n)\sum_{i=1}^{n} M_i^2} \qquad (3\text{-}6)$$

where M_i is the i^{th} crack-opening moment and n is the total number of crack-opening moments (n is generally different for the static and dynamic calculations)

(4) The percent displacement-controlled loading is then

$$F_s = \frac{\text{static } M_{rms}}{\text{total } M_{rms}} \times 100 \qquad (3\text{-}7)$$

This definition of inertial mixture is illustrated in Figures 3.63 to 3.66. As seen in the figures, the RMS values of effective crack-opening moment change with time and hence, the percent static loading also changes with time. The value of F_s at crack break-through was the value used in the experimental design. The time averaged definition given above for percent static loading is attractive in that F_s is always a positive number, whereas if the definition was strictly taken as the ratio of static to total moment at one instant, F_s could possibly be negative, depending upon the dynamics of the system. The definition given above is cumbersome, however, because two long finite element calculations are needed, one dynamic and one static.

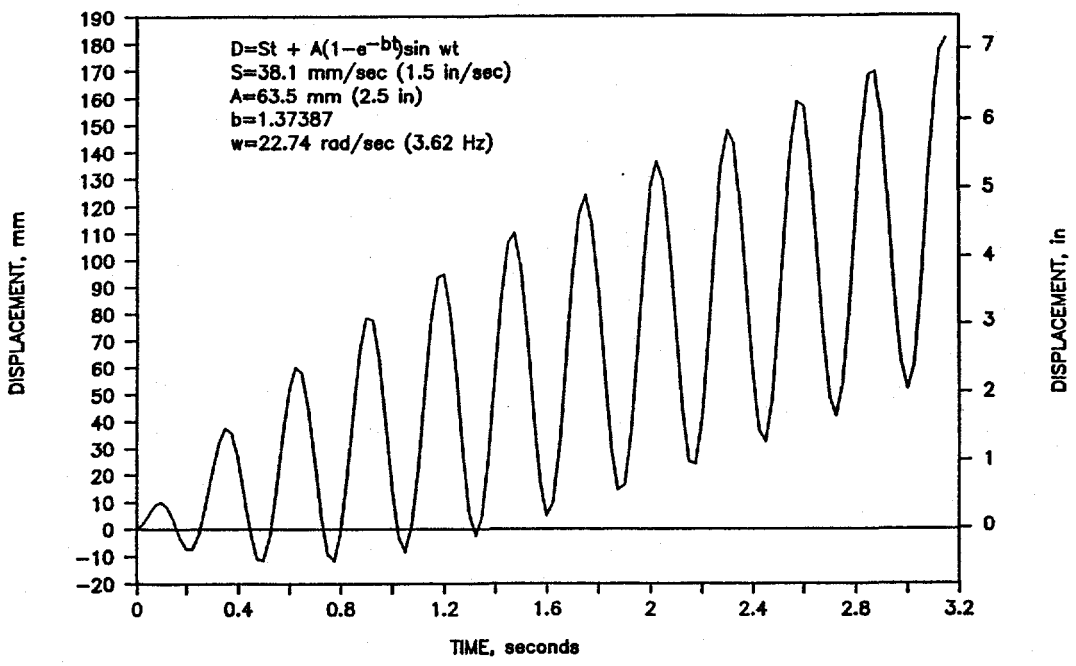

Figure 3.63 Actuator forcing function for consideration of ratio of inertial to displacement-controlled moments I1.3-10/90-F3.63

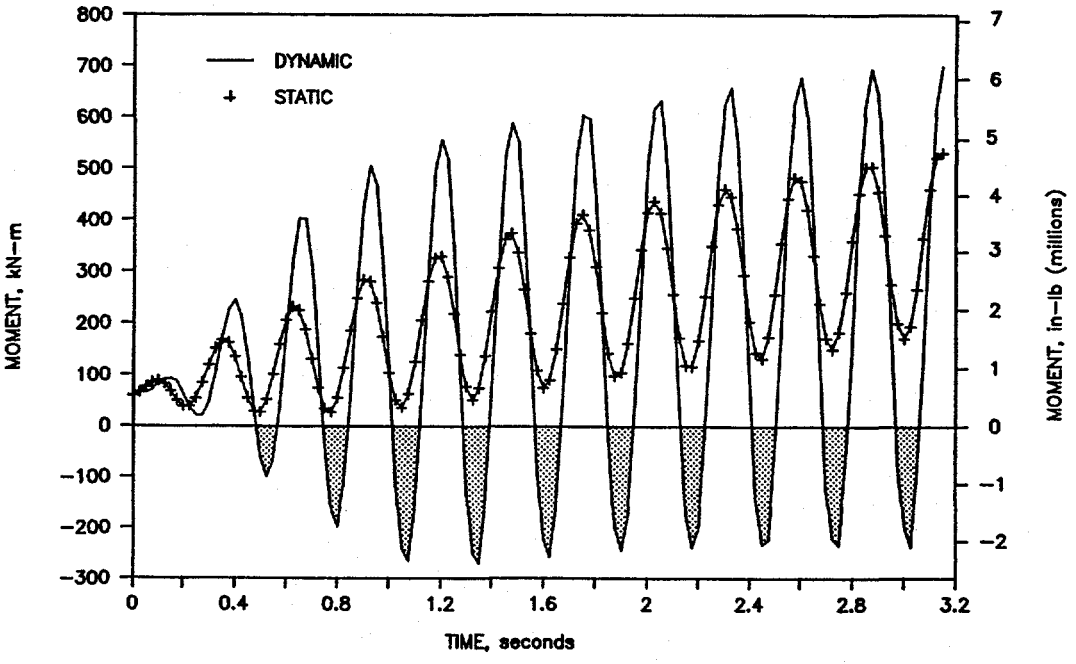

Figure 3.64 Crack location moment for consideration of ratio of inertial to displacement-controlled moments I1.3-10/90-F3.64

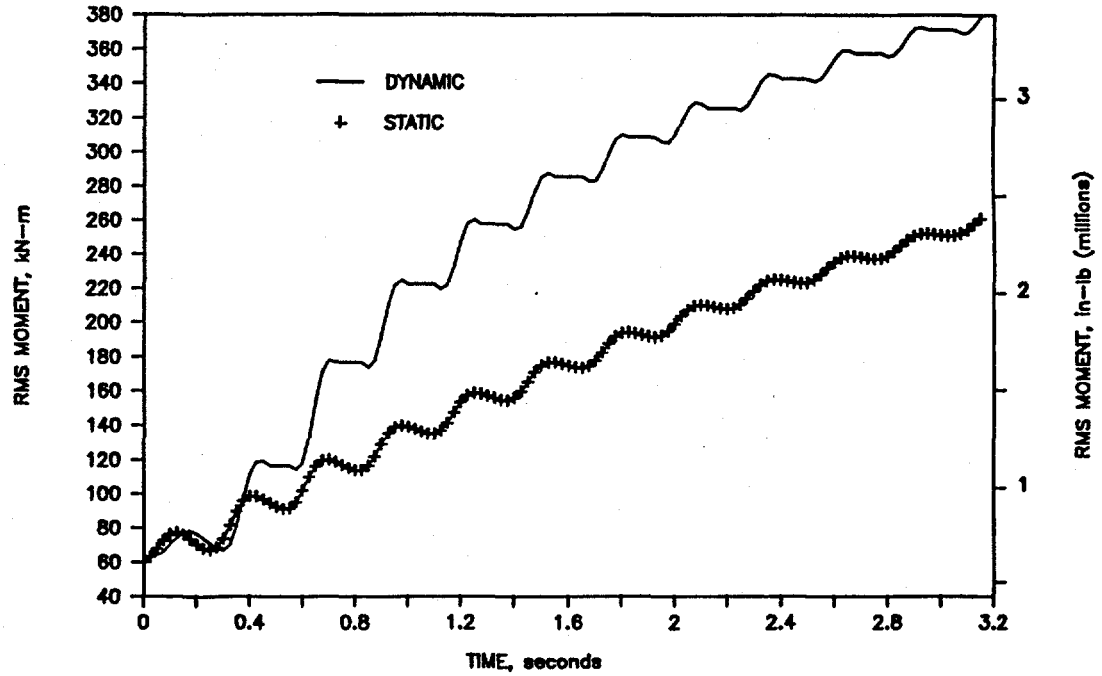

Figure 3.65 Effective crack-opening moment (RMS) for consideration of ratio of inertial to displacement-controlled moments I1.3-10/90-F3.65

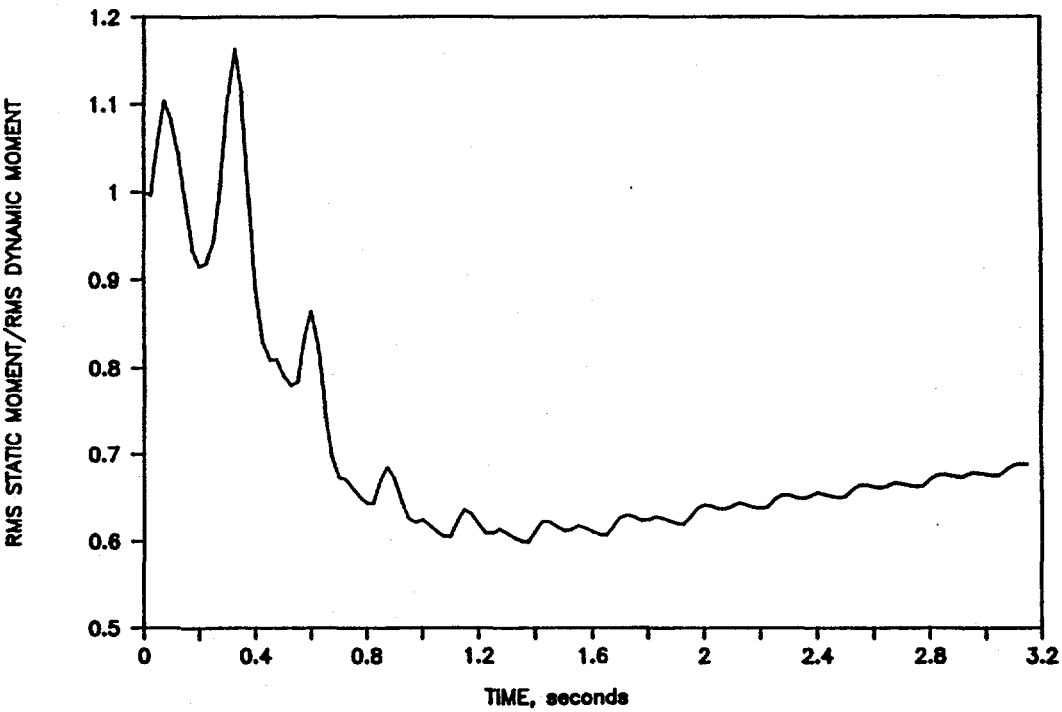

Figure 3.66 Predicted fraction of static loading in a cracked-pipe experiment I1.3-10/90-F3.66

After some investigation, it was determined that the percent static loading at crack penetration by the above definition was very nearly equal to the instantaneous ratio of the static moment to the total moment at the same actuator displacement. It was also argued that the percent static loading ought not to have history dependence, as in the definition given above, because the crack only responds to its instantaneous loading. In addition, there seemed to be some confusion in terminology as to what exactly was meant by static loading, i.e., whether thermal and pressure induced moments were included. Therefore, in the interest of simplifying the design process and eliminating ambiguity, the definition of the mixture of displacement- and inertial-controlled loading was changed to

$$F_i = \frac{M_T - M_s}{M_T} \times 100 \qquad (3\text{-}8)$$

where F_i is the percent inertial loading, M_T is the total moment at maximum load calculated in a dynamic analysis, i.e., a simulation of the experiment, and M_s is the moment calculated in a static analysis and caused by thermal and pressure loading combined with actuator displacement equal to the displacement of the actuator at failure in the dynamic simulation. This definition was used in the design of the three stainless steel experiments.

In addition to the percent inertial loading, the stress ratio (R) is another parameter of interest in these types of experiments. The IPIRG Subtask 1.2 experiments showed that stress-ratio had some effect on the maximum moment capacity of the specimens. Hence, one of the secondary considerations that was applied to the design of the Subtask 1.3 experiments was a bias toward more negative stress-ratios. Basically, if two experiment designs were judged equally acceptable on the primary criteria, then the one with the more negative stress-ratio would be used. For the purposes of this study, the stress-ratio was defined as:

$$R = \frac{\text{most recent minimum moment or stress prior to failure}}{\text{failure moment or stress}} \qquad (3\text{-}9)$$

3.3.6.2 Design Methodology

The methodology for selecting a forcing function followed a three step process:

- Estimation of the structural behavior of the cracked pipe section
- Dynamic finite element analyses of the piping system using the estimated crack response, and an assumed forcing function
- Iteration on the constants in the forcing function equation to satisfy the criteria discussed in the previous section.

The analyses performed in the experiment design were fundamentally identical to the analyses done during the system design. In this case, however, refined estimates of the cracked section structural behavior for the specific materials and for the pipe and flaw geometry were used, as well as the measured damping of the overall pipe system.

In preparing to design the experiments, at least two estimates of the moment-rotation response of the crack were considered in an attempt to get some bounds on the expected behavior. The first estimate was always the estimate derived from the companion quasi-static pipe fracture data. The remaining estimates were

from J-estimation schemes for surface-cracked pipe as implemented in a version of the NRCPIPE computer program, i.e., SC.TKP which uses a thick-shell formulation or SC.TNP which uses a thin-shell assumption (Ref. 3.7).

Using quasi-static pipe fracture data as one estimate of the moment-rotation behavior of the cracked section required a number of corrections to the basic data; pipe size, flaw size, internal pipe pressure, and possibly test temperature. The basic steps in the process of generating moment-rotation estimates were as follows:

(1) Using load-line displacement, load, CMO displacement, and machine compliance from the quasi-static data, create a basic moment-rotation curve for the quasi-statically tested crack (see System Design discussion for details).

(2) If the test temperature of the quasi-static data was not 288 C (550 F), calculate a temperature correction factor to be applied to the moments based on flow stress

$$f_t = \frac{\sigma_f(288C)}{\sigma_f(\text{quasi-static temperature})} \qquad (3\text{-}10)$$

(3) Using Net-Section-Collapse analysis as the basis, calculate a moment modification factor for pipe size and flaw size

$$f_g = \frac{M(\text{Subtask 1.3 flaw and pipe size})}{M(\text{quasi-static flaw and pipe size})} \qquad (3\text{-}11)$$

where M() is the moment from the Net-Section-Collapse analysis.

(4) Correct the moments from the basic moment-rotation curve by multiplying them by the two factors

$$M' = f_t f_g M \quad . \qquad (3\text{-}12)$$

(5) If the test pressure of the quasi-static data was not 15.5 MPa (2,250 psi), make a further adjustment to the moment rotation curve as follows:

(a) Reduce all moments by the following factor

$$\Delta M = M(\text{quasi-static pressure}) - M(15.5\ \text{MPa})$$

where

M() is the moment calculated from the Net-Section-Collapse analysis with the corrected test temperature, flaw size, and pipe size.

(b) Shift the moment-rotation curve along the rotation axis so that the curve passes through the origin.

It should be noted that this method of making the pressure correction is somewhat different from what was used in the system design.

The second method used to estimate the behavior of the crack for the design of the experiments was to use J-estimation schemes. In this procedure, a surface-crack version of the NRCPIPE computer program was used to generate moment-rotation curves using material specific stress-strain and J-R curve data. In generating these moment-rotation curves, different assumptions were occasionally made:

(1) Quasi-static and dynamic properties were considered

(2) Two different J-estimation schemes for the surface crack were used - thin pipe (SC.TNP) and thick pipe (SC.TKP) analyses (Ref. 3.7)

(3) For the weld experiments, the effect of the presence of the weld crown was investigated

(4) Different crack depths were evaluated.

In all cases, the moment-rotation curves from the J-estimation scheme program were pressure corrected as described above, because the surface-crack NRCPIPE program only considers pure bending loads.

The various possible moment-rotation curves for a given material were plotted together to find the upper and lower bounds. The forcing function parameters were adjusted so that both the upper and lower bound cases would meet the primary criteria. In many cases, some of the moment-rotation curves were eliminated from consideration as being extremely unlikely or not technically justifiable, i.e., the SC.TKP J-estimation scheme is too conservative for design of experiments, so the SC.TNP analysis was used. For these cases, generally, only a "best guess" case was actually used to design the experiment.

3.3.6.3 Design Summary

Table 3.5 summarizes the important results of all of the pretest forcing function design predictions. Predicted servo-hydraulic system requirements were well within the design capacity of the test system. Stress-ratio never really played any significant role in the design of the forcing function, although it certainly may have an effect on fracture behavior.

It is important to note that the data presented in Table 3.5 are not to be construed as blind predictions of the experiments. Rather, they are the product of trying to find forcing function parameters that could be expected to cause the actual pipe specimen to fail within the performance envelope of the test system. There are inconsistencies in the input data used to generate the results shown in Table 3.5; wall thicknesses, pipe diameters, and crack lengths were not necessarily the same as the Subtask 1.3 specimens. Some of the cases that were conceptually thought of as "upper bound" and "lower bound" were actually only high and low values, with nothing to substantiate whether or not they were bounding. In retrospect, it is clear that the quality of some of the early pretest calculations was poorer than the last ones that were done, i.e., the procedures used to design the forcing function were refined as more was learned from each experiment. In addition, differences in test parameters used in the pretest design calculations versus actual test parameters (i.e., such as a much deeper flaw in one case) tend to make the pretest calculations compare poorly with the actual test results. However, in spite of the limitations of the calculations used to design the forcing functions, the forcing functions selected generally proved to be good choices for meeting the objectives of the subtask.

Table 3.5 Pretest forcing function design predictions

Experiment	Test Material	Cycles to Surface Crack Penetration	Maximum Moment, kN	Inertial Loading, Percent	Basis
1.3-2	Carbon Steel Base Metal	6	610	~31	4112-8[(a)]
1.3-3	Stainless Steel Base Metal	15	667	52	SC.TNP, quasi-static properties
		8	400	55	SC.TKP, quasi-static properties
1.3-4	Carbon Steel Weld	15	595	51	4141-8[(a)]
		7	340	54	SC.TKP, dynamic properties
1.3-5	Stainless Steel Weld	9	445	45	SC.TNP, dynamic properties, no crown
		6	336	42	SC.TNP, dynamic properties, no crown, J_D-R reduced by a factor of 4 for fully reversed cyclic loading
1.3-7	Aged Cast Stainless Steel	11	676	58	SC.TNP, dynamic properties

(a) Degraded Piping Program experiment number.

The efficacy of the procedures used to design the experiments has been borne out by the results of the experiments. Except for the cases where the initial crack depth was not accurately known before the test was conducted, the pretest predictions have been close to the experimental results. Even with some unexpected flaw depths, however, the servo-hydraulic system has been kept within its capabilities. The predicted percent inertial loading at surface-crack penetration has not agreed well with the results from some of the experiments, principally because crack growth on earlier cycles has caused the bending moment at surface-crack penetration to be lower than the previously attained maximum moment for the test, see Figure 3.67. The percent inertial loading at surface-crack penetration is highly dependent on the instant of breakthrough, and typically this has happened as moment was rising, rather than near a

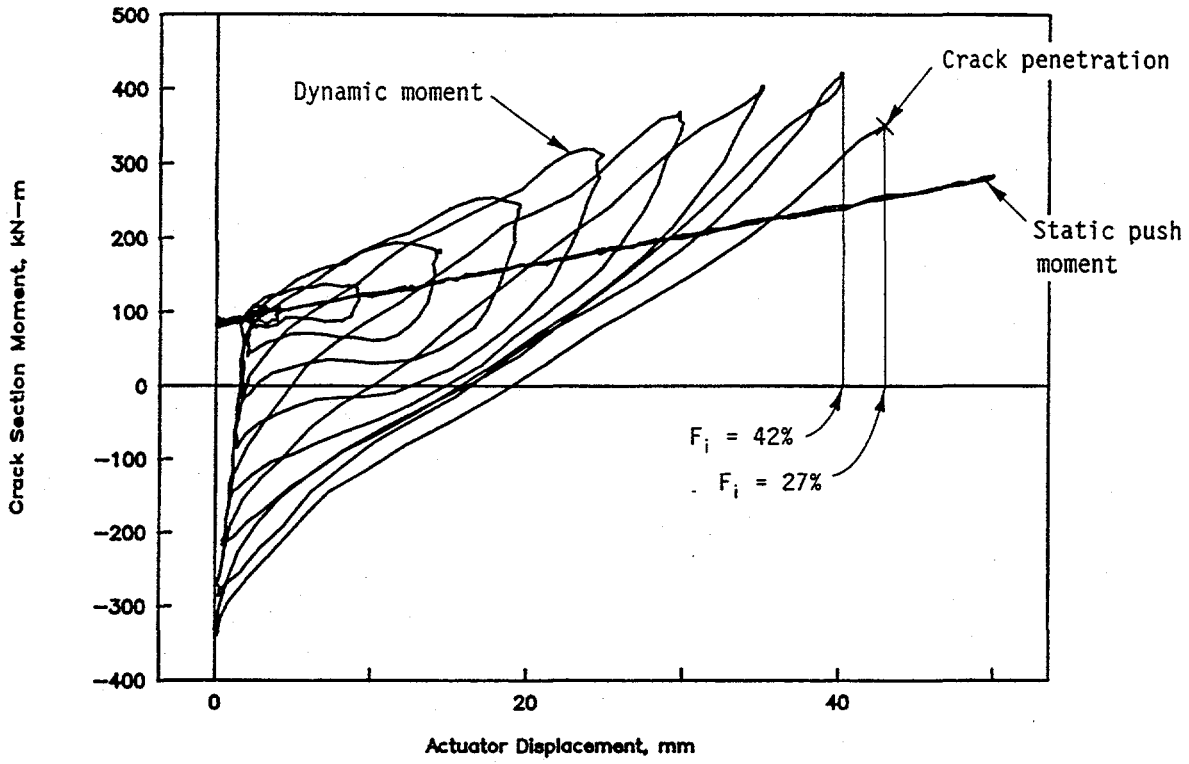

Figure 3.67 Percent inertial loading at maximum moment and at surface-crack penetration

I1.3-10/90-F3.67

maximum. This has tended to reduce the percent inertial loading at surface-crack penetration in some of the experiments.

3.3.7 Test Procedures

Six experiments were conducted as a part of IPIRG Subtask 1.3, one uncracked pipe experiment and five cracked pipe experiments. The following section describes the procedures used to conduct each of the experiments. The test results will be discussed later.

3.3.7.1 Uncracked Pipe Experiment

Although referred to as a single uncracked pipe experiment, under the title of Experiment 1.3-1, there was actually a series of six separate tests.

(1) Pipe-system pressurization test

(2) System damping test

(3) System natural frequency test

(4) Room temperature dynamic test

(5) PWR static test

(6) PWR dynamic test.

In addition, within the system natural frequency test, three methods were used to measure the natural frequencies of the pipe loop under various conditions. In actuality, there were more data generated in this "experiment" then in any of the cracked pipe experiments.

Pipe-System Pressurization

The first test of Experiment 1.3-1 was a simple pressurization of the pipe loop. The purposes of this test were to cycle all of the strain gages to remove any bonding-induced nonlinearities and to collect data to verify analytical predictions of displacements due to pressurization.

The procedure for the test consisted of applying a small preload to the system with the actuator to remove any backlash in the spherical bearings (clearances in the spherical bearings were designed to accommodate differential thermal expansion when the pipe is heated to 288 C (550 F), resulting in a somewhat loose fit at room temperature), followed by repeated cycles of pressurizing the loop with water to approximately 15.5 MPa (2,250 psi), and release of the pressure. Displacements at selected locations on the pipe loop were recorded at each step. The test was conducted at room temperature.

System Damping

The second test of Experiment 1.3-1 was a damping test of the pipe loop. The purpose of this test was to determine the amount of damping in the pipe loop so that accurate predictions of the dynamic response of the pipe loop could be made.

The procedure for the test consisted of applying a small amplitude [on the order of 1.3 mm (0.05 inch)], sinusoidal displacement to the pipe loop with the actuator, at a frequency below the first natural frequency of the system. The frequency of the excitation was increased until the resonant frequency of the pipe loop was found, as evidenced by large motions of the pipe loop and large actuator loads. At this point, the excitation was removed, the actuator held fixed, and the system allowed to come to rest as indicated by the load falling to a static value. The decrease in amplitude of the actuator force with time can be correlated with the amount of damping in the system. Actuator load was recorded continuously during the process. The test was conducted at room temperature, with the pipe filled with water in an unpressurized condition.

System Natural Frequencies

The third test of Experiment 1.3-1 was a natural frequency test of the pipe loop. The purposes of this test were to determine the natural frequencies of the piping system for comparison with analytical predictions, and to provide a basis for selecting the excitation frequency for the dynamic tests.

The system natural frequencies were determined in a number of ways: from a system ring-down; using an instrumented hammer, accelerometer, and spectral analyzer; and using an accelerometer and spectral analyzer with energy input by the actuator. In addition to using a number of different methods to determine natural frequencies, the frequencies were measured for the system under various conditions of pressure, temperature, and actuator preload. All loading involved only elastic stresses in the pipe loop.

Room Temperature Uncracked Dynamic Test

The fourth test of Experiment 1.3-1 was a room temperature dynamic test. The objectives of this test were to: (1) gain experience running the IPIRG Subtask 1.3 facility while in a condition that was relatively benign, i.e., not at PWR temperature, (2) generate data for comparison with analytical predictions of the motion of the system, (3) provide data for the selection of high stress locations for permanent gages to be applied to the elbows, and (4) generate data to calibrate a "load cell" for measuring moment at the future crack location.

The complete details of the test procedure can be found in IPIRG Quality Assurance Document IPI-PP-1.3, Revision 3, which essentially describes the procedures for conducting a Subtask 1.3 pipe-system experiment. For reference, a copy of the IPIRG Quality Assurance Document IPI-PP-1.3, Revision 3 is provided in Appendix C.

Conditions for this test were pipe loop and test specimen filled with water at room temperature and pressurized to 15.5 MPa (2,250 psi). The pipe was not insulated during this test.

The design basis displacement forcing function (command) for the actuator was a sinusoidal function starting with negligible amplitude, growing continuously in amplitude with time to some maximum, and then decreasing in amplitude back to zero. The equation which defined the design basis command signal was:

$$U_x = \{S_{ff}*t + A_{ff}*[1-\exp(-b_{ff}*t)]*\sin(\omega*t)\}*\exp(-c_{ff}*t) \qquad (3\text{-}13)$$

where,

U_x	= actuator displacement
t	= time, seconds
S_{ff}	= 38.1 mm/sec (1.50 inches/sec)
A_{ff}	= 101.6 mm (4.00 inches)
b_{ff}	= 1.38922
c_{ff}	= 1.04244
ω	= 22.745 rad/sec (3.62 Hz).

Figure 3.68 is a plot of the design forcing function. This function was selected on the following bases: (1) It was of the same basic form as the function to be used for the cracked pipe experiments, (2) The frequency for the excitation is approximately 80 percent of the first natural frequency of the pipe loop, and (3) the amplitudes were selected to keep the pipe in its elastic regime. **Note: there are slight differences between the command signal, Equation 3-13, and the actual displacements of the actuator. Hence, the measured actuator displacement is the displacement-time history that should be used in analyses of any of these experiments.**

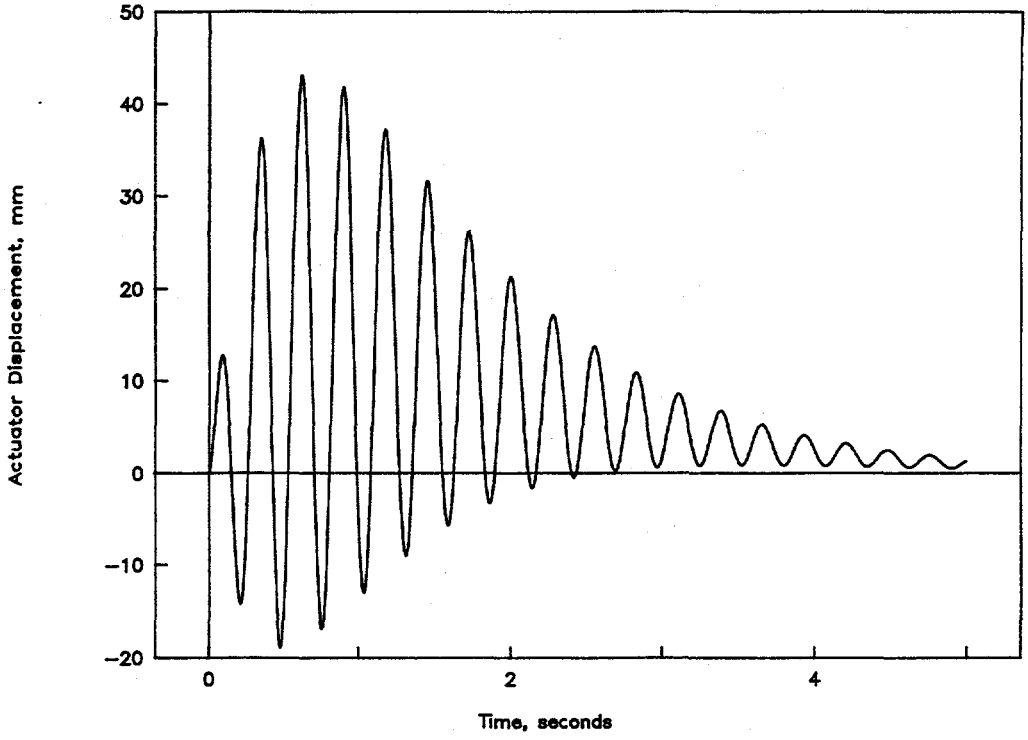

Figure 3.68 Design basis forcing function for Experiment 1.3-1 uncracked-pipe dynamic tests I1.3-10/90-F3.68

PWR Uncracked Static Push Test

The fifth test of Experiment 1.3-1 was a PWR condition static push test. The objectives of this test were to gain experience running the IPIRG Subtask 1.3 facility at PWR conditions prior to running a dynamic test and to generate data for comparison with analytical predictions of the motion of the system.

The test was conducted, essentially, according to IPIRG Quality Assurance Document IPI-PP-1.3, Revision 3, by substituting manual extension of the actuator for computer control.

Conditions for this test were pipe loop and test specimen filled with water at 288 C (550 F) and 15.5 MPa (2,250 psi) internal pressure. The actuator, under displacement control, was extended manually from the pre-test stress free location in increments of approximately 12.5 mm (0.50 inches) to a maximum displacement of 100 mm (3.9 inches) and then returned to the zero location in the same step-wise fashion.

PWR Uncracked Dynamic Test

The final test of Experiment 1.3-1 was a PWR condition dynamic test. The objectives of this test were to: (1) gain experience running the IPIRG Subtask 1.3 facility at PWR conditions prior to running a test with a cracked specimen, (2) generate data for comparison with analytical predictions of the motion of the system, and (3) generate data to calibrate a "load cell" for measuring moment in the future crack section.

The uncracked PWR dynamic test immediately followed the PWR static push test. The test procedures for the PWR dynamic test are essentially as documented in IPIRG Quality Assurance Document IPI-PP-1.3, Revision 3.

Conditions for this test were pipe loop and test specimen filled with water at 288 C (550 F) and 15.5 MPa (2,250 psi) internal pressure. This is the PWR condition.

The design basis displacement forcing function (command) for the PWR uncracked dynamic test was the same as for the room temperature uncracked dynamic test previously described. It was a sinusoidal function starting with negligible amplitude, growing continuously in amplitude with time to some maximum, and then decreasing in amplitude back to zero. The equation which defines the design basis command signal is:

$$U_x = \{S_{ff}*t + A_{ff}*[1-\exp(-b_{ff}*t)]*\sin(\omega*t)\}*\exp(-c_{ff}*t) \qquad (3\text{-}14)$$

where,

U_x = actuator displacement
t = time, seconds
S_{ff} = 38.1 mm/sec (1.50 inches/sec)
A_{ff} = 101.6 mm (4.00 inches)
b_{ff} = 1.38922
c_{ff} = 1.04244
ω = 22.745 rad/sec (3.62 Hz).

Figure 3.68 is a plot of the design basis command signal. This function was identical to the room temperature dynamic test design basis forcing function, and thus provides a basis for direct comparison of the two tests. Equation 3-14 was only the design basis for the displacement forcing function and it does not necessarily reflect the actual motion of the actuator during the test. Hence, the measured actuator displacement is the displacement time history that should be used in analyses of this test.

3.3.7.2 Cracked Pipe Experiments

The objective of the cracked pipe experiments was to gather experimental data for assessing the stability of a circumferential crack in a representative piping configuration subjected to combined dynamic inertial and displacement-controlled stresses.

The test procedures for the cracked pipe experiments are documented in IPIRG Quality Assurance Document IPI-PP-1.3, Revision 3.

Conditions for the cracked pipe experiments were pipe loop and test specimen filled with water at 288 C (550 F) and 15.5 MPa (2,250 psi) internal pressure. This is the PWR condition.

The design basis displacement forcing function (command) for the cracked pipe experiments was a sinusoidal function superimposed on a static push. The function started with negligible amplitude and grew continuously in amplitude with time until attenuated by an external shut-down device. The equation which defines the design basis command signal is:

$$U_x = S_{ff}*t + A_{ff}*[1-\exp(-b_{ff}*t)]*\sin(\omega*t) \quad (3\text{-}15)$$

where,

U_x = actuator displacement
t = time, seconds
S_{ff}, A_{ff}, b_{ff} = equation constants
ω = 22.745 rad/sec (3.62 Hz).

Table 3.6 summarizes the forcing function equation constants for each of the cracked pipe experiments. Figures 3.69 through 3.71 are plots of the design basis or command forcing functions. Equation 3-15 was only the design basis for the displacement forcing function and it does not necessarily reflect slight differences between the programmed and actual motion of the actuator during the experiments. The

Table 3.6 Cracked pipe forcing function equation parameters
$(U_x = S_{ff} + A_{ff}\,[1-\exp(-b_{ff}t)]\,\sin(\omega\,t)$

Experiment Number	Specimen	S_{ff}, mm/sec (in/sec)	A_{ff}, mm (in)	b_{ff} -	ω, rad/sec (Hz)
1.3-2	Carbon Steel Base Metal	25.4 (1.00)	63.5 (2.50)	0.83353	22.745 (3.62)
1.3-3	Stainless Steel Base Metal	9.53 (0.375)	241.3 (9.50)	0.04042	24.819 (3.95)
1.3-4	Carbon Steel Weld	9.53 (0.375)	152.4 (6.00)	0.04042	24.819 (3.95)
1.3-5	Stainless Steel Weld	9.53 (0.375)	241.3 (9.50)	0.04042	24.819 (3.95)
1.3-7	Aged Cast Stainless	9.53 (0.375)	241.3 (9.50)	0.04042	24.819 (3.95)

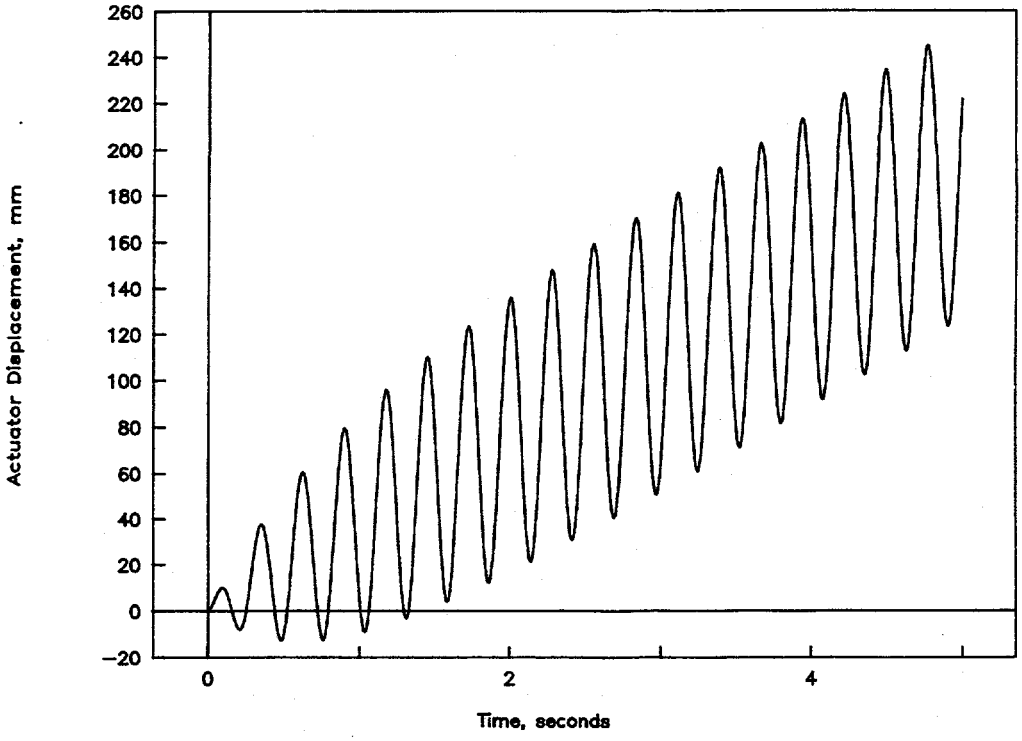

Figure 3.69 Design basis forcing function for Experiment 1.3-2 (carbon steel base metal) I1.3-10/90-F3.69

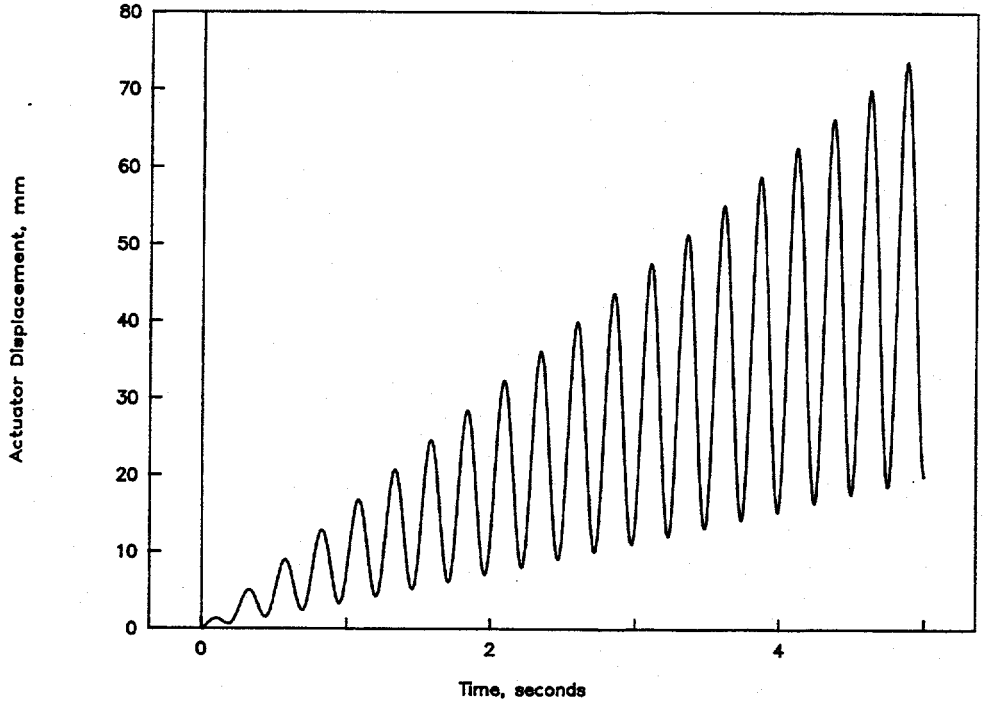

Figure 3.70 Design basis forcing function for Experiment 1.3-4 (carbon steel weld) I1.3-10/90-F3.70

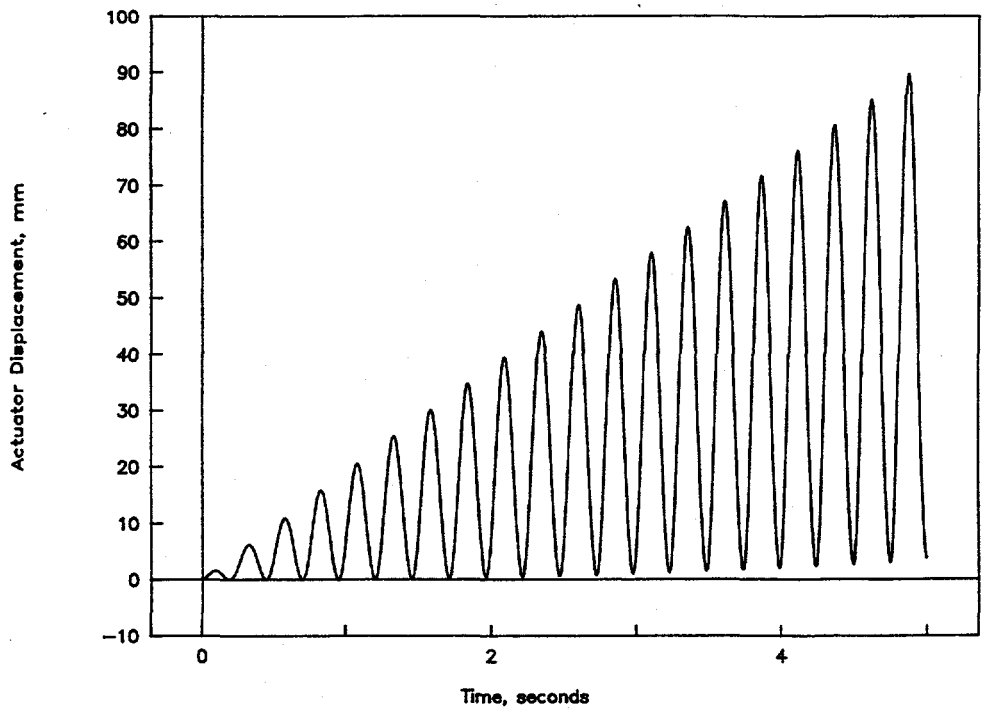

Figure 3.71 Design basis forcing function for Experiments 1.3-3, -5, and -7 (stainless steel base metal, stainless steel weld, aged cast stainless steel) I1.3-10/90-F3.71

measured actuator displacement is the displacement time-history that should be used in analyses of the experiments.

In all of the cracked pipe experiments, the forcing function was attenuated by the external shut-down device which was triggered by loss of pressure in the pipe loop test section. For the carbon steel base metal experiment, the shut-down pressure trigger was set at 3.4 MPa (500 psi). For all of the remaining cracked pipe experiments, the shut-down pressure trigger was set at 5.2 MPa (750 psi).

3.3.8 Data Reduction

The raw data from the cracked pipe experiments consisted of voltages from all of the transducers as a function of time. The data, which were stored digitally by the data acquisition system, were operated on in Lotus 1-2-3® spreadsheets and Fortran programs to generate the engineering data for the experiments. The assumptions and procedures used to conduct the data reduction are discussed below.

3.3.8.1 Basic Data Reduction Procedures

Before discussing the data reduction procedures, it is important to have an idea of the format of the raw data. In all of the cracked pipe experiments and the uncracked pipe dynamic tests, high-level analog voltages from the signal conditioning for the transducers were digitized at a 200 Hz rate. The range of the analog-to-digital converters was ±10 volts with a resolution of 5 mv (12-bit A/D conversion). Data were acquired by four computers for a total of 30 seconds, with data acquisition commencing several seconds prior to starting the forcing function. The data were stored by the data acquisition system as ASCII print

files. Each file included an experiment identifier header, a date and time stamp, channel description headers, and 16 channels of data. Six thousand lines by sixteen columns of data were generated per data acquisition computer, resulting in a total of about 4 Mbyte of data stored in four 1 Mbyte files.

Once the data were saved on floppy disks, the disks made read only, and the disks duplicated, reducing the data for the experiments followed a ten step process:

(1) Trim the initial portions of the raw data to eliminate the portions prior to the actuator starting to move. A Fortran program was used for this purpose.

(2) Using Lotus 1-2-3®, review the data to establish the useful duration of the event and then truncate the worksheets accordingly.

(3) Plot all of the data "as is" in voltages using Lotus 1-2-3®.

(4) Remove extraneous "spikes" from the data by reviewing the data on a channel-by-channel basis using Lotus 1-2-3®. Linear interpolation was used to replace the inappropriate data.

(5) Convert voltage data to engineering data using the appropriate conversion factors in Lotus 1-2-3®.

(6) Remove the starting offsets from the strain gage data to eliminate unknown amounts of heat-up induced drift.

(7) Determine the initial static moments at the locations where moments are calculated using an ANSYS® model of the piping system. The initial static loading consisted of PWR pressure and temperature with zero displacement of the actuator for the cracked pipe experiments. This is the condition that existed just prior to actuator motion in the tests.

(8) Convert the dynamic strain gage data (Step 6) into stresses and total moments using a Fortran program. The program requires the initial static moments calculated in Step 7 as inputs.

(9) Convert the measured string potentiometer displacements into global X-Y-Z displacements using a Fortran program.

(10) Make plots of all of the reduced data using Lotus 1-2-3®.

During the process outlined above, a record of the operations performed on the data sets was kept, and intermediate worksheets were saved.

The process of reducing the data is, for the most part, very simple, given the conversion factors from volts to engineering units. The only items requiring assumptions and more involved computations were calculations of global X-Y-Z displacements, stresses, moments and determination of crack initiation and crack growth. Appendix A provides a description of the procedures for converting the string potentiometer data into global X-Y-Z displacements. Appendix B provides a description of the procedures for converting the strain gage data into stresses and moments.

3.3.8.2 Data Reduction Uncertainties

The reduction of raw voltages into basic engineering quantities does not introduce any uncertainty beyond that associated with the measurements themselves. That is, strictly multiplying a voltage by a conversion factor does not change the basic uncertainty. However, when several pieces of basic engineering data are combined in some fashion to derive other quantities, the uncertainties associated with each of the basic measurements also combine to increase the overall uncertainty. Global X-Y-Z displacements are an example of the latter in which three measured vectors and initial measured geometry are combined. The uncertainty in global X may be considerably greater than the sum of the uncertainties associated with each of the measured vector lengths. To place some bounds on the uncertainty of the derived Subtask 1.3 data, an analysis of the data reduction procedures was performed.

To calculate the uncertainty of a derived quantity, the mathematical expression for the derived quantity at a particular point is expressed as a Taylor's series. Keeping only the linear terms, the total uncertainty can be expressed as

$$\Delta W = \Sigma \, (\partial W/\partial x_i)\Delta x_i \qquad (3\text{-}16)$$

where $W = f(x_1,x_2,...,x_i)$. To calculate the total uncertainty, the value of each of the parameters, x_i, must be known, as well as the associated uncertainty, Δx_i.

Uncertainty for the four derived quantities reported later in the Results Section, hanger reaction force at Node 6, pipe displacements, crack section rotation, and crack section moment, has been calculated. Included in the calculations are the uncertainties associated with the diameter of the Node 6 hanger jacks, initial measured vector lengths and geometry of the string potentiometer fixtures, Young's modulus, Poisson's ratio, and pipe section properties, as well as the uncertainties in the measured transducer outputs.

Table 3.7 summarizes the results of the data reduction uncertainty analysis. As indicated above, the uncertainty is a function of the value of the derived quantity. In this case, values typical of what was seen at surface-crack penetration in the experiments have been assumed as a basis. In addition, in some cases (i.e., global displacements) the uncertainty is also reported for an initial pretest condition. Several items deserve a comment:

- Node 21 displacements are inherently more uncertain than the other displacements due to the geometry of the string potentiometers.
- The uncertainty of the RVDT-based pipe rotation, which was only used on the first two experiments, is moot because the RVDT's were very noisy and so no rotation data were reported. The LVDT-based rotation measuring system was much better, not only from a signal-to-noise basis, but also from an uncertainty standpoint.
- Moment uncertainty is quoted for the worst case strain accuracy and likely strain accuracy conditions. The likely strain accuracy condition is consistent with comparisons made to analytical predictions.

Table 3.7 Data reduction uncertainty summary

Parameter	Basis	Uncertainty
Node 6 Force	500 kN	±10 kN
Crack Displacement		
X	0 mm	±8.05 mm
Y	0 mm	±8.02 mm
Z	0 mm	±3.15 mm
X	-25.4 mm	±8.23 mm
Y	-152.4 mm	±6.55 mm
Z	0 mm	±3.40 mm
Elbow 3 Displacement		
X	0 mm	±8.00 mm
Y	0 mm	±8.18 mm
Z	0 mm	±3.15 mm
X	152.4 mm	±10.59 mm
Y	-152.4 mm	±8.38 mm
Z	0 mm	±4.85 mm
Node 21 Displacement		
X	0 mm	±5.64 mm
Y	0 mm	±5.64 mm
Z	0 mm	±3.15 mm
X	-25.4 mm	±16.56 mm
Y	-152.4 mm	±18.87 mm
Z	0 mm	±16.92 mm
Crack Section Rotation		
RVDT	0.01 rad	±0.00258 rad
LVDT	0.01 rad	±0.00077 rad
Crack Section Moment		
Worst case	600 kN-m	±152 kN-m
Likely	600 kN-m	±83 kN-m

Reducing basic engineering data into derived quantities can introduce significant additional uncertainties into the results of experiments. For the most part, the IPIRG Subtask 1.3 derived data meet engineering expectations, ± 10 percent. Clearly, however, it is essential to try to directly measure quantities rather than to have to resort to deriving them.

3.4 Results of Experiments

In this section, the results of the pipe experiments will be presented. The results are grouped and presented in three basic categories. First, those results which illustrate the system performance of the experimental facility will be presented. Second, the results which address the issue of piping-system response will be presented. Third, the results which address the issue of fracture behavior will be presented.

3.4.1 Facility Performance

In many ways, the overall performance of the facility exceeded expectations. Great care was taken during the design phase to ensure that the as-built experimental facility could be easily modeled analytically. Hydrostatic bearings were incorporated in the facility design at the two vertical supports to produce a near frictionless restraint in the horizontal plane, a condition that is easily modeled in a finite element program. The very low measured value of system damping (0.5 percent) even at large amplitudes of motion (pipe motions, not actuator motions), is evidence of the success at translating the modeling into hardware. (The results of the system damping tests will be discussed in greater detail later herein.)

Great care was taken to insure that the two fixed ends remained fixed throughout the course of the experiments. The piping loop at the two fixed ends was bolted, via a 1,500-pound-class weld-neck flange, to a large steel frame which was buried in a large, heavily reinforced concrete mass. In order to assess the degree of movement at these two locations during the course of the experiments, accelerometers were mounted to the steel frame immediately adjacent to the large weld-neck flanges. By double integrating the accelerometer data, an assessment of the pipe motions at these locations could be made. Figures 3.72 through 3.74 show the results of the integration of the Node 1 accelerometer data for the stainless steel base metal experiment. For this particular experiment, the accelerometer data were augmented by string potentiometer data (see Figures 3.75 and 3.76). In comparing Figures 3.72 and 3.75 and Figures 3.73 and 3.76, one can see that the degree of agreement between the two instrumentation approaches is good.

In examining Figures 3.72 through 3.74, one can also see that the amount of motion at this location up to the point of surface-crack penetration is indeed negligible, less than 0.005 mm (0.0002 inch). These numbers are several orders of magnitudes less than the displacements applied to the piping system at the actuator. Consequently, an analyst is safe in mathematically describing the boundary conditions for Nodes 1 and 31 as fixed in all directions.

The last issue of facility performance that should be mentioned is the performance of the servo-hydraulic system. Table 3.8 compares the system capabilities with the performance of the servo-hydraulic system under test. There were significant margins on actuator stroke for all of the experiments. Actuator force, up to the point of surface-crack penetration never exceeded 45 percent of the rated force capacity. After break-through, while the system was blowing down and the shut-down device was active, the actuator force increased to a maximum of 82 percent of rated capacity.

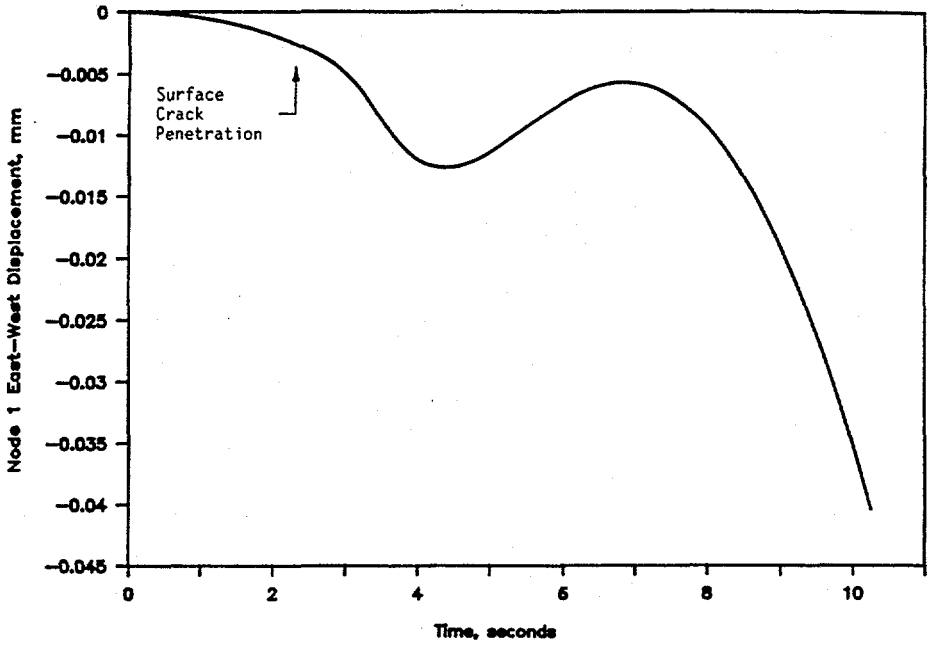

Figure 3.72 Node 1 east-west (x direction) displacements inferred from accelerometer data as a function of time for stainless steel base metal experiment

DRB/1.3-3/F25

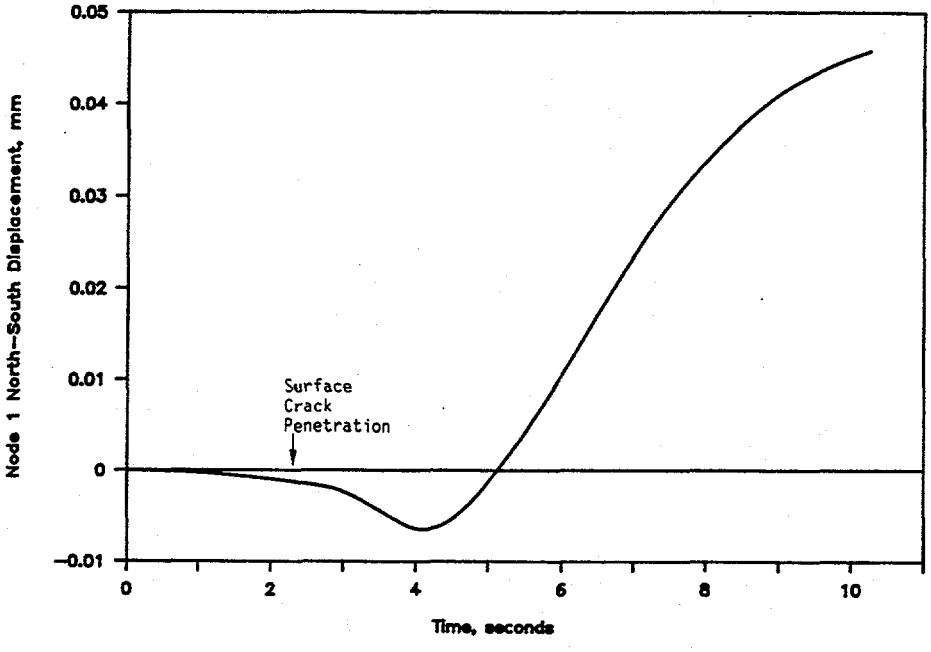

Figure 3.73 Node 1 north-south (y direction) displacements inferred from accelerometer data as a function of time for stainless steel base metal experiment

DRB/1.3-3/F26

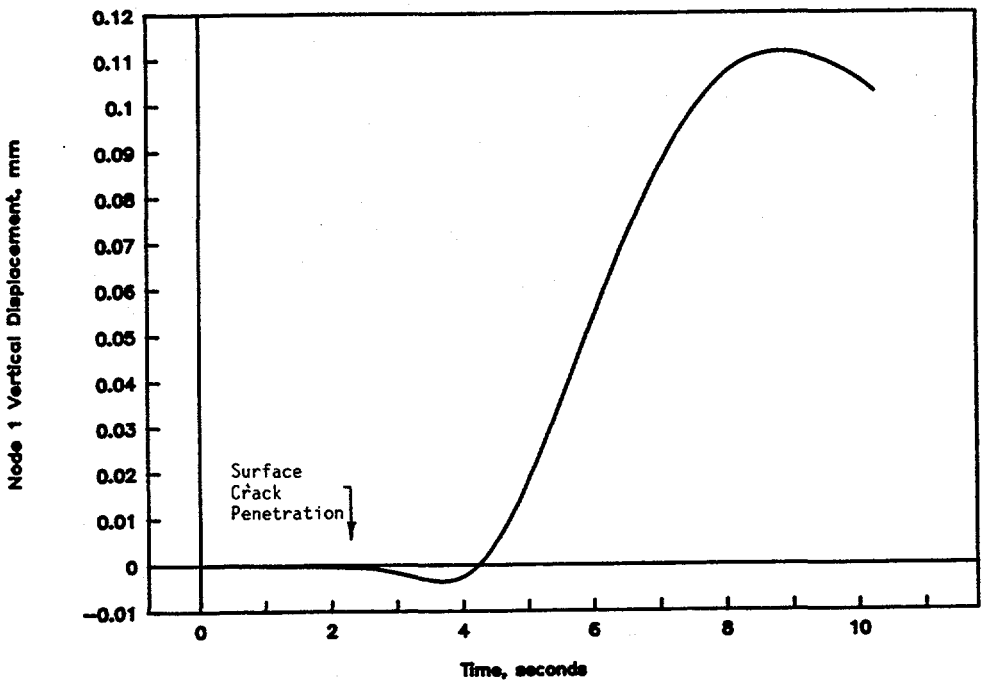

Figure 3.74 Node 1 vertical (z direction) displacements inferred from accelerometer data as a function of time for stainless steel base metal experiment

DRB/1.3-3/F27

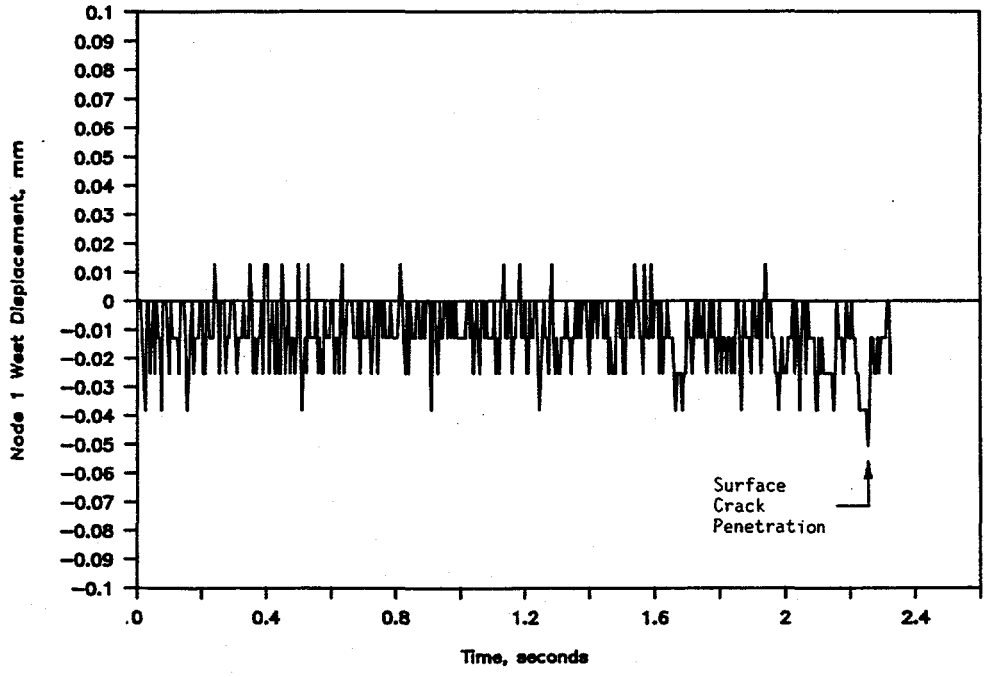

Figure 3.75 East-west displacements of Node 1 fixed end as measured using a string potentiometer versus time for stainless steel base metal experiment

DRB/1.3-3/F28

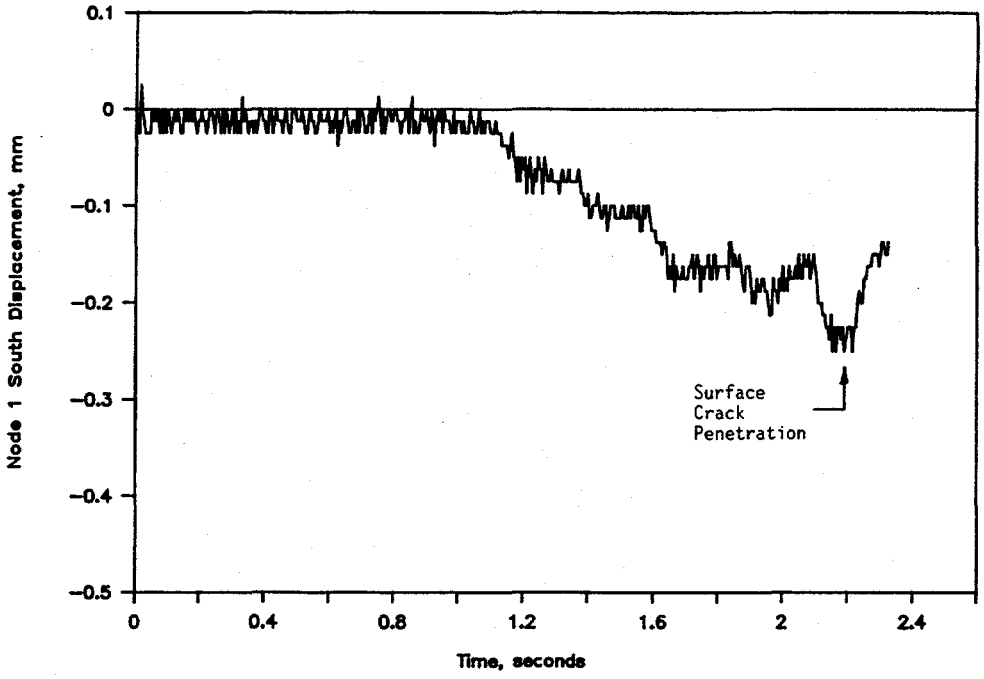

Figure 3.76 North-south displacement of Node 1 fixed end as measured using a string potentiometer versus time for stainless steel base metal experiment DRB/1.3-3/F29

Table 3.8 IPIRG 1.3 servo-hydraulic performance

Experiment		Time	Umax, mm	Umin, mm	Fmax, kN	Fmin, kN	Servo Flow, liter/min	Oil Volume, liter
System Limit		--	381.0	-76.2	1,556.9	-1,556.9	7,571	378.5
1.3-1	Uncracked	end	40.5	-11.9	527.8	-228.8	2,337	34.1
1.3-2	CSBM	SC Penetration	39.0	-2.9	406.1	-26.1	1,882	5.5
		end	90.6	-3.6	1,252.4	-928.1	3,544	126.1
1.3-3	SSBM	SC Penetration	43.5	-0.2	563.5	-252.0	2,125	22.5
		end	61.4	-0.2	1,069.8	-924.2	3,440	119.5
1.3-4	CSW	SC Penetration	94.1	0.3	682.7	-63.7	2,855	105.1
		end	101.1	0.3	1,098.0	-785.5	3,368	192.8
1.3-5	SSW	SC Penetration	49.8	-0.2	610.3	-238.2	2,415	28.7
		end	64.8	-0.2	1,120.7	-959.3	3,477	129.1
1.3-7	ACS	SC Penetration	50.1	0.0	647.2	-210.0	2,383	28.8
		end	95.1	-7.4	1,282.2	-885.4	16,628	272.4

For all experiments except the aged cast stainless, the servovalve rated flow capacity did not exceed 45 percent of its limit at any time during the tests. The servovalve rated flow for the aged cast stainless test exceeded capacity by more than a factor of two, but only after surface-crack penetration. The consequence of exceeding the rated flow was that the system displacement was significantly different from the command displacement. In fact, the excessive flow occurred during the DEGB in Experiment 1.3-7 when accumulator pressure was down and the actuator could not develop full rated force. The force of the DEGB was high enough that it pushed the actuator back approximately 25 mm (1 inch) when the servovalve was fully open.

The accumulator oil volume was more than adequate for all of the tests. A performance limitation of the accumulators appears to have been reached, however, in the aged cast stainless experiment because of pressure decay.

3.4.2 Piping System Response

The data from this program will prove useful in assessing the validity of both piping system analysis codes and fracture codes. This section of the report presents those results which will be useful in assessing piping system analysis codes or methodologies. Some of these results (i.e., eigenvalue and damping) are from the uncracked pipe experiment while some (i.e., pipe displacements, reaction forces, etc.) are from both the uncracked and cracked pipe experiments.

3.4.2.1 System Deflections During Pressurization

The first test of the uncracked pipe-system experiment was a simple pressurization of the pipe loop. The purposes of this test were to cycle all of the strain gages to remove any bonding induced nonlinearities and to collect data to verify analytical predictions of displacements due to pressurization.

The procedure for the test consisted of pressurizing the pipe loop to 15.5 MPa (2,250 psi), and then releasing the pressure. Displacements were recorded at each step using strategically located dial gages. The test was conducted at room temperature.

Data collected for this test consisted of the system pressure, actuator load, and displacements at four points on the pipe loop. Pipe displacements were measured, in the X-Y plane only, using 0.025 mm (0.001 inch) per division dial indicators located as shown in Figure 3.77. All data were recorded manually in the laboratory record book for this test.

The data from the system pressurization test are given in Table 3.9 for three pressurization cycles. These data indicate: (1) the displacements are all very small due to pressurization, (2) the displacements are consistent with engineering intuition in terms of sign of the displacements when one considers lengthening of runs of capped end pipes, and (3) the displacements, within some tolerance, are fairly repeatable.

3.4.2.2 System Damping

As part of the uncracked pipe experiment, the piping system damping characteristics were evaluated. Appendix D provides a background discussion on the determination of damping in a structural system. The evaluation of the system damping consisted of applying a small amplitude, on the order of 1.3 mm (0.05 inch), sinusoidal displacement to the pipe loop with the actuator, at a frequency below the first

Table 3.9 Pressurization data from uncracked Experiment 1.3-1

Pressure		Actuator Load		Displacement							
				Location 1		Location 2		Location 3		Location 4	
MPa	psi	kN	lb	mm	in	mm	in	mm	in	mm	in
0	0	0	0	0.000	0.0000	0.000	0.0000	0.000	0.0000	0.000	0.0000
0	0	1.02	230	0.025	0.0010	-0.178	-0.0070	0.025	0.0010	-0.102	-0.0040
15.47	2,244	4.58	1,030	-0.978	-0.0385	-0.279	-0.0110	-0.927	-0.0365	0.229	0.0090
0	0	0	0	-0.051	-0.0020	-0.013	-0.0005	-0.025	-0.0010	0.025	0.0010
0	0	1.02	230	-0.025	-0.0010	-0.152	-0.0060	0.000	0.0000	-0.051	-0.0020
15.49	2,246	5.29	1,190	-0.965	-0.0380	-0.368	-0.0145	-0.914	-0.0360	0.203	0.0080
0	0	0.85	190	-0.051	-0.0020	-0.114	-0.0045	-0.025	-0.0010	-0.025	-0.0010
15.50	2,248	5.16	1,160	-0.965	-0.0380	-0.356	-0.0140	-0.914	-0.0360	0.190	0.0075
0	0	0.85	190	-0.051	-0.0020	-0.102	-0.0040	-0.025	-0.0010	-0.013	-0.0005
0	0	0	0	-0.051	-0.0020	0.025	0.0010	-0.025	-0.0010	0.051	0.0020

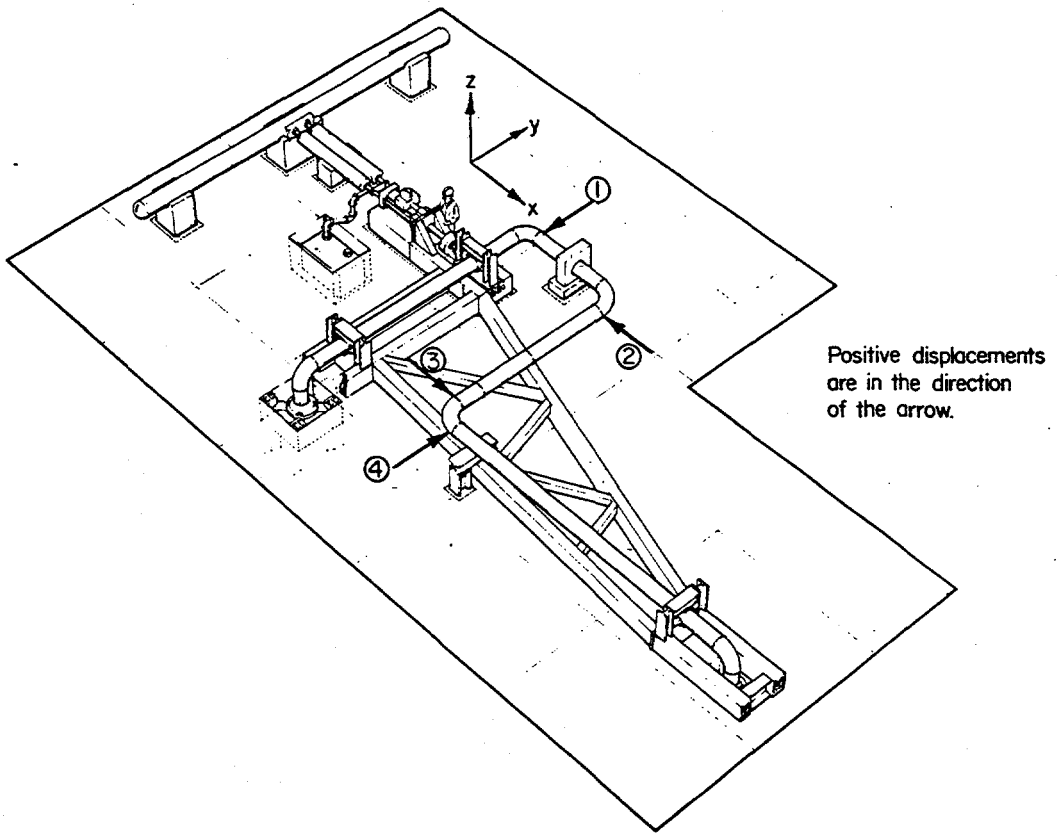

Figure 3.77 System pressurization test displacement measuring locations for room temperature uncracked pipe experiment DRB/1.3-1/F20

natural frequency of the system. The frequency of the excitation was then increased until the resonant frequency of the pipe loop was found, as evidenced by large motions of the pipe loop and large actuator loads. At this point, the excitation was removed, the actuator held fixed, and the system allowed to come to rest as indicated by the load falling to a static value. Actuator load was recorded continuously during the process. The test was conducted at room temperature, with the pipe filled with water in an unpressurized condition.

Data collected for this test consisted simply of actuator force as a function of time. The data were recorded on a Brush Mark 280, 2-channel, strip chart recorder. Sensitivity of the strip chart recorder was adjusted only for a reasonable output. Thus the recorded load is essentially uncalibrated (i.e., no conversion factor from volts to load was determined), although it is directly proportional to load. Per the discussion in Appendix D, a calibrated load was not necessary for this test.

Figure 3.78 shows the uncalibrated actuator load as a function of time for this system "ring-down" response test. Using the procedures outlined in Appendix D, the damping ratio using the logarithmic decrement over successive ten-cycle periods is shown in Figure 3.79. The data plotted in Figure 3.79 begin at 3 seconds on the abscissa, because prior to this time the actuator was still forcing the pipe loop and the response is not sinusoidal in nature. The average damping ratio, as calculated from the data in Figure 3.79, is approximately 0.5 percent.

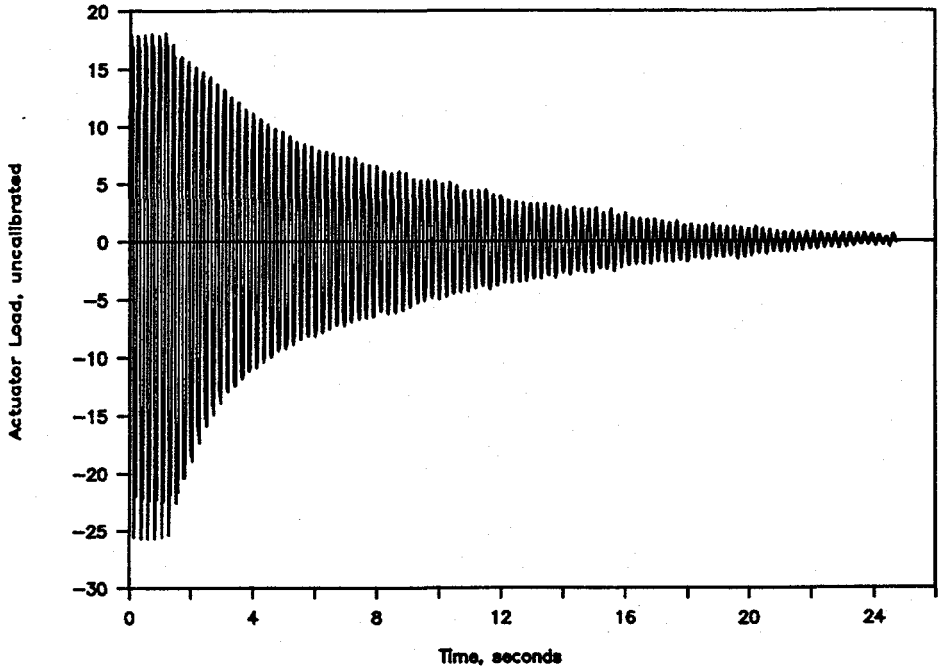

Figure 3.78 System "ring-down" response from Experiment 1.3-1

DRB/1.3-1/F21

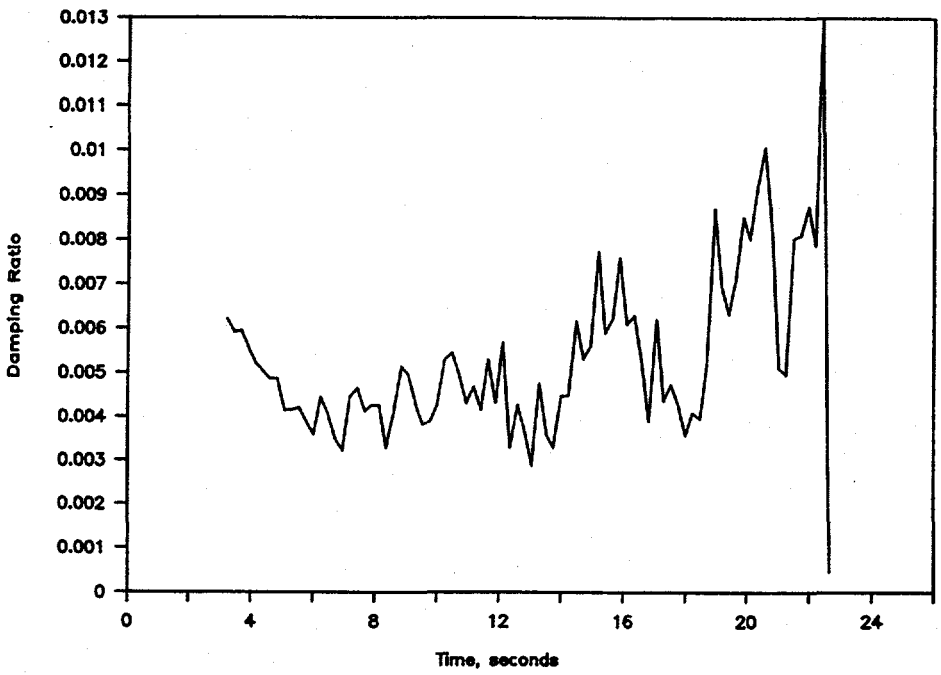

Figure 3.79 Damping ratio calculated using the logarithmic decrement over ten-cycle periods from Experiment 1.3-1

DRB/1.3-1/F22

3.4.2.3 Natural Frequency and Mode Shape Determination

As part of the uncracked pipe experiment, the first few natural frequencies for the piping loop were determined. The purposes of this test were to determine the natural frequencies of the piping system for comparison with analytical predictions, and to provide a basis for selecting the excitation frequency for the dynamic tests.

The system natural frequencies were determined in a number of ways: (a) from a system ring-down; (b) using an instrumented hammer, accelerometer, and spectral analyzer; and (c) using an accelerometer and spectral analyzer with energy input by the actuator. In addition to using a number of different methods to determine the natural frequencies, the frequencies were measured for the system under various conditions of pressure, temperature, and actuator preload.

System Ring-Down

The procedure for determining the system's first natural frequency by the ring-down method consisted of exciting the pipe loop with a small amplitude sinusoidal displacement, approximately 1.3 mm (0.05 inch), at a frequency just below the first natural frequency of the system. The frequency of the excitation was increased until the resonant frequency of the pipe loop was found, as evidenced by large motions of the pipe loop and large actuator loads. At this point, the excitation was removed, the actuator held fixed, and the system allowed to come to rest. The frequency of the actuator load signal during the ring-down is the system's first natural frequency. The test was conducted at room temperature, with the pipe filled with water in an unpressurized condition.

Data collected for this test consisted of actuator force as a function of time, as recorded on a Brush Mark 280, 2-channel, strip chart recorder. Sensitivity of the strip chart recorder was adjusted only for a reasonable output and thus, the recorded load is essentially uncalibrated (i.e., no conversion factor from volts to load was determined), although the recorded voltage is directly proportional to load. Only the frequency of the load response is important in this case.

Figure 3.80 shows a plot of the first natural frequency derived from the system ring-down data. For this plot, the frequency was calculated from successive ten-cycle periods, ignoring the data prior to three seconds because the actuator was still forcing the pipe. The average first natural frequency from Figure 3.80 is 4.28 Hz.

Instrumented Hammer Tests

In the instrumented hammer tests, transfer functions, as derived from pipe accelerations caused by a known impact force on the pipe, were used to determine the system's natural frequencies. The transfer function, which is the acceleration divided by the impact force, is calculated in real time by a Fast Fourier Transform (FFT) analyzer using the output of an accelerometer and an instrumented hammer. The hammer blows were applied manually. To ensure that all modes were excited, the accelerometer location and the point at which the hammer was struck were varied as shown in Figure 3.81. A sequence of 10 hammer blows for each hammer-accelerometer combination was used to average the data. The test was conducted at room temperature with the pipe filled with water at 15.4 MPa (2,230 psi). Two boundary conditions at the actuator location were investigated (see Figure 3.81), fixed in X, and free (actuator disconnected).

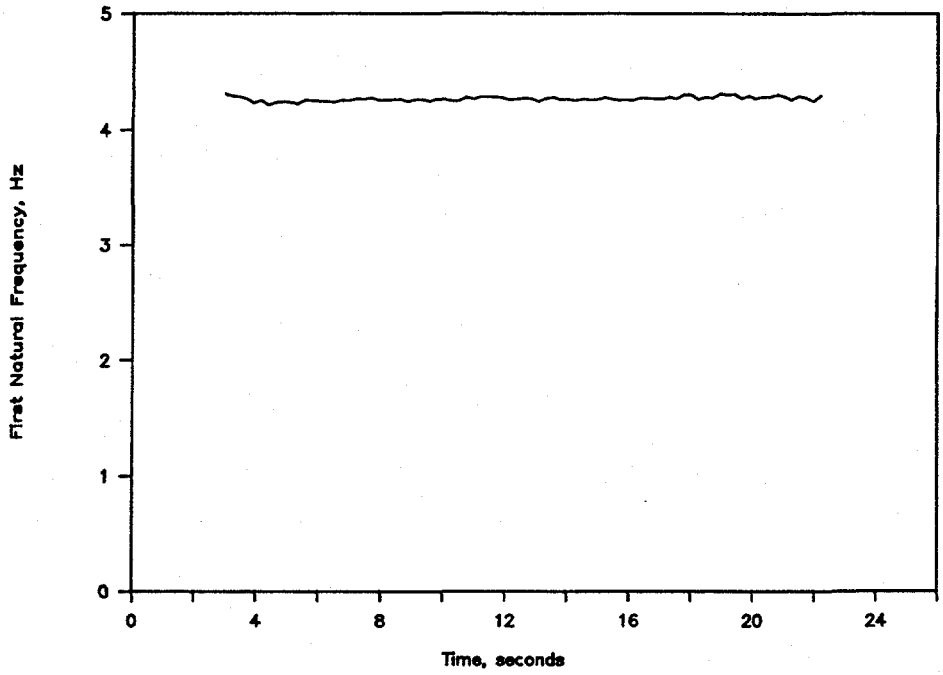

Figure 3.80 Natural frequency as calculated using successive ten-cycle periods of a system ring-down from Experiment 1.3-1

DRB/1.3-1/F24

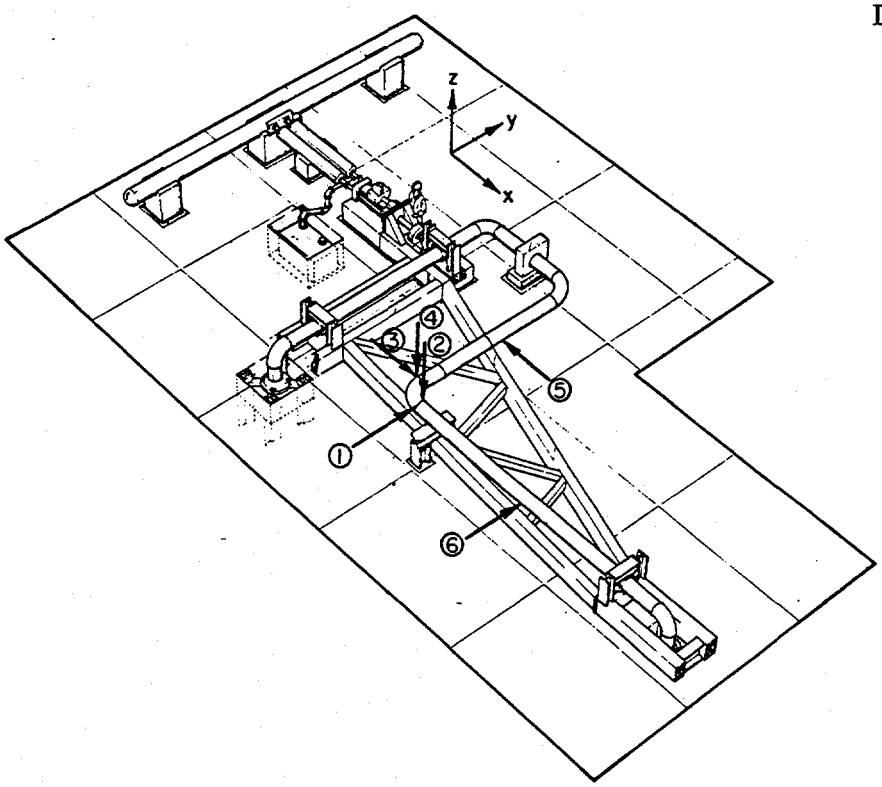

Figure 3.81 Accelerometer and force input locations for the instrumented hammer dynamic response measurements

DRB/A.3-1/F25

The selection of locations for the accelerometer and hammer impact was based upon finite element predictions of the pipe loop mode shapes. Figures 3.82 and 3.83 show plots of the predicted mode shapes for the actuator connected and actuator free conditions. Basically, the accelerometer was placed in locations that would experience predicted large motions when the pipe was struck in a certain direction.

The instrumentation used for the instrumented hammer tests consisted of a PCB Piezotronics GK291B50 instrumented hammer, a PCB Piezotronics Model 321A02 quartz accelerometer with built-in amplifier, a PCB Piezotronics 408D06 Battery Power Unit to power and condition the output of the accelerometer, and a Scientific Atlanta SD385, 2-channel FFT analyzer. The hammer was a 5.5 kg (12 pound) sledge with an integral load cell.

Using Figure 3.81 as a reference for accelerometer and hammer locations and Figure 3.82 as a framework for interpretation of the mode shapes, Figures 3.84 to 3.87 show the transfer functions for the actuator-connected boundary condition. Figure 3.84 shows a peak at 4.5 Hz, consistent with a predicted frequency of 4.42 Hz, using accelerometer and hammer locations consistent with Mode Shape A in Figure 3.82. A secondary peak around 18.0 Hz is also consistent with Mode Shape D. Likewise, using Positions 2 and 4 for the hammer blows and accelerometer, respectively, Figure 3.85 has a first peak at 13.9 Hz which is consistent with Mode Shape B, an out-of-plane mode. With the exception of the measured frequency of Mode Shape C, all of the acceleration/hammer locations, mode shapes, and frequencies are consistent with the predicted values. The somewhat low frequency measured for Mode Shape C, at least relative to the other predictions, cannot be readily explained.

The free actuator condition transfer function data are shown in Figure 3.88. The first frequency identified on the plot is 3.5 Hz. The second peak in the transfer function is at 6.0 Hz. Again, hammer and accelerometer locations, and measured frequencies are consistent with the predicted values shown in Figure 3.83.

Actuator Driven Excitation

A third method for measuring the natural frequencies of the IPIRG Subtask 1.3 pipe loop was employed just prior to the room temperature and PWR condition dynamic tests. In these tests, the actuator was used to displace the structure, as opposed to using an external source such as an instrumented hammer. A bandwidth-limited random noise signal was used as the actuator forcing function. Like the instrumented hammer test, acceleration was measured as an indicator of the response of the pipe to the force input. The procedure for determining the natural frequencies is conceptually similar to the one used in the instrumented hammer test, with a notable exception; peak acceleration was used as the dependent parameter instead of the transfer function (acceleration normalized by the impact force). This is a departure from typical practice and, therefore, deserves some comment.

When measuring the dynamic response of a structure, typically, a shaker (or an instrumented hammer) imparts a defined force to the structure. The response of the structure to the known force, in terms of acceleration, is measured. From forced vibration theory, this results in an easily implemented measurement called a transfer function which describes the dynamic response of a structure. In the present case, the actuator controls the displacement rather than the force on the structure. Mathematically, this is far more difficult to describe and the traditional transfer function measurement is not valid. When measuring the transfer function using the load cell at the actuator and an accelerometer on the structure, the first resonance of the structure could not be detected. The load cell was actually measuring the reaction force of the actuator trying to hold the pipe to small displacements, while the pipe was trying to increase

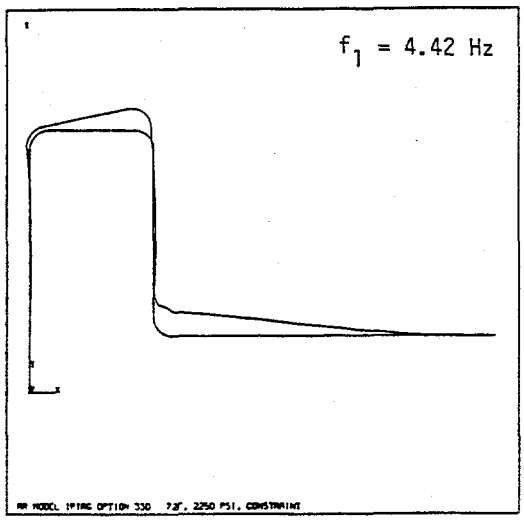

(a) Mode Shape A

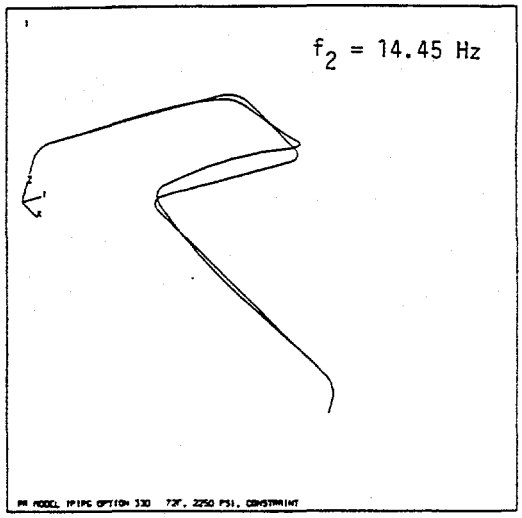

(b) Mode Shape B

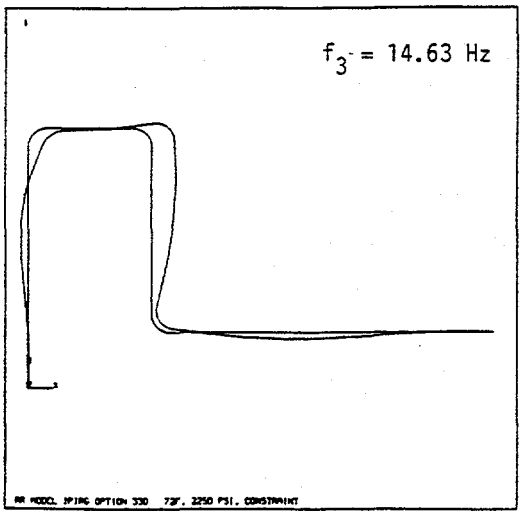

(c) Mode Shape C

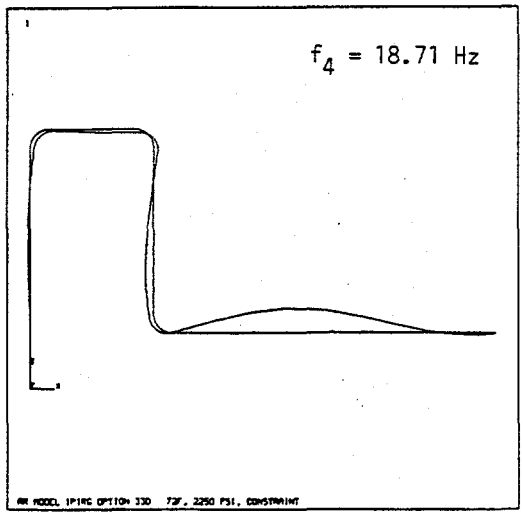

(d) Mode Shape D

Figure 3.82 Calculated mode shapes using ANSYS® for first four natural frequencies of the pipe loop with the actuator as a fixed node

DRB/1.3-1/F26

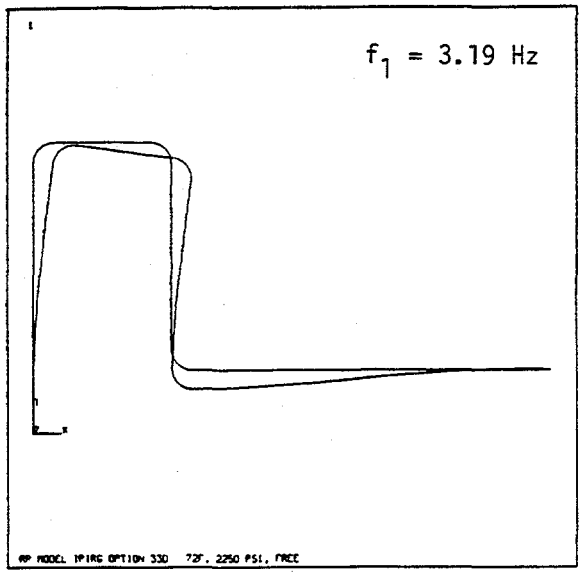

(a) Mode Shape E

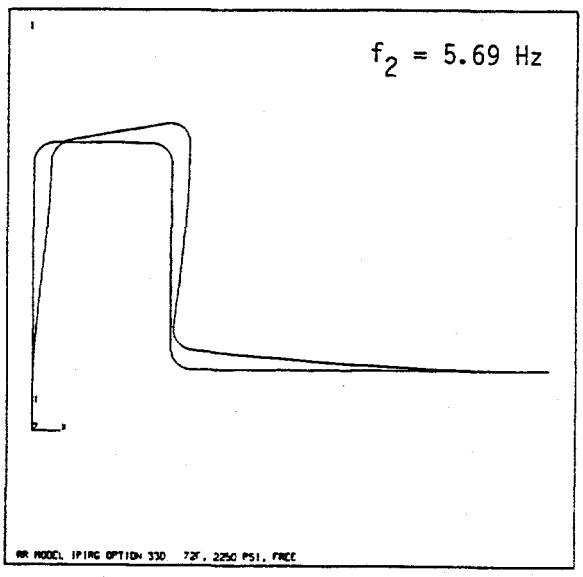

(b) Mode Shape F

Figure 3.83 Calculated mode shapes using ANSYS® for first two natural frequencies of the pipe loop with the actuator as a free node

DRB/1.3-1/F27

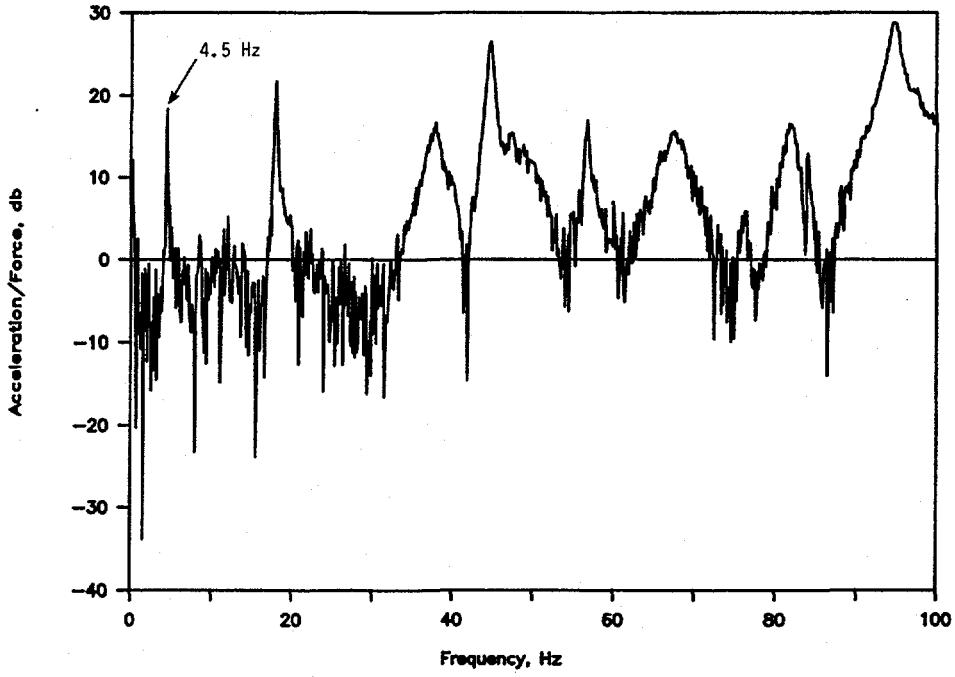

Figure 3.84 Transfer function with accelerometer at Position 1 and impact at Position 1, actuator connected - Mode Shape A

DRB/1.3-1/F28

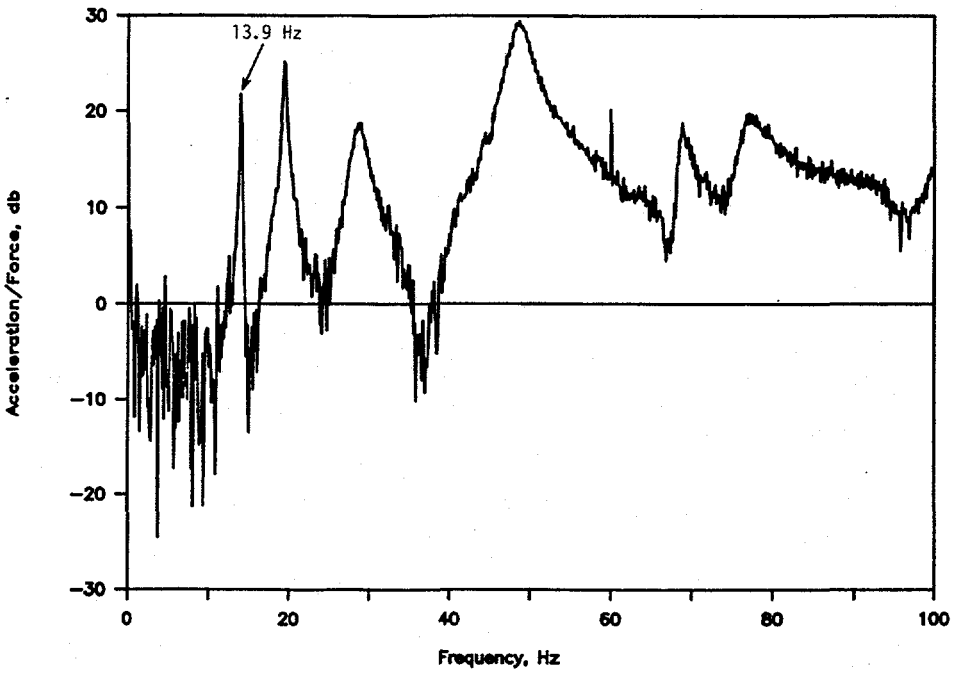

Figure 3.85 Transfer function with accelerometer at Position 4 and impact at Position 2, actuator connected - Mode Shape B

DRB/1.3-1/F29

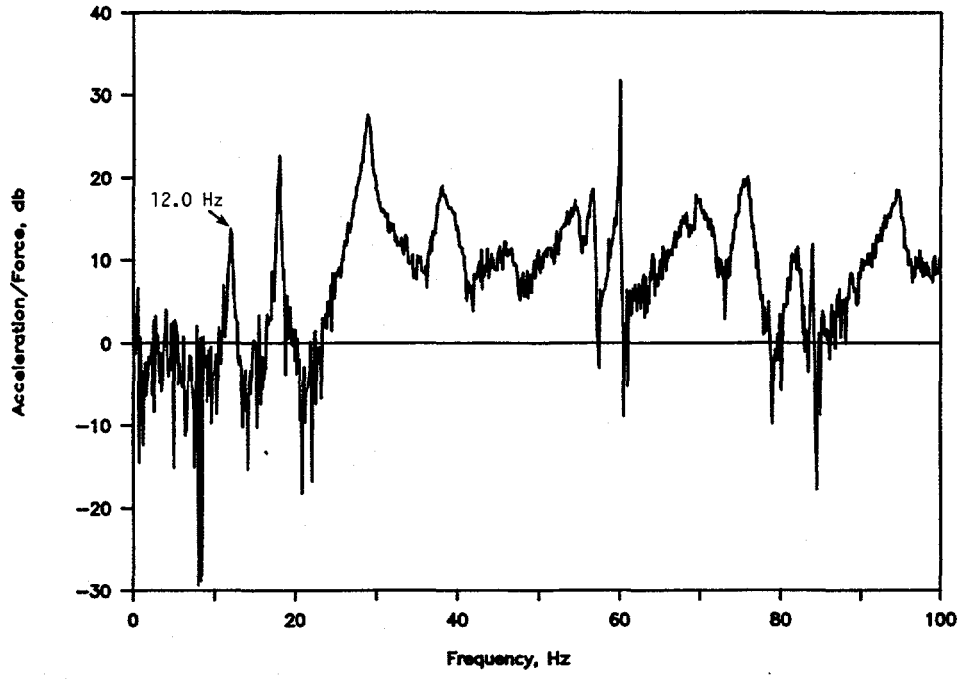

Figure 3.86 Transfer function with accelerometer at Position 5 and impact at Position 3, actuator connected - Mode Shape C

DRB/1.3-1/F30

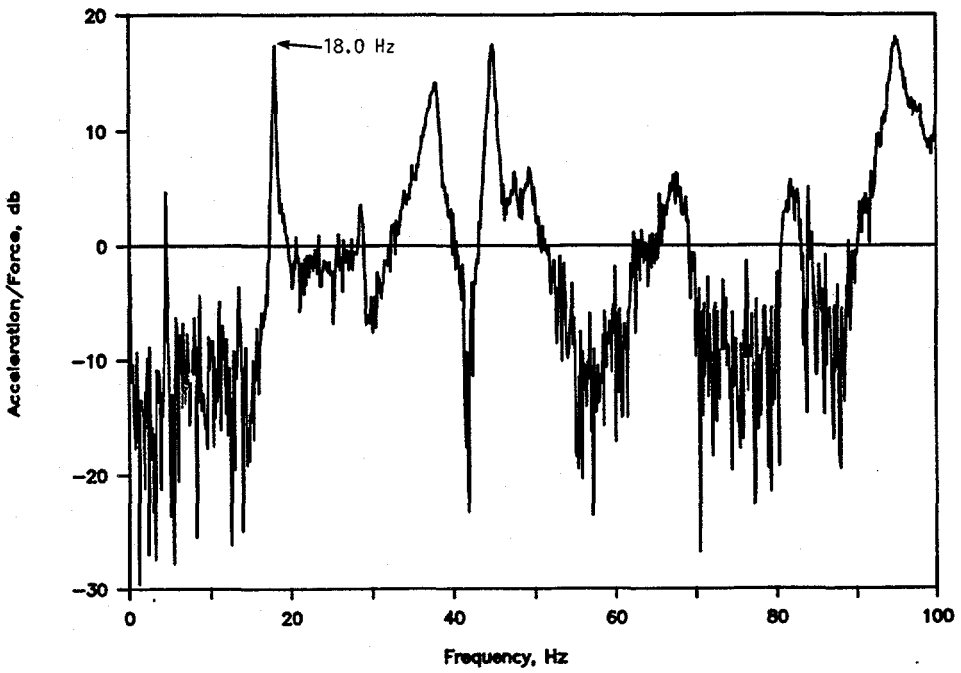

Figure 3.87 Transfer function with accelerometer at Position 6 and impact at Position 1, actuator connected - Mode Shape D

DRB/1.3-1/F31

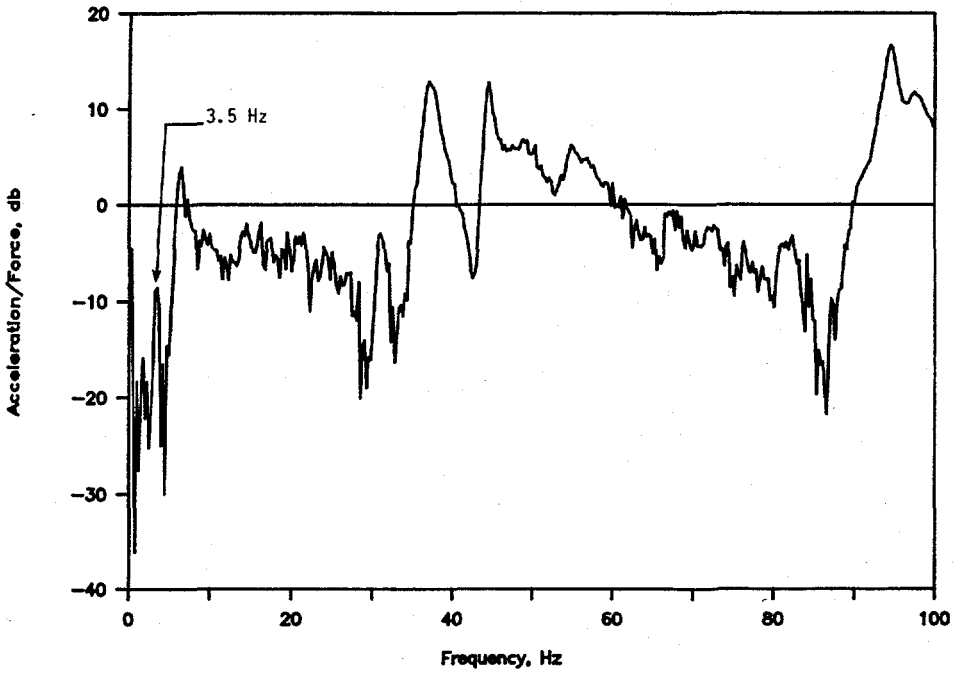

Figure 3.88 Transfer function with accelerometer at Position 1 and impact at Position 1, actuator free - Mode Shape E

DRB/1.3-1/F32

the range of motion at resonance. This caused the expected peak at resonance in the transfer plot to disappear. A plot of peak acceleration, however, shows the expected peaks at resonance.

The basic procedure for the actuator driven natural frequency determination consisted of applying a bandwidth-limited random noise displacement signal, so called pink noise (broad-band random noise with equal energy in each octave frequency band - see Figure 3.89), to the actuator and measuring the acceleration of the pipe in response to the pink noise. An FFT analyzer collected the acceleration response data for 30 seconds, averaged the data, and produced acceleration response spectra. For the room temperature test, two parameter variations were considered; internal pressure and actuator preload. For the PWR condition test, only the preload was varied. In both cases, the pipe was filled with water.

The instrumentation used for the actuator driven natural frequency test consisted of a Battelle-built pink noise generator, an Ectron 751 El-M563 amplifier to boost the output of the pink noise generator and to filter the output above 100 Hz, two accelerometers, and an FFT analyzer. For the room temperature test, the analyzer was a 2-channel Scientific Atlanta Model SD385, and the accelerometers were PCB Piezotronics 321A02 quartz accelerometers with built-in amplifiers, powered and amplified by a PCB Piezotronics 483A08 accelerometer amplifying power unit. For the PWR condition test, a 4-channel, Scientific Atlanta SD380 analyzer was used with PCB Piezotronics model 312A02 high temperature quartz accelerometers, PCB Piezotronics 4220 charge amplifiers, and a PCB Piezotronics 483A08 accelerometer amplifying power unit.

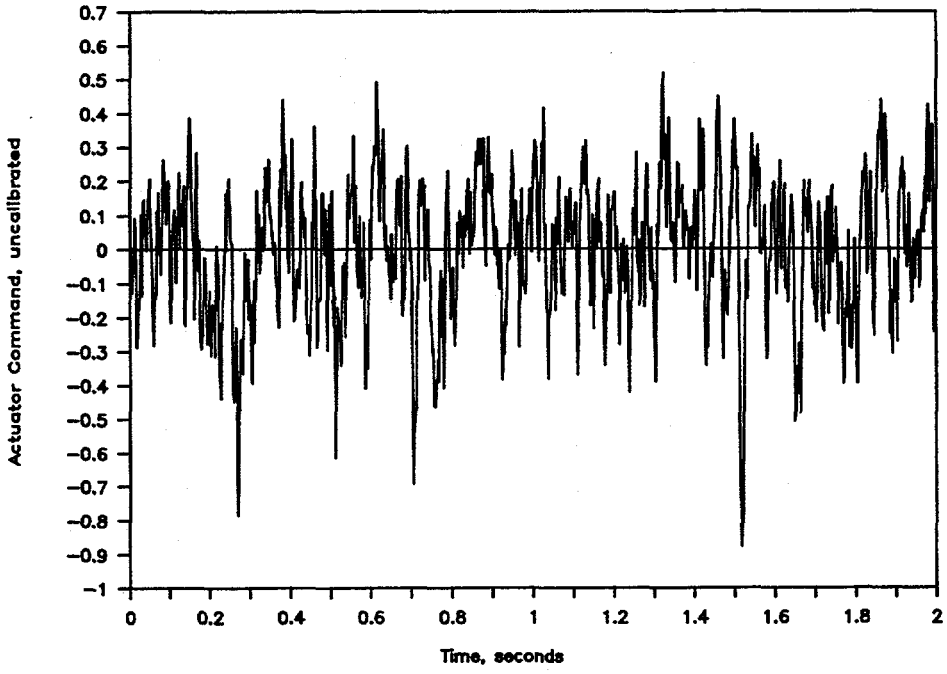

Figure 3.89 Typical pink noise actuator displacement input command signal
DRB/1.3-1/F33

The two accelerometers were located on the pipe as shown in Figure 3.90, one on the extrados of Elbow 3, and one on the top of the pipe at the junction of Elbow 3 and the straight pipe containing the test section. The Elbow 3 extrados position was chosen as a location that would likely experience significant motion for any of the in-plane modes shown in Figure 3.82, Modes A, C, or D. The other accelerometer was expected to respond to Mode B, the out-of-plane mode.

The results of the room temperature, actuator driven, natural frequency tests are shown in Figures 3.91 through 3.93. In comparing the three horizontal response spectra (accelerometer position 7), one concludes that a decrease in preload from 30.7 kN (6,900 lb) to 23.6 kN (5,300 lb) decreases the first natural frequency by 0.22 Hz (compare Figures 3.92 and 3.93), but pressure has no effect (compare Figures 3.91 and 3.92). The latter result is not intuitively obvious, but is consistent with analytical predictions using the ANSYS® code, which indicate that, except for some minor pressure stiffening of elbows, pressure does not stiffen and, hence, raise the natural frequency of a piping system. A second peak in horizontal acceleration occurs around 14 Hz for all three conditions which is consistent with Mode Shape C shown in Figure 3.82. All of the vertical spectra show a peak around 14 Hz, again consistent with Figure 3.82, Mode Shape B.

The acceleration response spectra under PWR conditions are shown in Figures 3.94 and 3.95. In these figures, the response in the vertical direction is only plotted for the first condition because the plot is virtually identical for the other preload condition. Vertical acceleration shows a peak at 13.35 Hz, a value somewhat lower than the room temperature test. The horizontal acceleration, on the other hand, shows one prominent peak at about 4.4 Hz, more or less independent of preload.

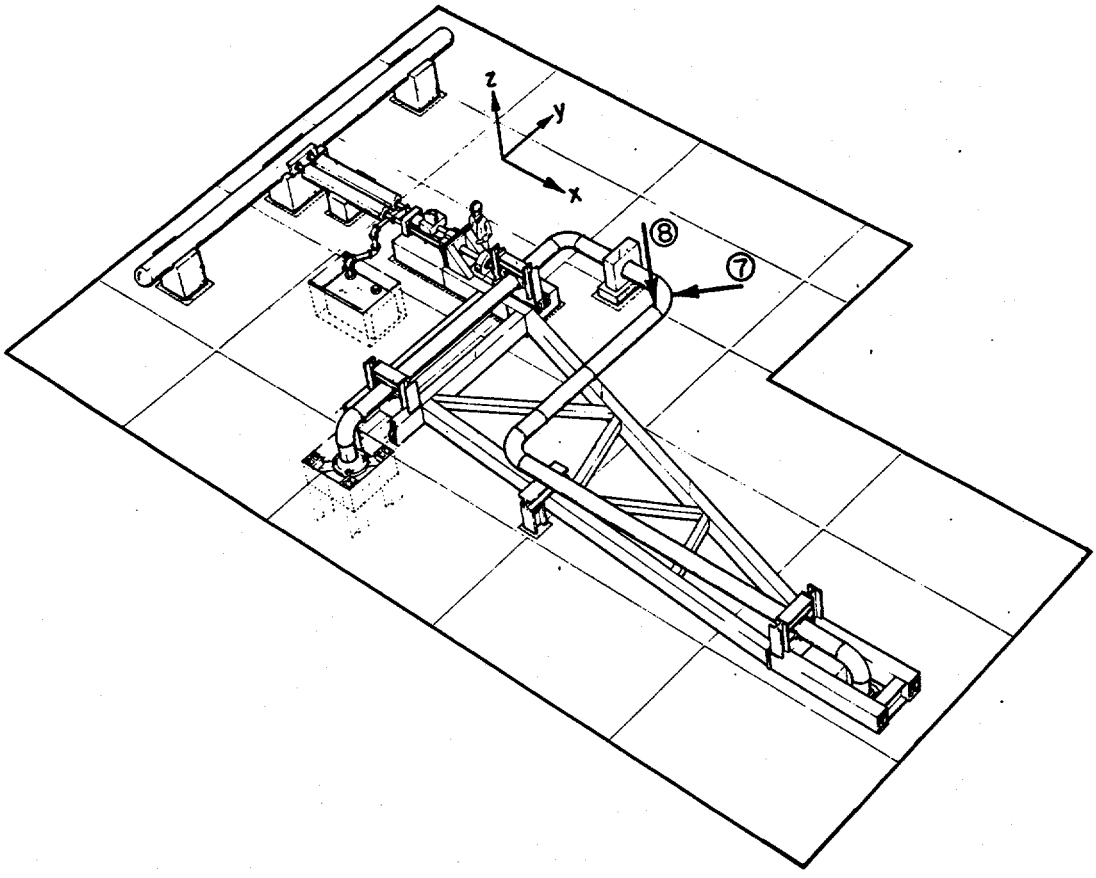

Figure 3.90 Accelerometer locations for actuator-driven excitation dynamic response measurements

DRB/1.3-1/F34

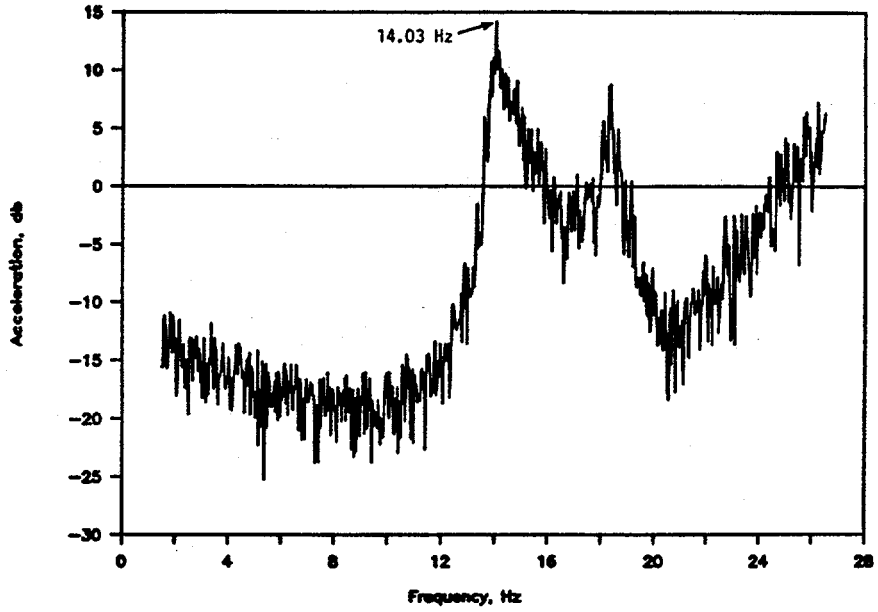

(a) Accelerometer Position 8

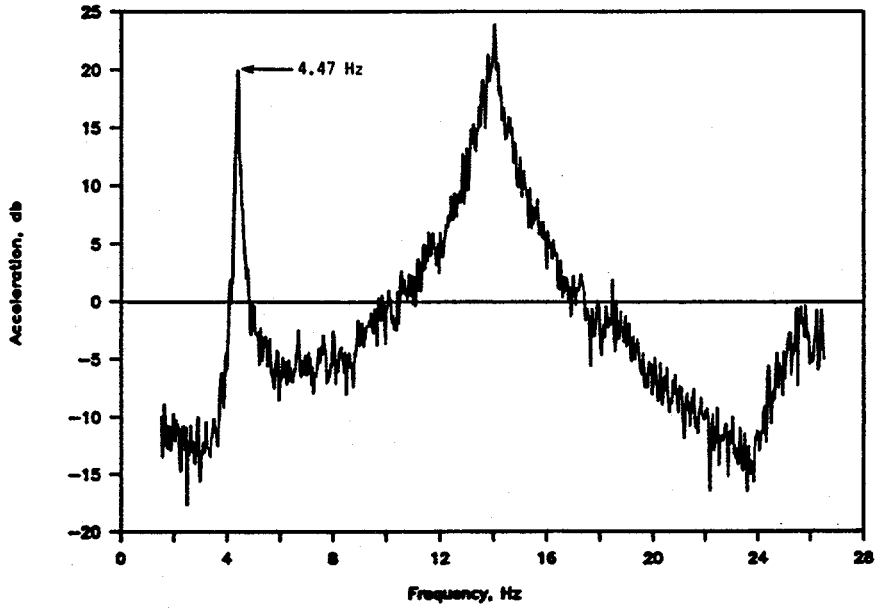

(b) Accelerometer Position 7

Figure 3.91 Frequency response with actuator controlled input displacement using a bandwidth-limited random noise excitation signal, internal pressure 15.4 MPa (2,238 psi), room temperature, actuator preload 30.7 kN (6,900 lbs) DRB/1.3-1/F35

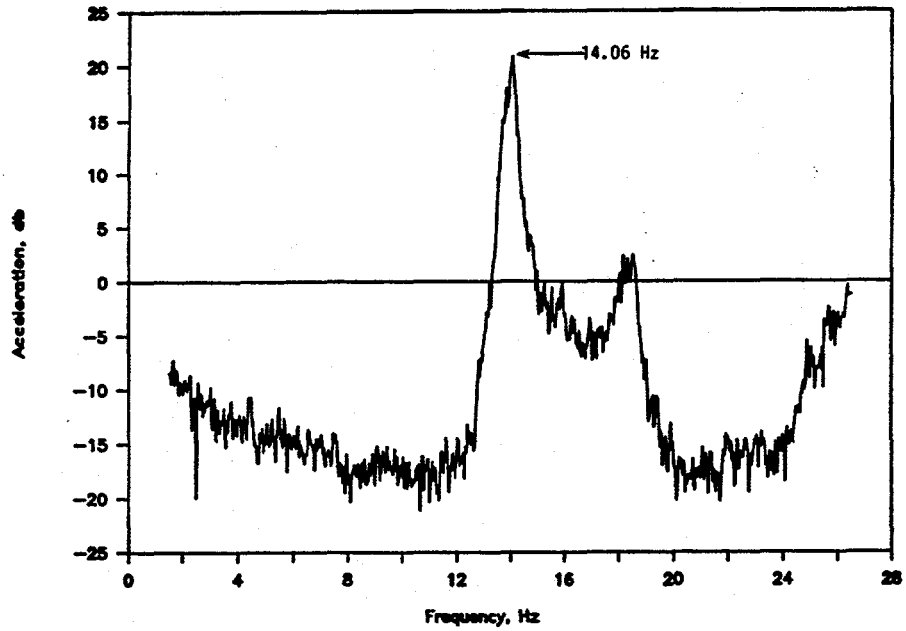

(a) Accelerometer Position 8

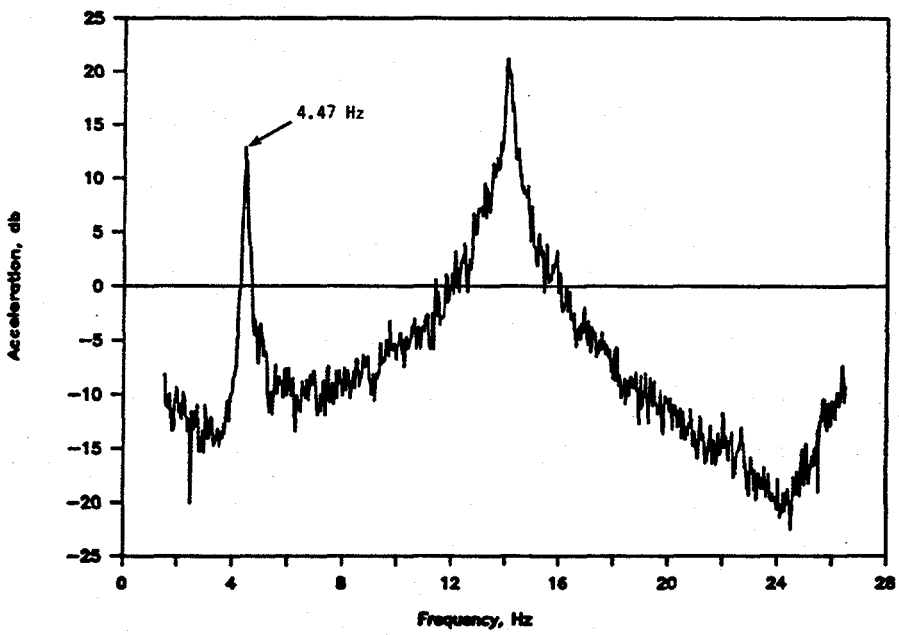

(b) Accelerometer Position 7

Figure 3.92 Frequency response with actuator controlled input displacement using a bandwidth-limited random noise excitation signal, internal pressure 0 MPa (0 psi), room temperature, actuator preload 30.7 kN (6,900 lbs) DRB/1.3-1/F36

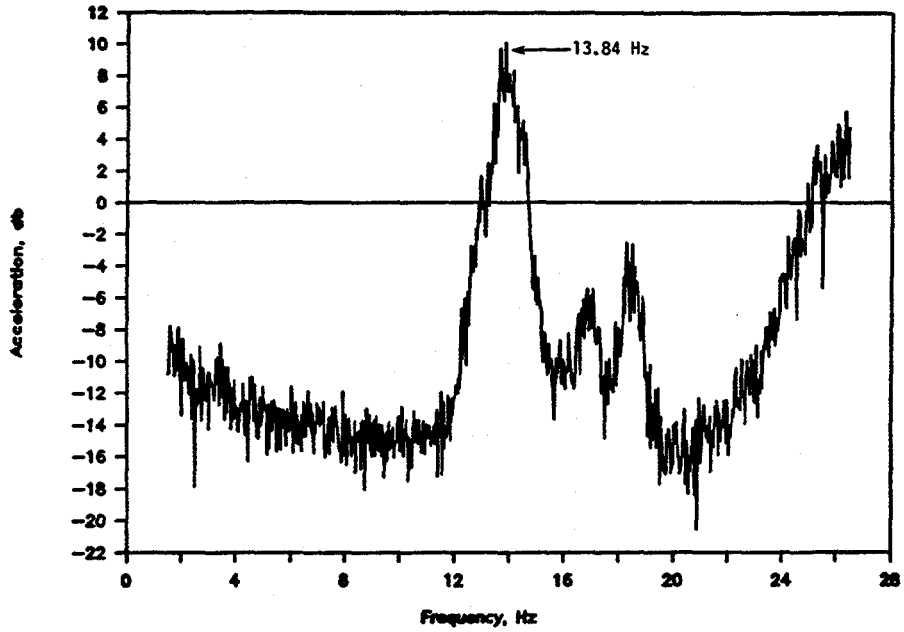

(a) Accelerometer Position 8

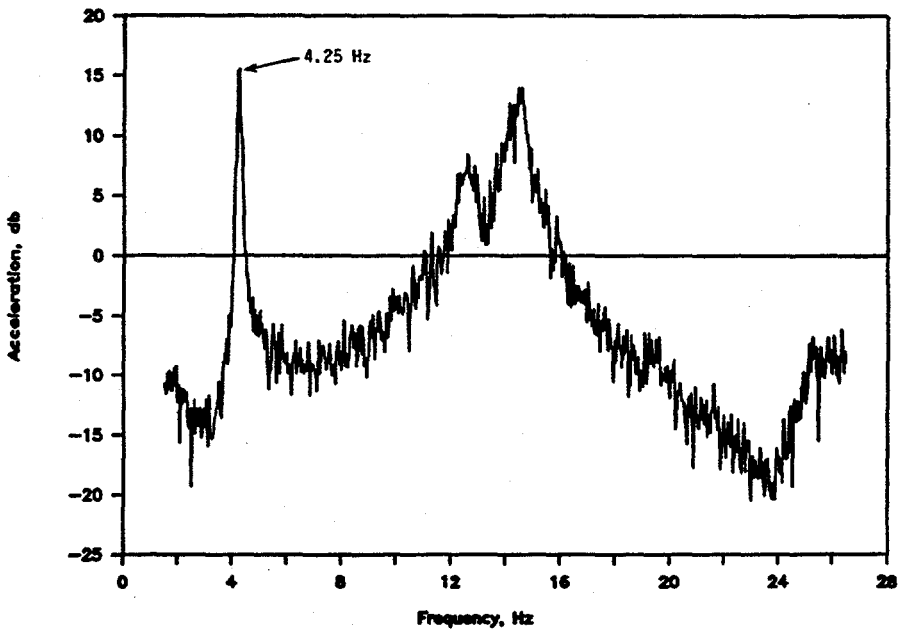

(b) Accelerometer Position 7

Figure 3.93 Frequency response with actuator controlled input displacement using a bandwidth-limited random noise excitation signal, internal pressure 0 MPa (0 psi), room temperature, actuator preload 23.6 kN (5,300 lbs) DRB/1.3-1/F37

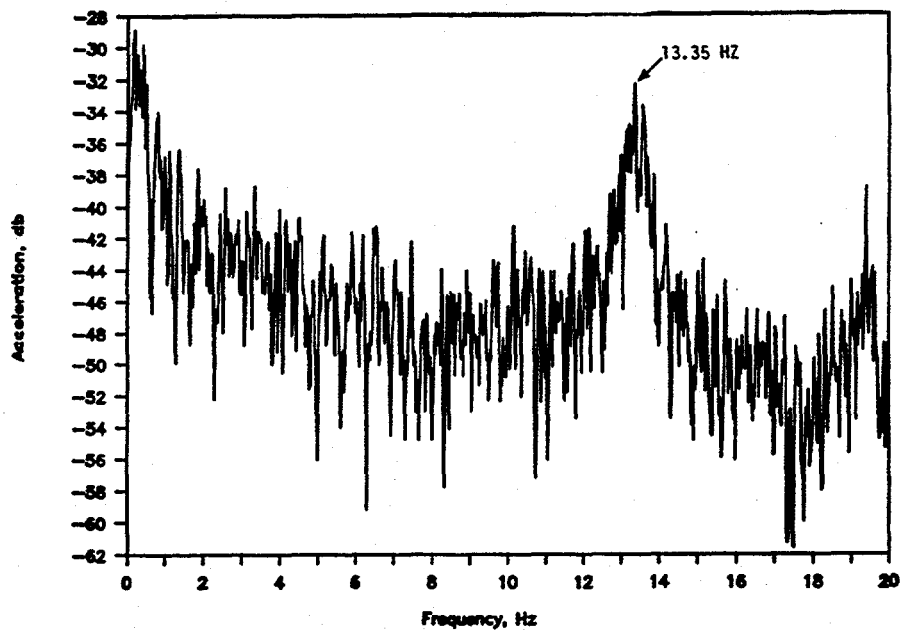

(a) Accelerometer Position 8

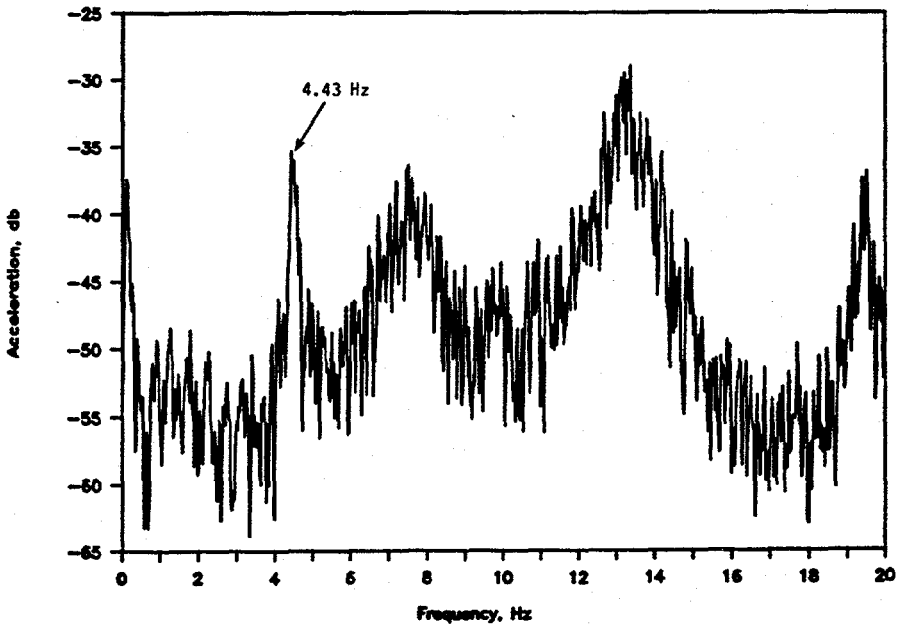

(b) Accelerometer Position 7

Figure 3.94 Frequency response with actuator controlled input displacement using a bandwidth-limited random noise excitation signal, internal pressure 15.6 MPa (2,257 psi), 292 C (557 F), actuator preload 31.1 kN (7,000 lbs) DRB/1.3-1/F38

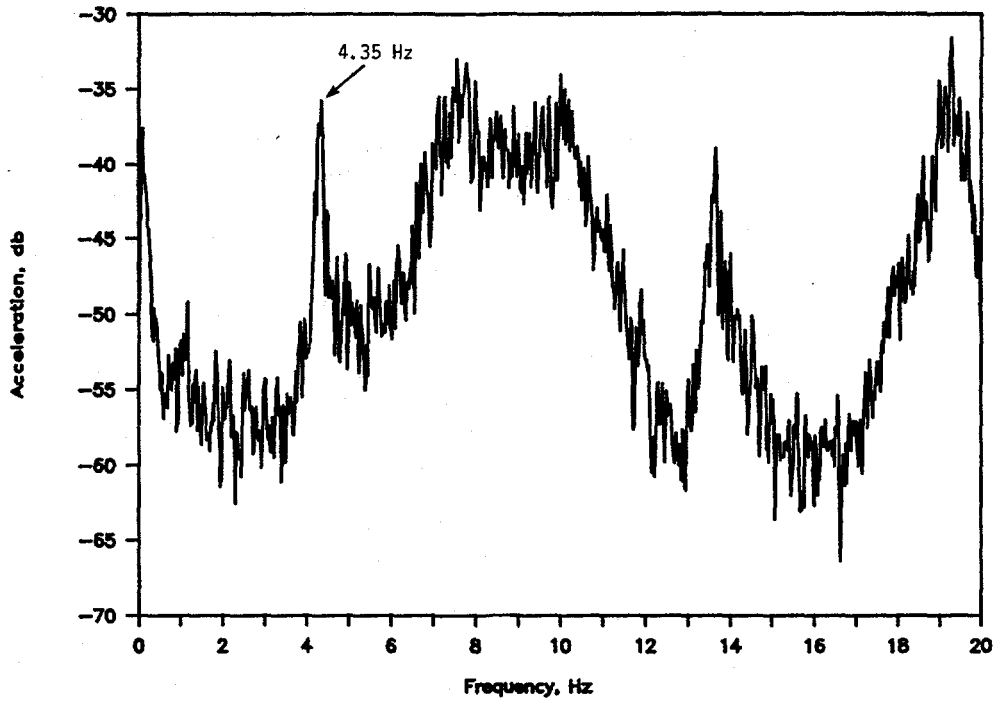

Figure 3.95 Frequency response at accelerometer Position 7 with actuator-controlled input displacement using a bandwidth-limited random noise excitation signal, internal pressure 15.6 MPa (2,257 psi), 292 C (557 F), actuator preload 4.4 kN (1,000 lbs)

DRB/1.3-1/F39

3.4.2.4 PWR Static Push

The objectives of this test were to gain experience running the IPIRG Subtask 1.3 facility at PWR conditions prior to running a dynamic test, and to generate data for comparison with analytical predictions of the motion of the system.

Conditions for this test were pipe loop and test specimen filled with water at 288 C (550 F) and 15.5 MPa (2,250 psi) internal pressure. The actuator, under displacement control, was extended manually from the pre-test (room temperature and zero pressure) stress free location in increments of approximately 12.5 mm (0.50 inches) to a maximum displacement of 100 mm (3.9 inches), and then returned to the zero location in the same step-wise fashion. Figure 3.96 shows the measured displacement-time trace.

The results of the uncracked pipe PWR static push are shown in Figures 3.96 through 3.102. The basic data for this test contain no particularly surprising features. The actuator load, Figure 3.97, exhibits a bit of hysteresis, but this is on the order of 1 percent of the full-scale load capacity of the load cell. The pipe global displacements at the crack, Elbow 3, and Node 21 are shown in Figures 3.98 through 3.100. For these plots the initial global displacements due to heat up and pressure have been subtracted from the data files. As expected, the pipe displacements plotted in Figures 3.98 through 3.100 show very little

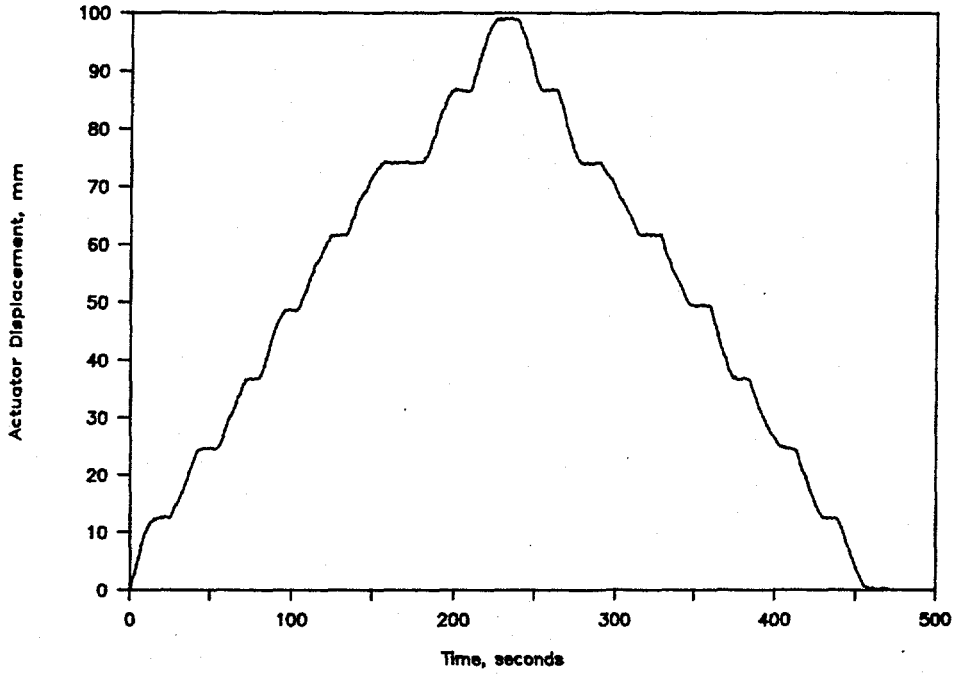

Figure 3.96 Actuator displacement for the PWR uncracked static push pipe test, Experiment 1.3-1

DRB/1.3-1/F72

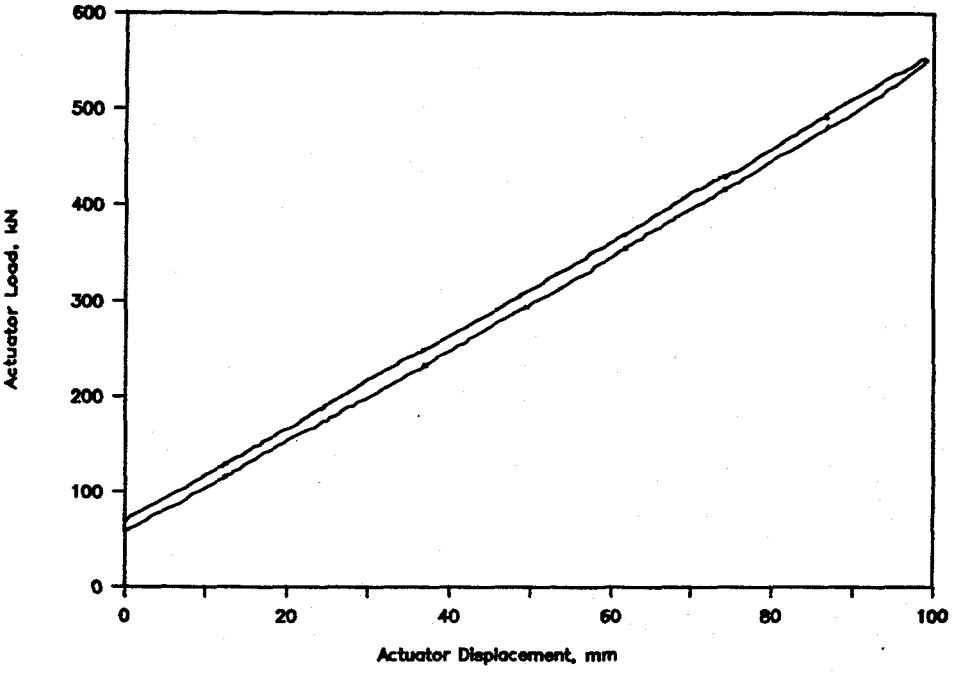

Figure 3.97 Actuator load for the PWR uncracked static push pipe test, Experiment 1.3-1

DRB/1.3-1/F73

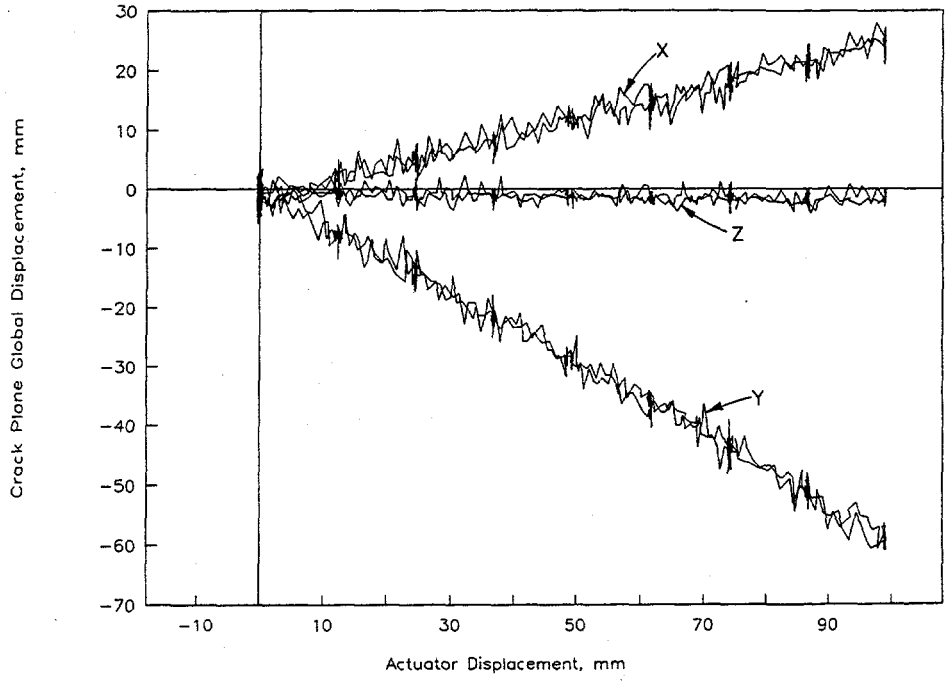

Figure 3.98 Crack plane global displacements from the PWR uncracked static push pipe test, Experiment 1.3-1

DRB/1.3-1/F87

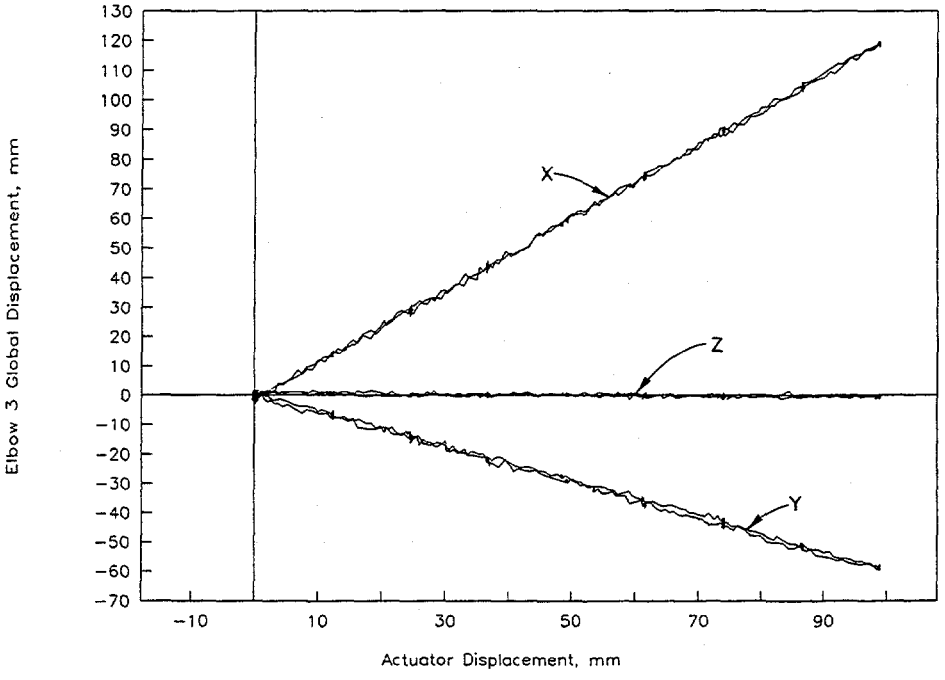

Figure 3.99 Elbow 3 global displacements from the PWR uncracked static push pipe test, Experiment 1.3-1

DRB/1.3-1/F88

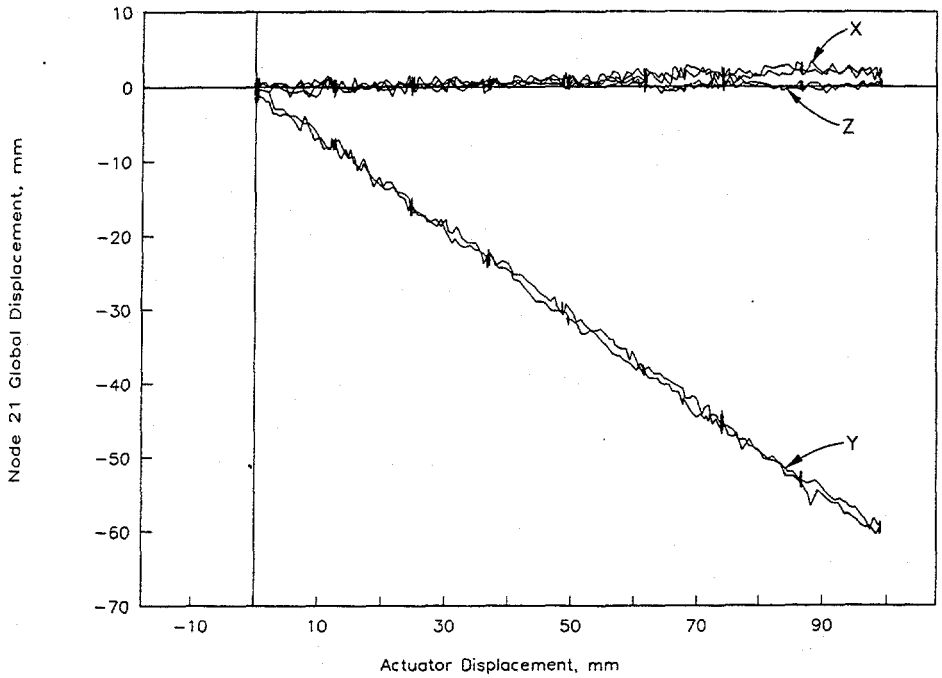

Figure 3.100 Node 21 global displacements from the PWR uncracked static push pipe test, Experiment 1.3-1

DRB/1.3-1/F89

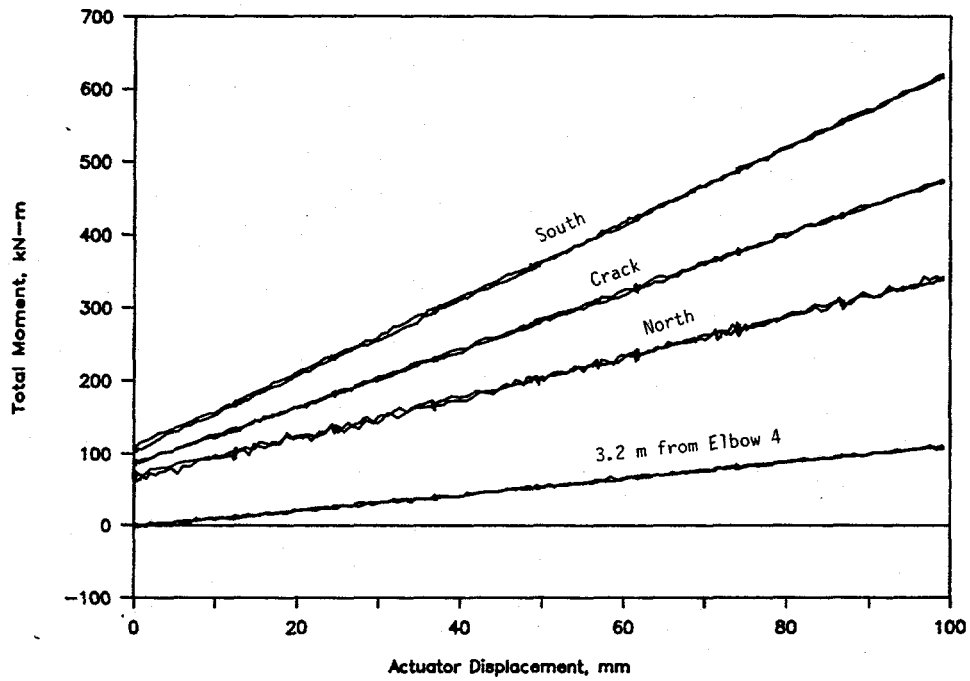

Figure 3.101 Total moment (using ANSYS® static value) from the PWR uncracked static push pipe test, Experiment 1.3-1

DRB/1.3-1/F90

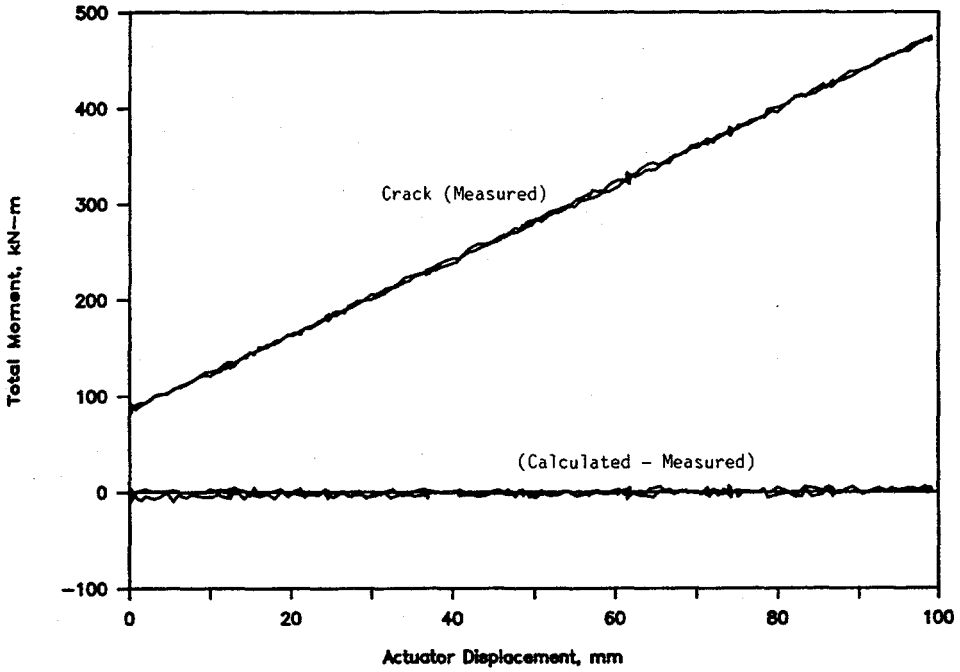

Figure 3.102 Performance of the moment "load cell" (calculated as average of the north and south end cap moments) from the PWR uncracked static push pipe test load-unload cycle, Experiment 1.3-1

DRB/1.3-1/F91

Z-direction motion and X- and Y-displacements that are consistent with each other. Figure 3.101 shows "total" moment developed in the vicinity of the future crack location and at a location 3.2 m (10.5 feet) north of Elbow 4. Because of a drift problem with the strain gages, the statically predicted moment from ANSYS® was added to all of the dynamic moments calculated from the strain gage data. Curiously, the location 3.2 m (10.5 feet) north of Elbow 4, the so called "moment gradient" measurement location, is a point of inflection at the static condition, as evidenced by a near zero moment about the Z axis at zero actuator displacement. Use of the moments at the north and south internal end caps to predict crack location moment was checked for this test. Figure 3.102, which contains both the load and unload data, confirms that the average of the north and south internal end cap moment values can be used to infer the moment at the test section for the cracked pipe experiments.

3.4.2.5 Actuator Loads

The applied loads at the actuator were measured using a load cell in the load train for all of the experiments. In comparing the applied load data for the different experiments, it was found that the data were consistent from one experiment to another. This was especially true for the stainless steel base metal, weld metal, and aged cast stainless experiments, because the same forcing function was used for each of these experiments. This consistency of data sets between experiments was also evident for the other data channels associated with the response of the piping system to the dynamic excitation. Due to this consistency of the data among experiments, piping system response data from only one of the experiments will typically be presented herein.

Figure 3.103 is a plot of the measured applied load at the actuator as a function of time for the stainless steel base metal experiment. When comparing the applied load data in Figure 3.103 to the applied displacement data for this same experiment, see Figure 3.104, one can see that the applied load data is approximately 90 degrees out of phase with the displacement data, i.e., when the applied displacement data is at a peak, the applied load data is going through zero. This is due to the piping system being excited near its natural frequency. In addition, it is also apparent that the load cell response has more than the forcing function frequency associated with it.

3.4.2.6 Node 6 Reaction Force

Figure 3.105 is a plot of the reaction force measured at Node 6 as a function of time for the stainless steel base metal experiment. Once the surface crack penetrated the pipe wall (at about 2.3 seconds), it is evident that the reaction forces became much greater.

There is an inconsistency in these data in that analysis suggests that the reaction force should start at a negative value with the dynamic component following the trend shown in Figure 3.105, Note that when one examines the Node-6 reaction force data for the aged cast stainless experiment, see Figure 3.106, one sees that the reaction forces do start negative, as expected, with the dynamic component following the downward trend previously exhibited by the stainless steel base metal data. The inconsistency associated with the stainless steel base metal data is probably a consequence of the long heatup for the system causing a shift in the static reaction load. Consequently, it would probably be more appropriate to report only the component of the reaction force associated with the dynamic shake. The ANSYS® calculated static value could be added to the dynamic values if desired.

3.4.2.7 Global Pipe Displacement

Motion of the pipe system was measured at three locations: Elbow 3, the crack location, and Node 21 (see Figure 3.26 for locations). The measurements made from the three potentiometers at each location were converted to X-Y-Z global coordinates using the methods outlined in Appendix A. Composite plots of the X, Y, and Z displacements for the stainless steel base metal experiment are presented in Figures 3.107 through 3.109 for Elbow 3, the crack plane, and Node 21, respectively. At all three locations, the Z directed motion (up-down) is negligible. The majority of the dynamic motion is in the Y direction with the X motions at the crack and Node 21 being primarily a static displacement caused by heat up. The X dynamic motion at Elbow 3 is significant due to its proximity to the actuator which is being forced in the X direction.

3.4.2.8 Pipe Pressure

For all except the last experiment, i.e., the aged cast stainless experiment, pressure was only measured at the test specimen. Furthermore, for the early experiments, the pressure data at the test specimen was influenced by the presence of the internal end caps at the test specimen. Once the surface crack penetrated the pipe wall, the end caps with the 12.7-mm (0.5-inch) diameter holes, restricted the fluid flow to the cracked test section such that the pressure at the test specimen decayed at an artificially high rate, see Figure 3.110.

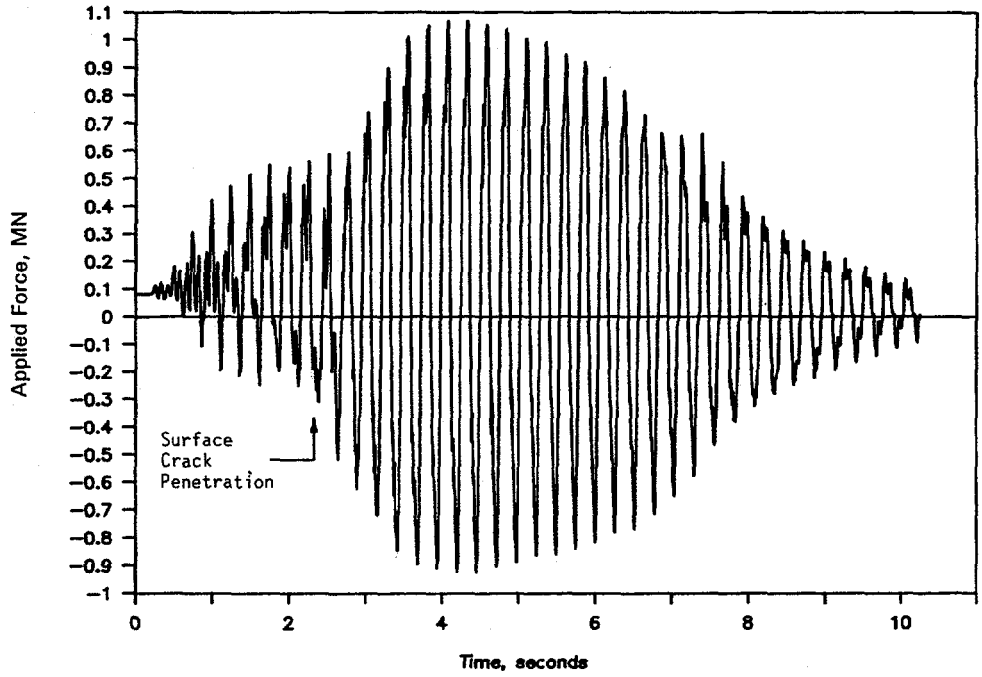

Figure 3.103 Applied force versus time from the stainless steel base metal experiment (1.3-3) DRB/1.3-3/F19

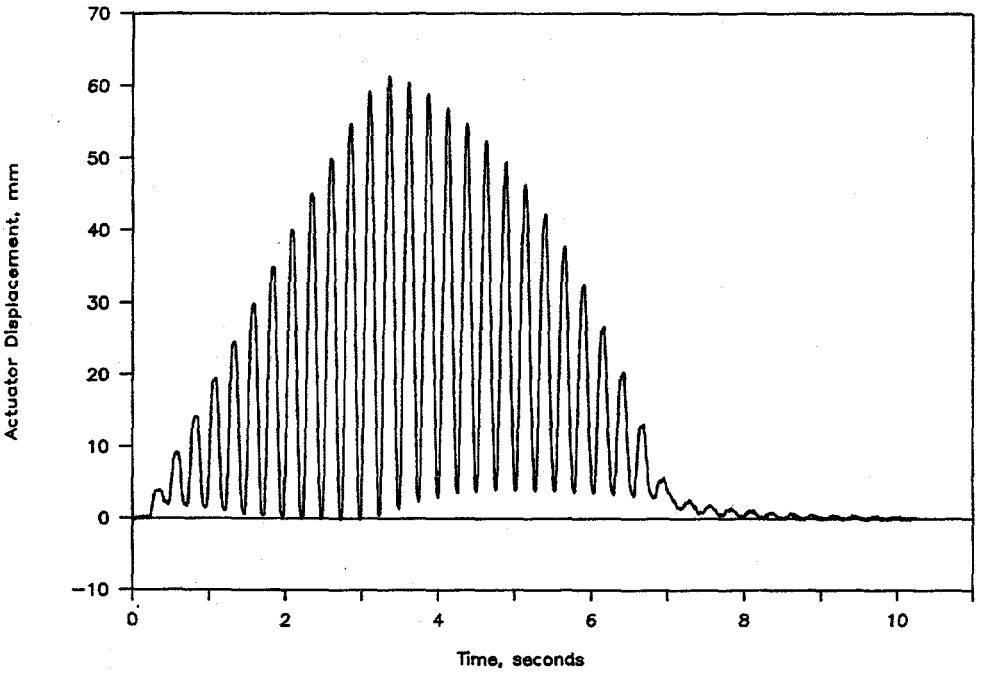

Figure 3.104 Actuator displacement versus time from the stainless steel base metal experiment (1.3-3)

DRB/1.3-3/F104

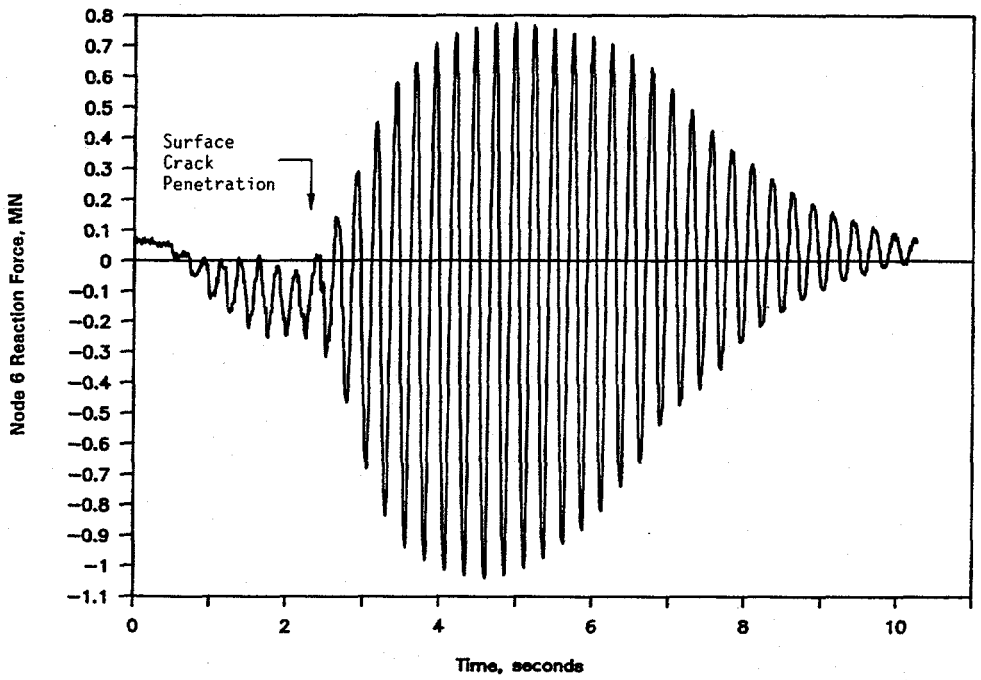

Figure 3.105 Reaction force at Node 6 versus time from the stainless steel base metal experiment (1.3-3)

DRB/1.3-3/F20

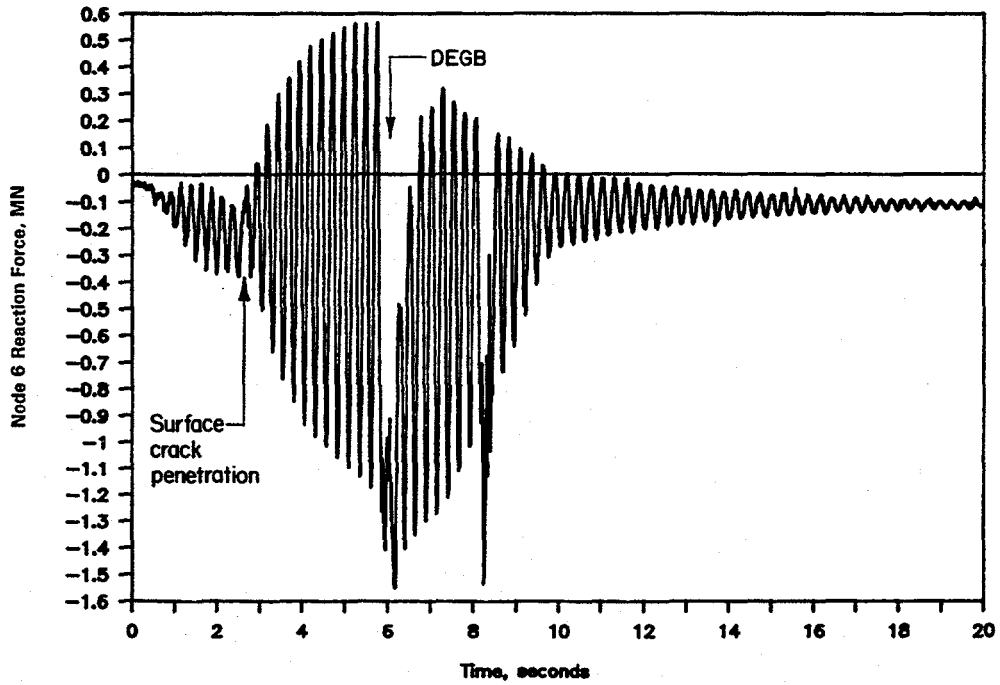

Figure 3.106 Node 6 reaction force versus time from the aged cast stainless steel experiment (1.3-7)

I-10/90-B21-PS

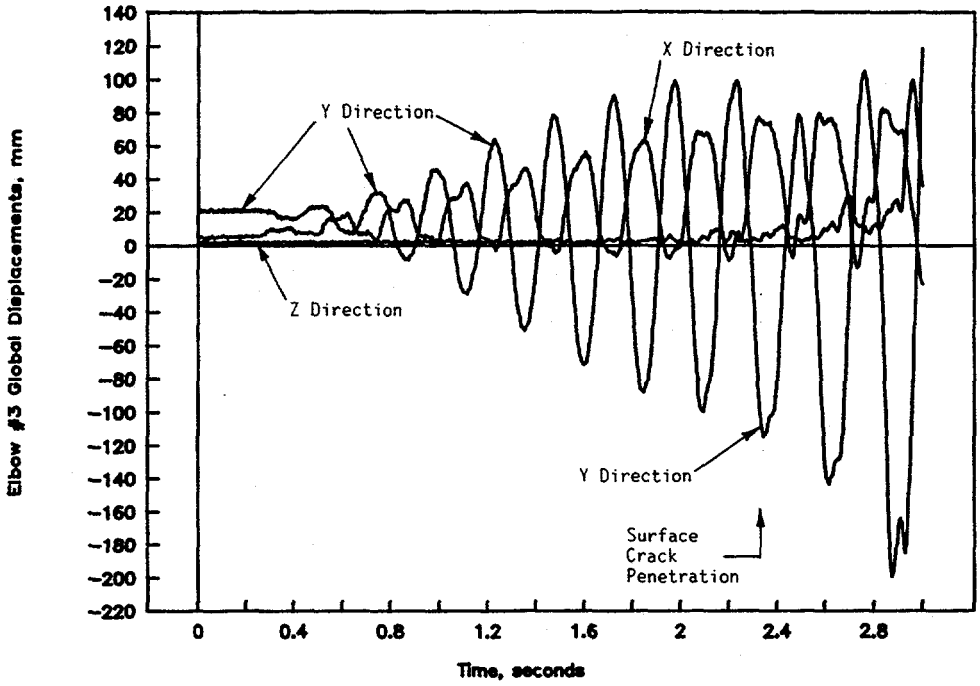

Figure 3.107 Composite plot of global displacements in X, Y, and Z directions for Elbow 3 as a function of time from the stainless steel base metal experiment (1.3-3)

DRB/1.3-3/F48

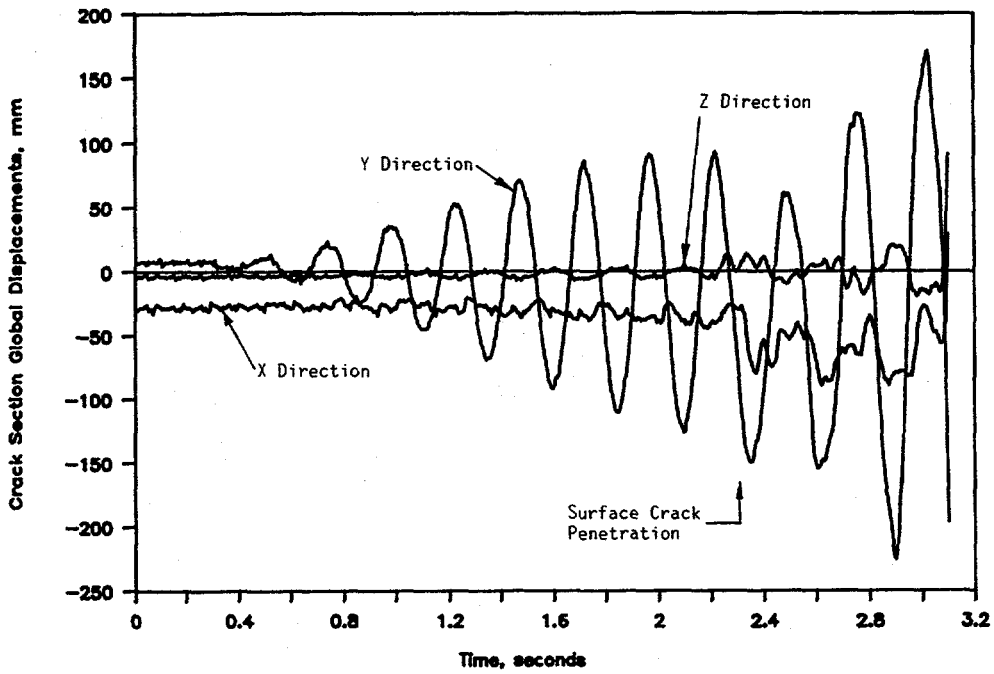

Figure 3.108 Composite plot of global displacements in X, Y, and Z directions for crack location as a function of time from the stainless steel base metal experiment (1.3-3)

DRB/1.3-3/F49

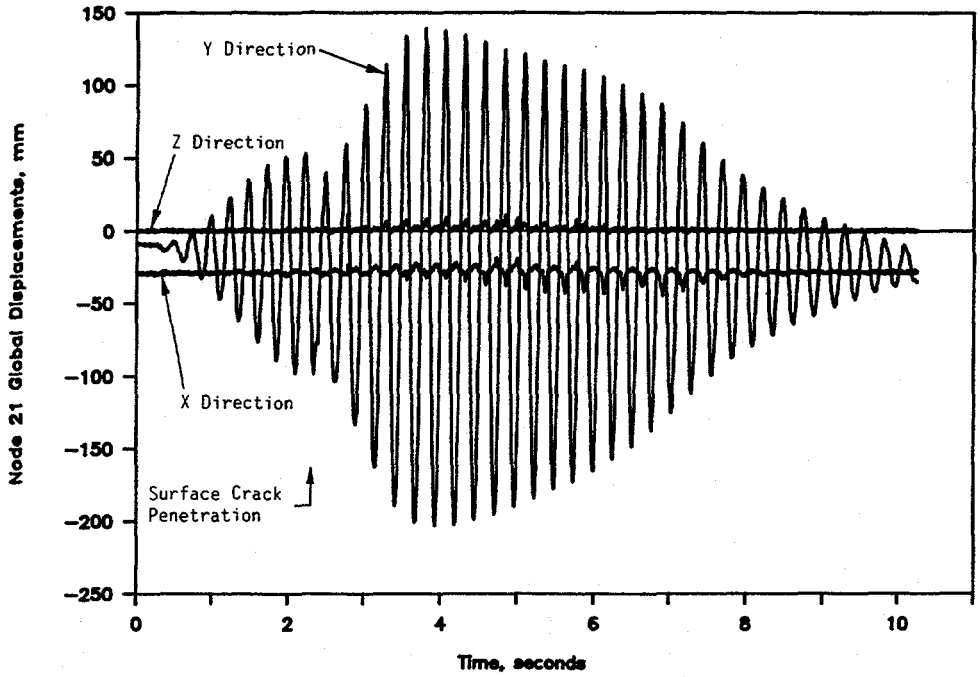

Figure 3.109 Composite plot of global displacements in X, Y, and Z directions for Node 21 as a function of time from the stainless steel base metal experiment (1.3-3)

DRB/1.3-3/F50

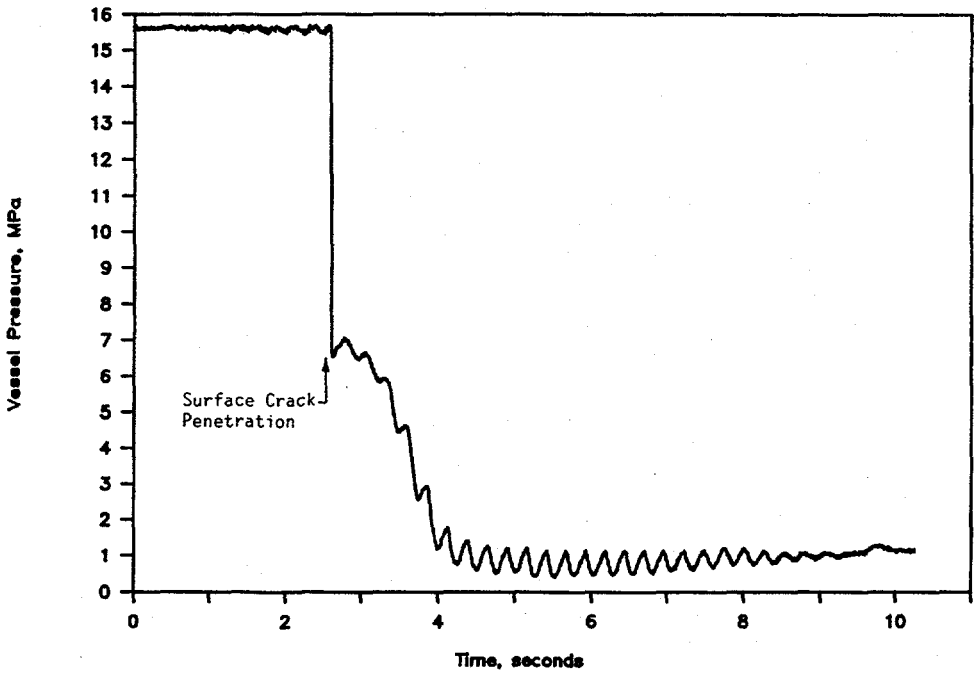

Figure 3.110 Internal pipe pressure versus time from the stainless steel weld experiment (1.3-5)

DRB/1.3-5/F20

For the aged cast stainless experiment (1.3-7), two additional pressure transducers were incorporated into the instrumentation plan and the internal end caps at the test specimen were removed. The additional pressure transducers were both attached to the piping loop in the north-south piping run which contains the crack. One transducer was attached to the piping loop 1.37 m (4.5 feet) south of the crack at the junction of the straight pipe run containing the crack and Elbow 4. The other transducer was attached to the piping loop 4.1 m (13.5 feet) north of the crack at the junction of the straight pipe run containing the crack and Elbow 3, see Figure 3.48. These transducers were incorporated into the instrumentation plan for this experiment to determine the pressure gradient in this pipe run after the surface crack penetrated the pipe wall.

Figures 3.111 through 3.113 are plots of the pressure data at these three locations as a function of time for the aged cast stainless experiment. Figure 3.114 presents the data for all three locations on the same plot. From Figure 3.114 one sees that there is virtually no evidence of a pressure gradient in this pipe run. The pressure at the crack is very nearly the same as the pressure at a location 4.1 m (13.5 feet), or ten pipe diameters, removed from the crack.

3.4.2.9 Elbow Strains

As part of the room temperature uncracked pipe experiment, conventional foil-back three-element strain gage rosettes were attached to the outside surface of Elbows 3 and 4 at the top, bottom, intrados, and extrados of the elbows, see Figure 3.60. Figures 3.115 through 3.122 are plots of elbow strain gage data as a function of time for the room temperature, uncracked pipe, dynamic test. It should be noted that the data shown in Figures 3.115 to 3.122 have had the static strains, due to pressurization, subtracted to be consistent with the presentation of the data for the elevated temperature tests. In addition to providing a measure of the strains and stresses in the elbows during the room temperature uncracked pipe experiment, these data were used to establish the locations for the permanent weldable strain gages to be attached to Elbows 2, 3, and 4. These permanent elbow gages were incorporated into the overall instrumentation plan to provide some measure of the damage done to the elbows during the subsequent dynamic cracked pipe experiments. Several points are worth noting with regard to Figures 3.115 through 3.122.

For one, the elbow strain gage rosettes all respond in phase with one another, except for the gages on the extrados (i.e., gages B3 and G3). On the extrados, the longitudinal gage is of opposite sign to the other two gages.

Second, for Elbow 3, the hoop gages (A1, B1, C1, D1) exhibit the highest dynamic values of strain for all four locations; top, bottom, extrados, and intrados. For these locations, the highest dynamic strain values observed (approximately 800 microstrain) were for the top and bottom hoop gages. For Elbow 4, the hoop gages exhibit the highest dynamic values of strain (approximately 550 microstrain) for the top and bottom surfaces of the elbow (F1, H1). However, for the intrados, the highest value of strain recorded (approximately 650 microstrain tensile and 1,000 microstrain compressive) was for the longitudinal gage (E3). For the extrados, the highest value of tensile strain (approximately 525 microstrain) was for the longitudinal gage (G3) while the highest value of the compressive strain (approximately 750 microstrain) was for the hoop gage (G1). These differences in strain data between Elbows 3 and 4 can be attributed to the fact that Elbow 3 is a Schedule 100 elbow while Elbow 4 is Schedule 160. During the dynamic event,

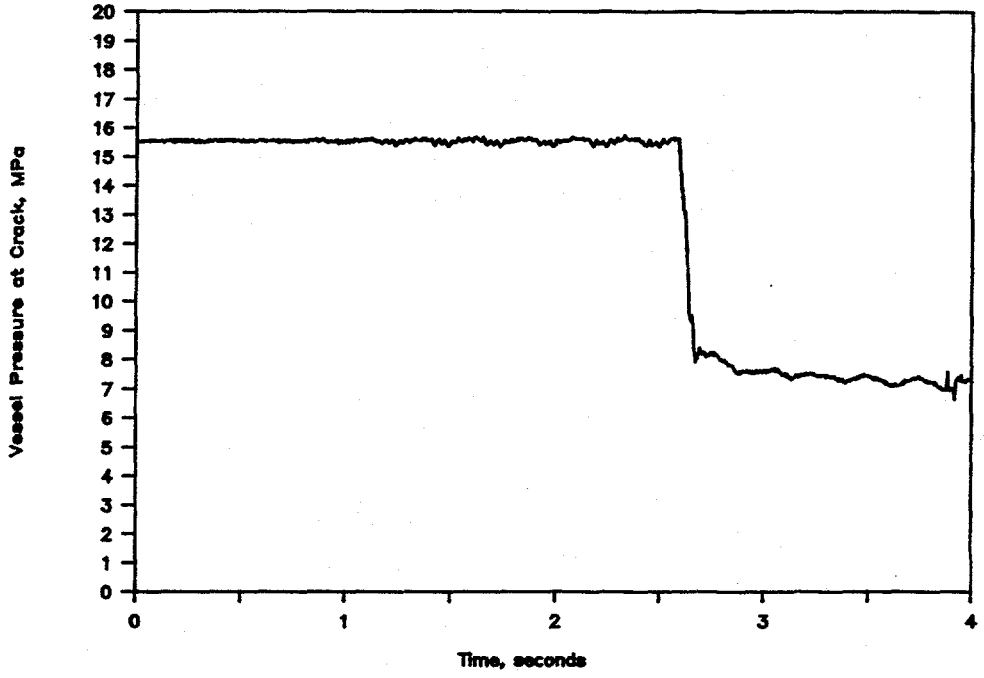

Figure 3.111 Vessel pressure at crack versus time from the aged cast stainless steel experiment (1.3-7)

I1.3-10/90-F3.111

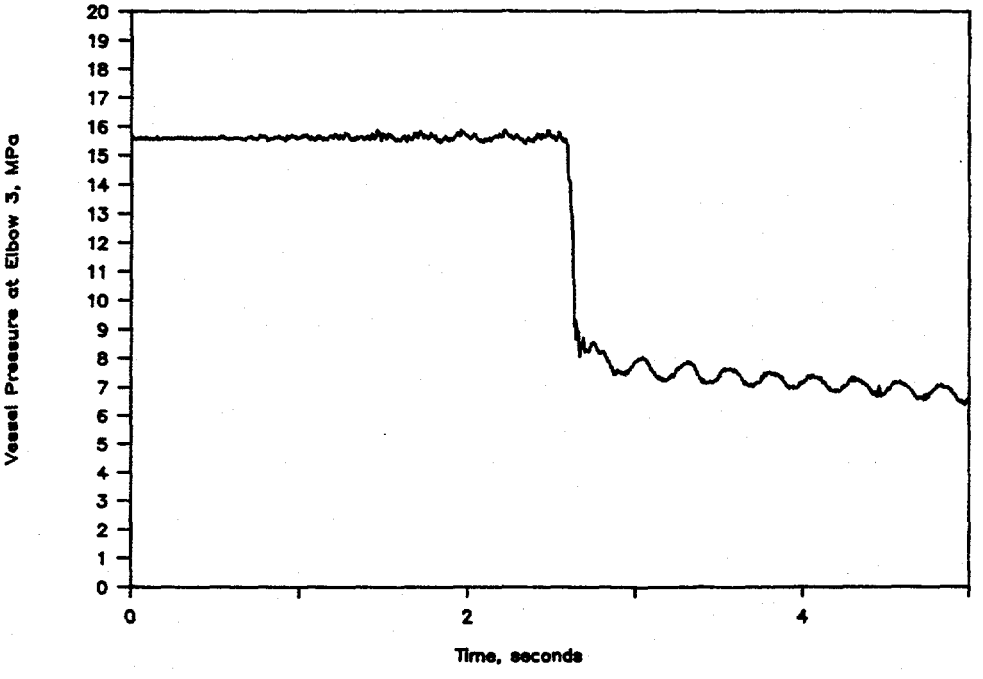

Figure 3.112 Vessel pressure at Elbow 3 versus time from the aged cast stainless steel experiment (1.3-7)

I1.3-10/90-F3.112

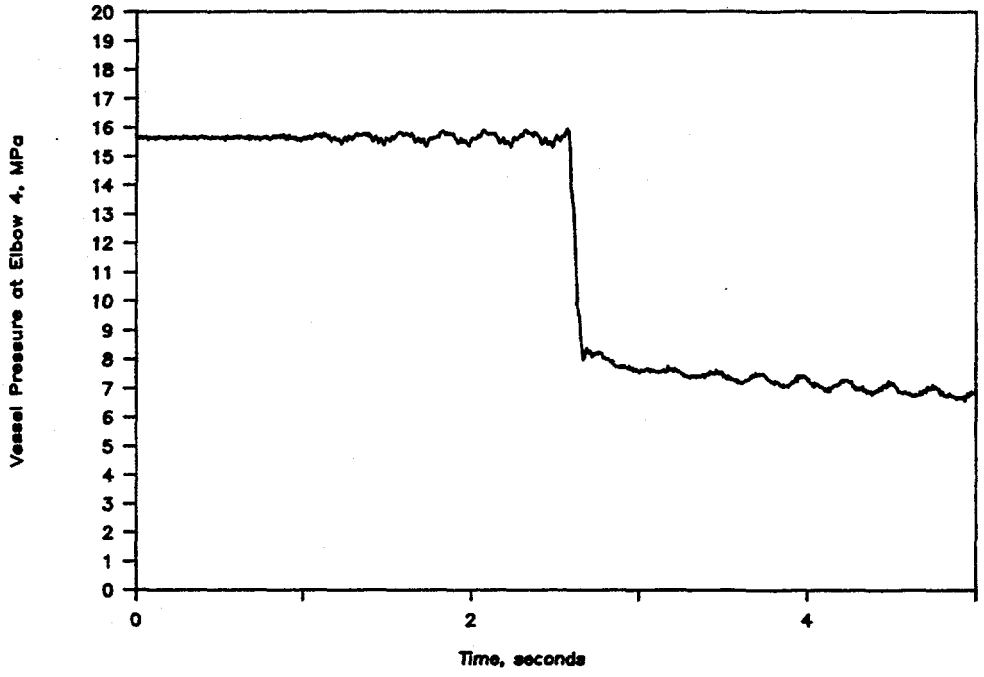

Figure 3.113 Vessel pressure at Elbow 4 versus time from the aged cast stainless steel experiment (1.3-7)

I1.3-10/90-F3.113

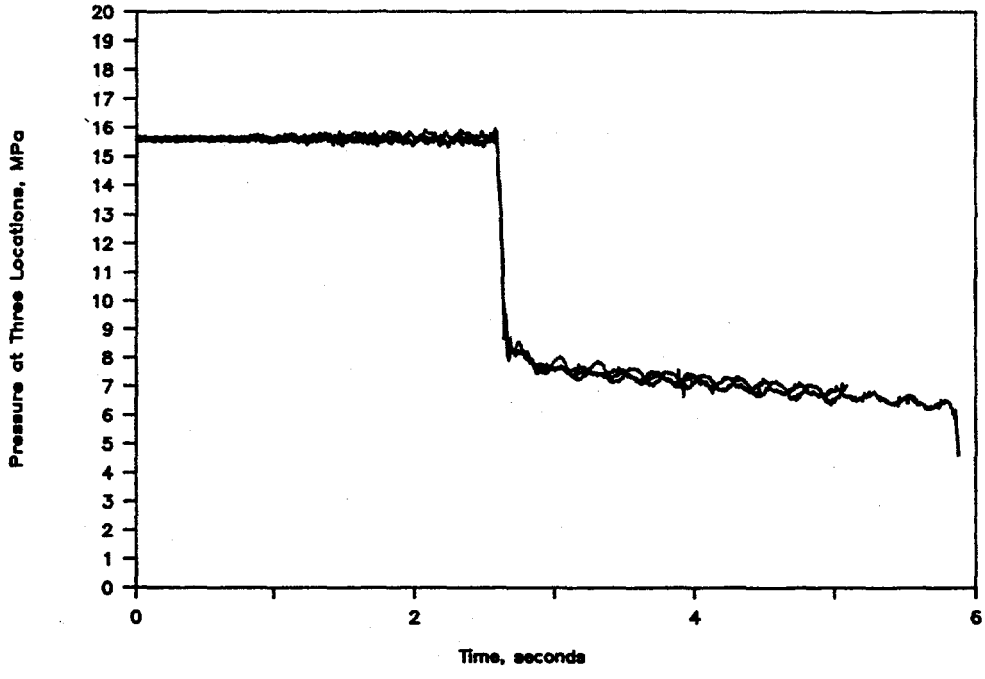

Figure 3.114 Vessel pressure at the three pressure transducer locations versus time from the aged cast stainless steel experiment (1.3-7)

I1.3-10/90-F3.114

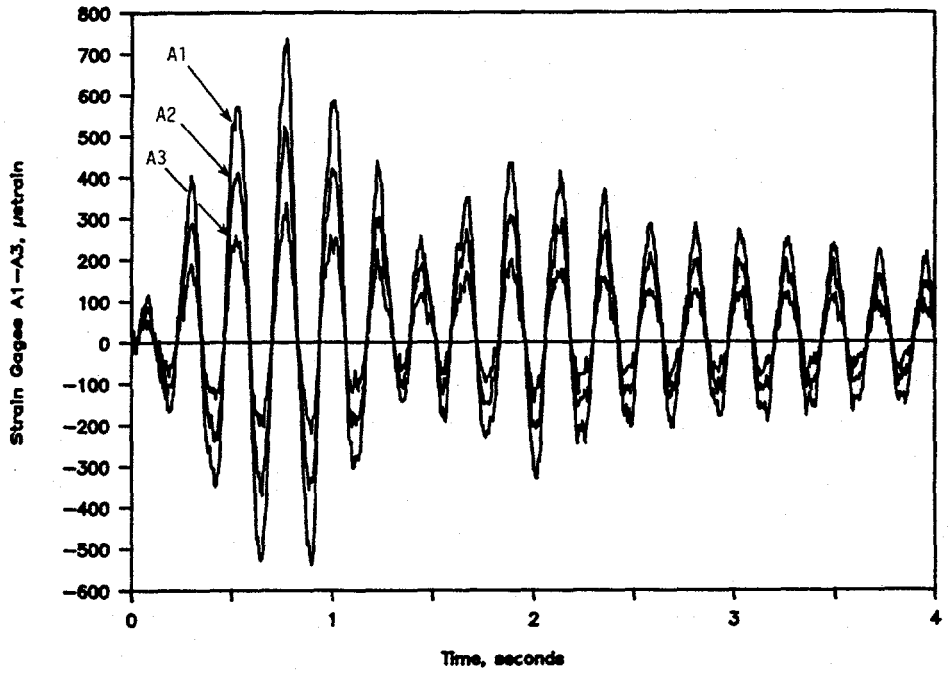

Figure 3.115 Dynamic strain gage rosette data on the top of Elbow 3 from the room temperature uncracked dynamic pipe test, Experiment 1.3-1 DRB/1.3-1/F52

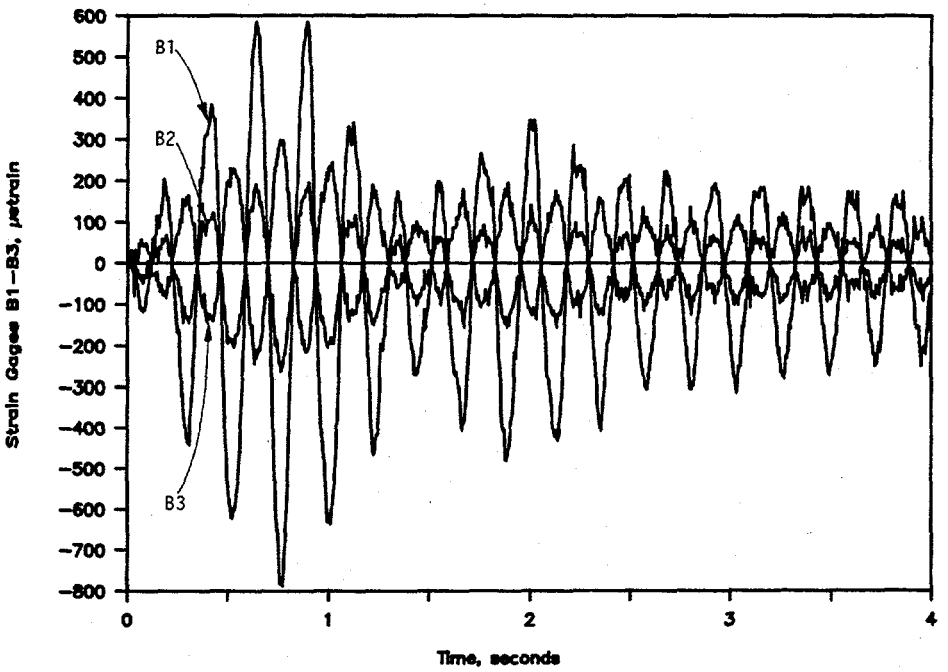

Figure 3.116 Dynamic strain gage rosette data on the extrados of Elbow 3 from the room temperature uncracked dynamic pipe test, Experiment 1.3-1 DRB/1.3-1/F53

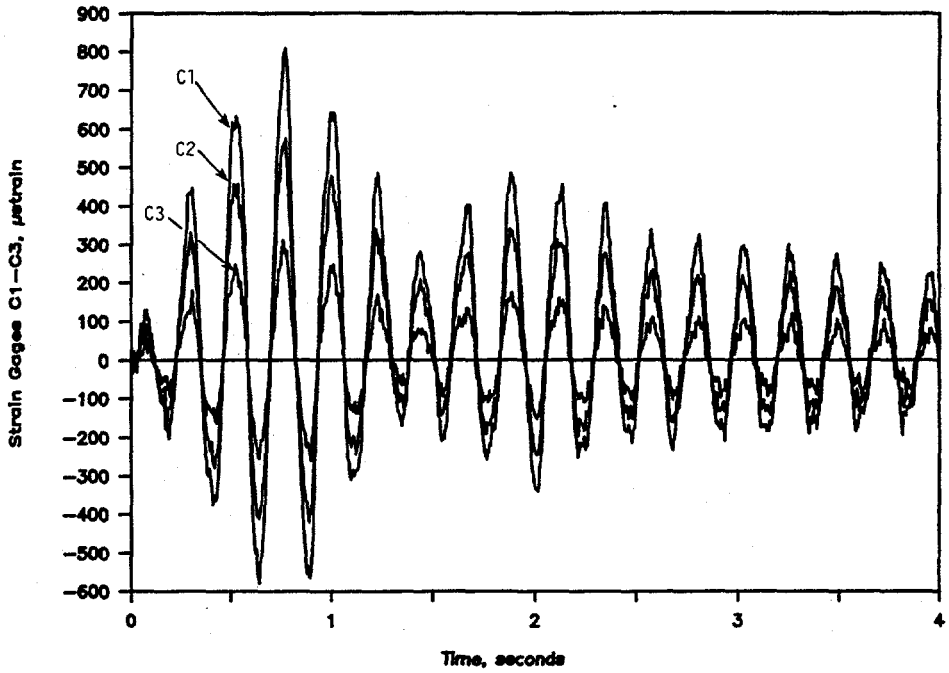

Figure 3.117 Dynamic strain gage rosette data on the bottom of Elbow 3 from the room temperature uncracked dynamic pipe test, Experiment 1.3-1 DRB/1.3-1/F54

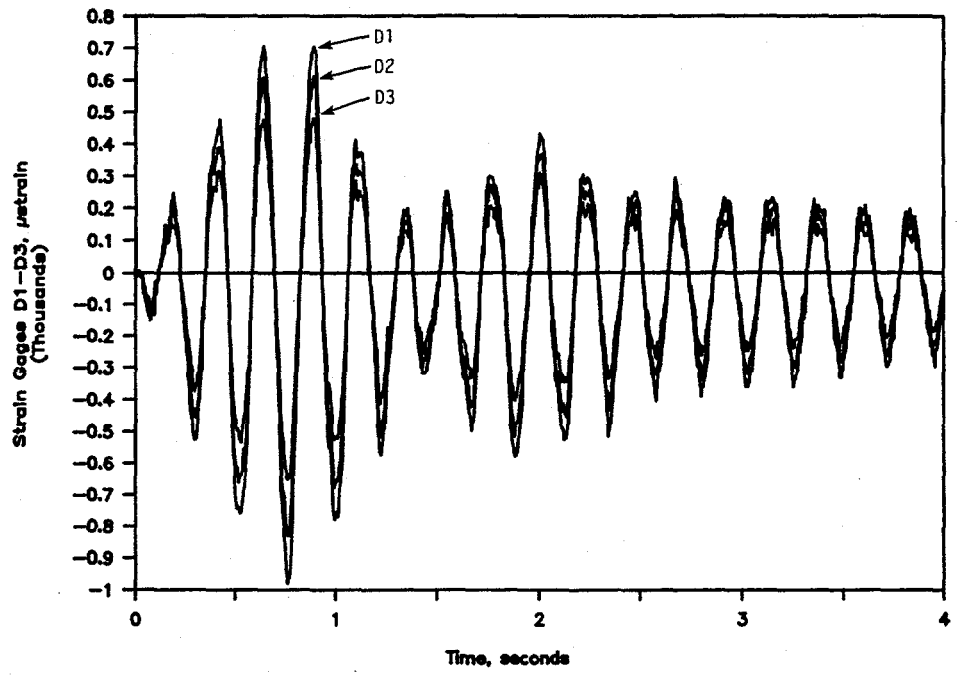

Figure 3.118 Dynamic strain gage rosette data on the intrados of Elbow 3 from the room temperature uncracked dynamic pipe test, Experiment 1.3-1 DRB/1.3-1/F55

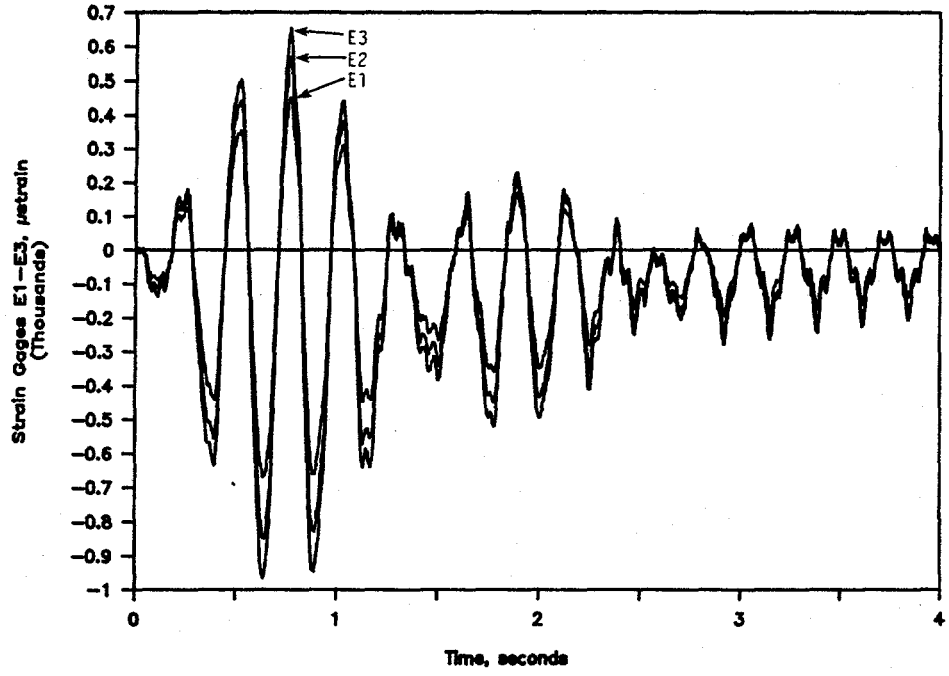

Figure 3.119 Dynamic strain gage rosette data on the intrados of Elbow 4 from the room temperature uncracked dynamic pipe test, Experiment 1.3-1 DRB/1.3-1/F56

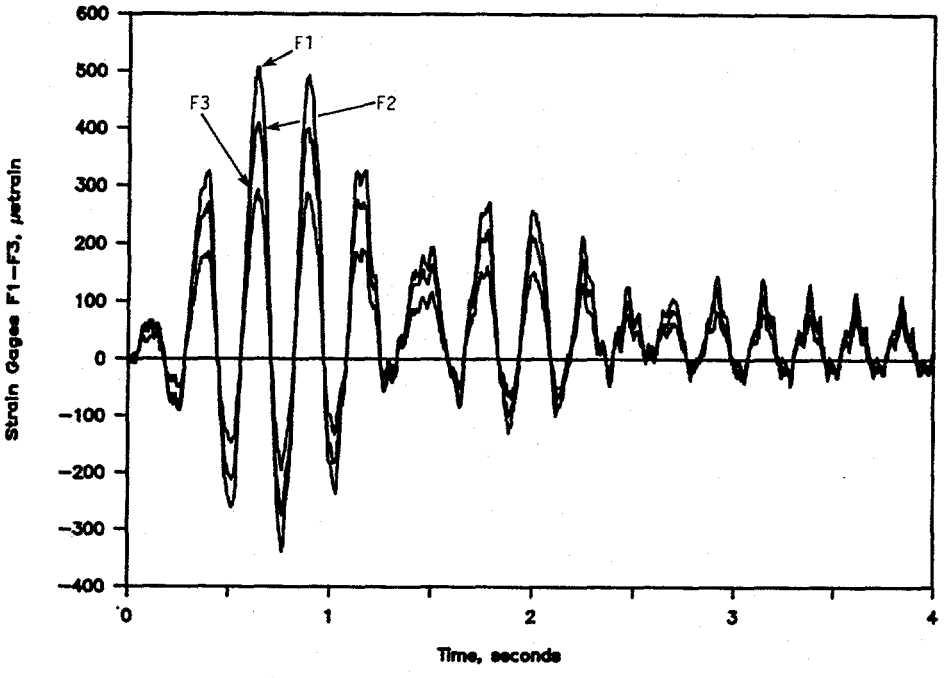

Figure 3.120 Dynamic strain gage rosette data on the top of Elbow 4 from the room temperature uncracked dynamic pipe test, Experiment 1.3-1 DRB/1.3-1/F57

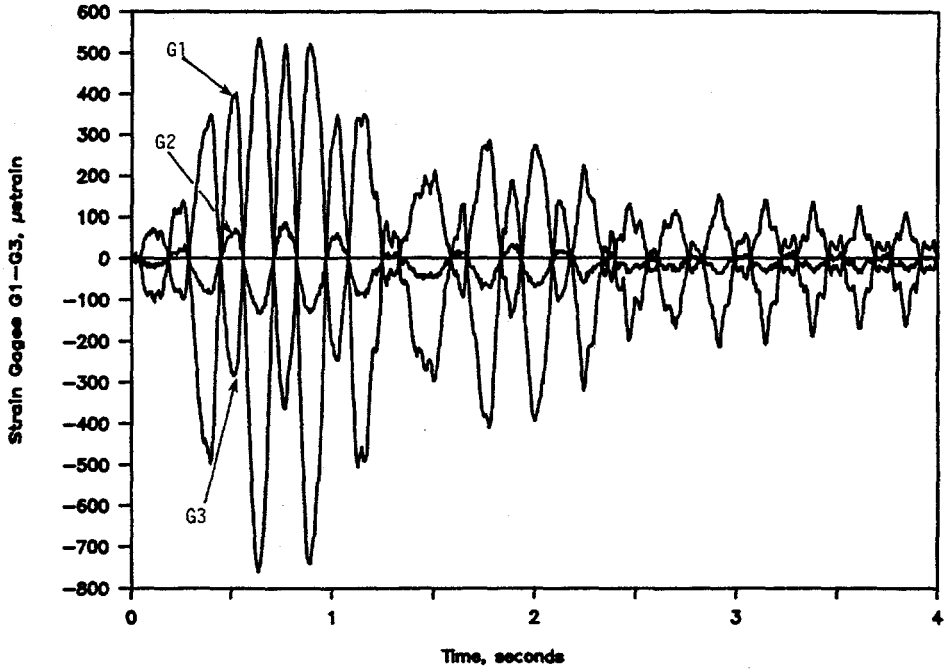

Figure 3.121 Dynamic strain gage rosette data on the extrados of Elbow 4 from the room temperature uncracked dynamic pipe test, Experiment 1.3-1 DRB/1.3-1/F58

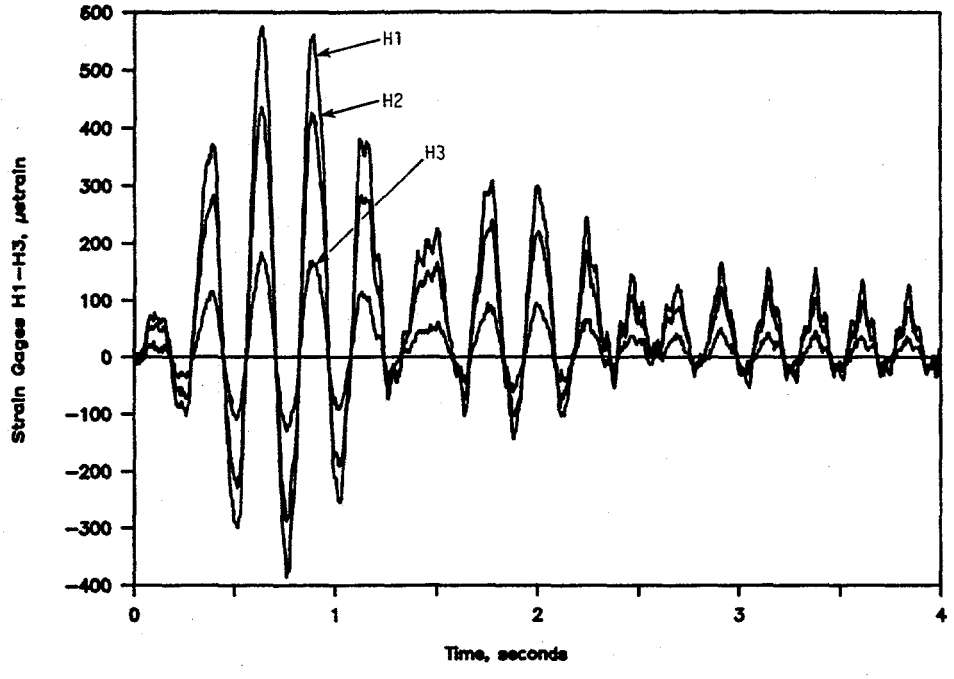

Figure 3.122 Dynamic strain gage rosette data on the bottom of Elbow 4 from the room temperature uncracked dynamic pipe test, Experiment 1.3-1 DRB/1.3-1/F59

the thinner Schedule 100 elbow tends to ovalize more than the Schedule 160 elbow such that a bending stress due to ovalization is induced in the elbow in the hoop direction. The heavier wall Schedule 160 elbow resists this ovalization, such that the elbow behaves more like a beam in bending with the higher strains being longitudinal strains occurring at the locations farthest from the neutral axis, i.e., the extrados and intrados.

3.4.2.10 Bending Moment Gradient

One question which arose early in the program concerned the magnitude of the bending moment gradient along the north-south pipe run which contains the crack. In order to address this question, additional permanent, weldable strain gages were attached to the pipe 3.7 m (10.5 feet) north of Elbow 4, see Figure 3.58. These gages, along with the gages at the north and south end caps and the gages at the crack for the uncracked pipe experiment, provided a fairly comprehensive picture of the bending moment gradient along this piping run. Figure 3.123 is a plot of the total bending moment (ANSYS® static value plus dynamic component from the dynamic strain gage data) as a function of time for the elevated temperature phase of the uncracked pipe experiment. From Figure 3.123, one can see that the bending moment decreases rapidly as one gets further from Elbow 4, i.e., from the south end cap to the location 3.2 m (10.5 feet) north of Elbow 4. A large portion of the difference between the moments along this pipe run is associated with the magnitude of the static contribution of moment as calculated via ANSYS®. If one plots only the dynamic component of moment from the dynamic strain gage data for these four locations as a function of time, see Figure 3.124, one sees a much smaller difference in moment. In other words, the bending moment gradient associated with the dynamic component of the moment is much less than the bending moment gradient associated with the static component of the bending moment.

3.4.3 Fracture Behavior

Data from this program will prove useful in assessing the validity of various fracture codes and methodologies. For example, data from this program will be useful in assessing the adequacy of the flaw-assessment criteria embodied in IWB-3640 and IWB-3650 of Section XI of the ASME Boiler and Pressure Vessel Code (Ref. 3.8). In this section of the report, those results which will be useful in assessing those codes or methodologies will be presented.

Table 3.10 presents the key experimental results from the five cracked pipe experiments. Included in Table 3.10 is the crack size, applicable material property data, maximum moment at the crack section, moment at surface crack penetration, the moment at crack initiation (if available), maximum moment, and moment at crack initiation from the companion quasi-static experiment (if appropriate), calculated percent inertial loading at maximum moment and surface-crack penetration, and calculated stress-ratio for each experiment. One point which should be emphasized is that it is difficult to make direct comparisons of results between experiments in that a number of the experimental variables were not held constant between experiments. For example, the forcing functions for the two carbon steel experiments were different from the forcing function for the three stainless steel experiments. The flaw size for the carbon steel base metal experiment was unintentionally deeper than that for the other experiments, while the flaw size for the aged cast stainless steel experiment was intentionally shallower than for the other experiments.

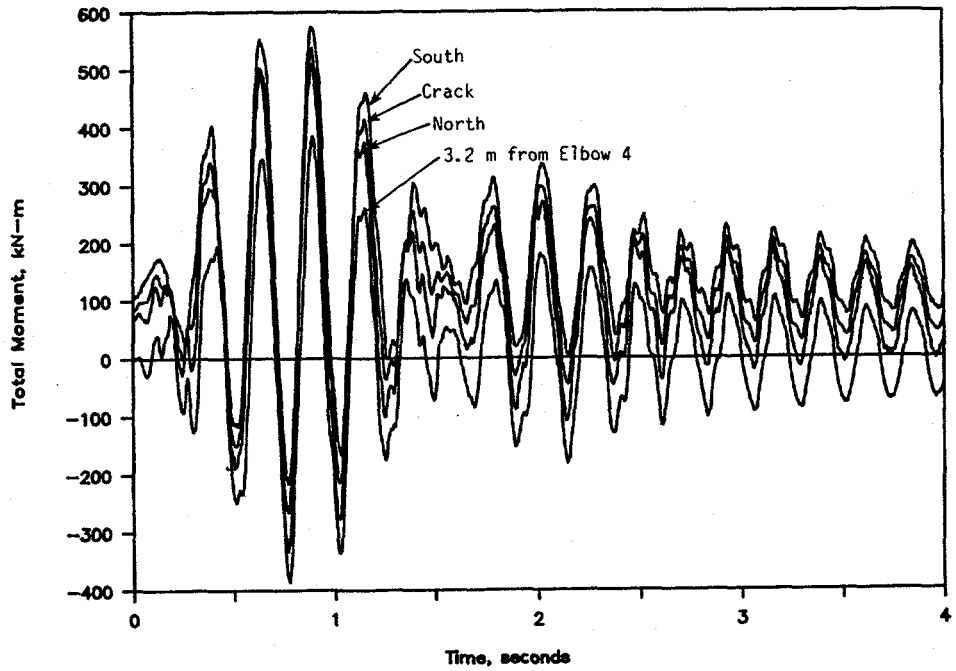

Figure 3.123 Total moment (using ANSYS® static value) from the PWR uncracked dynamic pipe test, Experiment 1.3-1

DRB/1.3-1/F112

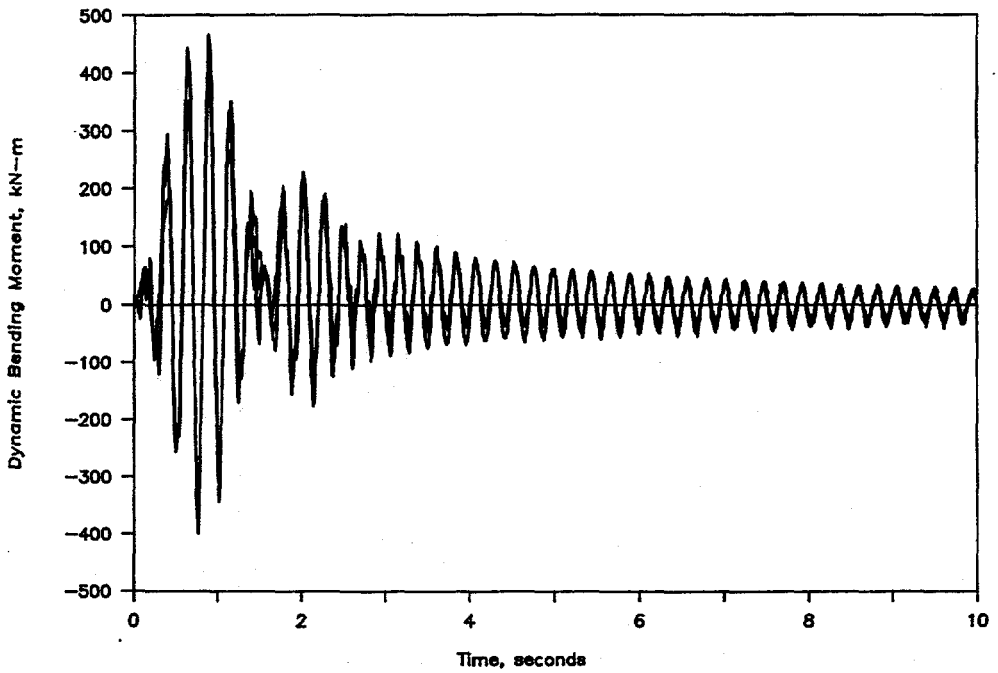

Figure 3.124 Dynamic moments at the crack, south end cap, north end cap, and location 1.83 m (6 feet) north of crack from the PWR uncracked dynamic pipe test, Experiment 1.3-1

I1.3-10/90-F3.124

Table 3.10 Key results from five cracked pipe-system experiments

Expt. Number	Test Mat'l	Max. d/t	θ/π[a]	Yield Strength, MPa[b]	Ultimate Strength, MPa[b]	J_I[b,c], kJ/m^2	Max. Moment at Crack, kN-m	Moment at Surface Crack Penetration, kN-m	Moment at Crack Initiation, kN-m	Max. Moment from Quasi-Static Expt., kN-m	Moment at Crack Init. from Quasi-Static Expt., kN-m	Percent Inertial Loading at Max. Moment	Percent Inertial Loading at Surface Crack Penetration	Stress Ratio (R) (Based on Moment)	Stress Ratio (R) (Based on Total Stress)
1.3-2	CSBM	0.727	0.438	237	610	129	341	341	--	(e)	(e)	30	30	-0.07	+0.23
1.3-3	SSBM	0.660	0.468	175	459	738	426	328	415	(e)	(e)	43	28	-0.81	-0.34
1.3-4	CSW	0.691	0.480	356[d]	556[d]	82[d]	618	618	--	594	423	28	26	-0.43	-0.18
1.3-5	SSW	0.635	0.440	258[d]	469[d]	55[d]	493	482	460	501	498	47	42	-0.66	-0.27
1.3-7	ACS[f]	0.533	0.500	201	578	88	590	543	504	672	660	55	51	-0.46	-0.20

(a) Based on the equivalent crack length (crack area/maximum crack depth) and inside pipe circumference.
(b) Based on quasi-static test data.
(c) C(T) specimen data with 20 percent sidegrooves.
(d) Weld metal properties.
(e) No data presented because comparison experiment was unpressurized.
(f) ACS = Aged cast stainless.

3.4.3.1 Crack Section Moments

Figures 3.125 through 3.129 are plots of the crack section moments as a function of time for the five cracked pipe experiments. These plots only present data up to the instant of surface-crack penetration. After the surface crack penetrates the pipe wall, a thrust load exists which acts as a shear force which invalidates one of the basic assumptions embodied in the moment calculations. Consequently, the crack section moment data past surface-crack penetration are suspect. For comparison purposes, the same scales have been used for each of these plots. Several points are worth noting with regard to Figures 3.125 through 3.129. First, one sees that the carbon steel base metal specimen failed very early at a relatively low moment. The fact that the carbon steel base metal failed at such a low bending moment can be attributed to the fact that the crack for the carbon steel base metal experiment was deeper than for the other experiments. The crack for the carbon steel base metal experiment was approximately 73 percent of the pipe wall thickness, while the cracks for the other experiments, excluding the aged cast stainless experiment, were nominally 66 percent of the pipe wall thickness. In addition, both the tensile strength and fracture toughness of this carbon steel material decreased at the higher strain rates typical of these pipe-system experiments (Ref. 3.9). Second, one sees that carbon steel weld and the aged cast stainless steel specimens failed at relatively high moments, approximately 600 kN-m (5,300,000 in-lbs), when compared to the other three experiments. The reason for the aged cast stainless specimen failing at such a high crack section moment was the flaw for that specimen was shallower than for the other specimens, i.e., 53 percent deep for the aged cast stainless steel specimen versus a nominal 66 percent deep flaw for the other specimens. The reason for the carbon steel weld specimen failing at such a high bending moment is probably a consequence of the fact that the yield strength of the carbon steel weld metal is significantly higher (anywhere from 33 to 103 percent higher) than the yield strength of the other materials.

3.4.3.2 Crack Section Rotations

Figures 3.130 through 3.132 are plots of the crack section rotation as a function of time for the three stainless steel specimens, i.e., the base metal, weld metal, and aged cast specimens. No data are provided for the carbon steel specimens because the carbon steel experiments used the rotation device based on the RVDT. The signal-to-noise ratio of this device was so poor that the resulting data were meaningless. The LVDT-based rotation device resulted in a much cleaner signal and, consequently, much more meaningful data. For comparison purposes the same scales have been used for each of these plots. Of note from Figures 3.130 through 3.132 is that the amount of rotation at surface-crack penetration for the stainless steel base metal experiment was approximately 50 percent greater than that for the stainless steel weld experiment, and nearly twice that for the aged cast stainless experiment. This observation is probably attributable to the fact that the toughness of the stainless steel base metal is significantly higher than the toughness for the other two stainless steel materials.

3.4.3.3 Crack Section Moment Rotation Behavior

The moment-rotation behavior out to surface-crack penetration for the three experiments where meaningful rotation data were collected is shown in Figures 3.133 through 3.135. In the case of the stainless steel base metal specimen, surface-crack penetration occurred on the ninth cycle. For the other two specimens, penetration occurred on the tenth cycle. The stainless steel base metal shows significantly more "ductility" than the other two specimens, probably as a consequence of its higher toughness.

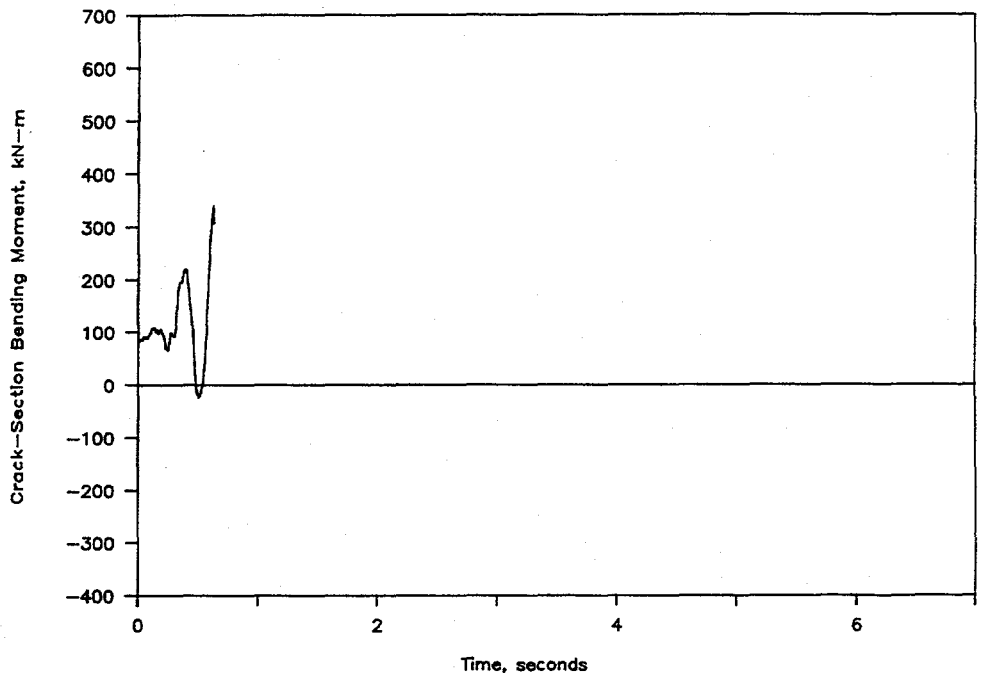

Figure 3.125 Calculated total crack section moment versus time from the carbon steel base metal experiment (1.3-2) (Note: time scale for Figures 3.125 to 3.129 is identical for comparison of all experiments)

I1.3-10/90-F3.125

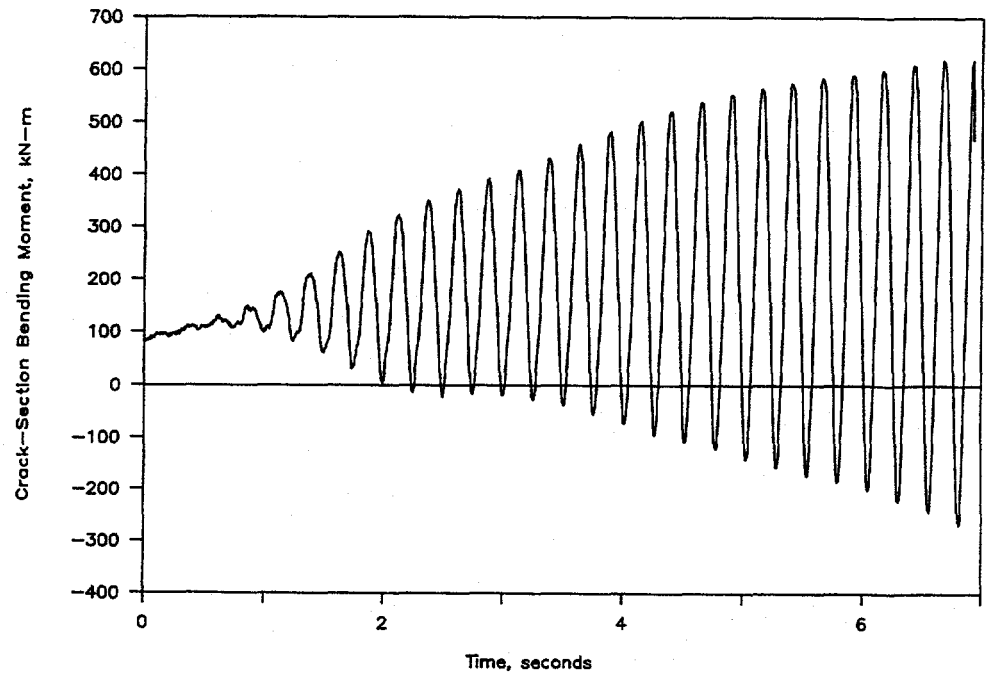

Figure 3.126 Total moment at crack section versus time from the carbon steel weld experiment (1.3-4)

I1.3-10/90-F3.126

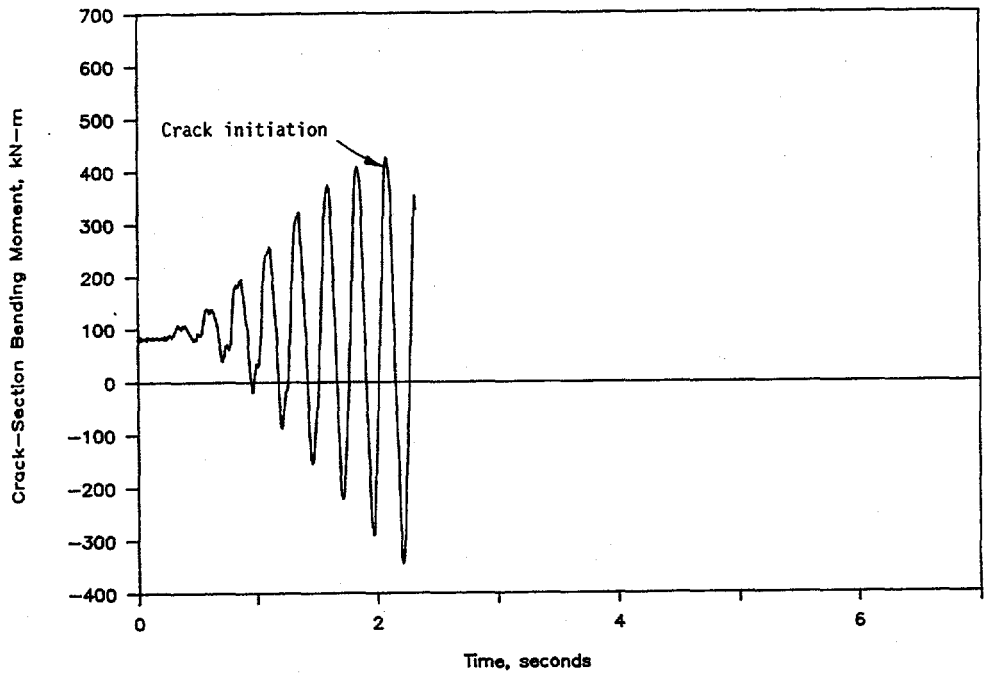

Figure 3.127 Total moment at the crack location as a function of time from the stainless steel base metal experiment (1.3-3) I1.3-10/90-F3.127

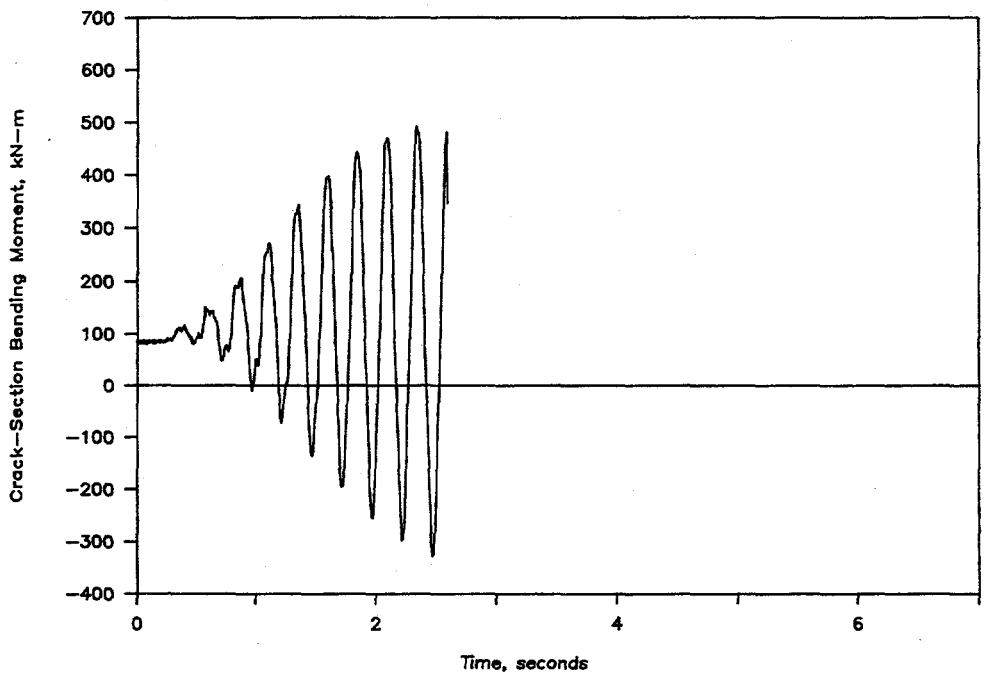

Figure 3.128 Total bending moment at the crack location versus time from the stainless steel weld experiment (1.3-5) I1.3-10/90-F3.128

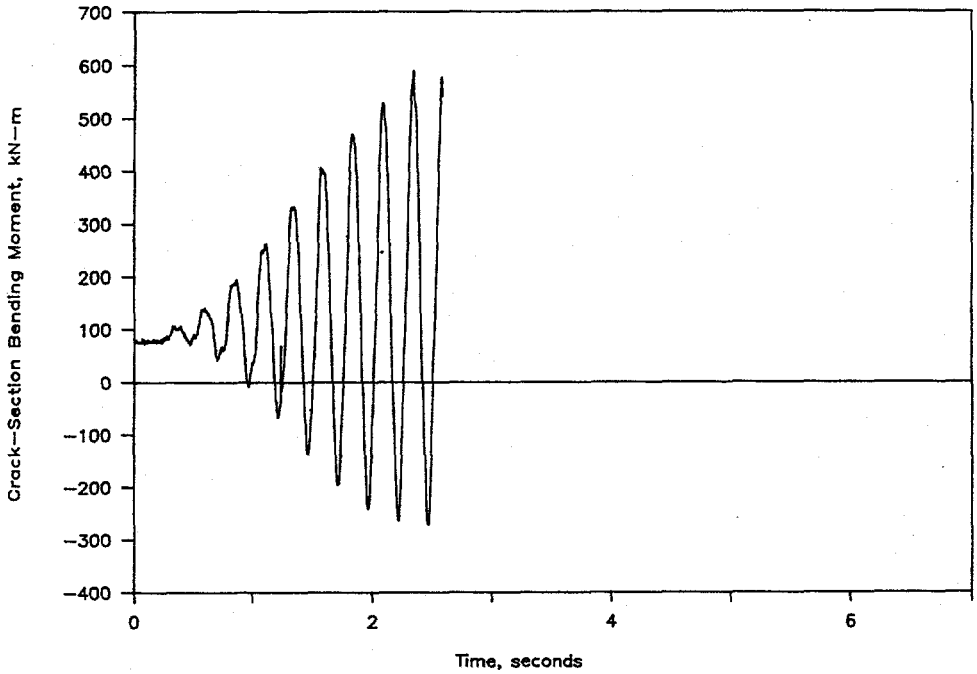

Figure 3.129 Total moment at the cracked section versus time from the aged cast stainless experiment (1.3-7) I1.3-10/90-F3.129

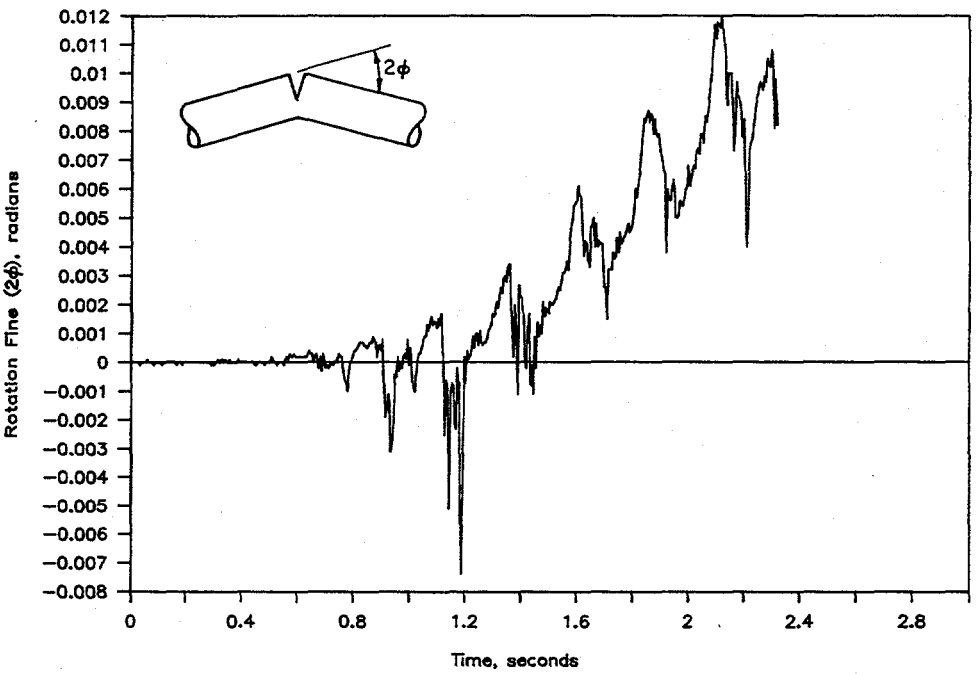

Figure 3.130 Fine rotation at the crack section versus time from the stainless steel weld experiment (1.3-3) I1.3-10/90-F3.130

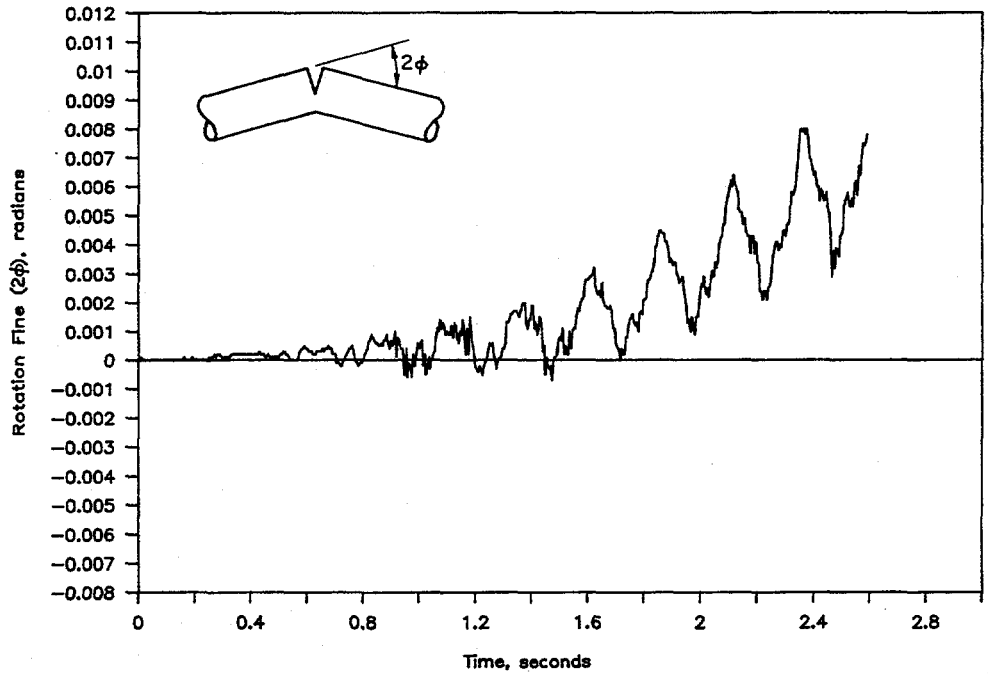

Figure 3.131 Fine rotation at the crack section versus time from the stainless steel weld experiment (1.3-5) I1.3-10/90-F3.131

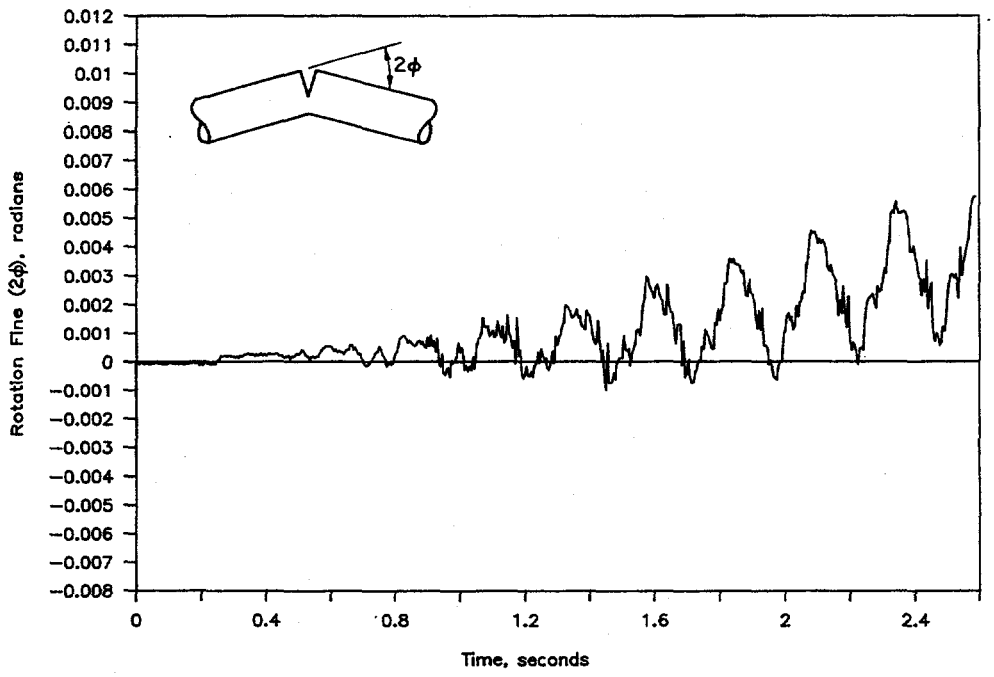

Figure 3.132 Fine rotation at the crack section versus time from the aged cast stainless steel experiment (1.3-7) I1.3-10/90-F3.132

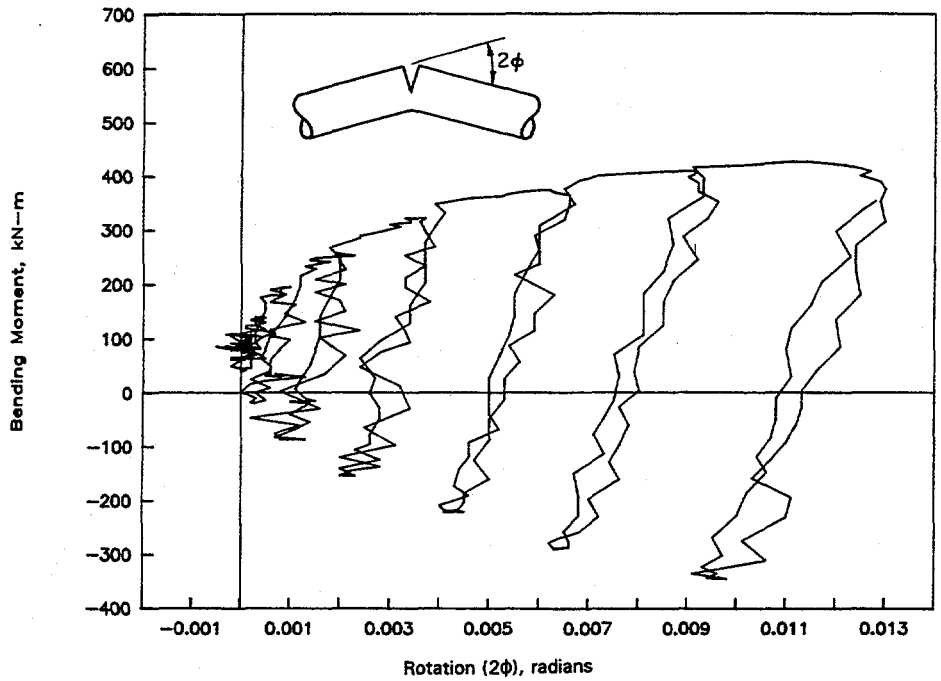

Figure 3.133 Crack section moment-rotation behavior from the stainless steel base metal experiment (1.3-3) I1.3-10/90-F3.133

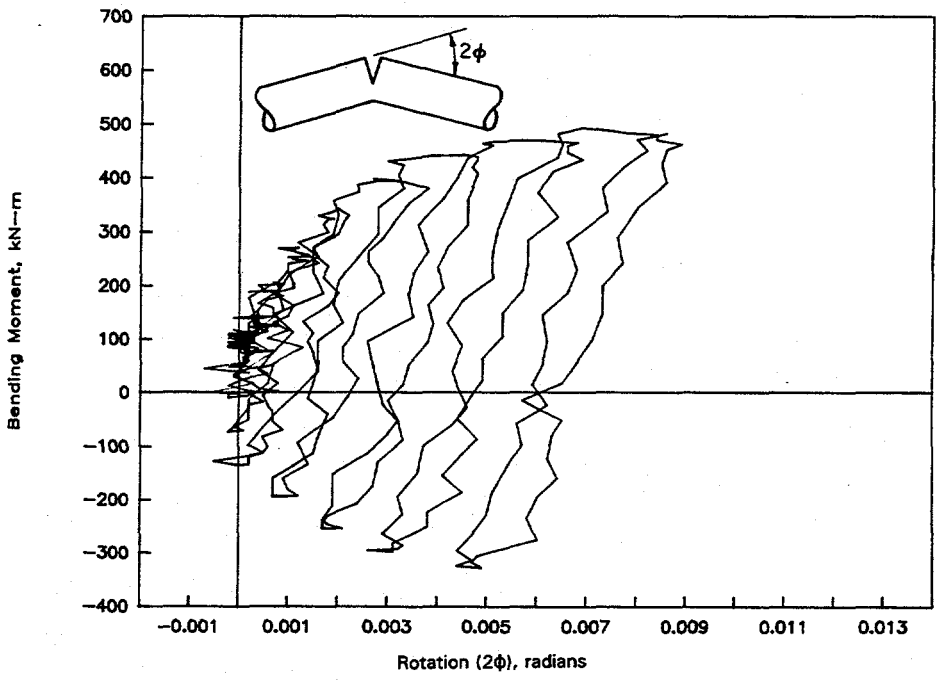

Figure 3.134 Crack section moment-rotation behavior from the stainless steel weld experiment (1.3-5) I1.3-10/90-F3.134

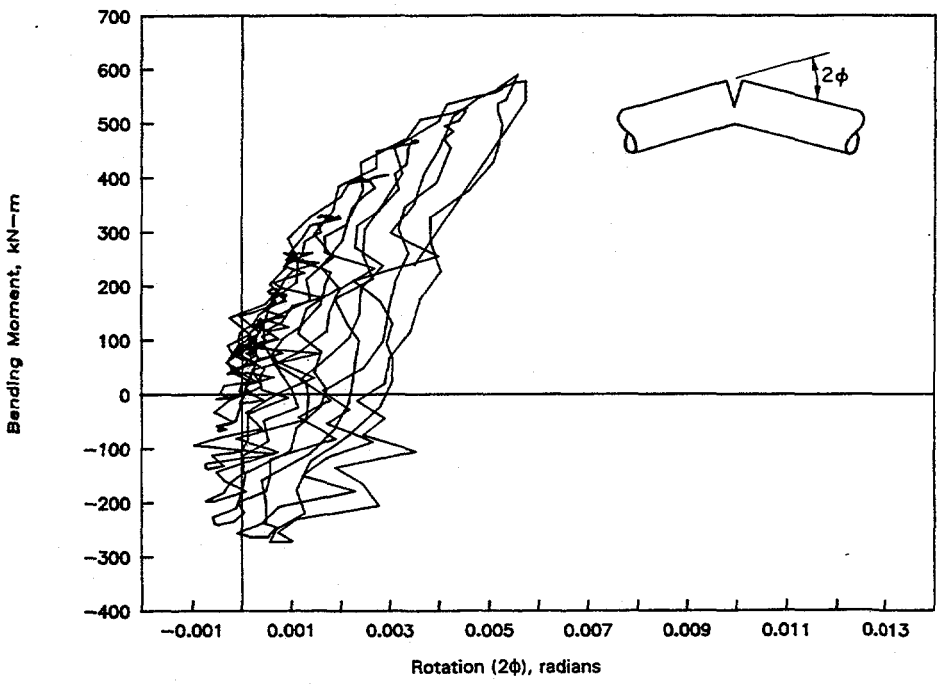

Figure 3.135 Crack section moment-rotation behavior from the aged cast stainless steel experiment (1.3-7) I1.3-10/90-F3.135

3.4.3.4 Crack-Mouth-Opening Displacements

Figures 3.136 through 3.139 are plots of the crack-mouth-opening displacements as a function of time for the carbon steel base metal experiment and the three stainless steel specimens. No data are provided for the carbon steel weld metal experiment because the LVDT mounted across the crack centerline for this experiment failed prior to the experiment. For comparison purposes, the same scales have been used for each of these plots. The stainless steel base metal specimen, which exhibited the most crack-opening displacement, had the largest value of J at crack initiation.

3.4.3.5 Crack Initiation/Crack Growth Data

Direct-current electric potential (d-c EP) data were recorded for the carbon steel weld metal experiment and the three stainless steel experiments in order to define the instant of crack initiation for the surface cracks and to estimate the extent of surface-crack growth and through-wall-crack growth once the surface cracks penetrated the pipe wall thickness. (Note, no d-c EP data are available for the carbon steel base metal experiment. Further note that it was not possible to interpret the d-c EP data for the carbon steel weld metal experiment due to the highly cyclic nature of the EP signals associated with this experiment. The large cyclic component associated with the carbon steel weld d-c EP data has been attributed to large self-induced voltages which occur during the elastic loadings.) Details of how the EP data were used to determine crack initiation and crack growth data for the stainless steel experiments are provided in Appendix E.

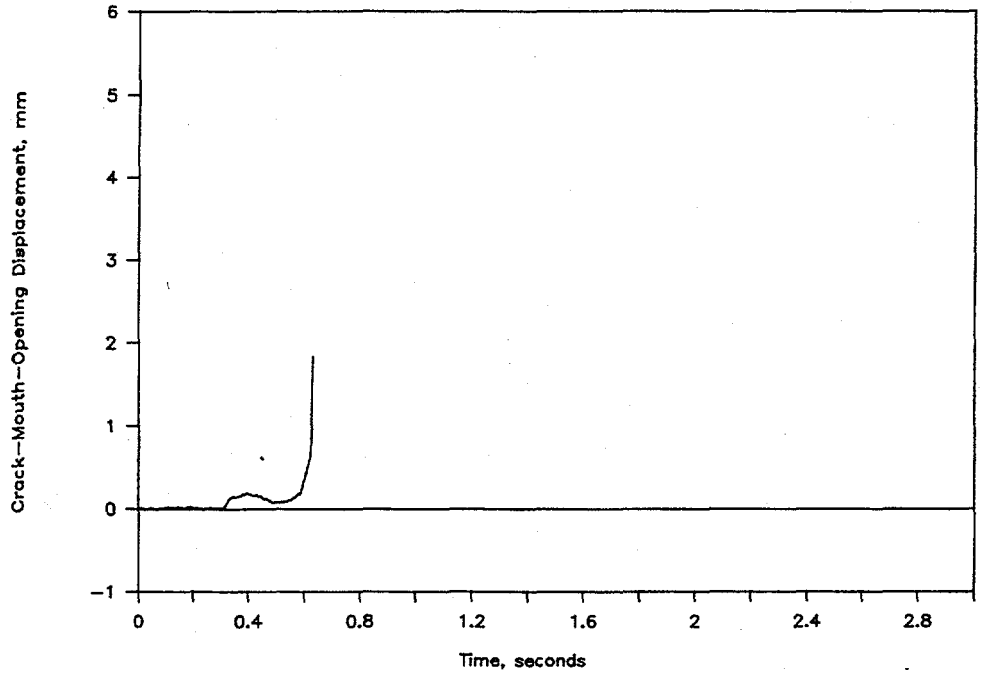

Figure 3.136 Crack-mouth-opening displacement versus time from the carbon steel base metal experiment (1.3-2) I1.3-10/90-F3.136

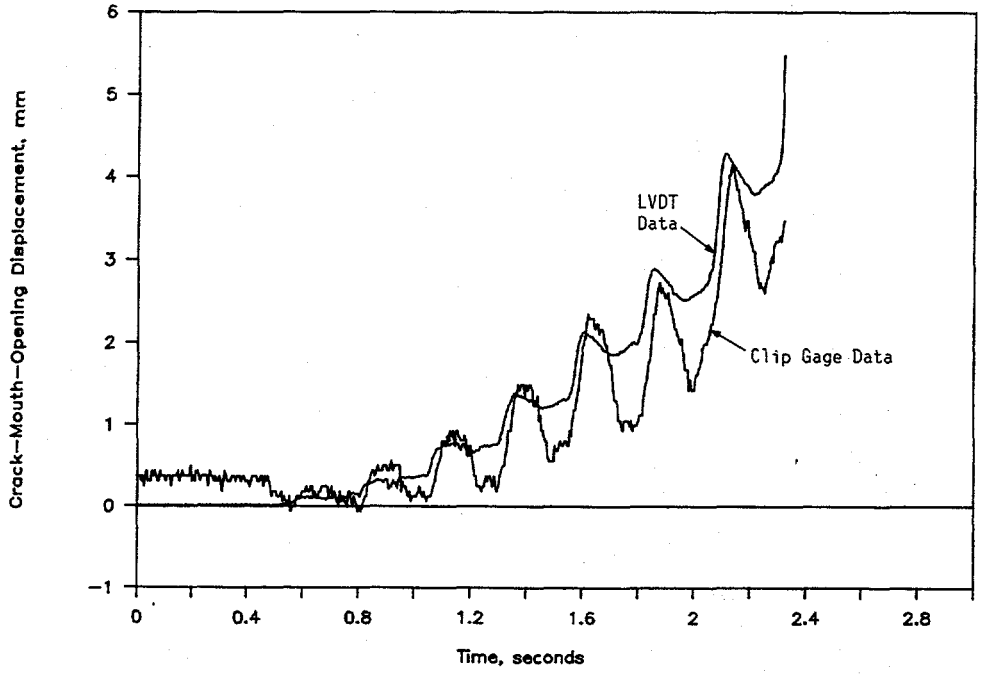

Figure 3.137 Crack-mouth-opening displacement data from LVDT and clip gage versus time from the stainless steel base metal experiment (1.3-3) I1.3-10/90-F3.137

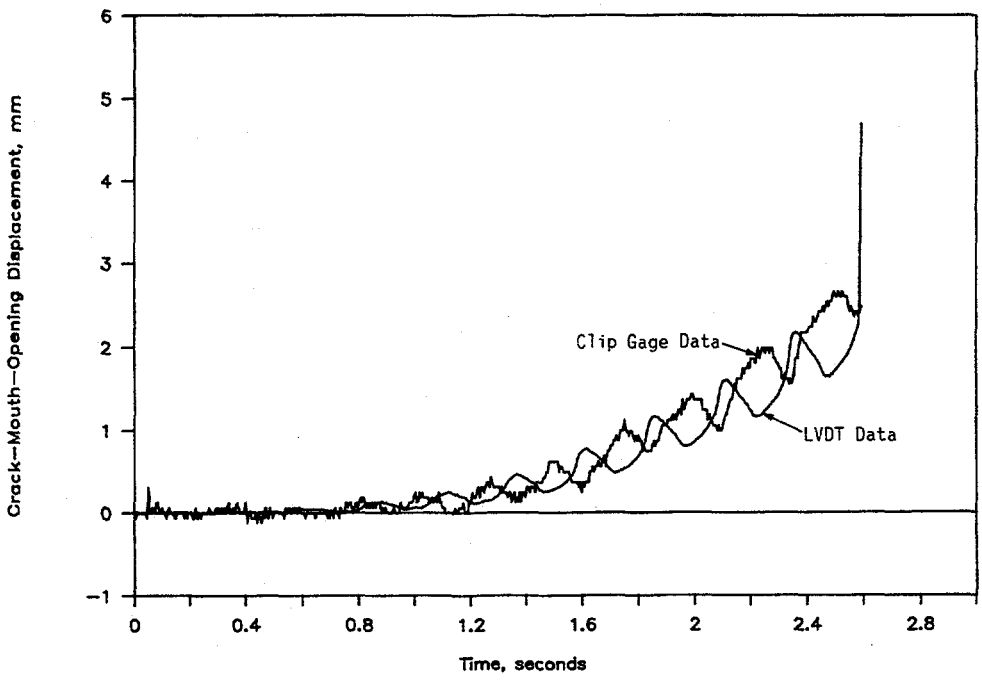

Figure 3.138 Crack-mouth-opening displacement (CMOD) data from LVDT and clip gage versus time from the stainless steel weld experiment (1.3-5) I1.3-10/90-F3.137

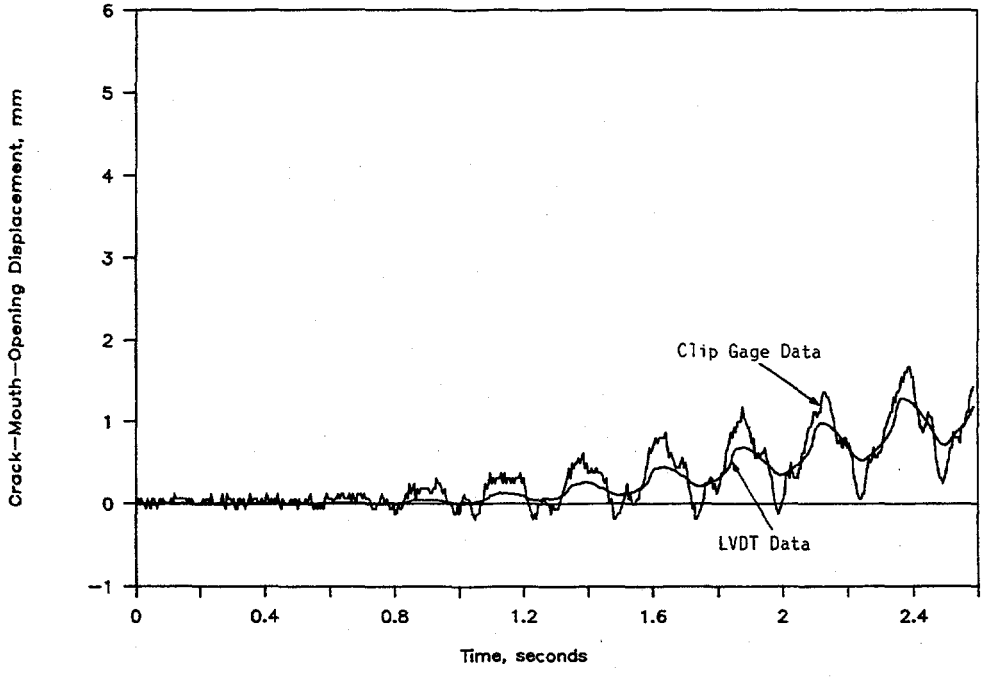

Figure 3.139 Crack-mouth-opening displacement data from LVDT and clip gage as a function of time from the aged cast stainless steel experiment (1.3-7) I1.3-10/90-F3.139

Using the procedures set forth in Appendix E, the crack section moment at the instant of crack initiation for the three stainless steel experiments was determined as shown in Table 3.10. From Table 3.10, it can be seen that the ratio of the moment at crack initiation to the maximum moment was 0.974 for the high toughness stainless steel base metal material while this same ratio was 0.854 for the lower toughness aged cast stainless material. Similar trends have been reported earlier (Ref. 3.2).

Figures 3.140 through 3.142 are plots of surface-crack growth (Δa) as a function of time for the three stainless steel specimens. The surface-crack growth data were obtained from the d-c EP data following the procedures specified in Appendix E. The horizontal plateaus of the curves are associated with the unloading portions of the loading history (i.e., that segment of the loading history where the applied moment and CMOD are either decreasing or increasing but at a value less than that obtained during the previous cycle).

Figure 3.143 is a plot of the through-wall crack length for the stainless steel base metal experiment as a function of time, based on the calibration curve shown in Appendix E. During the unloadings, appropriate crack lengths were input into the data files to provide a smooth curve, i.e., to avoid apparent negative crack growth from cyclic unloadings.

Figure 3.144 is a plot of the through-wall crack velocity at one crack tip for the stainless steel base metal experiment as a function of time for the period immediately following surface-crack penetration, i.e., the very steep portion of the curve in Figure 3.143, at about 2.3 seconds. From Figure 3.144 it can be seen that once the through-wall crack penetrates the pipe wall, the crack speed accelerates to approximately 20 meters/second (65 feet/second) in the first 10 milliseconds. It then slows to a nearly steady state fracture speed during the tearing phase of the fracture event beyond the time shown on the graph. The fracture speed during the subsequent cyclic growth of the simple through-wall crack was approximately 0.08 m/second (0.25 feet/second), which is significantly slower than the growth along the initially surface-flawed region.

3.4.3.6 Flaw Stability

Each of the cracked pipe experiments conducted as part of this effort exhibited similar behavior from the viewpoint of flaw stability. For each experiment, there was a small amount of stable surface-crack growth through the thickness from the initial surface crack, after which the surface crack propagated rapidly through the remaining pipe wall thickness. Once the surface crack propagated through the pipe wall, it continued to grow rapidly around the pipe circumference to the ends of the machined portion of the surface crack. This rapid surface-crack growth and subsequent rapid through-wall crack growth was one event. The time interval between the onset of rapid surface-crack growth and the arrest of the resultant through-wall crack was on the order of 0.025 seconds.

After this initial event, the through-wall cracks for each of the experiments continued to grow due to subsequent cyclic loadings. Figure 3.145a is a close-up photograph of the fracture surface at the end of the surface crack for the carbon steel base metal experiment. The distinct lines evident on this fracture surface are associated with the fracture arrest/reinitiations which occurred during the unloadings and subsequent reloadings. Figure 3.145b is a sketch of the fracture surface shown in Figure 3.145a which highlights the

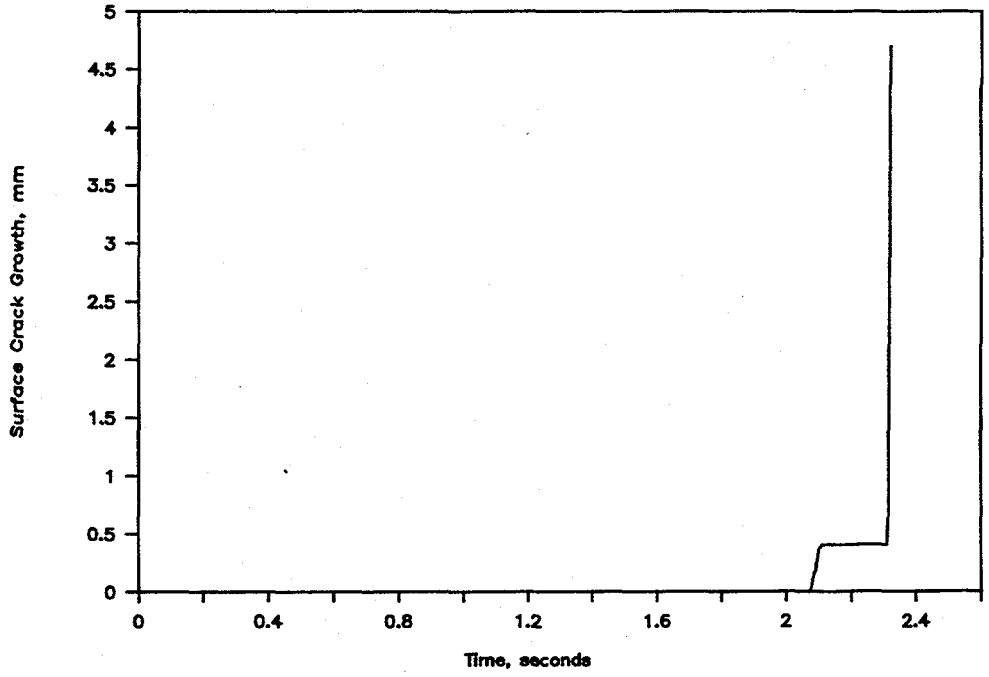

Figure 3.140 Surface crack growth versus time from the stainless steel base metal experiment (1.3-3) I1.3-10/90-F3.140

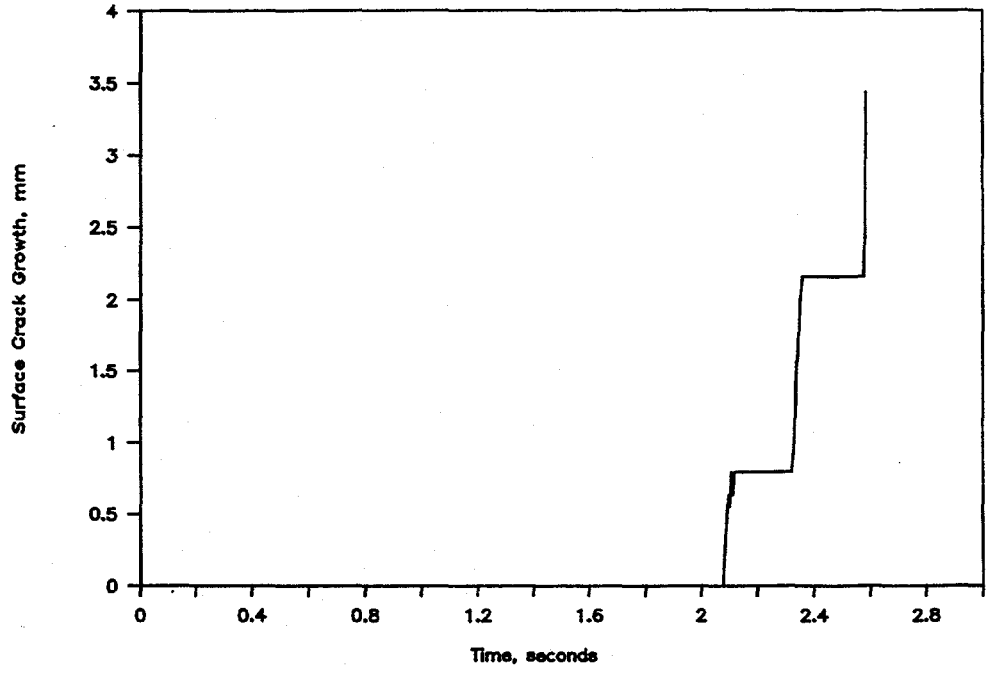

Figure 3.141 Surface crack growth versus time from the stainless steel weld experiment (1.3-5) I1.3-10/90-F3.41

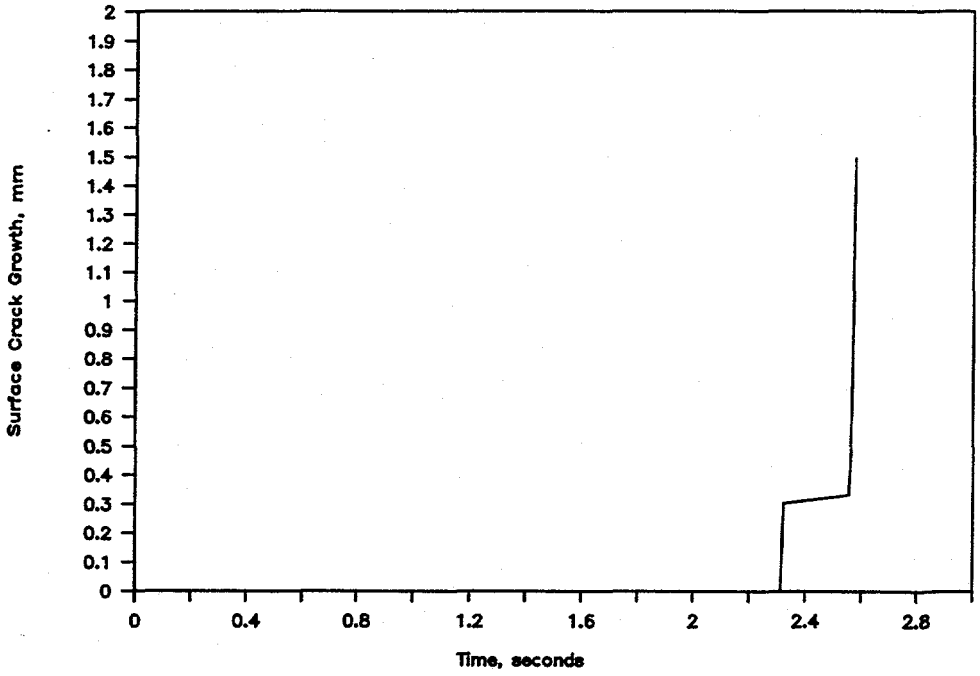

Figure 3.142 Surface crack growth versus time from the aged cast stainless steel experiment (1.3-7) I1.3-10/90-F3.142

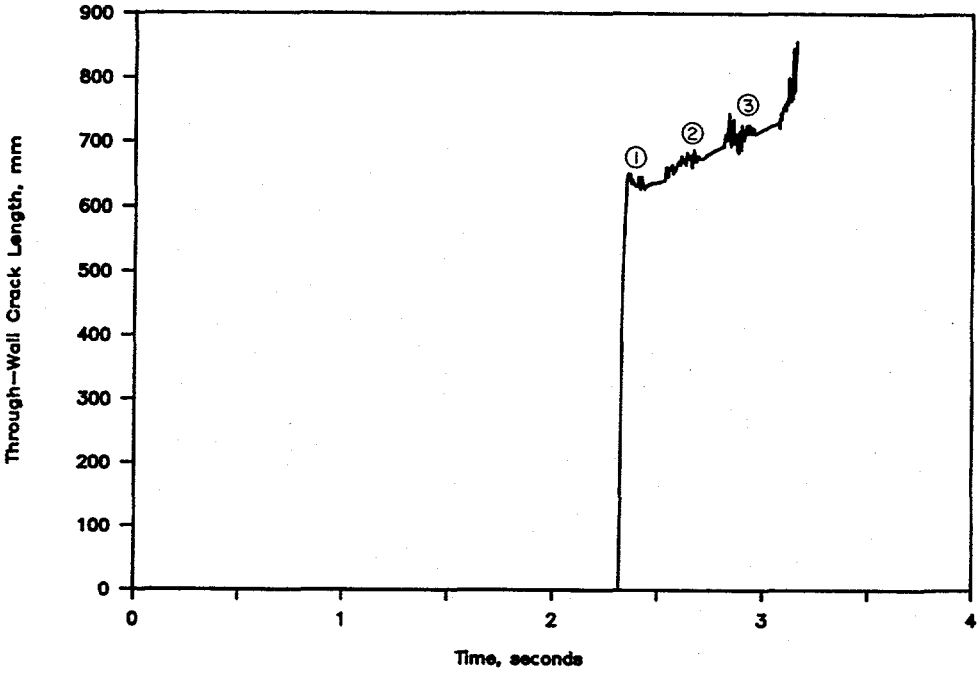

Figure 3.143 Total through-wall-crack length (2c) versus time from the stainless steel base metal experiment (1.3-3) I1.3-10/90-F3.143

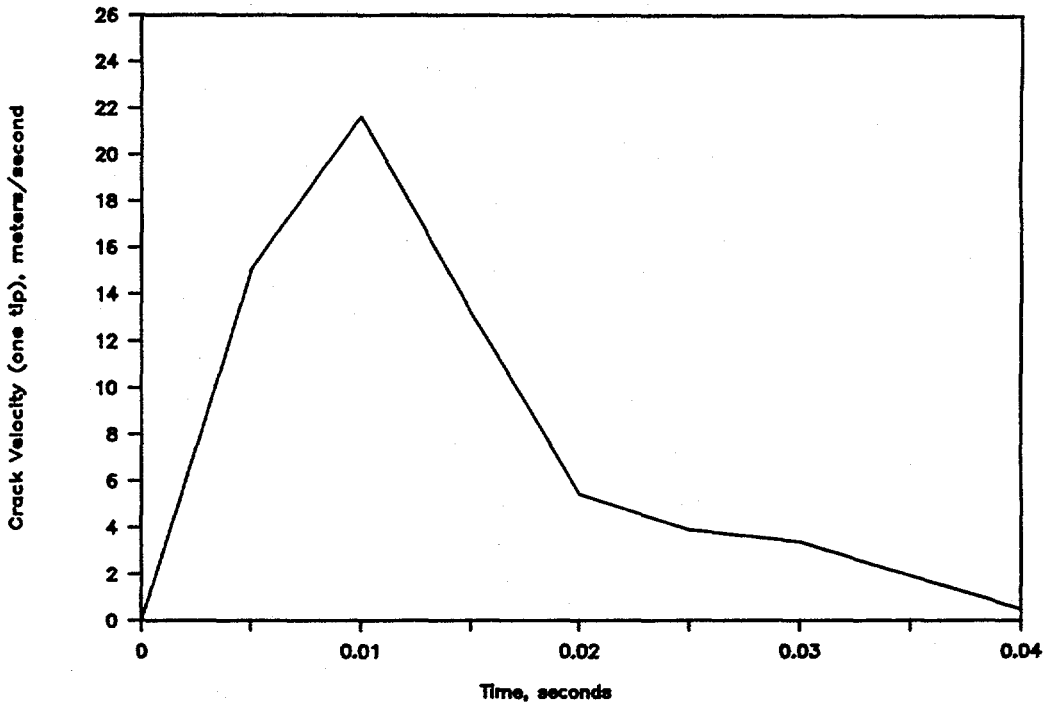

Figure 3.144 Crack velocity (at one crack tip) as the crack is transitioning from a surface crack to a through-wall crack as a function of time from the instant of surface crack penetration from the stainless steel base metal experiment (1.3-3) DRB/1.3-3/F41

(a)

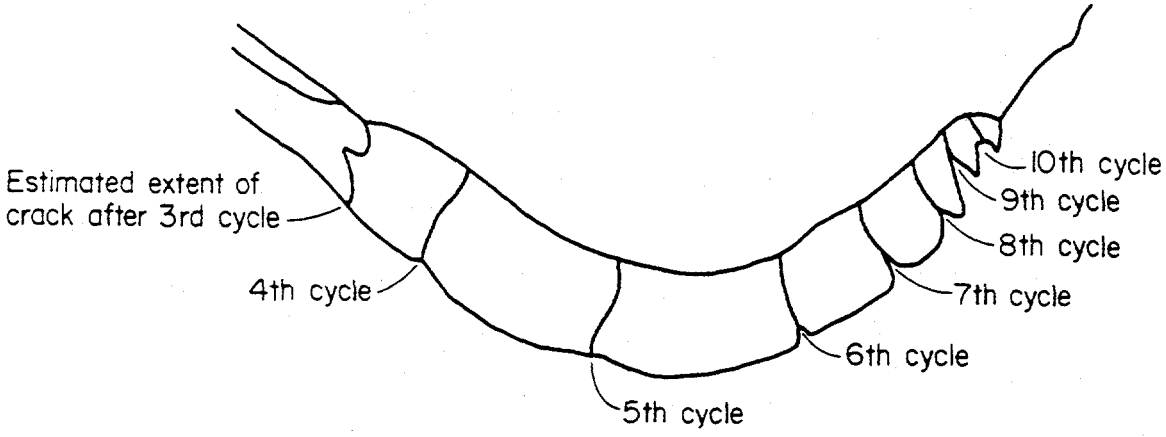

(b)

Figure 3.145 Close-up photograph of fracture surface from the carbon steel base metal experiment (1.3-2) at one crack tip (a) and a sketch of same fracture showing crack closure marks (b) (crack closure marks were used to estimate extent of the crack at various times during the event, see measurements in Table 3.11) DRB/1.3-2/F37

arrest/reinitiation lines. Measurements were taken on the outside pipe surface of the distance between the various arrest/reinitiation lines and the center of the machined surface crack. Those measurements are provided in Table 3.11.

The behavior exhibited in Figure 3.145 is typical of what was seen for each of the pipe fracture experiments. The main difference in fracture surface appearance between experiments was that the carbon steel base metal fracture turned out of the circumferential plane once the crack propagated past the ends of the initial surface crack, see Figure 3.146. Similar behavior has been observed for other carbon steel specimens in both static experiments (i.e., Degraded Piping Program experiments (Ref. 3.2) and dynamic experiments (i.e., IPIRG Subtask 1.1 and 1.2 experiments [Refs. 3.5 and 3.10).

Figures 3.147 and 3.148 are similar to Figures 3.145a and 3.145b except these figures are for the stainless steel base metal experiment. Figure 3.147 is a close-up photograph of the fracture surface at one of the crack tips. Figure 3.148 is a sketch of this same fracture surface showing the location of the crack closure marks which were visually evident on the fracture surface. These crack closure marks were used to estimate the extent of the crack at various times during the fracture event. Measurements were taken on both the inside and outside pipe surfaces of the distance between the various arrest/reinitiation lines. Those measurements are provided in Table 3.12.

Figure 3.149 is a close-up photograph of the fracture surface at one crack tip for the carbon steel weld experiment. Figure 3.150 is a sketch of this fracture surface highlighting the arrest/reinitiation lines. Measurements of the extent of the through-wall-crack length at various times during the fracture event are provided in Table 3.13.

Figure 3.151 is a close-up photograph of the fracture surface at one crack tip for the stainless steel weld experiment. Figure 3.152 is a sketch of the fracture surface shown in Figure 3.151 highlighting the arrest/reinitiation lines. Measurements of the extent of the through-wall crack at various times during the fracture event for this experiment are provided in Table 3.14.

Note, no crack closure marks were visually evident on the fracture surface of the aged cast stainless steel experiment due to the large grains affecting the fracture appearance. Consequently, no estimate of through-wall crack extent is possible for this experiment.

Figure 3.153 is a plot of the distance between the crack closure marks as a function of cycle (directly related to time) for the four experiments for which crack closure marks were evident on the fracture surface. The data used to generate Figure 3.153 were obtained from Tables 3.11 through 3.14. Of note from Figure 3.153 is that the crack extension between cycles tends to initially increase and then decrease as the applied loadings die out. The crack extension between cycles was significantly greater for the carbon steel base metal experiment than for the other three experiments, even though the maximum applied moment prior to surface-crack penetration was significantly less for this experiment, see Table 3.10. The significant crack extension for the carbon steel base metal experiment was attributed to the lower tearing resistance of this material at dynamic loading rates, see Tables 2.10 to 2.13. The value of dJ/da at dynamic loading rates for this carbon steel base metal was 58 MJ/m^3 (8,360 $in\text{-}lbs/in^3$), compared with values of 102 to 485 MJ/m^3 (14,700 to 70,300 $in\text{-}lbs/in^3$) for the other three materials. Further note that this carbon steel

Table 3.11 Crack length measurements from closure marks on the fracture surface from carbon steel base metal experiment (1.3-2)

	Projected Through-Wall Crack Length at Outside Surface From Center of Surface Crack	
Cycle	mm	(inch)
3	343	(13.5)
4	386	(15.2)
5	452	(17.8)
6	531	(20.9)
7	572	(22.5)
8	597	(23.5)
9	612	(24.1)
10	622	(24.5)

Table 3.12 Distance between the arrest/reinitiation lines on the stainless steel base metal fracture surface (Experiment 1.3-3)

Distance Between Line Numbers	Inside Surface		Outside Surface		Average	
	mm	(inch)	mm	(inch)	mm	(inch)
1 & 2	--	--	23	(0.9)	11.5	(0.45)
2 & 3	10	(0.4)	17	(0.65)	13	(0.52)
3 & 4	15	(0.6)	20	(0.8)	18	(0.7)
4 & 5	18	(0.7)	27	(1.05)	22	(0.87)
5 & 6	18	(0.7)	25	(1.0)	21.5	(0.85)
6 & 7	19	(0.75)	20	(0.8)	19.5	(0.77)
7 & 8	15	(0.6)	17	(0.65)	16	(0.62)
8 & 9	10	(0.4)	10	(0.4)	10	(0.4)
9 & 10	9	(0.35)	9	(0.35)	9	(0.35)
10 & 11	8	(0.3)	8	(0.3)	8	(0.3)
11 & 12	5	(0.2)	5	(0.2)	5	(0.2)
12 & 13	4	(0.15)	4	(0.15)	4	(0.15)

Table 3.13 Distance between crack closure marks on the fracture surface of carbon steel weld specimen (Experiment 1.3-4)

Crack Closure Mark Reference Numbers	Distance Between Crack Closure Mark Reference Numbers					
	Inside Surface		Outside Surface		Average	
	mm	(inch)	mm	(inch)	mm	(inch)
1-2	3.0	(0.12)	30.5	(1.20)	16.7	(0.66)
2-3	10.2	(0.40)	35.6	(1.40)	22.9	(0.90)
3-4	14.0	(0.55)	25.4	(1.00)	19.7	(0.77)
4-5	15.2	(0.60)	17.8	(0.70)	16.5	(0.65)
5-6	36.8	(1.45)	39.4	(1.55)	38.1	(1.50)
6-7	19.0	(0.75)	24.1	(0.95)	21.5	(0.85)
7-8	25.4	(1.00)	24.1	(0.95)	24.7	(0.97)
8-9	17.8	(0.70)	19.0	(0.75)	18.4	(0.72)
9-10	12.7	(0.50)	11.4	(0.45)	12.0	(0.47)
10-11	10.2	(0.40)	7.6	(0.30)	8.9	(0.35)
11-16	12.7	(0.50)	25.4	(1.00)	19.0	(0.75)

Table 3.14 Measurements taken on both the inside and outside pipe surface between the arrest/reinitiation lines evident on the stainless steel weld fracture surface (Experiment 1.3-5)

Distance Between Arrest/Reinitiation Lines	Outside Surface		Inside Surface		Average	
	mm	(inch)	mm	(inch)	mm	(inch)
1-2	17.8	(0.7)	--	--	8.9	(0.35)
2-3	21.6	(0.85)	--	--	10.8	(0.75)
3-4	26.7	(1.05)	20.3	(0.8)	23.5	(0.92)
4-5	45.7	(1.8)	38.1	(1.5)	41.9	(1.65)
5-6	38.1	(1.5)	34.3	(1.35)	36.2	(1.42)
6-7	35.6	(1.4)	27.9	(1.1)	31.7	(1.25)
7-End	73.7	(2.9)	66.0	(2.6)	69.8	(2.75)

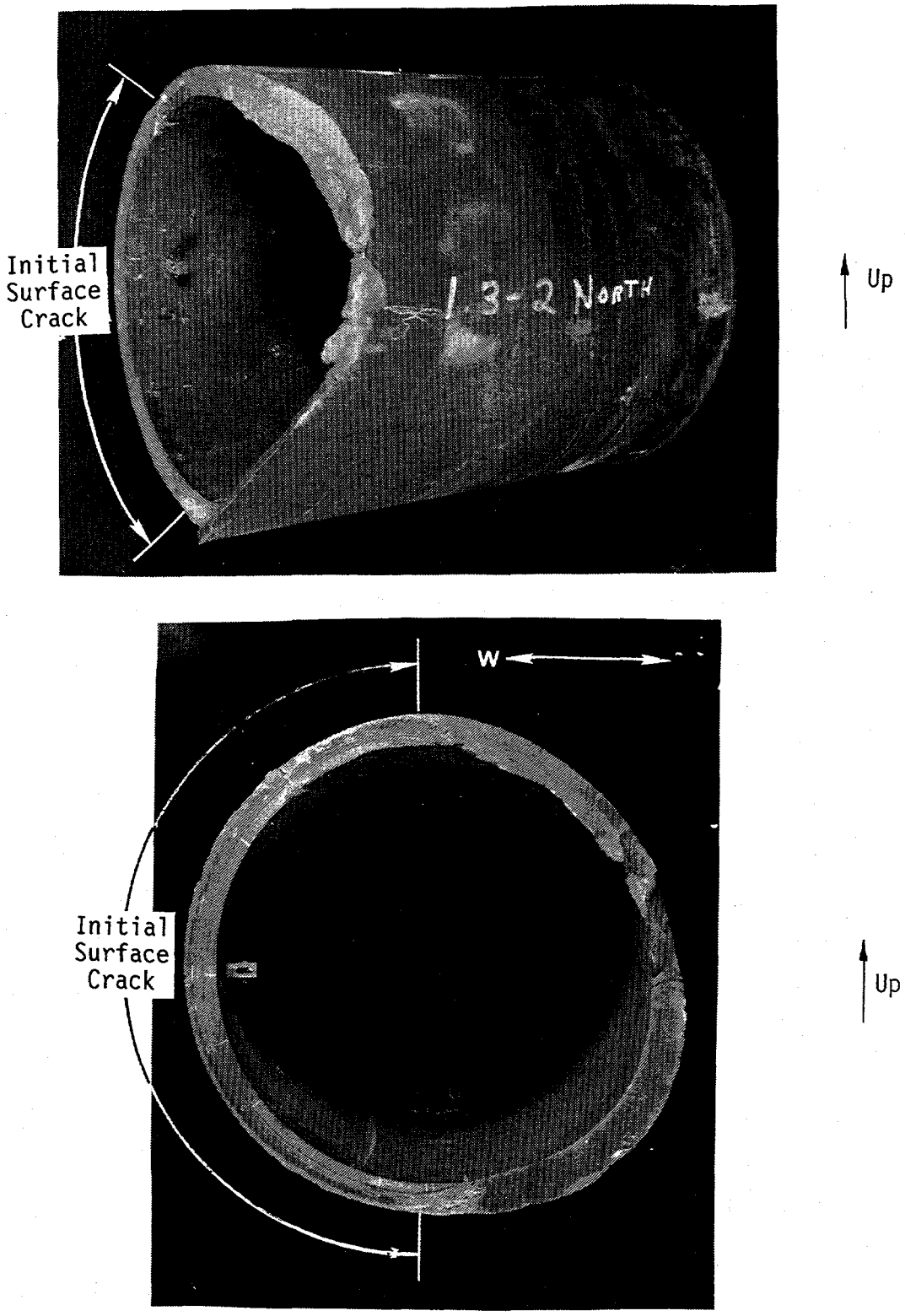

Figure 3.146 Overall views of carbon steel base metal fracture surface from Experiment 1.3-2

DRB/1.3-2/F36

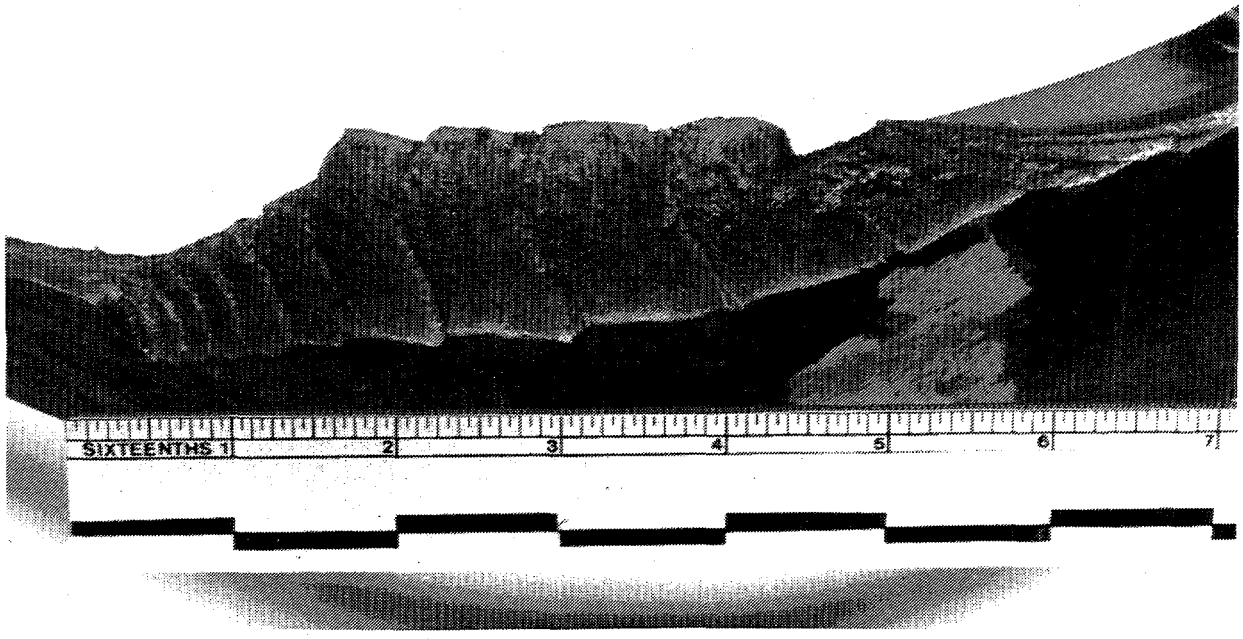

Figure 3.147 Fracture surface from the stainless steel base metal experiment (1.3-3) DRB/1.3-3/F56

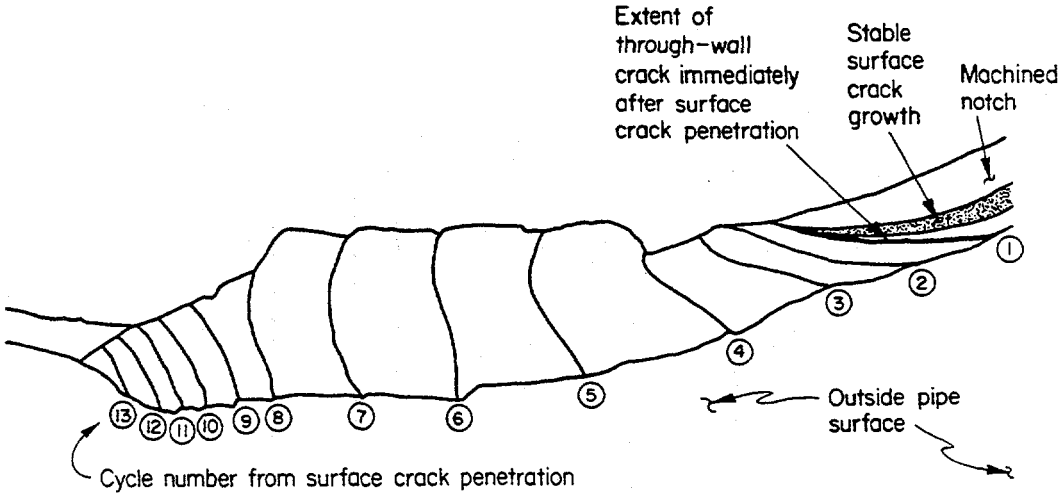

Figure 3.148 Sketch of the fracture surface shown in Figure 3.147 highlighting the arrest/reinitiation lines

I1.3-10/90-F3.148

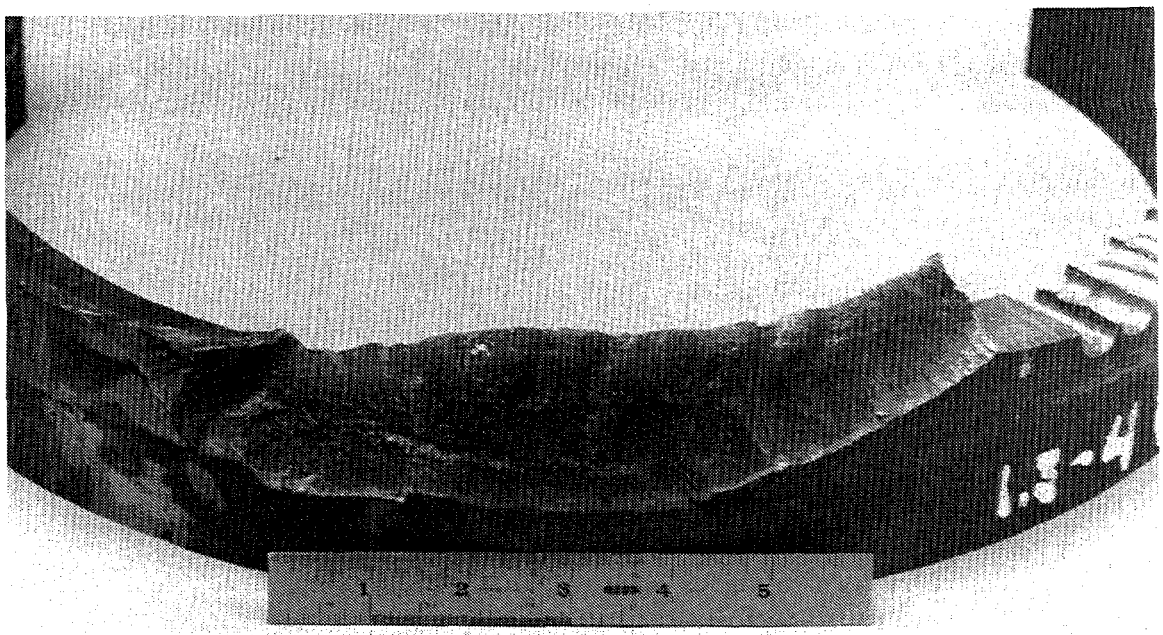

Figure 3.149 Fracture surface at one crack tip from the carbon steel weld experiment (1.3-4) F1.3-3/91-F3.149

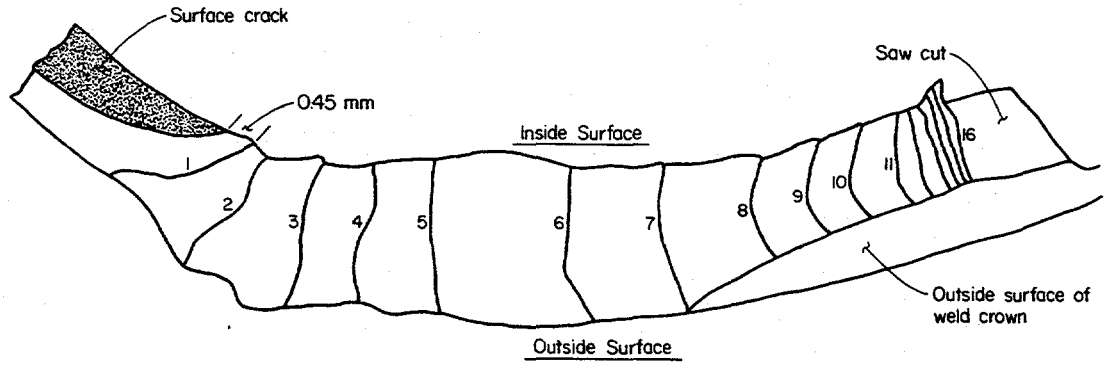

Figure 3.150 Sketch of fracture surface from the carbon steel weld experiment highlighting arrest/reinitiation lines

I1.3-10/90-F3.150

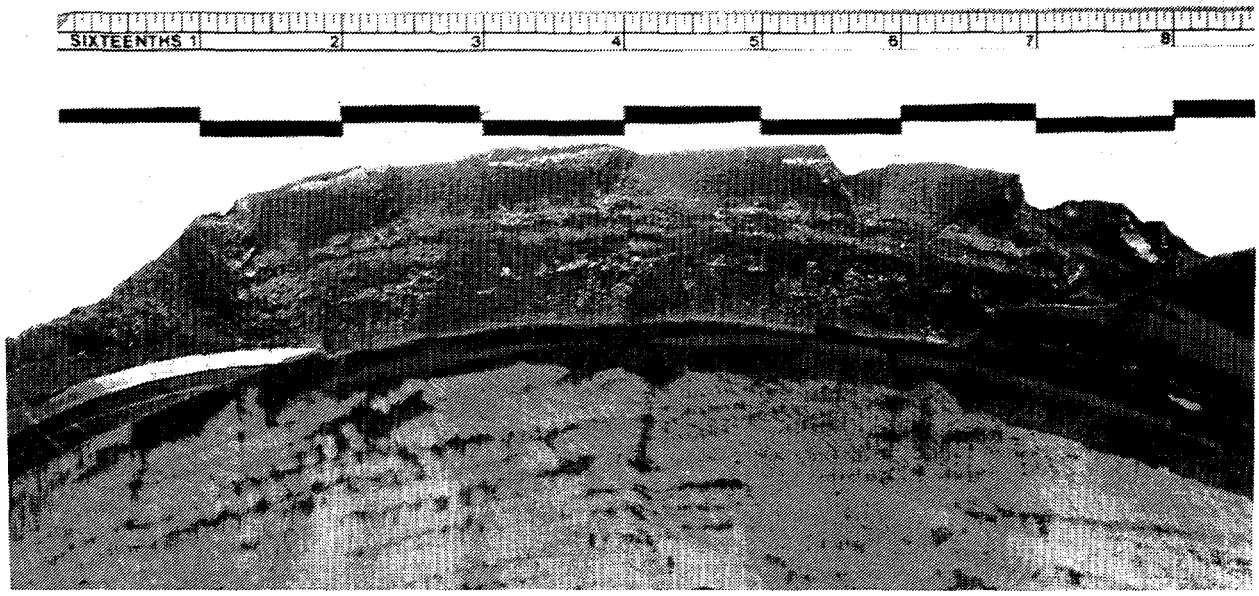

Figure 3.151 Close-up of the fracture surface at one crack tip from the stainless steel weld experiment (1.3-5) DRB/1.3-5/F52

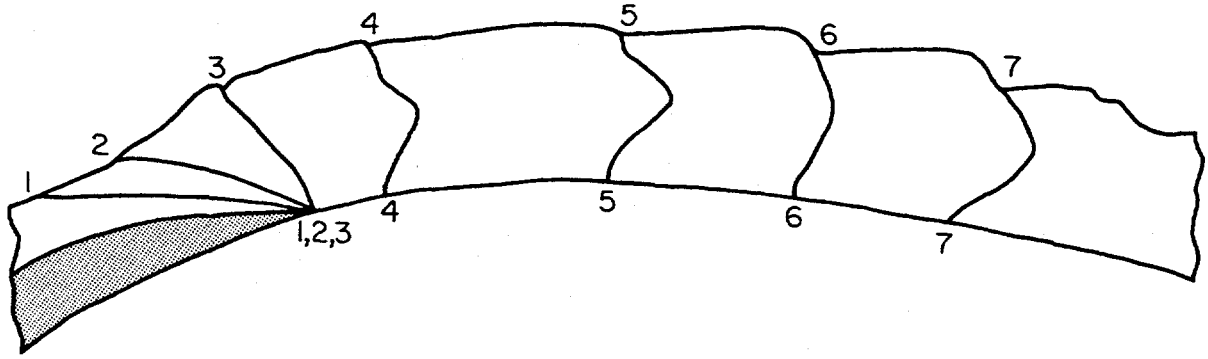

Figure 3.152 Sketch of fracture surface shown in Figure 3.151 highlighting the arrest/reinitiation lines DRB/1.3-5/F54

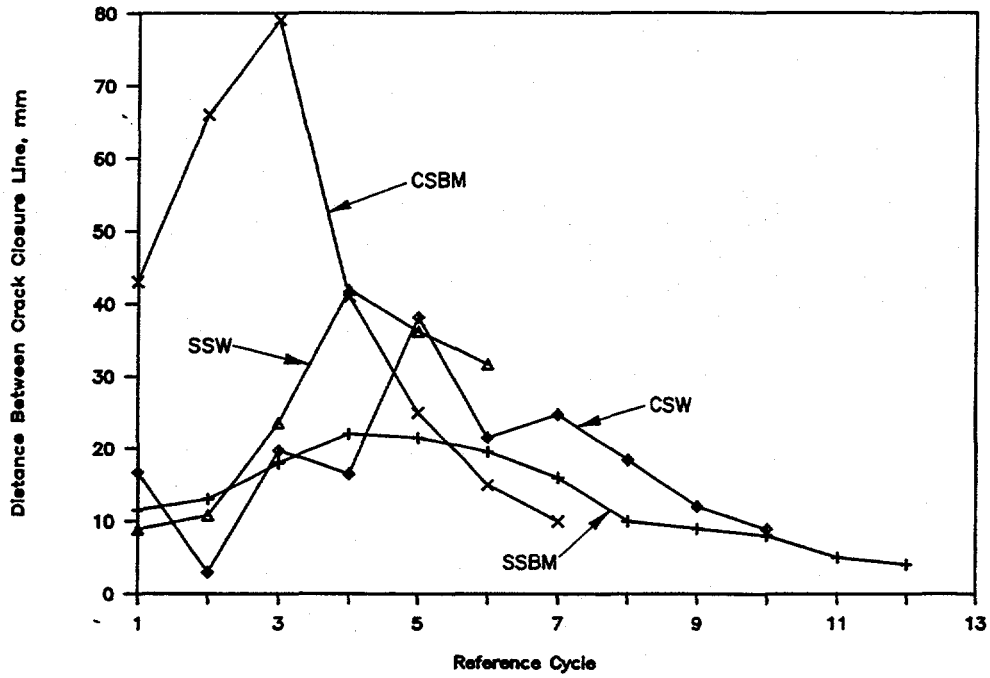

Figure 3.153 Distance between crack closure marks as a function of reference cycle (an indication of through-wall-crack velocity) for the carbon steel base metal and weld experiments and the stainless steel base metal and weld metal experiments F1.3-3/91-F3.153

base metal experiment was the only experiment of the four for which a complete severing of the pipe section occurred. (Note, the pipe section for the aged cast stainless experiment also severed, but that was an artifact of not attenuating the forcing function after surfaces crack penetration.

3.5 Observations

In this section, the results of the six pipe-system experiments will be briefly discussed. Note: any discussion comparing the results of these experiments to existing analytical tools will be deferred to Section 4.0 of this report.

As alluded to earlier, great care was taken in the design and construction of the experimental facility to ensure that the as-built experimental facility could be adequately modeled analytically. Hydrostatic bearings were incorporated in the facility design at the two vertical supports to obtain a near frictionless restraint in the horizontal plane at these two locations. Post-test examination of the brass sheets on which these bearings floated revealed only minor surface abrasions indicating that the bearings, and thus the piping loop, were indeed floating on a thin layer of oil throughout the tests. Thus, one can safely model these vertical supports as being free in the horizontal plane. In addition, in order to ensure that the two fixed ends remained fixed throughout the course of the experiments, the piping loop at the two fixed ends was attached to a large steel frame which was buried in a large heavily reinforced concrete mass. The accelerometer and displacement data from the stainless steel base metal experiment showed conclusively

that the displacements at the instrumented anchor point, Node 1, were indeed very small. The maximum displacements inferred from the accelerometer data up to the instant of surface-crack penetration were less than 0.005 mm (0.0002 inch). These displacements are four orders of magnitude less than the displacements applied to the piping system at the actuator. Therefore one can assume, without reservation, that the fixed ends are indeed fixed.

The experimentally determined damping value of 0.5 percent for the IPIRG Subtask 1.3 pipe loop is quite low compared to what is assumed for most piping analyses; i.e., 2-3 percent per ASME Section III, Division 1, Appendix N and up to 5 percent per ASME Code Case N-411-1. The reason for the low measured damping values lies in the hardware used to enforce the boundary conditions on the pipe system and the use of high strength pipe for the loop. In particular, the use of spherical bearings, linear bearings, and most importantly, hydrostatic bearings for the vertical supports, provides very little opportunity for energy to be dissipated as friction, even at large amplitudes of pipe motion. The use of high strength pipe for the loop also minimized plasticity and related energy absorption.

In reviewing Figure 3.79, it is apparent that the damping is not constant. In general, the damping appears to increase as the amplitude of motion decreases at increasing times. The increase can be attributed to friction damping starting to dominate the predominantly viscous damping at the earlier times. This is substantiated by Figure 3.154 which shows a plot of the successive amplitude ratios which is a measure of how close the actual damping is to being viscous in nature. In Figure 3.154, the amplitude ratio is nearly constant at early times, indicating that the damping is primarily viscous in nature. At later times, the amplitude ratio becomes more erratic indicating that other types of damping are becoming more important. Errors in digitization of the data which become more pronounced at longer times also contributed to the scatter in the amplitude ratio.

Table 3.15 is a summary of all of the measured first natural frequencies. Three items deserve some comment. First, the first natural frequency of the system for all of the test conditions evaluated for the case where the actuator is connected to the piping loop is approximately 4.5 Hz. This suggests that no special precautions are required to accommodate natural frequency changes when selecting a dynamic forcing function frequency other than the compliance change brought about when the surface crack becomes a through-wall crack in the cracked pipe tests. Second, the small change in frequency seen at the lower preloads in both the room temperature and PWR condition actuator driven tests can be easily explained. Because the random noise causes both positive and negative actuator motion about the static position, it is entirely likely that the benefit of the preload relative to any lash in the system is lost in the lower preload value as the actuator pulls on the pipe. An increase in preload in the PWR test is consistent with this hypothesis in that the frequency does not change.

Table 3.15 Summary of first natural frequency measurements from Experiment 1.3-1

Method	Temperature C	Temperature F	Pressure MPa	Pressure psi	Preload kN	Preload lb	Frequency, Hz
Ring-Down		RT	0	0	Fixed		4.28
Instrumented Hammer		RT	15.4	2,230	Fixed		4.5
Instrumented Hammer		RT	15.4	2,230	Free		3.5
Actuator Driven		RT	0	0	30.7	6,900	4.47
		RT	0	0	23.6	5,300	4.25
		RT	15.4	2,238	30.7	6,900	4.47
	292	557	15.6	2,257	31.1	7,000	4.43
	292	557	15.6	2,257	4.4	1,000	4.35
	292	557	15.6	2,257	89.0	20,000	4.48

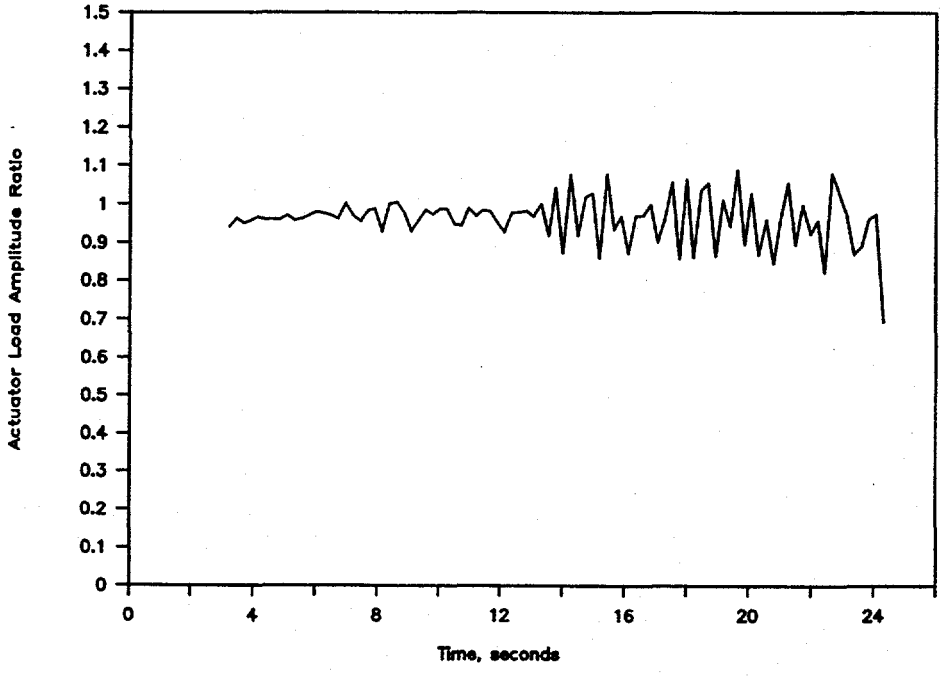

Figure 3.154 Ratio of successive amplitude cycles for assessment of the suitability of a viscous damping assumption DRB/1.3-1/F23

Last, no change in the natural frequency from room temperature and no pressure, to PWR conditions suggests that there is an interplay of parameters affecting the natural frequency. The effects of stiffening of elbows due to pressure, a decrease in the mass density of the water in the pipe, and a decrease in the modulus of elasticity of the pipe steel at high temperature must all balance. From the room temperature test, the change in frequency due to pressurization is insignificant. Therefore, mass and Young's modulus must decrease proportionately to maintain the same frequency. To be consistent with this experimental finding, analytical predictions of natural frequency must include all of these first-order effects to obtain correct predictions.

Although a detailed discussion of a comparison of the piping system response data (i.e., reaction forces, global displacements, and moments) to ANSYS® predictions will be deferred to Section 4 of the report, a few general comments regarding the piping system response data are worth noting. In Figures 3.107 through 3.109 one sees the Y-direction motions were the dominant dynamic motions associated with this piping system at all three locations where global displacements were made, i.e., Elbow 3, the crack, and Node 21. The displacements in the X-direction at the crack and Node 21 are static displacements caused by the heat-up. The X-direction dynamic motion at Elbow 3 is significant due to its proximity to the actuator which is being forced in the X-direction. The Z-direction displacements are negligible at all three locations. This general pattern of global displacements is consistent with the ANSYS® predicted mode shape presented in Figure 3.82 for the first natural frequency. For the first mode shape shown in Figure 3.82a, the Y-direction displacements are significant and the X- and Z-direction displacements are negligible. The second natural frequency mode shape, see Figure 3.82b, is an out-of-plane "flapping" mode for which significant Z-direction motions would be expected. The mode shapes for the third and fourth natural frequencies, see Figures 3.82c and 3.82d, are for other in-plane bending modes. However, for these cases, the X-direction motions are becoming significant. As a result, one can conclude that for the forcing function frequencies used in the Subtask 1.3 experiments, the pipe system responds predominantly in the first mode.

From Figure 3.114 one sees that once the surface crack penetrates the pipe wall, the internal pipe pressure at the crack immediately drops to the saturation pressure of the fluid at the temperature of the piping system. From Figure 3.114, one also sees that there is virtually no evidence of a pressure gradient in the piping run containing the crack. The pressure at the crack is very nearly the same as the pressure at a location 4.1 m (13.5 feet), or ten pipe diameters, removed from the crack. (The sensitivity of the pressure transducers and the 200 Hz filter used precluded the measurement of any high speed, small magnitude transients, i.e., reflective waves.) Furthermore, once the saturation pressure is reached after surface-crack penetration, the pressure at the crack tends to decay at a relatively slow rate, approximately 0.5 MPa/second (70 psi/second). With such behavior observed in a closed system with a small volume of water (3000 liters [800 gallons]), one can imagine that the pressure at the crack in an actual plant would be maintained near saturation for a significant length of time.

In reviewing the moment data, several points are worth noting. For one, Figures 3.123 and 3.124 demonstrate that the dynamic bending moment gradient along the north-south pipe run which contains the crack is minimal. There is a small gradient due to the pressure and thermal stresses, but the dynamic moment gradient due to the dynamic excitation of the piping system is negligible.

In comparing the moments at crack initiation to the maximum moments for the three stainless steel pipe-system experiments conducted as part of this subtask, one sees that the ratio of the moment at crack initiation to the maximum moment for the experiment increases as the toughness of the specimen increases. The ratio of the moment at crack initiation to the maximum moment for the high toughness stainless steel base metal specimen was 0.974 whereas the ratios for the lower toughness stainless steel

weld and aged cast stainless steel specimens were 0.933 and 0.854, respectively. Similar trends have been reported earlier (Ref. 3.2). Furthermore, when one examines the moment-time plot for the stainless steel base metal experiment, see Figure 3.127, one sees that the crack initiated near the peak of the cycle immediately prior to surface-crack penetration. The crack then penetrated the pipe wall on the next cycle at a moment 16 percent below the previously attained moment. This condition where the moment at surface-crack penetration is less than the moment for a previous cycle, has had an influence on the percent inertial loading for some of the experiments. The reduction in moment which is attributed to crack growth on earlier cycles, tends to reduce the percent inertial loading at surface-crack penetration, see Figure 3.67 and Table 3.10.

The percent inertial loading primarily influences the ultimate stability of the resultant through-wall crack once the surface crack penetrates the pipe wall. For a near instantaneous pipe break to occur, the inertially controlled loads at the crack section must be high when the surface crack penetrates the pipe wall. Of note from Table 3.10 is the fact that even for the aged cast stainless experiment, with its relatively high maximum moment and high percent inertial loading (51 percent) at surface-crack penetration, the resultant through-wall crack at surface-crack penetration was stable. Either the resultant through-wall crack had a greater fracture resistance than suspected, or the inertial loads decay so fast that they do not act on the crack for a sufficient length of time, or higher inertial loads are required to drive the resultant through-wall crack to a near instantaneous break. Based on the behavior of the aged cast stainless specimen, it is very doubtful that any of the other tests would have experienced an instantaneous instability had the surface cracks penetrated at maximum moment where the percent initial loading would have been high (see Table 3.10).

Figure 3.144 shows the through-wall crack velocity data as a function of time for the stainless steel base metal experiment. The data are for the period of time as the surface crack is transitioning from a part-through surface crack to a through-wall crack. The data are based on electric potential data. The peak velocity from Figure 3.144 is approximately 20 m/second (60 feet/second). As part of the Degraded Piping Program, through-wall crack speed measurements were made over the same regime (i.e., as the surface crack is transitioning into a through-wall crack) during a stainless steel submerged-arc weld (SAW) experiment using specially fabricated high temperature timing wires. The measured velocities from these timing wire measurements were in the range of 50 to 90 m/second (150 to 270 feet/second). One would intuitively expect the fracture velocity of the higher toughness base metal to be less than that observed for the weld. Furthermore, considering the differences in measurement techniques and the difficulties in making these measurements and interpreting the data, the discrepancies between the through-wall crack velocities for the two experiments is not that surprising.

One final comment with regard to the Subtask 1.3 pipe-system experiments. The end caps, used to minimize the amount of energy released in the event the pipe severed in two pieces, were removed for the final experiment, i.e., the aged cast stainless experiment. The rationale for removing these end caps was that it was felt that they may have been influencing the final stability of the resultant through-wall cracks because the axial stress in the test section decreased at an artificially high rate once the volume of water inside the test specimen rapidly depressurized. On the surface it appears that this was indeed the case. After the surface crack penetrated the pipe wall during the aged cast stainless experiment, it continued to grow until it reached a critical size for the applied stress level such that the pipe did in fact sever. However, it must be emphasized that the fact that the pipe severed may have been an artifact of how the test was set up for shutdown, more than the presence or absence of the end caps. (Obviously in a plant, an actual seismic event would not be "shut off" by a shutdown device.) In the previous tests, the shutdown pressure was set at 5.17 MPa (750 psi). Typically, after the surface crack penetrated the pipe wall, the applied loading continued to increase for another 2 or 3 cycles before the shutdown routine was activated

and the actuator began to return to its initial starting position. For the aged cast stainless test, the shutdown pressure was again set at 5.17 MPa (750 psi). However, without the end caps in place, the pressure at the test specimen was maintained near the saturation pressure, 7.5 MPa (1,100 psi). Consequently, the shutdown routine was never activated and the actuator displacement continued to increase. Obviously, the fact that the forcing function continued to increase contributed to the ultimate occurrence of a double-ended break.

3.6 References

3.1 "Piping and Fitting Dynamic Reliability Program," EPRI RP 1543-15, 1995.

3.2 Wilkowski, G. M., and others, "Degraded Piping Program-Phase II," Summary of Technical Results and Their Significance to Leak-Before-Break and In-Service Flaw Acceptance Criteria, March 1984-January 1989, by Battelle Columbus Laboratories, NUREG/CR-4082, Vol. 8, March 1989.

3.3 Kanninen, M. F., and others, "Instability Predictions for Circumferentially Cracked Type 304 Stainless Steel Pipes Under Dynamic Loadings," Final Report on EPRI Project T118-2, by Battelle Columbus Laboratories, EPRI Report Number NP-2347, April 1982.

3.4 Scott, P., and others, "The IPIRG-1 Pipe System Fracture Tests: Experimental Results, " ASME PVP Vol. 280, pp. 135-151, June 1994.

3.5 Scott, P., and others, "Stability of Cracked Pipe Under Inertial Stresses - Subtask 1.1 Final Report," NUREG/CR-6233, Vol. 1, August 1994.

3.6 Wilkowski, G. M., and others, "Degraded Piping Program-Phase II," Semiannual Report, by Battelle Columbus Division, NUREG/CR-4082, Vol. 6, April 1988.

3.7 Scott, P. M., and Ahmad, J., "Experimental and Analytical Assessment of Circumferentially Surface-Cracked Pipes Under Bending, " NUREG/CR-4872, April 1987.

3.8 ASME Boiler and Pressure Vessel Code, Section XI - "Rules for Inservice Inspection of Nuclear Power Plant Components," 1995 Edition, July 1995.

3.9 Marschall, C. W., Landow, M. P., and Wilkowski, G. M., "Loading Rate Effects on Strength and Fracture Toughness of Pipe Steels Used in Task 1 of the IPIRG Program," NUREG/CR-6098, October 1993.

3.10 Kramer, G., and others, "Subtask 1.2 Final Report -- Stability of Cracked Pipe Under Seismic/ Dynamic Displacement-Controlled Stresses," NUREG/CR-6233, Vol. 2, No. 1, July 1997.

4.0 ANALYSIS OF PIPE FRACTURE EXPERIMENTS

The specific objective of this effort was to assess different analyses that have been or may be used to predict and evaluate the fracture behavior and dynamic system response of the pipe-system experiments conducted in the IPIRG program. Quasi-static pipe fracture experiments from the NRC's Degraded Piping Program (Ref. 4.1) and a previous program conducted for EPRI at Battelle (Ref. 4.2) on the same pipes tested in the IPIRG program also are analyzed and compared with the IPIRG results. The analyses conducted include:

(1) Analyses of the piping system response data to determine dynamic variables such as damping,

(2) Elastic analyses of moments for the cracked pipe-system experiments,

(3) Fracture analyses to predict failure loads:

- Net-Section-Collapse,
- Dimensionless Plastic-Zone Screening Criterion,
- ASME Section XI flaw evaluation criteria,
- R6 analysis using the Revision 3 Option 1 method, and
- J-estimation scheme analyses,

(4) Normalized moment-rotation graph and J_i values calculated from dynamic pipe-system tests,

(5) Stability analyses,

(6) Dynamic analyses of cracked pipe experiments.

A short summary of the quasi-static pipe experiments is given first, and the above analyses are described in the sections that follow.

In conducting these analyses, quasi-static material properties were used consistently. While some material property data were obtained at higher loading rates, which were more representative of the loading rates in the pipe-system experiments, only the quasi-static properties were used in this section of the report. Those are the only properties commonly available and used in code analyses. The need to consider high rate properties in certain circumstances is evaluated in Section 5.

In Sections 4.3 and 4.4, the accuracy of predictions made using elastic stress analyses and fracture analyses are evaluated for the piping system experiments. Both of these analyses can give rise to inaccuracies, but they are quite different in character. The elastic analysis of stresses is an attempt to determine the stress that will arise during a hypothetical dynamic event. If it is assumed that elastic behavior predominates, then the actual stresses are typically overpredicted. The fracture analyses, on the other hand, predict maximum load-carrying capacity of a given crack geometry. In this case, the predicted maximum stresses are less than those measured in an experiment. This underprediction can be thought of as an underprediction of the fracture resistance of the cracked pipe.

The evaluation of inaccuracies that can arise from elastic calculations of expected moments and stresses for the pipe-system experiments is instructional. However, one must consider the fact that the Subtask 1.3 pipe system, as designed and constructed, is not typical of plant piping. Extensive efforts were made to minimize structural nonlinearities and inelasticity. High strength pipe and, in one case, a thicker elbow were used to minimize plasticity, and specially designed bearings were used at the supports to minimize friction. As a result, the elastic stress analyses are much more accurate than might be expected in analyzing actual plant piping. Furthermore, reuse of the piping system for all experiments could cause some further reductions in nonlinear behavior for the later experiments since the prior experimental loads could act as local shakedown events for some components.

4.1 Past Quasi-Static Pipe Fracture Experiment Results

For each of the IPIRG pipe-system fracture experiments, there was a companion quasi-static experiment conducted with a similar internal surface crack. The test specimens for these quasi-static experiments were fabricated from the same sections of pipe used in the IPIRG pipe-system experiments. The flaw sizes and weld procedures used in the IPIRG pipe-system experiments and quasi-static experiments were similar. There were some differences in test temperature and internal pressure, see Table 4.1. Because of these differences and slight differences in flaw sizes, direct comparison of the maximum moments at failure between the pipe-system experiments and quasi-static experiments should not be made. Rather, limit-load or fracture mechanics analyses should be used to predict the maximum moments for both sets of experiments. Then, the differences in the ratio of the measured to predicted maximum moments will show the relative differences between the quasi-static and dynamic pipe-system fracture behavior. In Section 4.5, basic moment-rotation results from the pipe-system experiments are normalized to remove slight differences in test parameters.

Table 4.1 Summary of related past quasi-static pipe fracture experiments

							Experimental Moment	
					Crack Geometry		Initiation	Maximum
Material	Pipe No.	Quasi-Static Test No.	Temp., C	Pressure, MPa	θ/π	d/t	kN-m	kN-m
A106B	F29	4112-8[a]	288	0	0.53	0.66	689	748
TP304 Base	A8	EPRI 13S[b]	RT	0	0.48	0.66	970	1,260
A106 SAW	F29W	4141-9[a]	288	15.51	0.50	0.67	419	594
SS SAW	A8W	4141-4[a]	288	11.03	0.50	0.69	443	445
Aged Cast SS	A40	4143-1[a]	288	15.51	0.50	0.55	656	672

(a) Reference 4.1.
(b) Reference 4.2.

4.2 Analysis of Pipe-System Response Data

The IPIRG Subtask 1.3 pipe loop and the individual experiments were designed using the analytical tools and methodologies discussed in the System Design Analysis and the Experiment Design sections, Sections 3.2 and 3.3.6, of this report. In these sections, conceptual approaches were presented, without any rigorous

attempt to compare the responses predicted by the analyses with experimental test data. So that we can begin to understand where the limitations are in our ability to predict pipe fracture behavior, a comparison of analytical predictions and experimental data for pipe-system response is needed.

As part of IPIRG Subtask 1.3, the state-of-the art for analyzing a flaw in a dynamically loaded piping system has been advanced. The prediction of the behavior of a flawed pipe system under combined inertial and displacement-controlled loading involves two essential elements: (1) local behavior of the flaw, and (2) the response of the overall piping system. This predictive capability has been advanced by coupling the structural analyses with crack behavior in a single dynamic finite element analysis.

In order to predict the dynamic behavior of a piping system containing cracks, the uncracked piping system must be correctly modeled. The important structural features of the system must be identified and included in the model, otherwise, the efforts to couple fracture behavior with the structural analysis will be wasted.

The IPIRG Subtask 1.3 pipe system was designed so that it could be modeled analytically in a straightforward fashion, as previously indicated. Great care was taken to provide boundary conditions that can be accurately modeled in a finite element analysis, and sources of nonlinear structural behavior were reduced. This was done to force the focus of the results of the experiments on the fracture behavior, rather than on any ambiguity in the piping system response. As a consequence, many features of the IPIRG Subtask 1.3 pipe loop are not typical of plant piping; there probably are no expansion loops in operating plants that use hydrostatic bearings for vertical hangers. The use of this device does, however, have a beneficial effect on the ability to understand the experimental data. The use of high strength pipe for the loop material was also beneficial in reducing structural nonlinearities. The determinations of analytical accuracies for the IPIRG pipe system, described in Sections 4.3 and 4.4, are instructive, but should be viewed with an understanding of how this system is different from plant piping.

Of all of the possible piping system response characteristics that are important to model correctly in a cracked pipe analysis, system damping and system natural frequencies are paramount. System damping has a strong effect on the amount of energy available to load the crack. If the system natural frequencies are correctly predicted, then one can be more confident that the mass and stiffness of the structure are being properly modeled in the analysis.

4.2.1 System Damping

The amount of damping typically assumed in plant piping analysis is on the order of 2 to 5 percent (Refs. 4.3, 4.4). This level of damping is generally caused by friction at supports and hangers, local plasticity in the pipe loop material, and deliberate introduction of damping through the use of snubbers. In most cases, the amount of damping in a real pipe system is not purely viscous and is a nonlinear function of the amplitudes of motion. Both of these characteristics (i.e., nonviscous and nonlinear behavior) make it difficult to both measure real damping or implement it in an analysis.

For the IPIRG Subtask 1.3 pipe loop, great care was taken to minimize damping by eliminating points where friction forces could act as an energy sink and by the use of high strength pipe to control plasticity. As a consequence, the measured damping in the IPIRG Subtask 1.3 system is on the order of 0.5 percent, even at very large amplitudes of motion. The damping was also found to be almost purely viscous, especially at large amplitudes.

The effect of the low damping on system response and the importance of using the correct amount of damping are illustrated in Figures 4.1 through 4.4. Figures 4.1 and 4.2 present comparisons of analytical predictions with experimental results for an analysis with 5 percent damping, while Figures 4.3 and 4.4 present comparisons for an analysis with 0.5 percent damping. The most significant difference between the 5 percent and 0.5 percent damping cases can be seen in the moment plots, Figures 4.1 and 4.3, at 1.2 to 1.6 seconds. In the 5 percent damping case, the analytically predicted moment amplitude remains fundamentally sinusoidal in nature. For the 0.5 percent damping case, a pipe-system transient that is not damped out alters the response. This transient is also evident in the experimental data. In addition, over the complete time range for the event in Figures 4.1 and 4.3, the 5 percent damping case shows significant amplitude discrepancies and nearly a 180 degree phase lag after 2.8 seconds. For the actuator force, the difference between the 5 percent damping case and the 0.5 percent damping case predictions is a thirty percent reduction of force and a significant phase lag for the 5 percent damping case. The modest discrepancies between the 0.5 percent damping analysis and the measured values from the experiment can probably be attributed to inherent numerical damping in the finite element time integration scheme.

4.2.2 System Natural Frequencies

Correct prediction of system natural frequencies indicates that the mass and stiffness of a system have been properly modeled. A good comparison gives confidence that subsequent static and dynamic pipe-system analyses are properly founded.

In a finite element model, properly modeling a system involves specification of the elastic and density properties of the materials, definition of the geometry, and correct application of boundary conditions. Errors in any of these can lead to serious discrepancies between predictions and the companion measurements.

The natural frequencies of the IPIRG Subtask 1.3 system were measured a number of ways, as discussed previously. Table 4.2 summarizes and compares the measurements with the frequencies predicted by Battelle's analysis using the ANSYS® code. Except for some modest differences in the second and third frequencies, the comparisons are very favorable. In fact, the disagreement at the higher frequencies is not of any great concern, because the pipe-system response in all IPIRG experiments is dominated by its motion at the first natural frequency. It is essential, however, to get the first mode correct since the test frequency used in the IPIRG test matrix is very close to this first natural frequency.

Table 4.2 Comparison of measured and predicted natural frequencies for Subtask 1.3 pipe loop

	p = 15.5 MPa, T = 20 C				
	F_1	F_2	F_3	F_4	p=15.6 MPa T=297 C
Measured	4.5	12.0	13.9	18.0	4.43
Analysis[a]	4.42	14.45	14.63	18.72	4.23

(a) Battelle results using ANSYS®.

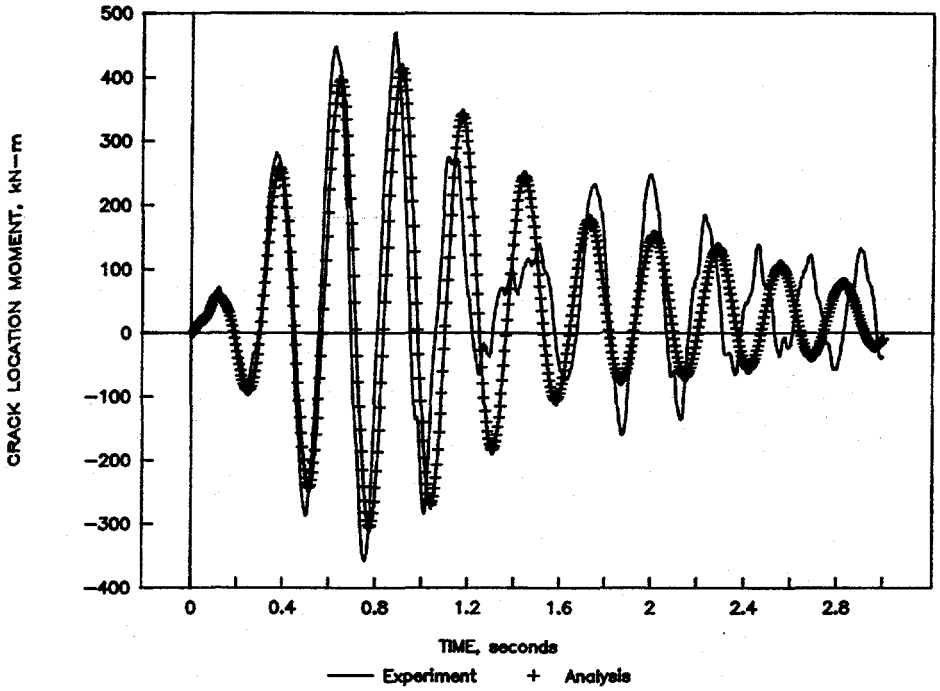

Figure 4.1 Crack location moment for the uncracked room temperature dynamic shake, analysis with 5 percent damping F1.3-10/90-F4.1

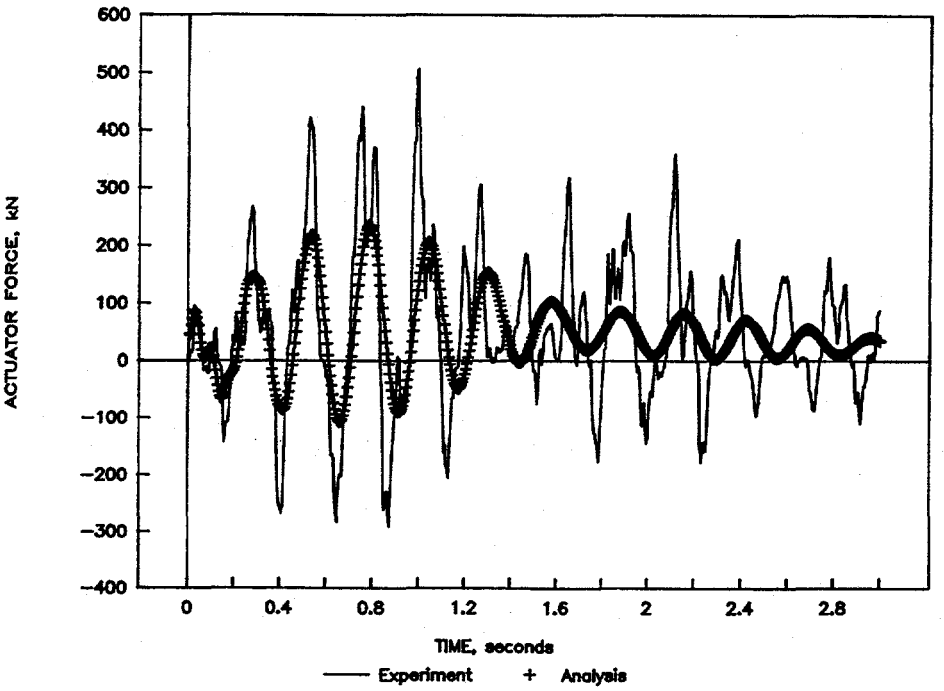

Figure 4.2 Actuator force for the uncracked room temperature dynamic shake, analysis with 5 percent damping F1.3-10/90-F4.2

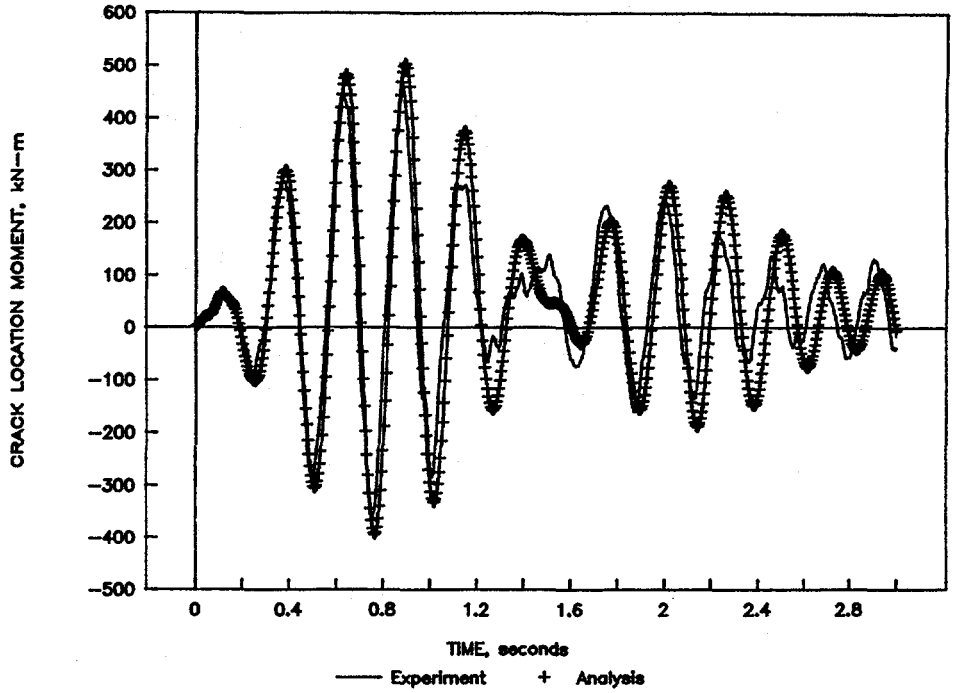

Figure 4.3 Crack location moment for the uncracked room temperature dynamic shake, analysis with 0.5 percent damping F1.3-10/90-F4.3

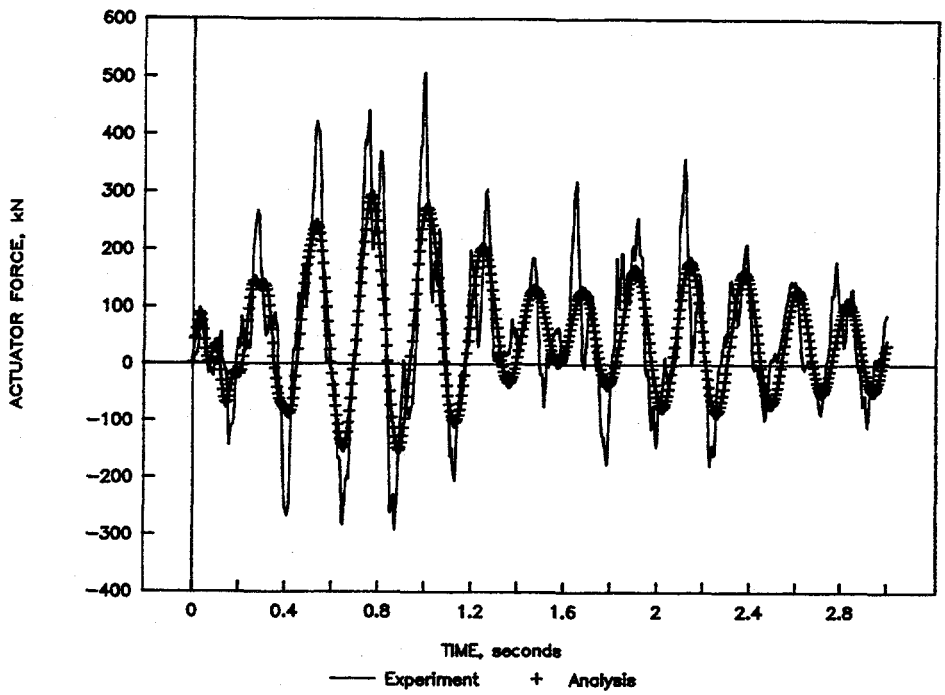

Figure 4.4 Actuator force for the uncracked room temperature dynamic shake, analysis with 0.5 percent damping F1.3-10/90-F4.4

Beyond the fact that the analysis and measurements compare well, both at PWR and pressurized room temperature conditions, the other interesting item in the data in Table 4.2 is the fact that the first natural frequency is substantially the same at room temperature and at PWR temperature. This suggests that there must be offsetting effects from the changes in density of the water and Young's modulus with temperature.

4.3 Elastic Analyses of Cracked Pipe-System Experiments

In the design of nuclear plant piping systems, elastic analysis is used for engineering design purposes. Seismic loads are determined by the response spectrum method which essentially involves modal analysis where typically the seismic anchor motion (SAM)[a] stresses are not included.

If nonlinear behavior occurs, the actual stresses or moments will normally be less than the elastically calculated values. The size of this difference will depend on whether the analysis considers the total stresses, the total stresses minus the seismic anchor motion stresses, or only the inertial stresses.

Recent work in the EPRI/NRC Piping Reliability Program has involved defining the failure mechanism for uncracked pipe subjected to seismic loading (Refs. 4.5, 4.6). These experiments involved either carbon or stainless steel small-diameter pipe tested at ambient temperature. One pipe-system experiment on 152-mm (6-inch) diameter carbon steel produced failure at a load level 34 times greater than that permitted by the ASME Code (Ref. 4.6). They also showed that the failure mechanism was by ratcheting and eventual fatigue, rather than by collapse. This work has resulted in proposed changes to the ASME piping design stress analysis procedures.

In the IPIRG Subtask 1.1 final report on "Stability of Cracked Pipe Under Inertial Stresses", a similar analysis was made of the degree to which the maximum moment calculated using an elastic analysis differed from the experimentally measured maximum moment (Ref. 4.7). This analysis involved a linear-elastic uncracked-pipe calculation for each pipe experiment to determine the maximum moment, and a comparison of these results with the experimental moments at failure. The Subtask 1.1 experiments involved inertial loading of nominal 152-mm (6-inch) diameter pipe with relatively large through-wall cracks (37-percent of the circumference) or large surface cracks (50-percent of the circumference in length and 66-percent of the wall thickness in depth). The experiments were conducted with an internal pressure of 15.5 MPa (2,250 psi) and a temperature of 288 C (550 F). Because the test pipe was a straight section with two actuators in the center and large masses on the ends, see Figure 4.5, there were only pressure, dead-weight, and inertial stresses. There were no thermal expansion stresses or displacement-controlled stresses that would be similar to SAM stresses. A measure of the difference between calculated and measured moments was defined as the moment calculated by an elastic analysis of an uncracked pipe segment, at the same time the experimental maximum moment occurred, divided by the maximum experimental moment. The ratios, for the IPIRG Subtask 1.1 experiments, ranged from 1.07 to 1.8.

(*) SAM stresses arise during a seismic event due to differential displacements of two pipe anchors. These are displacement-controlled stresses rather than inertially controlled stresses.

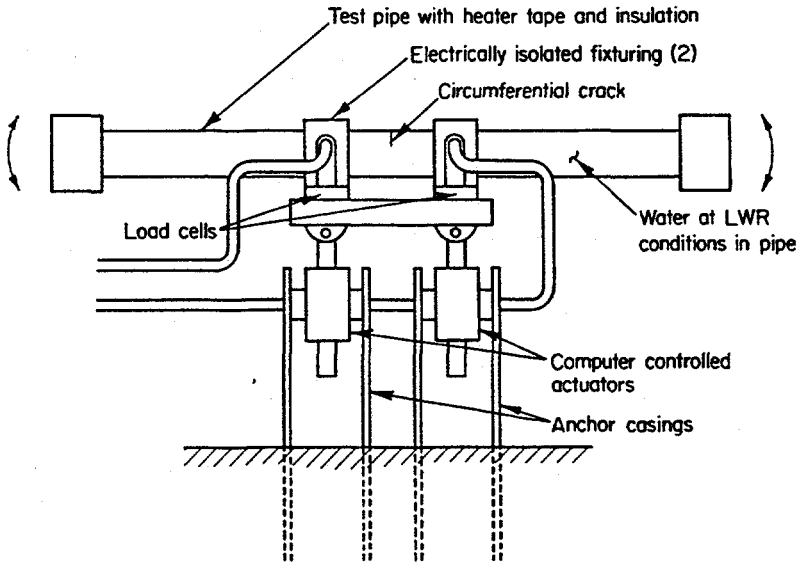

Figure 4.5 Schematic of IPIRG Subtask 1.1 inertial loading pipe system I1.1-8/89-F3.1

These ratios are much lower than those determined in the EPRI/NRC Piping and Fitting Reliability program which conducted experiments on unflawed pipe. In the IPIRG experiments of Subtasks 1.1 and 1.3, nonlinear behavior was intentionally minimized except at the crack plane itself. The close agreement between maximum moments calculated under elastic assumptions and measured maximum moments are, therefore, not necessarily typical of plant piping which may involve significant structural nonlinearities. While the observed modes of failure are completely different for these two programs, it is interesting to compare the calculated-to-measured ratios on the basis of crack size as seen in Figure 4.6. As the crack size is reduced from the sizes considered in the IPIRG experiments, more nonlinear behavior is expected and the ratios are expected to increase. Discontinuous behavior in this graph may be expected if there is a change of failure mode, but as the crack size approaches zero the calculated-to-measured ratio should approach the values observed in the EPRI/NRC program.

Various ways of defining the accuracy of linear elastic stress analyses when compared with measured stresses or moments were discussed in an IPIRG round-robin workshop. The resulting linear elastic stress analysis ratios will be denoted by the acronym ESR, with appropriate identifiers attached. Some of the ratios of calculated to measured quantities used in that workshop were used to evaluate the IPIRG cracked pipe-system experiments. This involved using ANSYS® to determine the elastic stresses for the uncracked pipe system. The experimentally measured displacement history was used as input. The ratios resulting from the elastic stress analysis were determined in the following manner:

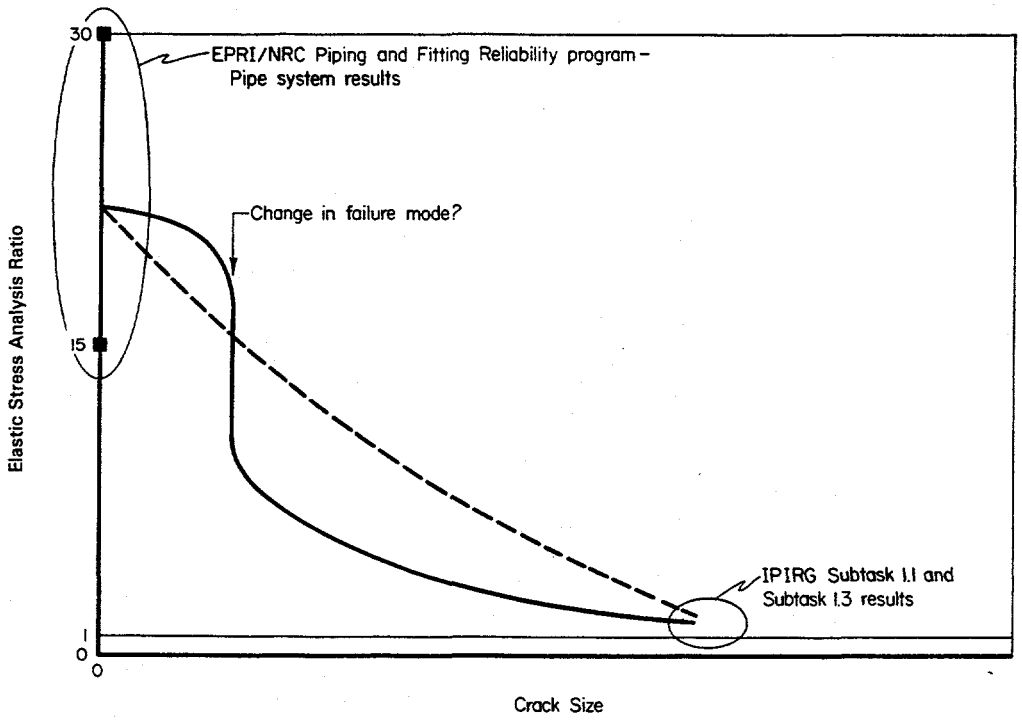

Figure 4.6 Accuracy of elastic stress analyses in predicting experimental stresses F1.3-10/90-F4.6

(1) Total bending moment ratio, $ESR_{(Tot.\ Mom.)}$ Determine the maximum moment, $M_{(Tot.\ el.)}$, that occurs during a dynamic elastic analysis using the measured actuator displacement time history up to the time of maximum experimental moment. Divide this by the experimental maximum moment, $M_{(Tot.\ exp.)}$.

$$ESR_{(Tot.\ Mom.)} = M_{(Tot.\ el.)}/M_{(Tot.\ exp.)} \quad (4\text{-}1)$$

(2) Total stress ratio, ESR(Tot. σ) Using the calculated elastic moments from Case (1), calculate the elastic bending stresses, $\sigma_{(Tot.\ el.\ bend\ \sigma)}$, then add the elastic pressure-induced axial tensile stress, $\sigma_{(ten.)}$, to get the total elastic longitudinal stress. Divide this by the experimental bending stress at maximum bending moment, $\sigma_{(expt.\ bend\ \sigma)}$ plus the pressure-induced axial tensile stress, $\sigma_{(ten.)}$. The denominator is the total experimental stress.

$$ESR_{(Tot.\sigma)} = \frac{\sigma_{(Tot.\ el\ bend\ \sigma)} + \sigma_{(ten)}}{\sigma_{(expt.\ bend\ \sigma)} + \sigma_{(ten)}} \quad (4\text{-}2)$$

where

σ(Tot. el. bend σ) $= M_{(tot.\ el.)}D_o/(2I)$

$\sigma_{(ten.)} = pD_o/(4t)$

$I = \pi(D_o^4 - D_i^4)/64$

D_o = Outside diameter

D_i = Inside diameter

t = Pipe thickness

p = Internal pressure

(3) Total stress minus SAM ratio, $ESR_{(\sigma\text{-SAM})}$ Subtract the seismic anchor motion (SAM) bending stresses from the total calculated elastic stress from Case (2), $\sigma_{(Tot.\ el.)}$, then divide by the experimental total stress, $\sigma_{(Tot.\ expt.)}$. For the analyses of these pipe-system experiments, the SAM stresses are calculated by:

(a) determining the value of the actuator displacement at the time in the experiment corresponding to maximum moment,

(b) applying this actuator displacement to a static linear elastic analysis of the pipe system to determine the seismic anchor motion moment ($M_{(SAM\ el.)}$) and the seismic anchor motion stress, $\sigma_{(SAM\ el.)}$ which equals $M_{(SAM\ el.)}D_o/(2I)$.

Note, the static linear elastic finite element analysis in Step (b) does not include the effects of pressure and temperature. This procedure might be considered as being similar to a stress analysis evaluation (required by ASME Section XI) where SAM stresses are not included, but inertial, pressure, thermal expansion and dead-weight stresses are.

$$ESR_{(\sigma\text{-SAM})} = [\sigma_{(Tot.\ el.)} - \sigma_{(SAM\ el.)}]/\sigma_{(Tot.\ expt.)} \quad (4\text{-}3)$$

where

$$\sigma_{(Tot.\ el.)} = \sigma_{(Tot.\ el.\ bend\ \sigma)} + \sigma_{(ten.)}$$

$$\sigma_{(Tot.\ expt.)} = \sigma_{(expt.\ bend\ \sigma)} + \sigma_{(ten.)}$$

(4) Inertial stress ratio, ESR_I From the calculated elastic total moment, $M_{(Tot.\ el.)}$, subtract the moment due to the seismic anchor motion stresses, thermal expansion stresses, dead-weight stresses, and pressure induced stresses. All of the moments to be subtracted can be determined from a static push analysis at temperature and pressure which is termed $M_{(SP\ el.)}$. The actuator displacement at the time of maximum moment is determined from the experiment as in Case (3). This actuator displacement was used in the static push elastic analysis to get $M_{(SP\ el.)}$. The denominator is the total experimental moment, $M_{(Tot.\ exp.)}$, minus the experimental static push moment, $M_{(SP\ exp.)}$. The $M_{(SP\ exp.)}$ was

measured in the static uncracked pipe experiment and includes pressure and thermal expansion stresses.

$$ESR_I = \frac{M_{(Tot.\ el.)} - M_{(SP\ el.)}}{M_{(Tot.\ exp.)} - M_{(SP\ exp.)}} \quad (4\text{-}4)$$

Note that all of the ratios for elastic stress analyses are ratios of some calculated quantity to its experimental equivalent. Since it is desirable to overpredict the actual stresses, it is desirable for these ratios to be greater than one. Similar ratios will be defined for fracture analyses. However, for the fracture analysis ratios, the ratio of experimental to analytical stresses is used. This is because it is desirable to have the predicted failure stresses lower than the actual failure stresses, in which case the fracture ratios will also be greater than one.

Table 4.3 lists, for each experiment, the values of moment and stress calculated at the instant of experimental maximum moment, using elastic assumptions for each experiment, as well as the experimental moment and stresses, and the various elastic stress ratios. The maximum experimental moments at the test section listed in Table 4.3 were calculated from measured strains using the data reduction procedures described in Appendix B. The elastic finite element results shown in Table 4.3 were calculated with the ANSYS® computer program, using nominal pipe diameter and wall thicknesses throughout the model. The use of nominal values is justified on the basis that most of the pipe was reasonably close to nominal size and that there was good agreement between experimental results and analytical predictions of natural frequencies, static behavior, and dynamic time histories.

The results in Table 4.3 show that the elastic stress ratio for just the inertial stresses, ESR_I, was in general the highest, except for Experiment 1.3-2. This experiment had a large component of SAM stresses. The other ESR_I values are in the range of 1.3 to 2.6. Calculations made by CEA for pure inertial loading of a cracked pipe gave margins ranging from 2 to 3 (Ref. 4.8).

Table 4.3 shows what impact the choice of elastic stress ratio definition can have for these pipe-system experiments. In most cases the variation in margin for a given experiment is roughly a factor of 1.5 (largest ratio divided by the smallest). However, this variation was a factor of 3 for Experiment 1.3-4. It is not immediately clear which elastic-stress-ratio definition is the most appropriate for all cases, and the most suitable choice may depend on the specific application.

The calculated elastic stress ratio is probably most directly influenced by the amount of nonlinear behavior experienced in a particular experiment. Low overall system stresses means that the system remains elastic, the elastic finite element calculations tend to be close to the experimental values, and, therefore, the ESR values are close to unity. Factors which tend to increase stresses and nonlinearities, thereby increasing the ESR values are shallow cracks and/or tougher materials which cause higher stresses in the rest of the piping system.

If we look at the elastic stress ratios for the different materials, we see that the carbon steel base metal experiment had the lowest ratio. This is consistent with arguments presented above, that this experiment had a deep crack and a lower toughness. The carbon steel weld experiment, on the other hand, had a more shallow crack resulting in higher failure loads and a higher ESR. The higher failure loads for the carbon steel weld experiment may also be due to the much higher strength of the weld metal and potential strengthening by the existence of the external weld crown.

Table 4.3 Evaluations of margins resulting from elastic stress analysis for IPIRG pipe-system experiments

Experiment No.	1.3-2	1.3-3	1.3-4	1.3-5	1.3-7
Material	CS Base	SS Base	CS Weld	SS Weld	Cast SS
Experimental results					
$M_{(Tot.\ exp.)}$, kN-m	341.0	426.2	618.4	492.7	590.1
$M_{(SP\ exp.)}$, kN-m	238.1	241.0	442.4	262.3	262.8
Max moment displacement, mm	38.97	39.72	91.00	45.15	45.26
Time to Max. moment, sec.	0.625	2.080	6.670	2.335	2.340
$\sigma_{(expt.\ bend)}$, MPa	125.5	144.8	230.3	170.1	215.9
$\sigma_{(Tot.\ exp.)}$, MPa	186.4	206.4	292.5	232.8	274.2
$\sigma_{(ten.\ exp.)}$, MPa	60.9	61.5	61.2	62.7	58.3
Elastic Calculated Values					
$M_{(Tot.\ el.)}$, kN-m	324.1	591.0	882.1	617.3	676.3
$M_{(SP\ el.)}$, kN-m	233.4	236.3	431.6	257.0	257.4
$\sigma_{(Tot.\ el.\ bend)}$, MPa	116.2	211.8	316.2	221.3	242.4
$\sigma_{(ten.\ el.)}$, MPa	60.0	60.0	60.0	60.0	60.0
$\sigma_{(Tot.\ el.)}$, MPa	176.2	271.9	376.2	281.3	302.5
$\sigma_{(SAM\ el.)}$, MPa	53.2	54.2	124.2	61.6	61.8
$\sigma_{(t=0)}$, MPa[1]	30.5	30.5	30.5	30.5	30.5
Calculated Elastic Stress Analysis Ratios					
$ESR^{(2)}_{(Tot.\ Mom.)}$	0.95	1.39	1.43	1.25	1.15
$ESR_{(Tot.\ \sigma)}$	0.95	1.32	1.29	1.21	1.10
$ESR_{(\sigma\text{-}SAM)}$	0.66	1.05	0.86	0.94	0.88
ESR_I	0.88	1.92	2.56	1.56	1.28

(1) Stresses due to bending only.
(2) ESR = Ratio of calculated to measured moments or stresses.

An attempt has been made to try to understand the accuracy of elastic analyses by calculating one simple independent parameter. It is clear, however, that all of the factors in the experiment--crack geometry, material properties, and forcing function--interact. Further analysis of the data will be required to unravel these interactions and to resolve inconsistencies.

It should be stressed again that certain aspects of these experiments are not typical of what might be expected in plant piping. If the experiments had been conducted with shorter cracks, or if the piping system had been constructed of material having the same strength as the cracked test section, rather than of high strength pipe and elbows, then there would have been more nonlinearities, and the elastic stress analysis ratios may have been much larger. These are factors that are easier to examine analytically than experimentally for a pipe system. However, more data will be needed to evaluate and verify the effects of individual parameters, in particular crack size, on the accuracy of an elastic stress analysis. Data are also needed for pipe and pipe-system experiments having shorter cracks and more nonlinear behavior which would simulate more realistic conditions as found in actual plant piping. The application of such ratios would be useful from the standpoint of both LBB analysis and in-service flaw acceptance criteria at service load levels where the stresses are above yield in the pipe or pipe fittings.

4.4 Fracture Analyses of Cracked Pipe-System Experiments

4.4.1 Pipe-System Experiments

In Section 4.3, we discussed the elastic stress analysis ratios which provide a measure of the accuracy of linear elastic stress analysis as applied to particular cracked pipe experiments. In this section, we will discuss similar measures of the accuracy of failure prediction methodologies. These will be measures on the fracture resistance of the cracked pipe. The predicted failure loads will be compared with the experimental failure loads.

The fracture analysis methodologies evaluated in this section are:

- Net-Section-Collapse (Refs. 4.2 and 4.9),
- Dimensionless Plastic-Zone Screening criterion (Ref. 4.10),
- ASME Section XI flaw evaluation procedures, i.e., IWB-3640 for austenitic pipe and IWB-3650 for ferritic pipe (Refs. 4.11 and 4.12),
- R6 analysis using the Revision 3 Option 1 method (Refs. 4.13, 4.14, and 4.15), and
- J-estimation scheme analyses, i.e., SC.TNP and SC.TKP (Ref. 4.16).

A general note of caution should be kept in mind when conducting such calculations. A common cause of errors in calculated values often occurs from incorrect use of mean radius versus outer radius, and thin shell versus thick shell formulations in calculating bending and axial tension stresses. Such discrepancies can produce differences of up to 8-percent for the pipe size used in this program. For the ASME Section XI flaw evaluation analyses in particular, it is necessary to use thin shell equations with the outer radius rather than mean radius for the axial stress calculation, since that is what the ASME code requires.

In this section, companion pipe fracture experiments conducted under quasi-static loading rates will also be analyzed and compared with the IPIRG pipe-system experiments. These quasi-static experiments were conducted under four-point bending, and were summarized in Section 4.1.

For the analyses of the IPIRG pipe-system experiments, the experimental failure stress comes from the moment determined from the strain gage "moment cell". However, it should be noted that the total experimental stress included the "dynamic" moment or stress calculated from the "moment cell" plus the moment or stress due to temperature, pressure, and dead-weight loads which is a calculated value based on ANSYS®.

4.4.2 Net-Section-Collapse Analyses

The Net-Section-Collapse (NSC) analysis is a limit-load analysis that was first proposed for application to stainless steel pipe with circumferential through-wall cracks (Ref. 4.9). It was subsequently verified for different diameter stainless steel pipes with circumferential surface and through-wall cracks (Ref. 4.2).

The solutions developed in References 4.2 and 4.9 had the following assumptions embedded in their formulation.

(1) The analysis was based on thin shell theory. Thick shell formulations have been developed, but are not used in this report because they do not provide significantly different answers for the Subtask 1.3 pipe geometry.

(2) It was assumed that the pipe remains circular. At high loads the pipe will ovalize, and will lose moment-carrying capacity as documented experimentally (Refs. 4.1 and 4.2). However, analytical corrections to account for this effect do not presently exist. Development of these corrections is one objective of the NRC's "Short Cracks in Piping and Piping Welds" program.

(3) Another limitation in the original Net-Section-Collapse formulation is that pressure contribution on the crack faces is not considered. Pressure corrections exist but have been found to be small for the Subtask 1.3 crack geometries, and, therefore, are not presented in this report.

(4) The material is assumed to be sufficiently tough so that there is negligible crack growth prior to reaching maximum load. The pipe cross section is also assumed to become fully plastic with the net-section stress reaching a constant value. The critical net-section stress at maximum load is called the flow stress.

Several different definitions of flow stress have been used in the Net-Section-Collapse analysis. The most frequently used value is the average of the yield and ultimate strengths. Results from the Degraded Piping Program pipe fracture experiments (Ref. 4.10) have shown that if the flow stress is defined as 1.15 times the average of the yield and ultimate strengths, then the experimental results match the predictions better. The yield and ultimate strength values were the average values from all quasi-static tensile test specimens for the material of interest. Note, in all comparisons made here, only the quasi-static yield and ultimate strength properties are used to determine the flow stress. A discussion of the effect of dynamic properties is found in Section 5.

Another definition of flow stress comes from the ASME Section XI flaw evaluation procedures (Refs. 4.11 and 4.12). Here, the flow stress is defined as $3S_m$ for stainless steels, and $2.4S_m$ for carbon steels, where S_m is the design stress intensity from Section III of the ASME Boiler and Pressure Vessel code. The term S_m(Code) is used in this report when using the S_m values from Section III of the ASME code. In Section III one also has the option to calculate an S_m based on actual properties. This S_m value is referred to as S_m(Actual) in this report. Using S_m(Actual) accounts for material variability, and essentially evaluates every pipe experiment as if the material for that experiment had the ASME Code properties for the pipe experiment temperature.

Although there is a lack of common agreement concerning modifications to the Net-Section-Collapse analysis for either short through-wall cracks (see Refs. 4.2 and 4.17), or for deep surface cracks (see Refs. 4.18 and 4.19), the basic equations given in Appendix F of this report are believed to be reasonably applicable for these pipe experiments since relatively large surface cracks were used.

Tables 4.4(a) and (b) summarize the calculated stresses from the Net-Section-Collapse analysis and the experimental stresses from the stainless steel and carbon steel experiments, respectively. The ratio of the experimental stress to the predicted stress is a measure of the accuracy of the Net-Section-Collapse calculations. Stress is considered to be the sum of the bending and axial stresses.

4.4.2.1 Stainless Steel Pipe Evaluations

Both the dynamic IPIRG experiments and the corresponding quasi-static pipe fracture experiments were evaluated for each material. For the stainless steels, there was a base metal test on wrought TP304, an SAW test with a crack in the center of the weld in the wrought TP304 pipe, and an artificially aged centrifugally cast stainless steel, CF8M. Of these, the quasi-static TP304 base metal test was conducted at room temperature, while the other tests were conducted at 288 C. The lower test temperature affects the relative comparison since $3S_m$ divided by the average of yield and ultimate strength is much lower at room temperature than at 288 C (550 F).

For the weld experiments, the heights of the weld crowns are neglected in determining the pipe thicknesses and the d/t ratios of the flaws.

TP304 Base Metal Experiments

For the TP304 stainless steel base metal pipe experiments, the experimental maximum stresses are below the NSC predicted result for IPIRG pipe Experiment 1.3-3, see Table 4.4(a). For the quasi-static pipe test, the experimental maximum stress is above the NSC predicted values except for the case when the flow stress is defined as 1.15 times the average of the yield and ultimate strengths.

This indicates that the dynamically loaded stainless steel base metal cracked pipe had a lower load-carrying capacity than the quasi-statically loaded pipe. When using the flow stress definition of $3S_m$, the ratio of the measured-to-calculated maximum stress for the dynamic experiments is significantly less than the ratio for the quasi-static tests. This is probably due to the effect of using $3S_m$ as flow stress at room temperature in the quasi-static pipe test.

Table 4.4a Net-Section-Collapse analysis of stainless steel pipe experiments

Material Type Pipe No.	TP304 Base DP2-A8		TP304 SAW DP2-A8W		Aged CF8M DP2-A40	
Loading Rate	**Dynamic**	**QS**	**Dynamic**	**QS**	**Dynamic**	**QS**
Experiment No.	**IPIRG (1.3-3)**	**EPRI (13S RT)**	**IPIRG (1.3-5)**	**DP3-II (4141-4)**	**IPIRG (1.3-7)**	**DP3-II (4143-1)**
D_o, mm	415.8	413.5	416.1	413.5	400.3	399.6
Thickness, mm	26.19	28.32	25.68	26.19	26.59	26.30
θ/π	0.468	0.475	0.440	0.500	0.500	0.500
d/t	0.660	0.660	0.635[a]	0.670[a]	0.533	0.550
$\sigma_{(f1)} = (\sigma_y+\sigma_u)/2$, MPa	318.3	519.2	318.3	318.3	389.5	389.5
$\sigma_{(f2)} = 1.15(\sigma_y+\sigma_u)/2$, MPa	366.1	597.1	366.1	366.1	448.9	447.9
$\sigma_{(f3)} = 3S_m$(Code), MPa	350.4	413.7	350.4	350.4	361.7	361.7
Experimental Values						
Pressure, MPa	15.51	0.000	15.51	11.03	15.51	15.51
Expt. Moment, kN-m	425.9	1260.4	493.1	501.5	589.8	672.1
Calculated Values						
Axial stress, MPa	50.21	0.000	51.46	35.46	47.02	47.48
Expt. σ_b, MPa	144.9	407.7	170.1	172.7	215.4	248.3
Predicted $\sigma_b(1)$, MPa	177.7	389.7	195.8	183.9	293.2	283.9
Predicted $\sigma_b(2)$, MPa	214.9	448.1	235.4	218.7	345.6	335.2
Predicted $\sigma_b(3)$, MPa	203.4	310.5	223.4	208.1	267.8	259.1
Ratio of Experimental to Calculated Stresses						
Experimental/NSC(1)[b]	0.856	1.046	0.897	0.949	0.771	0.893
Experimental/NSC(2)[b]	0.736	0.910	0.773	0.819	0.668	0.773
Experimental/NSC(3)[b]	0.769	1.313	0.806	0.855	0.834	0.965

(a) d/t without including height of weld crown.
(b) (Experimental bending stress + axial stress)/(Predicted bending stress + axial stress).

Table 4.4b Net-Section-Collapse analysis of carbon steel pipe experiments

Material Type Pipe No.	A106B Base DP2-F29		A106B SAW DP2-F29W	
Loading Rate	**Dynamic**	**QS**	**Dynamic**	**QS**
Experiment No.	**IPIRG (1.3-2)**	**DP3-II (4112-8)**	**IPIRG (1.3-4)**	**DP3-II (4141-8)**
D_o, mm	403.9	402.6	402.6	403.2
Thickness, mm	25.71	26.42	25.48	25.37
θ/π	0.438	0.532	0.480	0.500
d/t	0.727	0.662	0.691[a]	0.670[a]
$\sigma_{(f1)} = (\sigma_y+\sigma_u)/2$, MPa	423.4	423.4	423.4	423.4
$\sigma_{(f2)} = 1.15(\sigma_y+\sigma_u)/2$, MPa	486.9	486.9	486.9	486.9
$\sigma_{(f3)} = 2.4\ S_m$(Code), MPa	299.3	299.3	299.3	299.3
Experimental Values				
Pressure, MPa	15.51	0.000	15.51	15.51
Expt. Moment, kN-m	341.0	748.2	618.0	594.0
Calculated Values				
Axial stress, MPa	49.56	0.000	49.92	50.25
Expt. σ_b, MPa	125.5	271.4	230.6	222.0
Predicted $\sigma_b(1)$, MPa	239.9	299.5	238.5	241.6
Predicted $\sigma_b(2)$, MPa	285.8	344.5	284.5	288.2
Predicted $\sigma_b(3)$, MPa	149.0	211.6	147.3	149.3
Ratio of Experimental to Calculated Stresses				
Experimental/NSC(1)[b]	0.605	0.906	0.973	0.932
Experimental/NSC(2)[b]	0.522	0.788	0.839	0.804
Experimental/NSC(3)[b]	0.882	1.283	1.423	1.364

(a) d/t without including height of weld crown.
(b) (Experimental bending stress + axial stress)/(Predicted bending stress + axial stress).

Stainless Steel SAW Experiments

For the SAW stainless steel pipe experiments, the base metal strength properties were used. Table 4.4(a) shows that the experimental maximum stress is below the NSC predicted results for both the dynamic and quasi-static experiments for all definitions of flow stress.

The ratios for the dynamic experiments are slightly less than the quasi-static ratios. This indicates that the dynamically loaded, stainless steel, weld-metal-cracked pipe had slightly lower load-carrying capacity than the quasi-statically loaded pipe.

Cast Stainless Steel Experiments

For the aged-cast-stainless-steel pipe experiments, the experimental maximum stress is below the NSC predicted results for the dynamic experiment. The quasi-static test results are also below the NSC predicted values.

The ratio of experimental maximum stress to NSC predicted maximum stress is seen to be consistently lower for the dynamic test than those for the quasi-static experiment. This also indicates that the dynamically loaded aged-cast stainless steel pipe had a lower load-carrying capacity than the quasi-statically loaded pipe.

Summary of NSC Comparisons for Stainless Steel Pipe Experiments

With the exception of the room temperature base metal quasi-static experiment (EPRI 13S), the Net-Section-Collapse analysis consistently overpredicted the maximum experimental stress. This is not unexpected since the SAW and aged cast stainless steels may be low enough in toughness that a predictive analysis approach based on elastic-plastic fracture mechanics is needed rather than Net-Section-Collapse analysis.

The results showed that the wrought stainless steel had a lower load-carrying capacity at the dynamic loading rate of the IPIRG pipe-system experiments than at the quasi-static rate. This was also true for the aged cast stainless steel pipe. The SAW pipe experiment showed only slight differences at the IPIRG pipe-system dynamic loading rate than at the quasi-static loading rate.

4.4.2.2 Carbon Steel Pipe Evaluations

There were two pairs of carbon steel pipe experiments. One was for a surface crack in the A106 Grade B pipe base metal, while the other pair of experiments were for a similar crack in a low toughness carbon steel SAW. These materials were used in an IPIRG pipe-system test and in a Degraded Piping Program quasi-static pipe bend test.

The quasi-static properties for the A106B base metal were used to determine the flow stress for both the base metal and the weld metal tests. The height of the weld crown was ignored in the weld metal test.

A106 Grade B Experiments

For both experiments, the experimental maximum stress is considerably lower than the NSC predicted failure stress when using actual properties, see Table 4.4(b). This is not unexpected in that the toughness

of this material is sufficiently low that fully plastic conditions would not exist, and thus, the Net-Section-Collapse analysis would not be appropriate. When using the ASME definition of flow stress, $2.4S_m$, the measured quasi-static pipe test failure loads are less than the predicted values. This is due to the actual properties of this steel being well above the Code minimum values.

The ratios of measured-to-calculated maximum stress are considerably lower for the dynamic IPIRG experiment than they are for the quasi-static test. This relative disagreement may be reflective of the lower strength and toughness of this A106B material at seismic loading rates, see Section 2 of this report.

Carbon Steel SAW Experiments

For the carbon steel SAW pipe-system experiment, IPIRG Experiment 1.3-4, the experimental failure stresses are lower than the NSC predicted values when using actual properties to define the flow stress, see Table 4.4(b). When using the flow stress definition of $2.4S_m$, the predictions of the maximum load are underpredicted. The relative comparison of the dynamic IPIRG pipe-system test result with the quasi-static test result shows the IPIRG pipe test failed at a slightly higher stress than the companion quasi-static pipe fracture experiment.

Summary of NSC Comparisons for Carbon Steel Pipe Experiments

These results show that the carbon steel SAW cracked pipe had a higher load-carrying capacity than the base metal cracked pipe. This is somewhat surprising since the weld metal fracture toughness is lower than the base metal toughness at quasi-static rates. However, the weld metal fracture toughness is greater than the base metal toughness at dynamic rates (see Tables 2.10 and 2.12). In addition, the yield and ultimate strengths are considerably higher for the weld metal than the base metal, perhaps indicating that the weld strength should be taken into account in some manner. Such an evaluation is a subject of the U.S. NRC's "Short Cracks in Piping and Piping Welds" program (Ref. 4.20).

Another important difference is that the base metal load-carrying capacity was decreased significantly by the dynamic loading rates in the pipe-system test; whereas, the SAW showed a slightly higher load-carrying capacity at the higher loading rates.

4.4.2.3 Dimensionless Plastic-Zone Screening Criterion

In order to identify cases where fully plastic conditions exist (that is, where the NSC analysis should be appropriate), a Dimensionless Plastic-Zone Screening Criterion has been developed as part of the Degraded Piping Program (Ref. 4.10). The Dimensionless Plastic-Zone Screening Criterion is a semi-empirical relationship in which the ratio of the maximum predicted stress to the calculated NSC stress is a function of a Dimensionless Plastic-Zone Parameter (DPZP). The DPZP is the ratio of the plastic-zone size, using Irwin's relationship, to the distance from the crack tip to the neutral axis. This relationship is shown in Figure 4.7 with a large amount of experimental data. In this figure, the NSC stress is based on a flow stress equal to the average of the actual yield and ultimate strengths of the materials.

Four curves are shown in Figure 4.7, where the relationship between the ratio of the experimental stress to the predicted NSC stress and the DPZP is given below.

$$P/P_{nsc} = (2/\pi) \arccos (e^{-C(DPZP)}) \qquad (4\text{-}5)$$

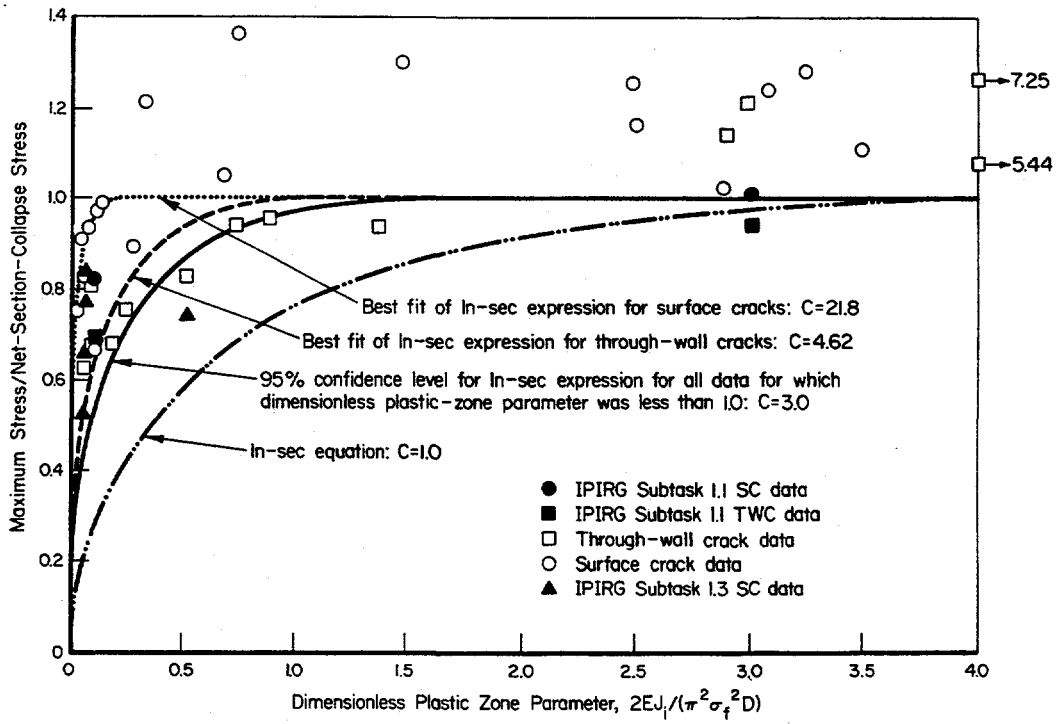

Figure 4.7 Schematic showing comparison of IPIRG pipe fracture data to Degraded Piping Program data using Dimensionless Plastic-Zone Parameter [$\sigma_f = (\sigma_y+\sigma_u)/2$ for all data] F1.3-10/90-F4.7

where,

$$DPZP = 2EJ_i/(\pi^2\sigma_f^2D) \quad (4\text{-}6)$$

P = total failure stress
P_{nsc} = NSC predicted tension and bending stress
E = elastic modulus
J_i = J at crack initiation (may be J_{Ic})
σ_f = flow stress = $(\sigma_y + \sigma_u)/2$
D = nominal pipe diameter
C = statistically based parameter

The factor "C" was selected based on a statistical fit of the pipe fracture data. The three upper curves in Figure 4.7 are for different values of "C" based on three different statistical fits of the data. The solid curve shows a 95-percent confidence level curve for all the data for which the DPZP was less than one.

The value of "C" for this curve is 3.0. For the best fit of the through-wall-cracked pipe and surface-cracked pipe data, the values of C were statistically determined to be 4.62 and 21.8, respectively.

The predicted maximum bending stresses from the Dimensionless Plastic-Zone Parameter analysis are presented in Tables 4.5(a) and 4.5(b) for the stainless and carbon steel experiments, respectively. A value of 21.8 for C was used for these analyses. The ratio of the experimental-to-predicted stress is the measure of accuracy for this fracture analysis. Stress is considered to be the sum of the bending stress and axial stress.

4.4.2.4 Stainless Steel Pipe Evaluations

For the three IPIRG stainless steel pipe-system experiments, the values of the DPZP are 0.654, 0.049, and 0.054 for the TP304 base metal, SAW weld, and aged cast stainless steels, respectively. With the exception of the TP304 base metal experiment (EPRI 13S), values for the three quasi-static pipe tests are similar. The DPZP for the quasi-static TP304 base metal experiment was 0.758 due to the higher toughness of this material at ambient temperature. These calculations were made using the quasi-static material properties. Since the DPZP values are less than one, Net-Section-Collapse conditions should not necessarily be satisfied. Using a value for C of 21.8 (best fit of the surface cracked pipe data), results in the predicted-to-NSC ratios, P/P_{NCS}, shown in Table 4.5(a). These values are 1.00 for both TP304 base metal experiments, 0.78 for both weld metal experiments, and 0.80 for both cast stainless steel experiments.

As shown in Table 4.5(a), the ratios of the experimental-to-predicted failure stress are close to or larger than one for all cases except the IPIRG base metal cracked-pipe experiment. In each case the ratio is less for the dynamic pipe system test than for the quasi-static test. This trend is consistent with the NSC evaluations.

4.4.2.5 Carbon Steel Pipe Evaluations

For the IPIRG carbon steel pipe-system experiments, the values of the DPZP are 0.07 and 0.045 for the A106 Grade B base metal and SAW experiments, respectively. Values for the two quasi-static pipe tests are similar. These values were calculated using the quasi-static tensile test and the quasi-static, monotonically loaded, C(T)-specimen, J_i values. Since the DPZP values are less than one, Net-Section-Collapse conditions should not necessarily be satisfied. Using C = 21.8 as previously for the stainless steel experiments, the DPZP predicted-to-NSC stress ratios were determined to be 0.86 for the base metal and 0.75 for the SAW experiments. These predictions are given in Table 4.5(b).

The experimental-to-predicted failure stress ratios were significantly below one (0.704) for the dynamic IPIRG A106 Grade B base metal experiment, and slightly above one (1.053) for the companion quasi-static pipe test, (4112-8). As was noted for the Net-Section-Collapse analysis, this is perhaps reflective of the lower toughness and strength at dynamic loading rates for this A106 Grade B pipe.

For the carbon steel SAW, the experimental-to-predicted failure stress ratios were well above one for both the dynamic and quasi-static experiments. As with the NSC evaluation, the SAW displays a higher load-carrying capacity than comparable cracks in the base metal even though the base metal thoughness is

Table 4.5a DPZP analysis of stainless steel pipe experiments

Material Type Pipe Number	TP304 Base DP2-A8		TY304 SAW DP2-A8W		Aged CF8M DP2-A40	
Loading Rate	**Dynamic**	**QS**	**Dynamic**	**QS**	**Dynamic**	**QS**
Experiment No.	**IPIRG (1.3-3)**	**EPRI (13S RT)**	**IPIRG (1.3-5)**	**DP3-II (4141-4)**	**IPIRG (1.3-7)**	**DP3-II (4143-1)**
D_o, mm	415.8	413.5	416.1	413.5	400.3	399.6
Thickness, mm	26.19	28.32	25.68	26.19	26.59	26.30
$\theta\pi$	0.468	0.475	0.440	0.500	0.500	0.500
d/t	0.660	0.660	0.635[a]	0.670[a]	0.533	0.550
$\sigma_f = (\sigma_y+\sigma_u)/2$, MPa	318.3	519.2	318.3	318.3	389.5	389.5
J_i, kJ/mm^2	738.9	2,278.8	55.0	55.0	88.00	88.00
E, GPa	183.0	183.0	183.0	183.0	183.0	183.0
Experimental Values						
Pressure, MPa	15.51	0.000	15.51	11.03	15.51	15.51
Expt. Moment, kN-m	425.9	1,260.4	493.1	501.5	589.8	672.1
Calculated Values						
Axial stress, MPa	50.21	0.000	51.46	35.46	45.94	46.46
Expt. σ_b, MPa	144.9	407.7	170.1	172.7	215.4	248.3
DPZP	0.654	0.758	0.049	0.049	0.054	0.054
P/P_{nsc}[b]	1.000	1.000	0.776	0.778	0.799	0.799
Predicted σ_b, MPa	177.7	389.7	140.3	135.1	225.8	218.4
Ratio of Experimental to Calculated Stresses						
Experimental/Predicted[c]	0.856	1.046	1.156	1.220	0.962	1.114

(a) d/t without including height of weld crown.
(b) Value of C = 21.8 for average surface crack predictions.
(c) (Experimental bending stress + axial stress)/(Predicted bending stress + axial stress).

Table 4.5b DPZP analysis of carbon steel pipe experiments

Material Type Pipe No.	A106B Base DP2-F29		A106B SAW DP2-F29W	
Loading Rate	**Dynamic**	**QS**	**Dynamic**	**QS**
Experiment No.	**IPIRG (1.3-2)**	**DP3-II (4112-8)**	**IPIRG (1.3-4)**	**DP3-II (4141-8)**
D_o, mm	403.9	402.6	402.6	403.2
Thickness, mm	25.71	26.42	25.48	25.37
$\theta\pi$	0.438	0.532	0.480	0.500
d/t	0.727	0.662	0.691[a]	0.670[a]
$\sigma_f = (\sigma_y+\sigma_u)/2$, MPa	423.4	423.4	423.4	423.4
J_i, kJ/mm^2	129.4	129.4	82.0	82.0
E, GPa	193.0	193.0	193.0	193.0
Experimental Values				
Pressure, MPa	15.51	0.000	15.51	15.51
Expt. Moment, kN-m	341.0	748.2	618.0	594.0
Calculated Values				
Axial stress, MPa	49.56	0.000	49.92	50.20
Expt. σ_b, MPa	125.5	271.4	230.1	221.6
DPZP	0.070	0.070	0.045	0.045
P/P_{nsc}[b]	0.860	0.861	0.753	0.752
Predicted σ_b, MPa	199.3	257.7	166.8	169.1
Ratio of Experimental to Calculated Stresses				
Experimental/Predicted[c]	0.704	1.053	1.292	1.239

(a) d/t without including height of weld crown.
(b) Value of C = 21.8 for average surface crack predictions.
(c) (Experimental bending stress + axial stress)/(Predicted bending stress + axial stress).

higher than the weld metal toughness at quasi-static loading rates. The higher load-carrying capacity for the SAW may be due to the higher strength of the weld metal which is not accounted for in the analysis.

The base metal evaluations show a significantly lower ratio of experimental-to-predicted failure stress for the dynamic pipe-system experiment than for the quasi-static test. However, in the SAW the dynamic ratio is slightly greater than the quasi-static ratio. This is consistent with the comparisons using the NSC evaluation.

4.4.3 ASME Section XI Flaw Evaluation Procedures

Within Section XI of the ASME Boiler and Pressure Vessel Code, flaw evaluation procedures for cracks in austenitic and ferritic piping have been developed. The austenitic pipe flaw evaluation procedures are in Article IWB-3640 and Appendix C. These were developed first in 1985, and have been modified to include procedures for evaluation of cracks in lower toughness welds (Refs. 4.11 and 4.21).

The ferritic pipe flaw evaluation procedures are given in the ASME Code as Appendix H (Ref. 4.12) as well as Article IWB-3650.

4.4.3.1 Stainless Steel Pipe Evaluations

The ASME flaw evaluation procedure for cracks in stainless steel base metal are essentially the same as the Net-Section-Collapse analysis procedure, previously discussed in this report. The major differences between these two analysis procedures are:

- The flow stress is defined as $3S_m$ in the ASME code rather than the average of yield and ultimate strength,
- For flux welds, i.e., SAW and SMAW, the ASME procedure uses a Z-factor to account for the toughness being much lower than the base metal.
- For combined tension and bending, the Net-Section-Collapse analysis and the ASME Code use slightly different expressions to calculate the shift in the neutral axis, i.e., the β terms differ slightly, see Equations 4.7a and 4.7b.

For the ASME analysis,

$$\beta = 0.5(\pi - \theta d/t - \pi P_m/\sigma_f) \qquad (4\text{-}7a)$$

and for the Net-Section-Collapse analysis,

$$\beta = 0.5[\pi - \theta d/t - \pi R_i^2 p/(2R_m t\sigma_f)] \qquad (4\text{-}7b)$$

Using the ASME β term for the pressurized pipe experiments in this analysis lowers the predicted failure stress approximately 5 percent below the Net-Section-Collapse predicted failure stress when both analyses use the same flow stress and a Z-factor of 1.

Table 4.6(a) gives the ratio of the experimental maximum stress to the maximum stress predicted by the ASME Section XI IWB-3640 analysis procedure using the exact pipe and crack dimensions. These results do not include the ASME safety factors of 2.78 for normal and test conditions, or the 1.39 safety factor for emergency and faulted loads.

Calculations of the predicted failure stress were made using the S_m definition of flow stress in two different manners for distinctly different reasons.

The first definition of flow stress involved using the S_m defined from Tables I-1.1 and I-1.2 of Section III in the ASME Code. This provides a direct comparison of the experiments to the ASME Code procedures.

The second definition of the flow stress was created to evaluate the technical basis of the Code and is an attempt to analyze the pipes as if they had the properties defined in Section III from the ASME Code. In this program we did not try to procure pipes with Code properties. To account for our pipe having a higher strength than the Code values, an S_m value was calculated using the actual (quasi-static) properties of the pipe tested. The term S_m(Actual) was defined in the spirit of ASME Section III Article 2110 as the lowest of:

(1) one-third of the actual room temperature ultimate tensile strength (for both ferritic and austenitic pipes)

(2) one-third of the actual ultimate strength at the pipe test temperature (for both ferritic and austenitic pipes)

(3) two-thirds of the actual yield at room temperature (for both ferritic and austenitic pipe)

(4) two-thirds of the actual yield strength at the pipe test temperature (for only ferritic pipes), or 90 percent of the actual yield strength at the pipe test temperature (for only austenitic pipes).

For the A106 Grade B pipe and weld experiments, Condition 4 governed the determination of S_m(Actual). For the TP304 stainless steel base metal and welded pipe experiments at 288 C, Condition 2 governed. However for the room temperature TP304 quasi-static test, Condition 3 governed the determination of S_m(Actual). For the aged cast stainless steel, the actual aged properties were used, and Condition 4 governed the determination of S_m(Actual).

Using this definition of S_m(Actual) accounts for material variability, and essentially evaluates every pipe experiment as if the test pipe had ASME Code properties.

Table 4.6a ASME Section XI IWB-3640 analysis of stainless steel pipe experiments

Material Type Pipe No.	TP304 Base DP2-A8		TP304 SAW DP2-A8W		Aged CF8M DP2-A40	
Loading Rate	**Dynamic**	**QS**	**Dynamic**	**QS**	**Dynamic**	**QS**
Experiment No.	**IPIRG (1.3-3)**	**EPRI (13S RT)**	**IPIRG (1.3-5)**	**DP3-II (4141-4)**	**IPIRG (1.3-7)**	**DP3-II (4143-1)**
D_o, mm	415.8	413.5	416.1	413.5	400.3	399.6
Thickness, mm	26.19	28.32	25.68	26.19	26.59	26.30
$\theta\pi$	0.468	0.475	0.440	0.500	0.500	0.500
d/t	0.660	0.660	0.635[a]	0.670[a]	0.533	0.550
$\sigma_f = 3S_m$(Code), MPa	350.4	413.7	350.4	350.4	361.7	361.7
$\sigma_f = 3S_m$(Actual)[b], MPa	453.1	589.3	453.1	453.1	543.2	543.2
Experimental Values						
Pressure, MPa	15.51	0.000	15.51	11.03	15.51	15.51
Expt. Moment, kN-m	425.9	1,260.4	493.1	501.5	589.8	672.1
Calculated Values						
Axial stress, MPa	61.6	0.000	62.8	43.5	58.4	58.9
Expt. σ_b, MPa	144.9	407.7	170.2	172.7	215.4	248.3
Z-factor	1.000	1.000	1.560	1.560	1.000[d]	1.000[d]
Predicted σ_b, $3S_m$(Code), MPa	176.5	290.7	103.1	103.3	237.9	229.2
Predicted σ_b, $3S_m$(Actual), MPa	252.3	414.3	155.0	148.7	391.4	379.7
Ratio of Experimental to Calculated Stresses						
Experimental/Predicted [$3S_m$(Code)][c]	0.867	1.402	1.404	1.473	0.924	1.066
Experimental/Predicted [$3S_m$(Actual)][c]	0.658	0.984	1.070	1.125	0.609	0.700

(a) d/t without including height of weld crown.
(b) S_m(Actual) = lower of $\sigma_u/3$ at room temperature, $\sigma_u/3$ at 288 C, $2\sigma_y/3$ at room temperature, or $0.9\sigma_y$ at 288C.
(c) (Experimental bending stress + axial stress)/(Predicted bending stress + axial stress).
(d) Assumed since values not given for aged cast stainless steel in Reference 4.11.

Table 4.6b ASME Section XI analysis of carbon steel pipe experiments

Material Type Pipe No.	A106B Base DP2-F29		A106B SAW DP2-F29W	
Loading Rate	**Dynamic**	**QS**	**Dynamic**	**QS**
Experiment No.	**IPIRG (1.3-2)**	**DP3-II (4112-8)**	**IPIRG (1.3-4)**	**DP3-II (4141-8)**
D_o, mm	403.9	402.6	402.6	403.2
Thickness, mm	25.71	26.42	25.48	25.37
$\theta\pi$	0.438	0.532	0.480	0.500
d/t	0.727	0.662	0.691[a]	0.670[a]
$\sigma_f = 2.4S_m$(Code), MPa	299.3	299.3	299.3	299.3
$\sigma_f = 2.4S_m$(Actual)[b], MPa	379.0	379.0	379.0	379.0
Experimental Values				
Pressure, MPa	15.51	0.000	15.51	15.51
Expt. Moment, kN-m	341.0	748.2	618.0	594.0
Calculated Values				
Axial stress, MPa	60.9	0.000	61.3	61.6
Expt. σ_b, MPa	125.6	271.4	230.8	221.8
Z-factor	1.473	1.473	1.620	1.620
Predicted σ_b, $2.4S_m$(Code), MPa	64.7	134.9	52.0	53.0
Predicted σ_b, $2.4S_m$(Act.)[b], MPa	102.7	170.8	86.6	88.1
Ratio of Experimental to Calculated Stresses				
Experimental/Predicted[$2.4S_m$(Code)][c]	1.484	2.012	2.579	2.475
Experimental/Predicted[$2.4S_m$(Actual)][c]	1.140	1.589	1.975	1.893

(a) d/t without including height of weld crown.
(b) S_m(Actual) = lower of $\sigma_u/3$ at room temperature, $\sigma_u/3$ at 288 C, $2\sigma_y/3$ at room temperature, or $2\sigma_y/3$ at 288 C.
(c) (Experimental bending stress + axial stress)/(Predicted bending stress + axial stress).

For the weld experiment, the base metal S_m values are used. Also for the weld experiment, the Z-factor was calculated to be 1.56, which acts as a stress multiplier to account for failure at lower loads resulting from the lower toughness of the SAW. The Z-factor is determined from the following equations from the Code case.

For NPS $\geq$ 24

$$Z = 1.30\,[1 + 0.010(\text{NPS} - 4)] \text{ and} \qquad (4\text{-}8a)$$

For NPS < 24

$$Z = 1.56 \qquad (4\text{-}8b)$$

where,

NPS = nominal pipe size (diameter), inches.

The ASME Code for austenitic pipe flaw evaluations requires that, if the pipe is less than 24 inches in diameter, the Z-factor be based on a diameter of 24 inches rather than the actual smaller diameter. The Z-factor for 24-inch diameter pipe is 1.56 and was used in the analysis of these experiments. Note that the Z-factor is applied to the bending stress as well as pressure-induced axial stress.

As with the Net-Section-Collapse and DPZP analyses, the measure of accuracy for predicted failure stresses is the ratio of experimental-to-predicted failure stress. Stress is considered to be the sum of bending and axial stress.

TP304 Base Metal Experiments

For the stainless steel base metal pipe experiments, the IPIRG Experiment 1.3-3 experimental maximum stress was below the ASME Code predictions. The quasi-static pipe test, conducted at room temperature, had experimental failure stresses well above the predicted failure stresses when using $3S_m$(Code). When the actual properties are used to determine the S_m values, the ratios of experimental-to-calculated stresses drop considerably and even the quasi-static test gives a ratio that is slightly less than one.

Also note, that the IPIRG dynamic pipe-system test had a much lower failure stress than the quasi-static pipe test. This is mainly due to the fact that the quasi-static experiment was conducted at room temperature.

Stainless Steel SAW Experiments

For the SAW pipe experiments, both the dynamic and quasi-static test predictions produce ratios of experimental-to-calculated stress greater than one. The dynamic ratios are very close to the quasi-static values.

Cast Stainless Steel Experiments

The ASME Section XI analysis procedure is the same for the cast stainless steel as the wrought stainless steel since the ferrite number for the cast stainless is less than 20. When using the Code definition of S_m, the experimental failure stress is slightly lower than the predicted value for the dynamic IPIRG test. But, the experimental value is slightly higher than predicted for the quasi-static test. Once again, the dynamic ratio of experimental-to-predicted stress is slightly lower than the quasi-static ratio.

If, on the other hand, the actual properties are used to define an S_m(Actual) for the calculations, then the failure stresses are considerably overpredicted. Note, that the actual flow stress is well above the Code value. Also note, that the aged strength properties at quasi-static rates were used to determine S_m(Actual). According to tests by Framatome, who aged this material, the aging raised the yield strength by approximately 7 percent, see Reference 4.22. However, this 7-percent increase accounts for only a small amount of the difference between the S_m(Code) and S_m(Actual) values.

4.4.3.2 Carbon Steel Pipe Evaluations

The ASME ferritic pipe flaw evaluation procedure is similar to the austenitic procedure. However, it is slightly more complicated than the austenitic procedure to account for failure being below Net-Section-Collapse stresses for a flaw in the base metal. The major differences between the ASME ferritic pipe flaw evaluation procedure and the Net-Section-Collapse analysis are:

- The flow stress used for ferritic pipe is $2.4S_m$ in the ASME Code.
- For combined tension and bending, the Net-Section-Collapse analysis and the ASME β terms differ slightly, see Equations 4-7a and 4-7b.
- In the ASME procedure there is a screening criterion used to assess if limit-load, elastic-plastic fracture, or linear-elastic fracture analyses should be used.
- There is a simple stress multiplier used for the elastic-plastic analysis method to account for the lower toughness.

The stress multiplier, Z, used for a crack in the base metal (Material Category 1 for base metals and SMAWs in Reference 4.12) is

$$Z = 1.20[1 + 0.021A(NPS - 4)] \quad (4\text{-}9)$$

where

$A = [0.125(R_m/t) - 0.25]^{0.25}$ for $5 \le R_m/t \le 10$, or
$A = [0.4(R_m/t) - 3.0]^{0.25}$ for $10 < R_m/t \le 20$,
R_m = mean pipe radius,
t = pipe thickness, and
NPS = nominal pipe size (diameter), inches.

The lower limit for the pipe diameter for the ferritic pipe flaw evaluation code is 4 inches. Hence the nominal pipe diameter of 16 inches was used. (This is different than the IWB-3640 procedure which requires the use of a Z-factor for 24-inch-diameter pipe if the pipe is smaller than 24 inches in diameter.) For the pipe in this effort, the R_m/t is approximately 7.4. Hence, A is approximately 0.904 and Z is 1.473 for the base metal experiment.

For a ferritic SAW, Material Category 2 in the Code case, the Z-factor is defined by

$$Z = 1.35[1 + 0.0184A(NPS - 4)] \quad (4\text{-}10)$$

The Z-factor for the SAW tests is 1.620.

A106B Base Metal Experiments

The predicted ASME failure stresses, without the ASME safety factors, are given in Table 4.6(b). For the base metal experiments, the ASME approach using S_m(Code) gives much lower calculated failure stresses than measured in the experiments, with the experimental values being approximately 1.5 higher for the dynamic IPIRG experiment and 2.0 higher for the quasi-static experiment.

If S_m(Actual) is used to predict the failure stresses, then the ratios of experimental-to-calculated stresses are considerably lower. However, these ratios for both the dynamic IPIRG experiment and quasi-static Degraded Piping Program experiment are still above one.

A106B SAW Experiments

For the carbon steel SAW experiments, failure stresses are significantly greater than the ASME IWB-3650 predicted maximum stresses. This was true for both the dynamic IPIRG and the quasi-static Degraded Piping Program Experiments. In fact, the actual carbon steel SAW failure stresses (bending plus axial) are higher than the A106B base metal failure stresses. If the actual properties of the base metal are used to calculate an S_m(Actual), the ratios of experimental-to-calculated stresses are still significantly greater than one.

4.4.3.3 Summary of ASME Code Evaluations

These results show that the ratios of experimental-to-calculated stresses, using the ASME IWB-3650 flaw evaluation analysis procedure for ferritic pipe, can be significant. For the austenitic pipe IWB-3640 procedures, the ratios are high for the SAW, but significantly lower for base metal cracks in the TP304 stainless steel and the aged cast stainless steel.

Predictions of failure stress using an S_m from the actual properties at the test temperature show that the dynamic IPIRG experiments on stainless steel base metal cracks fail at significantly lower failure stresses than calculated.

Although the use of a calculated S_m(Actual) is probably not used in practice, this exercise supports the practice of not using S_m(Actual). Furthermore, these results suggest the past stainless steel pipe fracture data base should be re-examined using the S_m(Actual) approach. Since this approach analyzes the pipe experiments as if all experiments have the Code lower-bound properties, this evaluation could impact changes in the ASME IWB-3640 flaw evaluation analysis.

4.4.4 R6 Analysis Using The Revision 3 Option 1 Method

The R6 method is a fracture prevention design criterion developed by CEGB (Refs. 4.13, 4.14 and 4.15). The most recent refinement is referred to as R6 Revision 3 (Ref. 4.15). Within this version there are three options. The first option is the simplest, and does not require the use of the material stress-strain curve input. The second option requires the use of the material stress-strain curve, and hence is slightly more complicated. The third option allows the use of any appropriate elastic-plastic fracture mechanics analysis,

e.g., the EPRI/GE method, to create the appropriate failure assessment curve. In this last option, the R6 method essentially would give the same predictions as the J-estimation scheme analysis given in Section 4.4.5 of this report. For the R6 analysis in this section, predictions using the Option 1 method will be compared with the experimental results. As with the previous analysis methods discussed, the ratio of the experimental-to-predicted failure stresses is the inherent margins for this fracture analysis.

4.4.4.1 R6 Rev. 3 Option 1 Calculational Procedure Used

In the Option 1 procedure, a fixed failure assessment curve is used for any material, crack or structural geometry. The failure assessment curve has a load or stress ratio (L_r or S_r) axis along the abscissa of a graph, and toughness ratio, using either the K or J fracture parameters, along the ordinate, see Figure 4.8.

The load ratio or L_r term is the applied load divided by the limit load. The limit load is the Net-Section-Collapse predicted load for circumferentially cracked pipe. For a pipe under pressure and bending, such as the IPIRG pipe-system experiments, one could interpret this ratio as being the total applied stress (bending plus tension from the pressure) divided by the total stress predicted from the Net-Section-Collapse analysis,

$$L_r = (\sigma_b + \sigma_t)/(\sigma_{bNSC} + \sigma_t) \tag{4-11a}$$

Alternatively, one could use the ratio of the applied bending stress divided by the Net-Section-Collapse predicted bending stress.

$$L_r = \sigma_b/\sigma_{bNSC} \tag{4-11b}$$

where

σ_b = MR_o/I (4-11c)
M = bending moment
R_o = outside radius
I = $\pi R_o^3 t$ (4-11d)
t = pipe thickness
σ_t = $R_i^2 p/(R_o^2 - R_i^2)$ (4-11e)
R_i = inside radius
p = internal pressure

and

$$\sigma_{bNSC} = (2\sigma_y/\pi)[2\sin\beta - (d/t)\sin\theta] \tag{4-12a}$$

where

σ_y = yield strength
d = surface crack depth
θ = half of surface crack length, radians
β = $[\pi - \theta d/t)]/2 - \pi(R_i^2 p)/(4R_m t\sigma_y)$ (4-12b)

Note that in the R6 method, the yield strength, not the flow stress, is used in the limit-load equation. The ratio of the flow stress to the yield strength can be used as the cut-off point along the L_r axis to be consistent with Net-Section-Collapse analyses, see Figure 4.8.

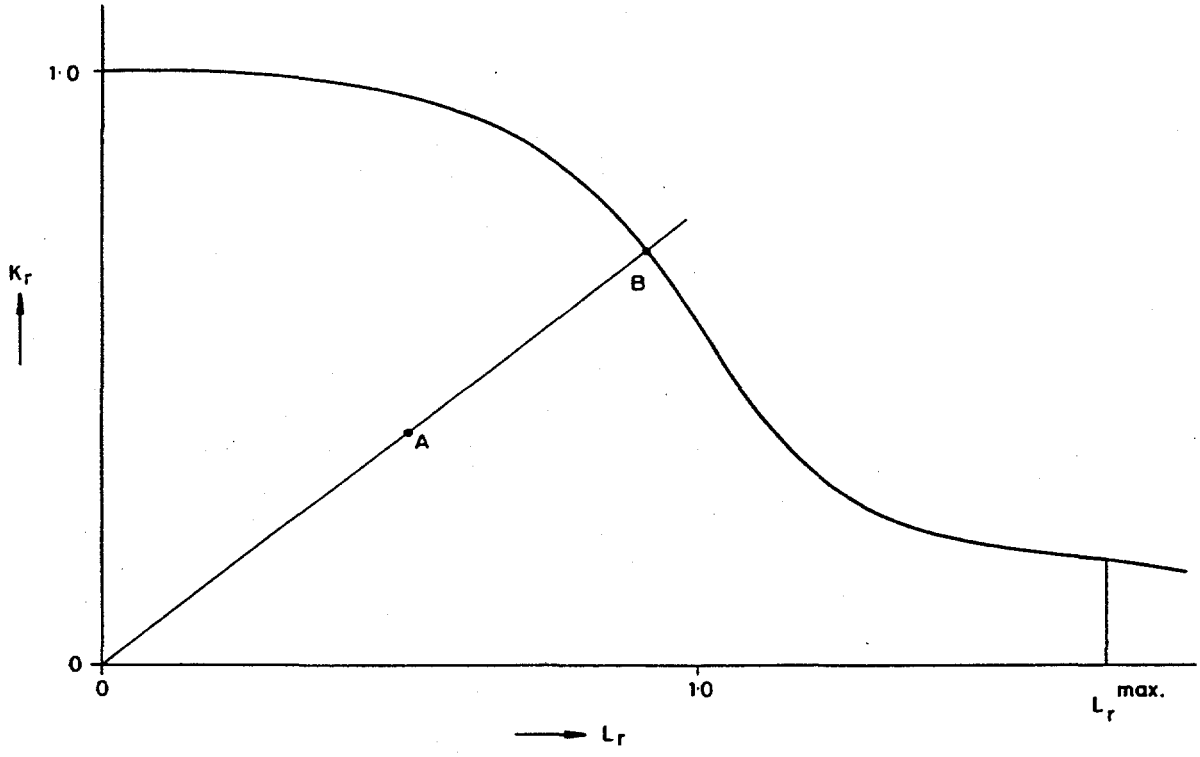

Figure 4.8 R6 Option 1 failure analysis diagram

F1.3-10/90-F4.8

The toughness or K_r term is the ratio of the applied linear elastic stress intensity factor, K_I, to the toughness of the material, $K_r(a)$, where $K_r(a)$ can be a function of crack growth from the J-R curve of the material.

$$K_r = K_I/K_r(a) \tag{4-13}$$

where

$$K_r(a) = (JE)^{0.5} \tag{4-14}$$

and

J = the value of J for the corresponding Δa from the J-R curve of the material
E = Elastic modulus.

Furthermore

$$K_I = K_{Im} + K_{Ib} \tag{4-15}$$

where, the terms K_{Im} and K_{Ib} are defined in this report by the solutions given in the ASME Section XI ferritic pipe flaw evaluation procedure, Appendix H (Ref. 4.12).

$$K_{Im} = F_m(\pi d)^{0.5}\sigma_t \tag{4-16a}$$

$$K_{Ib} = F_b(\pi d)^{0.5}\sigma_b \tag{4-16b}$$

where

$$F_m = 1.1 + (d/t)\{0.15241 + 16.772[(d/t)(\theta/\pi)]^{0.855} - 14.944(d/t)(\theta/\pi)\} \tag{4-16c}$$

$$F_b = 1.1 + (d/t)\{-0.09067 + 5.0057[(d/t)(\theta/\pi)]^{0.565} - 2.8329(d/t)(\theta/\pi)\} \tag{4-16d}$$

The Option 1 failure assessment curve, K_r-L_r curve, has the following relationship.

$$K_r = (1 - 0.14L_r^2)[0.3 + 0.7\exp(-0.65L_r^6)] \tag{4-17}$$

As part of this assessment of the R6 analysis method, moments at crack initiation and maximum load were calculated. In the maximum load calculations, the crack growth was incremented causing $K_r(a)$ to increase, K_I to increase, and σ_{bNSC} to decrease.

Normally in a design situation, one takes the applied stress and yield strength to calculate a L_r and K_r. This point is plotted on the failure assessment diagram (see Point A in Figure 4.8). If the point falls under the curve, it is considered safe. If it is above the curve it is considered a failure. The safety margin is generally calculated by dividing the length of line OB by the length of line OA. Line OB is drawn from the origin of the graph through Point A to the failure assessment curve. Line OA is drawn from the origin to point being assessed. This procedure assumes that all stresses are proportional, which may not be true for the combined pressure and bending pipe-system experiments being evaluated in this report.

For these experiments, one may be interested in the margin of safety of the moment with the pressure remaining constant. This makes the definition of the L_r term important.

In the analysis conducted, the definition of the L_r term used is the one given in Equation 4-11b. This gives the margin of safety on the moment.

One can directly solve for σ_b on the failure assessment curve using the following procedure. First, note that the K_r term takes on the form

$$K_r = A_1\sigma_b + A_2 \tag{4-18}$$

where

$$A_1 = (\pi a)^{0.5}F_b/K_r(a)$$
$$A_2 = K_{Im}/K_r(a)$$

If we define L_r in the form of

$$L_r = \sigma_b / A_3 \tag{4-19}$$

where

$A_3 = \sigma_{bNSC}$

Then combining Equations 4-18 and 4-19 gives,

$$K_r = A_1 A_3 L_r + A_2 \tag{4-20}$$

Equations 4-17 and 4-20 can then be combined to eliminate K_r and get only terms involving L_r.

$$A_1 A_3 L_r + A_2 = (1 - 0.14 L_r^2)[0.3 + 0.7\exp(-0.65 L_r^6)] \tag{4-21}$$

L_r can be determined numerically by iteration, and then σ_b can be determined from the failure assessment diagram from the L_r value.

In the calculations, the quasi-static J_D-R curve at the pipe test temperature was used. The yield strength used was the average of the measured values from quasi-static tests at the pipe test temperature. The cut-off point on the L_r axis was the ratio of the flow stress to the yield strength, where the flow stress was the average of the yield and ultimate strengths. For the case of a crack in a weld, the base metal strength and the weld metal J_D-R curve were used.

4.4.4.2 Results

Using the analysis procedure described above, the predicted failure points from the R6 Revision 1 Option 1 analysis procedure were determined. The accuracy of the method was measured as the ratio of the experimental-to-predicted stresses. As with the other analyses, these stresses include the pressure induced axial tension stress, i.e., $(\sigma_b + \sigma_t)_{experimental}/(\sigma_b + \sigma_t)_{predicted}$. Also note that the experimental stresses in this comparison are all assumed to be primary stresses, i.e., the thermal expansion and seismic anchor motion stresses are considered to be primary stresses as well as the pressure, dead-weight and inertial stresses. The effect of considering the thermal expansion and seismic anchor motion stresses as secondary stresses is discussed in Section 5 of this report, and would have the effect of lowering the calculated margins.

The results given in Table 4.7 show that the initiation and maximum stresses are calculated to be less than the experimental values for all the dynamic IPIRG and quasi-static pipe fracture experiments. The ratios of measured-to-calculated stresses are greater for the quasi-static experiments than for the dynamic IPIRG experiments in all cases except the carbon steel SAW.

4.4.5 J-Estimation Scheme Predictions Using SC.TNP and SC.TKP

For cases where limit-load analyses are inappropriate, due to low toughness or large diameter pipe, elastic-plastic analysis may be needed to obtain a more accurate estimate of the loads at crack initiation and

Table 4.7 R6 Revision 3 Option 1 analysis of dynamic IPIRG and quasi-static pipe fracture experiments[a]

			R6 Option 1 Moments		Experimental Moments				Ratio of Experimental to Calculated Stresses	
			Init.	Max.	Init.	Max.	M_{exp}/M_{pred}		$\frac{(\sigma_b + \sigma_t)_{exp}}{(\sigma_b + \sigma_t)_{pred}}$	
Material	Test No.	Loading	kN-m	kN-m	kN-m	kN-m	Init.	Max.	Init.	Max.
A106B	1.3-2	Dynamic	293	294	N.D.[b]	341	N.D.	1.16	N.D.	1.14
A106B	4112-8[c]	Quasi-static	484	488	689	748	1.42	1.53	1.42	1.41
TP304	1.3-3	Dynamic	303	304	415	426	1.37	1.40	1.25	1.27
TP304	EPRI 13S[c,d]	Quasi-static	918	946	970	1,260	1.06	1.33	1.06	1.33
CS SAW	1.3-4	Dynamic	263	267	N.D.	618	N.D.	2.31	N.D.	1.88
CS SAW	4141-8	Quasi-static	269	273	419	594	1.56	2.18	1.37	1.79
SS SAW	1.3-5	Dynamic	299	365	460	493	1.54	1.35	1.46	1.24
SS SAW	4141-4[e]	Quasi-static	230	245	443	445	1.93	1.82	1.64	1.57
CF8M	1.3-7	Dynamic	350	363	N.D.	504	1.44	1.62	1.39	1.46
CF8M	4143-1	Quasi-static	329	341	656	672	1.99	1.97	1.73	1.70

(a) Test at 288 C and 15.5 MPa internal pressure unless otherwise noted.
(b) N.D. = not determined
(c) No internal pressure.
(d) Room temperature.
(e) Internal pressure 11.03 MPa.

maximum load. The elastic-plastic analysis would also predict loads which were less than experimentally obtained values.

Various methods exist to predict the maximum loads for circumferentially cracked pipe in pure bending. This can be accomplished by detailed finite element analyses or by simpler approximate closed-form solutions. Detailed finite element analysis could be used in an application phase type of calculation along with the material fracture resistance curve to determine the strength of the cracked pipe during crack growth. Many different fracture mechanics parameters have been proposed, but the J-Integral parameter is the most frequently used parameter in the nuclear industry. Several closed-form equations for J exist that give approximate elastic-plastic fracture mechanics solutions for circumferentially cracked pipe. These are frequently referred to as J-estimation schemes. The J-estimation scheme results in this section can be considered the same as an R6 Option 3 analysis. The ratio of the experimental-to-predicted failure stresses is the inherent margins in this fracture analysis.

The following sections on the J-estimation scheme analyses contain:

- a description of the material property input for the analyses, and
- the results from the surface-cracked pipe J-estimation scheme analyses.

4.4.5.1 Material Property Input for J-Estimation Scheme Analyses

The necessary material property data input for these analyses are:

- the elastic modulus, yield and ultimate strengths,
- the Ramberg-Osgood parameters of the stress-strain curve, and
- the J-R curve of the material.

Tensile Test Data

The yield and ultimate strength of the materials under quasi-static and dynamic (strain rate of approximately 1 sec^{-1}) conditions were documented in Section 2 of this report. The elastic modulus was taken from handbook values, since it could not be accurately determined from the tensile test data which were obtained with a large-displacement extensometer.

Stress-Strain Curve Fits

The stress-strain curves from both the quasi-static and dynamic tests were used to determine the Ramberg-Osgood constants. The fit of the curves that gave the best regression coefficient was used. The Ramberg-Osgood fits of the stress-strain curves are shown in Figures 4.9 through 4.11. Only the quasi-static stress-strain curves were used in the surface crack J-estimation scheme analyses. Generally the engineering stress-strain curve was used, with the strain range being between just beyond the elastic region and the ultimate strength.

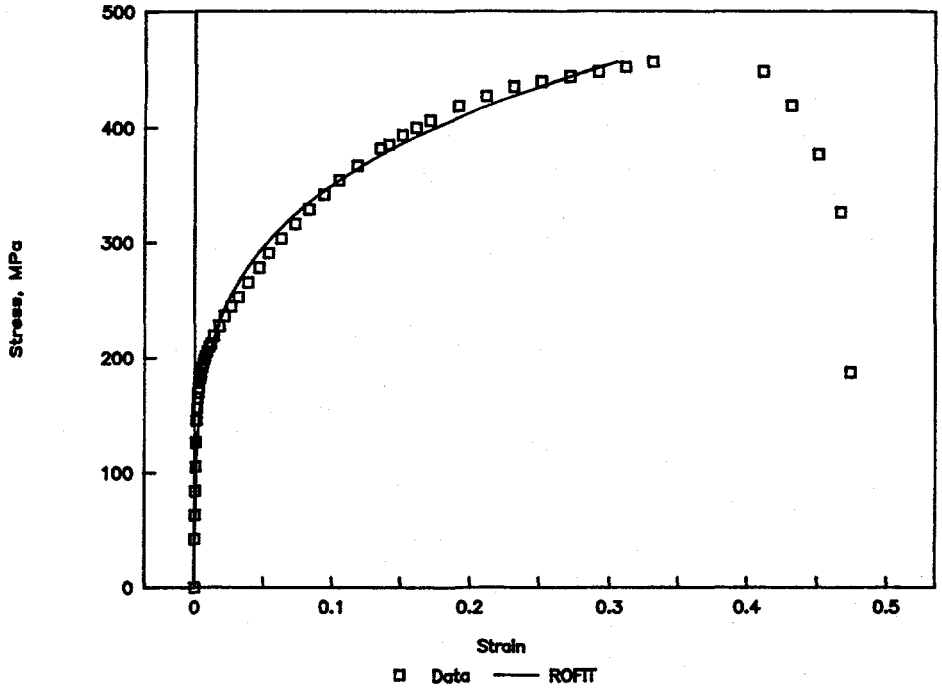

(a) Quasi-static at 288 C (550 F)

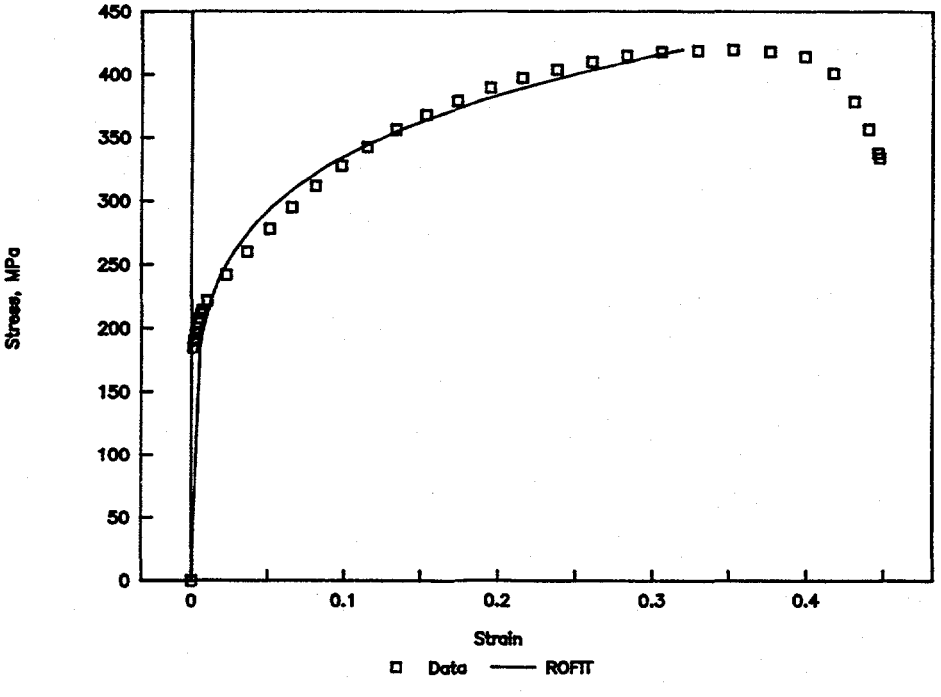

(b) Dynamic ($\dot{\epsilon}$=1/sec) at 288 C (550 F)

Figure 4.9 Ramberg-Osgood fit of TP304 stainless steel Pipe A8 stress-strain curves F1.3-10/90-F4.9a&b

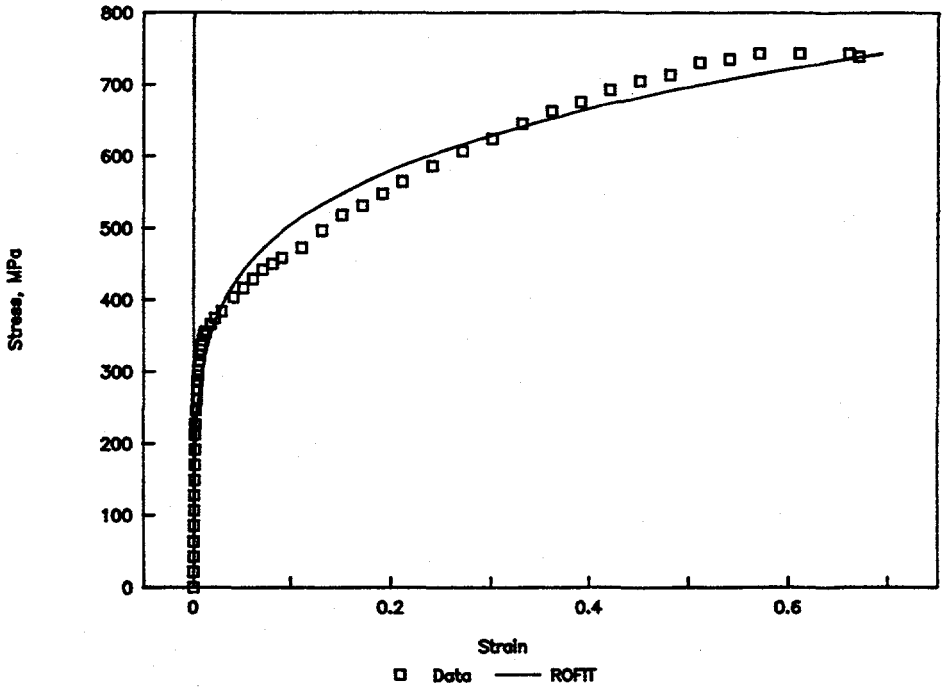

(c) Quasi-static at 20 C (68 F)

Figure 4.9 (continued)

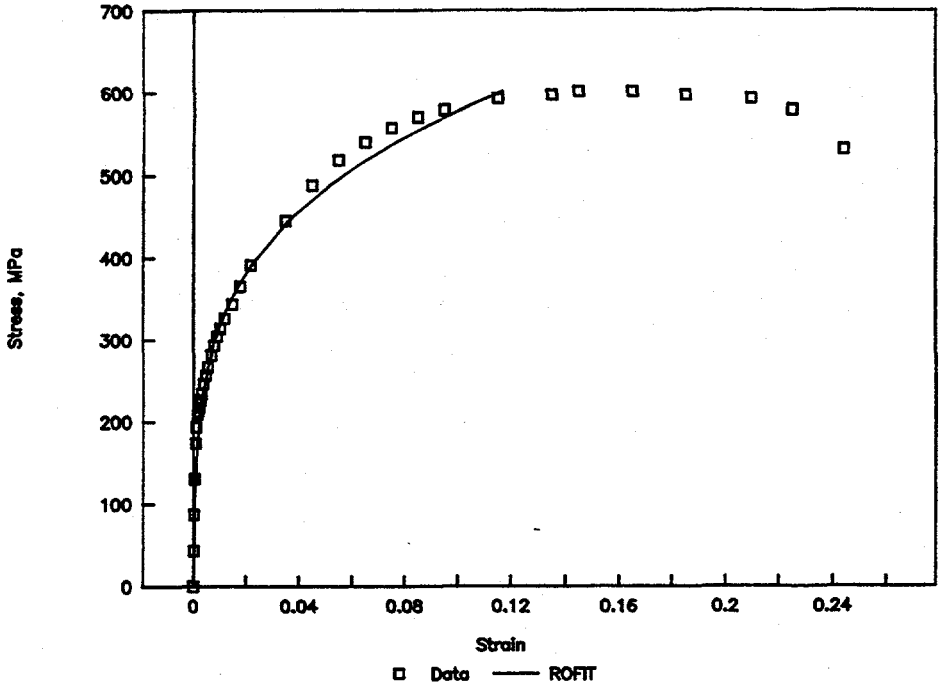

(a) Quasi-static at 288 C (550 F)

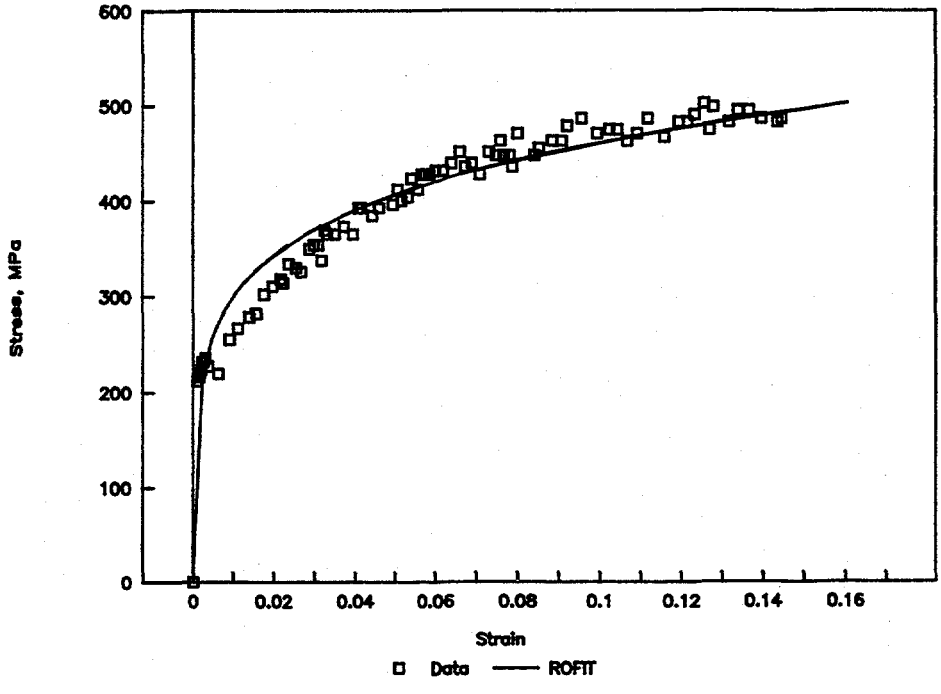

(b) Dynamic ($\dot{\epsilon}$=1/sec) at 288 C (550 F)

Figure 4.10 Ramberg-Osgood fits of A106 Grade B Pipe F29 stress-strain curves F1.3-10/90-F4.10a&b

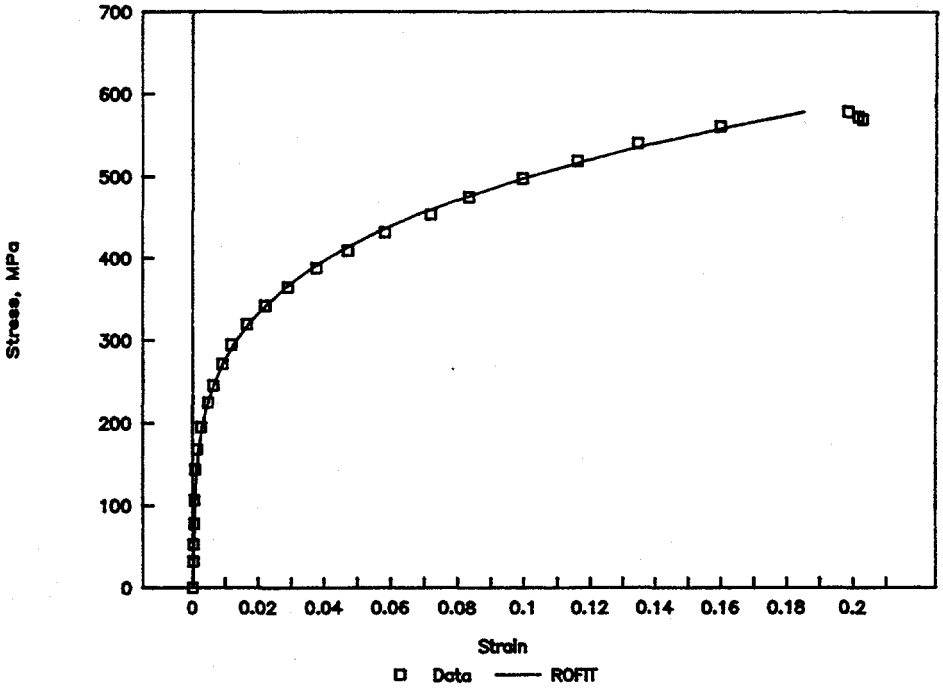

(a) Quasi-static at 300 C (572 F)

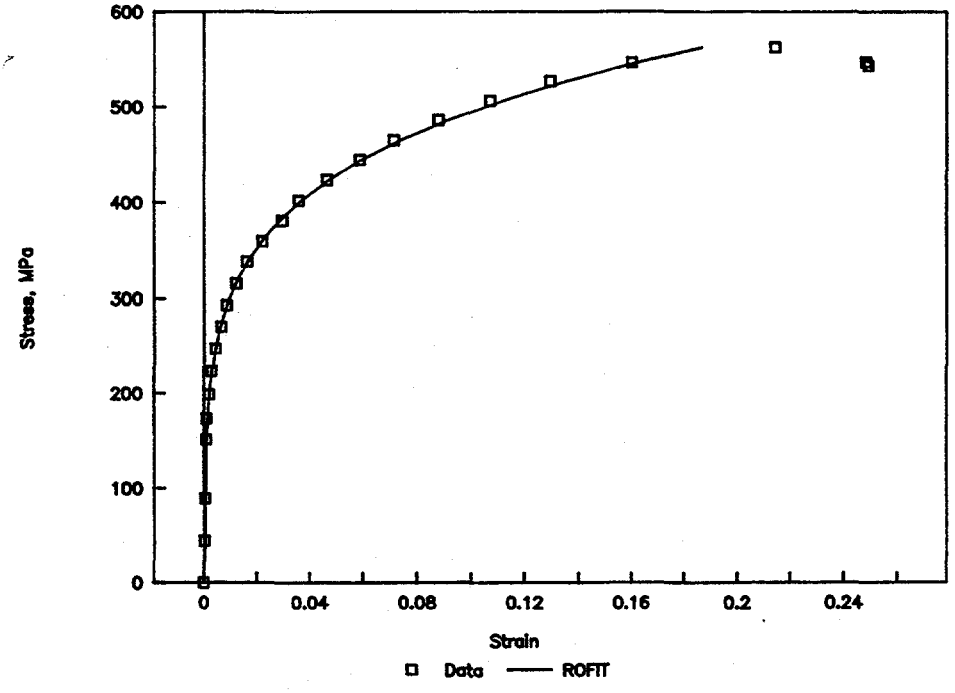

(b) Dynamic ($\dot{\epsilon}$=1/sec) at 300 C (572 F)

Figure 4.11 Ramberg-Osgood fits of CF8M Pipe A40 stress-strain curve F1.3-10/90-F4.11a

Extrapolated J-R Curves

The J-R curves used in the pipe predictions were from the monotonic quasi-static side-grooved C(T) specimens, see Section 2 of this report. Both the J_D-R and J_M-R curves were used. For the surface crack analysis, there is very little crack growth from initiation to maximum load. Hence, from a practical point of view, it doesn't matter if the J_D- or J_M-R curves are used.

4.4.5.2 J-Estimation Schemes Considered

There are very few J-estimation scheme analyses available for finite-length circumferential surface-cracked pipe. Some of the existing methods are:

EPRI/GE	- EPRI report NP-5596 (Ref. 4.23)
R6	- CEGB report R/H/R6-Rev. 3 (Ref. 4.15), and
SC.TNP and SC.TKP	- NRC report NUREG/CR-4872 (Ref. 4.16).

The EPRI/GE method uses an h_1 function to calculate the plastic contribution of J. The h_1 values are calculated from finite element analyses. Currently, there are very few values of h_1 for combined tension and bending. In fact, for the experiments conducted in this program, it was not possible to use this analysis since there were no h_1 values available to use in an interpolation for crack lengths of 180 degrees.

The R6 method was discussed in Section 4.4.4. Results of an analysis using R6 Revision 3 Option 1 were discussed. Revision 3 Option 3 provides for the use of elastic-plastic fracture mechanics analyses. One such analysis method is the J-estimation scheme using SC.TNP and SC.TKP solutions.

The SC.TNP and SC.TKP solutions were developed in the U.S. NRC Degraded Piping Program (Ref. 4.16). These solutions essentially use the EPRI/GE 360-degree surface-cracked pipe solution for pure tension to develop new h-functions for calculation of the plastic component of J, J_p, for finite-length surface-cracked pipe in bending. These solutions were implemented in the NRCPIPE Code during the Degraded Piping Program, and hence were available to assess the experimental data. Since past results showed that more accuracy is obtained using the SC.TNP solution, only this analysis procedure was used to assess these data.

4.4.5.3 Modification of SC.TNP for Tension and Bending

The prediction of initiation and maximum moment for the circumferentially surface-cracked pipe experiments in this study is complicated by the combined tension and bending loads, as well as the load reversals prior to crack initiation. A predictive analysis method should include the effect of load reversals both on the crack driving force (i.e., applied J) and on the material's crack growth resistance (i.e., J-R curve). In the present analysis, the reverse loading effects are ignored. The quasi-static stress-strain curves are used with the quasi-static J-R curve. Quasi-static properties were used to reflect the more normal situation in which dynamic data are not available.

Even with the above simplifications, prediction of surface-cracked pipe behavior is a difficult analysis problem awaiting further research. At present, the SC.TNP and SC.TKP methods appear to be the most detailed, short of full three-dimensional finite-element analysis. Even so, the method does not currently

include the effect of internal pressure or tension on J. The key equation from Reference 4.16 is the plastic component of J which is given by:

$$J_p = \alpha\epsilon_o\sigma_o(1 - d/t)dh_1(k\sigma/P_o)^{n+1} \quad (4\text{-}22)$$

The H_1 function corresponds to an axisymmetrically cracked pipe loaded in tension and α, ϵ_o, n, and σ_o are the constants corresponding to a Ramberg-Osgood representation of the material's uniaxial (tension) stress-strain curve. As discussed in Reference 4.16, the facts that there is a less than 360-degree surface crack, and the pipe is subjected to remote bending (rather than tension), are included in the analysis by modifying the applied stress (σ) term in Equation 4-22.

The effect of internal pressure is addressed in an approximate way, by ignoring possible loading path effects on plastic deformation, and replacing the axial tension in the uncracked ligament ahead of the crack by an additional applied moment. The equivalent moment, M_{eq}, from the pressure-induced axial tensile stress is calculated as being approximately equal to the difference of the Net-Section-Collapse predicted stress under pure bending and the Net-Section-Collapse predicted stress under combined bending and tension for the internal pressure. (The Net-Section-Collapse equations given in Appendix F were used.) With the above approximations and assumptions, analyses were performed for all the pipe experiments. In the analyses, loading was increased monotonically until initiation, and then instability were predicted.

4.4.5.4 Results of SC.TNP Comparisons with Pipe Fracture Experiments

The results of all the pipe predictions are given in Table 4.8 which includes: (1) the SC.TNP predicted moments at crack initiation and maximum load, (2) the experimental moments at crack initiation and maximum load, (3) the ratio of the experimental moments to the predicted moments for crack initiation and maximum load, and (4) the ratio of the total experimental stress to the predicted total stress at crack initiation and maximum load.

TP304 Pipe Fracture Experiments

For both the dynamic and quasi-static TP304 stainless steel base metal crack experiments, the ratio of the experimental-to-predicted moments and failure stresses are less than one for both crack initiation and maximum loads, see Table 4.8.

A relative comparison of the fracture mechanics ratios show a larger value for the quasi-static test than for the dynamic IPIRG test. This is consistent with the Net-Section-Collapse, DPZP, ASME Section XI and R6 relative comparisons.

Stainless Steel SAW Pipe Fracture Experiments

Unlike the stainless steel base metal experiments, for the stainless steel SAW experiments, the ratio of the experimental-to-predicted moments and failure stresses are greater than one by the SC.TNP analysis, see Table 4.8. The dynamic and quasi-static fracture analysis ratios are nearly the same for the stainless steel SAW experiments, see Table 4.8.

Aged Cast Stainless Steel Pipe Fracture Experiments

The aged cast stainless steel quasi-static pipe fracture experiment is predicted to have larger experimentally measured moments at crack initiation and maximum load than calculated values. By contrast, the ratio of

Table 4.8 SC.TNP analysis of dynamic IPIRG and quasi-static pipe experiments[a]

			SC.TNP Moments		Experimental Moments				Ratio of Experimental to Calculated Stresses	
			Init.	Max.	Init.	Max.	M_{Exp}/M_{Pred}		$(\sigma_b+\sigma_t)_{exp}/(\sigma_b+\sigma_t)_{pred}$	
Material	Test No.	Loading	kN-m	kN-m	kN-m	kN-m	Init.	Max.	Init.	Max.
A106B	1.3-2	Dynamic	498	530	N.D.[b]	341	N.D.	0.64	N.D.	0.72
A106B	4112-8[c]	QS	688	729	689	748	1.00	1.03	1.00	1.03
TP304	1.3-3	Dynamic	500	570	415	426	0.83	0.75	0.87	0.80
TP304	EPRI 13S[c,d]	QS	1,234	1,268	970	1,260	0.79	0.99	0.79	0.99
CS SAW	1.3-4	Dynamic	422	490	N.D.	618	N.D.	1.26	N.D.	1.21
CS SAW	4141-8	QS	432	499	423	594	0.98	1.19	0.98	1.15
SS SAW	1.3-5	Dynamic	265	389	460	493	1.74	1.27	1.47	1.19
SS SAW	4141-4[e]	QS	290	396	498	501	1.72	1.27	1.53	1.21
CF8M	1.3-7	Dynamic	512	658	504	590	0.98	0.90	0.99	0.91
CF8M	4143-1	QS	498	630	660	672	1.33	1.07	1.26	1.06

(a) Test at 288 C and 15.5 MPa internal pressure unless otherwise noted.
(b) N.D. = not determined
(c) No internal pressure.
(d) Room temperature.
(e) Internal pressure 11.03 MPa.

measured-to-calculated moments for the aged cast stainless steel dynamic pipe fracture experiment is less than one at both crack initiation and maximum load.

A106 Grade B Pipe Fracture Experiments

For the A106 Grade B base metal quasi-static pipe fracture experiment, the ratio of the experimental-to-predicted moments and failure stresses are slightly greater than one for both crack initiation and maximum loads, see Table 4.8. For the dynamic experiment, the SC.TNP analysis overpredicted the maximum experimental moments and stresses and thus gave ratios of experimental-to-predicted moments and failure stresses which are less than one.

Carbon Steel SAW Pipe Fracture Experiments

For the carbon steel SAW pipe fracture experiments, the ratio of the experimental-to-predicted moments and failure stresses are greater than one for maximum loads, see Table 4.8. For the quasi-static carbon steel SAW experiment, the SC.TNP analysis slightly overpredicted the experimental moments and stresses at crack initiation. These comparisons also show that the carbon steel SAW had higher load-carrying capacity than the carbon steel base metal cracked pipe. This is consistent with the results from the other analyses.

The relative comparison of the dynamic and quasi-static safety margins shows that the carbon steel SAW had a slightly (i.e., 5 percent) higher load-carrying capacity under dynamic loading than the quasi-static loading. This is consistent with the Net-Section-Collapse, DPZP, ASME Section XI and R6 relative comparisons.

4.4.5.5 Summary of SC.TNP Predictions

The range of the experimental-to-predicted maximum loads was from 0.72 to 1.21 when using the total stress ratio. The lowest prediction was for the IPIRG carbon steel base metal test, which had an experimental-to-predicted ratio of 0.72. If the lower dynamic material properties were used for the predictions for the dynamic carbon steel experiment, then this ratio would be closer to the average value of the rest of the experiments.

The relative comparisons of the dynamic and quasi-static fracture mechanics analysis margins, showed that all materials but the carbon steel SAW had a lower load-carrying capacity under dynamic loading conditions.

4.5 Normalized Moment-Rotation Results

Thus far, comparisons have only been made between quasi-static and dynamic experiments on the basis of ratios of maximum experimental moments or stresses to predicted moments or stresses. That is, all experimental data, both static and dynamic, have been normalized to eliminate the effects of differences in specimen geometry (pipe and crack dimensions). No attempt has been made in this process to make comparisons between different materials. All the IPIRG experiments analyzed had the same internal pressure.

In order to make comparisons between different materials, the data again have to be normalized. In this case, however, rather than making the comparison on the basis of a single parameter, i.e., maximum moment, a second parameter, rotation due to the crack, is introduced to provide not only a "strength" perspective, but also a "ductility" perspective in the comparison. Furthermore, the area under the moment-rotation curve is also proportional to the J-integral fracture resistance of the material. Hence, a relative comparison of the moment-rotation curves from the pipe tests will reflect the relative toughness of the materials in these pipe-system experiments.

The procedure used to normalize experimental moment-rotation data relies upon the SC.TNP J-estimation scheme, Reference 4.16, to put all of the experimental data on a common basis. That is, all differences in geometry, (i.e., crack depth, crack length, pipe diameter, and wall thickness), are eliminated so that only differences in material properties remain. The detailed procedure for performing the normalization is as follows:

(1) Select an arbitrary reference basis flaw and pipe size.

(2) For each material, perform two SC.TNP J-estimation analyses: the first one uses the as-tested flaw and pipe size, while the second one uses the reference basis flaw and pipe size. In both cases, the as-tested quasi-static material properties are to be used.

(3) Calculate the moment normalization parameter, using the maximum moment in the two SC.TNP analyses, as:

$$N_m = M_{reference}/M_{as\text{-}tested}$$

(4) Calculate the rotation normalization parameter using the rotation at maximum moment in the two SC.TNP analyses as:

$$N_\phi = \phi_{reference}/\phi_{as\text{-}tested}$$

(5) Normalize the Subtask 1.3 measured experimental data by multiplying all test moments by N_m and all test rotations by N_ϕ.

(6) Repeat Steps (2) through (5) for each different material.

The moment-rotation curves that result from the normalizations will be estimates of the moment-rotation behavior for each material with the reference flaw and pipe size.

The procedures described above were used to normalize the IPIRG Subtask 1.3 moment-rotation data. Unfortunately, for reasons discussed in Section 3 of the report, there are no rotation data for the carbon steel base metal and carbon steel weld experiments, so only the three stainless steel experiments can be compared. The reference basis flaw and pipe size chosen for the normalization were a $d/t = 0.66$ and $\theta/\pi = 0.468$ flaw in a 416 mm (16.37 inch) diameter by 26.2 mm (1.031 inch) thick pipe, with the crack length based on equivalent crack length and inside pipe circumference. This flaw and pipe size were chosen because they are the flaw and pipe size from the Subtask 1.3 stainless steel base metal experiment, and because they are reasonably close to the originally planned 66 percent deep, 50 percent long flaws to be used in the experiments.

For the three Subtask 1.3 stainless steel experiments, the six normalization factors (one for moment and one for rotation for each experiment) were all on the order of 0.98, except for the aged cast stainless moment normalization factor which was 0.93. The reason that all of the normalization factors are so close to 1.0 is that the flaw geometry differences between the as-tested and reference cases are insignificant. The 0.93 normalization factor for the aged cast stainless bending moment is a reflection of the shallow flaw used in that experiment, d/t = 0.53, when compared with the reference case. (Note, the flaw size for the aged cast stainless experiment was intentionally made more shallow so that it would match the flaw size used in the companion quasi-static Degraded Piping Program experiment.) To determine whether the linear normalization procedure was reasonable, all of the as-tested J-estimation scheme data were multiplied by the normalization factors to see if the resulting curve is a good approximation of the reference J-estimation curve. Figure 4.12 shows the two J-estimation curves and the normalized as-tested curve for the aged cast stainless specimen. Clearly, linearly normalizing the complete as-tested curve gives a very good approximation to the reference curve.

Figure 4.13 is a plot of the normalized moment-rotation behavior for the three stainless steel IPIRG Subtask 1.3 experiments. In reviewing Figure 4.13, it is evident that the higher toughness stainless steel base metal specimen had far more rotational "ductility" than either of the other two specimens.

The efficacy of the normalization procedure can be seen in Figure 4.13 by the fact that all three normalized moment-rotation curves lie basically on top of one another initially. This is expected because during the early part of the loading, the behavior of the crack is essentially linear and dominated by the elastic modulus of the material.

The toughness of the different materials in terms of J, is proportional to the area under the moment-rotation curves. From an inspection of the three different curves, first impressions are that the stainless steel base metal is the toughest material since the area under the moment-rotation curve is the largest. This is consistent with the C(T) specimen results given in Section 2 of this report. Furthermore, the relative comparison of the aged cast stainless steel and stainless steel SAW moment-rotation curves are relatively close, indicating the toughness of these materials are relatively close. Again, this is consistent with the C(T) specimen results presented in Section 2 of this report. However, the area under the moment-rotation curve for the stainless steel base metal is only about a factor of 2 greater than the area under the curves for the aged cast stainless steel and stainless steel SAW. From the C(T) specimen J-R curves for these materials, it would be expected that the difference would be a factor of 5 or more. Hence, either the stainless steel base metal is behaving more like the lower toughness materials, or the lower toughness materials are behaving more like the high toughness stainless steel. To make this distinction, it is necessary to calculate values of the toughness from the pipe experiment moment-rotation data.

4.6 Calculation of J_i from Subtask 1.3 Experiments

The calculation of the toughness at the initiation of ductile tearing in the Subtask 1.3 experiments is possible by using the experimental moment versus rotation data up to the rotation where crack initiation occurred. These data were compared together in the normalized graph in Figure 4.13. The method used to calculate the J values from the experimental data is referred to as an η-factor J-estimation scheme method. In this method, the J is equal to

$$J_{Total} = J_e + J_p \qquad (4\text{-}23)$$

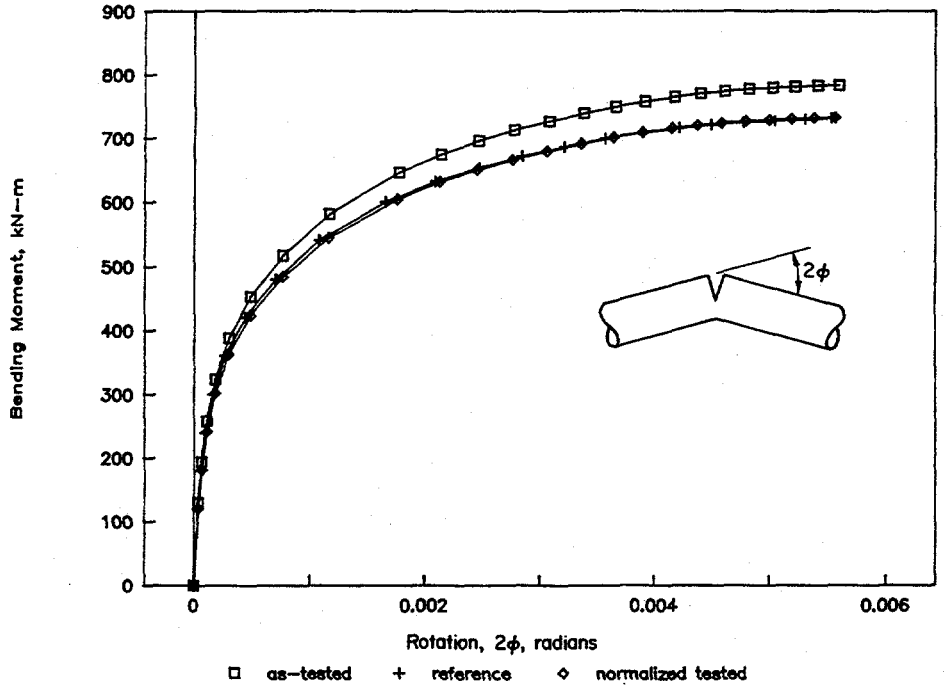

Figure 4.12 Moment-rotation curve normalization assessment

F1.3-10/90-F4.12

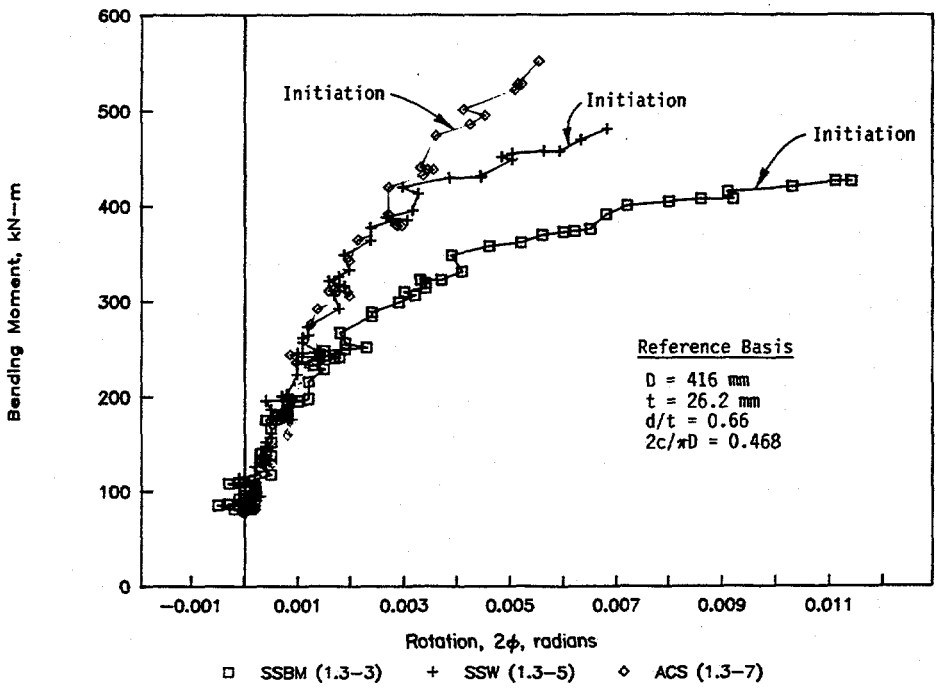

Figure 4.13 IPIRG Subtask 1.3 normalized moment-rotation data

F1.3-10/90-F4.13

where

J_e = elastic contribution of J
J_p = plastic contribution of J

Elastic solutions of J are available from Reference 4.12, where

$$J_e = (K_{Im} + K_{Ib})^2/E' \quad (4\text{-}24)$$

$$K_{Im} = [P_a/(2\pi R_m t)]F_m(\pi d)^{0.5} \quad (4\text{-}25)$$

$$K_{Ib} = [M/(\pi R_m^2 t)]F_b(\pi d)^{0.5} \quad (4\text{-}26)$$

and

P_a	=	$\pi R^2 p$ = axial force
R_m	=	mean radius
p	=	pressure
t	=	thickness
E'	=	$E/(1-\nu^2)$
E	=	elastic modulus
ν	=	Poisson's ratio
M	=	moment
d	=	surface crack depth

$$F_m = 1.1 + (d/t)[0.15241 + 16.772[\theta d/(t\pi)]^{0.855} - 14.944[\theta d/(t\pi)] \quad (4\text{-}27)$$

$$F_b = 1.1 + (d/t)[-0.09967 + 5.0057[\theta d/(t\pi)]^{0.565} - 2.8329[\theta d/(t\pi)] \quad (4\text{-}28)$$

θ	=	half crack angle, radians

The plastic contribution of J is calculated from Equation 4-29.

$$J_p = \eta \int_0^{\phi_i} M d\phi^c_p \quad (4\text{-}29)$$

From Pan (Ref. 4.24)

$$\eta = -[1/(2R_m t)](F_x/F) \quad (4\text{-}30)$$

where

$$F_x = \frac{-0.5 \cos[(\pi-\theta)(1-\gamma)/2][1 - t/R_m + t^2/(3R_m^2)]}{[1 - t/(2R_m)]} \quad (4\text{-}31)$$

$$\gamma = \frac{[\theta/(\theta-\pi)](1-d/t)[1-(1-d/t)t/(2R_m)]}{[1-t/(2R_m)]} \quad (4\text{-}32)$$

$$F = \{\mathrm{Sin}[(\pi-\theta)(1-\gamma)/2] - 0.5\mathrm{Sin}(\theta)\}^* [1 - t/R_m + t^2/(3R_m^2)] + [0.5\mathrm{Sin}(\theta)(1-d/t)][1-(t/R_m)(1-d/t) + t^2(1-d/t)^2/(3R_m^2)] \quad (4\text{-}33)$$

Note that this η-factor solution is for a pipe in pure bending. However, the Subtask 1.3 experiments involve combined pressure and bending. To account for the pressure in the η-factor J_p solution, an equivalent moment, M_{eq}, for the pressure was calculated. This was done using the Net-Section-Collapse equations for a crack in a pipe and solving for the failure moment in pure bending and for combined bending and pressure. The difference of the two was the equivalent moment due to the internal pressure.

This equivalent moment was added to the applied moments in the M-ϕ relations in Figure 4.13 to give total equivalent moments as if the pipes were in pure bending.

The final calculation involved the integration of the M-ϕ curves for the plastic rotations only up to the point of crack initiation. This was done graphically for the stainless steel base metal (1.3-3) experiment, the stainless steel weld metal (1.3-5) experiment, and the aged cast stainless steel base metal (1.3-7) experiment.

Table 4.9 summarizes the parameters in these calculations. The results gave J_i values of 104 kJ/m^2 (594 in-lb/in^2) for the aged cast stainless steel, 315 kJ/m^2 (1,800 in-lb/in^2) for the stainless steel SAW, and 560 kJ/m^2 (3,200 in-lb/in^2) for the stainless steel base metal. Of these values, the surface-crack stainless steel weld J_i value from the pipe experiment is significantly higher than either the quasi-static or dynamic C(T) specimen J_i value. (The height of the weld crown was ignored in the stainless steel weld calculations.) The aged cast stainless steel surface crack J_i value is only 10 percent below the dynamic C(T) specimen J_i value. The stainless steel base metal surface crack J_i value was a factor of 2.1 below the average J_i values of the dynamic C(T) specimens.

Further discussions on the significance of these results are given in Section 5 of this report.

4.7 Stability Analyses

The focus of this section is an assessment of the stability of cracked-pipe systems under combined inertial and displacement-controlled loading. It is important to first define what is meant by stability. Most crack stability criteria predict the start of unstable crack growth, and potential arrest of the instability is seldom considered. In prior sections, predictions of crack initiation and maximum moment were made. Under load-controlled conditions, maximum moment can be considered a stability criterion, since it is almost invariably followed by rapid crack growth. In this section instability will refer to rapid fracture. Furthermore, because we are primarily interested in whether or not a double-ended guillotine break (DEGB) is predicted to occur, primary attention will be directed toward stability of through-wall cracks which occur after the surface crack penetrates the pipe wall. Using this definition of stability, a surface crack will experience some maximum load and, under continued loading, the surface crack will penetrate

the wall and typically propagate to the ends of the surface crack. In a purely displacement-controlled situation, and in the absence of a large amount of system compliance, the through-wall crack will arrest well before the pipe has experienced a DEGB, (see the IPIRG Subtask 1.2 report (Ref. 4.25). In a purely load-controlled situation, the resulting through-wall crack from most surface crack geometries will almost

Table 4.9 Parameters in J_i values calculated from IPIRG Subtask 1.3 experiments

Material	Stainless Steel Base Metal	Stainless Steel SAW	Aged Cast Stainless Steel
Expt. No.	1.3-3	1.3-5	1.3-7
Outer diameter,[a] mm	416	416	416
Thickness,[a] mm	26.2	26.2	26.2
d/t[a]	0.66	0.66	0.66
θ/π[a]	0.468	0.468	0.468
E, GPa	182.7	182.7	182.7
Equivalent moment due to pressure, kN-m	174.8	174.8	168.3
Total equivalent moment, kN-m	589	616	672
Plastic energy to crack initiation,[b] kN-m-rad	3.75	2.38	0.736
J_i, kJ/m^2	560	315	104

(a) Diameter, thickness, a/t, and θ/π are values for normalized M-ϕ curves.
(b) Including M_{eq} due to pressure, and using only plastic area from normalized M-ϕ curves.

certainly experience an instability. (Note: short deep surface cracks can have failure loads less than a through-wall crack with the same length (Refs. 4.18 and 4.19). In those cases an instability of the through-wall crack would not necessarily be expected.) For cases of combined loading, such as existed in the Subtask 1.3 experiments, instability of the through-wall crack will not necessarily start at the maximum moment. The combined loading cases are of primary interest because they are the most likely to occur in plant piping.

The analyses presented in this section are based on quasi-static considerations. That is, it is assumed that the application of loads is much slower than the fracture event. If this is not true, then these methods will have some built-in inaccuracy. Although it is recognized that seismic loading is inherently dynamic, the state of the art for pipe fracture instability predictions, particularly for combined loading, is still quite primitive, and most involve quasi-static approaches. Failure of the quasi-static methods to adequately predict instability should only be taken as an indication of a need for further development. Likewise, correct predictions on limited data should be viewed skeptically since the agreement may only be fortuitous.

In the following, the stability of the surface cracks and the through-wall cracks that exist after a surface crack penetrates the pipe wall is considered. It is shown that the surface crack will be unstable, and that it will typically propagate at least to the end of the preexisting surface crack. Two analysis methods are considered. The first is the fully plastic J/T approach, and the other is the Energy Balance Stability analysis developed in the NRC's Degraded Piping Program.

4.7.1 J/T Stability Analysis

The J-integral/tearing modulus, J/T, stability analysis is one method currently used to make an assessment of the stability of cracked structures. Paris and co-workers popularized the methodology (Ref. 4.26). A rather extensive compilation of J/T solutions for various loading modes (displacement-controlled and load-controlled) and assumed material behavior can be found in Reference 4.27.

Simply stated the J/T instability criteria for either a surface or through-wall cracked pipe can be expressed as:

$$J_{applied} > J_{Ic} \tag{4-34a}$$

and

$$T_{applied} > T_{material} \tag{4-34b}$$

If the applied J is greater than J_{Ic}, the crack will initiate. Then, if the applied tearing modulus is greater than the material's tearing resistance, an instability will occur.

Graphically, the generalized J/T methodology is shown in Figures 4.14 and 4.15. In the left-hand part of Figure 4.14, an applied J is computed as a function of load for the given pipe, crack, and material. Applied J is also calculated as a function of applied T and plotted on the right-hand side of the figure. Next a J/T curve representing the material's crack growth resistance, as typically developed from a compact (tension) specimen J-R curve, is plotted on the right-hand portion of the figure from data shown in Figure 4.15. Instability is predicted to start when the applied and material J/T curves intersect. It is generally assumed, that once the instability starts, it will continue until the specimen or structure is broken in half.

As indicated previously, there are a number of different possible loading and material assumptions that can be made when performing a J/T stability analysis. For the IPIRG Subtask 1.3 piping system, the fully plastic J/T solution is probably most applicable. For circumferential through-wall-cracked pipe, the fully plastic J/T methodology is given in References 4.28 and 4.29. This analysis is briefly reviewed prior to presenting the results of J/T predictions for the IPIRG pipe-system experiments.

4.7.1.1 Through-Wall Crack Fully Plastic J/T Stability Analysis

The fully plastic J/T analysis makes the inherent assumption that the cracked pipe is at limit-load conditions during stable crack growth. Secondly, the current equations are based on either load-controlled stresses or displacement-controlled stresses for a compliant system. The load-controlled stability prediction should correspond to instability at Net-Section-Collapse predicted loads since fully

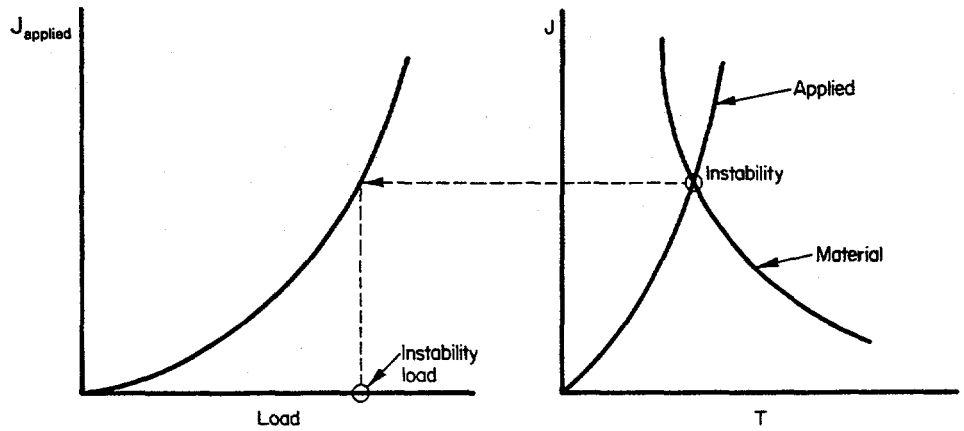

Figure 4.14 J/T stability assessment methodology

F1.3-10/90-F4.14

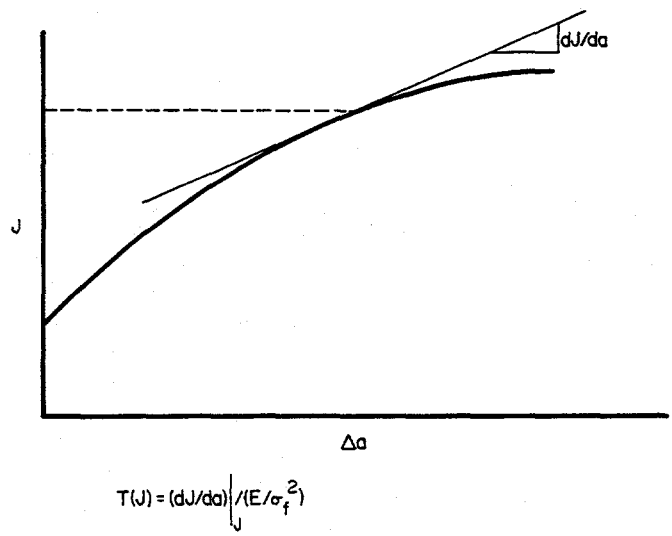

Figure 4.15 Material J/T behavior

F1.3-10/90-F4.15

plastic behavior is an inherent assumption in the analysis. Consequently, only the displacement-controlled analysis method was evaluated.

The applied J value is

$$J = \sigma_f R_m F_j \phi_k \tag{4-35}$$

where

σ_f = flow stress
F_j = $\sin(\theta/2) + \cos\theta$
ϕ_k = critical crack kink angle
R_m = pipe mean radius
2θ = total circumferential crack angle, radians.

The critical crack kink angle is an assumed value in the prior work, and in Reference 4.28 it is recommended to be 1 degree.

The applied tearing modulus is

$$T_{applied} = F_1(\theta) L_{eff}/R_m + F_2(\theta) JE/(\sigma_f^2 R_m) \tag{4-36}$$

where

$F_1(\theta)$ = $2F_j^2/\pi$
$F_2(\theta)$ = $[\cos(\theta/2) - 2\sin\theta]/2F_j$
L_{eff} = EI/k
I = area moment of inertia
k = system rotational stiffness
J = J-integral
σ_f = material flow stress, $(\sigma_y+\sigma_u)/2$
σ_y = material yield stress
σ_u = material ultimate stress
E = Young's modulus.

The system rotational stiffness, k, is determined from a piping code, such as ANSYS®, and is a measure of the elastic energy stored in the piping. Details of determining the system rotational stiffness are given in Reference 4.28. It involves putting a hinge element at the crack location in the piping system being analyzed and determining the relative rotation of the two sides of the hinge when a unit moment is applied.

The material tearing modulus, $T_{material}$, is defined as

$$T_{material} = dJ/da\ (E/\sigma_f^2) \tag{4-37}$$

The evaluation of stability is made by following the generic J/T procedures described previously.

4.7.1.2 Surface Crack Fully Plastic J/T Stability Analysis

The surface crack J/T stability equations are very similar to the through-wall crack equations with the exceptions of:

$$F_j = \sin[\theta d/(2t)] + (1/\theta)\sin\theta \quad (4\text{-}38)$$

$$F_1(\theta) = 2R_m F_j^2/(\pi t) \quad (4\text{-}39)$$

$$F_2(\theta) = [\theta R\cos(\theta d/2t)]/(2F_j t) \quad (4\text{-}40)$$

4.7.1.3 Results of Fully Plastic J/T Analysis of the IPIRG Pipe-System Experiments

The J/T displacement-controlled stability calculations were made considering both the quasi-static and dynamic properties. Additionally, rather than using the assumed value of 1 degree for the critical kink angle, ϕ_k, the SC.TNP-calculated rotation due to the crack at surface crack penetration was used. For the surface crack analysis, the initial slope of the J_D-R curve for small amounts of crack growth was used. For the through-wall crack stability analysis, the J_M-R curve was used in the large crack growth region where the slope of the curve is essentially constant.

All of the surface-cracked experiments exhibited a limited instability, i.e., an instability started, but the crack arrested with a through-wall flaw length close to the initial surface flaw length. The J/T analysis correctly predicted the start of an instability for all surface crack experiments.

All of the resultant through-wall-cracks in the IPIRG pipe-system experiments were predicted to be stable using the fully plastic J/T displacement-controlled analysis, independent of whether quasi-static or dynamic material properties were used. Tables 4.10 and 4.11 summarize the J/T calculations using quasi-static and dynamic material properties, respectively. These were correct predictions. Both the carbon steel base metal and aged cast stainless steel pipes severed into pieces by the end of the experiment, but only after numerous loading cycles and associated stable cyclic through-wall-crack growth. This is discussed in further detail in Section 5.

4.7.2 Elastic-Plastic Energy Balance Analysis

The Energy Balance Stability method is a technique that was developed in the Degraded Piping Program to predict the onset of an instability and to estimate the crack length at arrest for either through-wall or surface-cracked pipe in combined tension and bending. It uses elastic-plastic J-estimation schemes to calculate the moment-rotation response of a cracked pipe to determine the energy absorbed in the fracture process, and the elastic energy in the pipe system, as calculated by an elastic pipe stress analysis code, to determine the energy available to drive the instability. It has been verified for some limited cases by quasi-static compliant surface-cracked pipe fracture experiments (Ref. 4.30).

The basic process used to perform an energy balance stability assessment is shown in Figures 4.16 to 4.18. In Figure 4.16(a), the moment-rotation behavior of a surface crack is shown. The crack is assumed to be a plane of zero thickness, with all effects of the pipe on either side excluded. At any point on the loading curve, the shaded area describes the elastic energy that is stored in the cracked pipe. In Figure 4.16(b), the elastic energy stored in the attached piping is shown, assuming that all of the piping remote from the crack remains elastic and that the loading and unloading compliances are equal and linear. Figure 4.16(c) is the

Table 4.10 Fully plastic J-T stability calculations using quasi-static properties

C(T) Spec. #	A106 B Exp't 1.3-2 DP2-F29-17	CS SAW Exp't 1.3-4[a] DP2-F29W12	TP304 Exp't 1.3-3 DP2-A8-43	SS SAW Exp't 1.3-5[a] DP2-A45W-54	Aged CF8M Exp't 1.3-7 DP2-A40-GOO-6
C(T) size	1T	1T	1T	10T	1T
Diameter, mm	403.9	402.6	415.8	416.1	400.3
Thickness, mm	25.7	25.5	26.2	25.7	26.6
Radius, mm	189.1	188.6	194.8	195.2	186.9
σ_y, MPa	237	237	176	176	205
σ_u, MPa	610	610	459	459	603
dJ/da(sc), MJ/m^3	89.0	68.0	524.0	69.4	317.2
dJ/da(twc), MJ/m^3	66.2	34.4	257.6	48.9	100.0
E, GPa	193.060	193.060	182.718	182.718	182.718
I, m^4	0.000548	0.000539	0.000611	0.000603	0.000548
σ_f, MPa	423	423	318	318	390
d/t	0.727	0.691	0.660	0.635	0.533
Theta, radians	1.376	1.508	1.470	1.382	1.571
L_{eff}, mm	18,832	18,510	19,856	19,582	17,805
L_{eff}/R_m	99.6	98.2	101.9	100.3	95.3
ϕ_c(sc), radians	0.00323	0.00304	0.02339	0.00633	0.00559
$J_{applied}$(sc), kN-m/m^2	308.7	281.5	1,650.6	444.5	440.1
ϕ_c(twc), radians	0.01308	0.01432	0.10408	0.02658	0.03154
$J_{applied}$(twc), kN-m/m^2	867.2	854.5	4,954.4	1,356.2	1,682.6
$T_{applied}$(sc)	941.4	954.9	1,021.9	874.1	820.8
$T_{material}$(sc)	95.7	73.1	951.8	126.1	380.9
Surface-crack stable?	No	No	No (Marginal)	No	No
$T_{applied}$(twc)	40.0	30.8	1.2	34.3	21.1
$T_{material}$(twc)	71.2	37.0	468.0	88.7	120.1
Through-wall crack stable?	Yes	Yes (Marginal)	Yes	Yes	Yes

(a) Used base metal data.

Table 4.11 Fully plastic J/T stability calculations using dynamic properties

Material	A106 B	CS SAW	TP304	SS SAW	Aged CF8M
Experiment #	Exp't 1.3-2	Exp't 1.3-4[a]	Exp't 1.3-3	Exp't 1.3-5[a]	Exp't 1.3-7
C(T) specimen #	DP2-F29-17	DP2-F29W12	DP2-A8-43	DP2-A45W-54	DP2-A40-GOO-6
C(T) specimen size	1T	1T	1T	10T	1T
Diameter, mm	403.9	402.6	415.8	416.1	400.3
Thickness, mm	25.70	25.48	26.19	25.68	26.59
Radius, mm	189.1	188.6	194.8	195.2	186.9
σ_y, MPa	232	232	195	195	231
σ_u, MPa	507	507	424	424	570
dJ/da(sc), kN/mm^2	61.6	99.8	499.7	193.1	253.0
dJ/da(twc), kN/mm^2	32.8	38.6	362.6	76.5	127.6
E, GPa	193.1	193.1	182.7	182.7	182.7
I, mm^4	0.00055	0.00054	0.00061	0.00060	0.00055
σ_f, MPa	370	370	310	310	401
d/t	0.727	0.693	0.660	0.635	0.533
Theta, radians	1.376	1.508	1.470	1.382	1.571
L_{eff}, mm	18,832	18,510	19,856	19,582	17,805
L_{eff}/R_m	99.6	98.2	101.9	100.3	95.3
ϕ_c(sc), radians	0.00220	0.00392	0.00236	0.00804	0.00669
$J_{applied}$(sc), kN-m/m^2	182.9	316.8	162.7	551.3	522.4
ϕ_c(twc), radians	0.01915	0.03236	0.17719	0.05486	0.06517
$J_{applied}$(twc), kN-m/m^2	1,107.9	1,683.9	8,231.3	2,731.5	3,448.3
$T_{applied}$(sc)	939.9	958.1	963.5	879.3	823.5
$T_{material}$(sc)	87.0	141.0	953.0	368.2	287.9
Surface-crack stable?	No	No	No (Marginal)	No	No
$T_{applied}$(twc)	37.6	24.2	-26.7	24.1	11.1
$T_{material}$(twc)	46.3	54.6	691.6	146.0	145.1
Through-wall crack stable?	Yes	Yes	Yes	Yes	Yes

(a) Used base metal data.

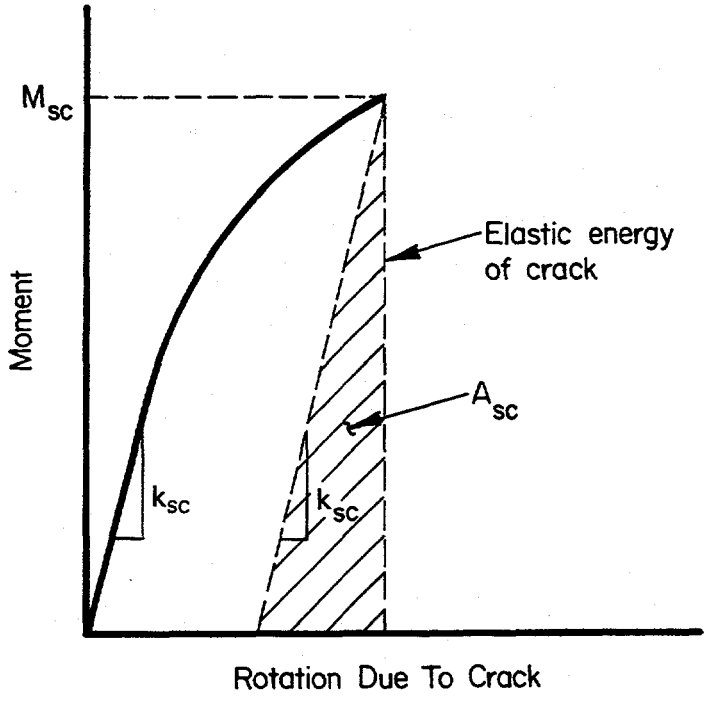

(a) Surface crack behavior

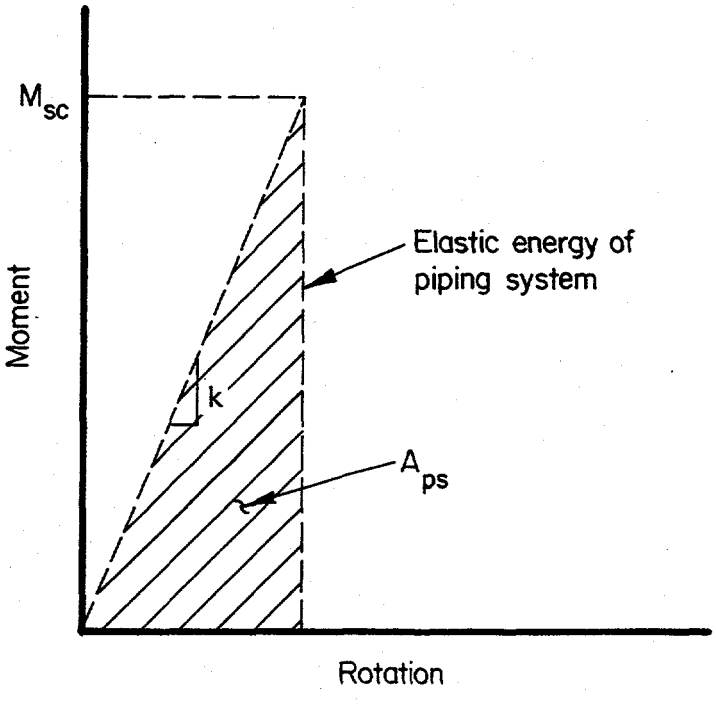

(b) Pipe-system behavior

Figure 4.16 Energy available for driving an instability

F1.3-10/90-F4.16a&b

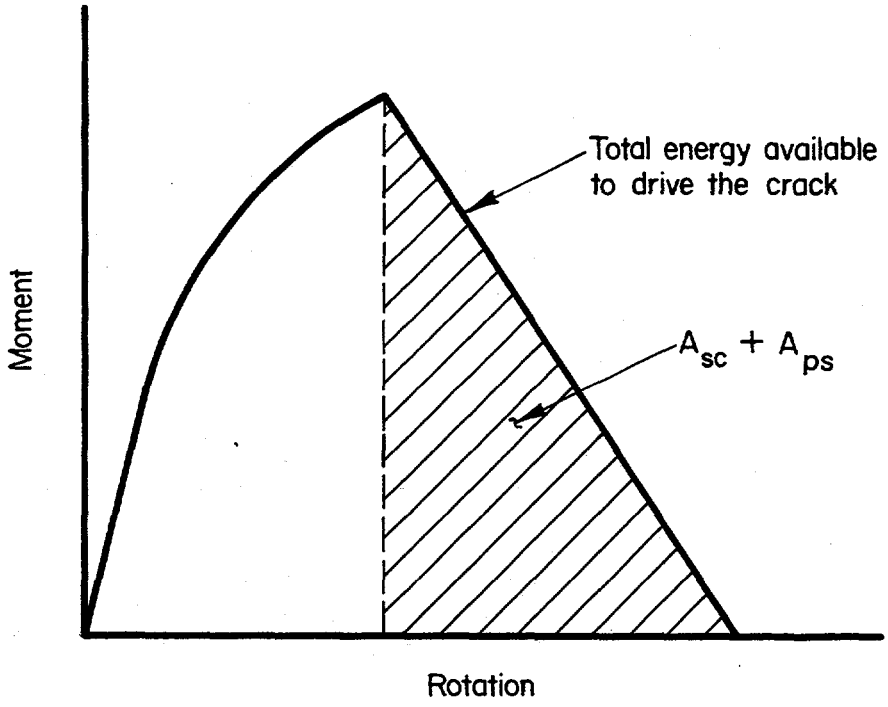

(c) Combined energy

Figure 4.16 (continued)

F1.3-10/90-F4.16c

sum of the energies shown in Figures 4.16(a) and 4.16(b). This is the total energy available to drive a surface crack as a through-wall crack.

The energy absorbed by a through-wall crack growing from length θ_0, the original length of the surface crack, to some final length θ_{tot} is shown in Figure 4.17. Figure 4.18 shows the energy being absorbed to propagate the through-wall crack being made equal to the available elastic energy from the crack and the attached piping system. Stability is determined by whether or not the predicted arrest point is above or below the load-controlled moment: a predicted arrest moment below the load-controlled moment implies instability.

The data needed to perform an energy balance analysis are the moment-rotation prediction of the initially surface-cracked pipe, the moment-rotation prediction for the resulting through-wall cracked pipe with the same circumferential crack length as the initial surface crack length, and the elastic compliance of the pipe system. Surface-cracked pipe moment-rotation predictions can be made using the SC.TNP J-estimation scheme that was previously discussed in this report (Ref. 4.16). Circumferential through-wall cracked pipe moment-rotation curves can be calculated using the LBB.ENG J-estimation scheme (Ref. 4.31). The calculational procedure is discussed in a later section. The pipe-system compliance can be determined with a finite element computer program using the methodology outlined in Reference 4.29.

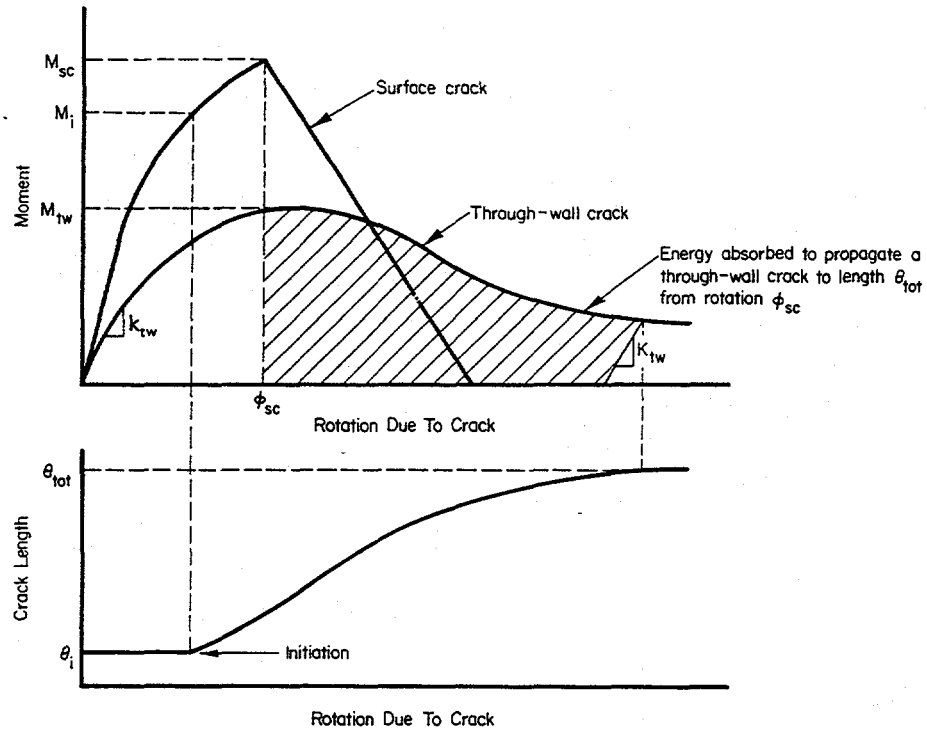

Figure 4.17 Through-wall crack propagation behavior

F1.3-10/90-F4.17

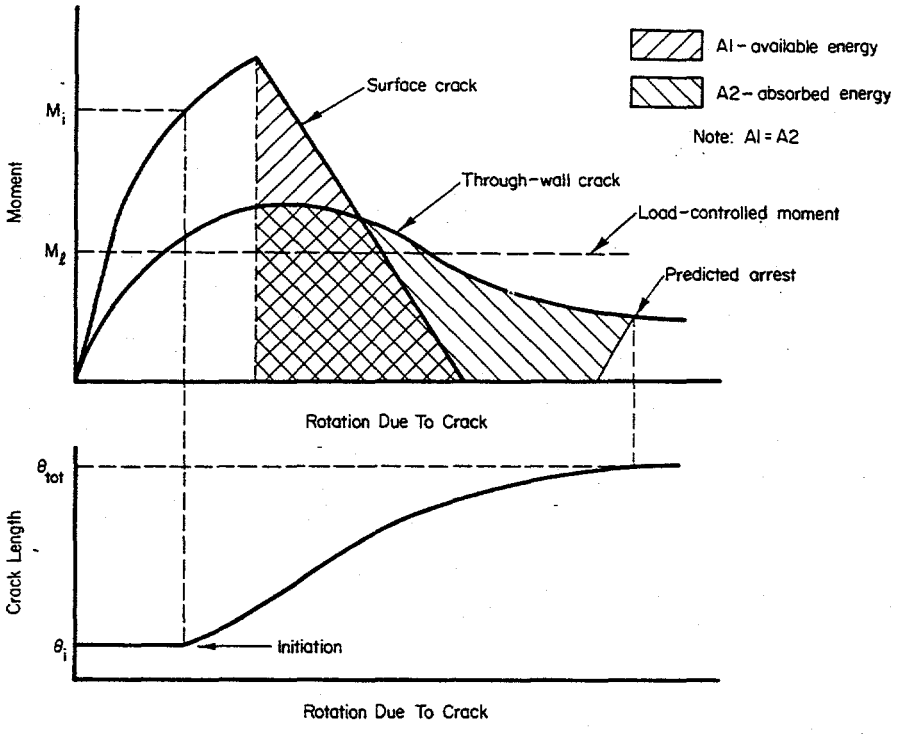

Figure 4.18 Balanced available and absorbed energies

F1.3-10/90-F4.18

For an Energy Balance Stability Analysis of a pipe system, it is necessary to identify load-controlled versus displacement-controlled moments. Displacement-controlled moments are moments which are relieved by pipe-system deformation. Thermal expansion and anchor displacements cause displacement-controlled moments. Load-controlled moments, on the other hand, are moments which are not shed as a result of deformation. Dead-weight loading and eccentric axial forces from pressure cause load-controlled moments. for the Subtask 1.3 system case, the only significant load-controlled moment of consequence is the moment caused by the eccentric axial forces from the internal pressure. The dead-weight loads are insignificant.

To account for the pressure induced moment, several possible approaches may be considered. One method is to incorporate the axial tensile forces in the calculations of the moment-rotation curves of the surface and through-wall-cracked pipe analyses. This is the most straightforward approach, but J-estimation schemes including pressure and bending of pipe have not been validated to date. Another approach is to conduct the moment-rotation calculations under pure bending, and then determine an equivalent load-controlled bending moment caused by the axial tensile load. This is the method that was used here. The equivalent bending moment, M_{eq} was determined by using the Net-Section-Collapse analysis:

$$M_{eq} = M_b - M_{b+p} \tag{4-41}$$

where M_b is the moment calculated by the Net-Section-Collapse analysis at failure for pure bending of the through-wall crack, and M_{b+p} is the moment calculated by the Net-Section-Collapse analysis at failure for combined bending and pressure of the through-wall crack. The original EPRI NP-192 Net-Section-Collapse equations (Ref. 4.9), as per Appendix F in this report, were used to perform the calculations. It should be noted that M_{eq} contains terms that include induced bending effects from the axial tension from the internal pressure. If the pipe system restrains the induced bending, then the M_{eq} will be less. This is a discussion point in Section 5.

4.7.2.1 Results of Energy Balance Stability Analysis of the IPIRG Pipe-System Experiments

The energy balance stability analyses utilized the SC.TNP surface-crack J-estimation scheme analysis for pure bending to establish surface-crack moment rotation curves. The through-wall crack moment-rotation curves were determined using the NRCPIPE code with the LBB.ENG method (see Ref. 4.31). Based on experience from the Degraded Piping Program (Ref. 4.1) the LBB.ENG method with the J_M-R curve has been found to give the most accurate prediction of the moment-rotation behavior of through-wall cracks past maximum load. Calculations performed in the Degraded Piping Program and during the design of the IPIRG Subtask 1.3 experiments showed that the SC.TNP analysis predicts the surface crack behavior quite well. (Either the J_D- or J_M-R curves can be used for the surface-cracked pipe SC.TNP predictions since the crack growth is small and, hence, there is little difference between J_D and J_M values). The system compliance was determined using the ANSYS® finite element computer program.

The input parameters for the J-estimation scheme analyses are the material properties, crack, and pipe geometry. A Ramberg-Osgood fit of the stress-strain curve was used to describe the material stress-strain response. Quasi-static stress-strain data were used for the surface-crack calculations, while the dynamic stress-strain curve at a strain rate of approximately 1 sec^{-1} was used for the through-wall-crack calculations. For the J-resistance curve, the dynamic J_M-R curve was used from C(T) specimen tests. Because through-wall moment-rotation response is needed well beyond the range of crack growth obtained in the C(T) tests,

it was necessary to extrapolate the J_M-R curves. This was done by linear extrapolation of the data with Δa values from 10 to 30 percent of the ligament (Ref. 4.32).

An equivalent crack length was used in the surface crack SC.TNP analysis. This equivalent crack length was determined by taking the area of the initial surface crack and dividing by the maximum surface crack depth. This accounts for the tapered nature at the ends of the surface cracks which were machined with a 152-mm (6-inch) diameter cutter, in most experiments.

4.7.2.2 Energy Balance Predictions

The energy balance stability diagrams for the five experiments conducted in IPIRG Subtask 1.3 are shown in Figures 4.19 to 4.23. In these figures, two load-controlled moments are shown: the higher one assumes that the PWR pressure (15.5 MPa) remains on the pipe throughout the rapid fracture process, while the lower one represents the load-controlled moment that would exist when the pressure drops to the saturation pressure at 288 C (550 F). Table 4.12 summarizes the energy balance predictions. This assumes that all the dynamic stresses are considered as displacement-controlled stresses.

Table 4.12 Summary of energy balance stability predictions

		Assuming Only Pressure Stresses are Load-Controlled			Assuming Pressure and Inertial Stresses are Load-Controlled
Experiment	Flaw Material	p=15.5 MPa	$p=p_{sat}$	Predicted Crack Growth at Arrest for $p=p_{sat}$, mm	$p=p_{sat}$
1.3-2	A106B	Unstable	Marginally Unstable	---	Unstable
1.3-4	CS SAW	Unstable	Stable	91.55	Unstable
1.3-3	TP304	Stable	Stable	19.94	Unstable
1.3-5	SS SAW	Marginally Stable	Stable	43.49	Unstable
1.3-7	Aged CF8M	Unstable	Stable	69.58	Unstable

A second assumption about the dynamic moments is that the inertial components are load-controlled. The experimental inertial moments at maximum load can be determined from Table 4.3 where,

$$M_{inertial} = M_{(Tot.\ exp.)} - M_{(SP\ exp.)} \tag{4-42}$$

If the inertial moments are added to the equivalent moment for the saturation pressure, then the total load-controlled moments are above all the through-wall crack curves in Figures 4.19 to 4.23. Hence, the energy balance analysis considering inertial contributions as load-controlled moments predicts a total instability for all IPIRG pipe-system experiments. This is conservative since only two of the five experiments resulted in complete severances, and then only after numerous loading cycles past the surface crack penetration. In these two experiments, the initial surface crack instability was arrested, most probably due to the inertial unloading which invalidates the energy balance analysis assumptions. Because there are no dynamic considerations in the Energy Balance (or J/T) analysis, arrest due to inertial unloading cannot be predicted.

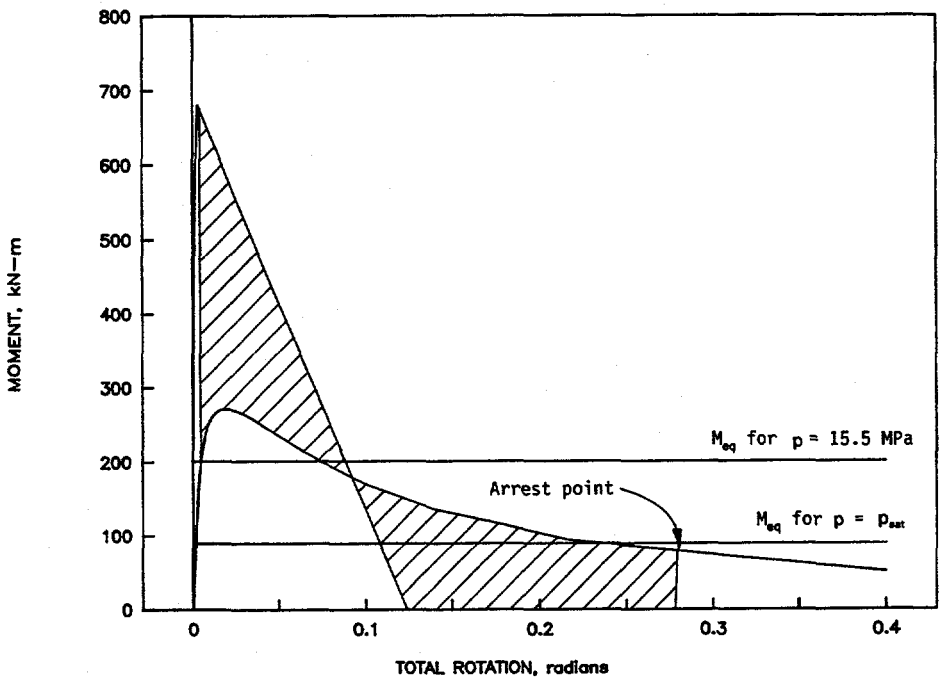

Figure 4.19 Energy balance predictions for IPIRG Experiment 1.3-2 on A106 Grade B pipe F1.3-10/90-F4.19

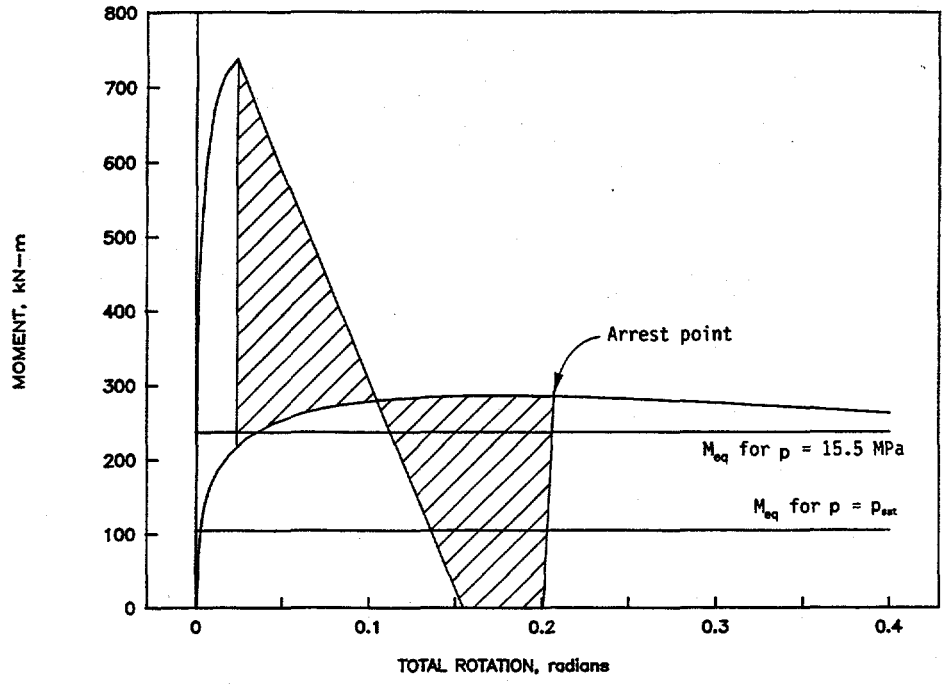

Figure 4.20 Energy balance predictions for IPIRG Experiment 1.3-3 on TP304 stainless steel pipe F1.3-10/90-F4.20

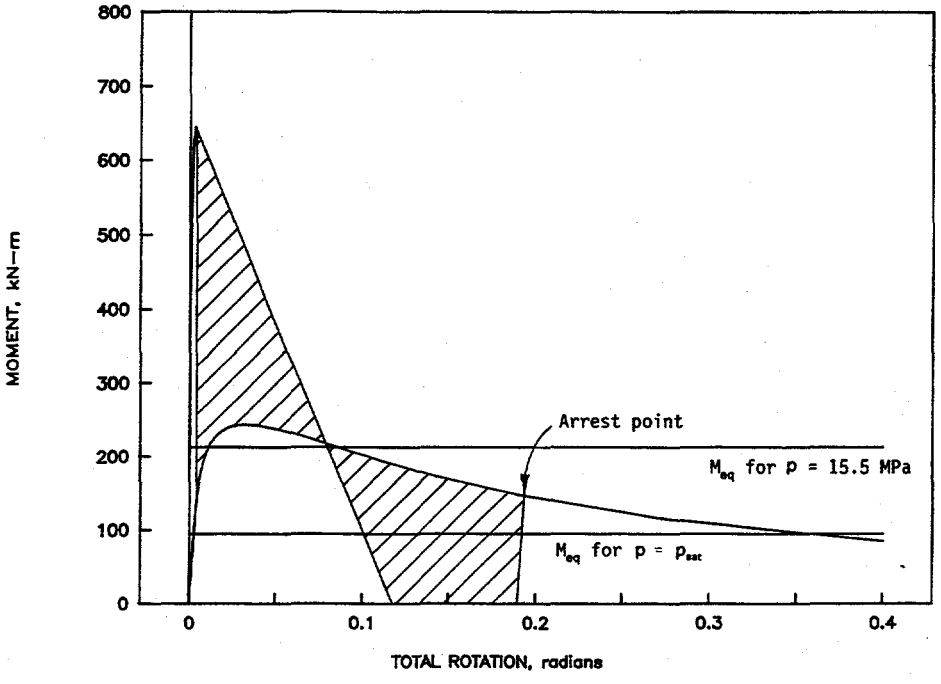

Figure 4.21 Energy balance predictions for IPIRG Experiment 1.3-4 with the crack in a carbon steel SAW F1.3-10/90-F4.21

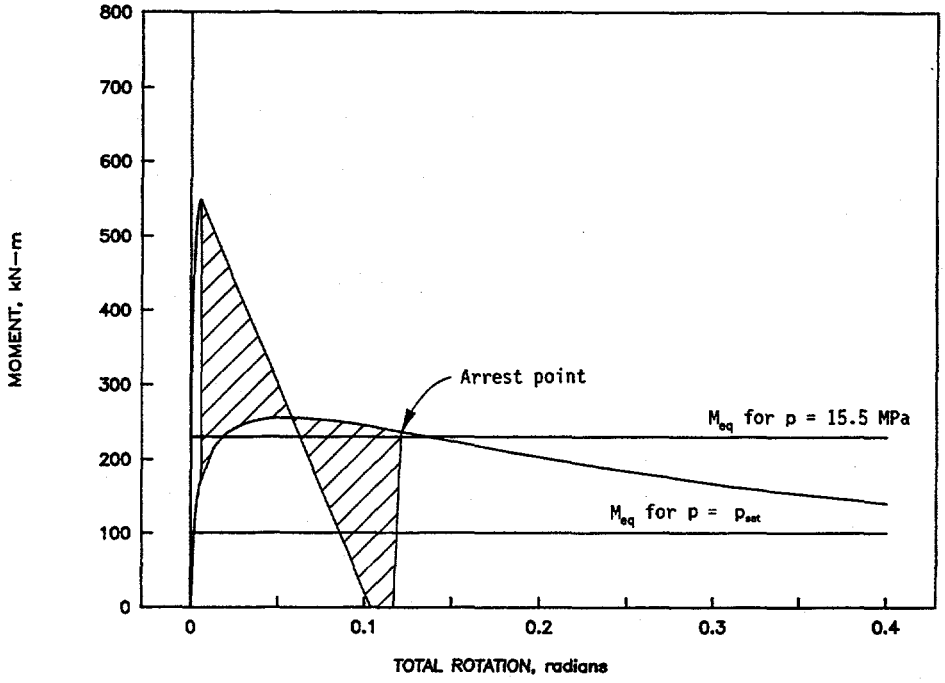

Figure 4.22 Energy balance predictions for IPIRG Experiment 1.3-5 with the crack in a stainless steel SAW F1.3-10/90-F4.22

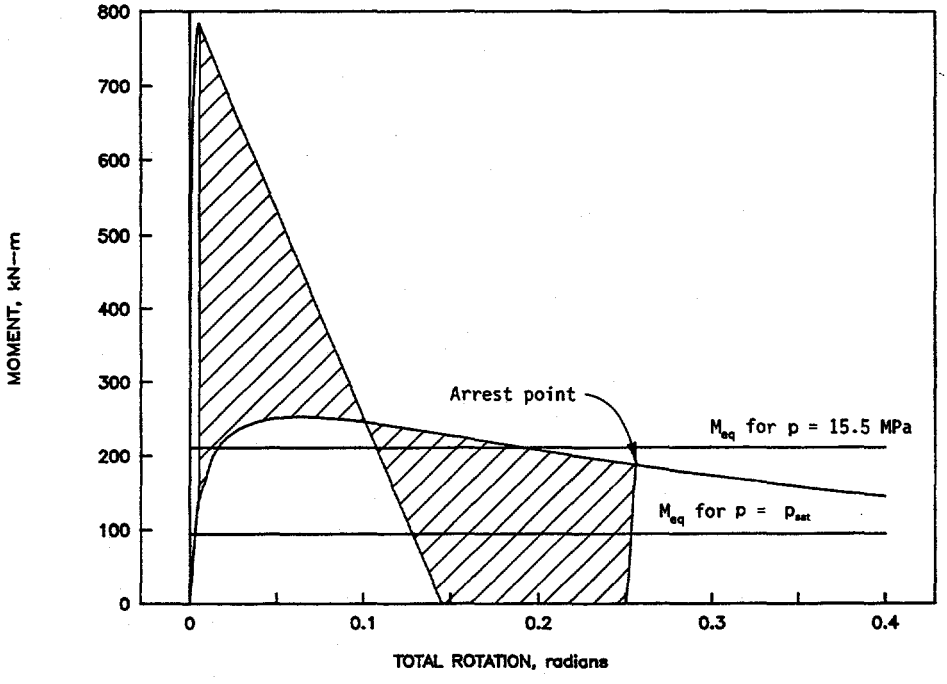

Figure 4.23 Energy balance predictions for IPIRG Experiment 1.3-7 with the crack in an aged CF8M pipe F1.3-10/90-F4.23

4.7.3 Summary of Stability Analysis Predictions

Table 4.13 summarizes the results of the J/T and energy balance stability predictions. The table includes the most likely case for the energy balance, the case where the equivalent load-controlled moment is based

Table 4.13 Summary of stability predictions

			Energy Balance, M_{eq} for $p=p_{sat}$	
Experiment	**Flaw Material**	**J/T**	**p_{sat}=Load Controlled**	**p_{sat}+Inertial=Load Controlled**
Through-Wall Cracks				
1.3-2	A106B	Stable	Unstable (Marginal)	Unstable
1.3-4	CS SAW	Stable	Stable	Unstable
1.3-3	TP304	Stable	Stable	Unstable
1.3-5	SS SAW	Stable	Stable	Unstable
1.3-7	Aged CF8M	Stable	Stable	Unstable
Surface Cracks				
1.3-2	A106B	Unstable	Unstable	
1.3-4	CS SAW	Unstable	Unstable	
1.3-3	TP304	Unstable	Unstable	
1.3-5	SS SAW	Unstable	Unstable	
1.3-7	Aged CF8M	Unstable	Unstable	

on the saturation pressure. The table further considers both the case where the load-controlled stresses are only due to the equivalent moment from the saturation pressure, and the case where the load-controlled stresses are due to the sum of the equivalent moments due to inertia and the saturation pressure. The J/T analysis considers all the moments as displacement-controlled. Both the J/T and energy balance methods correctly predict the start of the surface crack instability.

For the resulting through-wall cracks, the J/T analysis predicts stability for all the experiments. When considering the load-controlled moment being only due to the saturation pressure, the energy balance analysis predicts stability for all but the carbon steel base metal. Aside from the energy balance prediction of instability for Experiment 1.3-2, these predictions are nominally consistent with the experimental results

in that the double-ended breaks in Experiments 1.3-2 and 1.3-7 occurred only after a number of cycles of stable through-wall crack growth. If the energy balance considers the load-controlled stresses as the inertial plus saturation pressure equivalent moments, then the energy balance predicts complete instability for all experiments. This would be a conservative, but perhaps an overly conservative approach. Stability predictions are discussed further in Section 5.

4.8 Dynamic Analysis Predictions

In Section 4.2 of this report, it was demonstrated that a basic dynamic structural analysis is reasonably accurate, with proper modeling of the system. The next step includes a crack in the model to try to predict the behavior of the pipe system when it contains a crack. The mechanics of including a crack have been discussed in the System Design and Experiment Design sections in Section 3 of this report. The following provides a few selected comparisons between experimental data of cracked pipe experiments and analyses to evaluate the nonlinear spring simplified approach.

4.8.1 Carbon Steel Base Metal

In analyzing this experiment it was first necessary to calculate the moment versus crack rotation curve for the surface crack. This was done by conducting an SC.TNP analysis using dynamic J-R curve properties. The pressure at 15.5 MPa was used to calculate an equivalent moment, using Net-Section-Collapse equations, which was subtracted from the SC.TNP calculated moments.

The carbon steel base metal experiment (Experiment 1.3-2), was the first experiment to be conducted, and so it generated the first real pipe-system data that could be compared with the cracked pipe finite element analysis. The design of the experiment, using a 66 percent deep flaw, predicted that the cracked section would need to reach approximately 610 kN-m (5.3 x 10^6 in-lb) of moment for the surface crack to penetrate the pipe wall, and that this would happen at about 1.7 seconds into the test. The experiment was conducted, and the maximum moment at failure was 341 kN-m (3.0 x 10^6 in-lbs) at 0.625 seconds. Figure 4.24 shows the test design analysis prediction and the experimental data. Clearly, the experiment design overpredicted the moment capacity of the cracked section.

Post-test investigation into the cause of the overprediction determined that the crack was deeper than expected, 72.7 percent rather than the desired 66 percent. This increase in depth, amounting to 1.8 mm (0.073 in) out of a thickness of 25.7 mm (1.012 in), had a dramatic influence on the maximum moment-carrying capacity of the cracked specimen. Subsequent reanalysis of the test using the actual forcing function and a 75-percent deep flaw showed much better agreement with the experiment. (A 75-percent depth was used since preliminary post-test information indicated that this was the actual flaw size.) Figures 4.25 and 4.26 are comparisons of cracked section moment and the actuator force for the experiment and the analysis with the deeper flaw. Interpolating the failure moments for the two analyses, 610 kN-m (5.3 x 10^6 in-lbs) for the 66-percent deep flaw and 235 kN-m (2.0 x 10^6 in-lbs) for the 75-percent deep flaw, to a 72.7-percent deep flaw, the expected failure moment would be 330 kN-m (2.9 x 10^6 in-lbs), nearly perfect agreement with the test, and the predicted time to failure would be within 2 percent of the experimental result.

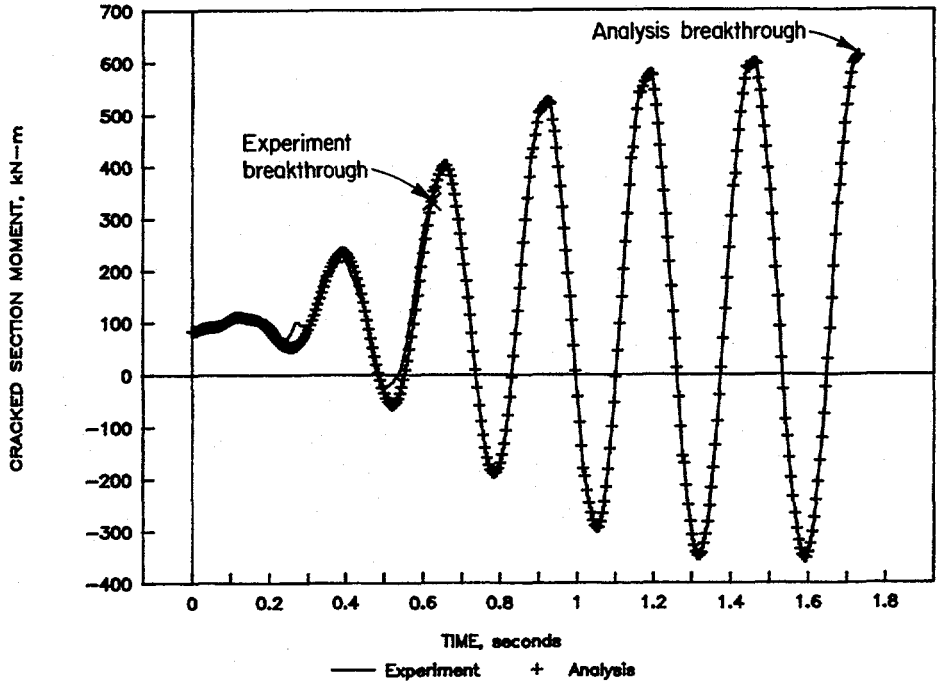

Figure 4.24 Comparison of pre-test predictions of cracked section moment to carbon steel base metal experiment (1.3-2) results (Analysis with 66 percent deep flaw) F1.3-10/90-F4.24

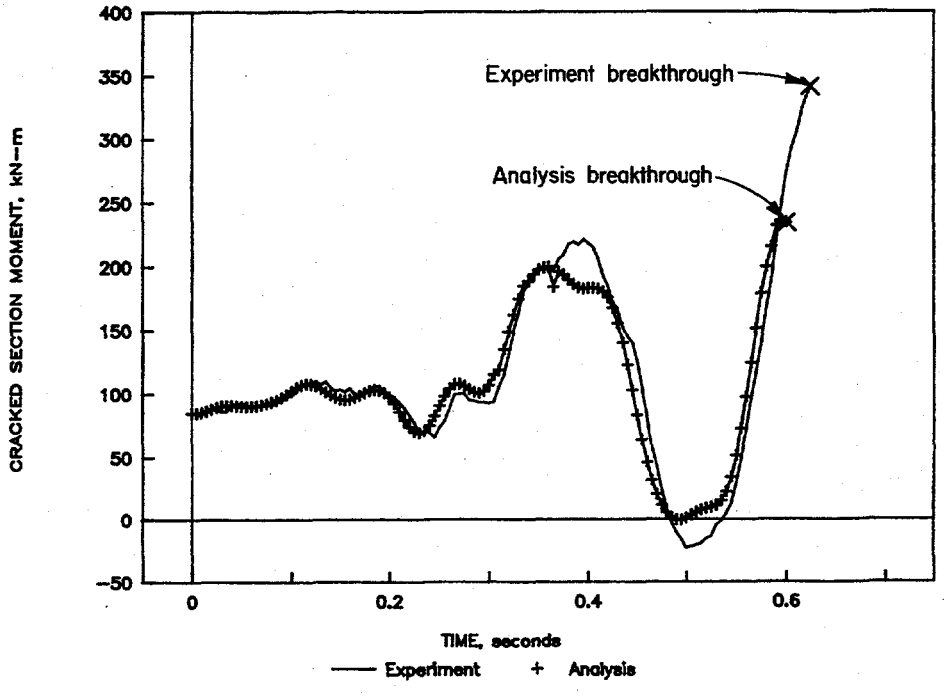

Figure 4.25 Comparison of post-test prediction of cracked section moment and experiment results for the carbon steel base metal experiment (1.3-2) (Analysis with 75 percent deep flaw; actual flaw depth 72.7 percent deep) F1.3-10/90-F4.25

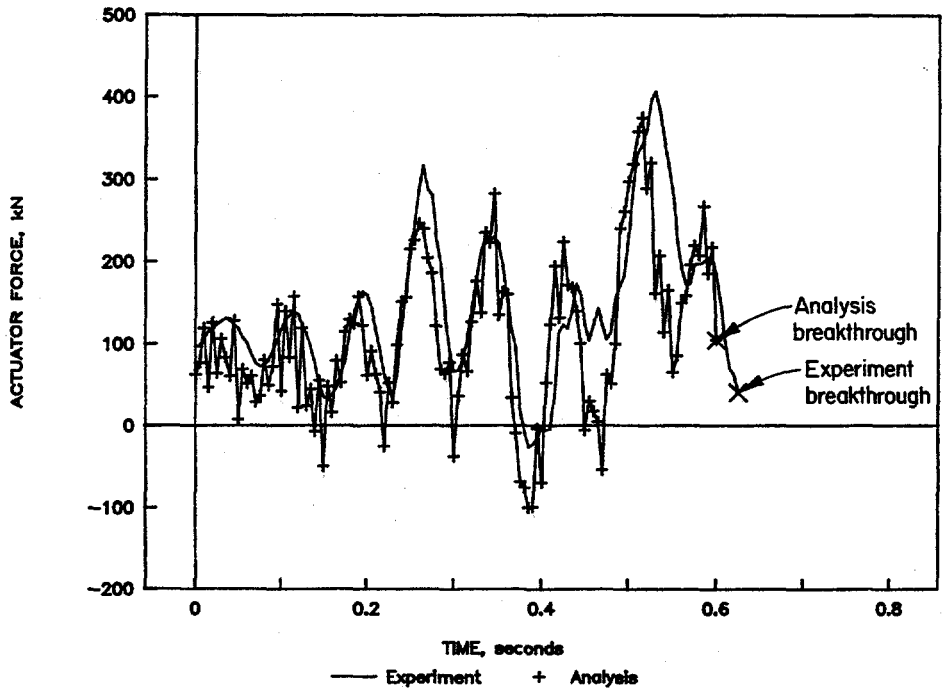

Figure 4.26 Comparison of actuator force prediction and experimental results for the carbon steel base metal experiment (1.3-2) (Analysis with 75 percent deep flaw)
F1.3-10/90-F4.26

4.8.2 Stainless Steel Base Metal

A detailed comparison between experiment and analysis also was made for the stainless steel base metal experiment (Experiment 1.3-3). This experiment was the subject of the Fifth IPIRG Workshop Analysis Round Robin. Figures 4.27 through 4.29 show typical comparisons of analysis with experiment. Other comparisons were made for moments at another location, displacements at various locations, and hanger loads. In general, all of the comparisons are exceptional. The analysis used the measured post-test flaw geometry and the experimental actuator displacement time history for input. The moment-rotation curve for the dynamic analysis was generated from J-R curve and stress-strain curve data using the procedure described in the Experiment Design section of this report. For this material, the J-R curves and tensile properties were relatively close at quasi-static and dynamic loading rates.

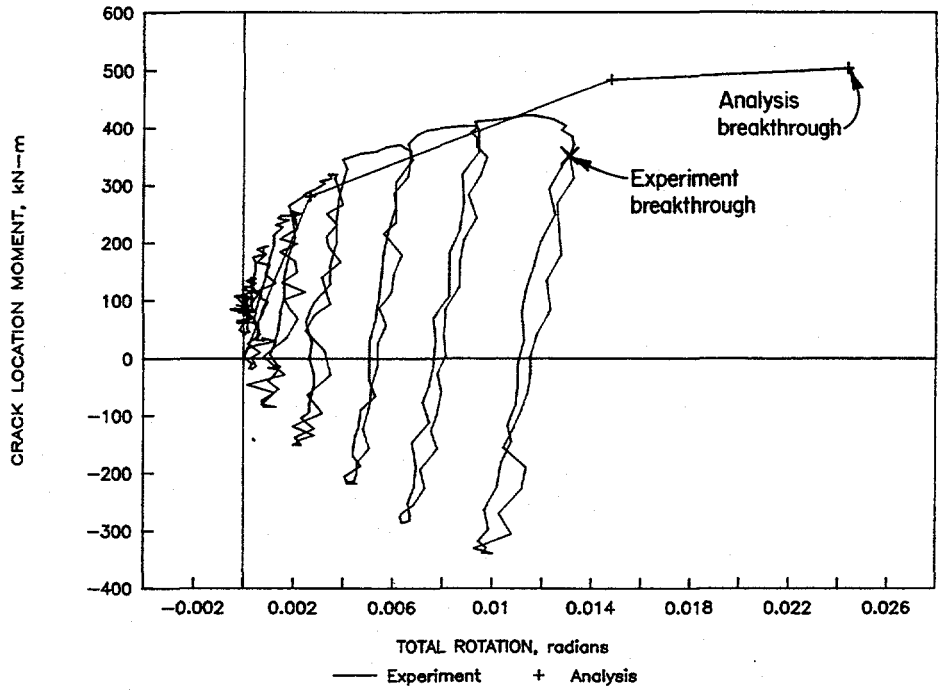

Figure 4.27 Comparison of moment-rotation curves of SC.TNP analysis with the stainless steel base metal experiment (1.3-3) F1.3-10/90-F4.27

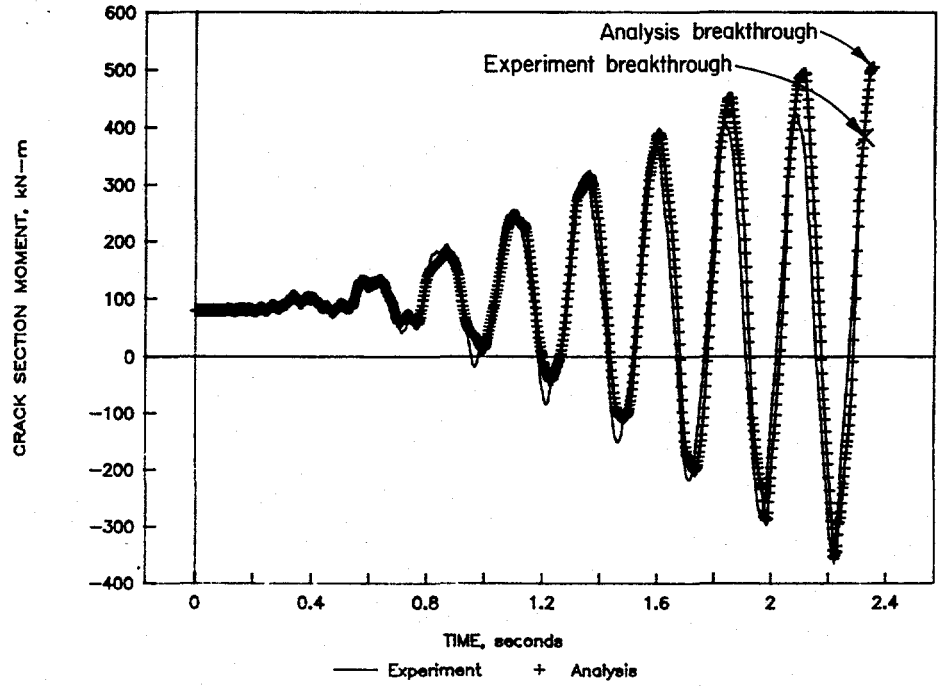

Figure 4.28 Comparison of the crack section moment predictions and experimental results for the stainless steel base metal experiment (1.3-3) F1.3-10/90-F4.28

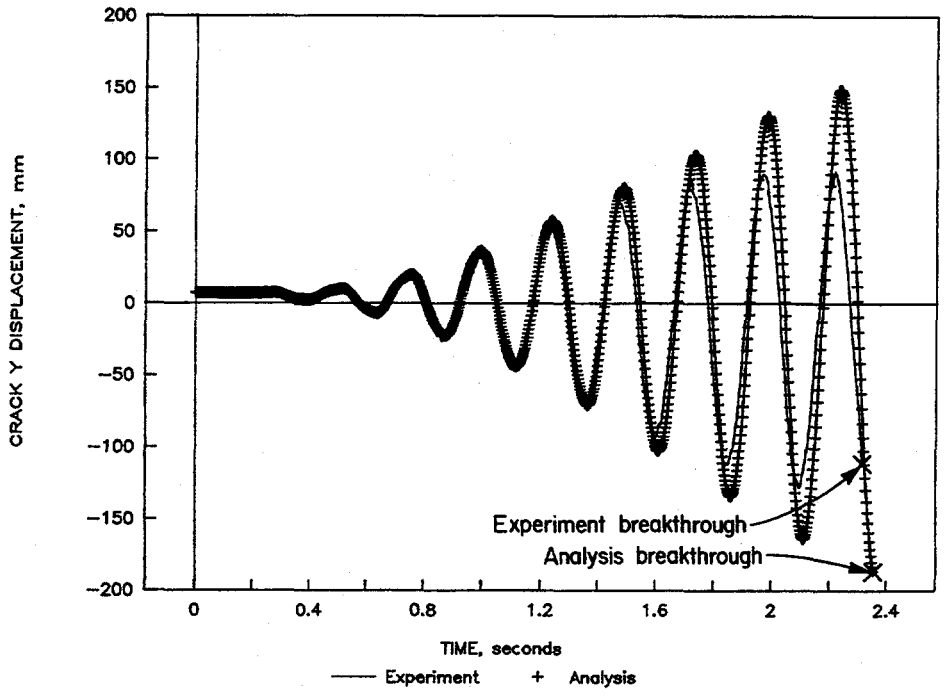

Figure 4.29 Comparison of the crack section displacement predictions and experimental results for the stainless steel base metal experiment (1.3-3) F1.3-10/90-F4.29

The experimental moment-rotation curve plotted in Figure 4.27 is reasonably bounded by the curve used as input to the analysis, in terms of general shape and magnitudes of moments. Rotation tends to be overestimated by the J-estimation scheme, but this overestimation does not seem to have seriously impaired the prediction of the failure time in the finite element analysis. It is worth noting that surface crack penetration in this experiment occurred at a moment that was significantly lower than the moment achieved on the prior cycle, due to crack growth during the prior cycle. The SC.TNP calculations past maximum load are not considered reliable, and hence are not used in modeling the moment-rotation curve for the dynamic analysis. Furthermore, current limitations in the ANSYS® code do not allow for negative stiffnesses in the moment-rotation curve modeling by the spring-slider approach employed. Even with this modest shortcoming, the moment predictions are quite reasonable.

The displacement comparison shown in Figure 4.29, is typical of the other displacement comparisons made for this experiment. The agreement, while not perfect, is still quite good. The fact that the displacements predicted by analysis are somewhat greater than the experimental data is consistent with the predicted moment being larger than the experimental moment. In general, the primary source of the small discrepancies between analysis and the experiments is the inability of the fracture mechanics analyses to predict the correct moment-rotation input for the crack.

4.8.3 Summary of Piping System Response Analysis

The comparisons shown have illustrated that it is possible to conduct nonlinear finite element analyses of a cracked pipe system and get meaningful predictions of both system and crack behavior. As noted earlier, damping must be properly characterized, the structural modeling must be properly performed, (i.e., mass

and stiffness must be correct), and the inputs to the analysis, forcing function and flaw size, must be known. In addition, the fracture mechanics portion of the analysis must be able to correctly predict the moment-rotation behavior of the cracked section of pipe. If any of these are not well known, the comparisons between the experiments and analysis would not be as good. Small changes in flaw size (depth), errors in the damping, ignoring the decrease in modulus of elasticity, or an incorrect estimation of moment-rotation behavior due to the crack can all drastically affect the predicted dynamic behavior of a pipe system with a crack.

Although the nonlinear time-dependent cracked pipe finite element analysis discussed here is reasonably straightforward, it is probably not suitable for routine application in plant piping design. However, in a research context, the cracked pipe analysis does provide a way to assess the effects of various parameters on pipe-system performance and flaw behavior without having to perform a large number of expensive experiments. It would be inappropriate to suggest that the analysis methodology discussed here is mature and extensively verified, but the successful design of the IPIRG Subtask 1.3 facility and the limited comparisons made with it for the Subtask 1.1 (Ref. 4.7) and Subtask 1.3 experimental results suggest that it is a viable tool.

Some other applications for this methodology would be to:

(a) Assess what would be the margins in the elastic stress analysis if the entire IPIRG pipe-system loop were fabricated from the same strength material as the test section rather than the high strength pipe and elbows that were used. Or what would be the margins for typical pipe loop configurations.

(b) Assess what the margins would be with more prototypical size flaws such as those considered in LBB and in-service flaw evaluations.

4.9 References

4.1 Wilkowski, G. M., and others, "Degraded Piping Program -Phase II," Summary of Technical Results and Their Significance to Leak-Before-Break and In-Service Flaw Acceptance Criteria, March 1984-January 1989, by Battelle Columbus Division, NUREG/CR-4082, Vol. 8, March 1989.

4.2 Kanninen, M. F., and others, "Instability Predictions for Circumferentially Cracked Type 304 Stainless Steel Pipes Under Dynamic Loadings," Final Report on EPRI Project T118-2, by Battelle Columbus Laboratories, EPRI Report Number NP-2347, April 1982.

4.3 ASME Boiler and Pressure Vessel Code, Section III, Division 1, Appendix N, American Society of Mechanical Engineers, 1989.

4.4 ASME Boiler and Pressure Vessel Code, Code Case N-411-1, American Society of Mechanical Engineers, 1989.

4.5 Tang, H. T., Duffey, R. B., Sing, A., and Bausch, P., "Experimental Investigation of High Energy Pipe Leak and Rupture Phenomena," ASME Special Publication PVP Volume 98-8, *Fracture, Fatigue and Advanced Mechanics*, 1985.

4.6 "Piping and Fitting Dynamic Reliability Program," EPRI RP 1543-15, 1995.

4.7 Scott, P., and others, "Stability of Cracked Pipe under Inertial Stresses - Subtask 1.1 Final Report," NUREG/CR-6233, Vol. 1, August 1994.

4.8 Brochard, J., Petit, M., and Millard, A., "A Special Cracked Pipe Element for Leak Before Break Application," Transactions of 10th SMiRT, Volume G, pp 357-362, August 1989.

4.9 Kanninen, M. F., and others, "Mechanical Fracture Predictions for Sensitized Stainless Steel Piping with Circumferential Cracks," Final Report, EPRI NP-192, September 1976.

4.10 Wilkowski, G. M. and Scott, P. M., "A Statistical Based Circumferentially Cracked Pipe Fracture Mechanics Analysis for Design or Code Implementation," *Nuclear Engineering and Design*, Vol. 111, pp 173-187, 1989.

4.11 ASME Boiler and Pressure Vessel Code, Section XI, Appendix C, 1995 Edition, July 1995.

4.12 ASME Boiler and Pressure Vessel Code, Section XI, Appendix H, 1995 Edition, July 1995.

4.13 Harrison, R. P., Loosmore, K., Milne, I., and Dowling, A. R., "Assessment of the Integrity of Structures Containing Defects," CEGB Report R/H/R6, 1976: R/H/R6-Rev. 1, 1977.

4.14 Milne, I., "Failure Assessment Diagrams and J Estimates: A Comparison for Ferritic and Austenitic Steels," CEGB Report RD/L/2208N81, 1982.

4.15 Milne, I., Ainsworth, R. A., Dowling, A. R., and Stewart, A. T., "Assessment of the Integrity of Structures Containing Defects," R/H/R6-Rev. 3, Published by Central Electric Generating Board, England, May 1986.

4.16 Scott, P. M. and Ahmad, J., "Experimental and Analytical Assessment of Circumferentially Surface-Cracked Pipes Under Bending," NUREG/CR-4872, April 1987.

4.17 Maricchiolo, C., and Milella, P. P., "Fracture Behavior of Carbon Steel Pipes Containing Circumferential Cracks at Room Temperature and 300 C," *Nuclear Engineering and Design*, 111, pp 35-46, 1989.

4.18 Wilkowski, G. M. and Eiber, R. J., "Evaluation of Tensile Failure of Girth Weld Repair Grooves in Pipe Subjected to Offshore Laying Stresses," ASME *Journal of Energy Resources Technology*, Vol. 103, March 1981.

4.19 Kurihara, R., Ueda, S. and Sturm, D., "Estimation of the Unstable Fracture of Pipe with a Circumferential Surface Crack Subjected to Bending," *Nuclear Engineering and Design*, Vol. 106, pp 265-273, 1988.

4.20 Wilkowski, G. M., and others, "Short Cracks in Piping and Piping Welds," Semi-Annual Report, March-September 1990, NUREG/CR-4599, Vol. 1, No. 1, May 1991.

4.21 "Evaluation of Flaws in Austenitic Steel Piping," (Technical basis document for ASME IWB-3640 analysis procedures), prepared by Section XI Task Group for Piping Flaw Evaluation, EPRI Report NP-4690-SR, April 1986.

4.22 Meyzaud, V., Ould, P., Balladon, P., Bethmont, M., and Soulat, P., "Tearing Resistance of Aged Cast Austenitic Stainless Steels," presented at NUCSAFE 88, Avignon, France, October 1988.

4.23 Kumar, V., and German, M., "Elastic-Plastic Fracture Analysis of Through-Wall and Surface Flaws in Cylinders," EPRI report NP-5596, January 1988.

4.24 Pan, J., "Some Considerations on Estimation of Energy Release Rates for Circumferentially Cracked Pipe," in *Journal of Pressure Vessel Technology*, Vol 106, pp 391-398, November 1984.

4.25 Kramer, G., and others, "Subtask 1.2 Final Report - Stability of Cracked Pipe Under Seismic/Dynamic Displacement-Controlled Stresses,"NUREG/CR-6233, Vol. 2, No. 1, July 1997.

4.26 Tada, H., and Paris, P., "Tearing Instability Handbook," NUREG/CR-1221, January 1980.

4.27 Zahoor, A., "Ductile Fracture Handbook, Volume 1, Circumferential Through-wall Cracks," EPRI Report Number NP-6301-D, June 1989.

4.28 Tada, H., Paris, P., and Gamble, R., "Stability Analysis of Circumferential Cracks in Reactor Piping Systems," NUREG/CR-0838, June 1979.

4.29 Zahoor, A., and Gamble, R., "Leak Before Break Analysis for BWR Recirculation Piping Having Multiple weld Locations," EPRI report NP-3522-LD, April 1984.

4.30 Wilkowski, G. M., and Kramer, G., "An Energy Balance Approach to Estimate the Initiation and Arrest of Ductile Fracture Instability in Circumferentially Cracked Pipe," in ASME Special publication PVP Vol. 167, pp 103-114, July 1989.

4.31 Brust, F. W., "Approximate Methods for Fracture Analyses of Through-Wall Cracked Pipes". NRC Topical Report by Battelle Columbus Division, NUREG/CR-4853, February 1987.

4.32 Wilkowski, G. M., Marschall, C. W., and Landow, M., "Extrapolation of C(T) Specimen J-R Curves," in ASTM STP 1074, pp 56-84, 1990.

5.0 DISCUSSION AND SIGNIFICANCE OF RESULTS

5.1 Significance of Material Characterization Efforts

The results of the material characterization efforts for the materials used in this effort were reported in detail in Reference 5.1. Material characterization tests included uniaxial tensile tests in the longitudinal orientation and compact tension [C(T)] tests in the L-C orientation. Except for the aged cast stainless tests, all tests were conducted at 288 C (550 F). The aged cast stainless steel tests were conducted at 300 C (572 F). For some of the materials, quasi-static test data at other temperatures were available from the Degraded Piping Program (Ref. 5.2). Specimens were tested under displacement control with monotonically increasing displacement at a constant rate, unlike the IPIRG pipe-system experiments for which the loading was cyclic. Strain rates in tensile tests and the time rate of change in J, dJ/dt, in the C(T) specimen tests were designed to approximate those in the Subtask 1.3 pipe-system experiments.

Within the strain rate and loading rate ranges considered, the results of material characterization tests revealed important differences in the behavior of carbon steels and stainless steels. The two carbon steels (A106B and a SAW) were found to be susceptible to dynamic strain aging, i.e., aging that occurs simultaneously with plastic straining and which depends on both the temperature and strain rate. Because of its susceptibility to dynamic strain aging, the carbon steel base metal was found to have a significantly higher ultimate strength but slightly lower yield strength at 288 C (550 F) than at room temperature, whereas the stainless steel base metals displayed decreasing strength (lower yield and ultimate strengths) with increasing temperatures, as is commonly expected for metallic materials.

While the increased tensile strength at elevated temperatures for the carbon steels could be considered advantageous, it was accompanied by several potentially negative effects. First, elevated temperature tensile strength was diminished significantly as strain rate was increased, though strength values remained in excess of ASME code values for the pipe examined. Second, dynamic rates of loading decreased the fracture resistance for C(T) specimens of the A106B base metal tested at 288 C (550 F). Dynamic loading lowered the value of J at crack initiation (J_i) by 35 percent and the value of dJ/da by 45 percent for the A106B material. For reasons that are not yet understood, the carbon steel weld metal behaved differently than the base metal in the C(T) tests, even though the two materials behaved similarly in tensile tests. In the dynamic C(T) tests at 288 C (550 F), the fracture resistance of the weld metal, both J_i and dJ/da, was approximately 50 percent higher than the quasi-static fracture resistance.

In addition to the loss of strength and fracture resistance in dynamic tests, the A106B base metal displayed another undesirable trait that is not well understood, but which also is believed to be associated with dynamic strain aging. This steel exhibited bursts of unstable crack extension between periods of stable tearing. Similar behavior was observed for a 152-mm (6-inch) diameter A106B pipe used in Subtasks 1.1 and 1.2 (Refs. 5.3 and 5.4). The C(T) specimens from the smaller pipe tested in Subtasks 1.1 and 1.2 showed unstable cracking in both the quasi-static and the dynamic C(T) tests, whereas the C(T) specimens of the larger pipe evaluated in Subtask 1.3 showed crack jumps only in the quasi-static tests.

In contrast to the results for the carbon steels, the stainless steels exhibited no pronounced deleterious effects of dynamic testing. Ultimate tensile strength values from the dynamic tests were within approximately $\pm$ 5 percent of those from the quasi-static tests. Yield strength values were raised, and

fracture resistance was increased. The increase in fracture resistance was modest in the case of the wrought TP304 base metals, and substantial for the SAW metal and the aged CF8M base metal.

The results of these material characterization tests suggest that it would be prudent to use dynamic strength and toughness properties to evaluate flawed carbon steel pipes that are suspected of being susceptible to dynamic strain aging. For stainless steel pipes, on the other hand, quasi-static strength and toughness data probably are adequate for pipe flaw analysis.

5.2 Significance of Pipe-System Experiments

This section discusses the significance of the pipe-system experiments from the viewpoint of observations of the experimental results. Significance from the analytical aspects are discussed in Section 5.3.

5.2.1 Stability Issues

For each of the Subtask 1.3 experiments, once the internal surface crack penetrated the pipe wall it grew rapidly to approximately the ends of the machined surface crack. The crack velocity for the resulting through-wall-crack at one crack tip during this period was estimated from electric potential data to be approximately 20 m/second (65 feet/second) for the stainless steel base metal experiment, see Figure 3.144. Once the resultant through-wall crack reached the ends of the machined surface crack, and the applied loadings began to decrease, the crack temporarily arrested. When the applied moments at the crack section went into the compressive regime, and the associated rotations became negative, the crack faces began to close upon themselves. This was evident by sharp drops in the electric potential data, see Figure E-17 in Appendix E. As the crack faces closed upon themselves, a current path across the crack faces was re-established thus reducing the effective electrical resistance and the measured potential. This through-wall crack closure was also evident on the videotapes by the steam emanating from the crack which was choked off whenever the crack faces closed upon themselves.

Once the applied loadings, and the associated crack section rotations began to increase again, the through-wall crack faces would separate. This was evident from both the electric potential traces (sharp rise in EP) and videos (steam once again emanating from the crack). As the applied loadings and associated crack section rotations continued to increase, there was a gradual but steady rise in the electric potential trace, see Figure E-17. This gradual but steady rise in the EP signal was associated with stable through-wall crack growth. For the stainless steel base metal experiment, the magnitude of the through-wall crack velocity was estimated to be approximately 0.08 m/second (0.25 feet/second). This through-wall crack velocity during the loading cycles after surface crack penetration was several orders of magnitude slower than the growth along the initially surface-flawed region as the initial surface crack was changing into a through-wall crack.

For each of the five cracked pipe experiments, the resultant through-wall crack continued to grow in a stable manner (fracture speeds on the order of 0.1 m/second [0.3 feet/second]) whenever the applied loadings, and associated crack section rotations, were increasing. Once the applied loadings and crack section rotations would decrease, the through-wall crack would arrest. The extent of crack growth at each of these unloadings was evident through close examination of the fracture surface. At each of these arrests, crack closure marks were evident on the fracture surface, for example see Figures 3.145, 3.147,

3.149, and 3.151. This slow steady cyclic through-wall crack growth continued until either a DEGB occurred or the applied loadings were stopped. For the carbon steel base metal and aged cast stainless experiments, a DEGB condition was reached. The number of cycles after maximum load until a DEGB was reached for these two experiments were approximately 10 to 15. For the other three experiments, the applied loadings died out before a DEGB occurred. The number of cycles after maximum load for these three experiments was approximately 20.

This is in sharp contrast to what was observed for the Subtask 1.1 experiments. In the Subtask 1.1 experiments it was observed that once maximum moment was achieved, there were very few additional cycles (i.e., 2 or 3) until the pipe essentially reached a DEGB (Ref. 5.3). It was concluded that in considering the stability of a piping system subjected to pure inertial loading (i.e., the Subtask 1.1 experiments), the loading should be considered as being closer to a load-controlled situation than a displacement-controlled. Thus, one would expect a near instantaneous break. For the Subtask 1.3 experiments, with a mixture of inertial and displacement-controlled stresses (the percent inertial loading for the Subtask 1.3 experiments ranged from 26 to 51 percent, see Table 3.10), one would expect a larger number of cycles between maximum moment and a break.

One of the objectives of the IPIRG Subtask 1.3 experiments was to achieve a near instantaneous break in one or more of the experiments. In order to satisfy this objective it was decided to remove the end caps near the test specimen for the aged cast stainless experiment (1.3-7). The rationale behind this decision was that these end caps represented an artificial constraint that may have been affecting the ultimate stability of the resultant through-wall crack. These end caps, which had a small 13-mm (0.5-inch) diameter hole in each of them, restricted the flow of water to the test section once the surface crack penetrated the pipe wall. Their purpose was to reduce the rapid release of energy in the earlier experiments. Consequently, after surface crack penetration, the pressure at the test specimen decreased at an artificially high rate. By removing the end caps it was felt that the pressure in the crack section, and hence the axial stress, would be maintained, thus enhancing the chances of achieving a DEGB.

During the design of the aged cast stainless experiment, calculations were made to assess the critical through-wall crack length for the case of simple pressure loading. Figure 5.1 is a plot of the normalized nominal axial tensile stress (due to pressure) as a function of the normalized critical through-wall crack length. (The normalized axial tensile stress is the value predicted by the Net-Section-Collapse analysis and is normalized by the flow stress, where the flow stress is the average of quasi-static yield and ultimate strengths. The crack length is normalized by pipe circumference.) Assuming the pressure at the crack is maintained near the saturation pressure (7.2 MPa [1,050 psi]), the normalized axial tensile stress has a value of 0.06 for the aged cast stainless steel pipe experiment. Based on this value and Figure 5.1, it was estimated that the critical through-wall crack length would be approximately 63 percent of the pipe circumference.

It was estimated that the through-wall crack would grow to a length of 63 percent of the pipe circumference in 6 to 7 cycles after surface crack penetration. This estimate was based on the cyclic through-wall crack growth for the stainless steel base metal experiment evident in Figures 3.147 and 3.148 and Table 3.12. If one accounts for the inertial component of the bending stresses acting as a load-controlled component to the crack driving force, it was felt that the combined pressure-induced and inertial stresses may drive the resultant through-wall crack to an instability in as little as 1 or 2 cycles after surface crack penetration.

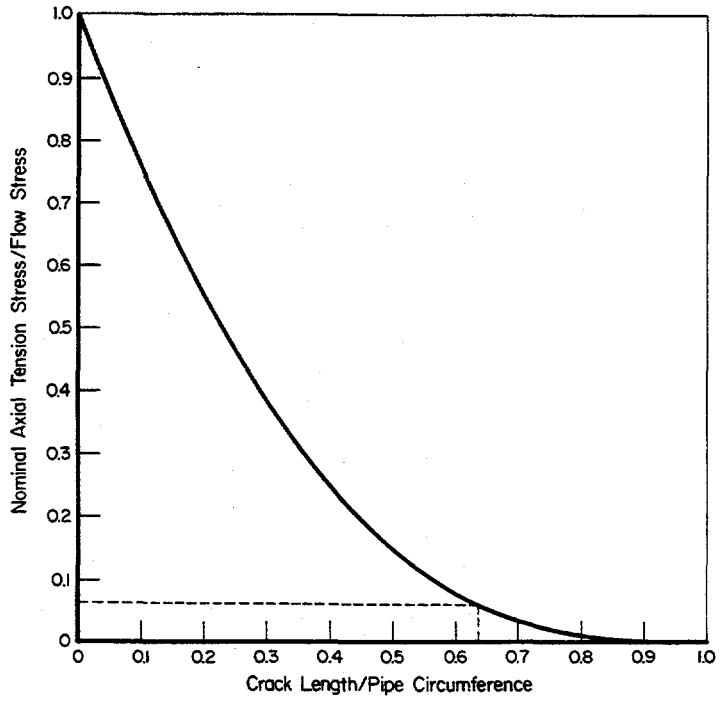

Figure 5.1 Predicted through-wall critical crack length based on Net-Section-Collapse analysis for axial tension stress as a function of the ratio of the crack length to pipe circumference I1.3-10/90-F5.1

As noted previously, the DEGB did not occur until 13 cycles after surface crack penetration. Furthermore, in examining the fracture surface and the videotape, it was apparent that the remaining ligament at the instant the crack section broke was only 75 mm (3 inches) in length, see Figure 5.2. The through-wall crack had grown to a length of 95 percent of the pipe circumference (instead of the predicted 63 percent) before a critical crack length was attained.

One possible explanation for this discrepancy is presented in Figure 5.3. Figure 5.3 shows two curves. The bottom curve is the same curve as shown in Figure 5.1. It is for the case where induced bending and rotations of the pipe due to pressure are allowed to occur freely, i.e., the ends of the test section are free to rotate. The top curve is for the case where these induced bending moments and associated rotations are restricted, i.e., the ends of the test section are completely fixed. Note that for the case of restricted rotations, the critical crack length is predicted to be 95 percent of the pipe circumference for a normalized tensile stress of 0.06. Consequently, it is possible that the remainder of the piping loop is restraining the induced bending and associated rotations such that the case of fixed ends gives the more accurate prediction. Another possible explanation is that the resulting thrust forces due to the escaping fluid through the through-wall crack are restricting the induced bending and associated rotations. In any event, this finding could impact leak-before-break analysis methods which are based on the Net-Section-Collapse, or other fracture analyses, that fail to take credit for this restriction of the induced bending moments and associated rotations. Consequently, the critical through-wall crack length in a pipe system for the leak-before-break analyses methods may be considerably greater than previously expected. This

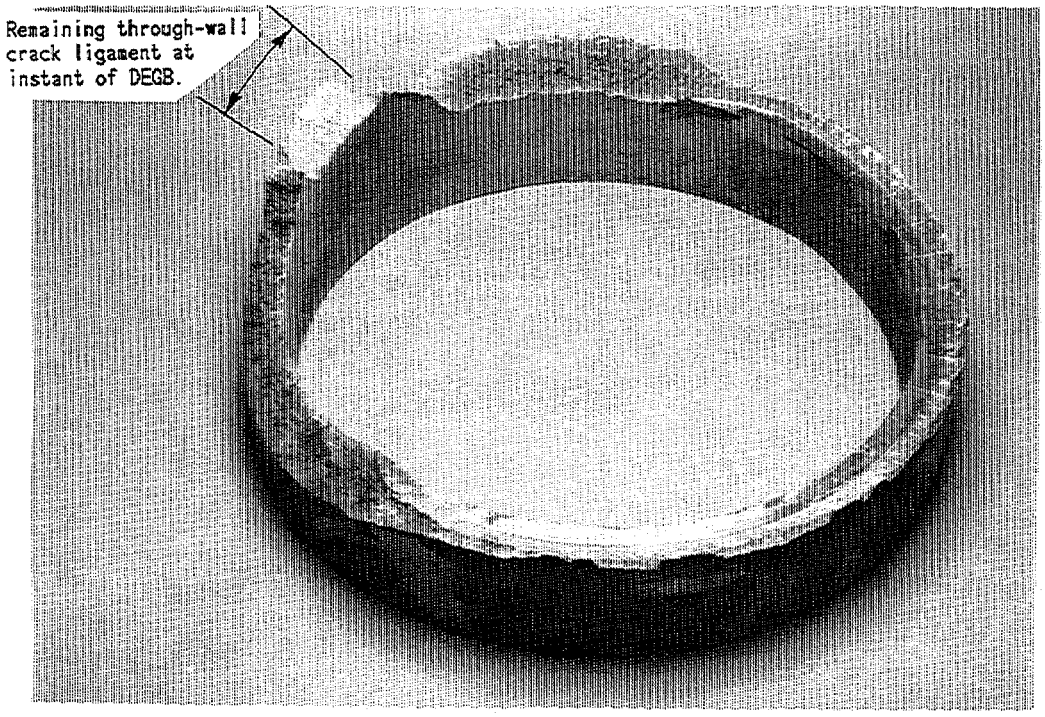

Figure 5.2 Photograph of fracture from aged cast stainless experiment (Experiment 1.3-7) I1.3-10/90-F5.2

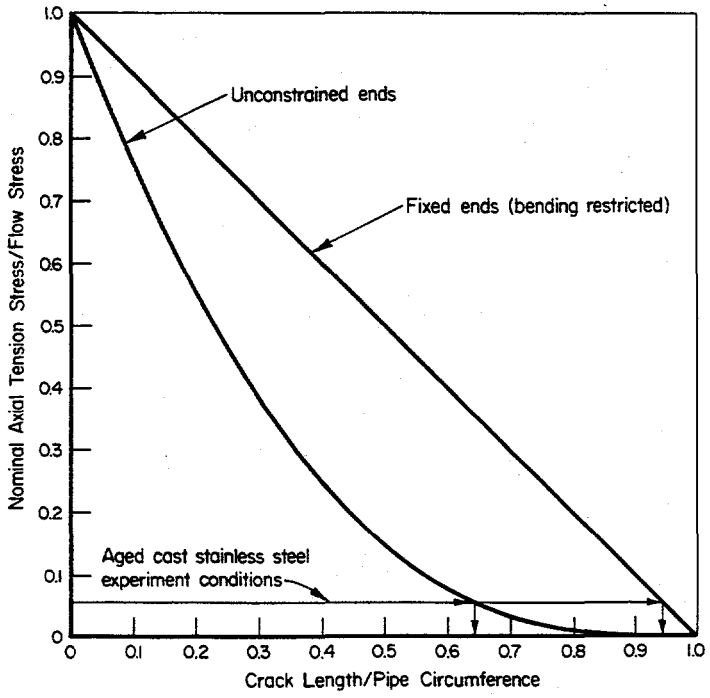

Figure 5.3 Net-Section-Collapse analyses predictions, with and without considering induced bending, as a function of the ratio of the through-wall crack length to the pipe circumference EB-3/91-RS13

is a beneficial aspect. A detrimental aspect may be that the restraint of the induced bending for a leaking through-wall crack may cause the crack opening area for leak rate considerations to be less than current calculational methods consider.

5.2.2 Effect of Cyclic Loading on Toughness

At the beginning of the program a literature review was undertaken to establish the effect of cyclic loadings on a material's fracture toughness. As a result of that literature review, it was concluded that there were limited data available on the effects of negative load ratios (i.e., minimum stress/maximum stress) on the apparent toughness of materials. The limited data that were available tended to suggest that cyclic loadings decreased the material's apparent fracture resistance.

As part of Subtask 1.2, a few critical pipe experiments were conducted to assess the effect of cyclic loading on a material's toughness. (Note, no laboratory C(T) specimens were evaluated as part of this effort.) What was found as a result of those pipe experiments was that two parameters, the stress ratio (R) and incremental cyclic plastic displacement, had a significant effect on the apparent toughness, at least for the case of a through-wall crack in a stainless steel pipe, see Figure 5.4. Figure 5.4 shows the crack-tip-opening-angle (CTOA), which is a measure of toughness, from the cyclic tests normalized to the CTOA from the corresponding monotonic test. The normalized CTOA is plotted as a function of the ratio of the load-line displacement (LLD) at crack initiation from the monotonic test to the incremental cyclic plastic displacement between loadings from the cyclic test, see Figure 5.5. (Note, the CTOA measurements used to generate Figure 5.4 were obtained optically.) From Figure 5.4 one can conclude that for the case of a through-wall crack in a stainless steel pipe, more negative stress ratios lower the apparent toughness of the material. Furthermore, for a given stress ratio, the smaller the value of the incremental cyclic plastic displacement, see Figure 5.5, the lower the apparent toughness.

An attempt was made to make a similar assessment for the Subtask 1.3 experiments of the effect of stress ratio and incremental cyclic plastic displacement on the fracture resistance. The effective stress ratio for the Subtask 1.3 experiments ranged from +0.23 to -0.34, with the average being approximately -0.15, see Table 5.1. (Note that internal pressure tends to raise the stress ratio.) Considering the stainless steel base metal experiment, which had the lowest effective stress ratio of -0.34, the ratio of the load-line displacement (LLD) at crack initiation to the incremental cyclic plastic displacement in moment-rotation space is approximately 2.5, see Figure 5.6. Based on these values one can see from Figure 5.7 that the effect of the cyclic loadings on the apparent toughness for this stainless steel experiment is expected to be minimal, i.e., less than 5 percent. The effect of cyclic loadings on the apparent toughness for the other Subtask 1.3 experiments should be even less because the effective stress ratios were less negative for those experiments. Consequently, all of the Subtask 1.3 experiments should be able to be effectively analyzed using monotonic specimen J-R curve data. A similar conclusion was reached for the Subtask 1.1 experiments (Ref. 5.3). The above conclusions, however, do assume that the CTOA empirical cyclic relation from the Subtask 1.2 through-wall-cracked TP304 stainless steel pipe experiments are generally applicable. Additional verification of this is desirable.

5.2.3 Additional Observations From Pipe-System Experiments

Several additional observations from the pipe-system experiments are worthy of note. For one, the pipe system experienced very little plastic deformation during the course of all but the last experiment.

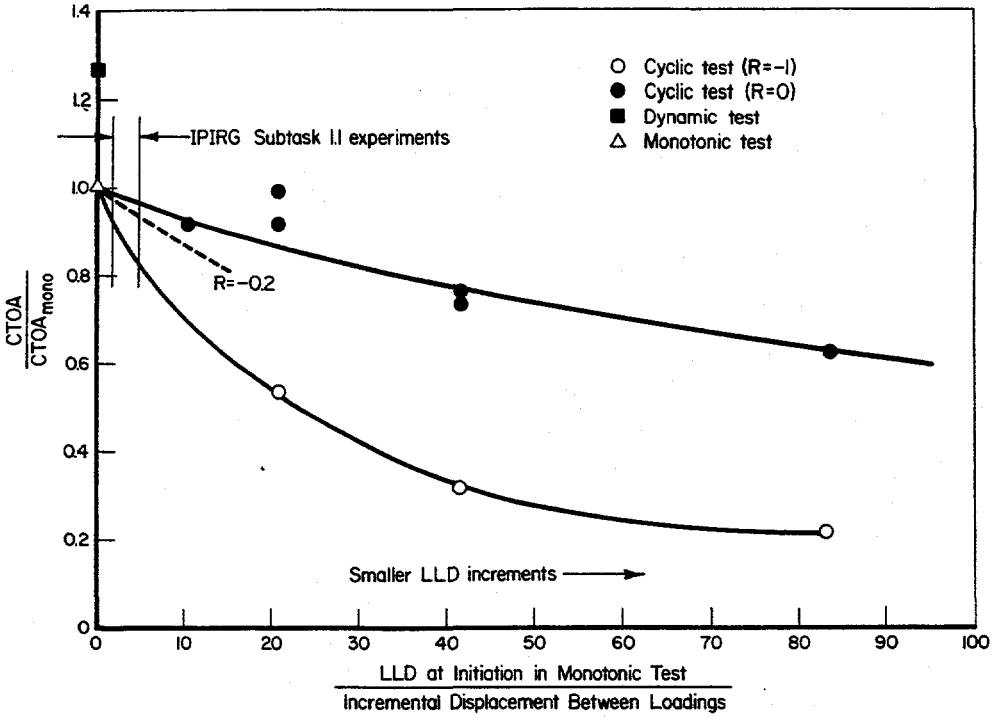

Figure 5.4 Effect of cyclic loading (stress-ratio and increment of cyclic plastic displacement) on apparent toughness for IPIRG Subtask 1.2 stainless steel TWC pipe experiments DRB/1.2-5/F25

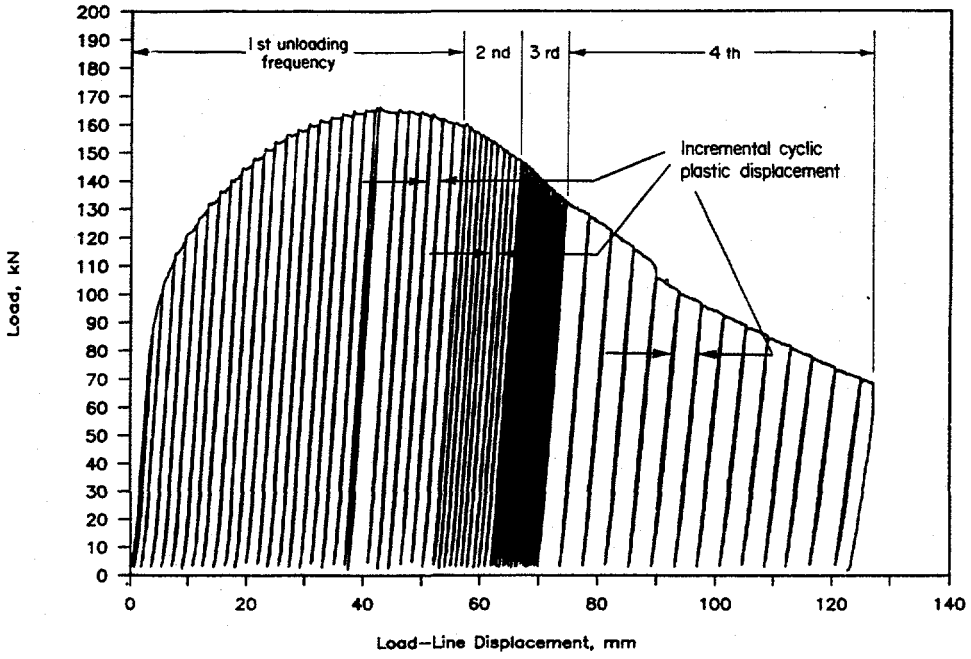

Figure 5.5 Measured load versus load-line displacement for Subtask 1.2 quasi-static reversed (R = 0) loading experiment (Experiment 1.2-3) I1.3-10/90-F5.5

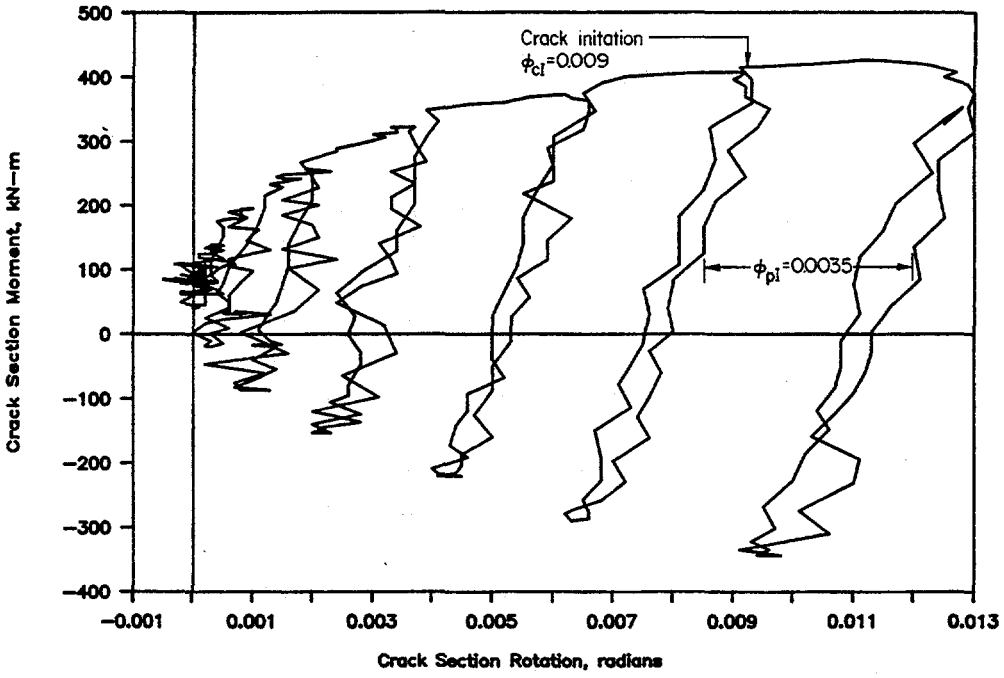

Figure 5.6 Crack section moment versus crack section rotation for stainless steel base metal pipe-system experiment (Experiment 1.3-3) I1.3-10/90-F5.6

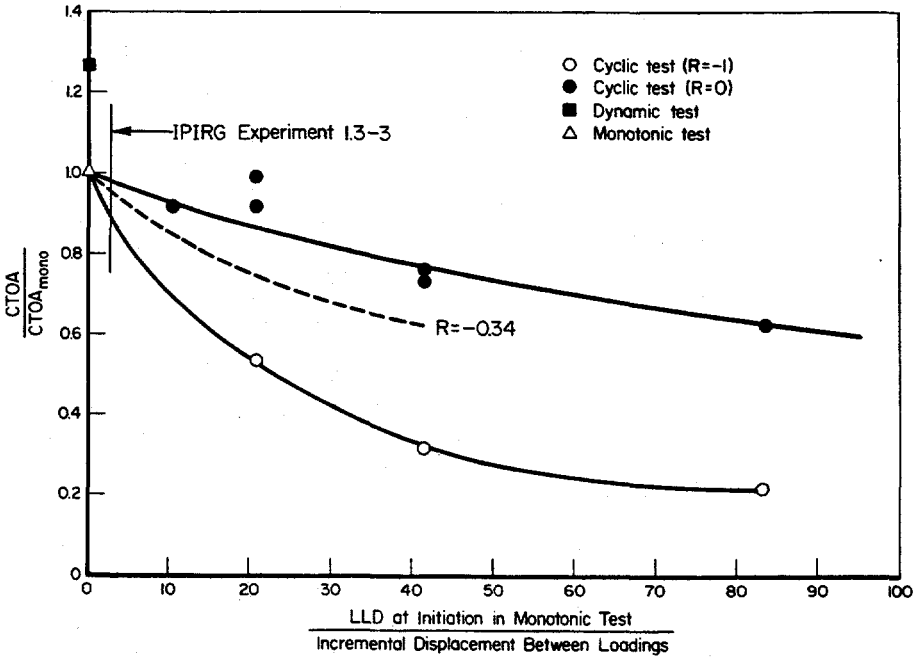

Figure 5.7 Effect of cyclic loading on apparent toughness for IPIRG Subtask 1.3 stainless steel base metal pipe-system experiment I1.3-10/90-F5.7

Table 5.1 Stress ratios (R) from IPIRG pipe-system experiments

Experiment Number	Test Specimen Material	Stress Ratio	
		M_{min}/M_{max}	$\frac{\sigma_{bmin} + \sigma_t}{\sigma_{bmax} + \sigma_t}$
1.3-2	CSBM	-0.07	+0.23
1.3-3	SSBM	-0.81	-0.34
1.3-4	CSW	-0.43	-0.18
1.3-5	SSW	-0.66	-0.27
1.3-7	Cast Stainless	-0.46	-0.20
	AVERAGE	-0.49	-0.15

Pre- and post-test measurements of the span across the elbows indicated that the elbows were not plastically deformed during the course of these experiments. Furthermore, the measured dynamic strains at the high stress locations on the elbows indicated that the strain levels were not excessive. In addition, after each test specimen was removed from the loop, the welding of the next test specimen into the piping loop required very little relative movement of the two ends of the pipe loop at the test section. Each of these observations support the contention that the piping loop experienced very little plastic deformation during the course of these experiments.

A second observation from the pipe-system experiments, which is probably worth noting, is that the blast effects of the steam emanating from the crack were significant. Calculations were made during the design of the pipe-system experiments to ensure that the pressure forces on the walls of the building were not excessive. Based on the work of Isozaki et al. (Ref. 5.5), it was concluded that by incorporating the end caps at the test specimen, that the pressure at the building walls from the release of the steam through a relatively small crack opening area would not damage the building. The calculations indicated that the pressure at a distance of 3 meters (10 feet) from the crack would be on the order of 0.12 kPa (0.02 psi). However, after the carbon steel base metal experiment, it was noted that the deflector shield, 3 meters (10 feet) from the crack (made from 6.3 mm [0.25 inch] thick steel plate) had a fairly significant bend in it. Since a 0.12 kPa (0.02 psi) pressure distributed over the entire 1.2 by 2.4 meter (4 by 8 feet) plate represents a total force of only 400 N (100 pounds), it was felt that the actual pressures were much greater than predicted. It should be noted that a number of assumptions were made in this analysis. Furthermore, Isozaki's analysis was empirical in nature and it was necessary to extrapolate his analysis beyond the region where he had experimental data.

A final observation of note from the pipe-system experiments has to do with the DEGB associated with the aged cast stainless experiment. Once the aged cast stainless specimen was completely severed at the crack section, the cable restraint system holding the two halves of the pipe loop together failed. When this happened, pipe whip caused by the large jet forces propelled the two halves of the loop in opposite directions (recall that there were no end caps for this experiment). The long east-west pipe run associated with the east half of the loop acted as a long moment arm creating a very high bending stress

at the girth weld adjacent to the hanger at Node 26, see Figure 3.26. The high bending stress at this girth weld caused an unexpected secondary failure at this weld. The pipe severed at this location and the long east-west pipe run from Node 26 to the crack was ejected from the building. This pipe section impacted a stack of pipe just to the south of the building with sufficient energy to launch several large pipe projectiles. One section of pipe from this stack, weighing approximately 330 kg (720 pounds), was launched into the air and came to rest 166 meters (544 feet) from the original stack. Another section of pipe, weighing approximately 1,000 kg (2,200 pounds), impacted a building approximately 30 meters (100 feet) from the original stack. In addition to these pieces of pipe, there were several smaller lengths of pipe that became projectiles. This suggests that the energy possessed by the section of the pipe loop which exited the building must have been quite large. The point to be made is that if a DEGB were to occur in a plant, and a pipe whip restraint failed, one could expect significant damage to occur in other parts of the plant.

5.3 Significance of Analytical Evaluations

The following points can be summarized from the analysis aspects from Section 4 of this report.

5.3.1 Elastic Stress Analysis Ratios

In the EPRI/NRC Piping Reliability program (Ref. 5.6), Code elastic stress analyses were assessed by comparisons with ambient temperature small diameter pipe-system experiments. Those experiments, however, were without initial cracks and the piping systems were constructed of one material. In contrast, the IPIRG system was constructed with high strength pipe, and, in one case, a thicker elbow was used intentionally to avoid plasticity at any location except the crack location. Damping was also minimized in the IPIRG experiments by the use of low friction supports. Hence, due to a lack of nonlinear behavior, the differences between elastic stress analyses and experimental measurements made during the IPIRG pipe-system experiments are probably as small as can practically be expected for the types of cracks and materials being evaluated.

The accuracy of elastic stress analyses were determined calculating the ratios of moments or stresses from an elastic analysis by the experimentally measured moments or stresses at the crack location. Although four different ratios were studied, perhaps the most meaningful are the ratio of calculated-to-measured total stresses, $ESR_{(Tot.\ \sigma)}$, and the ratio of calculated-to-measured total stress minus the seismic anchor motion stresses, $ESR_{(\sigma\text{-}sam)}$. The ratio on total stress, $ESR_{(Tot.\ \sigma)}$ is important because the total stress, including seismic anchor motion stresses, has been considered in the NRC's LBB analyses (Ref. 5.7). The $ESR_{(\sigma\text{-}sam)}$ ratio is important, because typical ASME code design analyses may not include the seismic anchor motion stresses.

In examining the results in Table 4.3, it can be seen that the ratio of calculated-to-measured total stress varied from 0.95 to 1.32. This is far less than the ratios of 15 to 30 observed in the EPRI/NRC Piping and Fitting Dynamic Reliability program on uncracked pipe, but are close to the results observed in the IPIRG Subtask 1.1 experiments (Ref. 5.3). (Note, the precise manner of calculating the elastic stress analysis ratio differed slightly between the IPIRG and EPRI/NRC Piping and Fitting Dynamic Reliability programs, but it is expected that the two methods would give the same order of magnitude for ratios of calculated-to-measured stresses.)

The use of $ESR_{(\sigma\text{-sam})}$ is an attempt to analyze the IPIRG pipe-system experiments in the spirit of the ASME piping design rules that may be used in some cases. Here, the seismic anchor motion stresses are not considered in the elastic analysis, but the experimental stresses include them. This identifies the consequence of ignoring the seismic anchor motion stresses for the IPIRG pipe system. As can be seen in Table 4.3, this analysis gave the lowest values of the elastic stress ratios, and in only one case was the $ESR_{(\sigma\text{-sam})}$ above one. The lowest value, 0.66, was for the carbon steel base metal experiment.

5.3.2 Inherent Accuracy of the Fracture Analyses

The details of the calculations of the ratios which gauged the accuracy of the various fracture analyses were given in Section 4.4 of this report. Table 5.2 summarizes those results for the various analyses. In this table only the maximum stress comparisons are given. Recall that all these analyses used only the quasi-static properties. This was done since dynamic properties of piping materials for an LBB or flaw evaluation are not generally available.

Table 5.2 includes the IPIRG experiments as well as the corresponding quasi-static experiments. The inherent accuracy of the fracture analyses are assessed by calculating the ratio of the experimental stress (bending plus tension) to the predicted stress (bending plus tension) at maximum bending moment. This ratio may be thought of as a measure of the difference between the measured and calculated pipe's resistance to fracture, whereas the elastic stress analysis ratios may be thought of as a measure of the difference between the measured and calculated values of stress or crack driving force.

5.3.2.1 Comparison of Various Fracture Analysis Methods

From Table 5.2 the following observations can be made about the various analyses.

- The Net-Section-Collapse analysis tends to overpredict the maximum experimental stress and, therefore, have low ratios of measured-to-calculated stresses. This was because some of the experiments were not limit-load failures and elastic plastic methods are required for a valid analysis.

- The Dimensionless Plastic-Zone Parameter analysis is one of the simplest means of modifying the Net-Section-Collapse analysis for elastic-plastic corrections. With the exception of the three dynamic IPIRG base metal experiments, the analysis produced ratios of the experimental-to-predicted load-carrying capacity of the pipe segments which were greater than one, and reasonably accurate. One reason for the IPIRG carbon steel base metal prediction of 0.704 being so far below 1.0 is that the analysis assumed quasi-static material property data. As alluded to earlier, both the strength and toughness of this material were significantly reduced at dynamic loading rates.

- The ASME Section XI flaw evaluation procedures for ferritic piping (IWB-3650) using the Code values of S_m, tended to have the highest ratios of experimental-to-calculated stresses. These ratios do not include the ASME Code applied safety factors of 2.78 for normal and test conditions and 1.39 for emergency and faulted conditions. The ratios of experimental-to-calculated stresses associated with the austenitic criterion (IWB-3640) tended to be much lower. The dynamic IPIRG pipe-system experiments with cracks in the TP304 stainless steel base metal and the artificially aged cast CF8M steel base metal had experimentally measured stresses less than the predicted stresses so that the ratios were less than one in these cases.

Table 5.2 Summary of experimental-to-predicted ratios of maximum stresses from fracture analyses (All values are based on total stress at maximum load)

Experiment Number	Material	Net-Section Collapse			DPZP	SME Section XI		R6 Opt. 1[a]	SC.TNP[a]
		$(\sigma_y + \sigma_u)/2$	$1.15(\sigma_y + \sigma_u)/2$	S_m(Code)	$(\sigma_y + \sigma_u)/2$	S_m(Code)	S_m(Actual)		
1.3-2	A106B	0.605	0.522	0.882	0.704	1.484	1.140	1.14	0.72
4112-8	A106B	0.906	0.788	1.283	1.053	2.012	1.589	1.41	1.03
1.3-3	TP304	0.856	0.736	0.769	0.856	0.867	0.658	1.27	0.80
EPRI 13S	TP304	1.046	0.910	1.313	1.046	1.402	0.984	1.33	0.99
1.3-4	CS SAW	0.973	0.839	1.423	1.292	2.579	1.975	1.88	1.21
4141-8	CS SAW	0.932	0.804	1.364	1.239	2.475	1.893	1.79	1.15
1.3-5	SS SAW	0.897	0.773	0.806	1.156	1.404	1.070	1.24	1.19
4141-4	SS SAW	0.949	0.819	0.855	1.220	1.473	1.125	1.57	1.21
1.3-7	CF8M	0.771	0.668	0.834	0.962	0.924	0.609	1.46	0.91
4143-1	CF8M	0.893	0.773	0.965	1.114	1.066	0.700	1.70	1.06

(a) Using J_D-R curve.

The low value for the CF8M experiment can be explained by the low toughness of this material after the artificial aging. The toughness of this material was closer to the toughness of the stainless SAW than of the stainless base metal. The ferrite number for this material is such that it could be analyzed using the IWB-3640 procedures. However, paragraph IWB-3641(c) further stipulates that for cast stainless steel materials, adequate toughness for the pipe to reach limit load after aging shall be demonstrated. Consequently, it would not be appropriate to assess this cracked pipe section using the procedures of IWB-3640. For this particular CF8M pipe, an elastic-plastic analysis is needed. Other CF8M pipes might retain sufficient toughness so that limit-load analyses could be used (see Ref. 5.8).

The low ratio for the TP304 base metal test, however, is not as explainable since this material has a high toughness in both the quasi-static and dynamic C(T) tests.

When using the actual properties to determine an S_m, the ratios of experimental-to-calculated stresses decreased significantly, and would be of concern for the TP304 and CF8M base metal experiments. This exercise shows that using the actual properties to define an S_m for the ASME approach should be done with caution. It also implies that for a pipe with Code minimum properties, the calculated stresses may be greater than the experimentally determined stresses.

- The R6 Option 1 analysis predicted the experimental failure stresses for all experiments to be less than the stresses measured in the experiments. While the amount by which the stresses are underpredicted is reasonable, the use of the Option-2 or 3 methods might increase the difference between the predicted and observed stresses associated with this approach.

  In these analyses, it was assumed that all the stresses were primary stresses. In reality, the thermal expansion and seismic anchor motion stresses are secondary stresses that are global in nature. Strictly following the R6 procedure in Reference 5.9 would treat the secondary stresses as only contributing to the elastic crack driving force in the failure assessment diagram. If such a procedure were used to analyze the IPIRG pipe-system experiments, the calculated stresses would be closer to the experimental values. Furthermore, all the quasi-static tests were conducted under displacement control, which could be considered as a secondary stress. Hence, ratio of the experimental-to-predicted stresses, using the R6 method, would decrease very significantly for these experiments. Without having gone through the precise calculations, one can see that the treatment of global secondary stresses as only making an elastic contribution to the fracture can significantly influence the accuracy of the fracture predictions in this analysis.

- The SC.TNP J-estimation analysis tended to give values closest to the experimental data with the exception of the dynamic IPIRG carbon steel base metal experiment. Again, this is probably an artifact of using quasi-static material property data to analyze this experiment which involved a material highly susceptible to dynamic strain aging effects. This method could also be considered as an R6 Option 3 analysis method.

5.3.2.2 Comparison of Dynamic Versus Quasi-Static Pipe Bend Fracture Behavior

An important consideration in this program was to see if dynamic pipe-system experiments are necessary, or if it is sufficient to conduct quasi-static pipe fracture experiments. In order to compare the results from the dynamic IPIRG pipe-system experiments with the quasi-static experiments it was necessary to normalize the results to account for differences in test temperature, pressure, or flaw size. It should be

noted, that the different analyses used for normalization have different effects, and the results require interpretation.

Table 5.2 summarizes the results for both the dynamic and quasi-static experiments using the various analyses to normalize the experimental differences. In this table, all the analyses use the quasi-static material properties. Several observations can be made about the dynamic behavior of the various materials tested.

- The dynamic IPIRG A106 Grade B carbon steel pipe-system experiment failed at the lowest relative stress level (relative to the quasi-static results) of any of the materials evaluated. This observation is consistent with the material property data that show that both the strength and toughness decreased at rates corresponding to seismic loading at 288 C (550 F). This is attributed to dynamic strain aging sensitivity of this particular pipe. Other carbon steels may be more or less sensitive to dynamic strain aging behavior. These results suggest that for such a steel, dynamic material properties may be needed to better assess the fracture stresses, and thereby make the calculated failure stress closer to the experimental measurement.

- The dynamic IPIRG TP304 stainless steel base metal pipe-system experiment tended to have the next lowest failure stresses relative to the quasi-static failure stresses of the five materials evaluated. This assessment is perhaps biased by the low ratios of experimental stresses to predicted stresses for the analyses that use S_m in their definitions of flow stress. For the room temperature quasi-static test, the $3S_m$ definition of the flow stress is much lower than the definition of flow stress using the average of the yield and ultimate strengths. This tends to make the room temperature maximum load quasi-static test prediction much lower relative to the dynamic 288 C (550 F) test prediction. The Net-Section-Collapse, DPZP, R6 and SC.TNP analyses all consistently show that the dynamic load-carrying capacity of this pipe was much lower than expected. Rate effects on material properties are not likely to provide the answer since the dynamic material properties are not much different than the quasi-static properties. From Table 3.4 it was observed that the likely uncertainty in the experimentally measured strain values, and consequently the moment values, was only 6.6 percent. Consequently, uncertainties in measured strain values cannot explain the entire discrepancy. Furthermore, Degraded Piping Program results indicated that the reproducibility of quasi-static experiments are typically within 5 percent.

  Another possible explanation is the potential for cyclic loading to reduce the apparent toughness of the material. This experiment (1.3-3) had the lowest stress-ratio (R) of all the IPIRG experiments. From the IPIRG Subtask 1.2 results (Ref. 5.4), this would tend to lower the apparent toughness. However, as noted earlier in Section 5.2, the stainless steel, Subtask 1.2, through-wall-cracked pipe observations on the effect of stress-ratio (R) and plastic incremental loading, suggest that cyclic loading effects may not provide the answer either. However, the relationship developed in Subtask 1.2 illustrating the effect of stress-ratio (R) and plastic increment was based exclusively on through-wall cracked pipe data. A different relationship may be appropriate for surface cracks, which could explain this discrepancy.

If the cyclic load history is a contributor to the lower failure stress of Experiment 1.3-3, then it may be worthwhile to examine the cyclic load histories for plants in service in a systematic manner.

Another possible explanation of the lower observed failure stresses for Experiment 1.3-3 may come from differences in the calculated J values from the surface-cracked pipe experiment to those from the C(T) test results. The surface-cracked pipe experiment and C(T) specimen J values are given in Table 5.3. The

Table 5.3 Comparison of surface-cracked pipe and C(T) specimen J_i values

Material	SC pipe J_i, kN-m^2 (From Subtask 1.3)	C(T specimen J_i, kN-m^2 QS	C(T specimen J_i, kN-m^2 Dyn	SC/C(T) QS	SC/C(T) Dyn
TP304 Base (Pipe A8)	560	738	1,215	0.76	0.46
TP304 SAW (A8W)	315	55	128	5.73	2.40
Aged Cast CF8M	104	88	116	1.18	0.90

J value at crack initiation in Experiment 1.3-3 using an η-factor approach (Ref. 5.10), were calculated to be only 76 percent of the quasi-static C(T) specimen values and only 46 percent of the dynamic C(T) specimen values. This is a significant discrepancy.

Verification that the toughness for the pipe experiment is more reasonable comes from the Plastic Zone Screening Criterion developed in the Degraded Piping Program. If the quasi-static C(T) specimen J_i value is used, then the actual failure stress is much less than predicted, see Figure 5.8. However, if the surface-cracked pipe η-factor J_i is used in the Dimensionless Plastic-Zone Parameter graph, then the stainless steel base metal experimental result falls much closer to the rest of the results from the Degraded Piping program and IPIRG surface-cracked pipe experiments, see Figure 5.8. Hence this is verification that the stainless steel in this surface-cracked pipe experiment behaved as if it had a much lower toughness than reflected in the C(T) specimen tests. The potential reasons for this are discussed further in Section 6 of this report.

- The carbon steel SAW was the only material that showed higher failure stresses at dynamic rates than at quasi-static rates, although the differences between the dynamic and quasi-static results are well within the scatter and uncertainty bounds for the experimental measurements. The fact that the carbon steel weld showed higher failure stresses at dynamic loading rates is not totally unexpected since the toughness of this weld was found to increase at the seismic loading rates in C(T) tests.

  However, this weld was in the same pipe used in the A106B base metal experiment (1.3-2). This material exhibited lower strength at higher strain rates. This may indicate that perhaps it is sufficient to use the quasi-static tensile properties to analyze a crack in this type of weld subjected to dynamic loadings. This is substantiated by results by Dr. Brickstad of Sweden, who showed by viscoplastic finite element analyses that the strain rates were sufficiently low in the uncracked pipe and most of the ligament, that quasi-static properties were sufficient for analysis of the entire pipe (Ref. 5.11).

  Another interesting aspect of the carbon steel SAW was that the behavior of the SAW compared to the base metal crack showed that the SAW had higher load-carrying capacity even at low strain rates. This is somewhat surprising, since the SAW toughness is lower than the base metal toughness at the quasi-static rates. Other carbon steel weld tests in the Degraded Piping Program

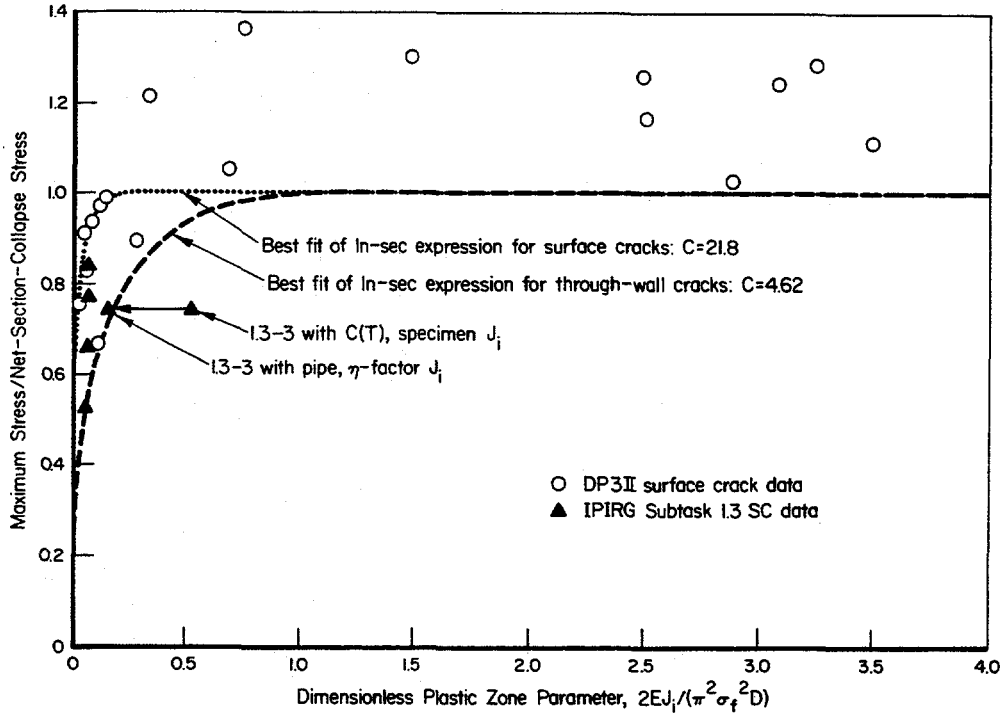

Figure 5.8 Effect of using Experiment 1.3-3 surface cracked pipe η-factor J_i value rather than quasi-static side-grooved C(T) specimen J_i value

I1.3-10/90-F5.8

(Ref. 5.8), also had higher failure loads than predicted. This may be due to the difference in the weld versus base metal strength, or possibly due to the increased thickness from the weld crown which adds additional thickness to the crack ligament.

- The stainless steel SAW cracked pipe had only a slightly lower load-carrying capacity (approximately 5 percent) in the IPIRG pipe-system experiment than in the quasi-static Degraded Piping Program experiment. This difference is within the normal scatter for these experiments, and hence is not considered significant.

- The artificially aged cast stainless steel cracked pipe had a lower relative load-carrying capacity in the IPIRG pipe-system experiment than in the quasi-static test for all analyses methods considered. This was surprising since the toughness of this CF8M pipe significantly increased under dynamic loading in the C(T) tests and the strength increased very slightly for the higher rate tensile tests, see Section 2.2.1. Clearly there is a discrepancy here between the laboratory specimen test results and the relative comparison of the pipe experiments at dynamic and quasi-static loading rates. The reason for this difference is unknown. Part, although not all, of this discrepancy may be explained by experimental scatter or uncertainty.

5.3.2.3 Assessment of Predictions Using Dynamic Properties

To assess if the use of the dynamic properties would improve the predictions of the various pipe experiments, additional calculations were made for the dynamic IPIRG pipe-system experiments. For the weld metal experiments dynamic tensile properties of the base metal and dynamic C(T) specimen toughness properties of the weld metal were used for these calculations.

Table 5.4 summarizes the ratios of the maximum experimental stress to the predicted stress when the dynamic properties were used. This was done for the Net-Section-Collapse, DPZP, R6 Option 1, and SC.TNP analyses. Since S_m is constant for quasi-static or dynamic loading, the ASME flaw evaluation procedures and Net-Section-Collapse analyses using S_m were not reevaluated. These results show:

- Carbon steel base metal. The agreement between the predictions for the dynamic IPIRG pipe-system experiments and the quasi-static experiments was improved for all methods by use of dynamic properties.

- Stainless steel base metal. The use of dynamic material properties (using C(T) specimen data for the J-R curves) in the analyses of the IPIRG stainless steel base metal experiment resulted in virtually no change when compared with the analyses where quasi-static properties were used. This was true for all analysis methods considered except the R6 Option 1 method. The use of dynamic properties resulted in a slight improvement in the accuracy for the R6 Option 1 approach.

- Carbon steel SAW. A general improvement in the accuracy of the predictions is realized for the Net-Section-Collapse (flow stress equal to the average of the yield and ultimate strengths) and SC.TNP analyses. The DPZP and R6 Option 1 methods showed virtually no change.

- Stainless steel SAW. The use of dynamic properties for the DPZP method resulted in a slight improvement in the accuracy of the predictions. A slight decrease in the accuracy of the predictions occurs for the R6 Option 1 approach. There was virtually no change for the Net-Section-Collapse method.

- Aged cast stainless steel. A slight decrease in the accuracy of the predictions occurs for all methods except the R6 Option 1 approach. The use of dynamic properties improved the accuracy of the predictions for the R6 Option 1 approach for this material.

In reviewing Table 5.4, it can be seen that in general, except for the carbon steel weld experiment, that even when dynamic tensile and C(T) specimen data were used in the analysis of the dynamic experiments, that the ratio of the experimental stress to the predicted stress was 5 to 30 percent lower for the dynamic IPIRG pipe-system experiments than for the companion quasi-static experiments. Consequently, the use of dynamic tensile and C(T) specimen data is not the total answer which explains all of the apparent discrepancies between the dynamic and quasi-static experimental results.

5.3.3 Stability Analyses

A summary of the fully plastic J/T and Energy Balance Stability analyses predictions, along with the experimental results, is presented in Table 5.5. Note that there are two sets of instability predictions.

Table 5.4 Summary of experimental-to-predicted ratios of maximum stresses from fracture analyses using both quasi-static and dynamic properties for the dynamic IPIRG pipe-system experiments and quasi-static properties for quasi-static experiments (all values are based on total stress at maximum load)

Expt. No.	Properties Used[a]	Material	Net-Section Collapse		DPZP	R6 Opt. 1	SC.TNP
			$(\sigma_y + \sigma_u)/2$	$1.15(\sigma_y + \sigma_u)/2$	$(\sigma_y + \sigma_u)/2$		
1.3-2	QS	A106B	0.605	0.522	0.704	1.14	0.72
1.3-2	DYN	A106B	0.700	0.603	0.856	1.19	0.81
4112-8	QS	A106B	0.906	0.788	1.053	1.41	1.03
1.3-3	QS	TP304	0.856	0.736	0.856	1.27	0.80
1.3-3	DYN	TP304	0.878	0.755	0.878	1.13	0.79
EPRI 13S	QS	TP304	1.046	0.910	1.046	1.33	0.99
1.3-4	QS	A106B SAW	0.973	0.839	1.292	1.88	1.21
1.3-4	DYN	A106B SAW	1.127	0.970	1.241	1.86	0.97
4141-8	QS	A106B SAW	0.932	0.804	1.239	1.79	1.15
1.3-5	QS	TP304 SAW	0.897	0.773	1.156	1.24	1.19
1.3-5	DYN	TP304 SAW	0.919	0.792	0.966	1.45	0.84
4141-4	QS	TP304 SAW	0.949	0.819	1.220	1.57	1.21
1.3-7	QS	Aged CF8M	0.771	0.668	0.962	1.46	0.91
1.3-7	DYN	Aged CF8M	0.750	0.650	0.882	1.28	0.81
4143-1	QS	Aged CF8M	0.893	0.773	1.114	1.70	1.06

(a) DYN = dynamic J_D-R curve and tensile test data at $\dot{\epsilon}$= 1/sec. QS = quasi-static J_D-R curve and quasi-static tensile test data.

Table 5.5 Summary of stability analyses

Expt. No.	Material	J/T[a]	Energy Balance[a]	Experiment
Surface Crack				
1.3-2	A106B	Unstable	Unstable	Unstable
1.3-3	TP304	Unstable	Unstable	Unstable
1.3-4	A106B SAW	Unstable	Unstable	Unstable
1.3-5	TP304 SAW	Unstable	Unstable	Unstable
1.3-7	Aged CF8M	Unstable	Unstable	Unstable

			Energy Balance			Experiment	
Expt. No.	Material	J/T[a]	(a)	(b)	(c)	Cycle During SC Penetration	Total Load History
Through-Wall Crack							
1.3-2	A106B	Stable	Stable	Unstable (Marginal)	Unstable	Stable	Unstable
1.3-3	TP304	Stable	Stable	Stable	Unstable	Stable	Stable
1.3-4	A106B SAW	Stable	Stable	Stable	Unstable	Stable	Stable
1.3-5	TP304 SAW	Stable	Stable	Stable	Unstable	Stable	Stable
1.3-7	Aged CF8M	Stable	Stable	Stable	Unstable	Stable	Unstable

(a) All stresses displacement controlled.
(b) M_{eq} for P_{sat} = load controlled.
(c) Inertial and M_{eq} for P_{sat} = load controlled.

One is for the surface crack instability and the other is for the stability of the resulting through-wall crack. Even if all the stresses are considered displacement-controlled, the surface crack in all experiments is properly predicted by both analyses to exhibit unstable behavior.

For the stability of the resulting through-wall crack, there are two columns to describe the experimental stability. One consideration reflects the situation at surface crack penetration and the other is the disposition of the through-wall crack at the end of the test. In this program there were two experiments where the pipe was completely severed by the end of the experiment. These were the carbon steel base metal and the aged cast stainless steel experiment. For these two experiments the "instability" occurred because the crack continued to grow after surface crack penetration due to cyclic ductile tearing as a result of continued cyclic loading. In all likelihood, if the applied loadings had continued further for the other three experiments, they would also have severed into two pieces. Neither the J/T nor the Energy Balance Stability analyses can account for this type of behavior.

The stability analyses used two different assumptions about the loading. The fully plastic J/T analysis assumes all the stresses are displacement controlled. The Energy Balance Analysis calculations were made assuming that either; (1) all stresses are displacement controlled, (2) only the pressure stresses are load-controlled components, or (3) both the pressure and inertial stresses are load-controlled components. When all stresses are considered as displacement controlled, both the J/T and Energy Balance Stability analyses predict the through-wall crack immediately after surface crack penetration to be stable for all experiments. When only the pressure induced longitudinal stresses (at the saturation pressure) are considered to be load controlled, the Energy Balance Stability analysis predicts all the through-wall cracks to be stable except the carbon steel base metal crack. When both the inertial and pressure stresses are considered load-controlled, the Energy Balance Stability analysis predicts all experiments to be unstable.

Superficially, it would appear that both analyses using displacement-controlled stress assumptions did a reasonable job of predicting the experimentally observed behavior. This may give some measure of confidence that the quasi-static methods are adequate for pipe-system stability analyses. However, under closer scrutiny, it appears that the correct predictions may only be fortuitous.

In the following, some of the inconsistencies in the J/T and Energy Balance Stability analysis will be discussed. In addition, some of the limitations of the methods will be presented, as well as some thoughts about the reasons for the inconsistencies. Finally, a possible methodology that overcomes the limitations of the current methods is discussed.

5.3.3.1 Inconsistencies in Quasi-Static Stability Analyses

The fully plastic J/T and Energy Balance Stability analyses display some glaring inconsistencies when compared with observed instability behavior. Focussing on the aged cast stainless experiment, the inconsistencies become very apparent. In that experiment, the crack remained stable until the through-wall crack grew to a length of 95 percent of the pipe circumference.

The fully plastic J/T analysis predicts increasing through-wall crack stability with longer through-wall cracks, which is counter to the evidence. The displacement-controlled assumption built into the fully plastic J/T analysis is thought to be one of the causes of this inconsistency. Considering one of the alternate J/T formulations, the GE/EPRI solution for load-controlled bending, a more accurate prediction

of stability can be made. To do so, it was assumed that the pressure stresses (at the saturation pressure) could yield an equivalent load-controlled moment, as was done in the Energy Balance Stability analysis. Additionally, it was assumed that the inertial stresses could also produce a load-controlled bending moment. These calculations showed that if one accounts for only the equivalent moment due to the pressure stress (i.e., one ignores the contribution of the inertial stresses towards the load-controlled component of the moments), the crack length would have to be much longer than the analysis was said to be valid for an instability to occur, i.e., $\theta/\pi >> 0.5$. For the case where load-controlled moments are considered to be the sum of the inertial and saturation pressure induced equivalent moments, the critical crack length for an instability event would be 52 percent of the pipe circumference for the cast stainless steel pipe experiment. For this experiment, the through-wall crack length at instability was 95-percent of the circumference. Hence, it would appear that there is general agreement between the experimental observations and the predictions when the analysis assumes that only the pressure stresses (at saturation pressure) yield an equivalent load-controlled moment. It appears that using the sum of the inertial and pressure induced stresses as load-controlled stresses for through-wall crack instability analysis is inappropriate.

The energy balance analysis does show the correct trend of increasing instability with increasing crack length. However, this analysis predicts that a crack 54 percent of the circumference is marginally stable when only the saturation-pressure-induced stress is considered as a load-controlled stress, Figure 5.9. If

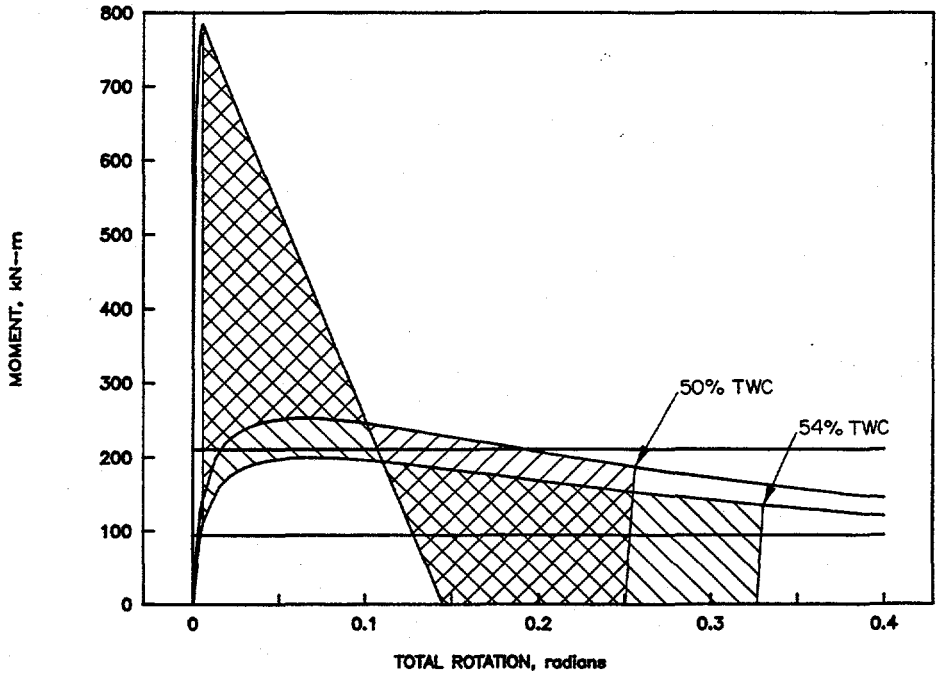

Figure 5.9 Energy balance for the aged cast stainless experiment (Experiment 1.3-7) for two different through-wall crack sizes I1.3-/90-F5.9

one also considers the inertial stresses as load-controlled stresses, the critical crack length would be even less. As noted above, the final instability for Experiment 1.3-7 did not occur until the through-wall crack was 95 percent of the pipe circumference.

5.3.3.2 Limitations in Quasi-Static Stability Analyses

The fully plastic J/T and Energy Balance Stability analyses are quasi-static based analyses that assume that the loads remain essentially static during the fracture event. During all of the IPIRG Subtask 1.3 experiments, the actuator motion after surface crack penetration did change and caused the loads to decrease at the crack. In addition, there were also inertial loads that were changing as the fracture propagated. In every case, the through-wall crack arrested when the loads dropped. Crack growth then reinitiated when the loads increased during the next cycle of loading. Subsequent crack growth continued in a cyclic tearing manner until the loading ceased, or the pipe severed. Neither of these stability analyses accounts for these phenomena.

In addition, J/T and Energy Balance Stability analyses are bending load driven formulations. In the IPIRG Subtask 1.3 piping system, there is a significant membrane stress due to internal pressure. In fact, the severing of the pipe in Experiment 1.3-7 was a result of a tensile failure of the remaining ligament, as opposed to a bending failure. An attempt has been made in the energy balance and load-controlled J/T analyses to incorporate the effect of the membrane stress by including a Net-Section-Collapse analysis based equivalent bending moment due to pressure. The results of such an approach for the Energy Balance Stability analysis, see Figure 5.10, are not encouraging as the analysis predicts an instability for a 54 percent long through-wall crack, a crack that certainly was stable in the experiment.

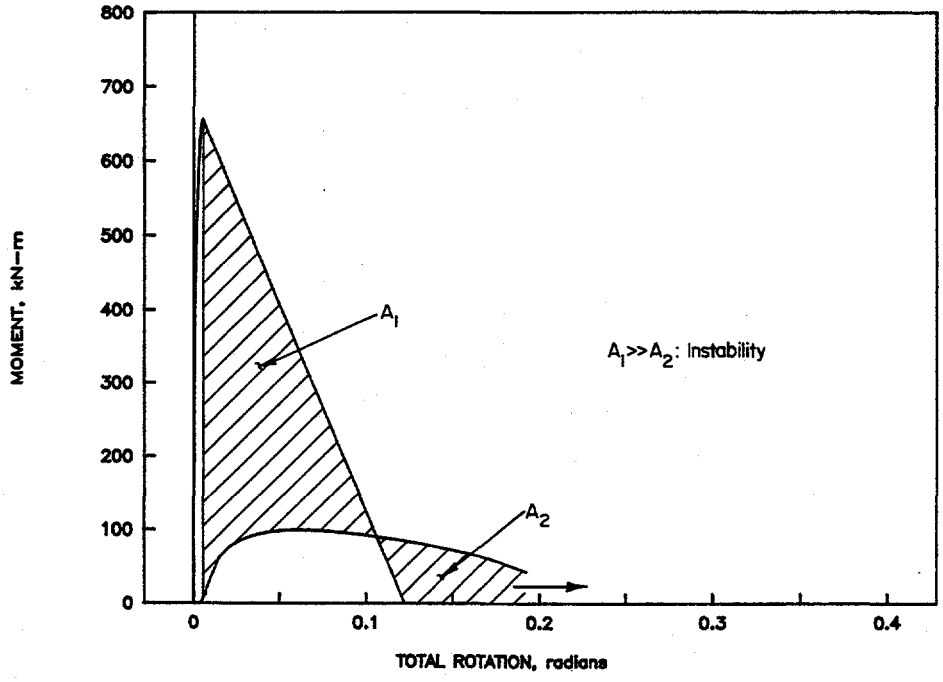

Figure 5.10 Pressure and bending energy balance for the aged cast stainless experiment (Experiment 1.3-7) I1.3-10/90-F5.10

Another limitation of the current quasi-static analyses is that they assume that there is no restraint of bending. That is, the through-wall cracked sections are assumed to be free to rotate without restriction. In fact, in the IPIRG Subtask 1.3 piping system, and probably in most plant piping, the piping remote from the crack provides a significant restraint to the free rotation of the through-wall cracked pipe section, thus making the through-wall crack much more stable than predicted by J/T or Energy Balance methods. Figure 5.3 shows an analytical assessment of the effect of restrained bending. Without induced bending, significantly longer flaws can be tolerated without failure. J/T and Energy Balance Stability analyses incorporate a piping system compliance feature, but in both cases, the piping system compliance is used to account for energy that could be used to drive the through-wall crack, rather than to incorporate a bending restraint feature.

5.3.3.3 Possible Sources of Inconsistency in Quasi-Static Analyses

Several sources of the inconsistencies between the experimentally observed behavior and the analytically predicted stability behavior have been mentioned previously. In addition to the items discussed above, two other factors may be affecting the predictions of stability; inertia of the pipe and jet thrust forces. Both of these phenomena could manifest themselves as higher "apparent" system stiffness, providing less system compliance for driving the through-wall crack and hence, more apparent stability.

Pipe rotational inertia, in this discussion, refers to the resistance of the pipe to rotation as a result of having to accelerate the pipe and its contents when the eccentric forces due to pressure at the through-wall crack are applied to the pipe. Basically, a massive pipe would provide much more resistance to further rotation than a small pipe. If the time to accelerate and rotate the pipe is short relative to the actuator forcing function frequency, then pipe rotational inertia probably plays no significant role in restraining pipe bending.

To investigate the role of pipe rotational inertia in enhancing stability, the idealized pipe-crack model shown in Figure 5.11 was used. In this model, the pipe system is replaced by two long infinitely rigid lengths of pipe connected by a rotational spring with a stiffness that approximates the stiffness of a typical though-wall crack. At time zero, a step function moment, M, equal to the Net-Section-Collapse equivalent pressure moment, is applied to the ends of the pipe. To assess the effect of pipe rotational inertia in enhancing stability, the dynamic rotational response of the pipe is calculated and compared to the IPIRG Subtask 1.3 pipe-system response.

Figure 5.12 compares the response of the pipe rotational inertia model with the static response of the IPIRG Subtask 1.3 pipe system containing a through-wall crack and forced by actuator displacements. In the inertia model, the pipe is assumed to be 3 m (10 feet) long and filled with water. The stiffness of the rotational spring in the inertia model approximated the tangent stiffness of the through-wall crack at the rotation when the surface crack was predicted to penetrate the pipe wall. The reference actuator displacements used in the comparison were the displacements at surface crack penetration of the aged cast stainless experiment, Experiment 1.3-7. Two observations can be made when comparing the pipe rotational inertia model response to the pipe-system response. First, the frequency of the rotational inertia model response is about five times the frequency of the response of the piping system due to actuator displacements. Second, the magnitude of the rotations of the inertia model are about five times greater than the actuator driven response. From these two observations, it can be concluded that pipe inertia played no significant role in enhancing the stability of the through-wall cracks in the IPIRG Subtask 1.3 system by resisting rotation of the pipe.

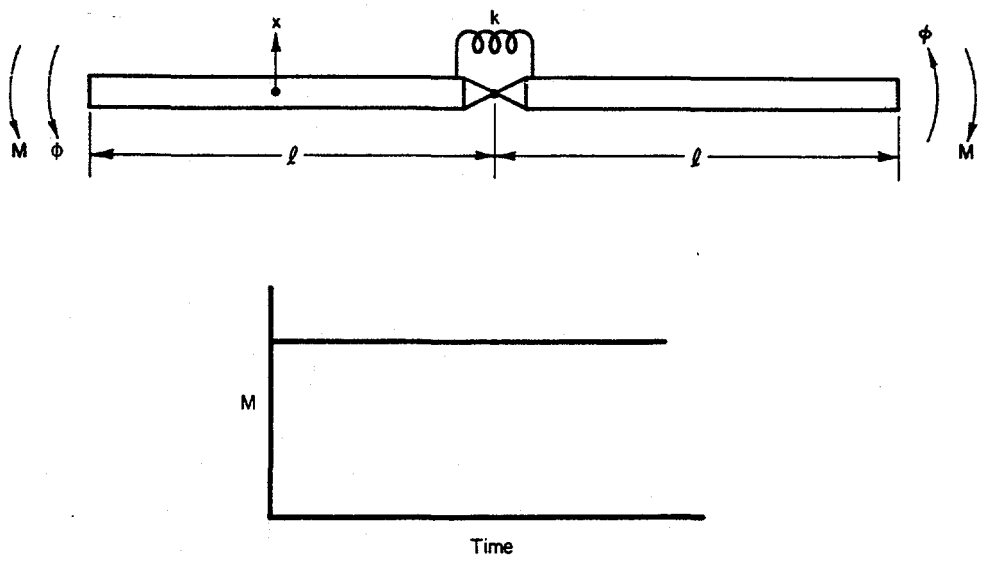

Figure 5.11 Model used to investigate the role of inertia in pipe stability
I1.3-10/90-F5.11

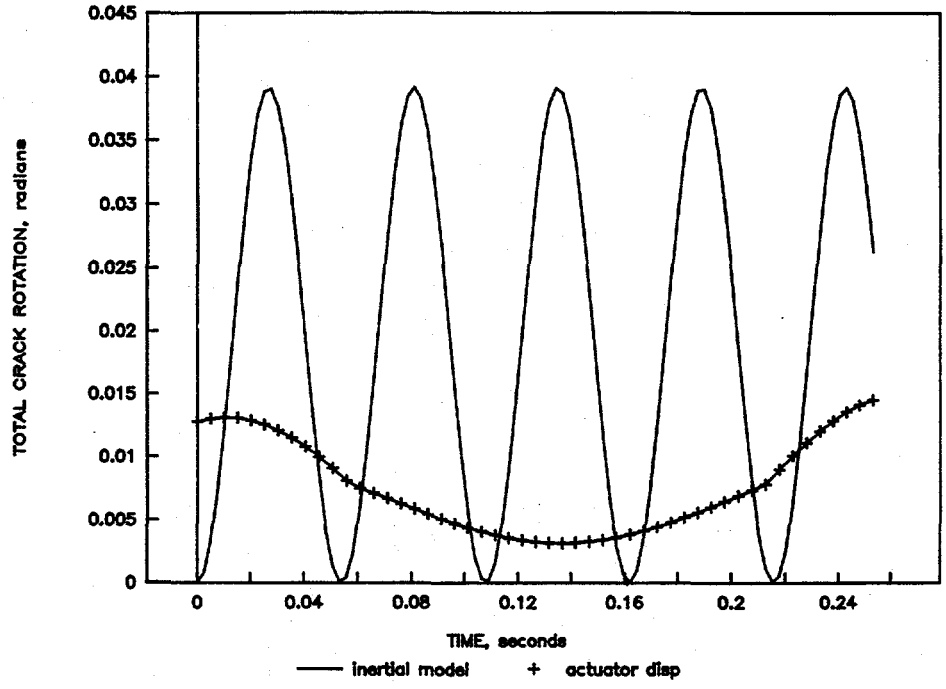

Figure 5.12 Comparison of pipe inertia model crack rotations and actuator displacement induced crack rotations
I1.3-10/90-F5.12

The second possible source of "apparent" system stiffness that was investigated was a thrust force caused by the steam jet escaping from the through-wall crack. Basically, the steam jet emanating from the crack tends to close the crack and limit crack rotations or reduce the inertial moments. To establish whether or not the jet thrust forces are of significant magnitude to have an impact on fracture stability, a finite element analysis including jet thrust forces was performed.

The essential features of the jet thrust force finite element model are shown in Figure 5.13. The starting point of the analysis was an NRCPIPE LBB.ENG2 through-wall crack J-estimation scheme analysis (Ref. 5.12). From this analysis, a through-wall crack moment-rotation curve was defined for the crack, and crack geometry data (COD and crack length) were established as a function of crack rotation. Given COD and crack length and an assumption that the crack shape was elliptical, the jet thrust force was calculated by integrating the pressure of the escaping steam over the crack opening area. The thrust of the escaping steam was assumed to be 1.26 times the saturation pressure times the crack opening area as per the recommendation of Reference 5.13. The pressure was applied to the finite element model normal to the center of the crack opening. Only static analysis was performed.

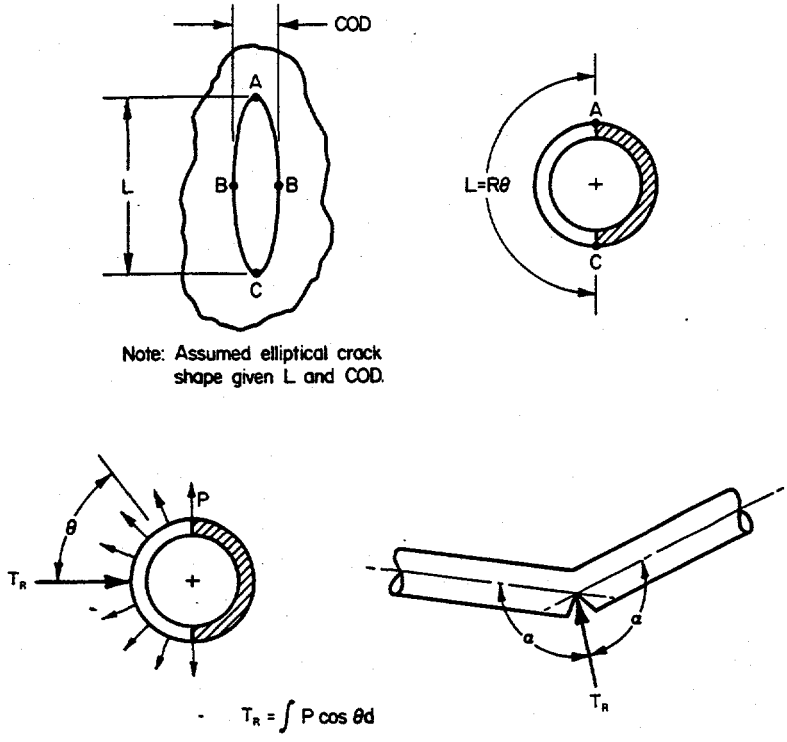

Figure 5.13 Finite element model of jet-thrust force

I1-3-10/90-F5.13

The calculation of the response of the pipe, including the effect of the jet thrust force is complicated by the fact that the thrust force is a function of the unknown rotation of the pipe. Basically, this is the classical "follower force" problem. Facilities within the ANSYS computer program allow this type of analysis to be performed, at least statically. In a departure from the practice used to design the Subtask 1.3 experiments, the ANSYS Nonlinear Spring Element was used for this study, as opposed to the previously discussed spring-slider model. The reason for using the ANSYS Nonlinear Spring is that it can accommodate what appear to be negative spring rates. This means that the portion of the through-wall crack beyond maximum load can be considered. (The Nonlinear Spring Element currently will not properly model unloading to, or less than, zero load, and hence it cannot be used for cyclic dynamic analysis).

To establish the effect of jet thrust forces, an analysis with and without the jet thrust force was conducted. In both cases, an IPIRG Subtask 1.3 system model was used. The crack was modeled using a 50 percent through-wall crack moment-rotation curve for the aged cast stainless material. Loads were applied to the piping system by static actuator displacement. Figures 5.14 through 5.16 show the essential inputs to the analysis, and Figure 5.17 shows the output.

From Figure 5.17, it is clear that the initial through-wall crack is not significantly affected by thrust loads. However, as the crack grows, the effect of the thrust forces becomes more and more pronounced, requiring more and more actuator displacement to obtain the same crack length. The implication of this analysis is that as the crack grows, thrust forces are going to contribute significantly to enhanced through-wall crack stability.

5.3.3.4 Advanced Dynamic Stability Analyses

It is clear from the discussions presented above that the stability of cracks in real piping systems involves many more phenomena than are embodied in the currently available quasi-static analysis methodologies. It is also not apparent that the current methods can be enhanced to include the features essential to making credible predictions consistent with all observed piping system responses. A spring-slider model dynamic analysis method was used to assess the dynamic behavior of the pipe system containing a surface crack up to maximum load. Unfortunately, the spring-slider model cannot be extended beyond maximum load to continue the dynamic analysis into the through-wall crack regime. The Nonlinear Spring Element was used in the jet thrust force calculations to consider loads past maximum. Limitations in the ANSYS Nonlinear Spring Element preclude its use in dynamic analyses, because it does not correctly model reloading.

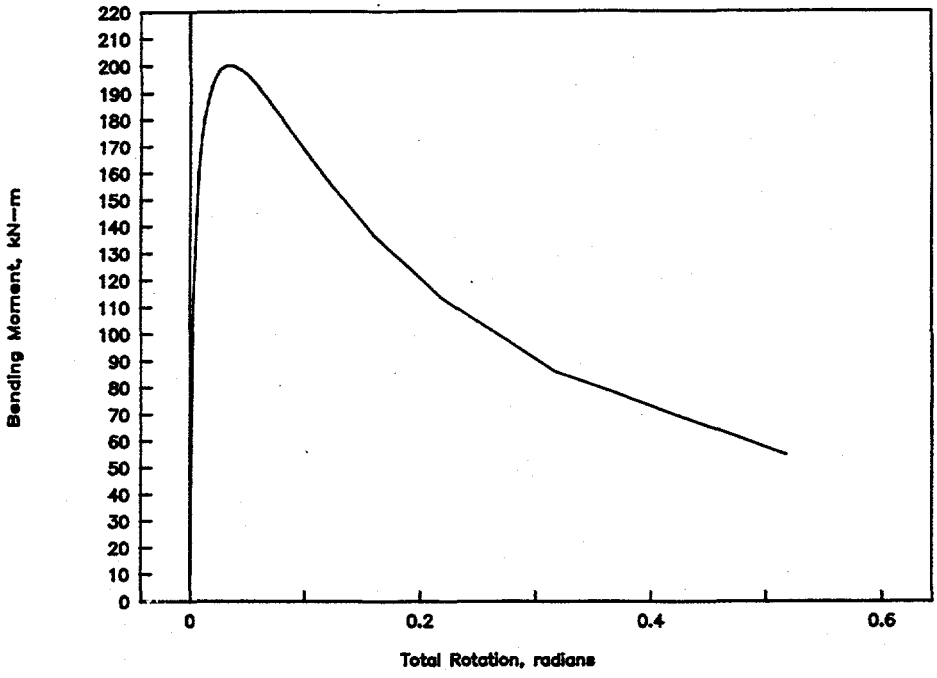

Figure 5.14 Through-wall crack moment-rotation response used in jet-thrust force analysis as predicted by LBB.ENG2 J-estimation scheme (50 percent TWC in aged cast stainless material) I1.3-10/90-F5.14

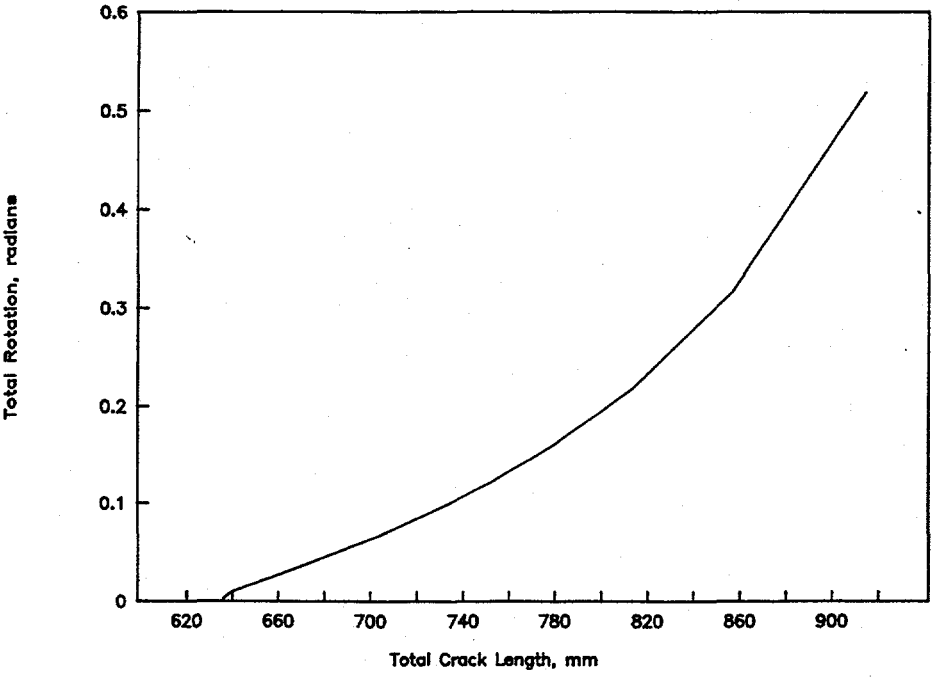

Figure 5.15 Crack rotation versus crack length response for the jet-thrust force analysis as predicted by LBB.ENG2 J-estimation scheme (50 percent TWC in aged cast stainless material) I1.3-10/90-F5.15

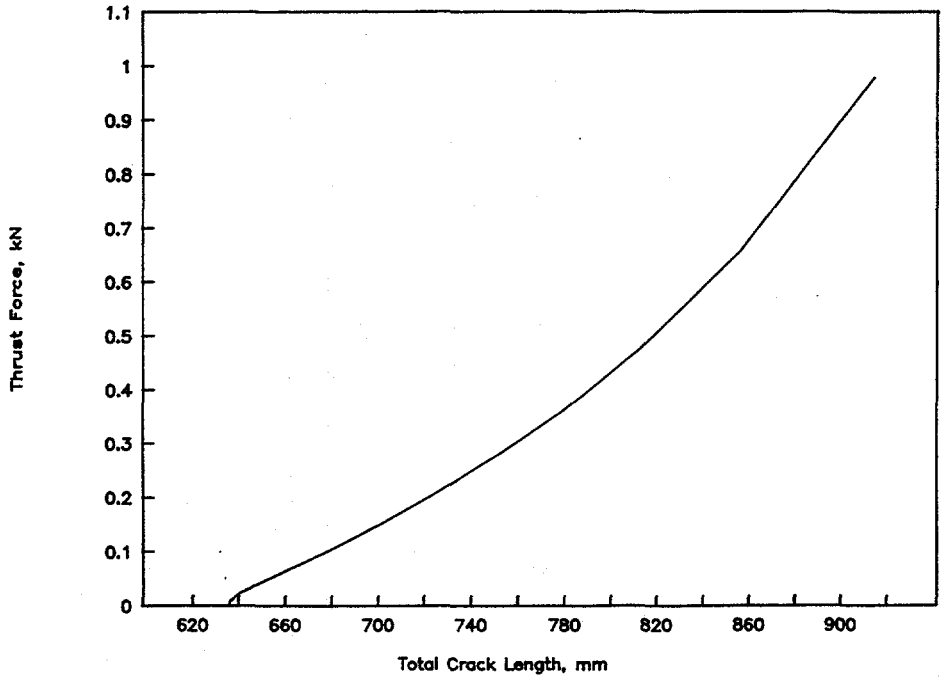

Figure 5.16 Jet-thrust for an initially 50 percent long TWC in aged cast stainless steel material
I1.3-10/90-F5.16

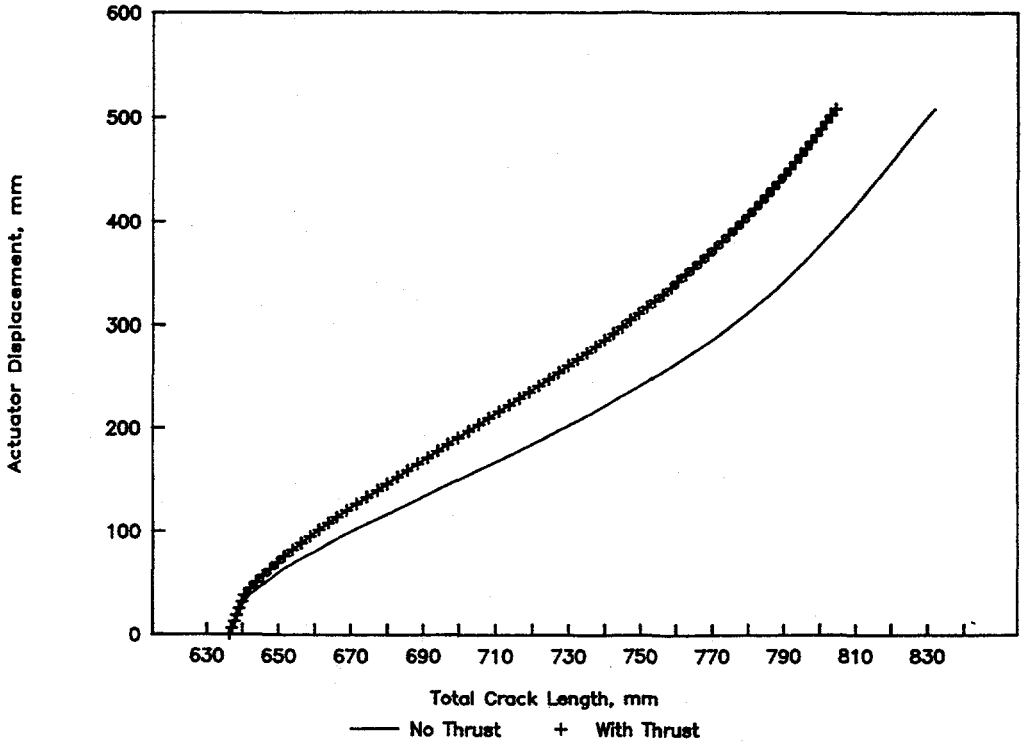

Figure 5.17 IPIRG Subtask 1.3 pipe system response when jet-thrust forces are and are not included from a through-wall crack
I1.3-10/90-F5.17

5.4 References

5.1 Marschall, C. W., Landow, M. P., and Wilkowski, G. M., "Loading Rate Effects on Strength and Fracture Toughness of Pipe Steels Used in Task 1 of the IPIRG Program," NUREG/CR-6098, October 1993.

5.2 Wilkowski, G. M., and others, "Degraded Piping Program -Phase II," Summary of Technical Results and Their Significance to Leak-Before-Break and In-Service Flaw Acceptance Criteria, March 1984-January 1989, by Battelle Columbus Division, NUREG/CR-4082, Vol. 8, March 1989.

5.3 Scott, P., and others, "Stability of Cracked Pipe under Inertial Stresses - Subtask 1.1 Final Report," NUREG/CR-6233, Vol. 1, August 1994.

5.4 Kramer, G., and others, "Stability of Cracked Pipe Under Seismic/Dynamic Displacement-Controlled Stresses - Subtask 1.2 Final Report," NUREG/CR-6233, Vol. 2, No. 1, July 1997.

5.5 Isozaki, T. and Miyazono, S., "Experimental Study of Jet Discharging Test Results Under BWR and PWR Loss of Coolant Accident Conditions," *Nuclear Engineering and Design*, 96, pp 1-9, 1986.

5.6 "Piping and Fitting Dynamic Reliability Program," EPRI RP 1543-15, 1995.

5.7 Solicitations for public comment on "Standard Review Plan 3.6.3 LEAK-BEFORE-BREAK PROCEDURES," *Federal Register*, Vol. 52, No. 167, Notices, pp 32626 to 32633, Friday, August 28, 1987.

5.8 Wilkowski, G. M., and others, "Degraded Piping Program - Phase II," Seventh Progress Report: October 1987 - January 1989, by Battelle Columbus Division, NUREG/CR-4082, Vol. 7, March 1989.

5.9 Milne, I., "Failure Assessment Diagrams and J Estimates: A Comparison for Ferritic and Austenitic Steels," CEGB Report RD/L/2208N81, 1982.

5.10 Pan, J., "Estimation of Energy Release Rates and Instability Analysis for a Pipe with a Circumferential Surface Crack Subjected to Bending," *Journal of Pressure Vessel Technology*, Vol. 108, pp 33-40, February 1986.

5.11 Brickstad, B., Swiss-Swedish Analysis Program: "Numerical Analysis of IPIRG Cracked Pipe Experiments with use of Nonlinear Fracture Mechanics," AB Statens Anläggningsprovning Report No. SA/Fou-RAPPORT, May 1989.

5.12 Brust, F. W., "Approximate Methods for Fracture Analyses of Through-Wall Cracked Pipes," NUREG/CR-4853, February 1987.

5.13 American Nuclear Society, "American National Standard Design Basis for Protection of Light Water Nuclear Power Plants Against the Effects of Postulated Pipe Rupture," ANSI/ANS-58.2-1988, American Nuclear Society, La Grange Park, IL, 1988.

6.0 SUMMARY OF FINDINGS

This section summarizes the major findings from Subtask 1.3 and the application of those findings towards plant design, Code criteria, and regulatory policy. The presentation of these findings is grouped by technical subject, and how those findings may be implemented into design or regulatory policy are discussed.

6.1 Material Characterization Efforts

6.1.1 Definite Findings

The material property testing data showed that the toughness and strength properties for all the stainless steels tested were affected very slightly by strain rate changes from quasi-static to seismic loading rates. Hence from the laboratory specimen data, quasi-static values are sufficient to analyze pipes made from these materials.

However, material properties of the carbon steel pipe and the carbon steel SAW investigated were affected significantly by strain rate changes from quasi-static to seismic loading conditions. This is believed to be due to the sensitivity of the carbon steel material to dynamic strain aging at LWR temperatures. Some carbon steel pipes may be more sensitive than others, and a screening criterion should be developed to determine which materials are sensitive. Such a criterion was developed in the U.S. NRC's "Short Cracks in Piping and Piping Welds" program for quasi-static loading (Ref. 6.1). If a material is found to be not susceptible to dynamic strain aging, then considerations of seismic loading rates lowering the toughness and strength is not a concern.

If a carbon steel is susceptible to dynamic strain aging, tensile and toughness testing at seismic loading rates may be appropriate to assess the magnitude of the effect on the fracture behavior of the pipe material of interest.

6.2 Significance of Cyclic Loading

Cyclic loading effects on the apparent toughness were reported in the literature and also found in the IPIRG displacement-controlled pipe experiments in Subtask 1.2 (Ref. 6.2). These results suggest that cyclic loading during the ductile tearing process can lower the apparent toughness. This may explain the lower failure stresses for the stainless steel and CF8M pipe-system experiments (1.3-3 and 1.3-7), but the empirical results to date are not sufficient to make such an assessment.

If cyclic loading histories are anticipated to have negative load ratios, then it may be desired to account for the uncertainty of cyclic loading on the fracture strength of the cracked piping system.

6.3 Findings on Comparison of J_i Values from Dynamic Pipe-System Experiments and C(T) Specimens

The J values at crack initiation were calculated from three of the IPIRG pipe-system experiments. (The other two experiments did not have rotation data of sufficient fidelity to allow such calculations to be made.) A significant difference existed for the stainless steel base metal and stainless steel weld experiments. There was good agreement for the aged cast stainless steel pipe experiment. The lower pipe toughness value for the stainless steel base metal experiment tends to explain why this pipe-system experiment had a lower failure stress than the corresponding quasi-static pipe experiment on the same material. This raises the question of how well C(T) specimen data can represent the fracture response of material in a piping system under dynamic and/or cyclic loading. At this point in time, we can only speculate that the differences may be due to cyclic loading or constraint effects.

6.4 Elastic Stress Analysis Ratios

When an elastic stress analysis is used to determine the stress at a location in a piping system and plastic behavior is anticipated, an inaccuracy associated with the elastic stress analysis exists. This type of inaccuracy (margin) was identified in the EPRI/U.S. NRC Piping and Fitting Dynamic Reliability program (Ref. 6.3.) That program reported margins estimated for an uncracked pipe system subjected to severe seismic loading of 20 to 34 (Ref. 6.3). Such a margin is a function of the magnitude of the applied loads, nonlinear behavior of the material, and geometry of the piping system.

Similar inaccuracies exist in the fracture evaluation of cracked piping. However for cracked piping, the difference between the experimental stresses and the calculated stresses will change as a function of the failure load expected for the crack of concern. Large cracks produce failure at low loads where there is relatively little plastic deformation. When there is little plastic deformation, the elastic analysis becomes more accurate, and the ratios of calculated-to-experimental stresses are close to one. In the limit, as the crack becomes smaller, the ratios from the IPIRG pipe-system experiments should approach those of the EPRI/U.S. NRC Piping and Fitting Dynamic Reliability program. This is schematically illustrated in Figure 6.1. Such ratios in the elastic analyses are very complicated to identify in a manner that can be used in a simplified design, code, or regulatory manner, but may be very significant for LBB size through-wall flaws, or smaller surface flaws than those used in the pipe-system experiments in this program.

Any changes to the ASME Code as a result of the EPRI/U.S. NRC Piping and Fitting Dynamic Reliability program should be viewed from the fact that the predicted-to-experimental ratios of stresses in the elastic stress analysis will be lower for cracked pipe than uncracked pipe, i.e., the piping reliability program ratios for uncracked pipe were 20 to 34, whereas the IPIRG cracked pipe-system experiments had ratios of 1.4 to slightly below one. The IPIRG inertially loaded cracked pipe experiments in Subtask 1.1 had calculated-to-experimental ratios of 1.8 to slightly below one (Ref. 6.4). (Note, Kot and others (Ref. 6.5) present data for the German HDR facility which indicate that their ratios from their elastic stress analyses were significantly less than 1.0 for most cases reported. They further indicated that the amount of plasticity associated with their piping system for the cases reported was minimal for the loads that were applied. The fact that their predicted-to-experimental ratios were less than 1.0 could possibly be attributed to poorly defined boundary conditions for this facility which adversely affects the fidelity of the analysis.) Note that the calculated-to-experimental stress ratios in the elastic stress analysis of the IPIRG experiments are

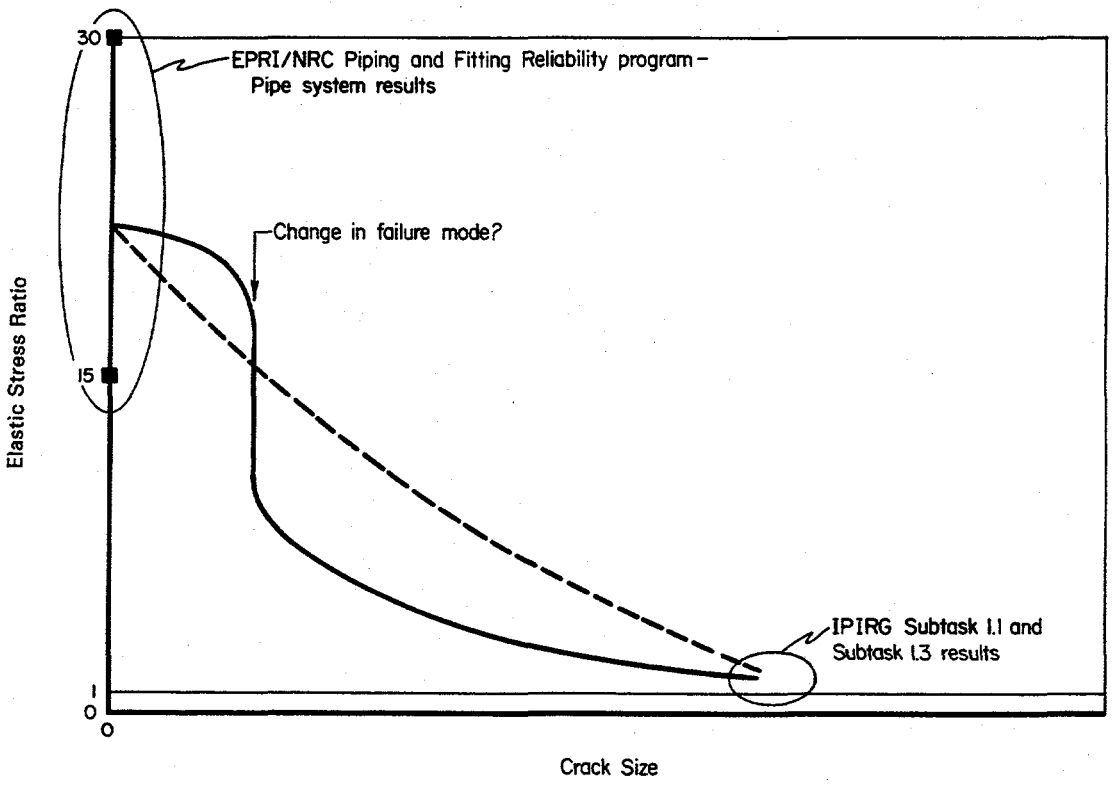

Figure 6.1 Postulated elastic stress ratios as a function of crack size

I1.3-10/90-F4.6

severe lower bounds. This is the result of the fact that the flaw sizes were large, higher strength pipe was used outside of the crack test section, a thicker elbow was used at a critical location to prevent plasticity, and low friction supports were used which minimized nonlinear boundary conditions.

The calculated-to-experimental ratios of stresses for the elastic stress analysis should be identified in such a manner that they could be used in either assessing proposed changes to the Code from the EPRI/U.S. NRC Piping and Fitting Dynamic Reliability program or incorporated in a simplified manner for LBB or in-service flaw evaluations at Level C or D conditions.

6.5 Inherent Accuracy of Fracture Analyses

Several different fracture analysis methods were used to predict the observed failure loads in cracked pipe experiments conducted in this subtask. These analyses include the following: the Net-Section-Collapse analysis, the Dimensionless Plastic-Zone Parameter (DPZP) analysis, the ASME Section XI flaw evaluation criteria, the R6 Option 1 method, and the SC.TNP J-estimation scheme. These methods were used to evaluate the dynamic IPIRG pipe-system experiments and the companion quasi-static pipe fracture experiments. This allowed for two assessments. First, the ratios of experimental-to-predicted failure stresses for each analysis method and each of the experiments were assessed, and second the relative assessment of the fracture behavior of each material under both the dynamic IPIRG pipe-system test conditions and the quasi-static test conditions was made. This later aspect is important in that it establishes whether or not the quasi-static pipe fracture data base used to verify existing Code criteria is sufficient. From this assessment the following findings were identified.

6.5.1 Net-Section-Collapse Analysis

The Net-Section-Collapse analysis method consistently overpredicted the maximum experimental stress. This was due to the fact that several of the materials had sufficiently low toughness that an elastic-plastic fracture analysis, or correction, was needed. This method should not be used unless there is a screening criterion that defines its range of validity.

6.5.2 DPZP Analysis

The Dimensionless Plastic-Zone Parameter analysis is a criterion for assessing whether conditions exist for using the Net-Section-Collapse analysis. Furthermore, the DPZP analysis gives an empirically derived, simplified correction to the Net-Section-Collapse analysis for elastic-plastic fracture considerations.

There were three experiments in which the predicted maximum stress was smaller than the experimental value when using the DPZP analysis and either quasi-static or dynamic C(T) specimen J_i values. For one of them (the stainless steel base metal) J_i values calculated from the pipe-system experiment brought the data more in line with other surface-cracked pipe data. The empirical "C" value for the surface-cracked pipe data generated to date may need to be adjusted to give a better statistical fit of the results to date. From observation of where the data falls compared with the predictions, this adjustment will be relatively small.

6.5.3 ASME Section XI Flaw Evaluation Criteria

The ASME Section XI flaw evaluation procedures were directly evaluated since these apply to surface-cracked pipe. There are two different criteria, one for austenitic pipe and one for ferritic pipe. The analyses conducted showed that they differ significantly in the values of the ratios of experimental-to-calculated stresses. Other considerations were how to analyze the weld crack experiments and how the ratios of experimental-to-calculated stresses would change if the actual properties were used to calculate an S_m for use in the flaw evaluation procedures.

6.5.3.1 Ferritic Pipe Flaw Evaluations

The ferritic pipe flaw evaluation procedure (IWB-3650) was found to overpredict the maximum experimental stress by a large amount. This criterion has been verified by the IPIRG experiments. In particular the IWB-3650 analysis procedure was found to substantially overpredict the maximum experimental stress for a carbon steel weld and also overpredict the maximum experimental stress for the A106 Grade B base metal, even with the loss in strength and toughness at dynamic rates.

6.5.3.2 Austenitic Pipe Flaw Evaluation

The austenitic pipe flaw evaluation procedure (IWB-3640) was found to give predictions of the failure loads that were greater than the experimental values but not overly so as was the case for the IWB-3650 analysis. The experimental-to-calculated stress ratios for the TP304 stainless steel and CF8M base metal dynamic IPIRG pipe-system experiments were significantly below one. In the quasi-static pipe fracture experiments, these ratios were above one for these materials. Consequently, the existing quasi-static pipe fracture data base used to verify IWB-3640 may not be sufficient.

The CF8M pipe test failed below the IWB-3640 prediction because of thermal aging of this particular experimental heat of French cast stainless steel. The aging of U.S. steels and CF8M steels from other countries may not be as severe because of lower niobium content. It may be necessary to develop a screening criterion for the use of IWB-3640 for cast stainless steel pipe in lieu of merely specifying that the ferrite number be less than 20.

6.5.3.3 Analysis of Weld Experiments

Both the ferritic and stainless steel weld IPIRG experiments had experimental-to-calculated stress ratios above one. This may be partially due to the fact that the height of the weld crown was ignored in determining the flaw-depth-to-thickness ratio. The weld crown increases the length of the remaining ligament and tends to add some conservatism if it is ignored. No attempts have been made to assess the various analyses if the weld crown were removed.

To minimize the experimental-to-calculated stress ratio, the weld crown should not be considered in determining the flaw-depth-to-thickness ratio for the fracture analysis of surface cracks.

6.5.3.4 Use of Actual or Code Minimum Properties

An evaluation was made using the actual properties of the material at temperature to determine an S_m to be used in the ASME flaw evaluation procedures. This was intended to assess the result of a user taking advantage of the strength of his pipe being greater than that in the ASME Section III Code tables. Using actual properties significantly lowered the experimental-to-calculated stress ratios in the flaw evaluation procedures. Some ratios were still less than one for the carbon steel base metal, the carbon steel weld, and the stainless steel weld, but the TP304 and CF8M pipe materials had significantly lower failure stresses than predicted. In fact, the increase in the ratio was greater than the applied safety factor of 1.39 for Level C and D service loads.

It is recommended that the actual properties not be used to determine an S_m for flaw evaluation procedures.

The experimental-to-calculated ratios determined on the basis of actual properties raises another possible concern. The use of an S_m calculated from the actual properties essentially makes every pipe appear to have the code minimum properties. As a result, the benefits realized for the actual strength being above the ASME Section III Code values are eliminated. On the other hand, this allows for a comparison of all pipe fracture experiments to the Code criteria without considering the experimental-to-calculated stress ratios. It may be worthwhile to further evaluate these Code criteria in this manner, particularly the austenitic flaw evaluation criterion.

6.5.4 R6 Option 1 Analysis

The R6 Option 1 analysis procedure gives experimental-to-calculated stress ratios that are the smallest for all of the R6 analysis procedures. Like the ASME Code flaw evaluation procedures, it is considered more as a design criterion than an accurate predictor of the experiments. It should be give ratios less than one in all cases. The comparisons with the experimental results indeed showed that the R6 Option 1 method overpredicted the maximum loads for all experiments evaluated in this report.

From these results, the R6 Option 1 method appears to give consistent results (ratios less than one) and can be recommended for use in practice as long as the thermal expansion and seismic anchor motion stresses are treated as primary stresses.

6.5.5 SC.TNP J-Estimation Scheme Analysis

The SC.TNP method is an elastic-plastic J-estimation scheme that was developed in the U.S. NRC's Degraded Piping Program for circumferentially surface-cracked pipe in pure bending. It was used with a method to account for pressure corrections. This approach tended to give the most accurate predictions, but predicted maximum loads less than the experimental loads for the A106B, TP304, and CF8M base metal, dynamic IPIRG pipe-system experiments.

6.6 Relative Comparison of IPIRG Dynamic Pipe-System Experiments with Quasi-Static Pipe Fracture Experiments

The relative comparison of the results from the dynamic IPIRG pipe-system experiments with the results from the various quasi-static experiments is an important consideration since all bases for pipe fracture codes to date have been based on the results from quasi-static pipe fracture experiments. The relative comparisons of the dynamic IPIRG pipe-system experiments with the quasi-static pipe experiments showed that the A106B, TP304, CF8M, and stainless steel weld pipe materials had lower load-carrying capacity in the dynamic IPIRG pipe-system experiments. Only the carbon steel weld material demonstrated a higher load-carrying capacity in the dynamic IPIRG pipe-system experiment.

6.7 Recommendations from Stability Evaluations

Stability evaluations were made by different analyses for the IPIRG pipe-system experiments involving circumferential surface cracks. These methods are intended to predict if rapid unstable fracture occurs (and estimate if a complete DEGB would occur) or if there would be a limited instability (surface crack penetration occurs, but the resultant through-wall crack remains stable). Additionally, some critical observations were made in Experiment 1.3-7 on the stability of the resulting through-wall crack in that experiment.

6.7.1 Recommendations on Stability Analysis of Surface-Cracked Pipe

The stability analyses evaluated were the fully plastic J/T and Energy Balance Stability criteria. Both of these analyses correctly predicted the stability behavior from the initial surface-crack break through, but neither appear capable of predicting further crack growth under cyclic loading to the point of a DEGB occurring. Perhaps the most conservative assumption would be to assume that inertia, dead-weight, and pressure stresses are load-controlled in a quasi-static stability analysis. For the IPIRG pipe-system experiments, this assumption would result in predictions of unstable through-wall crack behavior in all experiments. However, without exception, the experimental results indicated that the through-wall crack remained stable immediately after surface crack penetration. To evaluate if a complete break would occur for a short duration dynamic event requires a dynamic analysis using a nonlinear spring. Such a dynamic analysis may be useful for marginal cases, or for assessing the rate of crack instability. This would help to assess depressurization loads on the piping and reactor internal supports.

From the results to date, it is recommended to consider inertial, dead-weight, and pressure-induced stresses as load-controlled components for stability analyses of cracked piping systems under dynamic loading.

6.7.2 Recommendations From Observations on Stability of the Resulting Through-Wall Crack in Experiment 1.3-7

An interesting observation for the cast stainless steel test, Experiment 1.3-7, was that after the surface-crack instability, the resulting through-wall crack remained stable for a much longer amount of crack growth than expected. These results suggested that the induced bending and associated rotations from the pressure-induced axial tension loads are restrained by the pipe-system or possibly by the resulting thrust forces. Hence, the piping system had higher load-carrying capacity than analyzed by current through-wall crack analyses.

As a result of this, it is hypothesized that for through-wall-cracked pipe fracture analyses in LBB evaluations, elimination of the induced bending in the tension stress analysis would improve the load-carrying capacity of the piping system. This concept was previously proposed by Kraftwerk Union, Ref. 6.6. However, this restraint of the bending may have the detrimental effect of decreasing the crack-opening area for leak-rate determinations relative to the current calculation methods for normal operating conditions.

6.8 References

6.1 Marschall, C. W., and others, "Effect of Dynamic Strain Aging on the Strength and Toughness of Nuclear Ferritic Piping At LWR Temperatures," NUREG/CR-6226, October 1994.

6.2 Kramer, G., and others, "Stability of Cracked Pipe Under Seismic/Dynamic Displacement-Controlled Stresses - Subtask 1.2 Final Report," NUREG/CR-6233, Vol 2, July 1997.

6.3 "Piping and Fitting Dynamic Reliability Program," EPRI RP-1543-15, 1995.

6.4 Scott, P., and others, "Stability of Cracked Pipe under Inertial Stresses - Subtask 1.1 Final Report," NUREG/CR-6233, Vol. 1, August 1994.

6.5 Kot, C. A. et al., "High-Level Seismic Tests of Piping at the HDR," *Proceedings of SMiRT-10*, Division S, pp 87-92, 1989.

6.6 Bartholomé, G., Kastner, W., Keim, E., and Wellein, R., "Exclusion of Failure of the Pressure Retaining Coolant System - Part 2: Application to the Primary Coolant Piping," *International Symposium on Reliability of Reactor Pressure Components* (IAEA-SM-269/7), March 1983.

APPENDIX A

CALCULATION OF PIPE DISPLACEMENTS FROM STRING POTENTIOMETER DATA

APPENDIX A

CALCULATION OF PIPE DISPLACEMENTS FROM STRING POTENTIOMETER DATA

The basic data recorded for pipe displacement is the change in length of three vectors from fixed points to the pipe. The data reduction procedures for these data convert changes in the vector lengths to X-Y-Z global displacements. Those data reduction procedures are described in this appendix.

Figure A.1 shows the geometry of a typical pipe displacement measuring device. The point identified as (0,0,0) is attached to the pipe. When the pipe undergoes a displacement (x_i,y_i,z_i), the vector lengths from the point on the pipe to the fixed points change. The lengths of the three vectors are:

$$V_1 = \sqrt{(A - x_i)^2 + y_i^2 + (a - (C + z_i))^2} \qquad \text{(A-1)}$$

$$V_2 = \sqrt{x_i^2 + y_i^2 + (C + z_i)^2} \qquad \text{(A-2)}$$

$$V_3 = \sqrt{x_i^2 + (B - y_i)^2 + (b - (C + z_i))^2} \qquad \text{(A-3)}$$

Changes in the lengths of the three vectors from the initial configuration are measured by the string potentiometers. Knowing the initial geometry A, B, C, a, and b, (and hence initial vector lengths), Equations A-1 through A-3 are a set of three coupled nonlinear equations in x_i, y_i, and z_i that allow one to find the global displacements.

Equations A-1 through A-3 cannot be easily solved in closed form. To effect a reasonably easy solution, Newton's method for finding the roots of nonlinear equations in multiple degrees of freedom is invoked. Writing the three equations above as functions, F_1, F_2, and F_3, and displacements x_i, y_i, and z_i in a generalized form as X,

$$F_1 = V_1^2 - (A - X1)^2 + X2_2 + (a - (C + X3))^2 \qquad \text{(A-4)}$$

$$F_2 = V_2^2 - X1_2 + X2_2 + (C + X3)^2 \qquad \text{(A-5)}$$

$$F_3 = V_3^2 - X1^2 + (B - X2)^2 + (b - (C + X3))^2 \qquad \text{(A-6)}$$

$$X_1 = x_i \qquad \text{(A-7)}$$

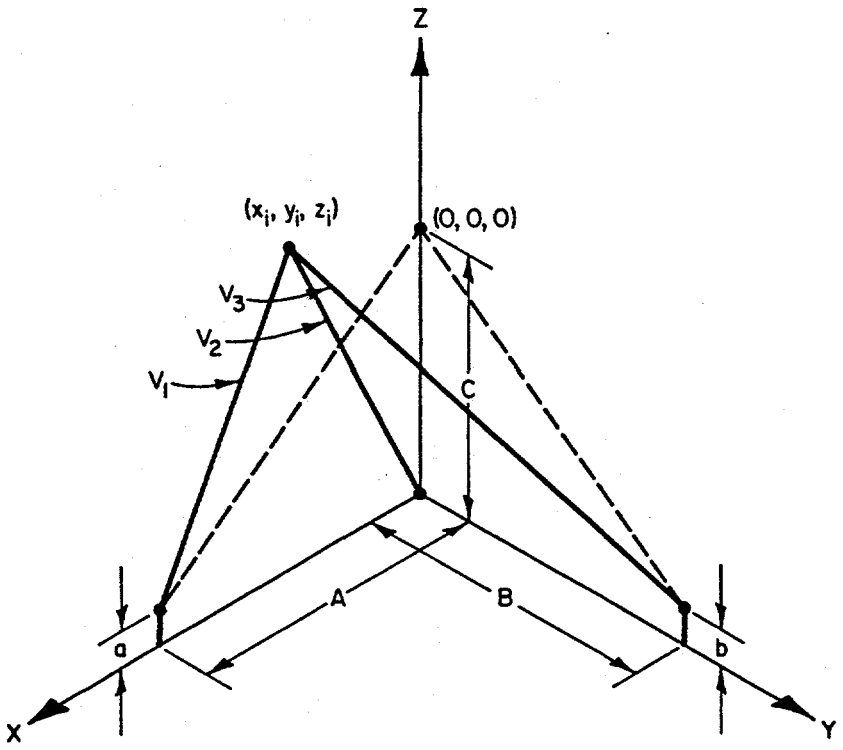

Figure A.1 Pipe displacement transducer geometry
DRB/1.3-1/FC-3

$$X_2 = y_i \tag{A-8}$$

$$X_3 = z_i \tag{A-9}$$

an iterative solution for X is written as:

$$\{X\}_{n+1} = \{X\}_n + [J]^{-1}\{F(X)_n\} \tag{A-10}$$

where [J] is the Jacobian defined as:

$$[J] = \begin{bmatrix} \partial F_1/\partial X_1 & \partial F_1/\partial X_2 & \partial F_1/\partial X_3 \\ \partial F_2/\partial X_1 & \partial F_2/\partial X_2 & \partial F_2/\partial X_3 \\ \partial F_3/\partial X_1 & \partial F_3/\partial X_2 & \partial F_3/\partial X_3 \end{bmatrix} \tag{A-11}$$

Given an initial guess for X, Equation A-10 can be used to iterate to a solution to any desired accuracy for each time step. A previously known solution is a very good guess, particularly with a reasonably fast data collection rate. Even with a poor guess, however, Equation A-10 is very convergent.

In practice, the string potentiometers were not positioned such that the center device was directly below the pipe after the first test. Rather, there was some positioning error offset that had to be accounted for. This was done by measuring the initial vector lengths of all of the potentiometers prior to pressurization and heat up and calculating the initial unloaded global displacements. These values were then subtracted from all subsequently calculated displacements.

APPENDIX B

CALCULATION OF STRESSES AND MOMENTS FROM STRAIN GAGE DATA

APPENDIX B

CALCULATION OF STRESSES AND MOMENTS FROM STRAIN GAGE DATA

Calculation of Stresses

The strain data provides basic information about the deformation of the material that they are attached to. They do not, however, directly provide information about stresses, and consequently, do not yield information that can be directly converted to bending moment. Therefore, special procedures were needed to reduce the strain data.

All of the strain gages used in these experiments were configured as quarter bridges, and therefore needed to be corrected for thermal effects. Specifically the indicated strains from the experiments needed to be corrected for apparent strain (i.e., the strain observed due to differences in the coefficients of thermal expansion between the strain gage and the pipe steel) at 288 C (550 F) and changes in gage factor from room temperature to 288 C (550 F). In order to ascertain the magnitude of the apparent strain and change in gage factor for the strain gages used in these experiments, a series of strain gage performance characteristic tests were conducted on a strain gage from the same manufacturing lot as the gages used in these experiments. These tests were conducted in accordance with ASTM Standard E251-86, "Standard Test Methods for Performance Characteristics of Bonded Resistance Strain Gages". The test specimen for this series of tests was fabricated from a sample of the ASTM A710 pipe loop material.

Figures B.1 and B.2 show the results of those tests. Figure B.1 is a plot of the apparent strain as a function of temperature for weldable strain gages attached to the A710 pipe steel substrate. From Figure B.1 it can be seen that the apparent strain at 288 C (550 F) is approximately -65 microstrain, i.e., one needs to numerically add 65 microstrain to the indicated strain values from the pipe experiment to determine the actual strain values. (Note, the actual strain is defined as the indicated strain minus the apparent strain.) Figure B.2 is a plot of the gage factor as a function of temperature. From Figure B.2 it can be seen that the gage factor does not change significantly as a function of temperature.

In performing the data reduction for the PWR uncracked pipe test, it was apparent that the strain gage data and hence the calculated moments just prior to actuator motion were not consistent with analytical predictions. Efforts to resolve this problem showed that although the total moment derived from the strain gages deviated significantly from what was expected, the dynamic components of the moments were reasonably consistent with the predictions. Furthermore, it was discovered that the discrepancies were of a random nature, i.e., some gages were higher and some were lower than needed to make the data consistent with the predictions, as opposed to a systematic discrepancy which would manifest itself as all gages being offset a similar amount. The discrepancies were traced to static drift in the strain gage measuring system, either the signal conditioning system or the gages themselves, due to the long heat-up period for the system. As a result, it was decided to treat the strain gages as strictly dynamic transducers for calculation of dynamic moments for all tests. Calculated static values of moment using ANSYS® finite element analyses were added to the measured dynamic data in order to get total moment data.

For the case of the room temperature tests, the drift problem would not occur and total strains could be used for moment and stress calculations. This was what was done in the case of the rosette strain gages on

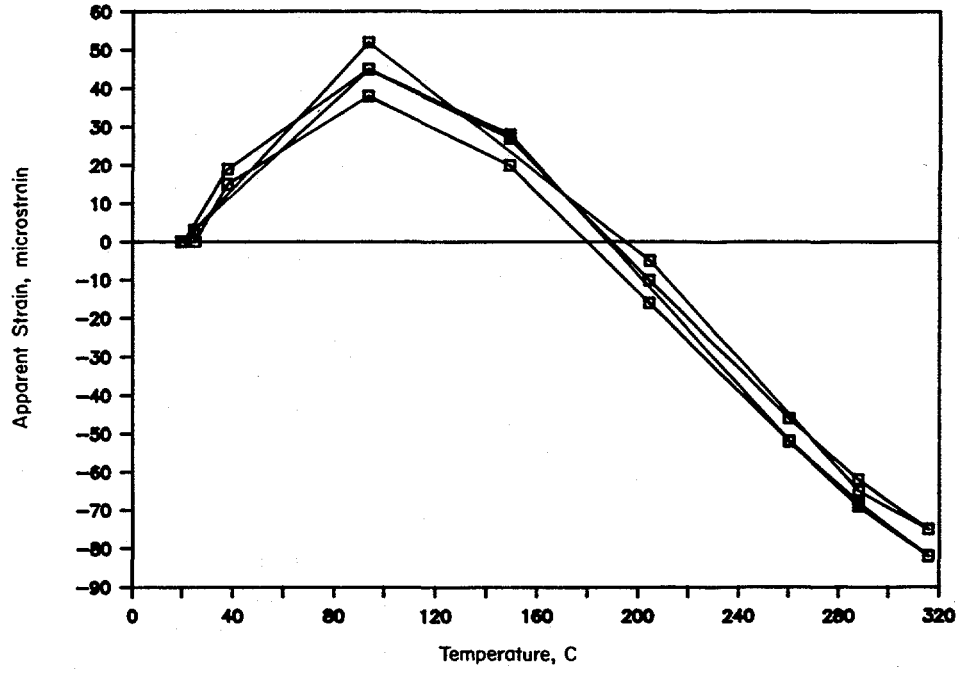

Figure B.1 Apparent strain correction for Eaton weldable strain gages
I-10/89-B42b-PS

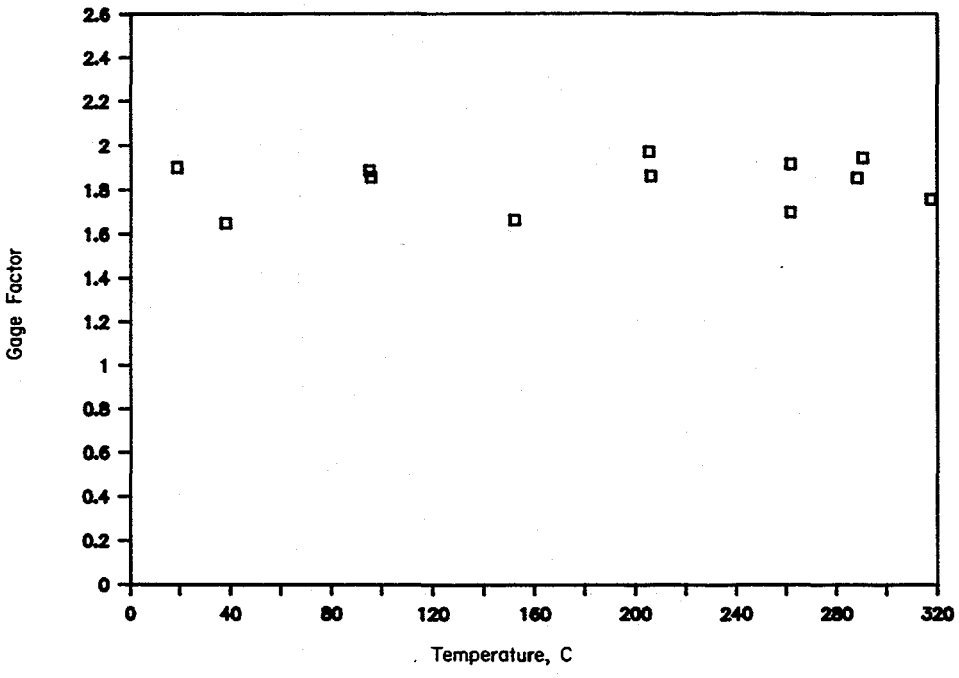

Figure B.2 Gage factor variation with temperature for Eaton weldable strain gages
I-10/89-B42a-PS

the elbows. For consistency, however, bending moments, even for the room temperature tests, were based on static calculations and dynamic measurements.

For a condition of plane stress and considering only dynamic components, the stress in terms of measured strains is written as:

$$\sigma_L = \frac{E}{(1 - \sqrt{v^2})} \quad (\epsilon_L + v\ \epsilon_h) \tag{B-1}$$

$$\sigma_h = \frac{E}{1 - \sqrt{v^2})} \quad (\epsilon_h + v\ \epsilon_L) \tag{B-2}$$

$$T = G \quad (2\epsilon_{45} - \epsilon_L - \epsilon_h) \tag{B-3}$$

where

σ_l	=	longitudinal stress
σ_h	=	hoop stress
τ	=	shear stress
ϵ_l	=	longitudinal strain
ϵ_h	=	hoop strain
ϵ_{45}	=	strain from 45-degree gage
E	=	Young's modulus
ν	=	Poisson's ratio
G	=	modulus of rigidity.

Equations B-1 through B-3 are used for locations where a three-element strain gage rosette has been applied. Engineering assumptions must be made to allow stresses to be calculated at other locations, i.e., where only a longitudinal gage has been applied.

At locations where only a longitudinal gage exists and where there is at least a 2-element rosette (hoop and longitudinal) gage somewhere at the same pipe cross-section, one can use the assumption that hoop stress is constant at that cross-section. Making that assumption, Equation B-2 can be used to solve for the hoop strain that would exist at the location that lacks a hoop gage. With the estimate of the hoop strain, Equation B-1 can be applied to calculate the longitudinal stress.

For the IPIRG data, the strains used in the equations come directly from the test. The modulus of elasticity at the test temperature was taken from the Young's modulus measurements done on the ASTM A710 material and reported in Section 2. Poisson's ratio was assumed to be 0.3. In several instances, failures of gages forced assumptions to have to be made regarding missing data. Failure of a hoop gage was accommodated by using the dynamic data from a nearby hoop gage. Failure of a longitudinal gage was accommodated by using the dynamic mirror image of the gage on the opposite side of the pipe. The

validity of these assumptions was substantiated by the consistency of the assumed strains with the rest of the dynamic strains for the test and consistency of the calculated moments with moments from the other tests. For the sake of brevity, the stresses calculated using B-1 to B-3 were never reported. Rather, they were only used as inputs for the calculation of pipe bending moments.

In addition to calculation of the basic stresses defined by Equations B-1 through B-3, von Mises stresses were calculated for the elbows in the room temperature uncracked pipe test. For this specific test and for the elbows only, the total strains were used in the calculations, because heat-up drift would not be a problem and because these gages were only on for one test. The equation for the von Mises stress under plane stress conditions and assuming a rectangular rosette is

$$\sigma_{vm} = \sqrt{\sigma_1^2 + \sigma_2^2 - \sigma_1\sigma_2} \qquad \text{(B-4)}$$

where

σ_{vm} = von Mises stress

σ_1, σ_2 = principal stresses

$$= E\left[\frac{(\epsilon_1 + \epsilon_h)}{2(1 - v)} \pm \frac{1}{2(1 + v)}\sqrt{(\epsilon_L - \epsilon_h)^2 + (2\epsilon_{45} - \epsilon_2 - \epsilon_h)^2}\right]$$

and all of the terms are as defined above.

Calculation of Bending Moments

The generalized calculation of moment in a pipe requires knowledge of the longitudinal stress around the complete circumference of the pipe. Under elastic conditions and assuming uniform wall thickness, the longitudinal stress at a given cross-section can be completely characterized by longitudinal stresses at three locations around the circumference. In principle, the three stresses may be located in many different positions around the circumference. However, one of two types of arrays is generally used, based on the deployment of strain gages: a 90-degree array or a 120-degree array. In the case of the IPIRG Subtask 1.3 experiments, the 90-degree array applies.

Figure B.3 shows a 90-degree array. For such an array, the longitudinal stress at any point (x,y) around a pipe of radius r is

$$\sigma = \frac{(\sigma_a + \sigma_c)}{2} + \frac{(\sigma_c - \sigma_a)}{2}\frac{X}{r} - \frac{(\sigma_a + \sigma_c - 2\sigma_b)}{2}\frac{y}{r} \qquad \text{(B-5)}$$

where σ_a, σ_b, and σ_c are the stresses at the three 90-degree locations. Stress σ is a maximum or minimum at

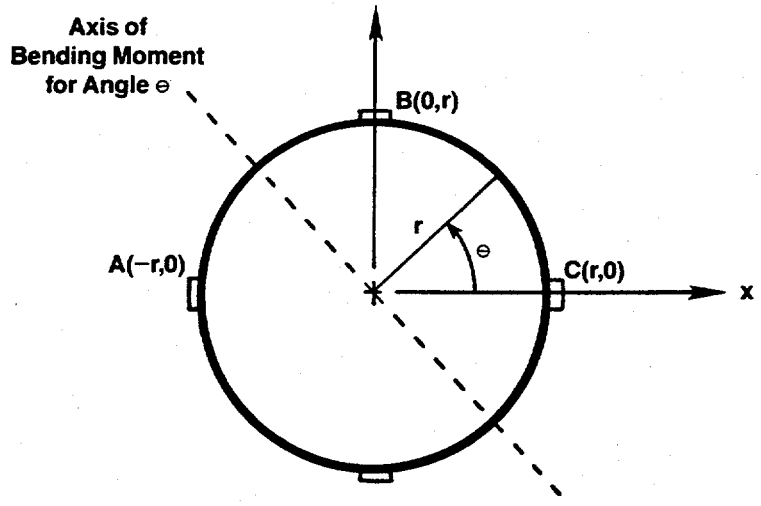

Figure B.3 90-degree array of known stresses from strain gage data used to determine pipe bending moments DRB/1.3-1/FC-1

$$\frac{x}{r} = \pm \frac{\sigma_c - \sigma_a}{\sqrt{2\sigma_a^2 + 2\sigma_c^2 - 4\sigma_a\sigma_b - 4\sigma_b\sigma_c + 4\sigma_b^2}} \quad \text{(B-6)}$$

$$\frac{y}{r} = \pm 1 - (x/r)^2 \quad \text{(B-7)}$$

Given the stress distribution defined by Equation B-5, the moment about any axis through the cross-section defined by the angle θ shown in Figure B.3 is

$$x = r \cos \theta \quad \text{(B-8)}$$

$$M = \frac{[\sigma(x,y - \sigma(-x,-y)]}{2} \frac{I}{r} \quad \text{(B-10)}$$

where

$$y = r \sin \theta \tag{B-9}$$

M	=	moment
σ(x,y)	=	stress from Equation B-5, location x,y
σ(-x,-y)	=	stress from Equation B-5, location -x,-y
I/r	=	section modulus (second moment of area/radius).

The tension in the pipe is given by

$$F = \frac{(\sigma_a + \sigma_c)}{2} A_p \tag{B-11}$$

where

F	=	pipe tensile force
σ_a	=	stress at location a
σ_c	=	stress at location c
A_p	=	cross-sectional area of the pipe.

If the stress is known only at two locations on opposite sides of the pipe, moment can only be calculated about the axis perpendicular to the line passing through the two points in the plane of the cross section.

Equations B-5 to B-11 can be used to calculate the bending moment about any axis of the pipe. For the IPIRG 1.3 system, the axes for calculation of bending moments are known ahead of time and the strain gages have been installed accordingly. Thus, Equation B-10 can be directly applied, using the stresses calculated on opposite sides of the pipe, without any additional calculations. Data reduction for the uncracked pipe tests to find the principal axes of bending indicated that the global X and Z axes (the vertical and horizontal axes through the pipe cross-section) were, for all practical purposes, the principal axes of bending.

In order to apply the equations for determining moment, the section modulus is needed, in addition to the stresses. For the crack plane, when gages were installed, and the location 3.2 m (10.5 feet) north of the Elbow 4, there is no difficulty; the section modulus was based on 406.4 mm (16 inch) diameter Schedule 100 [26.2 mm (1.031 inch) thick] pipe. At the locations 914 mm (36 inches) north and south of the crack location, however, there was some question about the actual section modulus due to the presence, in most of the tests, of internal end caps. Figure B.4 shows the geometry near the internal end caps. From Figure B.4, it is apparent that the strain gages are in a location that has a section modulus very nearly equal to the pipe itself. The end caps may stiffen the pipe in the hoop direction, but with the "plane sections remain

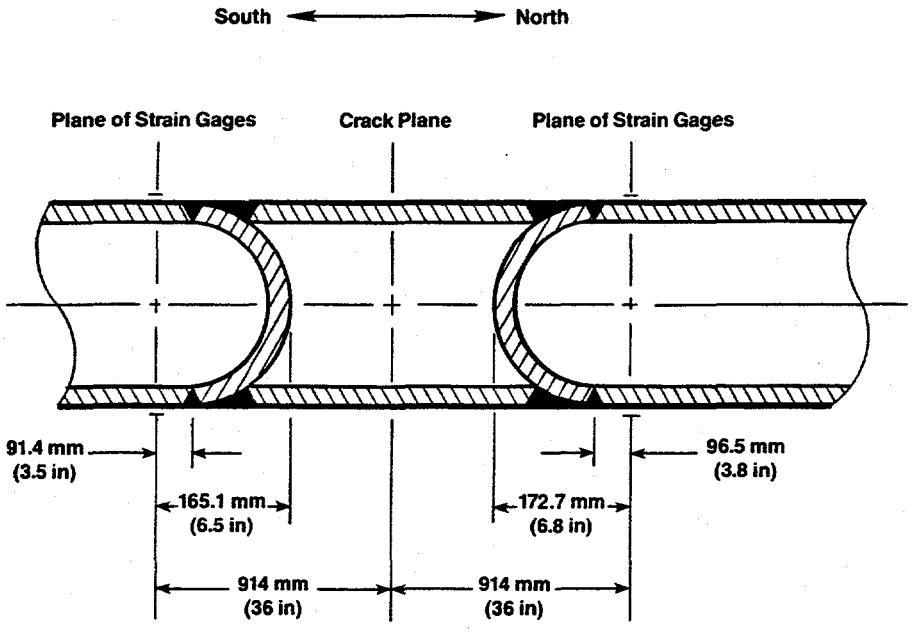

Figure B.4 Geometry of pipe and strain gages at the internal end caps
DRB/1.3-1/FC-2

plane" assumption of bending, the end caps should not affect the moment. Analysis of the moments at the internal end caps, in relation to the moments measured at the cracked section in the uncracked pipe tests and comparisons with analytical predictions, confirms this hypothesis. The nominal dimensions for the pipe were used in the moment calculations to keep it consistent with the calculated static moments and because the variations of the actual dimensions about the nominal were small.

Calculation of Crack Location Moment

In the uncracked pipe tests, strain gages were applied to the test specimen at the crack location, and these were used to calculate the moment using the procedures described above. For the cracked pipe experiments, however, there were no gages at the crack plane and so moment must be inferred from the moments measured nearest the crack, 914 mm (36 inches) north and south of the crack location. Figure B.4 shows the location of the strain gages at the 914 mm (36 inch) locations, and hence the locations where moments can be calculated, relative to the crack plane.

A gradient in moment exists along the pipe. However, from a free body diagram of the pipe loop, there are no externally applied in-plane shear forces acting on the pipe near the test section prior to penetration of a crack through the pipe wall, assuming that the contribution of inertial forces is small. Consequently, the shear force in the pipe must be constant and the moment gradient is linear. Thus, the moment at the crack must be the average of the moments at the north and south internal end caps.

The assertion that the crack section moment is the average of the moment at the north and south internal end caps was tested on the data from the room temperature dynamic test, the elevated temperature static push, and the elevated temperature dynamic test. By assuming that the crack section moment is a weighted average of the north and south end cap moments plus a constant, weighting coefficients can be calculated

by doing a least squares fit to the measured moment over the duration of each test. The resulting coefficients do indeed turn out to be very nearly 0.5 for the north and south moments with the constant very nearly equal to zero, as would be expected from the above discussion.

A word of caution is in order about the use of the moment coefficients for calculating cracked section moment; the coefficients only apply up to the point of crack break-through. Prior to crack break-through, there is a linear moment gradient which implies a constant shear force. After break-through, there is an additional shear force on the "moment load cell", the thrust force. This force alters the moment distribution, thereby invalidating the basic assumption used to derive the calibration coefficients. In addition, there is some question about the validity of the coefficients relative to St. Venant's principle, due to the proximity of the north and south end cap gages to the crack. The "characteristic length" is on the order of the pipe wall thickness prior to crack break-through, but is on the order of the pipe diameter after break-through. Although the calibration coefficients are probably applicable when the crack faces close, it is difficult to determine when this actually happens. The moment at the gage location, however, is always valid provided that the strain gages are functioning properly.

APPENDIX C

SUBTASK 1.3
QUALITY ASSURANCE (QA) PROCEDURES

IPI-PP-1.3
Revision 3

QUALITY ASSURANCE DOCUMENT

PROCEDURE FOR PERFORMING PIPE FRACTURE EXPERIMENTS UNDER COMBINED INERTIAL AND SEISMIC/DYNAMIC DISPLACEMENT CONTROLLED STRESSES (Subtask 1.3 of IPIRG Contract)

BATTELLE
505 King Avenue
Columbus, Ohio 43201-2693

Paul M. Scott

January 10, 1990
Date

APPROVED BY

1-17-90
Program Technical Manager Date

APPROVED BY

1/17/90
Section Manager Date

APPROVED BY

1/17/90
Program Manager Date

1/19/90
QA Manager Date

DOCUMENT REVISION RECORD

Title: Procedure for Performing Pipe Fracture Experiments Under Combined Inertial and Seismic/Dynamic Displacement Controlled Stresses (Subtask 1.3 of IPIRG Contract)

No. IPI-PP-1.3

Page i of i

INDEX OF PAGE REVISIONS

Page No.	i	ii	iii							
Rev. No.	3									

Page No.	1	2	3	4	5	6	7	8	9	10
Rev. No.	3	3	3	3	3	3	3	3	3	3

Page No.	11	12	13	14	15	16	17	18	19	20
Rev. No.	3	3	3	3	3	3	3	3	3	3

Page No.	21	22	23	24	25	26	27	28	29	30
Rev. No.	3	3	3	3	3	3	3	3	3	3

Page No.	31	32	33	34	35					
Rev. No.	3	3	3	3	3					

REVISION RECORD

Rev. No.	00	01	02	03	04	05	06	07	08	09
Date				1/19/90						
Approval				[signature]						

PROCEDURE FOR PERFORMING PIPE FRACTURE EXPERIMENTS UNDER COMBINED INERTIAL AND SEISMIC/DYNAMIC DISPLACEMENT CONTROLLED STRESSES (Subtask 1.3 of IPIRG Contract)

1.0 Scope

1.1 This document describes the test procedure for performing Subtask 1.3 "Crack Stability in Representative Piping Systems Under Combined Inertial and Seismic/Dynamic Displacement-Controlled Stresses" of the IPIRG program.

2.0 Objective

2.1 The objective of these experiments is to develop data to assess current analysis predictions for assessing the stability of a circumferential crack in a representative pipe configuration under combined dynamic inertial and displacement-controlled stresses.

3.0 Approach

3.1 A series of six pipe fracture experiments will be conducted to develop data on both stainless steel and carbon steel base metal and weld materials containing circumferential surface cracks. Table 1 provides a test matrix for this subtask.

3.2 One or more of these six experiments shall be designed such that a double-ended-guillotine-break (DEGB) is predicted to occur once the surface crack tears through the pipe wall.

3.3 Significant data that will be collected are: applied load; actuator displacement; reaction forces between pipe loop and framework; pipe strains, accelerations and displacements of the piping system at critical locations; pipe rotation at the crack section; electric potential; and crack-mouth-opening displacement data.

TABLE 1. TEST MATRIX FOR SUBTASK 1.3 EXPERIMENTS

Experiment Number	Material	Flaw Type
1.3-1	Carbon steel[a]	None
1.3-2	Carbon steel[a]	Surface crack in base metal[e]
1.3-3	Stainless steel[b]	Surface crack in base metal[f]
1.3-4	Carbon steel weld[c]	Surface crack in weld metal susceptible to dynamic strain aging[e]
1.3-5	Stainless steel weld[d]	Surface crack in submerge-arc weld (SAW)[e]
1.3-6	Contingent	To be determined

(a) A-106 Grade B carbon steel.
(b) SA-358 TP 304 stainless steel.
(c) Circumferential girth weld in A106 Grade B carbon steel.
(d) Circumferential girth weld in SA-358 TP304 stainless steel.
(e) Fatigue precracked specimen.
(f) Specimen is not precracked.

4.0 Experimental Preparation

4.1 Test Specimen

4.1.1 The pipe materials to be used in these experiments will be SA-358 TP304 stainless steel or A106 Grade B carbon steel and their associated weldments. The weldments to be evaluated are the low toughness flux weld variety. All pipe test specimens will be 406-mm (16-inch) nominal diameter, Schedule 100 pipe. Pipes which have non-uniform wall thicknesses will be machined prior to testing to produce a constant wall thickness.

4.1.2 A surface crack 50 percent of the pipe circumference in length and 55 to 60 percent of the wall thickness in depth will be machined into the carbon steel base metal, the carbon steel weld metal, and the stainless steel weld metal pipe specimens. The length and depth of the initial machined flaw for the stainless steel base metal specimen will be 50 percent of the pipe circumference in length and 66 percent of the wall thickness in depth. Once the simulated crack is machined, it will be instrumented with electric potential (EP) probes as shown in Figure 1 to be used to monitor crack initiation and crack growth. After instrumenting the test specimen with EP probes, the carbon steel base metal, carbon steel weld metal, and stainless steel weld metal specimens will be fatigue precracked by pressure cycling. The target depth of the fatigue precrack will be 66 percent of the pipe wall thickness. After precracking, the instrumented test specimen will be welded into the Subtask 1.3 piping loop.

4.2 Test Configuration

Figure 2 is a schematic of the piping loop that will be used in this subtask. The actuator that will be used to excite the piping loop is a Moog actuator with 1,535 kN (345,000 pounds) of force capacity at 20.7 MPa (3,000 psi) pressure and 457 mm (18 inches) of stroke. The actuator is equipped with an integral 7,580 lpm (2,000 gpm) servo valve. Loading fixtures will be used which allow for both axial translation and rotation of the pipe specimen. The welds tying the pipe loop together were fabricated by United McGill and inspected by them via X-rays.

4.3 Instrumentation

Figure 1 illustrates the specific location of the instrumentation on the piping loop in relation to the surface crack. The following data will be collected in each experiment:

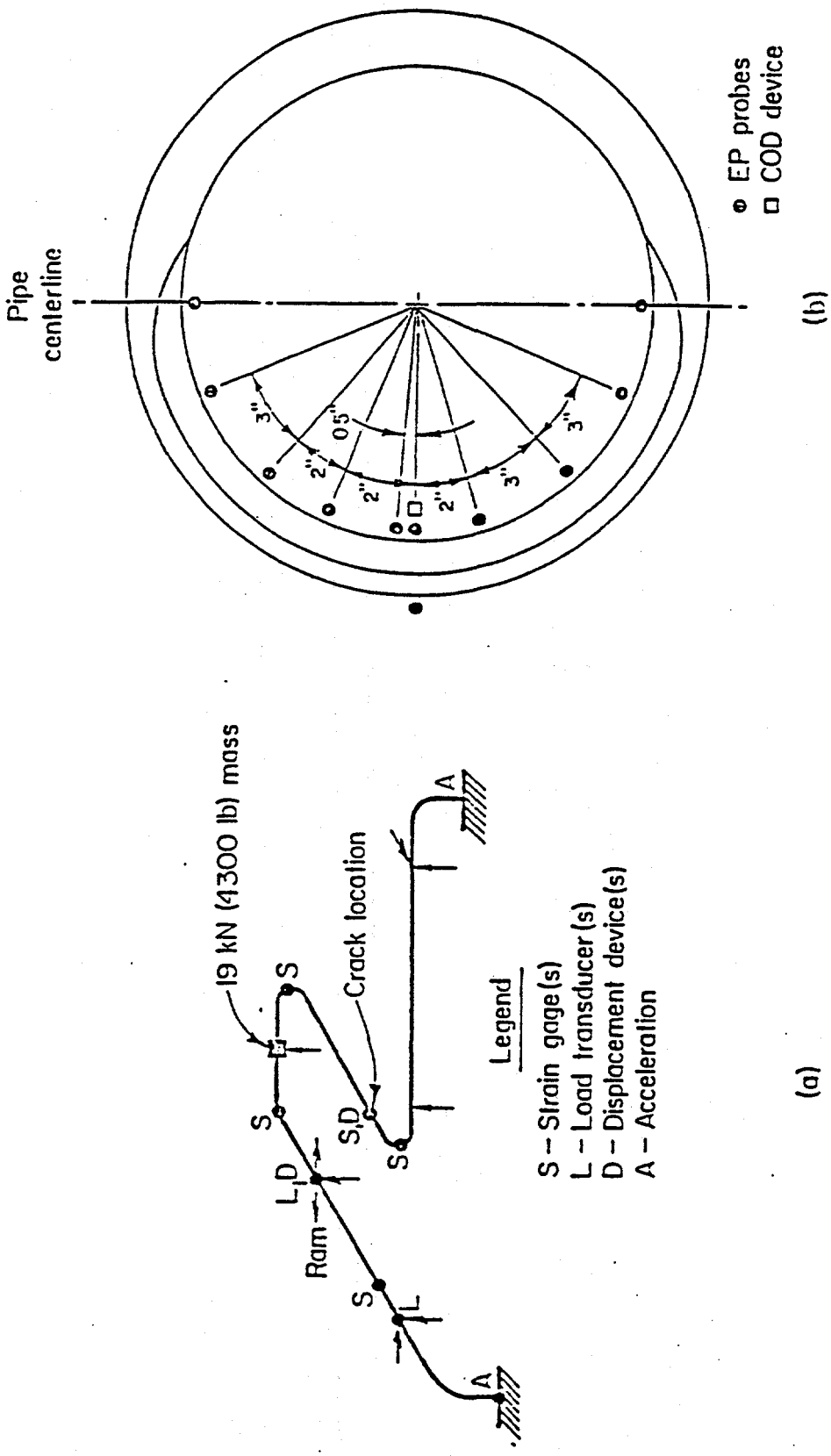

FIGURE 1. INSTRUMENTATION LAYOUT FOR SUBTASK 1.3

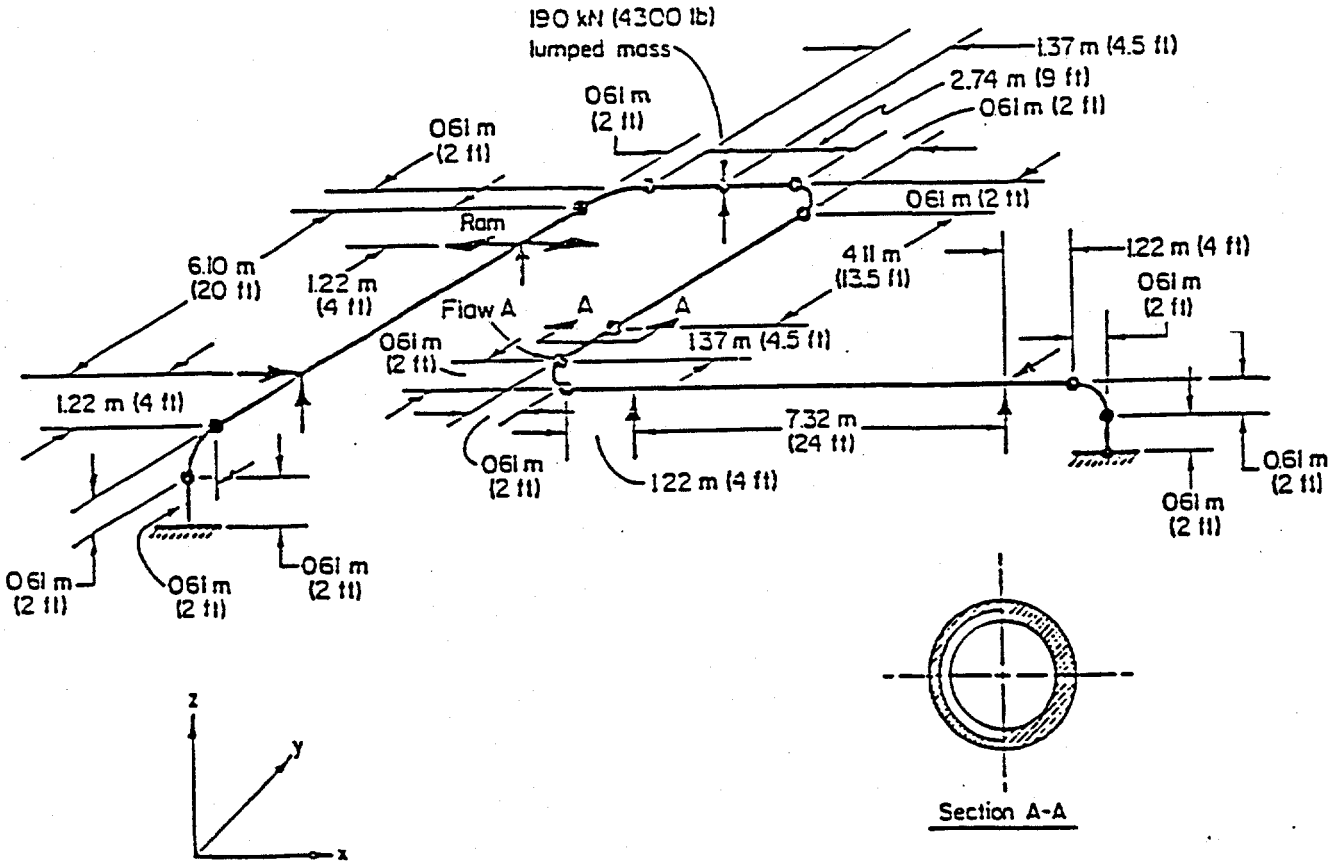

FIGURE 2. SKETCH OF THE PIPING CONFIGURATION FOR THE SUBTASK 1.3 EXPERIMENTS

4.3.1 Actuator load.

4.3.2 Actuator displacement.

4.3.3 Reaction loads between pipe loop and pipe frame at the X-Z hanger nearest the ram.

4.3.4 d-c EP measurements at multiple locations along the surface crack.

4.3.5 Base metal d-c EP.

4.3.6 Crack-mouth-opening (CMO) displacement at the crack centerline.

4.3.7 Pipe strains at critical locations.

4.3.8 Pipe displacements at critical locations.

4.3.9 Pipe rotations on each side of the surface crack.

4.3.10 Pipe temperature at multiple locations on the outside pipe surface.

4.3.11 Anchor accelerations.

4.3.12 Water temperature.

4.3.13 Internal pipe pressure.

4.3.14 Time.

4.4 Instrument Calibration

The instruments used to obtain test data will be calibrated prior to conducting the first pipe fracture experiment. All calibrations will be performed using the same signal conditioners, amplifiers, cables, etc. as will be used in the actual experiments. The following instruments shall be calibrated traceable to National Institute for Standards and Technology (NIST), formerly NBS, where standards are available.

4.4.1 Thermocouple probes and pressure transducers and their associated readouts will be calibrated by the Battelle Instrument Laboratory with standards traceable to NIST.

4.4.2 The load cell used to measure the applied load shall be calibrated to QA procedures by Battelle's Fatigue Laboratory using a load cell calibrated and traceable to NIST.

4.4.3 The crack-mouth-opening displacement, pipe displacement and pipe rotation instruments shall be calibrated by the Battelle Metrology Laboratory.

4.4.4 The ram displacement shall be calibrated in place using either a calibrated secondary LVDT or a dial gage with gage blocks.

4.4.5 All common measuring devices, such as calipers, micrometers, dial gages, etc., shall be calibrated and traceable to NIST and serial numbers will be recorded on appropriate data sheet.

4.4.6 The Battelle Instrument Laboratory and Metrology Laboratory maintain calibration capabilities traceable to NIST, where available, which are used to calibrate their own instruments and others used throughout the Laboratory.

4.4.7 Calibration cards for the instruments as indicated in Section 4.3 shall be forwarded to the Nuclear QA Manager; QA calibration stickers shall be attached to or near the instrument.

4.5 Perform each test as outlined in Sections 5 through 9 as applicable, and use data sheets as follows:

4.5.1 D1 for specimen preparation and test setup for uncracked pipe experiment.

4.5.2 D2 for test specimen preparation and installation of instrumentation for cracked pipe experiments.

4.5.3 D3 for pre-operational test procedures.

4.5.4 D4 for test procedures.

4.5.5 D5 for post test procedures.

4.6 Use BCD Laboratory Record Books (LRB) as necessary for additional information.

5.0 Specimen Preparation and Test Setup for Initial Uncracked Pipe Experiment

5.1 Specimen Preparation

5.1.1 Measure the OD of the test specimen (top to bottom and side to side) at future crack and strain gage locations and record on D1. [Note the measurement accuracy for these measurements will be ± 0.25 mm (± 0.010 inch).]

5.1.2 Measure the outside circumference of the pipe at the future crack and strain gage locations and record on D1. [The measurement accuracy for these measurements will be ± 1.6 mm (± 0.06 inch).]

5.1.3 Measure the pipe wall thickness at the future crack and strain gage locations and record on D1. (An ultrasonic thickness gage will be used to measure the wall thickness.) Calculate the average thickness for each location. [The measurement accuracy for these measurements will be ± 0.25 mm (± 0.010 inch).]

5.2 Pre-test Set-up Procedure

5.2.1 Instrument the piping loop with calibrated strain gages, accelerometers, thermocouples, displacement transducers, and pressure transducers as shown in Figure 1.

5.2.2 Install heater tapes and insulation on the pipe loop.

5.2.3 Instrument the test specimen with the following instrumentation:

5.2.3.1 Rotation Devices

5.2.3.2 Control Thermocouples

5.2.3.3 Monitoring Thermocouples

5.2.4 Charge the storage vessel and accumulators to the required nitrogen pressure as determined by the Task Leader (TL).
Note: THE GAS MUST BE NITROGEN NOT AIR.

5.2.5 The uncracked pipe experiment 1.3-1 is now ready for test. Proceed to Sections 7, 8 and 9 for test procedures and use appropriate data sheets.

6.0 Test Specimen Preparation and Installation of Instrumentation for Cracked Pipe Experiments

6.1 Cut test specimen to the required length as indicated by the Task Leader and stamp the identification in the appropriate location. See Table 1 for the test matrix.

6.2 Bevel the test specimen to a 37 degree included angle with a 1.6 mm (1/16-inch) to 3.2 mm (1/8-inch) land.

6.3 Machine the inside diameters of the specimen, as necessary, to obtain a constant wall thickness of 25.7 mm ± 0.5 mm (1.01 ± 0.02 inch) and record thickness on D2.

6.4 Measure the OD of the test specimen (top to bottom and side to side) at the specimen centerline and record on D2. [The measurement accuracy for these measurements will be ± 0.25 mm (± 0.010 inch).]

6.4.1 For the weld tests, measure and document the OD on each side of the weld.

6.5 Measure the outside circumference of the pipe at the specimen centerline and record on D2. [The measurement accuracy for this measurement will be ± 1.6 mm (± 0.06 inch).]

6.5.1 For weld tests, measure and document circumference on each side of weld.

6.6 Measure the pipe wall thickness at approximately 10 locations around circumference at specimen centerline and record measurements on D2. [The measurement accuracy for these measurements will be ± 0.25 mm (± 0.01 inch).]

6.7 Machine a circumferential surface crack (SC) into inside surface of pipe at the specimen centerline. Mark the centerline of the flaw on the O.D. of the pipe. The length of the SC for the carbon steel base metal, the carbon steel weld metal, and the stainless steel weld metal test specimens will be approximately 50 percent of the pipe circumference and the depth will be approximately 55-60 percent of the pipe wall thickness. The length and depth of the SC

for the stainless steel base metal experiment will be approximately 50 percent of the pipe circumference and 66 percent of the wall thickness, respectively.

6.8 Measure the length and depth of the SC as follows and record measurements on D2.

6.8.1 Length from tip-to-tip on the inside surface. [The measurement accuracy of this measurement will be ± 1.6 mm (± 0.06 inch).]

6.8.2 Depth at the crack centerline. The measurement accuracy of this measurement will be ± 0.25 mm (± 0.01 inch).]

6.9 Instrument the SC with electric potential probes (EP) as shown in Figure 1.

6.9.1 For the carbon steel base metal, the carbon steel weld metal, and the stainless steel weld metal specimens instrument with ten sets of EP probes as shown in Figure 1.

6.9.2 For the stainless steel base metal experiment, instrument with three EP probes as follows:

6.9.2.1 At the centerline of the crack

6.9.2.2 12.7 mm (0.5 inches) from each side of the crack centerline.

6.9.3 The axial spacing between each set of probes in Steps 6.9.1 and 6.9.2 is to be defined by the Task Leader. The actual spacing is to be measured and recorded on D2. This data is needed for the calibration of the electric potential signal. [The measurement accuracy for these measurements will be ± 0.8 mm (± 0.03 inch).]

6.10 Drill holes in the pipe at the 6 and 12 o'clock positions of the pipe (see Figure 1). Insert Conax fittings in each of these holes and weld in place. Route the EP leads out through the Conax fittings.

6.11 Instrument the exterior of the pipe specimen with a set of base metal EP probes. The probe spacing for the base metal probes should be 102 mm (4 inches). Record distance from crack plane.

6.12 Attach multiple lugs for the current leads for the constant current power supply to the exterior pipe surface. A sufficient number of lugs will be attached to the pipe to ensure a uniform current distribution.

6.13 Measure the initial EP signals for each set of EP probes and record on data sheet. (The measurement accuracy of these measurements will be $\pm$ 1 μV.)

Fatigue Precracking

Note: Items 6.14 through 6.19 apply only to the carbon steel base metal carbon steel weld metal, stainless steel weld metal experiments and possibly on the contingent test depending on the material selected.

6.14 Weld an end cap onto each end of the test specimen. Weld a 19 mm (3/4-inch) pipe fitting into one of the end caps.

6.15 Install the test specimens into the pressure cycling facility.

6.16 Pressure cycle the test specimens until the crack depth at the crack centerline is 66 percent of the wall thickness in depth. The minimum and maximum pressures for the pressure cycling will be provided by the Task Leader. In addition, the magnitude of the EP signal for a 66 percent deep crack will be provided based on the calibration curves given in the reference in Section 10.1.

6.17 Measure the final EP signals for the ten sets of interior EP probes and one set of exterior EP probes and document on data sheet. (The measurement accuracy of these measurements will be $\pm$ 1 μV).

6.18 Estimate the final flaw depth at the ten locations along the circumferential crack front and document on data sheet.

6.19 Cut the end caps off the test specimen and rebevel the ends for welding.

6.20 Mount a calibrated high temperature/high pressure LVDT across the crack centerline. Document the identification number for the LVDT on D2.

6.21 Spot weld a high temperature high pressure weldable strain gage across the centerline of the crack on the inside pipe surface.

Spot weld the ends only. This strain gage will serve as a back-up to the LVDT.

6.22 Measure the height of the LVDT above the inside pipe surface and axial spacing between crack, core fixture, and LVDT body, and document on D2. [The measurement accuracy of this measurement will be ± 0.8 mm (± 0.03 inch).]

6.23 Route the LVDT wires and the EP wires for the EP probes at the crack centerline, 12.7 mm (0.5 inches) from the crack centerline, and 50.8 mm (2 inches) from the crack centerline out through some of the existing Conax fittings. Note the EP probes at the other locations will not be used for the dynamic phase of the experiment.

6.24 Weld the instrumented test specimen into the piping loop.

6.25 Instrument the test specimen with the following instrumentation:

6.24.1 Rotation Device

6.24.2 Control Thermocouples

6.24.3 Monitoring Thermocouples

7.0 Pre-Operational Test Procedures

7.1 Connect all instrumentation to recording devices. Set gains and balance all bridges as appropriate. Document instrumentation set-up with scale and calibration factors in LRB.

7.1.1 Actuator displacement.

7.1.2 Output of load cell.

7.1.3 Pressure transducers on actuator.

7.1.4 Pressure transducers at hanger.

7.1.5 Pipe displacement devices.

7.1.6 Accelerometers.

7.1.7 Pipe pressure.

7.1.8 Strain gages.

7.1.9 Crack rotation devices.

7.1.10 Electric potential probes.

7.1.11 CMOD device.

7.1.12 Thermocouple at crack section.

7.2 Record Instrument Lab numbers of all instruments in LRB and verify that they are calibrated.

7.3 Wrap the piping loop with heater tapes.

7.4 Wrap the piping loop with insulation.

7.5 Connect the control thermocouples and heater tapes to the temperature controllers.

7.6 Fill the piping loop with water. As a preliminary step, make certain that the expansion tank has no water in it (purge it with air if necessary), then valve it off from the pipe loop. Open the vents in the piping loop, taking care so that any water that comes out during the fill does not wet any instrumentation. Draining the expansion tank assures that the maximum expansion space is available for the water and that the air in it is at atmospheric pressure. The venting of the pipe loop assures that the loop will be completely full of water.

7.7 Once the pipe loop is full of water, close the vent valves, turn off the water, and then open the valve between the expansion tank and the loop. Open the valve(s) between the expansion tank and the pressure source at JS-8.

7.8 Unlock garage doors to building. If outdoor weather conditions permit, the doors should be opened.

7.9 Perform visual inspection of the pipe loop, frame, and loading system to ensure that there are no tools, loose wires, etc. that may cause problems during the test.

7.10 Turn on cooling water for hydrostatic bearings and verify that there is water flow.

7.11 Turn on hydrostatic bearing pump, verify that the bearings are floating, and then adjust the pressure regulator at each of the bearings to 16.5 MPa (2400 psi).

7.12 Make certain that the transfer pump main power disconnect is on and the control switch is in the automatic position.

7.13 Close the main hydraulic supply line at the servovalve and open the accumulator drain valve.

7.14 Check the oil level in the main pump sump.

7.15 Set servovalve error to zero.

7.16 Verify that the output pressure of the #2 main pump (low pressure - 15.2 MPa (2200 psi)) is correct by turning on the pump. Turn off the pump when the pressure is confirmed.

7.17 Verify that the output pressure of the #1 main pump (high pressure - 20.7 MPa (3000 psi)) is correct by turning on the pump. Turn off the pump when the pressure is confirmed.

7.18 Set heater thermostat in pump room to 29C (85F) and verify that the heater operates.

7.19 Check the precharge pressure on the nitrogen supply vessel - 15.2 MPa (2200 psi).

7.20 Open the main hydraulic supply valve at the servovalve.

7.21 Open the servovalve pilot supply valve from JS-8.

7.22 Turn on cooling water for water circulation pump and verify flow.

7.23 Turn on water circulation pump and observe that it operates.

7.24 Turn on instrumentation cooling air fan.

7.25 Double check the condition of all instrumentation and zero all transducers.

7.26 Shunt calibrate all instrumentation for which it is possible to do so.

7.27 Record initial voltage outputs of all transducers.

7.28 Post barricades and warning signs to warn people to remain clear of the building.

7.29 CAUTION AT THIS TIME THE BUILDING AND THE IMMEDIATE SURROUNDINGS WILL REMAIN OFF LIMITS WHEN THE PIPE TEMPERATURE IS ABOVE 93C (200F)

7.30 Determine zero load actuator position.

7.30.1 Make certain that the servo-controller is disconnected from the D/A input and that the shunt bar is installed.

7.30.2 Verify that there is adequate oil in the JS-8 pump reservoir. There should be enough oil so that it will not need to be filled just prior to conducting the test.

7.30.3 Turn on cooling water to JS-8 pump.

7.30.4 Turn JS-8 pump output pressure to zero.

7.30.5 Turn on JS-8 pump.

7.30.6 Increase JS-8 pump output pressure to 10.3 MPa (1500 psi).

7.30.7 Make certain that the servo spool is moving freely and then set valve error to zero.

7.30.8 Turn on #2 main hydraulic pump (low pressure - 15.2 MPa (2200 psi)).

7.30.9 Verify that the servovalve inlet has low pressure on it.

7.30.10 Turn on #1 main hydraulic pump (high pressure - 20.7 MPa (3000 psi)).

7.30.11 Verify that the servovalve inlet has high pressure on it.

7.30.12 Move ram to zero load position and record offset setting.

7.30.13 Turn off main hydraulic pumps. (JS-8 pump remains on).

7.30.14 Verify that accumulators are draining (around 5 gpm).

7.30.15 When accumulators are drained, turn off JS-8 pump.

7.30.16 Set JS-8 pump output pressure to zero.

7.30.17 Turn off cooling water to JS-8 pump.

7.31 Record thermocouple readings, system pressure, and hydrostatic bearing pressure.

7.32 Turn on air compressor that supplies air for the battery contactor and the expansion tank bleed valve. Shut off compressor when it begins to cycle.

7.33 Turn on the heaters and pressurize the expansion tank to 7.6 MPa (1100 psi) with dry nitrogen. From this point until the completion of the test, the instrumentation room in JS-8 will be manned to monitor the progress of the heat-up cycle.

7.34 When the expansion tank is pressurized to 7.6 MPa (1100 psi), verify operation of bleed valve by reducing system pressure to 7.2 MPa (1050 psi). Make certain that there is sufficient air pressure to

close the valve, 0.6 MPa (80 psi). If air pressure is low, run air compressor until it begins to cycle.

7.35 At one hour increments, record thermocouple readings, system pressure, and hydrostatic bearing pressure.

7.36 At four hour increments, record voltage outputs of all transducers.

7.37 Whenever the pressure within the piping loop exceeds 15.5 MPa (2250 psi), bleed off the pressure to 13.7 MPa (2000 psi). Make certain that there is sufficient air pressure to open the valve, 0.6 MPa (80 psi). If air pressure is low, run air compressor until it begins to cycle. Record system water temperature and system pressure before and after reducing pressure.

7.38 Once the water and specimen have reached the test temperature of 288C (550F), allow the piping to soak at that temperature for a minimum of 1 hour.

7.39 Pressurize the piping loop and expansion tank to 15.5 MPa (2250 psi) with dry nitrogen. Record thermocouple readings, system pressure, and hydrostatic bearing pressure.

8.0 Test Procedures

8.1 Record voltage outputs of all transducers.

8.2 Check stability and drift of zero points on all instrumentation by comparing the initial transducer voltages to the voltages just prior to the test. Resolve any inconsistencies.

8.3 Prepare PC data acquisition.

8.3.1 Test functioning of the software.

8.3.1.1 Exit NB program, if it is running on the data acquistion computers, to ensure that all software flags are cleared.

8.3.1.2 Delete any existing MACHxx.DAT files.

8.3.1.3 Load NB data acquisition software using IP16 set-up files.

8.3.1.4 Turn off turbo mode, if applicable.

8.3.1.5 Reset trigger.

8.3.1.6 Execute the data acquisition program.

8.3.1.7 Trigger the system.

8.3.1.8 "QUIT" all of the computers when they are done writing files to disk.

8.3.1.9 Exit the NB program.

8.3.1.10 Verify that data have been recorded by looking to see if a file of the correct size has been written and that the timing channel was properly recorded.

8.3.1.11 Run "SPEED-DISK" to eliminate file fragmentation.

8.3.2 Turn off turbo mode, if applicable.

8.3.3 Reset trigger.

8.4 Prepare FM tape data acquistion.

8.4.1 Prepare Sangamo FM tape recorders.

8.4.1.1 Determine if there is enough tape for the test. Rewind as necessary.

8.4.2 Prepare Racal tape recorder.

8.4.2.1 Condition the tape by running it end-to-end one time. Make certain that the tape is completely rewound at the completion of the conditioning.

8.5 Verify the forcing function.

8.5.1 Make certain that the servo-controller is disconnected from the D/A input and that the shunt bar is installed.

8.5.2 Exit NB program, if it is running on the forcing function computer, to ensure that all software flags are cleared.

8.5.3 Load NB D/A software with the appropriate forcing function set-up file.

8.5.4 Execute the forcing function while recording the output on a strip chart recorder.

8.5.5 Verify that the correct function is programmed and that the function plus servo-controller offset voltage will not exceed 10 volts.

8.5.6 Make certain that the D/A output voltage is zero at the end of the verification process.

8.5.7 Exit the NB program.

8.6 Set-up shut down device.

8.6.1 Set shut-down voltage.

8.6.2 Test functioning of shut-down hardware.

8.6.2.1 Attach adjustable voltage source to shut-down test input. The input voltage should be approximately equal to the existing shut-down transducer voltage.

8.6.2.2 Exit NB program, if it its running on the forcing function computer, to ensure that all software flags are cleared.

8.6.2.3 Load NB program and verify set-up to ensure that the forcing function file(s) are correct.

8.6.2.4 Hold shut-down test switch in.

8.6.2.5 Arm shut-down device.

8.6.2.6 Run forcing function on PC. Reduce the test input voltage and verify that the forcing function is clamped to zero at the threshold voltage.

8.6.2.7 Release shut-down test switch.

8.6.2.8 Exit the NB program.

8.7 Turn off natural gas to building.

8.8 Open doors to building, if they are not already open.

8.9 Record thermocouple readings, system pressure, and hydrostatic bearing pressure.

8.10 Run air compressor until it cycles to ensure sufficient air pressure to close battery contactor.

8.11 On data acquisition system computers, exit NB, if it is running, to ensure that all software flags are cleared.

8.12 On data acquisition computers, load NB program and verify set-up to ensure that the IP16 set-up is still loaded.

8.13 On forcing function computer, exit NB, if it is running, to ensure that all software flags are cleared.

8.14 On forcing function computer, load NB program and verify set-up to

ensure that the correct forcing function set-up is still loaded.

8.15 Turn on video recorders.

8.16 Prepare the hydraulic system.

8.16.1 Verify that there is adequate oil in the JS-8 pump reservoir.

8.16.2 Turn on cooling water to JS-8 pump.

8.16.3 Set JS-8 pump output pressure to zero.

8.16.4 Turn on JS-8 pump.

8.16.5 Increase JS-8 pump output pressure to 10.3 MPa (1500 psi).

8.16.6 Make certain that the servo spool is moving freely and then set valve error to zero.

8.16.7 Turn on #2 main hydraulic pump (low pressure - 15.2 MPa (2200 psi)).

8.16.8 Verify that the servovalve inlet has low pressure on it.

8.16.9 Turn on #1 main hydraulic pump (high pressure - 20.7 MPa (3000 psi)).

8.16.10 Verify that the servovalve inlet has high pressure on it.

8.16.11 Move ram to initial zero load offset position.

8.16.12 Remove shunt bar and connect D/A output to servo-controller.

8.16.13 Set servo-controller span to 10.

8.17 Turn off heater tapes.

8.18 Turn off recirculation pump.

8.19 Execute the data acquisition program.

8.20 Arm shut-down device.

8.21 Start Sangamo FM tape recorders.

8.22 Start Racal tape recorder and clear overloads.

8.23 Trigger data acquisition system.

8.24 Close contact switch for battery.

8.25 Observe that battery voltage has been applied to specimen.

8.26 Execute forcing function.

8.27 Turn off main hydraulic pumps.

8.28 Set servo-controller span to zero.

8.29 Disconnect D/A input to servo-controller and install shunt bar.

8.30 Stop Sangamo FM tape recorders.

8.31 Stop Racal tape recorder.

8.32 "QUIT" all of the computers when they are done writing data to disk.

8.33 Exit NB on all computers.

8.34 Copy computer data to a new files.

8.35 Copy computer data to floppy disks and write protect them.

8.36 When accumulators are fully drained, turn off JS-8 pump.

8.37 Set JS-8 pump output pressure to zero.

8.38 Turn off cooling water to JS-8 pump.

9.0 Post-Test Procedures

9.1 Allow pipe loop to depressurize to atmospheric pressure before entering building.

9.2 Once the loop temperature is below 150 F, turn off hydrostatic bearing pump.

9.3 Assess any damage to the facility and/or building.

9.4 Take critical post test photographs.

9.5 Allow specimen to cool then remove insulation, heater tapes, and instrumentation from the piping loop in the vicinity of the crack.

9.6 Trace the crack opening profile. Record in LRB.

9.7 Take kink angle measurements. Record in LRB. [The measurement accuracy for these measurements will be $\pm$ 2.5 mm ($\pm$ 0.10 inch).]

9.8 Measure OD at the crack plane (top to bottom and side to side) and record in LRB. [The measurement accuracy for this measurement will be $\pm$ 0.25 mm ($\pm$ 0.01 inch).]

9.9 Measure pipe wall thickness at the crack centerline and selected other locations. [The measurement accuracy for this measurement will be $\pm$ 0.25 mm ($\pm$ 0.01 inch).]

9.10 Determine the extent of non-reusable pipe in the vicinity of the test specimen. Cut all of the non-reusable pipe from the piping loop.

9.11 Cut through the remaining ligament when authorized by task leader.

9.12 Cut the fracture surfaces from the length of non-reusable pipe.

9.13 Complete all LRB and Data Sheet Entries.

9.14 Deliver the LRB and fracture rings to the responsible engineer.

10.0 References

10.1 Hayashi, M., et.al., "Surface Crack Detection by Direct Current Potential Drop Technique", Mechanical Engineering Research Laboratory, Hitachi Works, Japan.

Data Sheet D-1
Uncracked Pipe

Test Material (Text Ref.) _____ Test ID No. _____

Work Performed by/Date _____/_____

(5.1.1) Measurement of OD(± 0.010 in.) at future crack and strain gage locations:

Future Crack Location	Strain Gage Location 1	Strain Gage Location
Top-to-bottom, _____inch	Top-to-bottom, ____ inch	Top-to-bottom, ____
Side-to-side, _____ inch	Side-to-side, ____ inch	Side-to-side, ____
Strain Gage Location 3	**Strain Gage Location 4**	**Strain Gage Location**
Top-to-bottom, _____ inch	Top-to-bottom, _____inch	Top-to-bottom, ____
Side-to-side, _____ inch	Side-to-side, _____inch	Side-to-side, ____

Gage Serial Number _____

(5.1.2) Measurement of circumference of pipe at future crack and strain gage locations(±0.06in.) _____/_____

_____ inch (future crack)
_____ inch (strain gage - Location 1)
_____ inch (strain gage - Location 2)
_____ inch (strain gage - Location 3)
_____ inch (strain gage - Location 4)
_____ inch (strain gage - Location 5)
Gage Serial Number_____

(5.1.3) Measurement of pipe wall thickness (±0.010in.) at future crack and strain gage locations are as follows: _____/_____

Future Crack				Strain Gages			
1.	_____	6.	_____	Location 1a	_____	Location 4a	_____
2.	_____	7.	_____	1b	_____	4b	_____
3.	_____	8.	_____	1c	_____	4c	_____
4.	_____	9.	_____	Location 2a	_____	Location 5a	_____
5.	_____	10.	_____	2b	_____	5b	_____
				2c	_____	5c	_____
				Location 3a	_____		
				3b	_____		
				3c	_____		

Average of 10 readings, _____ inch
Gage Serial Number_____

(5.2.1) Piping loop instrumented with strain gages, thermocouples, accelerometers, displacement transducers, and pressure transducers. _____/_____

(5.2.2) Heater tapes and insulation installed. _____/_____

(5.2.3) Test specimen instrumented with rotational devices, control thermocouples and monitoring thermocouples. _____/_____

(5.2.4) Nitrogen storage vessel and accumulators charged with nitrogen. _____/_____

Data Entries Reviewed by _____ Date_____
QA Review by _____ Date_____

Data Sheet D-2
Test Specimen Preparation and Installation of Instrumentation for Cracked Pipe Experiments

Test Material _____ Test ID No. _____
(Text Ref.) Work Performed by/Date

(6.1) Specimen cut to a length of 30-40 in.(length supplied by task leader).
Identification stamped in proper location _____/_____

(6.2) Test specimen beveled to a 37 degree included angle with a 1.6 mm (1/16-inch) to 3.2 mm (1/8-inch) land. _____/_____

(6.3) Wall thickness machined to 25.7 mm ± 0.5 mm (1.01 ± 0.020 inch).
Actual Measurement _____ inch _____/_____
Gage Serial Number_____

(6.4) Measurement of OD (to ±0.010 in.) at specimen centerline (top to bottom and side to side): _____/_____
Top-to-bottom _____ inch
Side-to-side _____ inch
Gage Serial Number_____

(6.4.1) For weld tests, measurement of pipe OD on each side of the weld;
Top-to-bottom: Side A _____ inch, Side B _____ inch
Side-to-side: Side A _____ inch, Side B _____ inch
Gage Serial Number_____ _____/_____

(6.5) Measurement of circumference of pipe at specimen centerline for base metal test;
_____ inch (± 0.06 in.) _____/_____
Gage Serial Number_____

(6.5.1) For weld tests, measurement of pipe circumference on each side of weld: _____/_____
_____ inch; Side A
_____ inch; Side B
Gage Serial Number_____

(6.6) Measurement of pipe wall thickness (inch;±0.01 in.) at 10 circumferential locations:

1	_____	6	_____
2	_____	7	_____
3	_____	8	_____
4	_____	9	_____
5	_____	10	_____

Avg. wall thickness: _____ inch _____/_____
Gage Serial Number_____

Data Entries Reviewed by _____ Date_____

QA Review by _____ Date_____

Data Sheet D-2 (Continued)

Test Material _____ Test ID No. _____

(Text Ref.)		Work Performed by/Date
(6.7)	Circumferential surface crack machined into inside surface of pipe at specimen centerline as required. Mark centerline of flaw on the OD of the pipe.	_____/_____
(6.8.1)	Length of SC from tip-to-tip on inside surface: _____ inch (± 0.06 in.) Gage Serial Number _____	_____/_____
(6.8.2)	Depth of SC: _____ inch (± 0.01 in.) Gage Serial Number _____	_____/_____
(6.9.3)	The SC instrumented with electric potential (EP) probes at required locations as shown in Figure 1. Measurement (± 0.03 in.) of spacing between each set of EP probes are as follows:	_____/_____

1. _____ 6. _____ 11. Exterior _____
2. _____ 7. _____
3. _____ 8. _____
4. _____ 9. _____
5. _____ 10. _____

Gage Serial Number _____

(6.10)	Holes drilled in pipe at 6 and 12 o'clock postions, Conax fittings installed and EP leads brought out through fittings	_____/_____
(6.11)	Exterior of pipe instrumented with a set of base metal EP probes having a spacing of 4 inches; Distance from Crack Plane _____ Gage Serial Number _____	_____/_____
(6.12)	Lugs installed for current leads	_____/_____
(6.13)	Initial EP signals for ten interior probes, one exterior probe measured, and base metal probes (± 1 μV)	_____/_____

Interior				Exterior	
1	_____ μV	6	_____ μV	11	_____ μV
2	_____ μV	7	_____ μV		
3	_____ μV	8	_____ μV	Base Metal	
4	_____ μV	9	_____ μV		
5	_____ μV	10	_____ μV	12	_____ μV

Gage Serial Number _____

NOTE: Items 6.14 through 6.19 apply only to the carbon steel base metal, carbon weld metal, and stainless steel weld metal experiments.

(6.14)	End cap welded to each end of test specimen and pipe fitting (3/4-inch) welded into one of the end caps.	_____/_____

Data Entries Reviewed by _____ Date _____

QA Review by _____ Date _____

Data Sheet D-2 (Continued)

Test Material _____ Test ID No. _____

(Text Ref.) Work Performed by/Date

(6.15) Test specimen installed into the pressure cycling facility. _____/_____

(6.16) Test specimen pressure cycled to obtain crack depth at crack centerline of 66 percent of wall thickness Minimum pressure; ____ psi
Maximum pressure; ____ psi
Target Magnitude of EP signal; ____ microvolt _____/_____

(6.17) Final EP signals for the ten sets of interior EP probes one exterior set of probes, and base metal probes. _____/_____
Interior: (± 1 μV)

1. _____ μV		6. _____ μV	
2. _____ μV		7. _____ μV	
3. _____ μV		8. _____ μV	
4. _____ μV		9. _____ μV	
5. _____ μV		10. _____ μV	
Base Metal:		Exterior:	
12. _____ μV		11. _____ μV	

Gage Serial Number_____

(6.18) Final flaw depth estimated at ten locations along circumferential crack front. _____/_____

1. _____ in.		6. _____ in.	
2. _____ in.		7. _____ in.	
3. _____ in.		8. _____ in.	
4. _____ in.		9. _____ in.	
5. _____ in.		10. _____ in.	

(6.19) End caps removed from test specimen and ends rebeveled _____/_____

(6.20) High temperature/high pressure LVDT installed across crack centerline.
ID No. of LVDT _____ _____/_____

(6.21) Spot weld high temperature strain gage across centerline of machine flaw. _____/_____

(6.22) Measurement of height of LVDT above inside pipe surface, ____ inch (± 0.03 in.) _____/_____
Gage Serial Number_____

(6.22.1) Measure axial spacing between crack, core fixture, and LVDT body.
Crack to core fixture _____ inch
Crack to LVDT body _____ inch _____/_____
Gage Serial Number_____

(6.23) LVDT wires and EP wires routed out through existing Conax fittings as required. _____/_____

Data Entries Reviewed by _____ Date_____
QA Review by _____ Date_____

Data Sheet D-2 (continued)

(Text Ref.)

(6.24)	Instrumented test specimen welded into piping loop as required	_____/_____
(6.25)	Test specimen instrumented with rotation device, control thermocouples and monitoring thermocouples as required	_____/_____

Data Entries Reviewed by _____ Date_____

QA Review by _____ Date_____

Data Sheet D-3
Pre-Operational Test Procedures

Test Material _____ Test ID No. _____

(Text. Ref.)		Work Performed
(7.1)	Instrumentation connected to recording devices, gains set and bridges balanced as required. Gains, scale, and calibration factors entered in LRB.	____/____
(7.2)	All instrumentation mounted on and connected to piping loop re-checked for valid calibration.	____/____
(7.3)	Heater tapes installed on loop as required.	____/____
(7.4)	Insulation installed as required.	____/____
(7.5)	Control thermocouples and heater tapes connected to temperature controllers.	____/____
(7.6)	Piping loop filled with water as required.	____/____
(7.7)	Vent valves at high point in loop closed, water turned off, and valve between piping loop and expansion tank opened. Valve(s) between expansion tank and pressure source in JS-8 opened.	____/____
(7.8)	Garage doors to building unlocked and, weather permitting, doors opened.	____/____
(7.9)	Visual inspection of pipe, frame, and hydraulic system completed.	____/____
(7.10)	Cooling water for hydrostatic bearing pump turned on and flow verified.	____/____
(7.11)	Hydrostatic bearing pump turned on, presure adjusted - 16.5 MPa (2400 psi), and operation of bearings verified.	____/____
(7.12)	Transfer pump power turned on and control switch verified to be in automatic mode.	____/____
(7.13)	Main hydraulic supply line closed and accumulator drain valve opened.	____/____
(7.14)	Oil level in sump checked.	____/____
(7.15)	Servovalve error set to zero.	____/____
(7.16)	Pump #2 pressure, 15.2 MPa (2200 psi) verified.	____/____

Data Entries Reviewed by _____ Date_____

QA Review by _____ Date_____

Data Sheet D-3 (Continued)
Pre-Operational Test Procedures

Test Material _____ Test ID No. _____

(Text. Ref.)		Work Performed by/Date
(7.17)	Pump #1 pressure, 20.7 MPa (3000 psi) verified.	/
(7.18)	Thermostat in pump room set to 27C (80F) and heater operation verified.	/
(7.19)	Precharge on nitrogen supply verified, 15.2 MPa (2200 psi).	/
(7.20)	Main hydraulic supply valve opened.	/
(7.21)	Servovalve pilot supply valve opened.	/
(7.22)	Cooling water for water circulation pump turned on and flow verified.	/
(7.23)	Water circulation pump turned on and operation verified.	/
(7.24)	Cooling air fan turned on.	/
(7.25)	Condition of all transducers checked and all transducers zeroed as required.	/
(7.26)	Instrumentation shunt calibrated.	/
(7.27)	Initial voltage outputs of all transducers recorded.	/
(7.28)	Barricades and warning signs posted.	/
(7.29)	Evacuation of building and immediate surroundings completed.	/
(7.30.1)	Servo-controller disconnected from the D/A input and shunt bar installed.	/
(7.30.2)	Adequate oil supply in JS-8 pump verified. Enough oil is in the sump so that it will not require filling at any time during the conduct of this test.	/
(7.30.3)	JS-8 pump cooling water turned on.	/
(7.30.4)	JS-8 pump output pressure set to zero.	/
(7.30.5)	JS-8 pump turned on.	/

Data Entries Reviewed by _____ Date _____

QA Review by _____ Date _____

Data Sheet D-3 (Continued)
Pre-Operational Test Procedures

Test Material (Text. Ref.) _____ Test ID No. _____

	Work Performed by/Date
(7.30.6) JS-8 pump pressure increased to 10.3 MPa (1500 psi).	____/____
(7.30.7) Free motion of the servovalve spool is observed. Valve error set to zero.	____/____
(7.30.8) Main pump #2 turned on.	____/____
(7.30.9) 15.2 MPa (2200 psi) at servovalve observed.	____/____
(7.30.10) Main pump #1 turned on.	____/____
(7.30.11) 20.7 MPa (3000 psi) at servovalve observed.	____/____
(7.30.12) Ram moved to zero load position. Offset setting recorded.	____/____
(7.30.13) Main hydraulic pumps turned off. (JS-8 pump still on).	____/____
(7.30.14) Draining of accumulators observed.	____/____
(7.30.15) After accumulators are drained, JS-8 pump turned off.	____/____
(7.30.16) JS-8 pump output pressure set to zero.	____/____
(7.30.17) Cooling water to JS-8 pump turned off.	____/____
(7.31) Thermocouple readings, system pressure, and hydrostatic bearing pressure recorded.	____/____
(7.32) Air compressor for battery contactor and operation of expansion tank bleed valve turned on. Compressor shut off when it begins to cycle.	____/____
(7.33) Heaters turned on and expansion tank pressurized with dry nitrogen to 7.6 MPa (1100 psi).	____/____
(7.34) With sufficient air pressure available to operate expansion tank bleed valve, operation of expansion tank bleed valve observed.	____/____

Data Entries Reviewed by _____ Date_____

QA Review by _____ Date_____

Data Sheet D-3 (Continued)
Pre-Operational Test Procedures

Test Material _____ Test ID No. _____
(Text. Ref.)

		Work Performed by/Date
(7.35)	Thermocouple readings, system pressure, and hydrostatic bearing pressure recorded hourly.	____/____
(7.36)	Output voltage of all transducers recorded every four hours.	____/____
(7.37)	Pressure reduced to 13.7 MPa (2000 psi) in pipe loop when it exceeds 15.5 MPa (2250 psi). System temperature and system pressure recorded before and after reducing pressure.	____/____
(7.38)	Pipe loop soaked at 288C (550F) for minimum of one hour.	____/____
(7.39)	Pipe loop pressurized to 15.5 MPa (2250 psi) with dry nitrogen. Thermocouple readings, system pressure and hydrostatic bearing pressure recorded.	____/____

Data Entries Reviewed by _____ Date_____

QA Review by _____ Date_____

Data Sheet D-4
Test Procedure

Test Material _____ Test ID No. _____
(Text. Ref.)

		Work Performed by/Date
(8.1)	Voltage outputs of all transducers recorded.	____/____
(8.2)	Stability and drift of all instruments checked and inconsistencies resolved.	____/____
(8.3.1.1)	NB program exited on data acquisition computers to clear software flags.	____/____
(8.3.1.2)	MACHxx.Dat files deleted.	____/____
(8.3.1.3)	NB data acquisition program loaded using IP16 files.	____/____
(8.3.1.4)	Turbo mode turned off.	____/____
(8.3.1.5)	Trigger reset.	____/____
(8.3.1.6)	Data acquisition program executed.	____/____
(8.3.1.7)	Data acquisition system triggered.	____/____
(8.3.1.8)	"QUIT" sequence executed after data files have been written to disk.	____/____
(8.3.1.9)	NB program exited.	____/____
(8.3.1.10)	Size of data files and presence of timing channel data in files verified.	____/____
(8.3.1.11)	"SPEED-DISK" software run.	____/____
(8.3.2)	Turbo mode turned off.	____/____
(8.3.3)	Trigger reset.	____/____
(8.4.1.1)	Sufficient tape on Sangamo tape recorders, or tape rewound.	____/____
(8.4.2.1)	Racal tape conditioned by running tape end-to-end. Tape completely rewound when done.	____/____
(8.5.1)	D/A output disconnected from the servo-controller and the shunt bar installed.	____/____
(8.5.2)	NB program exited on forcing function computer.	____/____

Data Entries Reviewed by _____ Date_____

QA Review by _____ Date_____

Data Sheet D-4 (Continued)
Test Procedure

Test Material (Text. Ref.) _____ Test ID No. _____

		Work Performed by/Date
(8.5.3)	NB forcing function program loaded with correct forcing function set-up file.	____/____
(8.5.4)	Forcing function executed and recorded on a strip chart recorder.	____/____
(8.5.5)	Correct forcing function obtained with total output voltage not exceeding 10 volts.	____/____
(8.5.6)	Zero output voltage observed at end of verification.	____/____
(8.5.7)	NB program exited.	____/____
(8.6.1)	Shut-down voltage set on shut-down device.	____/____
(8.6.2.1)	Adjustable voltage source attached to shut-down device test input with voltage exceeding existing shut-down transducer voltage.	____/____
(8.6.2.2)	NB program exited on forcing function computer to clear software flags.	____/____
(8.6.2.3)	NB forcing function program loaded and correct forcing function set-up file verified.	____/____
(8.6.2.4)	Shut-down device test switch pushed in.	____/____
(8.6.2.5)	Shut-down device armed.	____/____
(8.6.2.6)	Zero clamping of forcing function by shut-down device verified.	____/____
(8.6.2.7)	Shut-down test switch released.	____/____
(8.6.2.8)	NB program exited.	____/____
(8.7)	Natural gas to building turned off.	____/____
(8.8)	Doors to building opened, if not already.	____/____
(8.9)	Thermocouple readings, system pressure, and hydrostatic bearing pressure recorded.	____/____
(8.10)	Air compressor run until it cycles.	____/____

Data Entries Reviewed by _____ Date_____

QA Review by _____ Date_____

Data Sheet D-4 (Continued)
Test Procedure

Test Material _____ Test ID No. _____

(Text. Ref.)		Work Performed by/Date
(8.11)	NB program exited on data acquisition computers to clear software flags.	____/____
(8.12)	NB data acquisition program loaded and correct set-up verified.	____/____
(8.13)	NB program exited on forcing function computer to clear software flags.	____/____
(8.14)	NB forcing function program loaded and correct set-up verified.	____/____
(8.15)	Video recorders turned on.	____/____
(8.16.1)	Adequate oil supply in JS-8 pump verified.	____/____
(8.16.2)	JS-8 pump cooling water turned on.	____/____
(8.16.3)	JS-8 pump output pressure reduced to zero.	____/____
(8.16.4)	JS-8 pump turned on.	____/____
(8.16.5)	JS-8 pump pressure increased to 10.3 MPa (1500 psi).	____/____
(8.16.6)	Free motion of the servovalve spool is observed. Valve error set to zero.	____/____
(8.16.7)	Main pump #2 turned on.	____/____
(8.16.8)	15.2 MPa (2200 psi) at servovalve observed.	____/____
(8.16.9)	Main pump #1 turned on.	____/____
(8.16.10)	20.7 MPa (3000 psi) at servovalve observed.	____/____
(8.16.11)	Ram moved to initial zero load position.	____/____
(8.16.12)	Servo-controller shunt bar removed and D/A input connected.	____/____
(8.16.13)	Span set to 10.	____/____
(8.17)	Heater tapes turned off.	____/____
(8.18)	Recirculation pump turned off.	____/____

Data Entries Reviewed by _____ Date_____

QA Review by _____ Date_____

Data Sheet D-4 (Continued)
Test Procedure

Test Material _____ Test ID No. _____
(Text. Ref.) Work Performed

(8.19)	Data acquisition system executed.	____/____
(8.20)	Shut-down device armed.	____/____
(8.21)	Sangamo FM tapes started.	____/____
(8.22)	Racal tape started and overloads cleared.	____/____
(8.23)	Data acquisition triggered.	____/____
(8.24)	Battery contact closed.	____/____
(8.25)	Battery voltage observed on specimen.	____/____
(8.26)	Forcing function executed.	____/____
(8.27)	Main hydraulic pumps turned off.	____/____
(8.28)	Servo-controller span set to zero.	____/____
(8.29)	D/A input disconnected from servo-controller and shunt bar installed.	____/____
(8.30)	Sangamo FM tapes stopped.	____/____
(8.31)	Racal tape stopped.	____/____
(8.32)	"QUIT" executed after data files have been written to disk.	____/____
(8.33)	NB exited on all computers.	____/____
(8.34)	Data copied to new files.	____/____
(8.35)	Data copied to floppy disks and disks write protected.	____/____
(8.36)	Accumulators drained and JS-8 pump turned off.	____/____
(8.37)	JS-8 pump pressure set to zero.	____/____
(8.38)	Cooling water to JS-8 pump turned off.	____/____

Data Entries Reviewed by _____ Date_____

QA Review by _____ Date_____

Data Sheet D-5

Post Test Procedures

Test Material _____ Test ID No. _____

(Text Ref.)		Work Performed by/Date
(9.1)	Pipe loop depressurized to atmospheric pressure before entering building.	____/____
(9.2)	Hydrostatic bearing pump turned off once temperature in loop is below 150 F.	____/____
(9.3)	Damage to facility and building assessed.	____/____
(9.4)	Photographs taken of critical areas of test specimen and facility.	____/____
(9.5)	Insulation heater tapes and instrumentation in vicinity of crack removed.	____/____
(9.6)	Crack opening profile sketched and recorded in LRB.	____/____
(9.7)	Kink angle measurements made and recorded in LRB. (± 0.10 in.) Gage Serial Number_____	____/____
(9.8)	OD (top-to-bottom and side-to-side) at crack plane measured and recorded in LRB. (± 0.01 in.) Gage Serial Number_____	____/____
(9.9)	Pipe wall thickness at crack centerline and other selected locations measured and recorded in the LRB. (± 0.01 in.) Gage Serial Number_____	____/____
(9.10)	Non-reusable pipe cut out from piping loop.	____/____
(9.11)	Remaining ligament in test specimen cut through. (when authorized by task leader)	____/____
(9.12)	Fracture surfaces cut from the length of non-reusable pipe.	____/____
(9.13)	All LRB and Data Sheet entries completed and delivered to Test Engineer.	____/____
(9.14)	Fracture rings and LRB delivered to Task Leader.	____/____

Data Entries Reviewed by _____ Date_____

QA Review by _____ Date_____

APPENDIX D

BACKGROUND INFORMATION ON MEASUREMENT OF DAMPING

APPENDIX D

BACKGROUND INFORMATION ON MEASUREMENT OF DAMPING

During the cyclic excitation of the piping loop, energy is dissipated by and within the pipe and supporting structure. This dissipation of energy manifests itself by increasing the force required to dynamically excite the pipe, by increasing the amount of energy that must be put into the pipe system to get a surface crack to become a through-wall crack, and by altering its motion, relative to an undamped system. Because of these effects, the amount of damping plays a significant role in any prediction of the behavior of the pipe system and, consequently, the behavior of a crack in the system. To be able to make meaningful predictions of the system/crack behavior under dynamic loading, tests to establish the amount of damping in the IPIRG Subtask 1.3 piping system were conducted.

The damping of an actual system is a complex phenomenon involving several kinds of damping forces. The damping forces may be of a viscous nature (i.e., proportional to velocity), they may arise from friction at dry or unlubricated surfaces, or they may be attributable to imperfect elasticity or internal friction of the material. Furthermore, these damping forces may be linear in nature, as in the case of a viscous dash pot, they may be nonlinear, as in the case of Coulomb friction, or they may be frequency dependent. Consideration of damping in a system analysis or measurement of it can be complicated.

In performing system analyses and in measuring damping, it is usually assumed that all damping, regardless of its origin, can be treated as linear viscous damping, because it is mathematically convenient to do so. Making this assumption, and furthermore assuming that the system is subcritically damped, i.e., the motion "rings down" as in Figure D.1, the equations of motion for a single degree-of-freedom system yield expressions for the damping

$$\delta_d = \ln(x_1/x_2) \tag{D-1}$$

$$\delta_d = 2\pi\zeta/\sqrt{1 - \zeta^2} \tag{D-2}$$

where

δ_d = damping logarithmic decrement
x_1 = amplitude of motion (force) at some arbitrary time, t_1
x_2 = amplitude of motion (force) one cycle after t_1
ζ = damping ratio (fraction of critical damping).

The logarithmic decrement, and hence the damping, ζ, for a system can be determined from an experimental record of the damped free vibration of the system.

For a system that is lightly damped, the ratio of successive amplitudes may be near unity. To overcome possible measurement difficulties, Equation D-1 can be modified to relate the logarithmic decrement to the ratio of amplitudes separated by several cycles

$$\delta_d = (1/n) \ln(x_1/x_{n+1}) \qquad \text{(D-3)}$$

where,

δ_d = damping logarithmic decrement
x_1 = amplitude of motion (force) at some arbitrary time, t_1
x_{n+1} = amplitude of motion (force) n cycles after t_1.

For a linear viscous damper, successive ratios of amplitudes must all be equal. Failure to satisfy this criterion implies that part of the system damping is not purely viscous.

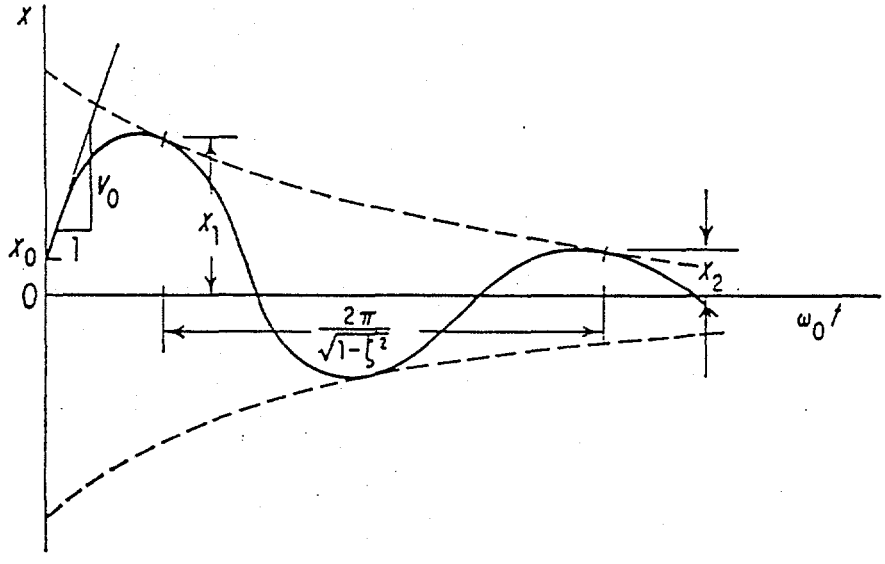

Figure D.1 Definitions used for system damping determination

APPENDIX E

ELECTRIC POTENTIAL DATA REDUCTION PROCEDURES

APPENDIX E

ELECTRIC POTENTIAL DATA REDUCTION PROCEDURES

Direct current electric potential (d-c EP) data were recorded for the carbon steel weld metal and the three austenitic experiments in order to define the instant of crack initiation for the surface cracks and to estimate the extent of surface crack growth and through-wall crack growth once the surface cracks penetrated the pipe wall thickness.

For each of these experiments, three sets of electric potential probes were mounted across the crack on the inside pipe surface, as shown in Figure E.1. The electric-potential data from these internal probes, along with the crack-mouth-opening-displacement data from the internally mounted LVDT, were to be used to define the instant of crack initiation for the surface cracks. In addition, three sets of electric-potential probes were mounted across the crack on the outside pipe surface, see Figure E.1. The data from these sets of probes were to be used to estimate the extent of through-wall crack growth. Finally, for each experiment a set of probes was attached to the pipe in the base metal remote from the influence of the crack to provide a baseline reference for the other potential drop data.

Figures E.2 through E.5 are plots of the base metal electric potential as a function of time for the carbon steel weld metal, stainless steel base metal, stainless steel weld metal, and aged cast stainless experiments, respectively. (Note, no electric-potential data are available for the carbon steel base metal experiment.) Immediately obvious in examining Figures E.2 through E.5 is that the base metal data for the carbon steel weld specimen has a large cyclic component associated with it. The base metal data for the three austenitic specimens also have a cyclic component, but the magnitude of the cyclic component is much smaller than it is for the carbon steel weld specimen. The cyclic component associated with the base metal EP data is also evident in the EP data at the crack centerline (internal) for the carbon steel weld metal experiment. This cyclic behavior made it futile to try to further interpret the EP data for the carbon steel weld metal experiment.

Similar behavior was also evident in the dynamic C(T) tests on the ferritic steels. The dynamic component in the EP data was attributed to a self-generating voltage similar to a piezoelectric effect in crystalline substances such as quartz. The self-induced voltage occurs during the elastic loading and is sensitive to the magnitude of the elastic stress and the strain rate. For the C(T) tests, this self-induced voltage precluded detection of crack initiation using the current densities normally used for quasi-static tests. The approach to overcome this problem for the C(T) J-R curve testing was to apply a large enough current to make the self-induced voltage become negligible. To extend this approach to the pipe fracture experiments, a very high amperage battery was used.

For the carbon steel weld metal and stainless steel base and weld metal experiments, the current supplied to the pipe specimen was on the order of 4,000 amps. This was apparently not enough current to overcome the self-induced voltage for the carbon steel weld experiment. In order to circumvent this problem for the last experiment, i.e., the aged cast stainless experiment, a different current wire arrangement was tried, see Figure E.6. For this experiment, the eight current wires coming from the battery were all attached to a single copper block which was silver soldered to the pipe, 76 mm (3 inches) from the crack plane at the crack centerline. In doing so, the current supplied to the pipe in the vicinity of the crack centerline increased four times from approximately 4,000 amps to approximately 16,000 amps.

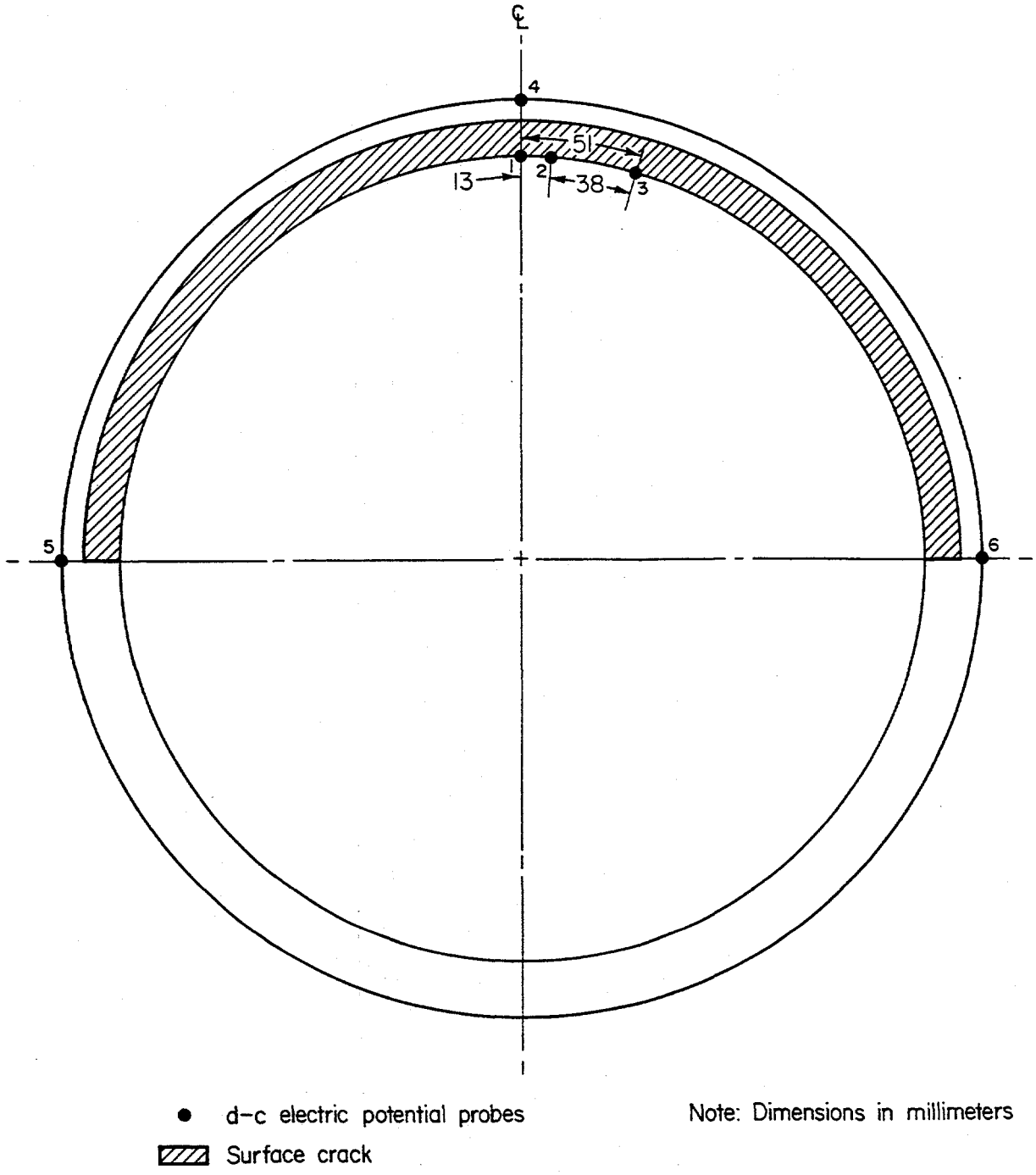

Figure E.1 Location of d-c electric potential probes at the crack plane for Subtask 1.3 experiments
QL/1.3-4/F3

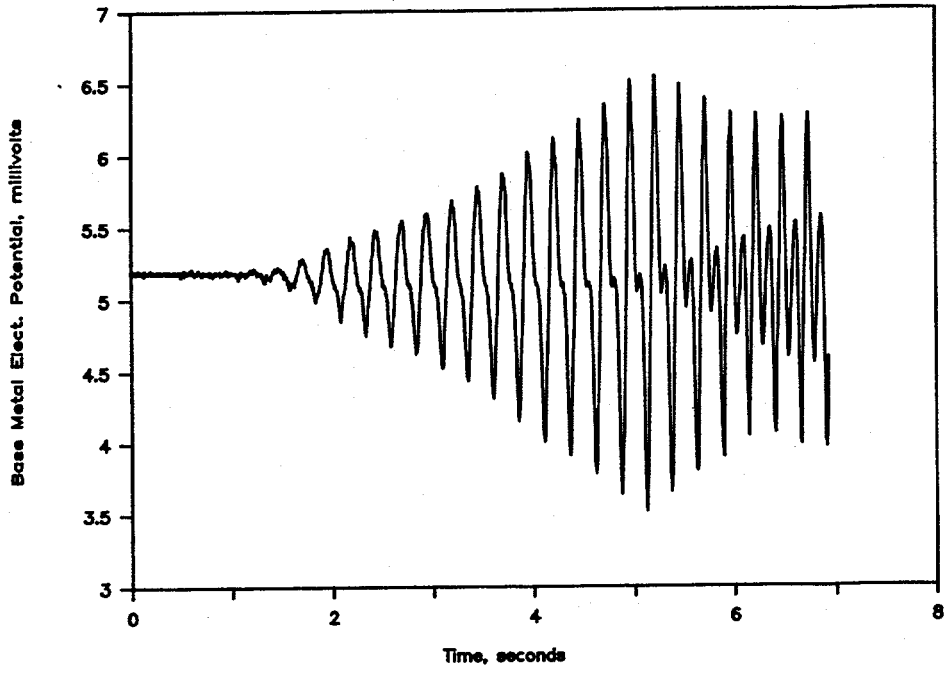

Figure E.2 Base metal d-c electric potential versus time for carbon steel weld experiment [101.6 mm (4 inch) probe wire spacing] DRB/1.3-4/F19

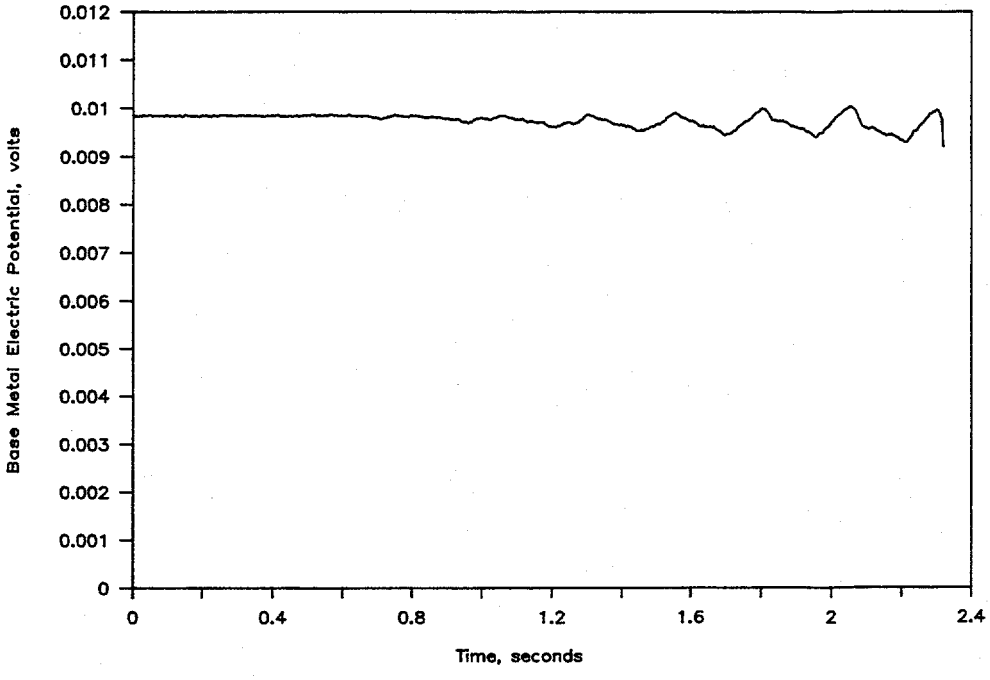

Figure E.3 Base metal electric potential versus time for stainless steel base metal experiment I1.3-10/90-FE3

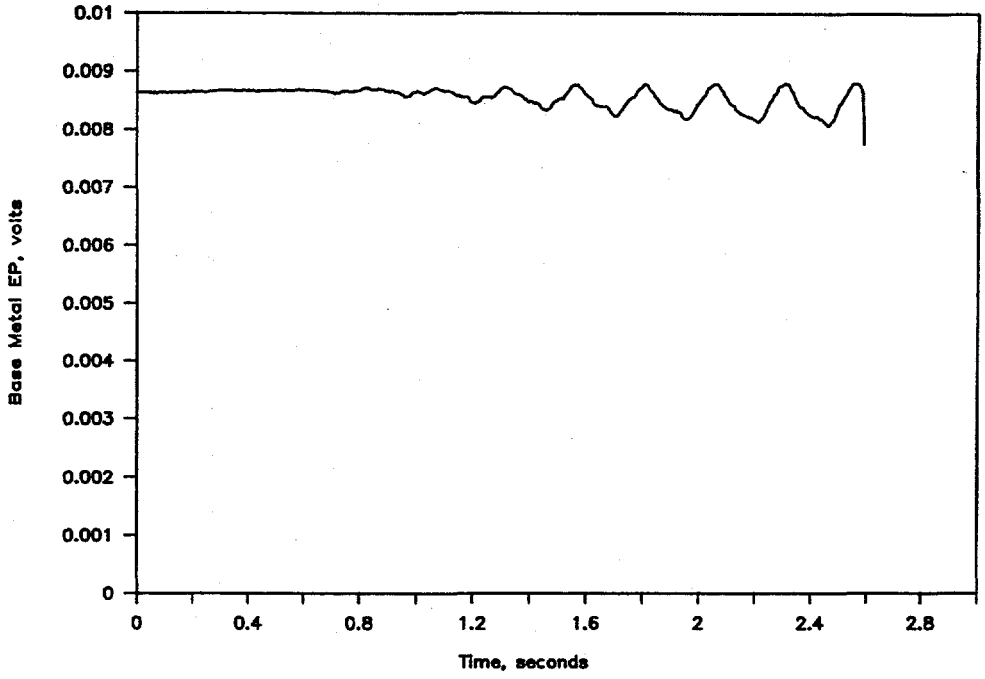

Figure E.4 Base metal electric potential (EP) versus time for stainless steel weld experiment
DRB/1.3-5/F24

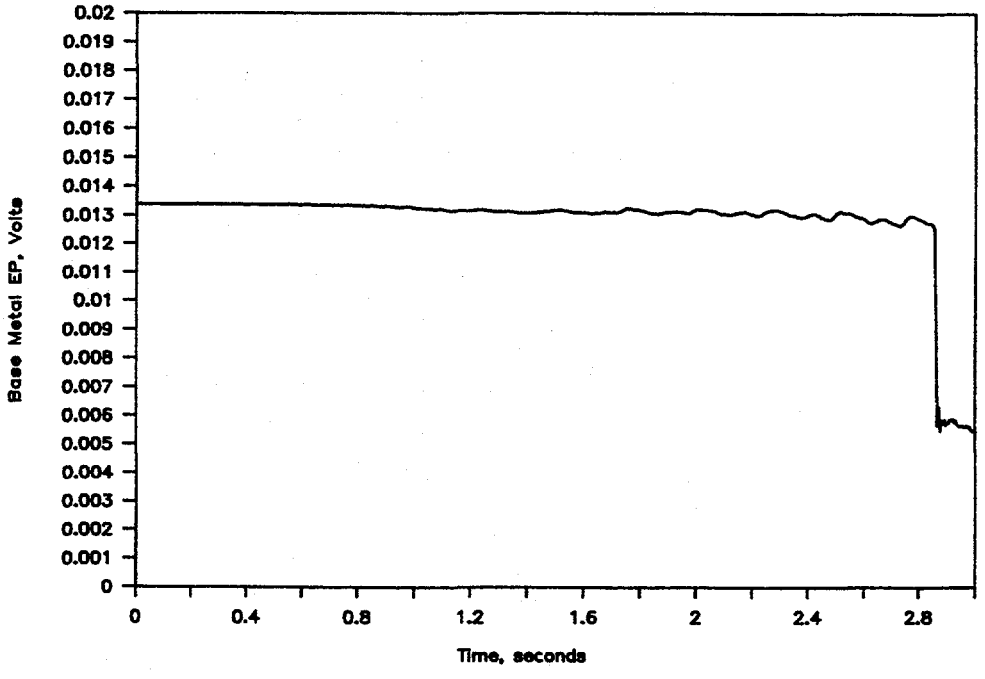

Figure E.5 Base metal electric potential versus time for aged cast stainless experiment
I1.3-10/90-FE5

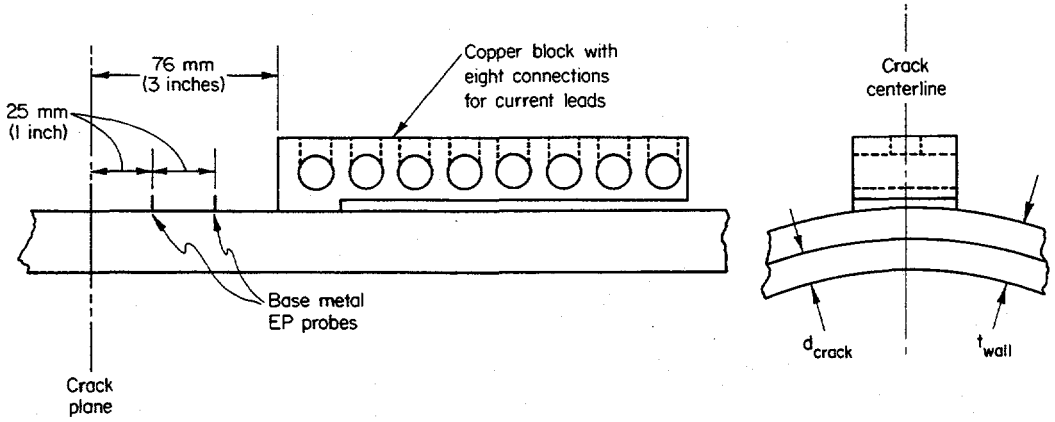

Figure E.6 Details of current wire arrangement for aged cast stainless experiment
I1.3-10/90-F3.55

Determining Crack Initiation

Figures E.7 through E.9 are plots of the electric potential at the crack centerline on the inside surface of the pipe as a function of the crack-mouth-opening displacement for the three austenitic experiments. By plotting the electric-potential data versus the CMOD, one can attempt to separate the change in EP due to plasticity from that due to surface crack extension. The point on the EP versus CMOD curve where the slope increases is generally defined as crack initiation. Close examination of Figure E.7 (stainless steel base metal) reveals that the slope of the EP versus CMOD curve is roughly the same for the fifth through eighth loading cycles. (The shift in EP between the seventh and eighth loading cycles is speculated to be caused by compressive plasticity effects which occurred during the unloading. The slope of the ninth loading cycle appears to be slightly steeper than that for the previous cycles, and the slope for the tenth cycle is significantly steeper. Consequently, it was speculated that the surface crack for the stainless steel base metal experiment initiated during the ninth loading cycle at a CMOD value of approximately 3.0 mm (0.12 inch). The crack section moment at the instant of crack initiation was approximately 415 kN-m (3,670,000 in-lbs).

Figure E.8 is a similar plot for the stainless steel weld metal specimen. In examining Figure E.8 one sees that there is a fairly distinct increase in slope of the EP versus CMOD data at a CMOD value of approximately 1.3 mm (0.05 inch). This increase in slope is indicative of crack initiation. The crack section moment at that instant was approximately 460 kN-m (4,070,000 in-lbs).

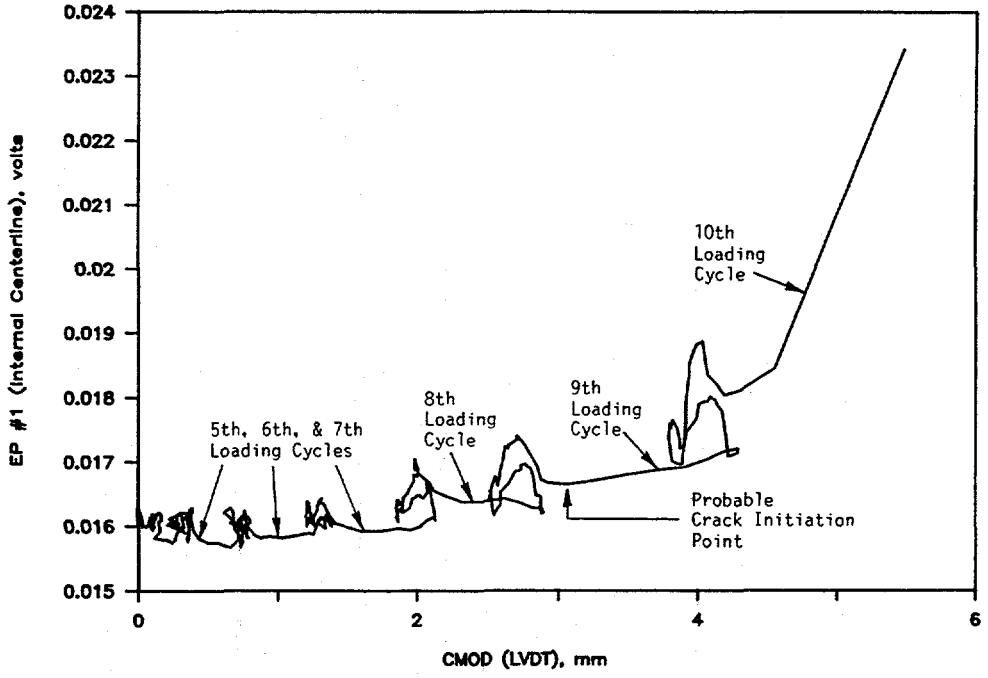

Figure E.7 Electric potential at the crack centerline (internal) versus crack-mouth-opening displacement for stainless steel base metal experiment DRB/1.3-3/F34

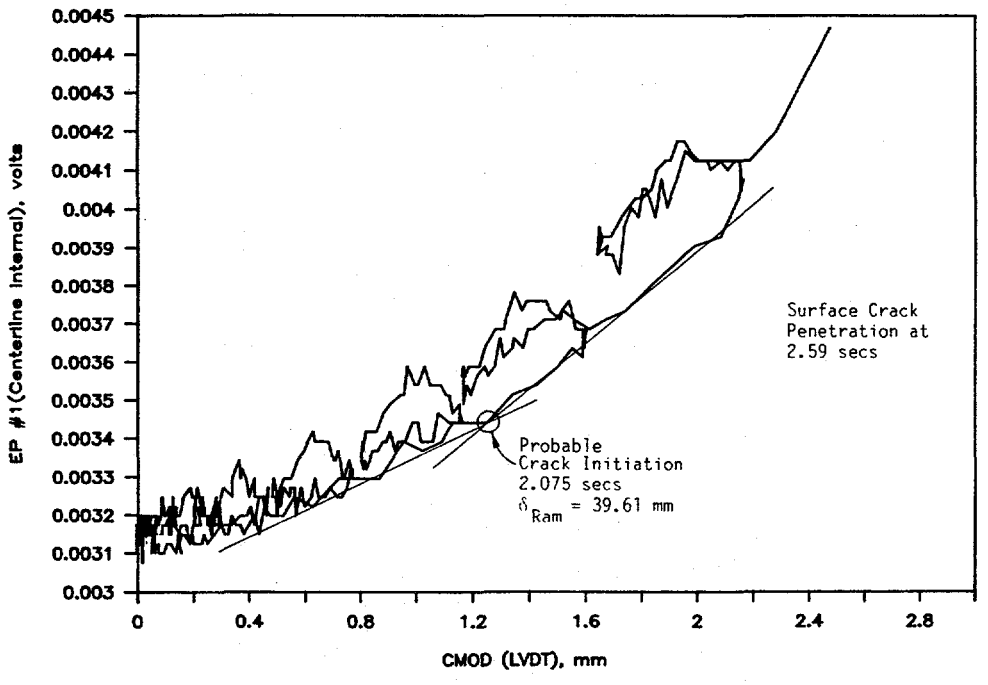

Figure E.8 Electric potential at the crack centerline (internal) versus crack-mouth-opening displacement for stainless steel weld experiment DRB/1.3-5/F33

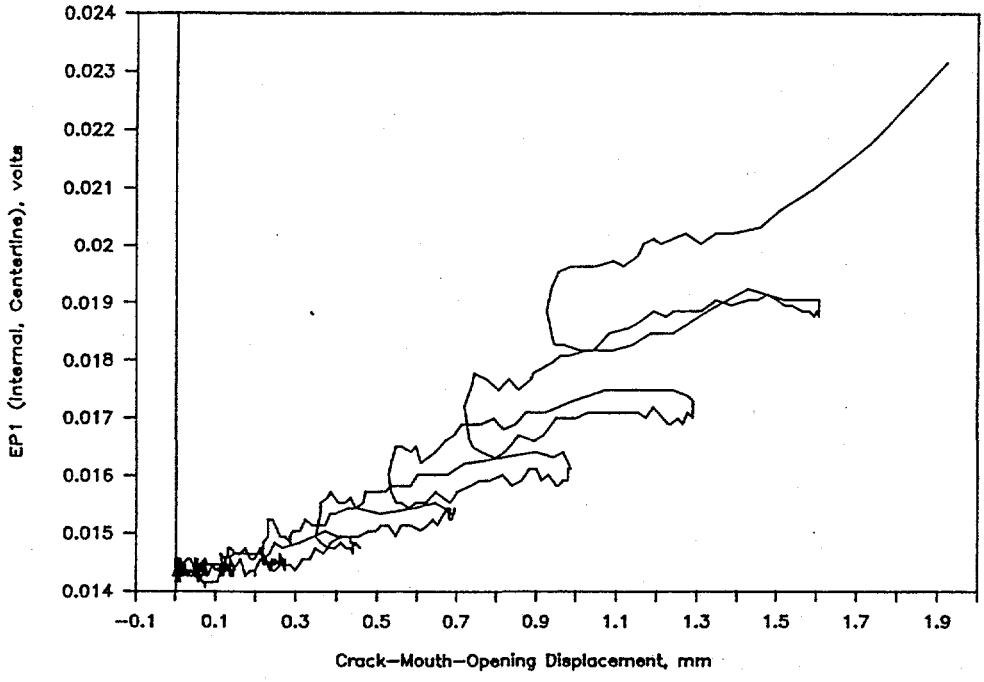

Figure E.9 Electric potential at the crack centerline (internal) versus crack-mouth-opening displacement for aged cast stainless experiment I1.3-10/90-FE9

Figure E.9 is a plot of the electric potential at the crack centerline on the inside surface as a function of crack-mouth-opening displacement for the aged cast stainless steel experiment. Figure E.10 isolates the last four cycles prior to surface crack penetration of Figure E.9. The arrows included on Figure E.10 were added to help differentiate the loading portion of the cycles from the unloadings. The large jumps in EP when the CMOD is not changing are speculated to be caused by compressive plasticity effects which occurred during the unloadings. Similar behavior was seen earlier for the stainless steel base metal experiment (see Figure E.7).

These large shifts in the EP data due to plasticity effects make it difficult to determine when the EP versus CMOD curve increases in slope. In order to overcome this problem, the EP data in Figure E.10 for the ninth, tenth, and eleventh cycles were shifted downward so that the EP data for succeeding cycles matches up with the EP data from the preceding cycle. In this way the shifts in EP data due to compressive plasticity were eliminated, see Figure E.11. In order to further clarify things, the EP data from Figure E.10 associated with the unloading portion of the cycles were also eliminated in Figure E.11. As a result of these actions, one sees a fairly distinct change in slope in the EP versus CMOD curve (indicative of crack initiation) for the aged cast stainless steel experimental data at a CMOD value of 1.23 mm (0.048 inch), see Figure E.11. The crack section moment at this instant in time was approximately 504 kN-m (4,460,000 in-lbs).

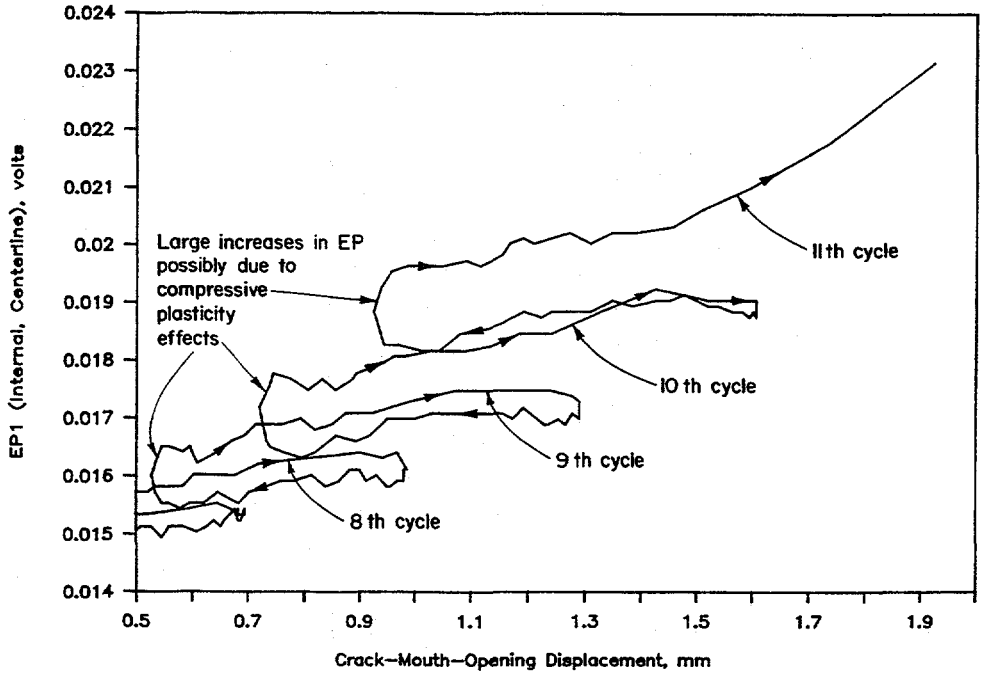

Figure E.10 Electric potential at the crack centerline (internal) versus crack-mouth-opening displacement for aged cast stainless experiment I1.3-10/90-FE10

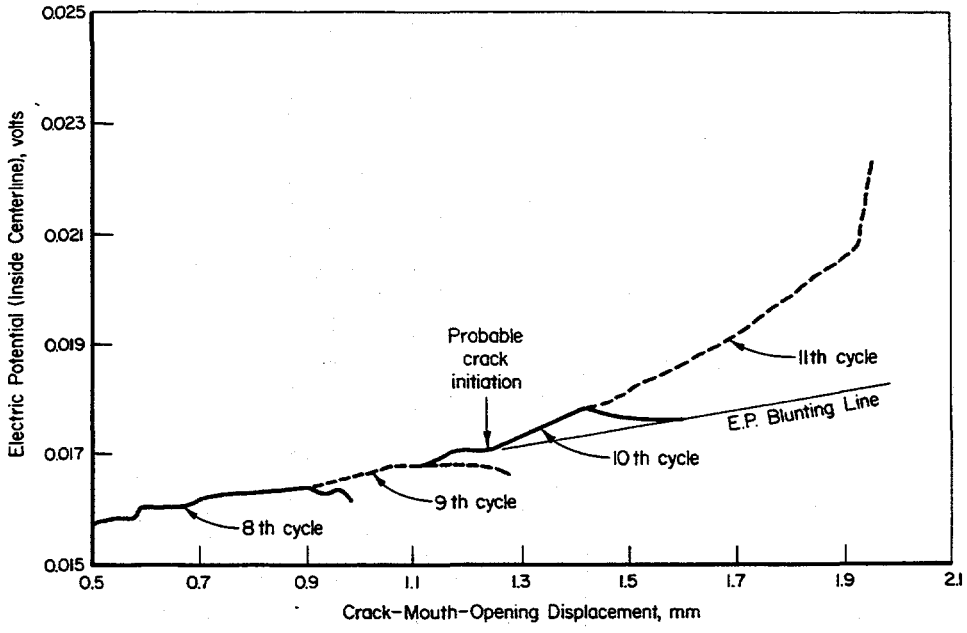

Figure E.11 Electric potential at the crack centerline (internal) with shifts in electric potential signal due to compressive plasticity removed versus crack-mouth-opening displacement for aged cast stainless experiment I1.3-10/90-FE11

Surface Crack Growth

In order to convert the electric-potential data after crack initiation, and prior to surface crack penetration, into surface crack growth data an appropriate calibration curve is needed. Typically, the electric potential calibration involves normalizing the electric-potential data across the crack to some normalizing parameter, usually either the base metal potential or the potential across the crack at some reference crack depth. The normalizing parameter accounts for differences in current densities between the calibration specimen and the test piece. The problem with normalizing the electric potential data to the base metal potential in this application is that the potential across the crack in the test piece is being heavily influenced by plasticity effects, while the base metal potential is not. Plasticity at the crack tip significantly increases the resistance of the material, making it seem as if one were dealing with two distinct materials. In order to deal with this problem, it was decided to use the potential across the crack at some reference crack depth as the normalizing parameter.

Figure E.12 is the surface crack depth calibration curve used through-out this program. The EP data used to generate Figure E.12 was developed using a 25-mm (1-inch) thick flat plate with machined notches of known depths. The reference crack depth is 58 percent of the pipe wall thickness. An exponential curve was fitted through the data in Figure E.12. The resulting expression is shown in Equation E-1.

$$d/t = 0.321 * \exp[(EP/EP_{0.58}) * 0.603] \qquad \text{(E-1)}$$

where,

d/t = the crack depth to wall thickness ratio
$EP/EP_{0.58}$ = the ratio of EP across the crack to the EP of the reference crack depth of 58 percent of the pipe wall thickness.

In order to use Figure E.12 or Equation E-1, one measures the depth of the initial surface crack post test. Next, one determines the ratio $EP/EP_{0.58}$ for that depth of surface crack using Figure E.12. Then one calculates the value for $EP_{0.58}$ using the previously determined ratio of $EP/EP_{0.58}$ and the value of EP across the crack at crack initiation determined using the procedures described previously in Figures E.7 through E.11. Once the value of $EP_{0.58}$ is established, the crack depth to wall thickness ratio is calculated at subsequent instances in time using the experimentally measured value of EP across the crack and Equation E-1. The surface crack depth, and thus the surface crack growth, are then established by multiplying the crack depth to wall thickness ratio by the pipe wall thickness. One further note of interest is that as part of these procedures, the original pipe wall thickness was used in establishing the surface crack depth and thus the surface crack growth values. This assumption introduced some degree of error in that the stainless steel specimens tend to neck down in the region of the remaining ligament such that procedures outlined above probably overpredict actual amount of surface crack growth. One other assumption that was imposed in establishing the amount of surface crack growth was that the effect of compressive plasticity on the EP signal was eliminated from the EP data. If a large jump in the EP signal was observed during one of the unloadings, the EP data was shifted downward so that the EP signal after the unloading matched up with the EP signal prior to the unloading, see Figures E.10 and E.11.

Figures E.13 through E.15 are plots of surface crack growth (Δa) as a function of time for the three stainless steel specimens. The flat regions of the curves are associated with the unloading portions of the loading history (i.e., that segment of the loading history where the applied moment and CMOD is either decreasing or increasing but at a value less than that obtained during the previous cycle).

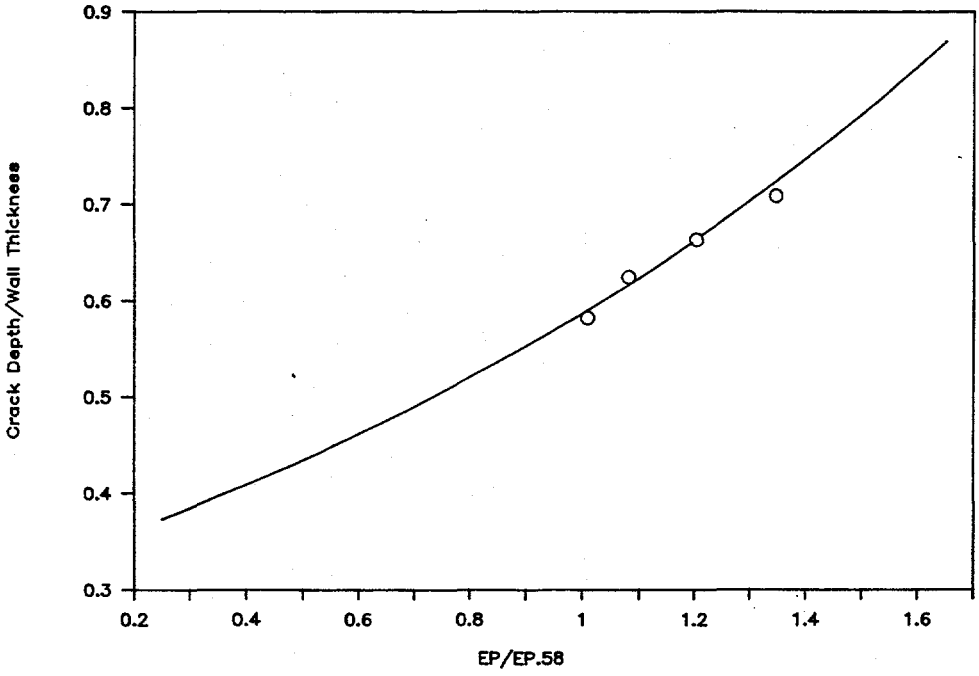

Figure E.12 Electric potential calibration curve for surface crack depths

I1.3-10/90-FE12

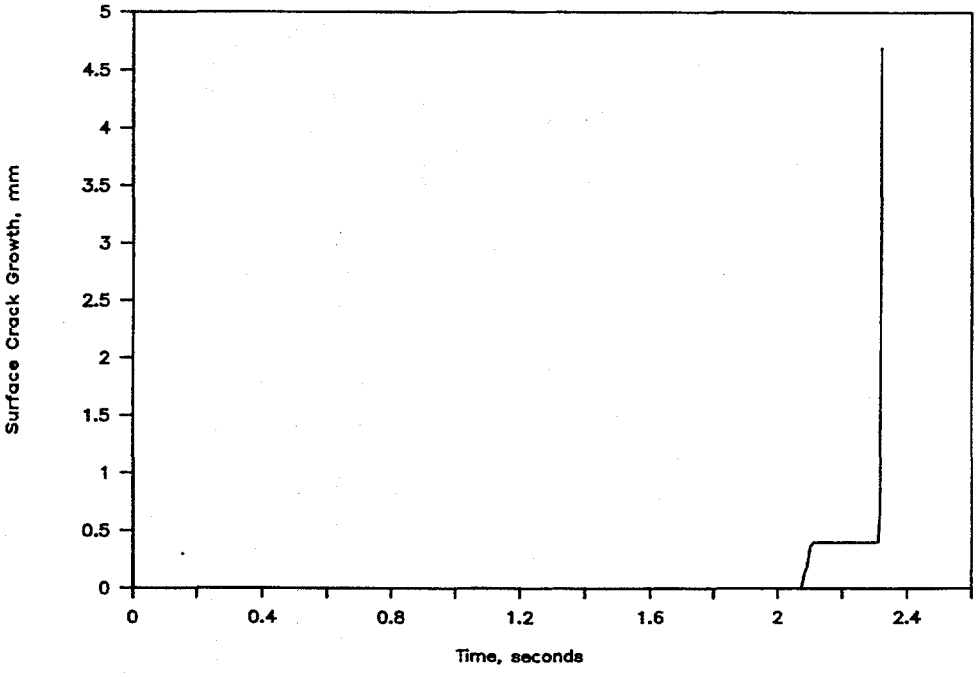

Figure E.13 Surface crack growth versus time for stainless steel base metal experiment

I1.3-10/90-F3.140

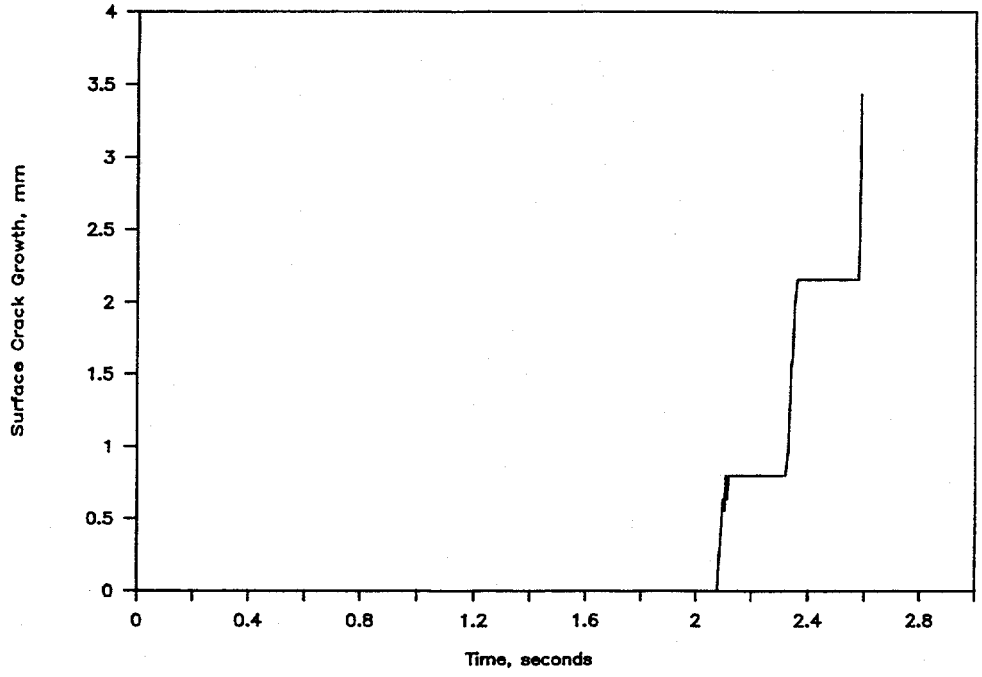

Figure E.14 Surface crack growth versus time for stainless steel weld experiment
I1.3-10/90-F3.141

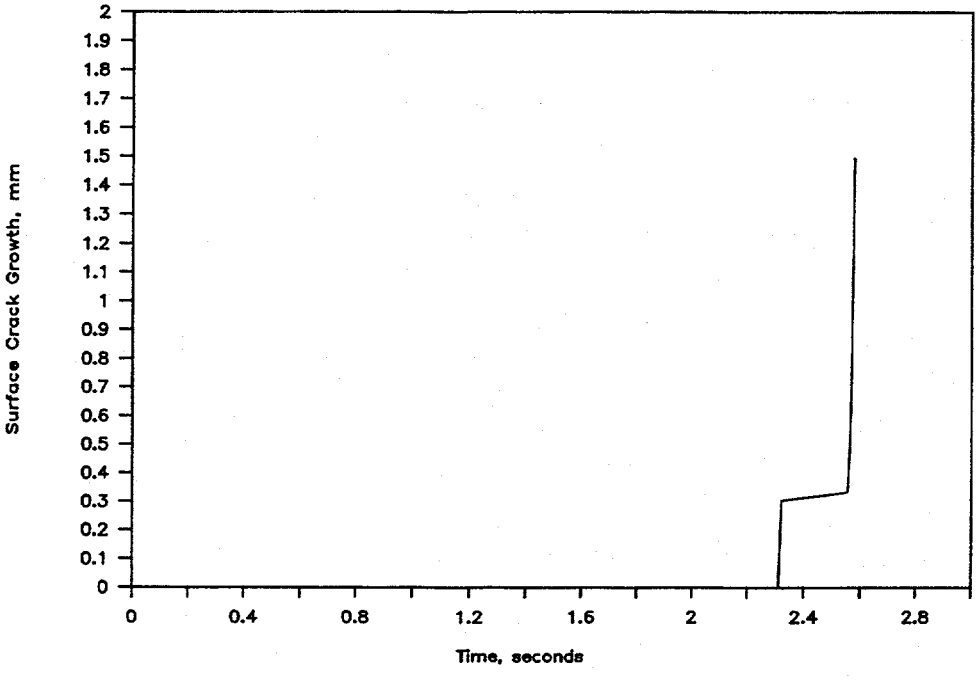

Figure E.15 Surface crack growth versus time for aged cast stainless experiment
I1.3-10/90-F3.142

Through-Wall Crack Growth

Figures E.16 and E.17 are plots of the electric potential at the crack centerline on the outside surface as a function of time for the stainless steel base metal experiment. The external EP data at the crack centerline are the data used to infer the extent of through-wall crack growth. No such data are presented for the two ferritic specimens for reasons previously discussed. No data are presented for the stainless steel weld experiment because the external EP data, after surface crack penetration, was of questionable quality. No data are presented for the aged cast stainless experiment because no EP-versus-crack-length calibration curve is known to exist for the current wire arrangement used for that experiment. Consequently, this discussion will focus on the data from the stainless steel base metal experiment.

Examination of Figure E.16 reveals that good EP data exist for three or four cycles after surface crack penetration. After three or four cycles the data become very noisy. Figure E.17 is a plot of the EP signal up to the instant when the data become noisy.

Because an existing d-c EP calibration curve exists for a circumferential through-wall cracked pipe for the case of a uniform current density, see Figure E.18, it was possible to convert the d-c EP data in Figure E.17 to through-wall crack length data. Figure E.19 is a plot of the through-wall crack length for the stainless steel base metal experiment as a function of time, based on the calibration curve shown in Figure E.18. During the unloadings, represented by sharp decreases in EP in Figure E.17, appropriate crack lengths were input into the data files to provide a smooth curve, i.e., to avoid apparent negative crack growth from cyclic unloadings.

Figure E.20 is a plot of the through-wall crack velocity at one crack tip as a function of time for the period immediately following surface crack penetration, i.e., the very steep portion of the curve in Figure E.19, at about 2.3 seconds. From Figure E.20 it can be seen that once the through-wall crack penetrates the pipe wall, the crack speed at one crack tip accelerates to approximately 20 meters/second (65 feet/second) in the first 10 milliseconds. It then slows to a nearly steady state fracture speed during the tearing phase of the fracture event beyond the time shown on the graph. The fracture speed during the subsequent cyclic growth of the simple through-wall crack was approximately 0.08 m/second (0.25 feet/second), significantly slower than the growth along the initially flawed region.

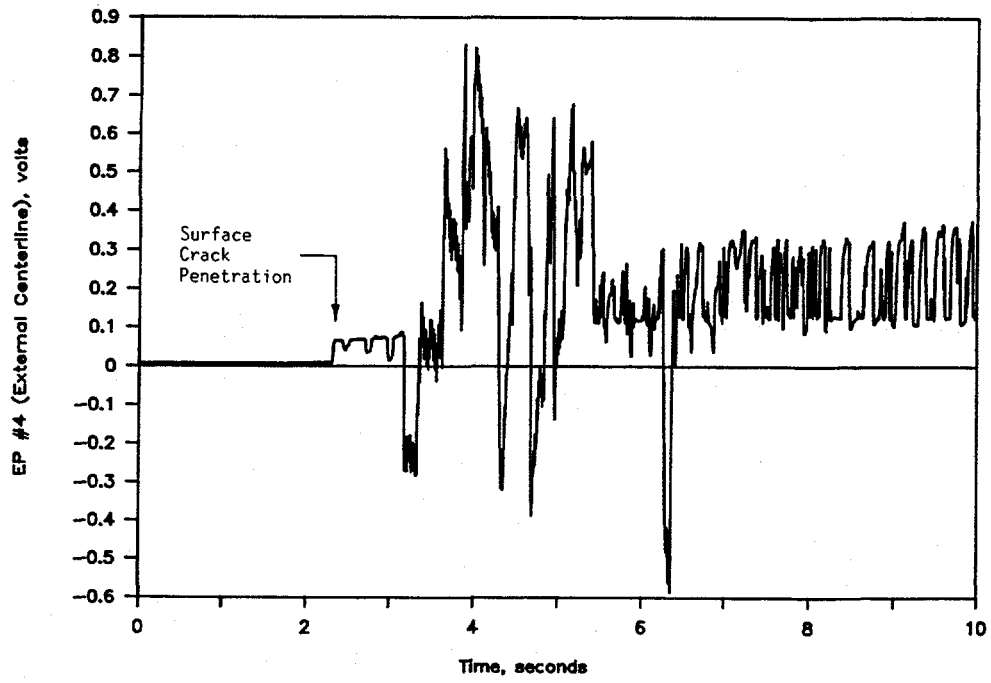

Figure E.16 Electric potential at the crack centerline (external) versus time for stainless steel base metal experiment DRB/1.3-3/F35

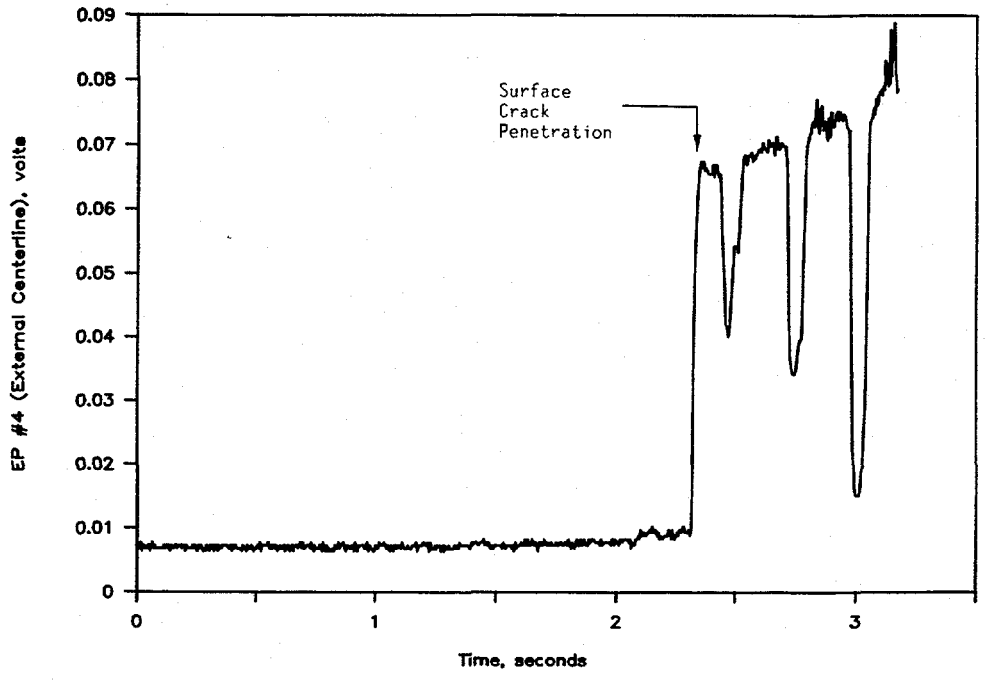

Figure E.17 Electric potential at the crack centerline (external) as a function of time for stainless steel base metal experiment DRB/1.3-3/F38

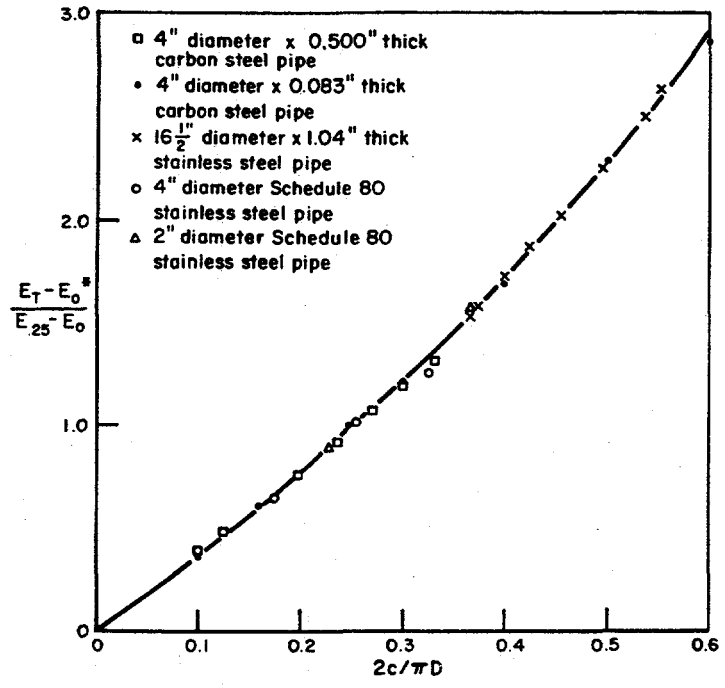

Figure E.18 Normalized d-c EP calibration for through-wall circumferential cracks in pipes (Current wires at least 3.25 diameters either side of crack plane, probe wires across center of crack.) E_T = total d-c EP, E_ϕ = d-c EP without crack, $E_{0.25}$ = d-c EP for crack 25 percent around circumference DRB/1.3-3/F39

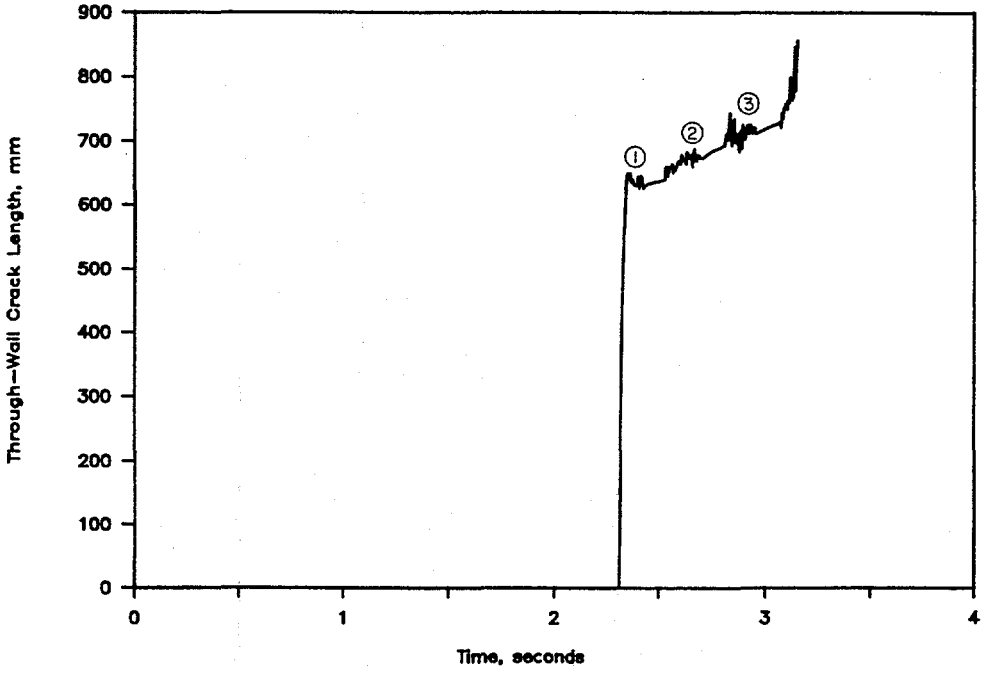

Figure E.19 Total through-wall crack length (2c) versus time for stainless steel base metal experiment DRB/1.3-3/F40

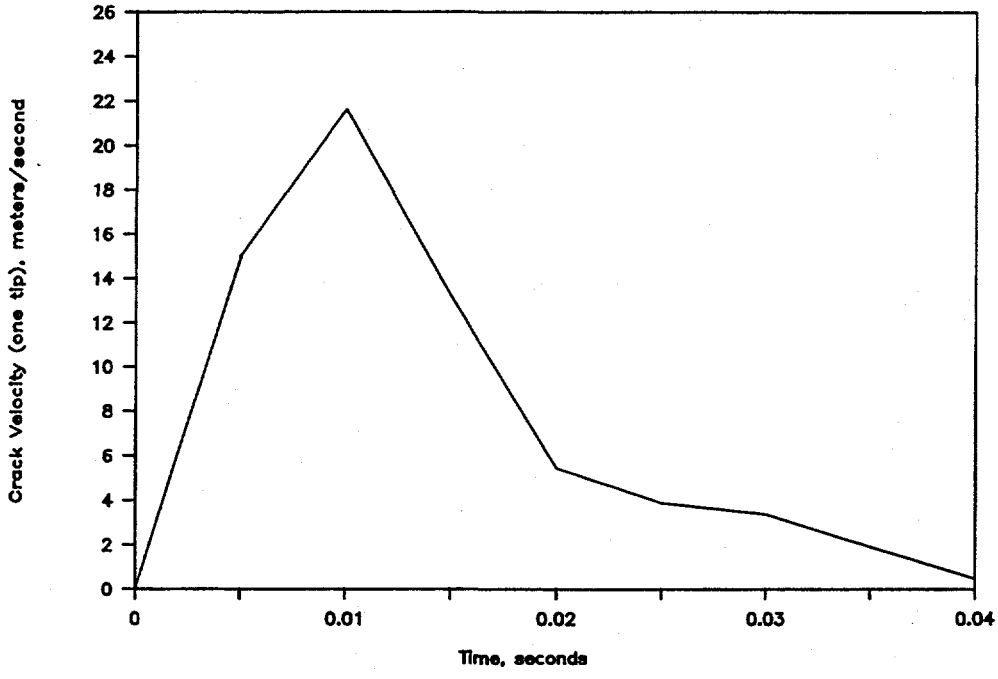

Figure E.20 Crack velocity (at one crack tip) as the crack is transitioning from a surface crack to a through-wall crack as a function of time from the instant of surface crack penetration for stainless steel base metal experiment DRB/1.3-3/F41

APPENDIX F

NET-SECTION-COLLAPSE ANALYSIS

APPENDIX F

NET-SECTION-COLLAPSE ANALYSIS

The Net-Section-Collapse concept for predicting the failure of a circumferentially cracked pipe was developed in EPRI Project RP585 (Ref. F.1). One major assumption in the Net-Section-Collapse analysis is that the material toughness is sufficiently high that failure is governed by the strength of the material (that is, flow stress or collapse stress) and is not sensitive to the material's toughness. Also, crack growth is not taken into account. The collapse stress is a value between the material's yield strength and ultimate strength and represents an average critical net-section stress reached throughout the flawed ligament of the structure (see Figure F.1).

For an unpressurized pipe with a circumferential through-wall crack subjected to pure bending, an idealized bending stress was assumed in the plane of the crack (as shown in Figure F.2). A free-body analysis shows that the point of stress inversion (β in Figure F.2) is

$$\beta \ \frac{\pi-\theta}{2} \qquad \text{(F-1)}$$

The bending moment predicted by the Net-Section-Collapse analysis can be determined by using Equation F-2:

$$M_{NSC} = 2\sigma_f R_m^2 t (2 \sin\beta - \sin\theta) \qquad \text{(F-2)}$$

where

M_{NSC} = Net-Section-Collapse analysis predicted bending moment
σ_f = flow stress or collapse stress
R_m = mean radius of the pipe
t = wall thickness of the pipe
θ = half the initial crack angle.

Equation F-2 was developed by integrating the forces around the pipe circumference and assuming the pipe retains a circular cross section.

From the bending moment in Equation F-2, one can calculate the bending stress (Mc/I) predicted by the Net-Section-Collapse analysis using Equation F-3,

$$\sigma_{nsc} = \frac{2}{\pi}\sigma_f (2 \sin\beta - \sin\theta) \qquad \text{(F-3)}$$

For an unpressurized pipe with a circumferential surface crack subjected to bending, that is, pure bending, an idealized bending stress was assumed in the plane of the crack as shown in Figure F.3. A free-body analysis shows that the point of stress inversion is

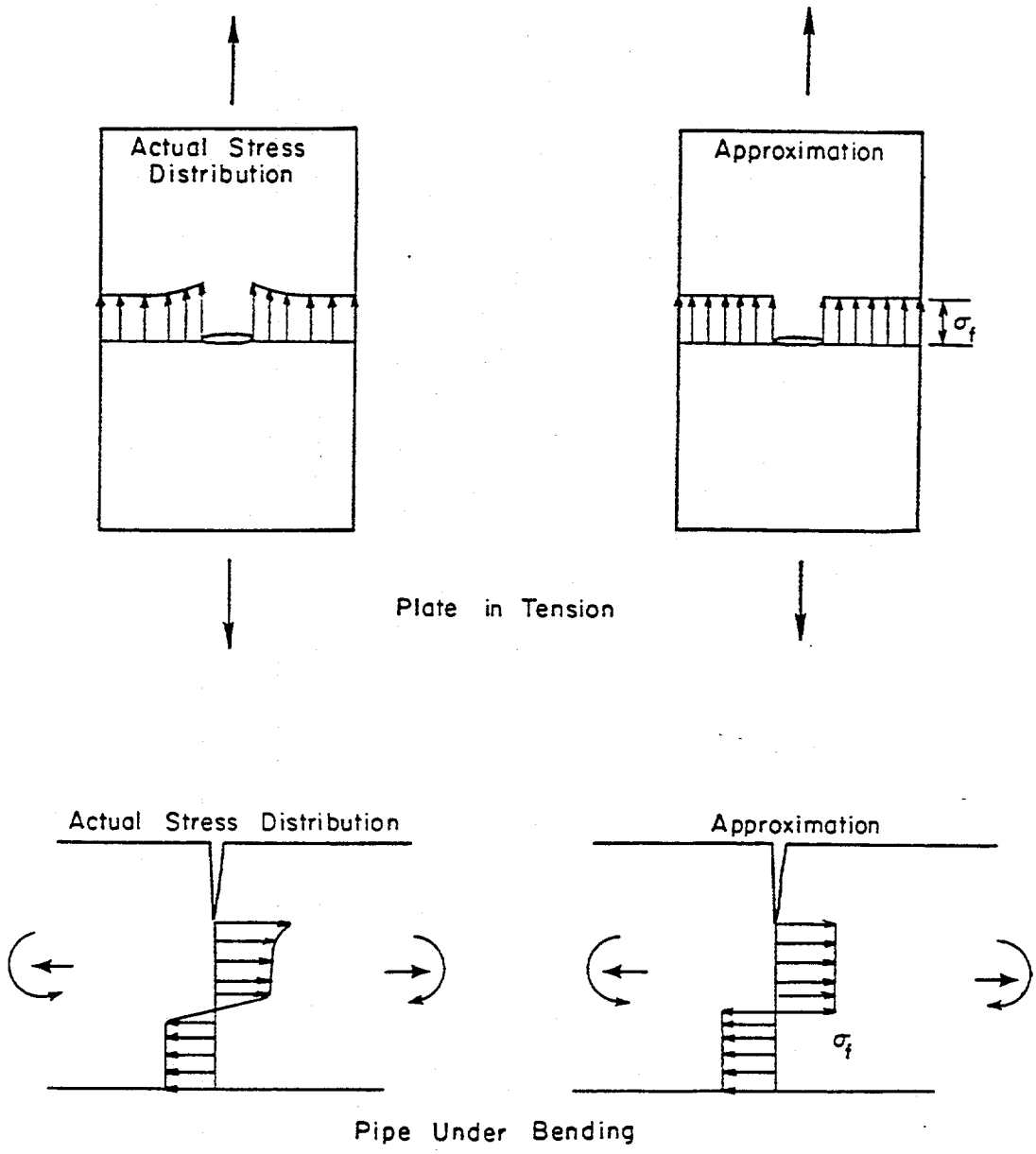

Figure F.1 Net-Section-Collapse criteria
T-4574-F2.1

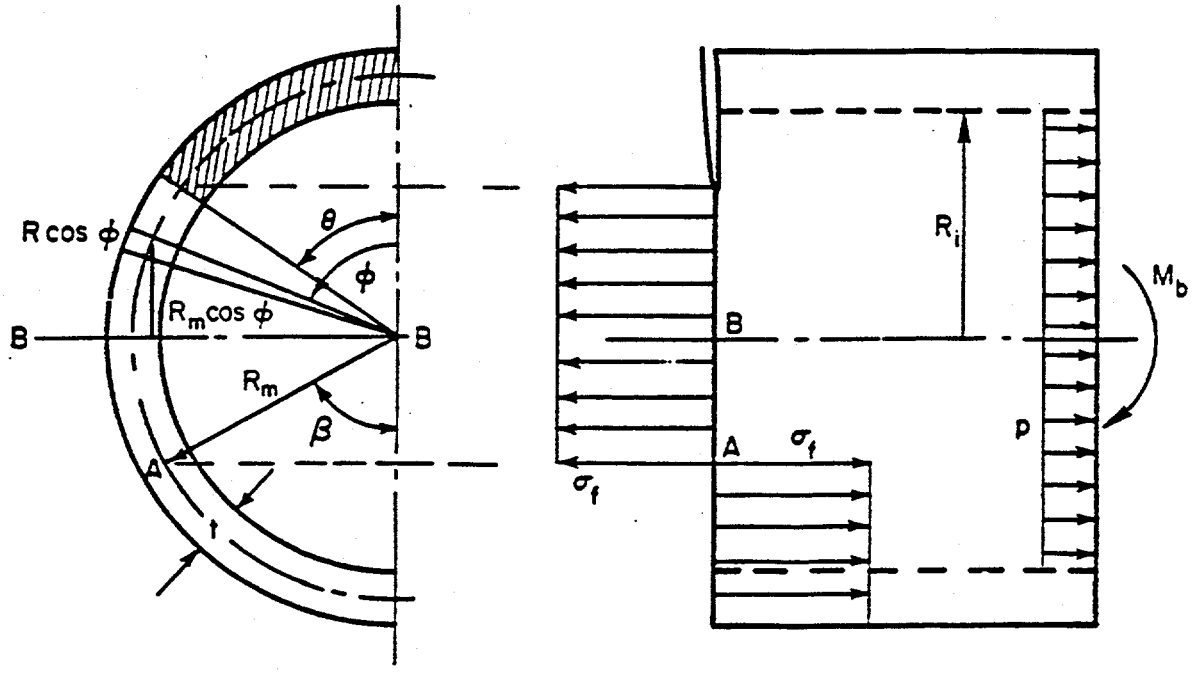

Figure F.2 Nomenclature and loading system for the application of the Net-Section-Collapse criterion to a pipe with a circumferential through-wall crack

T-4574-F2.2

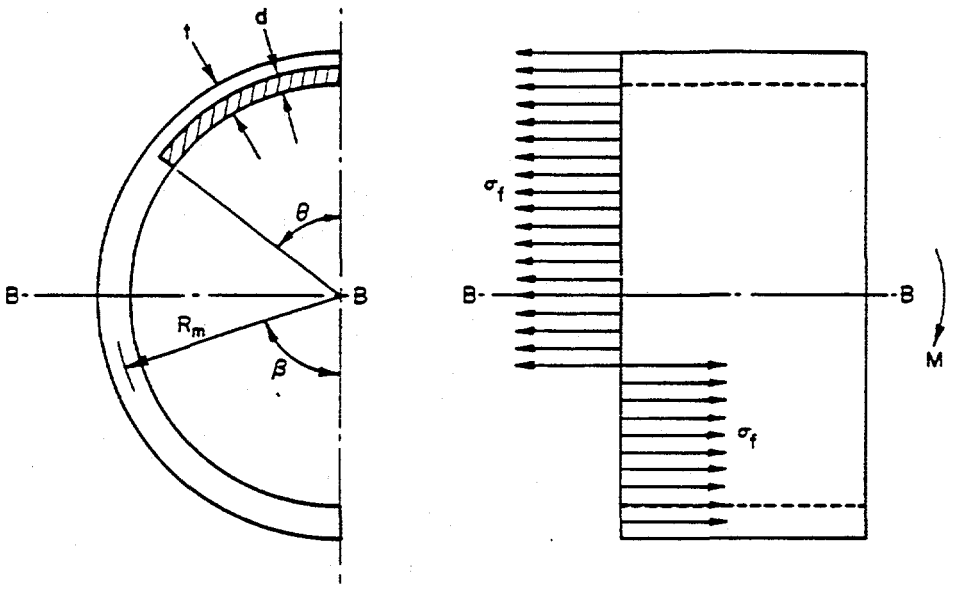

Figure F.3 Nomenclature and loading for the application of the Net-Section-Collapse criterion to a pipe with a circumferential surface crack subjected to pure bending SA-6/86-FA.3

$$\beta = \frac{\pi - (d/t)\theta}{2} \tag{F-4}$$

This assumes that the circumferential crack length, 2θ, is less than β; that is, the surface crack does not extend into the compressively stressed side of the pipe. The bending moment is then determined from Equation F-5.

$$M = 2\sigma_f R_m^2 t(2\ \sin\beta - (d/t)\sin\theta) \tag{F-5}$$

where

d = depth of the surface crack.

From the bending moment in Equation F-5 one can calculate the bending stress predicted by the Net-Section-Collapse analysis using Equation F-6,

$$\sigma_{nsc} = \frac{2}{\pi}\sigma_f\ (2\ \sin\beta - (d/t)\ \sin\theta) \tag{F-6}$$

For a pressurized pipe with a circumferential part-through surface crack subjected to bending, that is, combined pressure and bending, an idealized bending stress was assumed in the plane of the crack as shown in Figure F.4. A free-body analysis shows that the point of stress inversion in this case is

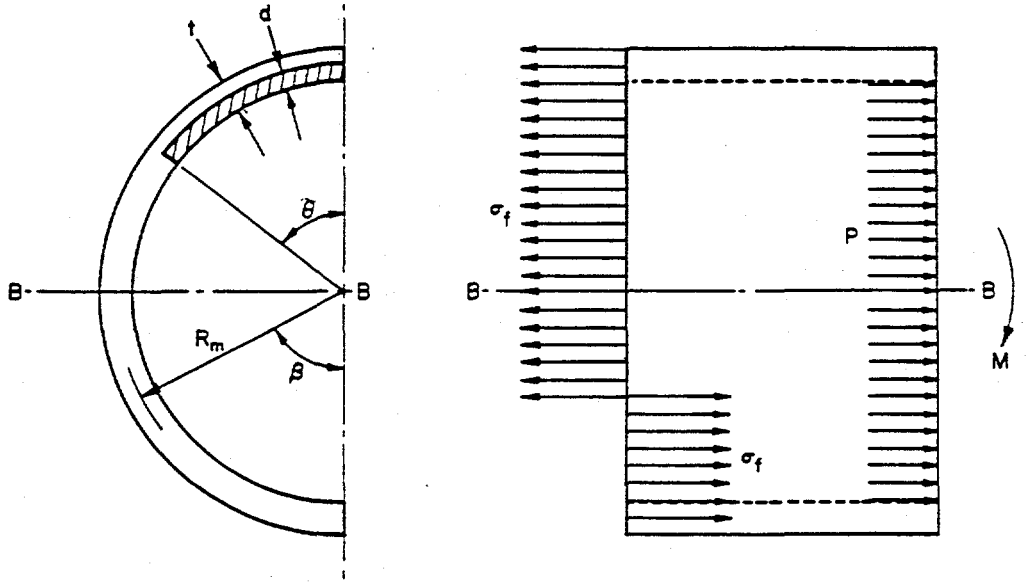

Figure F.4 Nomenclature and loading for the application of the Net-Section-Collapse criterion to a pipe with a circumferential surface crack subjected to combined pressure and bending SA-6/86-FA.4

$$\beta = \frac{\pi - (d/t)\theta}{2} - \frac{\pi R_i^2 p}{4 R_m t \sigma_f} \qquad \text{(F-7)}$$

where

R_i = inside radius of the pipe
p = internal pipe pressure.

Again this assumes that the circumferential crack length, 2θ, is less than β.

Knowing β, the predicted stress using the Net-Section-Collapse analysis can be calculated as above using Equation F-6. Thus, the only difference between surface crack Net-Section-Collapse formulations for the pure bending case and the combined pressure and bending case is in the determination of the stress inversion angle β. The pressure term shifts the neutral axis down away from the crack, thus lowering the predicted moment from the Net-Section-Collapse analysis.

For the case of a pipe section with a surface crack subjected only to pressure loads, that is, pure pressure, the formulation for Net-Section-Collapse stress can be developed by rearranging Equation F-5. Specifically for the case of pure pressure the applied bending moment is zero. For that to be the case Equation F-5 indicates that

$$2 \sin\beta = (d/t) \sin\theta \qquad \text{(F-8)}$$

Substituting Equation F-7 into Equation F-8 and solving for the axial stress, one finds that the predicted pure tension failure stress predicted by the Net-Section-Collapse analysis is

$$\sigma_{nsc} = \sigma_f \left[1 - \frac{\theta}{\pi} (d/t) - \frac{2}{\pi} \arcsin \left(\frac{d}{2t} \sin\theta \right) \right] \qquad \text{(F-9)}$$

References to Appendix F

F.1 Kanninen, M. F., Broek, D., Marschall, C. W.. Rybicki, E. F., Sampath, S. G., Simonen, F. B., and Wilkowski, G. M., "Mechanical Fracture Predictions for Sensitized Stainless Steel Piping with Circumferential Cracks," Final Report, EPRI NP-192, September 1976.

NRC FORM 335 (2-89) NRCM 1102, 3201, 3202

U.S. NUCLEAR REGULATORY COMMISSION

BIBLIOGRAPHIC DATA SHEET

(See instructions on the reverse)

1. REPORT NUMBER (Assigned by NRC, Add Vol., Supp., Rev., and Addendum Numbers, if any.)
NUREG/CR-6233, Vol. 3
BMI-2177

2. TITLE AND SUBTITLE
Crack Stability in a Representative Piping System Under Combined Inertial and Seismic/Dynamic Displacement-Controlled Stresses

Subtask 1.3 Final Report

3. DATE REPORT PUBLISHED
MONTH: June
YEAR: 1997

4. FIN OR GRANT NUMBER
B5702

5. AUTHOR(S)
P. Scott, R. Olson, G. Wilkowski, C. Marschall, and R. Schmidt

6. TYPE OF REPORT

7. PERIOD COVERED *(Inclusive Dates)*
7/10/86 - 7/9/91

8. PERFORMING ORGANIZATION – NAME AND ADDRESS *(If NRC, provide Division, Office or Region, U.S. Nuclear Regulatory Commission, and mailing address; if contractor, provide name and mailing address.)*
Battelle
505 King Avenue
Columbus, OH 43201

9. SPONSORING ORGANIZATION – NAME AND ADDRESS *(If NRC, type "Same as above"; if contractor, provide NRC Division, Office or Region, U.S. Nuclear Regulatory Commission, and mailing address.)*
Division of Engineering Technology
Office of Nuclear Regulatory Research
U. S. Nuclear Regulatory Commission
Washington, D. C. 20555-0001

10. SUPPLEMENTARY NOTES
M. Mayfield, NRC Project Manager

11. ABSTRACT *(200 words or less)*

This report presents the results from Subtask 1.3 of the International Piping Integrity Research Group (IPIRG) program. The objective of Subtask 1.3 is to develop data to assess analysis methodologies for characterizing the fracture behavior of circumferentially cracked pipe in a representative piping system under combined inertial and displacement-controlled stresses. A unique experimental facility was designed and constructed. The piping system evaluated is an expansion loop with over 30 meters of 16-inch diameter Schedule 100 pipe. The experimental facility is equipped with special hardware to ensure system boundary conditions could be appropriately modeled. The test matrix involved one uncracked and five cracked dynamic pipe-system experiments. The uncracked experiment was conducted to evaluate piping system damping and natural frequency characteristics. The cracked-pipe experiments evaluated the fracture behavior, pipe system response, and stability characteristics of five different materials. All cracked-pipe experiments were conducted at PWR conditions. Material characterization efforts provided tensile and fracture toughness properties of the different pipe materials at various strain rates and temperatures. Results from all pipe-system experiments and material characterization efforts are presented. Results of fracture mechanics analyses, dynamic finite element stress analyses, and stability analyses are presented and compared with experimental results.

12. KEY WORDS/DESCRIPTORS *(List words or phrases that will assist researchers in locating the report.)*
pipe system, surface crack, fracture mechanics, fracture toughness, elastic modulus, yield strength, ultimate strength, seismic, elbow, flaw evaluation, dynamic loading, cyclic loading, R6, ASME, carbon steel, stainless steel, submerged-arc weld, circumferential crack, J-integral, nuclear pipe, inertial stresses, displacement-controlled stresses

13. AVAILABILITY STATEMENT
Unlimited

14. SECURITY CLASSIFICATION
(This Page)
Unclassified
(This Report)
Unclassified

15. NUMBER OF PAGES

16. PRICE